A.B. Movchan (Ed.)

IUTAM Symposium on

Asymptotics, Singularities and Homogenisation in Problems of Mechanics

IUTAM

IUTAM Symposium on Asymptotics, Singularities and Homogenisation in Problems of Mechanics

SOLID MECHANICS AND ITS APPLICATIONS
Volume 113

Series Editor: G.M.L. GLADWELL
Department of Civil Engineering
University of Waterloo
Waterloo, Ontario, Canada N2L 3GI

Aims and Scope of the Series

The fundamental questions arising in mechanics are: *Why?, How?,* and *How much?*
The aim of this series is to provide lucid accounts written by authoritative researchers giving vision and insight in answering these questions on the subject of mechanics as it relates to solids.

The scope of the series covers the entire spectrum of solid mechanics. Thus it includes the foundation of mechanics; variational formulations; computational mechanics; statics, kinematics and dynamics of rigid and elastic bodies: vibrations of solids and structures; dynamical systems and chaos; the theories of elasticity, plasticity and viscoelasticity; composite materials; rods, beams, shells and membranes; structural control and stability; soils, rocks and geomechanics; fracture; tribology; experimental mechanics; biomechanics and machine design.

The median level of presentation is the first year graduate student. Some texts are monographs defining the current state of the field; others are accessible to final year undergraduates; but essentially the emphasis is on readability and clarity.

For a list of related mechanics titles, see final pages.

IUTAM Symposium on

Asymptotics, Singularities and Homogenisation in Problems of Mechanics

Proceedings of the IUTAM Symposium held in
Liverpool, United Kingdom, 8–11 July 2002

Edited by

A.B. MOVCHAN

University of Liverpool, United Kingdom

Created in the United States of America

Visit Springer's eBookstore at: http://www.ebooks.kluweronline.com
and the Springer Global Website Online at: http://www.springeronline.com

TABLE OF CONTENTS

PREFACE

This symposium was organised to provide cross-linking of research activities in the following areas of Applied Mathematics, Continuum Mechanics and Theoretical Physics:

- Perturbation problems for partial differential equations and their applications in mechanics;

- Homogenisation theory in models of composite structures;

- Fracture. Mathematical models of cracks in solids;

- Wave propagation, scattering;

- Models of photonic and phononic band gap composite materials;

- Models of dislocations in lattice structures;

- Asymptotic and numerical models of imperfect interfaces.

The topics covered in this volume represent the results of the recent work in wave propagation and scattering, asymptotics for eigenvalue problems, analysis of localised "defect modes", mathematical models of cracks and damage in solids, homogenisation approximations and models of composites, models of plates and shells, analysis of physical fields near non-smooth boundaries, modelling of gas and fluid flows, non-linear waves, models of combustion and advanced numerical methods. All the papers included in this volume have been carefully refereed. The Appendix, at the end of the volume, includes the complete programme of the meeting.

The International Scientific Committee responsible for the Symposium comprised of the following: Prof. A.B. Movchan (UK) - Chairman, Prof. I.D. Abrahams (UK), Prof. A. Aslanyan (Russia), Prof. D. Bigoni (Italy), Prof. H. Gao (Germany/USA), Prof. K.Z. Markov (Bulgaria), Prof. R.C. McPhedran (Australia), Prof. J. Salencon (France), Prof. W. Wendland (Germany).

On behalf of the Scientific Committee, I would like to acknowledge the financial support for the Symposium from

- International Union of Theoretical and Applied Mechanics,

- European Office of Aerospace Research and Developement, Air Force Office of Scientific Research, United States Air Force Research Laboratory,

- London Mathematical Society,

- Kluwer Academic Publishers,

- University of Liverpool.

I would like to thank my colleagues on the local Organising Committee, and members of the Scientific Committee, for their help and advice. The efficient running of the Symposium is due to the efforts of Dr Özgur Selsil and Mrs Alana Selsil, Mr Steven Platts, Mr Sirajul Haq, Mr Juan Bercial, Dr Sebastien Guenneau, Mr Julien Servant, Dr Natasha Movchan and Miss Nadya Movchan. Finally, I offer my special thanks to Mrs Joanna Seed for her invaluable contribution in organising and running the conference, as well as preparation of the volume of the conference proceedings.

Alexander Movchan

Chapter 1

Wave propagation and scattering

ASYMPTOTIC ANALYSIS OF HIGHER ORDER PERIPHERAL MODES IN ACOUSTIC WAVE SCATTERING BY AN ELASTIC CYLINDER OR SPHERE

J. Kaplunov[1], V. Kovalev[2] and M. Wilde[3]

[1] *Department of Mathematics, The University of Manchester,*
Oxford Road, Manchester M13 9PL, UK

kaplunov@ma.man.ac.uk

[2] *Department of Mathematics, Moscow State Academy of Device Building and Computer Science, Ul. Stromynka 20, GSP-6, Moscow 107846, Russia*

vlad_koval@mail.ru

[3] *Department of Mathematical Elasticity and Biomechanics,*
Saratov State University, Astrakhanskaya str. 83, Saratov, 410026,Russia

wildemv@mail.ru

Keywords: Asymptotic, scattering, Rayleigh, whispering gallery, elastic, cylinder, sphere.

Abstract   Higher order partial modes are studied in the case of harmonic scattering of plane acoustic waves by an elastic cylinder or sphere. Short-wavelength asymptotic models are developed for localized Rayleigh and whispering gallery peripheral waves and non-localized distortion peripheral waves. Approximate formulae are obtained including local estimations for resonant curves. An asymptotic classification is proposed for modal resonances. Comparison with exact solutions is presented.

INTRODUCTION

Evaluation of modal resonances of peripheral waves is the basic concept in the Resonance Scattering Theory investigating related contributions to the scattered field [5]. In this case asymptotic methods are of particular relevance because of very different features of peripheral waves associated with obstacle motions. They were mainly exploited for thin elastic shells (e.g. see [2]) characterized by a natural geometric parameter. Shell peripheral waves are similar to Lamb waves propagating in a flat layer.

This paper deals with acoustic wave scattering by an elastic cylinder or sphere. Peripheral waves involve now a generalization of flat Rayleigh waves and whispering gallery waves known originally for acoustic wave guides [1]. It is essential that the latter are characteristic only of curved bodies.

Below we establish asymptotic models oriented to short-wavelength vibrations of elastic bodies. An acoustic medium is treated on the basis of the Helmholtz equation defined over an infinite domain. Sometimes we also assume that acoustic impedance is small compared with elastic one.

The asymptotic models are utilized for deriving approximate formulae for higher order modal resonance components. All of these correspond to a rigid background. Elementary estimations for resonance frequencies, amplitudes and widths are also presented. The efficiency of the proposed formulae is demonstrated by comparison with computed exact solutions in the case of a plane harmonic incident wave.

The asymptotic models and formulae are especially useful for classifying higher order modal resonances of peripheral waves. These include Rayleigh resonances, dilatation and distortion whispering gallery resonances and resonances of non-localized distortion waves.

The developed methodology is not restricted only to bodies of canonical shapes allowing efficient numerical testing. More complicated geometries just require adapting traditional short-wavelength expansions for incident and scattered waves.

1.   STATEMENT OF THE PROBLEM

Consider harmonic acoustic wave scattering by a circular elastic cylinder or sphere. The problem involves the following dimensionless parameters

$$\gamma = \frac{c_2}{c_1}, \quad \kappa = \frac{\rho}{\rho_1}, \quad \varepsilon = \rho c / \rho_1 c_2 \tag{1.1}$$

$$k = \frac{\omega}{c}, \quad x = ka, \quad \beta_i = \frac{c_i}{c}, \quad x_i = \beta_i^{-1} x, \quad (i = 1, 2),$$

where c_1 and c_2 are dilatation and distortion wave speeds in solid, ρ_1 is solid density, c and ρ are sound speed and fluid density, respectively, a is cylinder or sphere radius, ω is circular frequency.

In the two-dimensional case the boundary conditions on the contact surface $r = a$ become

$$u_r|_{r=a} = \frac{1}{\rho c^2 k^2} \left. \frac{\partial (p_i + p_s)}{\partial r} \right|_{r=a},$$

$$\sigma_r|_{r=a} = -(p_i + p_s)|_{r=a}, \quad \sigma_{r\theta}|_{r=a} = 0, \tag{1.2}$$

where r and θ denote cylindrical or spherical co-ordinates, p_i is incident pressure, p_s is scattered pressure, u_r is radial solid displacement, σ_r and $\sigma_{r\theta}$ are radial and circumferential stresses in solid. The latter satisfy the Helmholtz equation for fluid motion and the elasticity equations (see e.g. [5]). In addition, the scattered pressure p_s should obey the radiation condition at infinity.

In cylindrical co-ordinates a plane acoustic wave may be expressed as

$$p_i = p_0 \sum_{n=0}^{\infty} E_n(-i)^n J_n(kr) \cos n\theta, \qquad (1.3)$$

where $E_0 = 1$, $E_n = 2$ $(n \geq 1)$, J_n is cylindrical Bessel function of first kind, p_0 is constant. Then we accept for the scattered pressure

$$p_s = p_0 \sum_{n=0}^{\infty} E_n(-i)^n B_n H_n^{(1)}(kr) \cos n\theta, \qquad (1.4)$$

where B_n are sought for coefficients, $H_n^{(1)}$ is Hankel function of first kind.

In this paper we concentrate on modal resonance components ζ_n (see [5] for more detail) in the case of backscattering $(\theta = 0)$. For an acoustically rigid background these take the form

$$\zeta_n = \frac{4}{\sqrt{\pi x}} \left| B_n + \frac{J_n'(x)}{H_n^{(1)'}(x)} \right|. \qquad (1.5)$$

Our main concern is a short-wavelength analysis assuming that

$$n \gg 1, \ x_1 \sim x_2 \sim x \sim n. \qquad (1.6)$$

For a sphere the formula (1.5) should be rewritten as

$$\zeta_n = \frac{4n_1}{x} \left| B_n + \frac{j_n'(x)}{h_n^{(1)'}(x)} \right|, \qquad (1.7)$$

where $n_1 = n + 1/2$, j_n and $h_n^{(1)}$ denote associated spherical functions.

2.   RAYLEIGH RESONANCES

Rayleigh modal resonances occur at $x < n\beta_2$ for a cylinder or at $x < n_1\beta_2$ for a sphere. For large n they may be analysed starting from the following equations written in terms of the Lame potentials φ and ψ

$$\Delta_{\mathrm{p}}\varphi + \beta_1^{-2}k^2\varphi = 0, \quad \Delta_{\mathrm{p}}\psi + \beta_2^{-2}k^2\psi = 0 \qquad (2.1)$$

with the "plane" Laplace operator

$$\Delta \mathrm{p} = \frac{\partial^2}{\partial r^2} + \frac{\partial^2}{\partial \theta^2}. \tag{2.2}$$

The displacements and stresses in the contact conditions (1.2) become

$$u_r = \frac{\partial \varphi}{\partial r} + \frac{\partial \psi}{\partial \theta}, \qquad \sigma_r = \rho_1 c^2 \left[-k^2 \varphi + 2\beta_2^2 \left(\frac{\partial^2 \psi}{\partial r \, \partial \theta} - \frac{\partial^2 \varphi}{\partial \theta^2} \right) \right],$$

$$\sigma_{r\theta} = \rho_1 c^2 \left[k^2 \psi + 2\beta_2^2 \left(\frac{\partial^2 \varphi}{\partial r \, \partial \theta} + \frac{\partial^2 \psi}{\partial \theta^2} \right) \right]. \tag{2.3}$$

The equations (2.1)–(2.3) coincide with those for plane strain presented in Cartesian co-ordinates. They are oriented to investigation of short-wavelength vibrations localized near cylindrical or spherical surfaces. The proposed model is derived by keeping only highest order derivatives in the original equations of linear elasticity for a circular cylinder or sphere (e.g. see [5]). In addition, the radial co-ordinate is fixed on the contact surface.

The coefficients B_n in the formulae (1.5) and (1.7) may be easily found from the equations (1.2) and (2.1)–(2.3) by substituting the series (1.3) and (1.4) or their analogues for spherical co-ordinates. The result is

$$B_n = -\frac{S f_n(x) - R f_n'(x)}{S g_n(x) - R g_n'(x)} \tag{2.4}$$

with

$$S = \kappa \beta_2^{-4} x^3 \alpha_1, \quad R = \left(2N^2 - \beta_2^{-2} x^2 \right)^2 - 4N^2 \alpha_1 \alpha_2,$$

$$\alpha_i = \sqrt{N^2 - \beta_i^{-2} x^2} \ (i = 1, 2), \tag{2.5}$$

where $f_n = J_n$, $g_n = H_n^{(1)}$ and $N = n$ for a cylinder and $f_n = j_n$, $g_n = h_n^{(1)}$ and $N = n_1$ for a sphere.

A further analysis [3] shows that for small relative impedances ε (see the formula (1.1)) resonance frequencies correspond to zeroes of the Rayleigh denominator R. It also reveals a linear dependence of the resonance width on its number.

In Fig. 1 modal resonance components computed by the formula (1.5) with the coefficients B_n defined by the formula (2.4) are compared with the relevant exact solution [5] for a cylinder. The exact solution is plotted by the thick line, while the thin one corresponds to the proposed approximation. The problem parameters are

$$c_1 = 6420 \text{ m/s}, \ c_2 = 3040 \text{ m/s}, \ c = 1493 \text{ m/s},$$

$$\rho = 1000 \text{ kg/m}^3, \ \rho_1 = 2700 \text{ kg/m}^3. \tag{2.6}$$
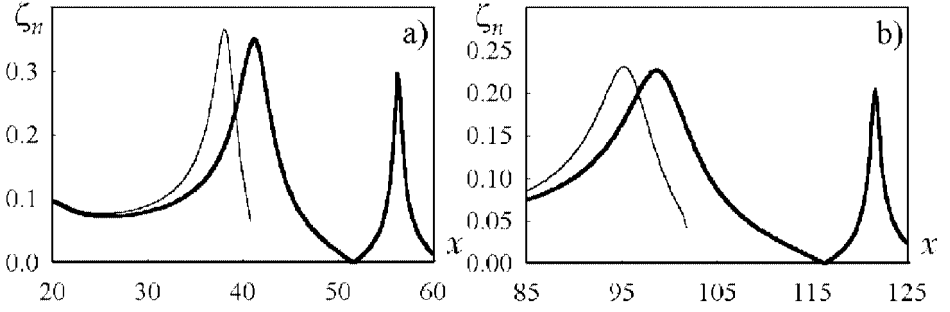
Figure 1   Comparison for domain $x < n\beta_2$ ($n = 20$ (a) and $n = 50$ (b)).

3.   WHISPERING GALLERY RESONANCES

For a cylinder we expand the Lame potentials as infinite series generated by the formula (1.3). For the partial potentials φ_n and ψ_n we obtain

$$\frac{d^2\varphi_n}{d\zeta^2} - \frac{1}{1-\zeta}\frac{d\varphi_n}{d\zeta} - \frac{n^2\varphi_n}{(1-\zeta)^2} + x_1^2\varphi_n = 0,$$

$$\frac{d^2\psi_n}{d\zeta^2} - \frac{1}{1-\zeta}\frac{d\psi_n}{d\zeta} - \frac{n^2\psi_n}{(1-\zeta)^2} + x_2^2\psi_n = 0 \tag{3.1}$$

with $\zeta = 1 - r/a$.

It is well known [1], that acoustic whispering gallery waves are localized within a narrow surface zone of thickness $O\left(x^{-2/3}\right)$. For elastic whispering gallery waves a similar behaviour takes place at

$$x = n\beta_2 + O\left(x_2^{1/3}\right) \tag{3.2}$$

for the distortion potential ψ_n and at

$$x = n\beta_1 + O\left(x_1^{1/3}\right) \tag{3.3}$$

for the dilatation potential φ_n.

In the case of the domain (3.2) we have in the leading order

$$\frac{d^2\psi_n}{dz^2} - 2\left(x_2^{-1/3}(n - x_2) + z\right)\psi_n = 0 \tag{3.4}$$

with $z = x_2^{2/3}\zeta$.

The solution of the equation (3.4), decaying as $\zeta \to \infty$, is

$$\psi_n(\zeta) = C_{2n}\mathrm{Ai}\left[(x_2/2)^{-1/3}\left(n - x_2(1 - \zeta)\right)\right], \tag{3.5}$$

where Ai denotes Airy function.

The leading order equation for the potential φ_n becomes

$$\frac{d^2\varphi_n}{d\zeta^2} - \alpha_1^2\varphi_n = 0, \quad \alpha_1 = \sqrt{n^2 - x_1^2}. \tag{3.6}$$

By taking into account asymptotic identities

$$\frac{d\varphi_n}{d\zeta} \sim x_2\varphi_n, \quad \frac{d\psi_n}{d\zeta} \sim x_2^{2/3}\psi_n$$

we get for displacements and stresses

$$u_{r,n} = \frac{1}{a}\left(-\frac{d\varphi_n}{d\zeta} + \frac{n}{1-\zeta}\psi_n\right),$$

$$\sigma_{r,n} = \frac{\rho_1 c^2 \beta_2^2}{a^2}\left[-x_2^2\varphi_n + 2\left(\frac{n^2\varphi_n}{(1-\zeta)^2} - \frac{n}{1-\zeta}\frac{d\psi_n}{d\zeta}\right)\right],$$

$$\sigma_{r\theta,n} = \frac{\rho_1 c^2 \beta_2^2}{a^2}\left[x_2^2\psi_n + 2\left(\frac{n}{1-\zeta}\frac{d\varphi_n}{d\zeta} - \frac{n^2\psi_n}{(1-\zeta)^2}\right)\right]. \tag{3.7}$$

The developed short-wavelength model describes vibrations of a cylinder over the domain (3.2). Straightforward transformations yield

$$\zeta_n = \frac{8}{(\pi x)^{3/2}}\frac{\frac{1}{x}D_2^{(2)}}{\left|D_1^{(2)} - \frac{1}{x}D_2^{(2)}\frac{H_n^{(1)}(x)}{H_n^{(1)'}(x)}\right|\left|H_n^{(1)'}(x)\right|^2}, \tag{3.8}$$

where

$$D_1^{(2)} = \frac{\left(2n^2 - x_2^2\right)^2}{\alpha_1} + 4n^2 x_2 \frac{\text{Ai}'(\tau_2)}{\text{Ai}(\tau_2)}\left(\frac{x_2}{2}\right)^{-1/3},$$

$$D_2^{(2)} = \kappa x_2^4, \quad \tau_2 = (n - x_2)\left(\frac{x_2}{2}\right)^{-1/3}. \tag{3.9}$$

Inspection of the formula (3.8) shows that in the case of small relative impedances whispering gallery modal resonances correspond to zeros of the function $D_1^{(2)}(x)$. It is clear that the function $D_1^{(2)}$ may vanish only provided that τ_2 belongs to the region $\tau_m + O\left(x_2^{-1/3}\right)$, where τ_m ($m = 1, 2, \ldots$) are zeros of the Airy function. Thus, the equation $D_1^{(2)} = 0$ defines the resonance frequencies $x_{n,m}$ occurring near the roots $x_{n,m}^0$ of the equation

$$x_2 = n - \tau_m(x/2)^{1/3}. \tag{3.10}$$

Its roots may be estimated as $x_{n,m}^0 = \beta_2\left(n - \tau_m(n/2)^{1/3}\right)$.

Let us obtain local approximations in the vicinities of the resonance frequencies $x_{n,m}$. By utilizing the asymptotic formula for Hankel functions as $n \to \infty$ for $x > n$ we have [4]

$$\zeta_{n,m} = A_{n,m} \frac{\Gamma_{n,m}}{|x - x_{n,m} + i\Gamma_{n,m}|}, \qquad (3.11)$$

where the amplitudes $A_{n,m}$ and the widths $\Gamma_{n,m}$ are given by

$$A_{n,m} = \frac{4}{\sqrt{\pi x_{n,m}}}, \quad \Gamma_{n,m} = \frac{\kappa x_{n,m}^3 \left(x_{n,m}^2 - n^2\right)^{-1/2}}{\beta_2^2 p_2(x_{n,m})}$$

$$p_2(x) = 4n^2 \left[\left(\frac{\text{Ai}'(\tau_2)}{\text{Ai}(\tau_2)}\right)^2 - \tau_2 \right] \left(\frac{x_2}{2}\right)^{-2/3}. \qquad (3.12)$$

The local formula (3.11) is valid for $x - x_{n,m} \ll \beta_2$ under the condition $\Gamma_{n,m} \ll \beta_2$. Numerical results are presented in Fig.2 for the problem parameters (2.6). The exact solution is shown by the solid line while the dash and dash-dotted ones correspond to the formulae (3.8) and (3.11), respectively.
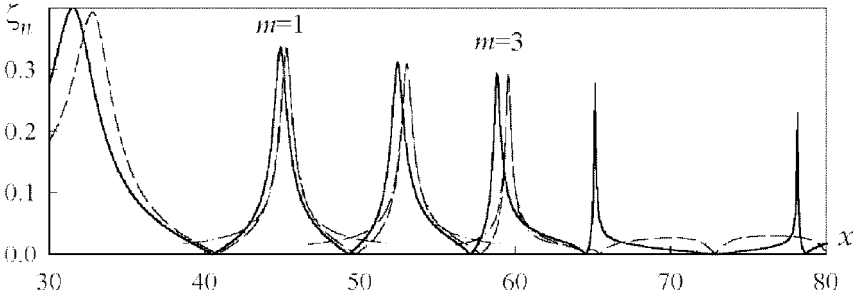
Figure 2   Comparison for domain $n\beta_2 < x < n\beta_1$ $(n = 15)$.

For the domain (3.3) an approximate equation for the dilatation potential φ_n is established similarly to that for the distortion potential ψ_n in the previous case. In terms of the variable $z = x_1^{2/3} \zeta$ it becomes

$$\frac{d^2 \varphi_n}{dz^2} - 2 \left(x_1^{-1/3}(n - x_1) + z\right) \varphi_n = 0 \qquad (3.13)$$

The potential ψ_n demonstrates now an oscillating behavior. By applying the WKB method and taking into account turning points we get [4]

$$\psi_n(\zeta) = C_n \left[\left(\frac{d\eta}{d\zeta}\right)(1 - \zeta) \right]^{-1/2} \text{Ai}(\eta), \qquad (3.14)$$

where

$$\eta(\zeta) = \left[\frac{3}{2}\int_{\zeta_0}^{\zeta}(-\mu^2)^{1/2}d\zeta\right]^{2/3}, \quad \mu(\zeta) = \sqrt{x_2^2 - \frac{n^2}{(1-\zeta)^2}}. \tag{3.15}$$

Here the turning point is defined by the formula $\zeta_0 = 1 - n/x_2$.

By making use the asymptotic behavior of the Airy function at infinity [4] we transform the solution (3.14) to

$$\psi_n(\zeta) = C_n\left(\frac{\alpha_2}{\overline{\zeta}\mu(\zeta)}\right)^{1/2}\cos\left[\overline{\zeta}\mu(\zeta) - n\arccos\left(\frac{nx_2^{-1}}{\overline{\zeta}}\right) - \frac{\pi}{4}\right], \tag{3.16}$$

where $\alpha_2 = \mu(0) = \sqrt{x_2^2 - n^2}$, $\overline{\zeta} = 1 - \zeta$.

Finally we have for modal resonance components

$$\zeta_n = \frac{8}{(\pi x)^{3/2}}\frac{\frac{1}{x}D_2^{(1)}}{\left|D_1^{(1)} - \frac{1}{x}D_2^{(1)}\frac{H_n^{(1)}(x)}{H_n^{(1)'}(x)}\right|\left|H_n^{(1)'}(x)\right|^2}, \tag{3.17}$$

where

$$D_1^{(1)} = -\frac{(x_2^2 - 2n^2)^2}{x_1}\frac{\text{Ai}(\tau_1)}{\text{Ai}'(\tau_1)}\left(\frac{x_1}{2}\right)^{1/3} + 4n^2\alpha_2\frac{\sin\chi}{\cos\chi},$$

$$D_2^{(2)} = \kappa x_2^4, \quad \tau_1 = (n - x_1)\left(\frac{x_1}{2}\right)^{-1/3},$$

$$\chi = \sqrt{x_2^2 - n^2} - n\arccos\left(\frac{n}{x_2}\right) - \frac{\pi}{4}. \tag{3.18}$$

For small relative impedances the equation $D_1^{(1)} = 0$ determines two resonance families. The first family is similar to what has been done before. The sought for estimate becomes $x_{n,m}^0 = \beta_1\left(n - \tau_m(n/2)^{1/3}\right)$.

For the second family we have Ai ~ 1. In this case the quantity $D_1^{(1)}$ may turn to zero under the condition $\cos\chi \ll 1$. Thus, in the case of the second family we observe non-localised peripheral waves associated with the distortion potential ψ_n.

Let $x_{n,m}^1$ be roots of the equation $x_1 = n - \tau_m'(x/2)^{1/3}$ (τ_m' are zeros of the Airy function derivative). We label then roots of the equation $D_1^{(1)} = 0$ as $x_{n,m,k}$, where $k = \overline{0,K}$ is root number within the interval $x_{n,m}^1 \leq x < x_{n,m+1}^1$ ($K \sim n^{1/3}$); in doing so, we use the indexes $m = 1$, $k = -1, -2, \ldots$ for roots beyond $x_{n,1}^1$.

Local approximation in the vicinities of the resonance frequencies $x_{n,m,k}$ can be written in the form of (3.11) with the triple index n, m, n. We have

$$A_{n,m,k} = \frac{4}{\sqrt{\pi x_{n,m,k}}}, \quad \Gamma_{n,m,k} = \frac{\kappa\beta_1}{p_1(x_{n,m,k})\sqrt{\beta_1^2 - 1}},$$

$$p_1(x) = \left(1 - 2\gamma^2\right)^2 \left[1 - \tau_1 \left(\frac{\mathrm{Ai}(\tau_1)}{\mathrm{Ai}'(\tau_1)}\right)^2\right] + 4\gamma^2 \left(1 - \gamma^2\right) \frac{1}{\cos^2 \chi}. \quad (3.19)$$

Numerical results are demonstrated in Fig. 3. All the notations and problem parameters are the same as above.
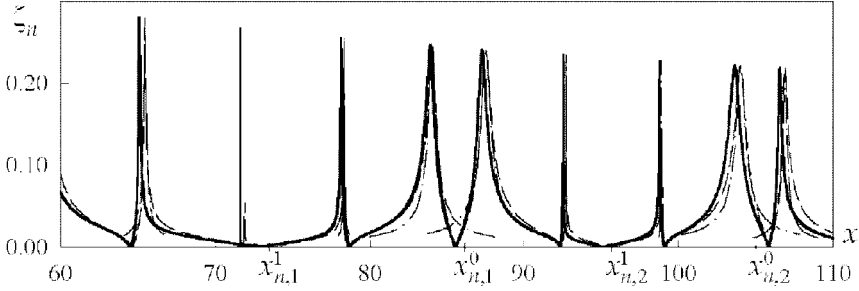
Figure 3   Comparison for domain $x > n\beta_1$ ($n = 15$).

The formula for p_1 indicates important features of modal resonances. In particular, if the frequency $x_{n,m,k}$ is close to a zero of the function $\mathrm{Ai}(\tau_1)$, i.e. close to $x_{n,m}^0$, then $p_1(x_{n,m,k}) \sim 1$. In this case the resonance width $\Gamma_{n,m,k}$ is of the same order as for the domain (3.2). For the resonance frequency $x_{n,m,k}$ occurring near a zero of the function $\cos \chi$ we have $p_1(x_{n,m,k}) \gg 1$. Therefore, the resonance width considerably decreases. Sharp spikes are associated with closely located zeroes of the functions $\cos \chi$ and $\mathrm{Ai}'(\tau_1)$.

For a sphere the formulae for resonance components and local approximations may be derived from those for a cylinder by substituting spherical Bessel functions instead of cylindrical ones, n_1 instead of n, $4n_1/x^3$ instead of $8/(\pi x)^{3/2}$ and introducing the amplitudes $4n_1/x_{n,m}$ and $4n_1/x_{n,m,k}$.

4.   CONCLUDING REMARKS

The paper is aimed to generalize the asymptotic methodology elaborated for thin elastic shells to the case of thick bodies. Peripheral waves, typical for the latter, are investigated in great detail. In particular, it is established that whispering gallery resonances may be separated into dilatation and distortion ones. The former interact with resonances of non-localised distortion waves. In contrast to Rayleigh resonances, the width of whispering gallery resonances as well as that of resonances associated with non-localised waves demonstrate a weak dependence on mode number. It might be expected that the proposed treatment is not restricted only to a circular cylinder or sphere. For more general geometries, short-wavelength

solutions of the Helmgoltz equation may be utilized [1] that generalize, in a sense, asymptotic expansions of Bessel functions.

Acknowledgments

References

[1] Babich, V M and V.S.Buldyrev, V S (1991) *Short-wavelength diffraction theory. Asymptotic methods.* Berlin: Springer-Verlag.

[2] Kaplunov, J D, Kossovich, L Yu and Nolde, E V (1998) *Dynamics of thin walled elastic bodies.* San Diego: Academic Press.

[3] Kaplunov, J D and Kovalev, V A (2000) *Approximation of the resonances of the Rayleigh wave in scattering of acoustic waves by elastic circular cylinders and spheres*, Izv. Ross. Akad. Nauk. Mekhanika Tverdogo Tela, **35**(4), 180-186 (Engl.transl.: Mechanics of Solids).

[4] Olver, F W J (1974) *Introduction to asymptotic and special functions.* NY: Academic Press.

[5] Veksler, N D (1993) *Resonance acoustic spectroscopy.* Berlin: Springer-Verlag.

EMBEDDING FORMULAS AND SINGULARITIES IN ACOUSTIC SCATTERING

C. M. Linton

Department of Mathematical Sciences

Loughborough University

Loughborough LE11 3TU, UK

C.M.Linton@lboro.ac.uk

Abstract   The solution to the scattering problem for a plane wave incident from an arbitrary angle on an arbitrary configuration of N parallel strips is shown to be related to $2N$ separate scattering problems for the same geometry, but with different boundary conditions. The number of separate problems that are required is shown to be determined by the number of singularities in the velocity field which in turn is given by the number of strip edges.

1.   INTRODUCTION

In [1] it was noted that the solution to the two-dimensional problem of scattering of a plane wave by a finite slit in an infinite, thin screen for arbitrary incident wave angle could be written in terms of the solution to the problem in which the incident wave is parallel to the screen. Such a relationship is an example of an embedding formula. It has been shown [2] that embedding formulas can be derived for the case of N slits; in this case the result for an arbitrary angle of incidence is determined from the solution to $2N$ separate problems (the reason this reduces to 1 in the case of a single slit is due to symmetry).

These problems are related to problems in which the slits and screen are interchanged (this is an example of Babinet's principle). Thus embedding formulas are easily derived for a finite number of collinear strips. Here we show that similar formulas can be derived when the strips are parallel, but not necessarily collinear; a situation which does not correspond directly to

any slit problem. However, the existence of embedding formulas for the case of N slits distributed over a number of parallel screens has recently been reported in [3].

The approach used in [2], [3] is extremely general and involves formulating the problem as an integral equation depending on a parameter (the incident wave angle) and then utilizing the specific structure of the kernel to generate relationships between solutions to the equations for different values of that parameter. Here we take a slightly different tack, one which is more problem specific but which sheds further light on the nature of embedding formulas. Integral equations again form the starting point, but rather than just relating solutions to these equations for different parameter values, we also relate the solutions to the singularities in the velocity field at the strip ends and in the process explain why the solution to a problem involving N strips/slits for any incident wave angle depends on precisely $2N$ separate problems.

2.   FORMULATION

We consider an array L consisting of N parallel strips:

$$L = \bigcup_{n=1}^{N} L_n, \qquad L_n = \{\mathbf{x} : a_n < x < b_n,\, y = \eta_n\},$$

where $\mathbf{x} = (x, y)$. A plane wave making an angle β with the x-axis is of the form $\mathrm{Re}\{f_\beta(\mathbf{x}) \exp(-\mathrm{i}\omega t)\}$, where

$$f_\beta(\mathbf{x}) = \mathrm{e}^{-\mathrm{i}k(x\cos\beta + y\sin\beta)}.$$

If Neumann boundary conditions are imposed on the strips, the total scattered field will be characterized by $f_\beta + \varphi_\beta$, where

$$(\nabla^2 + k^2)\varphi_\beta = 0 \qquad\qquad \mathbf{x} \in \mathbb{R}^2 \backslash L, \qquad\qquad (2.1)$$

$$\frac{\partial \varphi_\beta}{\partial y} = \mathrm{i}k\sin\beta\, f_\beta \qquad \mathbf{x} \in L, \qquad\qquad (2.2)$$

whereas if the boundary conditions are of Dirichlet type we have $f_\beta + \psi_\beta$, where ψ_β again satisfies the Helmholtz equation and

$$\psi_\beta = -f_\beta \qquad \mathbf{x} \in L.$$

The potentials φ_β and ψ_β also satisfy outgoing radiation conditions

$$\lim_{r\to\infty} r^{1/2}\left(\frac{\partial}{\partial r} - \mathrm{i}k\right)\varphi_\beta = 0, \qquad \lim_{r\to\infty} r^{1/2}\left(\frac{\partial}{\partial r} - \mathrm{i}k\right)\psi_\beta = 0,$$

where $r = \sqrt{x^2 + y^2}$, and conditions at the edges of the strips ($\nabla\psi_\beta$ and $\nabla\varphi_\beta$ have square root singularities at (a_m, η_m), (b_m, η_m), $m = 1, \ldots N$) which ensure regularity of the potentials throughout the fluid domain. These boundary-value problems possess unique solutions.

We will also consider N further (non-physical) problems with boundary conditions

$$\psi_\beta^{(n)} = -f_\beta^{(n)} \qquad \mathbf{x} \in L, \qquad n = 1, \ldots, N,$$

where

$$f_\beta^{(n)}(\mathbf{x}) = \begin{cases} f_\beta(\mathbf{x}) & \mathbf{x} \in L_n, \\ 0 & \mathbf{x} \in L\backslash L_n. \end{cases}$$

Note that $\psi_\beta = \sum_{n=1}^N \psi_\beta^{(n)}$.

It can be shown that the solutions φ_β, ψ_β, and $\psi_\beta^{(n)}$ are related. Consider the function

$$\varphi_\beta = \frac{\mathrm{i}}{k\sin\beta}\left(\frac{\partial\psi_\beta}{\partial y} + \sum_{n=1}^N \left[A_{0,\beta}^{(n)}\frac{\partial\psi_0^{(n)}}{\partial y} + A_{\pi,\beta}^{(n)}\frac{\partial\psi_\pi^{(n)}}{\partial y}\right]\right) \qquad \beta \neq 0, \pi.$$

(2.3)

By construction φ_β satisfies (2.1), (2.2) and the radiation condition, but will in general be singular at the edges of the strips. The constants $A_{0,\beta}^{(n)}$, $A_{\pi,\beta}^{(n)}$ are to be chosen so that φ_β is bounded at (a_n, η_n), (b_n, η_n), $n = 1, \ldots N$. The number of unknown constants is the same as the number of strip edges and this provides the reason why the embedding formulas given below require the solution of $2N$ separate problems.

All the above problems can easily be formulated as integral equations. If we define

$$\mathbf{x}' = (\xi, \eta), \quad R = |\mathbf{x} - \mathbf{x}'|,$$

then the problem for φ_β can be written as an integral equation for the unknown jump in the potential across each barrier. For numerical computations one would probably formulate the problem as a hypersingular integral equation, but for our purposes we use the fact that all the barriers are parallel to the x-axis to write the integral equation in the form

$$\left(\frac{\partial^2}{\partial x^2} + k^2\right)\int_L p_\beta(\mathbf{x}')H_0^{(1)}(kR)\,\mathrm{d}\xi = 2k\sin\beta\, f_\beta(\mathbf{x}), \quad \mathbf{x} \in L, \qquad (2.4)$$

where

$$p_\beta(x, \eta_n) \equiv \tfrac{1}{2}(\varphi_\beta(x, \eta_n^+) - \varphi_\beta(x, \eta_n^-)).$$

Note that $p_\beta(a_n, \eta_n) = p_\beta(b_n, \eta_n) = 0$. Once p_β has been determined, the solution is given everywhere in the fluid by

$$\varphi_\beta(\mathbf{x}) = -\frac{\mathrm{i}}{2}\frac{\partial}{\partial y}\int_L p_\beta(\mathbf{x}')H_0^{(1)}(kR)\,\mathrm{d}\xi. \qquad (2.5)$$

For ψ_β and $\psi_\beta^{(n)}$ we have

$$\int_L v_\beta(\mathbf{x}')H_0^{(1)}(kR)\,\mathrm{d}\xi = -2\mathrm{i}f_\beta(\mathbf{x}), \quad \mathbf{x} \in L, \qquad (2.6)$$

where

$$v_\beta(x, \eta_n) \equiv \tfrac{1}{2}(\partial\psi_\beta/\partial y|_{y=\eta_n^+} - \partial\psi_\beta/\partial y|_{y=\eta_n^-}),$$

and

$$\int_L v_\beta^{(n)}(\mathbf{x}')H_0^{(1)}(kR)\,\mathrm{d}\xi = -2\mathrm{i}f_\beta^{(n)}(\mathbf{x}), \qquad \mathbf{x} \in L, \qquad (2.7)$$

where

$$v_\beta^{(n)}(x, \eta_n) \equiv \tfrac{1}{2}(\partial\psi_\beta^{(n)}/\partial y|_{y=\eta_n^+} - \partial\psi_\beta^{(n)}/\partial y|_{y=\eta_n^-}),$$

and the solution to the Dirichlet problem is given in terms of v_β by

$$\psi_\beta(\mathbf{x}) = -\frac{\mathrm{i}}{2}\int_L v_\beta(\mathbf{x}')H_0^{(1)}(kR)\,\mathrm{d}\xi.$$

As $kr \to \infty$ ($x = r\cos\theta$, $y = r\sin\theta$), we have

$$\psi_\beta \sim \frac{\mathrm{e}^{\mathrm{i}(kr-3\pi/4)}}{(2\pi kr)^{1/2}}G_{\theta,\beta}, \qquad \varphi_\beta \sim \frac{\mathrm{e}^{\mathrm{i}(kr-3\pi/4)}}{(2\pi kr)^{1/2}}F_{\theta,\beta},$$

where the diffraction coefficients $G_{\theta,\beta}$ and $F_{\theta,\beta}$ are given by

$$G_{\theta,\beta} = \int_L f_\theta v_\beta, \qquad F_{\theta,\beta} = \mathrm{i}k\sin\theta\int_L f_\theta p_\beta. \qquad (2.8)$$

It follows from (2.4) and (2.6) that $G_{\theta,\beta} = G_{\beta,\theta}$ and $F_{\theta,\beta} = F_{\beta,\theta}$.

The particular form of the integral equation (2.4) is used because it can be written

$$\left(\frac{\partial}{\partial x} \pm \mathrm{i}k\right)\left(\frac{\partial}{\partial x} \mp \mathrm{i}k\right)\int_L p_\beta(\mathbf{x}')H_0^{(1)}(kR)\,\mathrm{d}\xi = 2k\sin\beta\, f_\beta(\mathbf{x}),$$

$$\mathbf{x} \in L,$$

from which, using integration by parts,

$$\left(\frac{\partial}{\partial x} \pm \mathrm{i}k\right)\int_L \left(\frac{\partial p_\beta}{\partial\xi}(\mathbf{x}') \mp \mathrm{i}k p_\beta(\mathbf{x}')\right)H_0^{(1)}(kR)\,\mathrm{d}\xi = 2k\sin\beta\, f_\beta(\mathbf{x}),$$

$$\mathbf{x} \in L.$$

Now we solve this pair of first-order ODEs, each defined on N intervals. For convenience, we use subscripts $+$ and $-$ as alternatives to π and 0, respectively, since then $(\partial/\partial x \pm ik)f_{\mp}(\mathbf{x}) = 0$. We obtain

$$\int_L \left(\frac{\partial p_\beta}{\partial \xi}(\mathbf{x}') \mp ik p_\beta(\mathbf{x}') \right) H_0^{(1)}(kR) \, d\xi$$

$$= \frac{2i \sin \beta}{\cos \beta \mp 1} \left(f_\beta(\mathbf{x}) + \sum_{n=1}^N c_{\mp,\beta}^{(n)} f_{\mp}^{(n)}(\mathbf{x}) \right), \qquad \mathbf{x} \in L, \quad (2.9)$$

in which $c_{\mp,\beta}^{(n)}$ are $2N$ constants of integration.

It then follows from (2.6) and (2.7) that

$$\frac{\partial p_\beta}{\partial x} \mp ik p_\beta = \frac{-\sin \beta}{\cos \beta \mp 1} \left(v_\beta + \sum_{n=1}^N c_{\mp,\beta}^{(n)} v_{\mp}^{(n)} \right), \qquad \mathbf{x} \in L, \qquad (2.10)$$

and hence (multiply by $f_{\mp}^{(m)}(\mathbf{x})$ and integrate over L)

$$G_{\mp,\beta}^{(m)} + \sum_{n=1}^N c_{\mp,\beta}^{(n)} G_{\mp,\mp}^{(m,n)} = 0, \qquad m = 1,\ldots,N, \qquad (2.11)$$

where

$$G_{\theta,\beta}^{(m,n)} = \int_L f_\theta^{(m)} v_\beta^{(n)} \, d\xi = G_{\beta,\theta}^{(n,m)}, \qquad (2.12)$$

and

$$G_{\theta,\beta}^{(m)} = \int_L f_\theta^{(m)} v_\beta \, d\xi = \int_L f_\beta v_\theta^{(m)} \, d\xi = \sum_{n=1}^N G_{\beta,\theta}^{(n,m)} = \sum_{n=1}^N G_{\theta,\beta}^{(m,n)}.$$

Equation (2.11) represents two $N \times N$ systems of equations for the constants $c_{\mp,\beta}^{(n)}$. Note that because of the symmetry properties of the diffraction coefficients, knowledge of $v_{\pm}^{(n)}$ is sufficient to be able to compute these constants. We note that

$$\sum_{m=1}^N \sum_{n=1}^N G_{\theta,\beta}^{(m,n)} = \sum_{m=1}^N G_{\theta,\beta}^{(m)} = G_{\theta,\beta}.$$

The constants $A_{\pm,\beta}^{(n)}$ defined in (2.3) and $c_{\mp,\beta}^{(n)}$ defined in (2.9) are related. Using (2.3), (2.6) and (2.7) we have, for $\mathbf{x} \in L$,

$$\int_L p_\beta(\mathbf{x}') H_0^{(1)}(kR) \, \mathrm{d}\xi$$

$$= \frac{2}{k \sin \beta} \left(f_\beta(\mathbf{x}) + \sum_{n=1}^{N} \left[A_{0,\beta}^{(n)} f_0^{(n)}(\mathbf{x}) + A_{\pi,\beta}^{(n)} f_\pi^{(n)}(\mathbf{x}) \right] \right). \quad (2.13)$$

If we differentiate with respect to x, use integration by parts, and then use (2.10) we can show that

$$A_{\pm,\beta}^{(n)} = \tfrac{1}{2}(1 \mp \cos \beta) c_{\pm,\beta}^{(n)}. \quad (2.14)$$

We also get (multiply (2.13) by $v_\theta(\mathbf{x})$ and integrate over L)

$$F_{\theta,\beta} = -\frac{\sin \theta}{\sin \beta} \left(G_{\beta,\theta} + \sum_{n=1}^{N} \left[A_{0,\beta}^{(n)} G_{0,\theta}^{(n)} + A_{\pi,\beta}^{(n)} G_{\pi,\theta}^{(n)} \right] \right), \qquad \beta \neq 0, \pi. \quad (2.15)$$

If we eliminate v_β from the two equations that make up (2.10) we obtain

$$\frac{\partial p_\beta}{\partial x} + \mathrm{i} k \cos \beta \, p_\beta = \tfrac{1}{2} \sin \beta \sum_{n=1}^{N} \left(c_{0,\beta}^{(n)} v_0^{(n)} - c_{\pi,\beta}^{(n)} v_\pi^{(n)} \right), \qquad \mathbf{x} \in L, \quad (2.16)$$

and this can be solved for p_β. For $\mathbf{x} \in L_m$ we thus have

$$p_\beta(x, \eta_m) = \tfrac{1}{2} f_\beta(x, \eta_m) \sin \beta$$

$$\times \int_{a_m}^{x} \sum_{n=1}^{N} f_{\pi-\beta}(\xi, \eta_n) \left(c_{0,\beta}^{(n)} v_0^{(n)}(\xi, \eta_n) - c_{\pi,\beta}^{(n)} v_\pi^{(n)}(\xi, \eta_n) \right) \, \mathrm{d}\xi, \quad (2.17)$$

which expresses p_β in terms of $v_0^{(n)}$ and $v_\pi^{(n)}$. The solution to the rigid-strip scattering problem for an arbitrary angle of incidence is thus determined, through (2.5), in terms of the solution to $2N$ integral equations of the form (2.7).

The relationships between the diffraction coefficients take particularly simple forms if we define

$$\mathcal{F}_{\theta,\beta} = (\cos \theta + \cos \beta) F_{\theta,\beta}, \qquad \mathcal{G}_{\theta,\beta} = (\cos \theta + \cos \beta) G_{\theta,\beta}, \quad \text{etc.}$$

From (2.8) and (2.17), we can derive

$$\mathcal{F}_{\theta,\beta} = \tfrac{1}{2} \sin \theta \sin \beta \sum_{n=1}^{N} \left(c_{0,\beta}^{(n)} G_{0,\theta}^{(n)} - c_{\pi,\beta}^{(n)} G_{\pi,\theta}^{(n)} \right)$$

and from (2.15) we then get

$$\mathcal{G}_{\theta,\beta} = -\sum_{n=1}^{N} \left(A_{0,\beta}^{(n)}\mathcal{G}_{0,\theta}^{(n)} + A_{\pi,\beta}^{(n)}\mathcal{G}_{\pi,\theta}^{(n)} \right). \tag{2.18}$$

Alternatively, using (2.11),

$$\mathcal{F}_{\theta,\beta} = \tfrac{1}{2}\sin\theta\sin\beta \sum_{n=1}^{N}\sum_{m=1}^{N} \left(c_{\pi,\beta}^{(n)}c_{\pi,\theta}^{(m)}G_{\pi,\pi}^{(n,m)} - c_{0,\beta}^{(n)}c_{0,\theta}^{(m)}G_{0,0}^{(n,m)} \right)$$

and

$$\mathcal{G}_{\theta,\beta} = \sum_{n=1}^{N}\sum_{m=1}^{N} \left(A_{0,\beta}^{(n)}A_{0,\theta}^{(m)}\mathcal{G}_{0,0}^{(n,m)} + A_{\pi,\beta}^{(n)}A_{\pi,\theta}^{(m)}\mathcal{G}_{\pi,\pi}^{(n,m)} \right),$$

from which the symmetry relations $F_{\beta,\theta} = F_{\theta,\beta}$ and $G_{\beta,\theta} = G_{\theta,\beta}$ are obvious. In fact, equation (2.18) follows from (2.15) if we impose the symmetry of F.

3. CONCLUSION

We have shown that the scattering problem for a plane wave incident from an arbitrary angle on an arbitrary configuration of N parallel strips can be related to $2N$ separate scattering problems for the same geometry, but with different boundary conditions. For a given geometrical configuration and frequency, we must solve $2N$ integral equations (each with the same logarithmically singular kernel) and invert two $N \times N$ systems of equations in order to determine the solution for any incident wave angle. This may lead to significant computational savings if solutions are required over a range of angles. The numerical solution of integral equations of the type given by (2.7) is discussed in [4].

Embedding formulas can also be derived for the case of N gaps in a breakwater which has finite thickness, see [5]. In this situation we require the solution to $4N$ problems, corresponding to the fact that there are now $4N$ corners. Although Babinet's principle does not apply here, it appears that it may be possible to derive embedding formulas for an array of rectangles, and work is currently underway to establish whether this is indeed the case and, if it is, what form such formulas would take.

References

[1] Marc H. Williams. Diffraction by a finite strip. *Q. J. Mech. Appl. Math.*, 35:103–124, 1982.

[2] N. R. T. Biggs, D. Porter, and D. S. G. Stirling. Wave diffraction through a perforated breakwater. *Q. J. Mech. Appl. Math.*, 53:375–391, 2000.

[3] N. R. T. Biggs and D. Porter. Wave scattering by a perforated duct. *Q. J. Mech. Appl. Math.*, 55:249–272, 2002.

[4] C. M. Linton and P. McIver. *Handbook of Mathematical Techniques for Wave/Structure Interactions*. Chapman & Hall/CRC, Boca Raton, 2001.

[5] N. R. T. Biggs and D. Porter. Wave diffraction through a perforated barrier of non-zero thickness. *Q. J. Mech. Appl. Math.*, 54:523–547, 2001.

NUMERICAL INVESTIGATION OF PHOTONIC CRYSTAL FIBERS BY SPECTRAL AND MULTIPOLE METHODS

A. Nicolet[†], S. Guenneau[‡], F. Zolla[†], C. Geuzaine[⋆], B. Kuhlmey[†] and
G. Renversez[†]

[†] *Institut Fresnel, UMR 6133, Faculté de Saint-Jérôme, case 161, F-13397 Marseille Cedex 20, France*

andre.nicolet@fresnel.fr, frederic.zolla@fresnel.fr, boris.kuhlmey@fresnel.fr, gilles.renversez@fresnel.fr

[‡] *Department of Mathematical Sciences, University of Liverpool, Liverpool L69 3BX, UK*
Current address: Blackett Laboratory, Imperial College, Prince Consort Rd., London SW7 2AZ, UK

s.r.l.guenneau@imperial.ac.uk

[⋆] *California Institute of Technology, Applied and Computational Mathematics, 1200 E. California Boulevard MC 217-50 Pasadena, CA 91125, USA*

geuzaine@acm.caltech.edu

Keywords: Microstructured optical fibres, finite elements, multipole method.

Abstract

In this paper, we investigate the propagation of electromagnetic waves along microstructured optical fibres (MOF) with a crystal cladding of finite extension in the transverse plane. In these so-called Photonic Crystal Fibres (PCF), many interesting and unusual phenomena may be observed. For instance, it appears that, for some range of frequencies, a defect in the crystal cladding gives rise to localized waves in the low index core (i.e. in the defect). It is worth noting that the methods reducing the system of equations to a single longitudinal (electric or magnetic) component cannot tackle these genuine vectorial propagation problems.

We first achieve this study with a variational numerical method i.e. a Finite Element Formulation with the electric field as the variable, where edge elements are used for discretizing the transverse field and nodal elements for the longitudinal field [4]. Finally, we compare our finite element method - which leads to a generalized eigenvalue problem- with another method co-developed by some of us [18, 11], which is based on the determination of poles of the scattering operator (multipole expansion method).

1.   INTRODUCTION

In the last decade, some advances have been made in a deeper under-standing of the propagating properties of a new class of electromagnetic waveguides. These structures [10], whose propagating properties depend on the geometry of a crystal lattice constituted of dielectric rods, have been called Photonic Crystal Fibers (PCF).

PCF rely on some periodic structures that induce the so-called photonic band gaps. This phenomenon, that mimics electronic band gaps in semi-conductors, prevent propagation of light in forbidden frequency gaps what is used to confined light in a central low index defect (PBG effect).

To study such structures, one approach is the supercell method [3] which is commonly employed for PCF (it assumes pseudo-periodic conditions on a cell which includes the waveguide cross-section): the main drawback comes from the assumption of periodicity in the transverse plane. In this paper we compare two alternative methods that do not rely on artificial period-icity. The first one is the Finite Element Method (FEM) which allows the modeling of complex geometries (e.g. PCF filled with rod cross-sections of different shapes) and takes into account the influence of the outer boundary of the guide [4]. Another approach which can take into account the finite size of the fibre cross-section, is the multipole method. In this method, the fields are expanded in Fourier-Bessel series, and a generalized scattering problem is solved[18, 11]. How can we justify the choice of these two meth-ods? The advantages of having two methods to solve the same problem is that comparing the results gives some confidence in their accuracy if they match and also that the methods may have complementary advantages so that they can rescue each other if one of them meets difficulty on a par-ticular problem. Therefore, it seems natural to choose the two methods as different as possible. It is quite the case between the multipole and the finite element methods. As a common feature, the two methods share the very classical fact that the unknown fields or functions are approxi-mated using a linear combination of given basis functions. Nevertheless, one can say that the approach of the multipole method is global while the finite element method is local. On the one hand the basis functions in the multipole method are solutions of the Helmholtz equations to be solved (excepted at the source point but it is not included in the domain where the solution is considered) as they are the field produced by a multipolar radiating source. Their linear combinations are themselves solutions and the problem is to pick the good one by choosing the right coefficients (i.e. the values of the equivalent multipolar charges). This is performed thanks

to the numerical expression of local conditions: continuity conditions of the field at the interfaces. On the other hand the basis functions in the finite element methods are simple (e.g. piecewise linear) functions with bounded support (of small size). In the case of Whitney elements [2], if basis functions do not match the Helmholtz equation, they locally respect the right continuity conditions at the interfaces e.g. tangential continuity for electric and magnetic fields represented by edge elements (that is the geometrical nature of the fields that determines the kind of element to be used) and so do their linear combinations. In this case, the Helmholtz equation itself (in weak variational form) is used to compute the numerical coefficients of the approximation. The purpose of this paper is to describe in the same framework the two methods, and to show that they give consistent results.

2.   COMMON HYPOTHESIS AND NOTATIONS

We consider an inhomogeneous waveguide of constant section Ω invariant along the z axis, whose permittivity profile ε is a piecewise constant function and with constant permeability $\mu = \mu_0$ (non magnetic). We are looking for electromagnetic fields solutions of the vector Maxwell system. Choosing a time dependance in $e^{-i\omega t}$ with ω denoting the angular frequency, related to the free space wavenumber by $\omega = k_0 c$, and taking into account the invariance of the guide along its z axis, we define time-harmonic electric and magnetic fields $\mathbf{E}$ and $\mathbf{H}$. Each mode is characterized by the value of γ, its propagation constant along the z axis, and the dependence of the fields ($\mathbf{V} = \mathbf{E}$ or $\mathbf{V} = \mathbf{H}$) is given by:

$$\mathbf{V}(\vec{r}, t) = \widetilde{\mathbf{V}} e^{i(\gamma z - \omega t)} \tag{2.1}$$

In each constant permittivity region of the waveguide, the fields ($\widetilde{\mathbf{V}}$) satisfy an Helmholtz equation.

3.   THE FINITE ELEMENT MODELING

In this formulation, $\widetilde{\mathbf{V}}$ depends on the cartesian coordinates x and y in equation (2.1). For the sake of simplicity, we consider that the boundary of the waveguide $\partial\Omega$ is infinite conducting, thereby avoiding to deal with an open problem (note that a judicious choice of coordinate transform allows this modeling [8]). We choose an electric field formulation, because the tangential trace of $\mathbf{E}$ is null, contrary to that of $\mathbf{H}$ on $\partial\Omega$. We achieve numerical computations with the help of finite elements. It involves both a transverse field in the section of the guide and a longitudinal field along its axis. The section of the guide is meshed with triangles and Whitney finite elements are used i.e. edge elements for the transverse field and nodal elements for the longitudinal field. The solution of the above problem is

then given by the minimum of the following residual

$$\mathcal{R}(\gamma; \mathbf{E}, \mathbf{E}') = \int_\Omega \mathrm{curl}_\gamma \, \mathbf{E} \cdot \overline{\mathrm{curl}_\gamma \, \mathbf{E}'} \, dxdy - \mu_0 \omega^2 \int_\Omega \varepsilon \mathbf{E} \cdot \overline{\mathbf{E}'} \, dxdy \qquad (3.1)$$

where $\mathrm{curl}_\gamma \, \mathbf{E}(x, y) = \mathrm{curl}\Big(\mathbf{E}(x, y)e^{i\gamma z}\Big)e^{-i\gamma z}$. It must be noticed that the penalty term involving the divergence of the field is not introduced in the discrete formulation because the use of Whitney elements guarantees the nullity of the divergence in weak sense [2, 8, 7]. The operator associated with this variational problem has a compact resolvent [8, 9] and its spectrum is therefore a discrete set of eigenvalues belonging to $[\dfrac{\gamma^2}{\varepsilon}; +\infty[$ which gives us a numerical criterion to eliminate invalid modes. The GetDP software [4] has been used to set up the finite element problem. The Lanczos algorithm solves the generalized eigenvalue problem [7]. Since we study propagating modes in a low-index default, they are associated with complex frequencies: these so-called leaky modes are similar to classical propagating modes, except they are attenuated as energy is lost to the crystal cladding. These modes initially decrease in amplitude away from the PCF, but eventually increase at large distances and diverge infinitely far from the PCF. Because real PCF have a finite crystal cladding (contrary to the assumption of [3]), all the propagating modes induced by PBG effects are leaky. It is therefore important that the losses associated with leaky modes be considered when calculating the modal properties of PCF. For this, we embed our PCF in a metallic jacket.

The finite element approach is currently limited by the use of the Lanczos algorithm that is only able to find real eigenvalues. Therefore, in order to be able to find leaky modes one has to consider either air (in a possibly infinite region using a transformation method [8]) around a finite silica fibre, either a metallic jacket at finite distance. The case of infinite silica matrix (using the already quoted transformation method to carry the jacket at infinity) does not converge numerically. Fortunately, when the numerical algorithm converges, the localized defect modes are quite insensitive to boundary conditions. Future developments include the use of Arnoldi algorithm[14, 15] in order to deal with complex eigenvalues.

In the case of a metallic jacket at finite distance (four pitches Λ from fibre center in the following numerical examples), the operator associated with the eigenvalue problem becomes bounded (and therefore has a discrete spectrum) and is still Hermitian (*i.e.* its eigenvalue are real). Physically, this may be seen as a trick used to prevent energy of the modes to leak far from the fibre.

We could take into account the losses of leaky modes via the computation of the current as the integral of the tangential magnetic field ($i\omega\mu_0\mathbf{J}_S = \mathbf{n}\wedge$

curl$_\gamma$ **E**) on the metallic cavity. Let us emphasize that $\mathbf{J}_S$ is an unknown of the problem which does not appear in the electric formulation ($\mathbf{n} \wedge \mathbf{E} = 0$). The Dirichlet homogeneous boundary conditions of the electric field do not actually involve wave reflection, since the propagation occurs along the z-axis. Such a condition for the magnetic field is not *adequate*, since the tangential magnetic field has an unknown value on the boundary i.e. the surface currents. For the sake of completeness, the reader can refer to [7] for a review on properties of PCF with a high central index (where a magnetic field formulation was used).

4.   THE MULTIPOLE METHOD

Our method is inspired by the one developed in our laboratory in the framework of two-dimensional photonic crystal theory [5]. It is generally named as the multipole method. The first step of the method is to elaborate a theory of scattering of an infinitely long MOF in conical (off-plane) mounting. In this formulation, $\widetilde{\mathbf{V}}$ depends on polar coordinates r and θ in equation (2.1). This theory is based on the use of the three elements: the Fourier-Bessel series describing the electromagnetic fields, the translation properties of Fourier-Bessel functions (also called Graf's theorem) which appear in the series, and the scattering matrices of the holes pierced in silica. In addition, the notion of generalized scattering matrix is employed for the external boundary of the silica fibre. The second step of the method is to find homogeneous solutions of this scattering problem. Noting the appropriate matrix $\mathcal{M}$, we must solve:

$$\mathcal{M}\tilde{\mathcal{B}} = 0. \tag{4.1}$$

A non-zero vector $\tilde{\mathcal{B}}$ verifying this equation represents a non-zero field verifying the Helmholtz equation and the boundary conditions: the field associated with this vector is a mode of the structure. The matrix $\mathcal{M}$ is a function of the geometry, the wavelength and the effective index $n_{eff} = \gamma/k_0$. Finding the modes for a given structure and wavelength thus leads to the search of zeros of the complex function $\det(\mathcal{M})$ of the complex variable n_{eff}.

The geometrical losses $\mathcal{L}$ in $dB.m^{-1}$ associated with the modes are directly obtained from the imaginary part of n_{eff}:

$$\mathcal{L} = \frac{20}{\ln(10)} \frac{2\pi}{\lambda} Im(n_{\mathtt{eff}}) \times 10^6 \tag{4.2}$$

where λ is in μm.

For circular inclusions, the boundary conditions are implemented analytically, so that in this case the only approximations is the truncation of

M	$\mathrm{Re}(n_{eff})$	$Im(n_{eff}) \times 10^6$
3	1.43852886240663	6.918242988502046
4	1.43838719374803	1.749096334333127
5	1.43836672605884	1.373925319699950
6	1.43836499998690	1.414928166193201
7	1.43836493475660	1.416468499483090
8	1.43836493461317	1.416459892560528
9	1.43836493424529	1.416475747100788

Table 1 Convergence of n_{eff} with M the truncation order of the Fourier-Bessel series. Results are for an higher order mode of the MOF described below at $\lambda = 1.45\,\mu\mathrm{m}$.

the Fourier-Bessel series. For non circular inclusions, differential or integral methods can be used to compute the scattering matrices associated with the inclusions [16]. If the inclusions overlap, our method is no longer appropriate. Symmetry properties of the fibers are accurately satisfied: for an usual MOF with a rotational symmetry of order 6 (for example a triangular lattice of circular holes), the fundamental mode is two-fold degenerate as expected by Mc Isaac's theory[17]. It is worth noting that these symmetry properties can be used to reduce significantly the size of the matrix $\mathcal{M}$, and therefore the computational time.

Our formulation also allows a self-consistency check of the computed results through a comparison between two different expansions of the fields: a local one and a global one (also called Wijngaard expansion). These expansions only match perfectly for untruncated series, and so their numerical difference can be used as an indicator of truncations errors and of the quality of the matrix null vector location[11]. A second test of convergence is provided by the stability of n_{eff} with respect to the increase of the truncation order M of the Fourier-Bessel series, this is illustrated in Table 1.

With the MOF geometry and the wavelength as inputs, the method gives the modes of the MOF as an output. Material dispersion can thus be included in a natural way in the MOF geometry, using for instance Sellmeier expansions[6, 1]. The dispersion parameter D is computed through

the usual formula from the real part of the effective index $\text{Re}(n_{eff})$ [1]:

$$D = -\frac{\lambda}{c}\frac{\partial^2 \text{Re}(n_{\text{eff}})}{\partial \lambda^2} \tag{4.3}$$

The reader interested in applying this theory can refer to papers [18, 11], and results on dispersion engineering can be found in [12, 13].

5.   NUMERICAL COMPARISONS

On one hand, we use a metallic jacket approach with Finite Elements i.e. the PCF is included in an outer metallic waveguide [8]. On the other hand, with our multipole method we consider an infinite silica matrix and therefore we deal with complex frequencies [11]. In both cases, the PCF consists of six air-holes ($n = 1$) of radius $2.5\mu m$ spaced in hexagonal arrangement by a pitch $\Lambda = 6.75\mu m$ in a matrix of silica ($n = 1.45$). The Getdp software [4] is used to set up the Finite Element Modeling (figure 1, left) and to retrieve the real part of the leaky mode's frequency calculated with the multipole method approach for the six holes honeycomb structure (figure 1, right). More precisely, the wavelength $\lambda = 1.45\mu m$ is set up in the multipole method and one obtains $n_{eff} = \gamma/k_0 = \gamma\lambda/2\pi = 1.445395345 + i\ 3.15\ 10^{-8}$ for the degenerate fundamental mode of the above C_{6v} MOF structure [17]. Then, for a given propagating constant $\gamma_{FEM} = 1.445395k_0 = 6.263232\mu m^{-1}$, we catch a leaky mode (figure 1, left) whose eigenvalue $\omega_{FEM} = 2\pi c/\lambda$ corresponds to a wavelength $\lambda_{FEM} = 1.449996\mu m$ that matches the initial value. We illustrate on figure 2 the impact of a perturbation on the geometry of the PCF on this leaky mode.

6.   CONCLUSION

We have numerically investigated the propagating modes in a 6 air-hole honeycomb fiber with a finite element modeling and a multipole method, both of which proved to be fast and efficient algorithms. The multipole method gives easy access to loss of the modes, whereas the finite element method is not restricted to a circular geometry for the fibres (cf. figure 2). A possible extension of this work is to explore further the numerical comparisons on larger linear systems i.e. for a large bunch of fibers in various geometrical configurations (the multipole method taking into account the possible symmetries) and for higher index contrasts (the edge-element approach being well adapted).
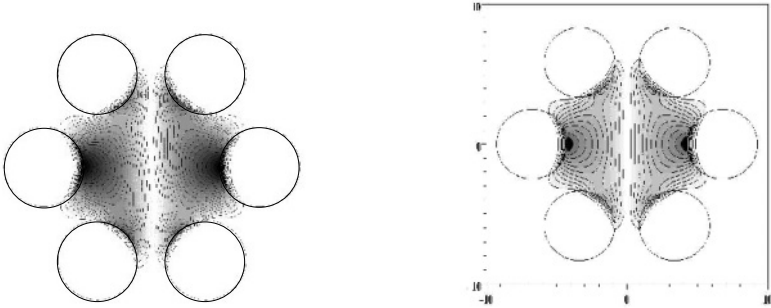
Figure 1   Longitudinal component E_z of the electric field **E** for the degenerate fundamental mode (E_z null along the vertical y-axis) in a 6-air-hole MOF (radii $= 2.5\mu m$) of pitch $\Lambda = 6.75\mu m$ for a normalized propagating constant $\gamma\Lambda = 42.276817$ (left: finite element modeling, right: multipole method with $M = 5$).
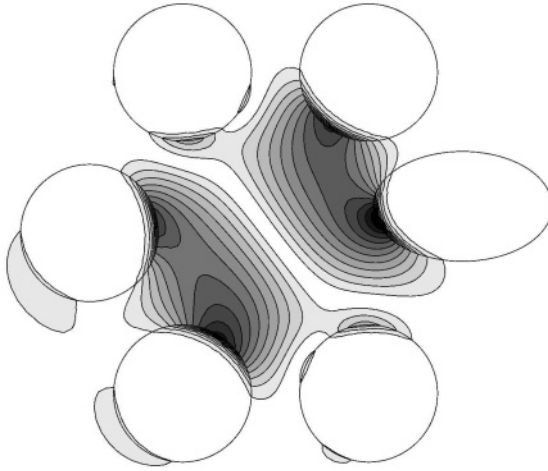
Figure 2   Eigenfield of figure 1 when breaking the hexagonal symmetry of the structure (the rightmost inclusion is now a shifted ellipse). This result is obtained with the Finite Element Method.

Acknowledgments

References

[1] G. P. Agrawal. *Nonlinear fiber optics.* Academic Press, 1989.

[2] A. Bossavit. Solving Maxwell equations in a closed cavity, and the question of spurious modes. *IEEE Trans. Mag*, 26:702-705, 1990.

[3] J. Broeng, S.E. Barkou, T. Sondergaard, A. Bjarklev. Analysis of air-guiding photonic bandgap fibers. *Optics Letters*, 24:1203-1205, 2000.

[4] P. Dular, C. Geuzaine, F. Henrotte, and W. Legros. A general environment for the treatment of discrete problems and its application to the finite element method. *IEEE Trans. Mag.*, 34(5):3395–3398, 1998.

[5] D. Felbacq, G. Tayeb, and D. Maystre. Scattering by a random set of parallel cylinders. *J. Opt. Soc. Am. A*, 9:2526–2538, 1994.

[6] J. W. Fleming. Material dispersion in lightguide glasses. *Electron. Lett.*, 14(11):326–328, May 1978.

[7] S. Guenneau. Homogénéisation des quasi-cristaux et analyse des modes dans des fibres optiques de type cristal photonique. *PhD Thesis*, Université de Provence, 2001.

[8] S. Guenneau, A. Nicolet, F. Zolla, and S. Lasquellec. Modeling of photonic crystal optical fibers with finite elements. *IEEE Trans. Mag.*, 38(2):1261-1264, 2002.

[9] S. Guenneau, S. Lasquellec, A. Nicolet, and F. Zolla. Design of photonic band gap optical fibers using finite elements. *The International Journal for Computations and Mathematics in Electrical and Electronic Engineering, COMPEL*, 21(4):534-539, 2002.

[10] J. C. Knight, J. Broeng, T. A. Birks, and P. St. J. Russell. Photonic band gap guidance in optical fibers. *SCIENCE*, 282:1476-1478, 1998.

[11] B. Kuhlmey, T. P. White, G. Renversez, D. Maystre, L.C. Botten, C. Martijn de Sterke, and R. C. McPhedran. Multipole method for microstructured optical fibers II: implementation and results. *J. Opt. Soc. Am. B*, 19(10):2331-2340, 2002.

[12] B. Kuhlmey, G. Renversez, D. Maystre, T. White, R. McPhedran, L. Botten and M. de Sterke. Multipole study of dispersion and losses of photonic crystal fibres. *SPIE Proceedings, Photonic Bandgap Materials and Devices, A. Adibi, A. Scherer and S. Lin editors*, 4655, 2002.

[13] B. Kuhlmey, G. Renversez and D. Maystre. Chromatic dispersion and losses of microstructured optical fibers. *Applied Optics*, 42(4):634-639, 2003.

[14] R. Lehoucq and J. A. Scott. An evaluation of software for computing eigenvalues of sparse nonsymmetric matrices. Preprint MCS-P547-1195, Argonne National Laboratory, 1996.

[15] R. Lehoucq. Implicitly Restarted Arnoldi Methods and Subspace Iteration, SIAM Journal on Matrix Analysis and Applications, 23(2):551-562, 2001.

[16] D. Maystre and P. Vincent. *in Electromagnetic theory of gratings* edited by R. Petit; Topics in Current Physics, Springer-Verlag, 22, 1981.

[17] P. R. Mc Isaac. Symmetry-induced modal characteristics of uniform waveguides-I: Summary of results. *IEEE Trans. on Microwave Theory Tech.*, 23(5):421–433, 1975.

[18] T. P. White, B. Kuhlmey, R. C. McPhedran, D. Maystre, G. Renversez, C. Martijn de Sterke, and L.C. Botten. Multipole method for microstructured optical fibers I: formulation. *J. Opt. Soc. Am. B*, 19(10):2322-2330, 2002.

METHOD OF HYPERELLIPTIC SURFACES FOR VECTOR FUNCTIONAL-DIFFERENCE EQUATIONS

Y.A. Antipov[1], V.V. Silvestrov[2]

[1] *Department of Mathematics, Louisiana State University,*
Baton Rouge LA 70803, USA
antipov@math.lsu.edu

[2] *Department of Mathematics, Chuvash State University,*
Cheboksary 428015, Russia
sil@chuvsu.ru

Abstract

A vector functional-difference equation of the first order with a special matrix coefficient is analysed. It is shown how it can be converted into a Riemann-Hilbert boundary-value problem on a union of two segments on a hyperelliptic surface. The genus of the surface is defined by the number of zeros and poles of odd order of a characteristic function in a strip. As an example, a new model problem for an anisotropic half-plane with imperfect interfaces which are illuminated by a plane electromagnetic wave at oblique incidence, is considered.

1. INTRODUCTION

The most powerful and general technique for exact solution of model problems in acoustic and electromagnetic scattering is Maliuzhinets' method [1]. For impedance boundary conditions, in general, this technique gives rise to a vector functional-difference equation

$$\mathbf{\Phi}(\sigma) = \mathbf{G}(\sigma)\Phi(\sigma - h) + \mathbf{g}(\sigma), \quad \sigma \in \Omega = \{\mathrm{Re}(s) = \omega\}, \qquad (1.1)$$

where $\mathbf{\Phi}(\sigma)$ is an unknown vector analytic in the strip $\Pi = \{\omega - h < \mathrm{Re}(s) < \omega\}$. The matrix $\mathbf{G}(\sigma)$ and the vector $\mathbf{g}(\sigma)$ are supposed to be known.

The method of exact solution of equations (1.1) rests on our ability to factorise the coefficient $\mathbf{G}$ of the problems, i.e. to split the matrix $\mathbf{G}$ into

two factors:

$$\mathbf{G}(\sigma) = \mathbf{X}(\sigma)[\mathbf{X}(\sigma - h)]^{-1}, \quad \sigma \in \Omega. \tag{1.2}$$

Here $\mathbf{X}(s)$ is analytic and non-singular in the strip Π. To the best of the authors' knowledge, classes of matrices admitting constructive difference factorisation (1.2) have not been studied. We of course disregard those cases when the matrix coefficient $\mathbf{G}$ can be diagonalised by multiplying the left- and right-hand sides of equation (1.1) by a constant matrix.

In this paper, we study the vector functional-difference equation (1.1) with the matrix coefficient of the form

$$\mathbf{G}(\sigma) = \begin{pmatrix} a_1(\sigma) + a_2(\sigma)f_1(\sigma) & a_2(\sigma) \\ a_2(\sigma)f_2(\sigma) & a_1(\sigma) - a_2(\sigma)f_1(\sigma) \end{pmatrix}, \quad \sigma \in \Omega, \tag{1.3}$$

where $a_1(\sigma), a_2(\sigma)$ are arbitrary Hölder functions on every finite segment of the contour Ω, $f_1(\sigma), f_2(\sigma)$ are arbitrary single-valued meromorphic functions in the strip Π such that $f_j(\sigma) = f_j(\sigma - h)$, $\sigma \in \Omega$, $j = 1, 2$. It is assumed that the function $f_1(s)$ and the characteristic function $f(s) = f_1^2(s) + f_2(s)$ have finite numbers of poles in the strip Π. The number of zeros of the function $f(s)$ in the strip Π is also finite.

We propose a procedure of exact solution based on the theory of Riemann-Hilbert boundary value problem on hyperelliptic surfaces.

2. VECTOR FUNCTIONAL-DIFFERENCE EQUATION OF THE FIRST ORDER

Let Π be a strip in the plane of a complex variable s: $\Pi = \{s \in \mathbf{C} : \omega - h < \mathrm{Re}(s) < \omega\}$, where ω is real and $h > 0$. Let Ω, Ω_{-1} be the boundaries of the strip: $\Omega = \{\mathrm{Re}(s) = \omega\}$, $\Omega_{-1} = \{\mathrm{Re}(s) = \omega - h\}$. Consider the following boundary-value problem of the theory of analytic functions:

Given a 2×2 matrix $\mathbf{G}(\sigma)$ and a vector $\mathbf{g}(\sigma)$ find a vector $\mathbf{\Phi}(s)$ analytic in the strip Π, continuous up to the boundary $\Omega \cup \Omega_{-1}$ apart from a finite number of poles $\beta_1, \beta_2, \ldots, \beta_t \in \Pi$ of orders $\tau_1, \tau_2, \ldots, \tau_t$ and satisfying the boundary condition

$$\mathbf{\Phi}(\sigma) = \mathbf{G}(\sigma)\mathbf{\Phi}(\sigma - h) + \mathbf{g}(\sigma), \quad \sigma \in \Omega. \tag{2.1}$$

At the ends of the strip, i.e. as $\mathrm{Im}(s) \to \pm\infty$, $\mathbf{\Phi}(s) = O(e^{b^\pm \, \mathrm{Im}(s)})$ with $b^\pm$ being real, finite and prescribed. The matrix $\mathbf{G}(\sigma)$ and the vector $\mathbf{g}(\sigma)$ satisfy the Hölder condition on every finite segment of Ω. At infinity, i.e. as $\sigma \to \omega \pm i\infty$, the components of the $\mathbf{G}(\sigma)$ and $\mathbf{g}(\sigma)$ may have a finite exponential growth not necessarily the same. The matrix $\mathbf{G}(\sigma)$ is also nonsingular on Ω.

Let $\lambda_1(\sigma)$, $\lambda_2(\sigma)$ be the eigenvalues of the matrix $\mathbf{G}(\sigma)$ and let $\lambda_1(\sigma) \neq \lambda_2(\sigma)$. We define a class of matrices representable in the form

$$\mathbf{G}(\sigma) = \mathbf{T}(\sigma)\mathbf{\Lambda}(\sigma)[\mathbf{T}(\sigma - h)]^{-1}, \quad \sigma \in \Omega, \tag{2.2}$$

where $\mathbf{\Lambda}(\sigma) = \mathrm{diag}\{\lambda_1(\sigma), \lambda_2(\sigma)\}$, and the matrix $\mathbf{T}(\sigma)$ admits a two-valued analytical continuation from the contour Ω into the strip apart from a finite number of poles, branch points and points where $\det \mathbf{T}(s) = 0$. It is also required that $\mathbf{T}(\sigma) = \mathbf{T}(\sigma - h)$, $\sigma \in \Omega$. The eigenvalues of the matrix

$$\mathbf{G}(\sigma) = \begin{pmatrix} G_{11}(\sigma) & G_{12}(\sigma) \\ G_{21}(\sigma) & G_{22}(\sigma) \end{pmatrix} \tag{2.3}$$

are given by

$$\lambda_j(\sigma) = \frac{1}{2}[G_{11}(\sigma) + G_{22}(\sigma) - (-1)^j \Delta^{1/2}(\sigma)], \quad j = 1, 2, \tag{2.4}$$

where

$$\Delta(\sigma) = [G_{11}(\sigma) - G_{22}(\sigma)]^2 + 4G_{12}(\sigma)G_{21}(\sigma). \tag{2.5}$$

Take the diagonalising matrix $\mathbf{T}(\sigma)$ in the form

$$\mathbf{T}(\sigma) = \begin{pmatrix} 1 & 1 \\ \frac{G_{22}(\sigma) - G_{11}(\sigma) + \Delta^{1/2}(\sigma)}{2G_{12}(\sigma)} & \frac{G_{22}(\sigma) - G_{11}(\sigma) - \Delta^{1/2}(\sigma)}{2G_{12}(\sigma)} \end{pmatrix}, \quad \sigma \in \Omega, \tag{2.6}$$

with $\det \mathbf{T}(\sigma) = -\Delta^{1/2}(\sigma)[G_{12}(\sigma)]^{-1}$. In order that the matrix $\mathbf{T}(\sigma)$ is meromorphic and two-valued, it is sufficient that

$$f_1(s) = \frac{G_{11}(s) - G_{22}(s)}{2G_{12}(s)}, \quad f_2(s) = \frac{G_{21}(s)}{G_{12}(s)}, \quad s \in \Pi, \tag{2.7}$$

are single-valued meromorphic functions in Π. Then the original matrix has the form

$$\mathbf{G}(\sigma) = a_1(\sigma) \begin{pmatrix} 1 & 0 \\ 0 & 1 \end{pmatrix} + a_2(\sigma) \begin{pmatrix} f_1(\sigma) & 1 \\ f_2(\sigma) & -f_1(\sigma) \end{pmatrix}, \quad \sigma \in \Omega, \tag{2.8}$$

where

$$a_1(\sigma) = \frac{1}{2}[G_{11}(\sigma) + G_{22}(\sigma)], \quad a_2(\sigma) = G_{12}(\sigma). \tag{2.9}$$

In the new notations, the eigenvalues λ_1, λ_2 and the matrix of transformation $\mathbf{T}$ become

$$\lambda_1(\sigma) = a_1(\sigma) + a_2(\sigma)f^{1/2}(\sigma), \quad \lambda_2(\sigma) = a_1(\sigma) - a_2(\sigma)f^{1/2}(\sigma), \tag{2.10}$$

$$\mathbf{T}(s) = \begin{pmatrix} 1 & 1 \\ -f_1(s) + f^{1/2}(s) & -f_1(s) - f^{1/2}(s) \end{pmatrix}, \tag{2.11}$$

where $f(s) = f_1^2(s) + f_2(s)$. Here $a_1(\sigma)$, $a_2(\sigma)$ are *arbitrary Hölder functions on* Ω (although they may be *discontinuous at infinity*), and $f_1(s)$, $f_2(s)$ are *arbitrary single-valued meromorphic functions in the strip* Π. They do not have poles on Ω. In the strip Π, the functions $f_1(s)$, $f(s)$ have finite numbers of poles. It is assumed that the number of zeros of the function $f(s)$ in the strip Π is also finite. We emphasise that the elements of the matrix $\mathbf{T}(s)$ are h-periodic or, equivalently, the functions $f_1(s)$, $f^{1/2}(s)$ are h-periodic.

3. SCALAR RIEMANN-HILBERT PROBLEM ON A HYPERELLIPTIC SURFACE

In this section we reduce the vector functional-difference equation (2.1) with the matrix coefficient (2.8) to a scalar Riemann-Hilbert problem on a Riemann surface. First, substitute the relation (2.2) into equation (2.1)

$$[\mathbf{T}(\sigma)]^{-1}\mathbf{\Phi}(\sigma) = \mathbf{\Lambda}(\sigma)[\mathbf{T}(\sigma-h)]^{-1}\mathbf{\Phi}(\sigma-h) + [\mathbf{T}(\sigma)]^{-1}\mathbf{g}(\sigma), \quad \sigma \in \Omega, \quad (3.1)$$

and introduce a new vector-function

$$\varphi(s) = [\mathbf{T}(s)]^{-1}\mathbf{\Phi}(s), \quad s \in \Pi, \tag{3.2}$$

with the components

$$\varphi_1(s) = \left(\frac{f_1(s)}{2f^{1/2}(s)} + \frac{1}{2}\right)\Phi_1(s) + \frac{\Phi_2(s)}{2f^{1/2}(s)},$$

$$\varphi_2(s) = \left(-\frac{f_1(s)}{2f^{1/2}(s)} + \frac{1}{2}\right)\Phi_1(s) - \frac{\Phi_2(s)}{2f^{1/2}(s)}, \quad s \in \Pi. \tag{3.3}$$

These formulae indicate that the functions $\varphi_1(s)$ and $\varphi_2(s)$ are multi-valued. They have branch points at the zeros and poles of odd order of the function $f(s)$.

Among these points there can also be the two infinite points at the upper and lower ends of the strip. From the theory of periodic meromorphic functions, by definition, the upper end $x + i\infty$ ($\omega - h \leq x \leq \omega$) of the strip is called a zero of order ν of a function $f(s)$ if $f(s) \sim Ae^{2\pi is\nu/h}$ as $\mathrm{Im}(s) \to +\infty$ ($A = \mathrm{const} \neq 0$). The point $x + i\infty$ is a pole of order ν if $f(s) \sim Ae^{-2\pi is\nu/h}$ as $\mathrm{Im}(s) \to +\infty$. The lower end $x - i\infty$ is treated similarly. Any h-periodic meromorphic function has the same number of poles and zeros in the strip of the periods (the poles and zeros including the upper and lower infinite points are counted according to the multiplicity). Therefore, the function $f^{1/2}(s)$ has an even number of the branch points (the infinite points $x \pm i\infty$ can be branch points as well). Let the branch points be $s_0, s_1, \ldots, s_{2\rho+1}$. In the case $\rho = -1$, the function $f(s)$ is either

a constant, or all its poles and zeros are of even order. Henceforth, it is assumed that $\rho \geq 0$. Apart from the branch points $s_0, s_1, \ldots, s_{2\rho+1}$, the functions $\varphi_1(s)$ and $\varphi_2(s)$ admit a finite number of poles in the strip Π. In addition to the prescribed poles $\beta_1, \beta_2, \ldots, \beta_t$ of the vector-function $\boldsymbol{\Phi}(s)$, the functions φ_1 and φ_2 have new poles. Their multiplicity and location are entirely defined by the poles of the function $f_1(s)$ and the zeros of even order of the function $f(s)$. Let all the poles of the functions $\varphi_1(s)$ and $\varphi_2(s)$ be $a_1, a_2, \ldots, a_m$ of orders $\nu_1, \nu_2, \ldots, \nu_m$.

By using (3.2) the coupled difference equation (3.1) reduces to two separate equations

$$\varphi_1(\sigma) = \lambda_1(\sigma)\varphi_1(\sigma - h) + g_1^\circ(\sigma), \quad \sigma \in \Omega,$$

$$\varphi_2(\sigma) = \lambda_2(\sigma)\varphi_2(\sigma - h) + g_2^\circ(\sigma), \quad \sigma \in \Omega, \tag{3.4}$$

with

$$g_1^\circ(\sigma) = \left(\frac{f_1(\sigma)}{2f^{1/2}(\sigma)} + \frac{1}{2} \right) g_1(\sigma) + \frac{g_2(\sigma)}{2f^{1/2}(\sigma)},$$

$$g_2^\circ(\sigma) = \left(-\frac{f_1(\sigma)}{2f^{1/2}(\sigma)} + \frac{1}{2} \right) g_1(\sigma) - \frac{g_2(\sigma)}{2f^{1/2}(\sigma)}, \quad \sigma \in \Omega. \tag{3.5}$$

and λ_1, λ_2 being the functions (2.10). To fix a branch of the function $f^{1/2}(s)$ we cut the strip Π by smooth curves $\Gamma_j \subset \Pi$ $(j = 0, 1, \ldots \rho)$ which do not intersect each other and join the branch points so that $\Gamma_j = s_{2j}s_{2j+1}$ $(j = 0, 1, \ldots \rho)$. The positive direction of Γ_j is chosen from s_{2j} to s_{2j+1}. Denote the limit value of the fixed branch on the left and the right sides of the cut as $[f^{1/2}(\sigma)]^+$ and $[f^{1/2}(\sigma)]^-$, respectively. Clearly, $[f^{1/2}(\sigma)]^+ = -[f^{1/2}(\sigma)]^-$, $\sigma \in \Gamma_j$.

Since the vector-function $\boldsymbol{\Phi}(s)$ must be single-valued in the strip Π, from (3.2), in addition, we get the following boundary condition on the system of curves Γ_j $(j = 0, 1, \ldots, \rho)$:

$$\mathbf{T}^+(\sigma)\varphi^+(\sigma) = \mathbf{T}^-(\sigma)\varphi^-(\sigma), \quad \sigma \in \Gamma_j. \tag{3.6}$$

This requirement recovers the linear relations between the limit values of the functions φ_1 and φ_2 on the curves Γ_j:

$$\varphi_1^+(\sigma) = \varphi_2^-(\sigma), \quad \varphi_1^-(\sigma) = \varphi_2^+(\sigma),$$

$$\sigma \in \Gamma_j \quad (j = 0, 1, \ldots, \rho). \tag{3.7}$$

Therefore, the original vector functional-difference equation (2.1) with the matrix coefficient (2.8) is equivalent to the system of two separate difference equations (3.4) and the two relations of Riemann-Hilbert type (3.7).

To reduce this new problem to a vector Riemann-Hilbert problem on a system of open contours, we map the s-strip Π onto a z-plane cut along the segment $[-1, 1]$. The mapping function and the inverse map are defined by

$$z = -i \tan \frac{\pi}{h}(s - \omega), \quad s = \omega + \frac{ih}{2\pi} \log \frac{1 + z}{1 - z}. \tag{3.8}$$

The contour Ω is mapped onto the upper side of the cut $[-1, 1]$ (the left bank with respect to the positive direction), the second side of the strip, Ω_{-1}, is mapped onto the lower side of the cut. The images of the upper and the lower infinite points of the strip Π, $x - i\infty$ and $x + i\infty$ ($\omega - h \leq x \leq \omega$), are the points $z = -1$ and $z = 1$, respectively. The function $\log[(1 + z)(1 - z)^{-1}]$ is real on the upper side of the cut. Introduce the following functions

$$F_j(z) = \varphi_j\left(\omega + \frac{ih}{2\pi} \log \frac{1 + z}{1 - z}\right), \quad z \in \mathbf{C},$$

$$l_j(t) = \lambda_j\left(\omega + \frac{ih}{2\pi} \log \frac{1 + t}{1 - t}\right), \quad t \in [-1, 1],$$

$$g_j^*(t) = g_j^\circ\left(\omega + \frac{ih}{2\pi} \log \frac{1 + t}{1 - t}\right), \quad t \in [-1, 1], \quad j = 1, 2, \tag{3.9}$$

and also the notations for the images of the branch points s_j and the poles a_k:

$$z_j = -i \tan \frac{\pi}{h}(s_j - \omega), \quad j = 0, 1, \ldots, 2\rho + 1,$$

$$\alpha_k = -i \tan \frac{\pi}{h}(a_k - \omega), \quad k = 1, 2, \ldots, m. \tag{3.10}$$

Let the cuts Γ_j be mapped onto curves γ_j ($j = 0, 1, \ldots \rho$). The curves $\gamma_j \subset \mathbf{C}$ and do not intersect each other and the segment $[-1, 1]$.

Thus, the system of equations (3.4), (3.7) is equivalent to the following vector Riemann-Hilbert problem

$$F_1^+(t) = l_1(t)F_1^-(t) + g_1^*(t), \quad t \in (-1, 1),$$

$$F_2^+(t) = l_2(t)F_2^-(t) + g_2^*(t), \quad t \in (-1, 1),$$

$$F_1^+(t) = F_2^-(t), \quad t \in \gamma_j,$$

$$F_2^+(t) = F_1^-(t), \quad t \in \gamma_j, \quad j = 0, 1, \ldots \rho. \tag{3.11}$$

Finally, we reduce this vector problem on the complex plane to a scalar problem on a Riemann surface. Let $\mathbf{R}$ be the two-sheeted surface of the algebraic equation

$$w^2 = q(z), \quad q(z) = (z - z_0)(z - z_1) \cdots (z - z_{2\rho+1}), \tag{3.12}$$

formed by gluing two copies $\mathbf{C}_1$ and $\mathbf{C}_2$ of the extended complex plane $\mathbf{C} \cup \infty$ cut along the system of the curves γ_j $(j = 0, 1, \ldots \rho)$. The positive (left) sides of the cuts γ_j on $\mathbf{C}_1$ are glued with the negative (right) sides of the curves γ_j on $\mathbf{C}_2$, and vice versa. This gives rise to a two-sheeted Riemann surface $\mathbf{R}$ of genus ρ. Then the function w, defined by (3.12), becomes single-valued on the surface $\mathbf{R}$:

$$w = \begin{cases} q^{1/2}(z), & z \in \mathbf{C}_1 \\ -q^{1/2}(z), & z \in \mathbf{C}_2, \end{cases} \tag{3.13}$$

where $q^{1/2}(z)$ is the branch chosen such that $q^{1/2}(z) \sim z^{\rho+1}$, $z \to \infty$.

Denote a point of the surface $\mathbf{R}$ with affix z on $\mathbf{C}_1$ by the pair $(z, q^{1/2}(z))$, and its counterpart on $\mathbf{C}_2$ by the pair $(z, -q^{1/2}(z))$. Introduce a function on the surface $\mathbf{R}$

$$F(z, w) = \begin{cases} F_1(z), & (z, w) \in \mathbf{C}_1 \\ F_2(z), & (z, w) \in \mathbf{C}_2. \end{cases} \tag{3.14}$$

Because of the third and forth conditions in (3.11), the function $F(z, w)$ is meromorphic everywhere on the surface except for the contour $\mathbf{L} = L_1 \cup L_2$, where $L_1 = (-1, 1) \subset \mathbf{C}_1$ and $L_2 = (-1, 1) \subset \mathbf{C}_2$. Therefore, the system (3.11) is equivalent to a scalar Riemann-Hilbert problem on the surface $\mathbf{R}$

$$F^+(t, \xi) = l(t, \xi) F^-(t, \xi) + g^*(t, \xi), \quad (t, \xi) \in \mathbf{L}, \tag{3.15}$$

where

$$l(t, \xi) = \begin{cases} l_1(t), & (t, \xi) \in L_1 \\ l_2(t), & (t, \xi) \in L_2, \end{cases} \quad g^*(t, \xi) = \begin{cases} g_1^*(t), & (t, \xi) \in L_1 \\ g_2^*(t), & (t, \xi) \in L_2, \end{cases} \tag{3.16}$$

and $\xi = w(t)$.

Without loss of generality, the Hölder function $l(t, \xi)$ does not vanish on the contour $\mathbf{L}$ and has definite limits at the end-points $t = \pm 1$. The function $g^*(t, \xi)$ is also a Hölder function on $\mathbf{L}$ except possibly the ends:

$$|g^*(t, \xi)| \leq A_0^{(j)} |t \mp 1|^{-\tilde{\nu}_j^\pm}, \quad (t, \xi) \in L_j \ (j = 1, 2), \quad t \to \pm 1, \tag{3.17}$$

where $A_0^{(j)} = \text{const}$. The parameters $\tilde{\nu}_j^\pm$ are defined from (3.5) by the behaviour at the points $\omega \pm i\infty$ of the functions $f_1(\sigma)$, $f^{1/2}(\sigma)$, $g_1(\sigma)$ and $g_2(\sigma)$.

A closed-form solution to the scalar Riemann-Hilbert problem (3.15) on a hyperelliptic surface is presented in [2] (see also [3]).

4. DIFFRACTION BY AN ANISOTROPIC IMPEDANCE HALF-PLANE

We give an example of a physical problem that can be solved by the technique presented. Consider scattering of an electromagnetic wave at skew incidence by an anisotropic half-plane with different impedances. Let the primary source be a plane wave incident obliquely whose z-components are

$$E_z^i = e_z e^{ik\rho \sin \beta \cos(\theta - \theta_0) - ikz \cos \beta},$$

$$Z_0 H_z^i = h_z e^{ik\rho \sin \beta \cos(\theta - \theta_0) - ikz \cos \beta}, \tag{4.1}$$

where (ρ, θ, z) are cylindrical coordinates, k is the wave number ($\mathrm{Im}(k) \leq 0$), Z_0 is the intrinsic impedance of free space, β is the angle of incident ($0 < \beta < \pi/2$), and e_z, h_z are prescribed parameters. In the most general case in which the impedance is anisotropic and differs on the upper and lower sides of the half-planes $\{0 < \rho < \infty, \theta = \pm\pi \mp 0, |z| < \infty\}$, the boundary conditions are [4]

$$E_\rho = \mp\eta_2^\pm Z_0 H_z, \quad \theta = \pm\pi \mp 0,$$

$$E_z = \pm\eta_1^\pm Z_0 H_\rho, \quad \theta = \pm\pi \mp 0, \tag{4.2}$$

where $\eta_1^\pm, \eta_2^\pm$ are the surface impedances of the upper ($\theta = \pi - 0$) and lower ($\theta = -\pi + 0$) half-planes, respectively. The boundary conditions (4.2) can also be written as

$$\frac{1}{\rho}\frac{\partial E_z}{\partial \theta} - \cos\beta \frac{\partial(Z_0 H_z)}{\partial \rho} \pm \frac{ik \sin^2 \beta E_z}{\eta_1^\pm} = 0, \quad \theta = \pm\pi \mp 0,$$

$$\frac{1}{\rho}\frac{\partial(Z_0 H_z)}{\partial \theta} + \cos\beta \frac{\partial E_z}{\partial \rho} \pm ik\eta_2^\pm \sin^2 \beta Z_0 H_z = 0, \quad \theta = \pm\pi \mp 0. \tag{4.3}$$

Represent the total field in the form of the Sommerfeld integral [1]

$$E_z(\rho, \theta, z) = \frac{e^{-ikz \cos \beta}}{2\pi i} \int_\gamma e^{ik\rho \sin \beta \cos \alpha} s_e(\alpha + \theta) d\alpha,$$

$$Z_0 H_z(\rho, \theta, z) = \frac{e^{-ikz \cos \beta}}{2\pi i} \int_\gamma e^{ik\rho \sin \beta \cos \alpha} s_h(\alpha + \theta) d\alpha, \tag{4.4}$$

where γ is the Sommerfeld contour, the functions $s_e(\alpha)$ and $s_h(\alpha)$ are analytic everywhere in the strip $-\pi < \mathrm{Re}(\alpha) < \pi$ apart from the point $\alpha = \theta_0$, where they have a simple pole with the residues defined by the incident field (4.1). At the infinite points $\alpha = x \pm i\infty$ ($|x| < \infty$), the

functions $s_e(\alpha)$ and $s_h(\alpha)$ are bounded. The boundary conditions (4.3) are satisfied if and only if the functions [5]

$$\Phi_1(\alpha + \pi) = \left(\sin\alpha + \frac{1}{\eta_1^+}\sin\beta\right) s_e(\alpha + \pi) - \cos\alpha\cos\beta s_h(\alpha + \pi),$$

$$\Phi_2(\alpha + \pi) = \left(\sin\alpha + \eta_2^+\sin\beta\right) s_h(\alpha + \pi) + \cos\alpha\cos\beta s_e(\alpha + \pi) \quad (4.5)$$

solve the following vector functional-difference equation

$$\mathbf{\Phi}(\sigma) = \mathbf{G}(\sigma)\mathbf{\Phi}(\sigma - 4\pi), \quad \sigma \in \Omega, \quad (4.6)$$

where

$$\mathbf{\Phi}(\sigma) = \begin{pmatrix} \Phi_1(\sigma) \\ \Phi_2(\sigma) \end{pmatrix}, \qquad \mathbf{G}(\sigma) = \begin{pmatrix} G_{11}(\sigma) & G_{12}(\sigma) \\ G_{21}(\sigma) & G_{22}(\sigma) \end{pmatrix}, \quad (4.7)$$

with

$$G_{11}(\sigma) = \frac{\Gamma_\sigma(1/\eta_1^-, -\eta_2^+)\Gamma_\sigma(1/\eta_1^+, -\eta_2^-) + \eta_2\eta_1^{-1}\cos^2\sigma\sin^2 2\beta}{D(\sigma)},$$

$$G_{22}(\sigma) = \frac{\Gamma_\sigma(-1/\eta_1^-, \eta_2^+)\Gamma_\sigma(-1/\eta_1^+, \eta_2^-) + \eta_2\eta_1^{-1}\cos^2\sigma\sin^2 2\beta}{D(\sigma)},$$

$$G_{12}(\sigma) = -\frac{\eta_0^-\sin\beta\sin 2\beta\sin 2\sigma}{\eta_1 D(\sigma)}, \quad G_{21}(\sigma) = \frac{\eta_0^+}{\eta_0^-}\eta_1\eta_2 G_{12}(\sigma),$$

$$D(\sigma) = \frac{\Gamma_\sigma(-1/\eta_1^+, -\eta_2^+)}{\Gamma_\sigma(1/\eta_1^+, \eta_2^+)}$$

$$\times[\Gamma_\sigma(-1/\eta_1^-, \eta_2^+)\Gamma_\sigma(1/\eta_1^+, -\eta_2^-) + \eta_2\eta_1^{-1}\cos^2\sigma\sin^2 2\beta],$$

$$\eta_0^+ = \eta_2^+ - \frac{1}{\eta_1^-}, \quad \eta_0^- = \eta_2^- - \frac{1}{\eta_1^+}, \quad \frac{1}{\eta_1} = \frac{1}{2}\left(\frac{1}{\eta_1^+} + \frac{1}{\eta_1^-}\right), \quad \eta_2 = \frac{\eta_2^+ + \eta_2^-}{2},$$

$$\Gamma_\alpha(a, b) = (\sin\alpha + a\sin\beta)(\sin\alpha + b\sin\beta) + \cos^2\alpha\cos^2\beta. \quad (4.8)$$

Equation (4.6) is a vector functional-difference equation of the first order with the shift $h = 4\pi$ subject to the additional condition of symmetry

$$\mathbf{\Phi}(\sigma) = \mathbf{\Phi}(2\pi - \sigma), \quad \sigma \in \Pi = \{-\pi < \mathrm{Re}(s) < 3\pi\}. \quad (4.9)$$

It is seen that the matrix (4.7) has the structure (2.8) required for the method to be applied. The key function of the method is

$$f(s) = f_1^2(s) + f_2(s) = \left[\frac{\eta_1(\eta_0^+ + \eta_0^-)\tan\beta}{4\eta_0^-\cos s}\right]^2 f^*(s), \quad (4.10)$$

where

$$f^*(s) = \left(\cos^2 s - \frac{1 - e_0 \sin^2 \beta}{\sin^2 \beta} \right)^2 + 16 e_1 \cos^2 s \cot^2 \beta,$$

$$e_0 = \frac{1}{\eta_0^+ + \eta_0^-} \left(\eta_0^+ \frac{\eta_2^-}{\eta_1^+} + \eta_0^- \frac{\eta_2^+}{\eta_1^-} \right), \quad e_1 = \frac{\eta_2 \eta_0^+ \eta_0^-}{\eta_1 (\eta_0^+ + \eta_0^-)^2}. \qquad (4.11)$$

The function $f^{1/2}(s)$ has 16 branch points in the strip $\Pi = \{-\pi < \mathrm{Re}(s) < 3\pi\}$. Because of its symmetry the problem (4.6) is equivalent to a scalar Riemann-Hilbert problem on a surface of genus 3 admitting a closed form-solution.

Acknowledgments

References

[1] G.D.MALIUZHINETS, *Excitation, reflection and emission of surface waves from a wedge with given face impedances*, Sov. Phys. Dokl., 3 (1958), 752-755.

[2] Y.A.ANTIPOV, V.V.SILVESTROV, *Vector functional-difference equation in electromagnetic scattering*, IMA J. Appl. Math., to appear.

[3] Y.A.ANTIPOV, V.V.SILVESTROV, *Factorisation on a Riemann surface in scattering theory*, Quart. J. Mech. Appl. Math., 55 (2002), 607-654.

[4] T.B.A.SENIOR, *Some problems involving imperfect half planes*, in Electromagnetic Scattering (ed. P.L.E.Uslenghi), (Academic Press, New York 1978) 185-219.

[5] T.B.A.SENIOR AND S.R.LEGAULT, *Diffraction by an anisotropic impedance half plane at skew incidence*, Electromagnetics, 18 (1998), 207-225.

DYNAMICS OF CHARGE ROTATORS AND LATTICE WAVES IN A PLASMA ENVIRONMENT

S.V. Vladimirov, M.P. Hertzberg, and N.F. Cramer

Department of Theoretical Physics, School of Physics, The University of Sydney, New South Wales 2006, Australia

S.Vladimirov@physics.usyd.edu.au

Keywords: Complex plasmas, lattice waves, rod-like particles, phase transitions, liquid plasma crystals

Abstract   Three dimensional rotatory modes of oscillations in a one-dimensional chain of rod-like charged particles or dust grains in a plasma are investigated. The dispersion characteristics of the modes are analyzed. The stability of different equilibrium orientations of the rods, phase transitions between the different equilibria, and a critical dependence on the relative strength of the confining potential are analyzed.

1.   INTRODUCTION

Recently, there has been an increasing interest in the properties of structures involving colloidal charged particles ("dust grains") levitating in a plasma [1]. The dynamic properties of the particle motion, formation of colloidal crystals and phase transitions in complex plasma systems are important fundamental questions related to the general theory of self-organization in open dissipative systems [1]. The cases already studied, experimentally and theoretically, mostly correspond to spherical grains, but there is growing interest in the properties of colloidal structures composed of elongated (cylindrical) particles [2, 3] levitating in the sheath region of a gas discharge plasma. In the experiments, various arrangements of such grains, levitating horizontally (i.e., oriented parallel to the lower electrode and perpendicular to the gravity force) and vertically (i.e., oriented perpendicular to the lower electrode and parallel to the gravity force) have been observed.

The oscillations of chains of point-like charged particles have previously been analyzed [4, 5]. Unlike point-like or spherical particles, elongated rotators exhibit a number of additional oscillations related to the new (rotational) degrees of freedom [6, 7]. Lattices composed of rod-like particles will therefore exhibit rotational oscillation modes, analogous to those existing in liquid crystals [8]. It is natural to expect that the excitation and interactions of all these modes will strongly affect the lattice dynamics, leading in particular to new types of phase transitions, as well as affecting those phase transitions already existing in lattices composed of spherical grains. Earlier we have briefly communicated the first results of the investigation of lattice oscillations in the one-dimensional chain consisting of rod-shaped particles [7] where characteristics of the modes associated with the motions and rotations of rods in the (vertical) plane of the chain were obtained. Here, we present a full three-dimensional analysis of the rotatory modes in the chain of rod-like particles, and analyze the critical dependence of the equilibrium and stability of such a chain on the external potential.

2.   BASIC EQUATIONS

Each rod-like particle is modeled as a rotator having two charges (and masses) concentrated on the ends of the rod, see Fig. 1, the upper charge being Q_a and the lower charge Q_b. For further simplicity, we assume that the charges are constant and the masses are equal. The rod of length L,
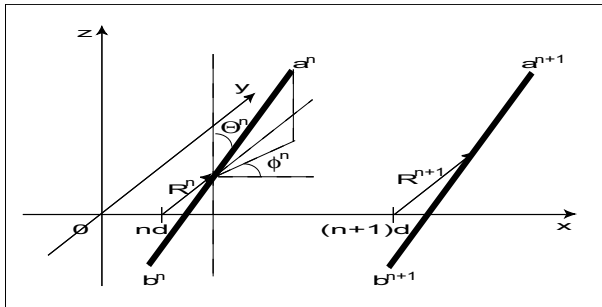
Figure 1   Geometry of rod.

connecting these two charges, has zero radius and mass. We consider a one-dimensional infinite linear chain of rods, with their centers of mass evenly separated by the distance d in equilibrium, along the x-axis.

The relevant forces are due to the external potentials and the interparticle interactions. The external potential Φ_{ext} is a combination of the

potentials due to both gravitation and the external electrodes. The inter-particle force is Coulombic in nature; since the dust grain is shielded by the surrounding plasma, there is an exponential decay of the interparticle potential with distance from each point charge, as follows from Debye-Hückel law. Hence, we can form the Lagrangian

$$\mathcal{L} = \frac{m}{2}\sum_n \left(\frac{d\mathbf{R}^n}{dt}\right)^2 + \frac{I}{2}\sum_n \left[\left(\frac{d\varphi^n}{dt}\right)^2 (\sin\theta^n)^2 + \left(\frac{d\theta^n}{dt}\right)^2\right]$$
$$- \left(\sum_n Q_a\Phi_a + \sum_n Q_a\Phi_b + \sum_n Q_b\Phi_a + \sum_n Q_b\Phi_b\right.$$
$$\left. + \sum_n Q_a\Phi_{\text{ext}} + \sum_n Q_b\Phi_{\text{ext}}\right), \quad (2.1)$$

where the sum is over all the particles, and I is the common rotational inertia of each particle. Here θ is the angle the rod makes with the z (vertical) axis, and φ is the angle the projection of the rod onto the $x - y$ (horizontal) plane makes with the x-axis (the direction of the chain of particles), see Fig. 1. The first two terms on the right hand side correspond to the kinetic energy, and terms like $Q_a\Phi_a$ describe the interaction on the upper charge Q_a of the nth particle with the potential Φ_a due to the upper charges Q_a of all the other particles, etc. Note the summation implied in the calculation of $\Phi_{a,b}$ for the nth particle is, in principle, over all the other particles. However, we shall only allow the two nearest neighbor interactions in our approximation.

Modes associated with the center of mass motion are analogous to those in chains of spherical particles [4, 5, 7] so here we investigate the rotational behavior, unique for rod-like particles, in detail. The Euler Lagrange equations of angular motion can then be written down for the nth particle,

$$\frac{d}{dt}\frac{\partial\mathcal{L}}{\partial\dot{\theta}^n} = \frac{\partial\mathcal{L}}{\partial\theta^n}, \quad (2.2)$$

and similarly for φ^n. In order to compute these derivatives we must write down the displacement vectors from each charge to each neighboring charge. Let $\mathbf{R}^n$ locate the center of mass of the nth dust grain, relative to the equilibrium position. We then define $\mathbf{S}^n$ to be the direction of the upper charge relative to the center of mass, so in spherical co-ordinates

$$\mathbf{S}^n = (\cos\varphi^n\sin\theta^n, \ \sin\varphi^n\sin\theta^n, \ \cos\theta^n). \quad (2.3)$$

We may now define the four displacement vectors *from* the charges on the $(n+1)^{\text{th}}$ grain *to* the charges on the nth grain as, for example,

$$\mathbf{r}_{aa}^{n+} = -d\mathbf{e}_x + (\mathbf{R}^n - \mathbf{R}^{n+1}) + \frac{L}{2}(\mathbf{S}^n - \mathbf{S}^{n+1}), \quad (2.4)$$

etc.; similar equations exist for the vectors from the charges on the $(n-1)^{\text{th}}$ grain to the charges on the nth grain.

The external potential can be approximated by a parabolic potential for small oscillations, whose minimum lies at the center of mass of a rod ($y = 0$, $z = 0$); note that the assumption of an infinite chain in the x-direction removes the need for a confining potential in that direction. We have

$$Q_a \Phi_{\text{ext}}(\mathbf{a}^n) + Q_b \Phi_{\text{ext}}(\mathbf{b}^n) = k_y y^2 + k_z z^2, \qquad (2.5)$$

where (y, z) are the coordinates of the upper charge Q_a. Note that the y-component of the external potential is purely electrical and the z-component is a combination of the electric and gravitational potentials.

We shall call the equilibrium colatitudinal and azimuthal angles, about which we consider small perturbations, θ_0 and φ_0 respectively, which are common to all particles. The analysis then proceeds as follows: let ϵ be a small perturbation of θ, so that $\theta^n = \theta_0 + \epsilon^n$; we may then approximate

$$\cos \theta^n = \cos \theta_0 - \sin \theta_0 \epsilon^n, \qquad (2.6)$$
$$\sin \theta^n = \sin \theta_0 + \cos \theta_0 \epsilon^n, \qquad (2.7)$$

and similarly for φ by letting η be a small perturbation from φ_0. Note that the linearizing process for terms like $\Phi_b'(\mathbf{r}_{ba}^{n+})/|\mathbf{r}_{ba}^{n+}|$ in fact involves taking the zeroth and first order terms in a Taylor expansion of six variables, namely ϵ^n, ϵ^{n+1}, ϵ^{n-1}, η^n, η^{n+1}, η^{n-1}. The full result for θ^n is long and complicated, and has only a numerical solution.

We next determine the common *equilibrium* orientation of the particles. Thus we set $\epsilon^n = \epsilon^{n+1} = \epsilon^{n-1} = \eta^n = \eta^{n+1} = \eta^{n-1} = 0$, and let the acceleration $\ddot{\theta}^n$ be zero. We find

$$\frac{Q_a L}{2} \left[\frac{\Phi_b'(\mathbf{r}_{ba}^{n+})}{|\mathbf{r}_{ba}^{n+}|} - \frac{\Phi_b'(\mathbf{r}_{ba}^{n-})}{|\mathbf{r}_{ba}^{n-}|} \right] d \cos \varphi_0 \cos \theta_0 - [a \leftrightarrow b]$$
$$- Q_a \frac{\partial \Phi_{\text{ext}}(\mathbf{a}^n)}{\partial \theta^n} - Q_b \frac{\partial \Phi_{\text{ext}}(\mathbf{b}^n)}{\partial \theta^n} = 0, \qquad (2.8)$$

where each term is to be evaluated at the relevant equilibrium orientation. Thus the external potential derivatives at each charge should vanish at the equilibrium; this occurs only at the y and z axes for a potential of the form (2.5), unless $k_y = k_z$. Similarly we must ensure

$$\left[\frac{\Phi_b'(\mathbf{r}_{ba}^{n+})}{|\mathbf{r}_{ba}^{n+}|} - \frac{\Phi_b'(\mathbf{r}_{ba}^{n-})}{|\mathbf{r}_{ba}^{n-}|} \right] d \cos \varphi_0 \cos \theta_0 = 0. \qquad (2.9)$$

The result is that equilibria exist in only the following orientations (unless $k_y = k_z$); $(\theta_0, \varphi_0) = (0, \varphi_0)$ (with φ_0 arbitrary) or $(\pi/2, 0)$ or $(\pi/2, \pi/2)$,
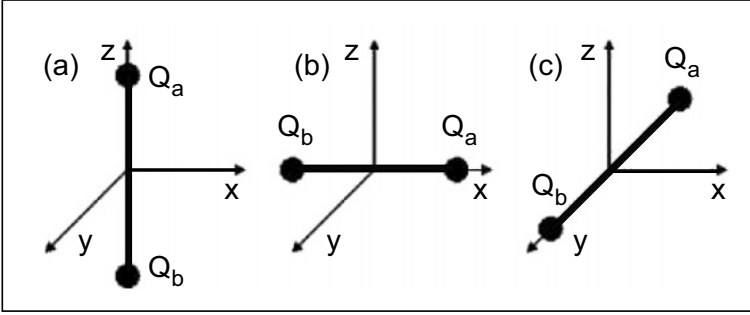
Figure 2   The three equilibrium orientations of the rod-like dust grains.

which we draw successively as shown in Fig. 2 (a), (b), and (c), respectively. If $k_y = k_z$, equilibrium exists for the orientation $(\theta_0, \pi/2)$, where θ_0 is arbitrary. Oscillations in θ about the second equilibrium have already been considered in Ref. [7], and oscillations in φ about that equilibrium can be obtained simply by exchanging k_y and k_z. Since φ is undefined for a vertically oriented rod, we concentrate here on the horizontal equilibrium case $(\pi/2, \pi/2)$.

3.   AZIMUTHAL MOTION

The perturbation equation describing small oscillations in azimuthal angle φ^n about the equilibrium Fig. 2(c), $\theta = \pi/2$, $\varphi = \pi/2$, can be written for the θ perturbation equation by rotating the y- and z-axes about the x-axis, so the new z-axis lies along the old y-axis. The equilibrium is now, in terms of the new polar angles, $(\theta'_0 = 0, \varphi'_0 = 0)$, and the perturbation η in the old angle φ is the negative of the perturbation η' in the new angle θ'. The resulting equation for η is

$$
I\ddot{\eta}^n = -\frac{L^2}{4}\left[Q_a\Phi''_a(d) - \frac{Q_a}{L_d}\Phi'_b(L_d)\right]\left(2\eta^n - \eta^{n+1} - \eta^{n-1}\right)
$$

$$
-\frac{d^2L^2}{4}\left[\frac{Q_a}{L_d^2}\Phi''_b(L_d) - \frac{Q_a}{L_d^3}\Phi'_b(L_d)\right]\left(2\eta^n + \eta^{n+1} + \eta^{n-1}\right)
$$

$$
+[Q_a \leftrightarrow Q_b] + \frac{L^2}{2}k_y\eta^n, \qquad (3.1)
$$

where $L_d^2 = L^2 + d^2$. Thus the ϵ and η behavior decouples. (In fact they decouple in all the above three equilibrium cases.) Note the presence of $2\eta^n - \eta^{n+1} - \eta^{n-1}$ in the first term. This term will vanish if all the rods rotate together. If we consider the upper charges Q_a all moving together,

it is apparent that this interaction should vanish, as a result of the $(n-1)^{\text{th}}$ and $(n+1)^{\text{th}}$ charges pushing in equal and opposite directions. However in the second term, the term $2\eta^n + \eta^{n+1} + \eta^{n-1}$ will not vanish. This is a consequence of the fact that as the rods rotate, the cross interaction between Q_a and Q_b (on adjacent rods) increases as they come closer together. The $(n+1)^{\text{th}}$ and $(n-1)^{\text{th}}$ contributions become unbalanced.

To investigate the existence of an oscillatory solution we compute the Fourier transform of Eq. (3.1), which gives the frequency ω as a function of the wavenumber k in the x-direction:

$$
I\omega^2 = +L^2 \left[Q_a \Phi_a''(d) - \frac{Q_a}{L_d} \Phi_b'(L_d) \right] \sin^2(kd/2)
$$

$$
+ \frac{d^2 L^2}{L_d^2} \left[Q_a \Phi_b''(L_d) - \frac{Q_a}{L_d} \Phi_b'(L_d) \right] \cos^2(kd/2)
$$

$$
+ [Q_a \leftrightarrow Q_b] - \frac{L^2}{2} k_y. \tag{3.2}
$$

Because of the Debye-Coulomb character of the potential in Eq. (3.2), the product $Q_a \Phi_a'$ is negative, while $Q_a \Phi_a''$ is positive, as is true for any potential that falls off with distance. The result is that the coefficients of the oscillatory sine and cosine terms in Eq. (3.2) are always positive. Thus the dust particles would always exhibit stable oscillations, except for the presence of the term $-k_y L^2/2$ from the external potential, which acts to pull the grains away from this equilibrium to the x-axis (where $y = 0$). These competing terms may then give rise to regions of stable behavior and regions of unstable behavior.

We may plot the dispersion relation, by selecting some typical values of the parameters involved: $m = 10^{-15}$kg, $Q = 10^3 e$ to $10^4 e$, and the plasma Debye length $\lambda_D = 300\mu$m. For the case $d \approx \lambda_D$, and for the particular choice of the external potential parameter $k_y = 10^{-10}$kg s^{-2} (which can be controlled in an experiment), the resulting dispersion relation is shown in Fig. 3. Note that the vertical axis is for the square of the normalized frequency $(\omega/\omega_0)^2$, where ω_0 is a typical dust plasma frequency with $\omega_0^2 = 3Q^2/(4\pi\varepsilon_0 m\lambda_D^3)$, which is normally a few hundred radians per second. The horizontal axis is a normalized wavenumber $k\lambda_D$. This plot clearly shows stable regions, corresponding to $\omega^2 > 0$, and unstable regions corresponding to $\omega^2 < 0$ (i.e ω imaginary.)

For a typical choice of the wavenumber, we can plot $(\omega/\omega_0)^2$ as a function of a normalized interparticle distance d/λ_D, (since d is typically of the order of the Debye length), as shown in Fig. 4. Clearly at close interparticle distances the motion is stable, as the particles oscillate under their mutual repulsion. However at large distances the external potential dominates, and the motion becomes unstable. This is a result of the interparticle

Figure 3 Normalized frequency squared versus normalized wavenumber for perturbations in the angle φ, traveling in the x direction. The equilibrium orientation is ($\theta_0 = \pi/2, \varphi_0 = \pi/2$). Here ω_0 is the dust plasma frequency, $d = \lambda_D$ and $k_y = 10^{-10} \text{kgs}^{-2}$.
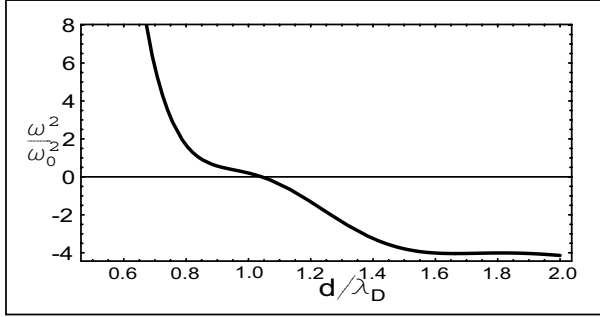
Figure 4 Normalized frequency squared versus interparticle distance for perturbations in the angle φ, travelling in the x direction. Here $k\lambda_D = 8$, and the other parameters are as for Fig. 3.

force decreasing with distance. Note that this instability will *always* arise at large distances, if $k_y > 0$. We reiterate that this horizontal motion is identical to the vertical case under the interchange $k_y \leftrightarrow k_z$.

4.   COLATITUDINAL MOTION

We now investigate the behaviour of the perturbation ϵ of the colatitudinal angle θ, recalling that ϵ and η completely decouple in the linear approximation. The equation of motion in the second (horizontal) equilib-

rium case is,

$$I\ddot{\epsilon}^n = -\frac{L^2}{4}\frac{Q_a}{d}\Phi'_a(d)(2\epsilon^n - \epsilon^{n+1} - \epsilon^{n-1})$$

$$+\frac{L^2}{4}\frac{Q_a}{L_d}\Phi'_b(L_d)(2\epsilon^n - \epsilon^{n+1} - \epsilon^{n-1})$$

$$+[Q_a \leftrightarrow Q_b] - \frac{L^2}{2}(k_z - k_y)\epsilon^n. \tag{4.1}$$

Note that this time *all* the dust particle interaction terms are of the form $2\epsilon^n - \epsilon^{n+1} - \epsilon^{n-1}$ and so the net force (apart from external influences) is zero if the rods rotate together. This expresses the fact that each plane (given by $\varphi_0 \equiv \pi/2$, and all θ_0 equal) is identical. Moreover, in the absence of an effective external potential (one in which $k_y = k_z$) there would exist equilibria at any θ_0 value, since we would have no preferred direction. The stability of cases such as these will be pursued in the next section.

Fourier transforming Eq. (4.1) leads to the following dispersion relation:

$$I\omega^2 = L^2\left[\frac{Q_a}{d}\Phi'_a(d) - \frac{Q_a}{L_d}\Phi'_b(L_d)\right]\sin^2(kd/2)$$

$$+[Q_a \leftrightarrow Q_b] + \frac{L^2}{2}(k_z - k_y). \tag{4.2}$$

Once again note the oscillatory dependence on wavenumber. The first term on the right hand side is this time *negative*, since $Q\Phi'(\mathbf{r}) < 0$ and $d < L_d$. Thus the dust particle's mutual repulsion causes instability. This results from the $Q_a\Phi_a$ interaction pushing away from equilibrium, dominating the cross interaction $Q_a\Phi_b$ that pushes back. Once again it is the fact that the dust grain's Debye-Coulomb potential falls off with distance that a net force results. Note the competing terms from the external potential. In the horizontal case one needs $k_z > k_y$ for the possibility of stability (of course wavenumber gaps are still possible). Note that similar dependence exhibit pairs of unbound spherical particles levitating in the confining potential in x- and z-directions [9] (other plasma collective effects such as the wake formation [6, 10] can also affect these arrangements). We also recall that the interchange $k_z \leftrightarrow k_y$ gives the vertical equilibrium case. By selecting $k_z > k_y$ the dispersion relation will be qualitatively the same as in Fig. 3.

However, the behavior of the frequency as a function of interparticle distance shows a noticeable difference to the azimuthal oscillation case, as shown in Fig. 5. Note the reversed characteristic, where stability now increases as the particles get further apart. We explain this as follows: at close distances the motion is highly unstable, since the repulsion due to the $Q_a\Phi_a$ and $Q_b\Phi_b$ terms is so strong. However in the far region, it is the sign of $k_z - k_y$ that determines stability.
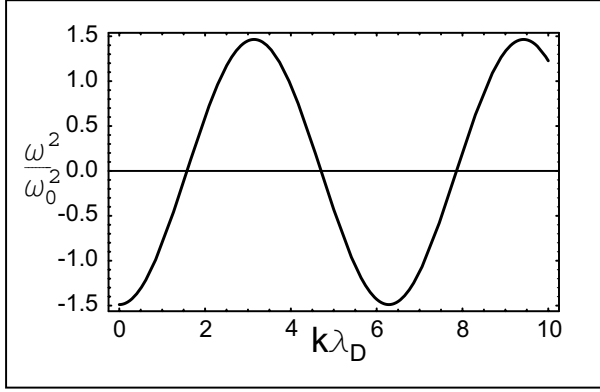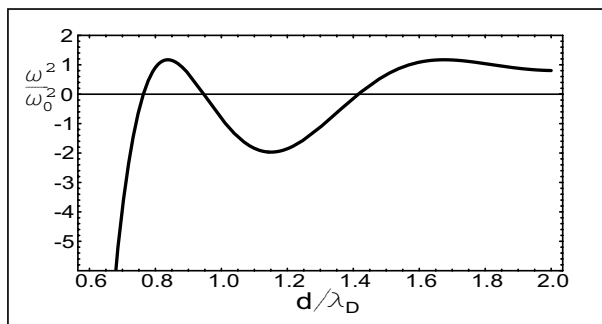
Figure 5 Normalized frequency squared versus interparticle distance for perturbations in the angle θ, traveling in the x direction. Here $k\lambda_D = 8$.

5. CONCLUSION

We found here that the different rotational modes of oscillation of rods are decoupled in the linear approximation. The specific behaviour was analysed through the dispersion relations. An oscillatory dependence on wavenumber was found, and a critical dependence on the relative strengths of the confining potential. The azimuthal and colatitudinal modes in fact showed opposite characteristics in the near and far interparticle distance regimes, respectively. The rods were then shown to move, or switch, to the relevant equilibrium, dependent on the confining parameters. This is a phase change phenomenon which has been observed in liquid crystals for instance.

Hence rods can undergo phase transitions from one state to another i.e vertical to horizontal and vice versa. These transitions have actually been observed in experiments [3]. Moreover, this has relations to processes in liquid crystals [8]. This is a state of matter between the solid and liquid phases, wherein rod shaped molecules exhibit a partial alignment, rather than a rigid array seen in crystals. The direction of this partial alignment (and phase) can be altered by an external influence.

The ability to line up rods, by alternating the relative sizes of the confining potentials, is a powerful tool. This can be of use in plasma coating for instance, if some rod shaped objects are used as the basis to give strength to a material. The nanotube industry is another exciting new area where this may have use [11]. The elongated shape of these carbon based molecules shows the obvious connection to our discussion of 'rods', although the particular rod shape analysed in this paper might differ from the true geometry of a nanotube.

Acknowledgments

References

[1] H.M. Thomas and G.E. Morfill, Nature **379**, 806 (1996).

[2] U. Mohideen, H. U. Rahman, M.A. Smith, *et al*, Phys. Rev. Lett. **81**, 349 (1998).

[3] B.M. Annaratone, A.G. Khrapak, A.V. Ivlev, *et al*, Phys. Rev. E **63**, 036406 (2001).

[4] S.V. Vladimirov, P.V. Shevchenko, and N.F. Cramer, Phys. Rev. E **56**, R74 (1997).

[5] S.V. Vladimirov, N.F. Cramer, and P.V. Shevchenko, Phys. Rev. E **60**, 7369 (1999).

[6] S.V. Vladimirov and M. Nambu, Phys. Rev. E **64**, 026403 (2001).

[7] S.V. Vladimirov and E.N. Tsoy, Phys. Rev. E **64**, 035402(R) (2001).

[8] S.Kumar, *Liquid Crystals: Experimental study of Physical Properties and Phase Transitions* (Cambride University, Cambridge, 2001).

[9] S.V. Vladimirov and A.A. Samarian, Phys. Rev. **65**, 046416 (2002).

[10] S.V. Vladimirov and M. Nambu, Phys. Rev. E **52**, 2172 (1995).

[11] M.S. Dresselhaus, G. Dresselhaus, *Carbon Nanotubes: Synthesis, Structure, Properties and Applications* (Springer, New York, 2001).

PROPAGATION OF ELASTIC WAVES ALONG INTERFACES IN LAYERED BEAMS

O. Avila-Pozos[1], A.B. Movchan[2] and S.V. Sorokin[3]

[1] *Instituto de Ciencias Básicas e Ingenieria, Universidad Autónoma del Estado de Hidalgo, Pachuca 42074, MEXICO*

avilap@uaeh.reduaeh.mx

[2] *Department of Mathematical Sciences, University of Liverpool*
Liverpool L69 3BX, UK

abm@liv.ac.uk

[3] *Marine Technical University of St. Petersburg, St. Petersburg, RUSSIA*

Abstract   An asymptotic model is proposed for the analysis of a *long-wave* dynamic model for a layered structure with an imperfect interface. Two layers of isotropic material are connected by a thin and soft adhesive: effectively the layer of adhesive can be described as a surface of discontinuity for the longitudinal displacement. The asymptotic method enables us to derive the *lower-dimensional* differential equations that describe waves associated with the displacement jump across the adhesive.

1.   INTRODUCTION

This paper is based on the work [1], [2], [3] on modelling of thin-walled layered structures with high contrast in the elastic properties of the layers. In real physical structures, these models describe adhesive joints. The challenge in the asymptotic analysis is that the problem involves two small parameters: a geometrical parameter characterising the normalised thickness of the beam, and a physical small parameter corresponding to a normalised Young's modulus of the interior adhesive layer. The limit problems depend on the relation between these parameters. The study of the corresponding static problems was presented in [3].

The new development given here is in the analysis of the wave propagation problem for a layered structure containing an adhesive joint. We shall study discontinuity waves propagating along the adhesive joint. It is appropriate to mention the relevant work [4] and [5] on the vibrational response of plates in vacuo and vibrations of multi-layered beams.

The paper is organised as follows. Sections 2 and 3 describe the geometry and governing equations. Section 4 contains an outline of the structure of the asymptotic expansions. The formal asymptotic algorithm is implemented in Section 5. Section 6 gives an example, which illustrates the lower-dimensional asymptotic model.

2. THE GEOMETRY OF THE SANDWICH BEAM

In this section we define the geometry of a two-dimensional isotropic thin layered structure with an adhesive joint. The formulation of the problem includes two small parameters: the normalised thickness of the structure and the relative stiffness of the adhesive (similar to [1] and [3]).

Let us consider a thin rectangular domain which consists of three layers:

$$\Omega_1 = \{\mathbf{x} \in \mathbb{R}^2 : |x_1| < l \, , \, \epsilon(h/2 - h_1) + \epsilon^2 h_0 < x_2 < \epsilon h/2 + \epsilon^2 h_0\},$$
$$\Omega_2 = \{\mathbf{x} \in \mathbb{R}^2 : |x_1| < l \, , \, -\epsilon h/2 < x_2 < -\epsilon h/2 + \epsilon h_2\},$$
$$\Omega_0 = \{\mathbf{x} \in \mathbb{R}^2 : |x_1| < l \, , \, -\epsilon(h/2 - h_2) < x_2 < -\epsilon(h/2 - h_2) + \epsilon^2 h_0\},$$

where l and h_i , $i = 0, 1, 2$, have the same order of magnitude. Also we define h as $h = h_1 + h_2$. The elastic materials of the regions Ω_i are characterised by the Youngs moduli E_i and by the values ν_i of the Poisson ratio. The index i throughout the paper takes the values $0, 1$ and 2. By λ_i, μ_i we denote the Lamé constants of the elastic materials which are given as

$$\lambda_i = \frac{E_i \nu_i}{(1 + \nu_i)(1 - 2\nu_i)}, \quad \mu_i = \frac{E_i}{2(1 + \nu_i)}. \tag{2.1}$$

The interface boundary includes two parts, S_+ and S_-, specified by

$$\begin{aligned} S_+ &= \{\mathbf{x} : |x_1| < l \, , \, x_2 = -\epsilon(h/2 - h_2) + \epsilon^2 h_0\}, \\ S_- &= \{\mathbf{x} : |x_1| < l \, , \, x_2 = -\epsilon(h/2 - h_2)\}. \end{aligned} \tag{2.2}$$

The upper and lower surfaces of the compound region are

$$\begin{aligned} \Gamma_+ &= \{\mathbf{x} : |x_1| < l \, , \, x_2 = \epsilon^2 h_0 + \epsilon h/2\}, \\ \Gamma_- &= \{\mathbf{x} : |x_1| < l \, , \, x_2 = -\epsilon h/2\}. \end{aligned}$$

3. FORMULATION OF THE PROBLEM

In this section we consider propagation of elastic waves and the state of plane strain in the three-layered medium introduced in Section 2. Thus, the

displacement field given by $\mathbf{u}^{(i)} = (u_1^{(i)}(\mathbf{x}, t), u_2^{(i)}(\mathbf{x}, t))$ with $\mathbf{x} = (x_1, x_2)$, satisfies the system

$$\mu_i \nabla^2 \mathbf{u}^{(i)} + (\lambda_i + \mu_i) \nabla \nabla \cdot \mathbf{u}^{(i)} = \rho_i \frac{\partial^2}{\partial t^2} \mathbf{u}^{(i)}, \mathbf{x} \in \Omega_i; \; i = 0, 1, 2. \quad (3.1)$$

Here t denotes the time variable and ρ_i the density of the material at the region Ω_i.

For the surfaces of the compound region Ω_ϵ we prescribe free-traction conditions:

$$\mu_i \left(\frac{\partial u_2^{(i)}}{\partial x_1} + \frac{\partial u_1^{(i)}}{\partial x_2} \right) = 0, \; (2\mu_i + \lambda_i) \frac{\partial u_2^{(i)}}{\partial x_2} + \lambda_i \frac{\partial u_1^{(i)}}{\partial x_1} = 0, \; \text{on} \quad (3.2)$$

on Γ_+ $(i = 1)$ and Γ_- $(i = 2)$. On the interface surfaces, the displacement and traction continuity conditions are given by

$$\mu_i \left(\frac{\partial u_2^{(i)}}{\partial x_1} + \frac{\partial u_1^{(i)}}{\partial x_2} \right) = \mu_0 \left(\frac{\partial u_2^{(0)}}{\partial x_1} + \frac{\partial u_1^{(0)}}{\partial x_2} \right), \quad (3.3)$$

$$(2\mu_i + \lambda_i) \frac{\partial u_2^{(i)}}{\partial x_2} + \lambda_i \frac{\partial u_1^{(i)}}{\partial x_1} = (2\mu_0 + \lambda_0) \frac{\partial u_2^{(0)}}{\partial x_2} + \lambda_0 \frac{\partial u_1^{(0)}}{\partial x_1},$$

$$\mathbf{u}^{(i)} = \mathbf{u}^{(0)},$$

on S_+ $(i = 1)$ and S_- $(i = 2)$. We are interested in the analysis of time-harmonic vibrations of the beam and propagation of waves along the thin interface layer.

4.   THE STRUCTURE OF THE ASYMPTOTIC EXPANSIONS

In this section, additionally to the analysis given in [6], two time-scales are defined for each component of the displacement vector.

Stretched variables ξ_i, $i = 0, 1, 2$, are introduced to describe the transverse behaviour of the fields across the thickness of the beam and are given as

$$\begin{aligned} \xi_0 &= \epsilon^{-2}(x_2 + \epsilon(h/2 - h_2) - \epsilon^2 h_0/2), \\ \xi_1 &= \epsilon^{-1}(x_2 - \epsilon^2 h_0 - \epsilon h_2/2), \\ \xi_2 &= \epsilon^{-1}(x_2 + \epsilon h_1/2). \end{aligned} \quad (4.1)$$

In this way one can verify that

$$\xi_i \in [-h_i/2, h_i/2], \; i = 1, 2; \; \xi_0 \in [-h_0/2, h_0/2] \quad (4.2)$$

and

$$\partial_{x_2} = \epsilon^{-2} \partial_{\xi_0}, \; \partial_{x_2} = \epsilon^{-1} \partial_{\xi_i}, \; i = 1, 2, \quad (4.3)$$

where the notation ∂_α means the partial derivative with respect to α.

Longitudinal vibrations of a thin-walled structure occur at higher frequencies compared to flexural vibrations; slow and fast time variables are used to describe flexural and longitudinal vibrations, respectively.

The displacement field $\mathbf{u}^{(i)}$ is sought in the form of the following asymptotic expansions

$$\mathbf{u}^{(i)} \sim \mathbf{u}^{(i,0)}(x_1, \xi_i, \tau, T) + \epsilon \mathbf{u}^{(i,1)}(x_1, \xi_i, \tau, T) + \epsilon^2 \mathbf{u}^{(i,2)}(x_1, \xi_i, \tau, T) \quad (4.4)$$

where T and τ are scaled variables. Assuming that $T = \epsilon t$, (the slow variable) and $\tau \equiv t$ (the fast variable), we obtain

$$\partial_t^2 = \partial_\tau^2 + 2\epsilon \partial_{\tau T}^2 + \epsilon^2 \partial_T^2. \quad (4.5)$$

The displacement field is split into two terms as follows

$$u_j^{(i)}(x_1, \xi_i, t) = \tilde{u}_j^{(i)}(x_1, \xi_i, \tau) + \bar{u}_j^{(i)}(x_1, \xi_i, T). \quad (4.6)$$

If one substitutes the series (4.4) into (3.1), the boundary conditions (3.2), and analyses the coefficients near like powers of ϵ, it follows that the following recurrence relations hold on the cross-section

$$\mu_i \partial_{\xi_i}^2 u_1^{(i,k)} + (\lambda_i + \mu_i)\partial_{\xi_i x_1}^2 u_2^{(i,k-1)} + (\lambda_i + 2\mu_i)\partial_{x_1}^2 u_1^{(i,k-2)} = \\ \rho_i \left\{ \partial_\tau^2 u_1^{(i,k-2)} + \partial_T^2 u_1^{(i,k-4)} \right\}, \quad (4.7)$$

$$(2\mu_i + \lambda_i)\partial_{\xi_i}^2 u_2^{(i,k)} + (\lambda_i + \mu_i)\partial_{\xi_i x_1}^2 u_1^{(i,k-1)} + \mu_i \partial_{x_1}^2 u_2^{(i,k-2)} = \\ \rho_i \left\{ \partial_\tau^2 u_2^{(i,k-2)} + \partial_T^2 u_2^{(i,k-4)} \right\}, \quad (4.8)$$

for $\Omega_i, i = 1, 2$. Due to the fact that the middle layer is softer than the others, we use the relationship $E_0 = \epsilon^3 E$, where $E \sim E_1 \sim E_2$ (see (2.1)) and obtain

$$\mu \partial_{\xi_0}^2 u_1^{(0,k)} + (\lambda + \mu)\partial_{\xi_0 x_1}^2 u_2^{(0,k-2)} + (\lambda + 2\mu)\partial_{x_1}^2 u_1^{(0,k-4)} = \\ \rho_0 \left\{ \partial_\tau^2 u_1^{(0,k-1)} + \partial_T^2 u_1^{(0,k-3)} \right\}, \quad (4.9)$$

$$(2\mu + \lambda)\partial_{\xi_0}^2 u_2^{(0,k)} + (\lambda + \mu)\partial_{\xi_0 x_1}^2 u_1^{(j,k-2)} + \mu \partial_{x_1}^2 u_2^{(0,k-4)} = \\ \rho_0 \left\{ \partial_\tau^2 u_2^{(0,k-1)} + \partial_T^2 u_2^{(0,k-3)} \right\}, \quad (4.10)$$

in Ω_0. As for the static case (see [1]), we have the following interface boundary conditions

$$\mu_i(\partial_{\xi_1} u_1^{(i,k)} + \partial_{x_1} u_2^{(i,k-1)}) = \mu(\partial_{\xi_0} u_1^{(0,k-2)} + \partial_{x_1} u_2^{(0,k-4)}),$$
$$(2\mu_i + \lambda_i)\partial_{\xi_1} u_2^{(i,k)} + \lambda_i \partial_{x_1} u_1^{(i,k-1)} = (2\mu + \lambda)\partial_{\xi_0} u_2^{(0,k-2)} + \lambda \partial_{x_1} u_1^{(0,k-4)},$$
$$u_j^{(0,k)} = u_j^{(i,k)} \quad j = 1, 2, \quad (4.11)$$

on S_+ $(i = 1)$ and S_- $(i = 2)$.

For the upper and lower surfaces we have

$$\mu_i(\partial_{\xi_1} u_1^{(i,k)} + \partial_{x_1} u_2^{(i,k-1)}) = 0, \tag{4.12}$$

$$(2\mu_i + \lambda_i)\partial_{\xi_1} u_2^{(i,k)} + \lambda_i \partial_{x_1} u_1^{(i,k-1)} = 0,$$

on Γ_+ $(i = 1)$ and Γ_- $(i = 2)$.

5.   FORMAL ASYMPTOTIC ALGORITHM

At each step of the asymptotic algorithm, solvability conditions of the model boundary value problems (BVP) on the cross-section are formulated and analysed.

For the transverse components, the following condition for the *slow components* is obtained

$$\boxed{\bar{u}_2^{(1,0)} = \bar{u}_2^{(2,0)} = \bar{u}_2^{(0,0)} \equiv \bar{u}_2^{(0)}.} \tag{5.1}$$

This means that to the leading-order, all points on the cross-section of the beam have the same transverse displacement in slow motions. This agrees with the Kirchhoff hypothesis adopted in the classical theory of flexural motions of elastic beams. For the *fast components* the solvability conditions of relevant model problems give a system of ordinary differential equations

$$\boxed{\frac{\rho_1 h_0 h_1}{\lambda + 2\mu}\partial_\tau^2 \tilde{u}_2^{(1,0)} + \tilde{u}_2^{(1,0)} - \tilde{u}_2^{(2,0)} = 0,} \tag{5.2}$$

$$\boxed{\frac{\rho_2 h_0 h_2}{\lambda + 2\mu}\partial_\tau^2 \tilde{u}_2^{(2,0)} + \tilde{u}_2^{(2,0)} - \tilde{u}_2^{(1,0)} = 0.} \tag{5.3}$$

These equations describe the transverse x_1-independent motion within a composite beam. With these conditions taken into account, the functions $u_2^{(i,2)}$ are given by

$$u_2^{(1,2)} = \frac{\lambda_1}{2\mu_1 + \lambda_1}\left[\frac{\xi_1^2}{2}(\partial_{x_1}^2 \tilde{u}_2^{(1,0)} + \partial_{x_1}^2 \bar{u}_2^{(1,0)}) - \xi_1(\partial_{x_1}\tilde{v}^{(1)} + \partial_{x_1}\bar{v}^{(1)})\right]$$

$$+\frac{\rho_1}{2\mu_1 + \lambda_1}\left[\frac{\xi_1^2}{2} - \frac{\xi_1 h_1}{2}\right]\partial_\tau^2 \tilde{u}_2^{(1,0)}, \tag{5.4}$$

$$u_2^{(2,2)} = \frac{\lambda_2}{2\mu_2 + \lambda_2}\left[\frac{\xi_2^2}{2}(\partial_{x_1}^2 \tilde{u}_2^{(2,0)} + \partial_{x_1}^2 \bar{u}_2^{(2,0)}) - \xi_2(\partial_{x_1}\tilde{v}^{(2)} + \partial_{x_1}\bar{v}^{(2)})\right]$$

$$+\frac{\rho_2}{2\mu_2 + \lambda_2}\left[\frac{\xi_2^2}{2} + \frac{\xi_2 h_2}{2}\right]\partial_\tau^2 \tilde{u}_2^{(2,0)}. \tag{5.5}$$

We note that

$$u_1^{(i,1)} = -\xi_i \left[\partial_{x_1} \tilde{u}_2^{(i,0)} + \partial_{x_1} \bar{u}_2^{(i,0)} \right] + \tilde{v}^{(i)}(x_1, \tau) + \bar{v}^{(i)}(x_1, T), \ i = 1, 2$$

The functions $\bar{v}^{(i)}$ satisfy second-order differential equations derived as solvability conditions (when $k = 3$) for model problems associated with "slow" motions.

$$\frac{4(\lambda_1 + \mu_1)}{2\mu_1 + \lambda_1} h_1 \partial_{x_1}^2 \bar{v}^{(1)} = \frac{\mu}{\mu_1 h_0} \left\{ \frac{h_1 + h_2}{2} \partial_{x_1} \bar{u}_2^{(0)} + \bar{v}^{(1)} - \bar{v}^{(2)} \right\}, \quad (5.6)$$

$$\frac{4(\lambda_2 + \mu_2)}{2\mu_2 + \lambda_2} h_2 \partial_{x_1}^2 \bar{v}^{(2)} = -\frac{\mu}{\mu_2 h_0} \left\{ \frac{h_1 + h_2}{2} \partial_{x_1} \bar{u}_2^{(0)} + \bar{v}^{(1)} - \bar{v}^{(2)} \right\}. \quad (5.7)$$

For the fast motions we obtain

$$\frac{4(\lambda_1 + \mu_1)}{2\mu_1 + \lambda_1} h_1 \partial_{x_1}^2 \tilde{v}^{(1)} + \frac{\rho_1 h_1}{\mu_1} \left\{ \frac{\lambda_1 h_1}{2(2\mu_1 + \lambda_1)} \partial_{x_1 \tau^2}^3 \tilde{u}_2^{(1,0)} - \partial_\tau^2 \tilde{v}^{(1)} \right\}$$
$$= \frac{\mu}{\mu_1 h_0} \left\{ \frac{h_1}{2} \partial_{x_1} \tilde{u}_2^{(1,0)} + \frac{h_2}{2} \partial_{x_1} \tilde{u}_2^{(2,0)} + \tilde{v}^{(1)} - \tilde{v}^{(2)} \right\}, \quad (5.8)$$

$$\frac{4(\lambda_2 + \mu_2)}{2\mu_2 + \lambda_2} h_2 \partial_{x_1}^2 \tilde{v}^{(2)} + \frac{\rho_2 h_2}{\mu_2} \left\{ \frac{\lambda_2 h_2}{2(2\mu_2 + \lambda_2)} \partial_{x_1 \tau^2}^3 \tilde{u}_2^{(2,0)} - \partial_\tau^2 \tilde{v}^{(2)} \right\}$$
$$= -\frac{\mu}{\mu_2 h_0} \left\{ \frac{h_1}{2} \partial_{x_1} \tilde{u}_2^{(1,0)} + \frac{h_2}{2} \partial_{x_1} \tilde{u}_2^{(2,0)} + \bar{v}^{(1)} - \bar{v}^{(2)} \right\}. \quad (5.9)$$

Taking into account solvability conditions for the Neumann BVP on the cross-section at the step $k = 4$ for the transverse displacement components we can establish the following equations:

$$\frac{1}{3} \frac{\mu_1(\mu_1 + \lambda_1)}{2\mu_1 + \lambda_1} h_1^3 \partial_{x_1}^4 \bar{u}_2^{(0)} - 2\mu_1 \frac{\lambda_1 + \mu_1}{2\mu_1 + \lambda_1} h_1^2 \partial_{x_1}^3 \bar{v}^{(1)} + \rho_1 h_1 \partial_T^2 \bar{u}_2^{(0)}$$
$$+ \frac{2\mu + \lambda}{8h_0^2} \left\{ \frac{\lambda_1 h_1}{2h_0(2\mu_1 + \lambda_1)} \partial_{x_1} \bar{v}^{(1)} + \frac{\lambda_2 h_2}{2h_0(2\mu_2 + \lambda_2)} \partial_{x_1} \bar{v}^{(2)} \right.$$
$$\left. \left[\frac{\lambda_1 h_1 h_0}{2\mu_1 + \lambda_1} - \frac{\lambda_2 h_2 h_0}{2\mu_2 + \lambda_2} \right] \partial_{x_1}^2 \bar{u}_2^{(0)} \right\} = 0, \quad (5.10)$$

$$\frac{1}{3} \frac{\mu_2(\mu_2 + \lambda_2)}{2\mu_2 + \lambda_2} h_2^3 \partial_{x_1}^4 \bar{u}_2^{(0)} + 2\mu_2 \frac{\lambda_2 + \mu_2}{2\mu_2 + \lambda_2} h_2^2 \partial_{x_1}^3 \bar{v}^{(2)} + \rho_2 h_2 \partial_T^2 \bar{u}_2^{(0)}$$
$$- \frac{2\mu + \lambda}{8h_0^2} \left\{ \frac{\lambda_1 h_1}{2h_0(2\mu_1 + \lambda_1)} \partial_{x_1} \bar{v}^{(1)} + \frac{\lambda_2 h_2}{2h_0(2\mu_2 + \lambda_2)} \partial_{x_1} \bar{v}^{(2)} \right.$$
$$\left. \left[\frac{\lambda_1 h_1 h_0}{2\mu_1 + \lambda_1} - \frac{\lambda_2 h_2 h_0}{2\mu_2 + \lambda_2} \right] \partial_{x_1}^2 \bar{u}_2^{(0)} \right\} = 0. \quad (5.11)$$

We remark that these equations do not involve *fast* functions $\tilde{u}_2^{(i,4)}, i = 1, 2$.

6.   ILLUSTRATIVE EXAMPLE AND CONCLUDING REMARKS

As shown in the previous section, the asymptotic algorithm allows one to find explicitly lower-dimensional differential equations describing longitudinal and flexural vibrations within a composite beam.

Slow motions occur in accordance with the equations (5.6),(5.7),(5.10) and (5.11). The equations for the transverse components involve the fourth-order derivative in x_1, which is consistent with classical results of the theory of elastic beams (see, for example, [8]). However the presence of an imperfect interface provides a coupling between the longitudinal and transverse displacements associated with a slow motion.

Fast motions are described by the second-order differential equations (5.2), (5.3), (5.8) and (5.9). These motions may involve a longitudinal displacement jump, and discontinuity waves might propagate along the soft interface. Since the transverse fast motions occur according to equations (5.2) and (5.3), which do not include derivatives with respect to x_1, the transverse vibrations do not generate waves propagating along the adhesive joint.

Next, we consider an illustrative example. Assume that the upper and lower layers have the same thickness $h_1 = h_2$ and made of the same material ($\mu_1 = \mu_2, \lambda_1 = \lambda_2, \rho_1 = \rho_2$). Combining equations (5.10) and (5.11), and using equations (5.6) and (5.7), we obtain

$$\frac{h_1^3}{3} \frac{\mu_1(\mu_1 + \lambda_1)}{2\mu_1 + \lambda_1} \partial_{x_1}^4 \bar{u}_2^{(0)} + \rho_1 h_1 \partial_T^2 \bar{u}_2^{(0)} = 0. \qquad (6.1)$$

Seeking a solution of this equation in the form

$$\bar{u}_2^{(0)} = A \exp\left(ikx_1 - i\Omega T\right)$$

we derive the corresponding characteristic equation

$$\frac{2h_1^3}{3} \frac{\mu_1(\mu_1 + \lambda_1)}{2\mu_1 + \lambda_1} k^4 - 2\rho_1 h_1 \Omega^2 = 0.$$

The previous equation reduces to the standard dispersion relation attributed to the Kirchhoff theory:

$$Dk^4 - \rho_l h_1 \Omega^2 = 0, \qquad (6.2)$$

where $D = \frac{Eh_1^3}{12(1-\nu_1^2)}$.

For the case of fast motions we obtain the following system of differential equations:

$$\frac{4(\lambda_1 + \mu_1)}{2\mu_1 + \lambda_1} h_1 \partial_{x_1}^2 \tilde{v}^{(1)} + \frac{\rho_1 h_1}{\mu_1} \left\{ \frac{\lambda_1 h_1}{2(2\mu_1 + \lambda_1)} \partial_{x_1 \tau^2}^3 \tilde{u}_2^{(1,0)} - \partial_\tau^2 \tilde{v}^{(1)} \right\}$$

$$-\frac{\mu}{\mu_1 h_0} \left\{ \frac{h_1}{2} \partial_{x_1} \tilde{u}_2^{(1,0)} + \frac{h_1}{2} \partial_{x_1} \tilde{u}_2^{(2,0)} + \tilde{v}^{(1)} - \tilde{v}^{(2)} \right\} = 0, \qquad (6.3)$$

$$\frac{4(\lambda_1 + \mu_1)}{2\mu_1 + \lambda_1} h_1 \partial_{x_1}^2 \tilde{v}^{(2)} + \frac{\rho_1 h_1}{\mu_1} \left\{ \frac{\lambda_1 h_1}{2(2\mu_1 + \lambda_1)} \partial_{x_1 \tau^2}^3 \tilde{u}_2^{(2,0)} - \partial_\tau^2 \tilde{v}^{(2)} \right\}$$

$$+\frac{\mu}{\mu_1 h_0} \left\{ \frac{h_1}{2} \partial_{x_1} \tilde{u}_2^{(1,0)} + \frac{h_1}{2} \partial_{x_1} \tilde{u}_2^{(2,0)} + \tilde{v}^{(1)} - \tilde{v}^{(2)} \right\} = 0, \qquad (6.4)$$

$$\frac{\rho_1 h_0 h_1}{2\mu + \lambda} \partial_\tau^2 \tilde{u}_2^{(1,0)} + \tilde{u}_2^{(1,0)} - \tilde{u}_2^{(2,0)} = 0, \qquad (6.5)$$

$$\frac{\rho_1 h_0 h_1}{2\mu + \lambda} \partial_\tau^2 \tilde{u}_2^{(2,0)} + \tilde{u}_2^{(2,0)} - \tilde{u}_2^{(1,0)} = 0. \qquad (6.6)$$

A solution for the homogeneous problem (6.3)–(6.6) is sought in the form

$$\tilde{v}^{(j)} = A_j \exp\left(ikx_1 - i\omega\tau\right),$$
$$\tilde{u}_2^{(j,0)} = B_j \exp\left(ikx_1 - i\omega\tau\right),$$

where $j = 1, 2$. The corresponding characteristic equation has the roots given by

$$\omega_1^2 = 0, \qquad (6.7)$$

$$\omega_2^2 = \frac{2(2\mu + \lambda)}{\rho_1 h_1 h_0}. \qquad (6.8)$$

The first root (6.7) is related to a uniform transverse displacement of all three layers, and the second root (6.8) corresponds to an anti-phase vibration of the upper and lower layers, relative to each other.

The equation

$$\omega^2 = \frac{4\mu_1(\mu_1 + \lambda_1)}{\rho_1(2\mu_1 + \lambda_1)} k^2, \qquad (6.9)$$

corresponds to uniform longitudinal motions of the whole layered structure, with no displacement jump across the adhesive layer.

The equation

$$\omega^2 = \frac{4\mu_1(\mu_1 + \lambda_1)}{\rho_1(2\mu_1 + \lambda_1)} k^2 + \frac{2\mu}{\rho_1 h_1 h_0} \qquad (6.10)$$

describes anti-phase longitudinal motions of the upper and lower layers, representing shear mode of motions.

We can see that there exists a cut-off frequency which is given by

$$\omega = \omega_3 = \sqrt{\frac{2\mu}{\rho_1 h_1 h_0}}. \tag{6.11}$$

If the frequency of the signal does not exceed the critical value ω_3, the displacement jump may not propagate along the imperfect interface. Let

$$k_1 = \frac{\mu_1 + \lambda_1}{\sqrt{2h_1 h_0 \mu_1 (\mu_1 + \lambda_1)}}, \tag{6.12}$$

$$k_2 = \frac{2\mu_1 + \lambda_1}{\sqrt{2h_1 h_0 \mu_1 (\mu_1 + \lambda_1)}}. \tag{6.13}$$

The intersection points of the dispersion curves given by (k_1, ω_2) and (k_2, ω_2), correspond to the resonance modes involving transverse and longitudinal vibrations.

References

[1] A. Klarbring and A.B. Movchan, *Asymptotic modelling of adhesive joints*, Mechanics of Materials, **28**(1998), 137–145.

[2] A.B. Movchan and N.V. Movchan, Mathematical Modelling of Solids with Non-regular Boundaries, 1995, CRC Press, New York, London, Tokyo.

[3] O. Avila-Pozos, A. Klarbring and A.B. Movchan, *Asymptotic model of orthotropic highly inhomogeneous layered structure*, Mechanics of Materials, **31**(1999), 101–115.

[4] S.V. Sorokin, *Introduction to Structural Acoustics*, Institute of Mechanical Engineering, Aalborg University, August 1995, Report No. 28.

[5] M.R. Maheri and R.D. Adams, *On the flexural vibration of Timoshenko beams and the applicability of the analysis to a sandwich configuration*, Journal of Sound and Vibration, **209**(1998), No 3, 419–442.

[6] O. Avila-Pozos, *Mathematical Models of Layered Structures with an imperfect interface and delamination cracks*, PhD Thesis *University of Bath*, 1999.

[7] A. Kozlov, V.G. Maz'ya and A.B. Movchan, Asymptotic analysis of fields in multi-structures, 1999, Oxford University Press, Oxford, New York.

[8] Z. Hashin, *Plane anisotrpic beams*, Journal of Applied Mechanics: Trans. ASME Series E, 1967, 257–262.

LOW FREQUENCY BAND GAPS
AND LOCALISED MODES FOR ARRAYS
OF COATED INCLUSIONS

S.B. Platts and N.V. Movchan

Department of Mathematical Sciences, M & O Building, University of Liverpool, L69 3BX, U.K.

S.Platts@liv.ac.uk, nvm@liv.ac.uk

Abstract   We study the scattering of plane elastic waves (pressure and shear) by a finite stack of gratings, infinite and periodic in the x-direction, of circular cylindrical elastic inclusions placed in an infinite elastic medium. The inclusions are connected to the surrounding medium via a thin soft elastic layer. The constitutive equations for the layer are derived using an asymptotic technique [1]. The problem is then solved using the method of multipole expansions. Results show regular arrays of cylinders which act as elastic polarisers (i.e. they reflect one type of wave and transmit the other) and elastic filters, structures that do not transmit elastic waves. We also demonstrate that an elastic inclusion surrounded by a thin soft "coating" layer is responsible for creating localised modes in the low frequency range.

1.   INTRODUCTION

This paper presents a development of the previous work [3]-[5] in which we studied the scattering of elastic waves by arrays of circular cylindrical defects. The defects were voids, perfectly bonded elastic inclusions or fluid filled cylinders. Here we develop the formulation by introducing a thin soft elastic layer which bonds the inclusions to the surrounding (infinite) medium. Using the asymptotic technique of [1] we derive constitutive equations corresponding to a so-called linear interface across which the tractions remain continuous and proportional to the jump in the displacement. The algorithm involves calculating the reflection and transmission matrices for a single grating, and employing this information in a recurrence procedure to find the overall reflection and transmission properties for a stack of gratings.

2. FORMULATION FOR A SINGLE LAYER

We consider the problem of a plane elastic wave propagating in an infinite elastic medium, containing an array of infinitely long circular cylindrical inclusions, aligned along the z-axis. The cylinder spacing in the x-direction is denoted by d, and in the y-direction by η. The cylinder radius is r_c. We study the case where each inclusion is connected to the surrounding medium via a thin soft elastic layer of thickness εR, with $\varepsilon << 1$. The medium, the inclusions and the interface layer are assumed to be isotropic, with Lame constants λ and μ for the medium, λ_0 and μ_0 for the inclusions, and λ_1 and μ_1 for the interface layer.

The vectors $\mathbf{u}$, $\mathbf{u}^{(0)}$ and $\mathbf{u}^{(1)}$ of amplitudes of elastic displacements within the matrix, inclusions and layer respectively satisfy the following equations:

$$(\mathcal{L} + \rho\omega^2)\mathbf{u}(\mathbf{r}) := \mu \triangle \mathbf{u}(\mathbf{r}) + (\lambda + \mu)\nabla(\nabla \cdot \mathbf{u}(\mathbf{r}))$$

$$+\rho\omega^2\mathbf{u}(\mathbf{r}) = \mathbf{0} \quad \text{within the matrix,} \qquad (2.1)$$

$$(\mathcal{L}_0 + \rho_0\omega^2)\mathbf{u}^{(0)}(\mathbf{r}) := \mu_0 \triangle \mathbf{u}^{(0)}(\mathbf{r}) + (\lambda_0 + \mu_0)\nabla(\nabla \cdot \mathbf{u}^{(0)}(\mathbf{r}))$$

$$+\rho_0\omega^2\mathbf{u}^{(0)}(\mathbf{r}) = \mathbf{0} \quad \text{within the inclusions,} \qquad (2.2)$$

$$(\mathcal{L}_1 + \rho_1\omega^2)\mathbf{u}^{(1)}(\mathbf{r}) := \mu_1 \triangle \mathbf{u}^{(1)}(\mathbf{r}) + (\lambda_1 + \mu_1)\nabla(\nabla \cdot \mathbf{u}^{(1)}(\mathbf{r}))$$

$$+\rho_1\omega^2\mathbf{u}^{(1)}(\mathbf{r}) = \mathbf{0} \quad \text{within the layer,} \qquad (2.3)$$

where ρ_i is the (finite) density of each material, and ω is the angular frequency. Across each surface we assume continuity in displacements and tractions, giving on the surface of each inclusion,

$$\sum_{j=1}^{3} \sigma_{ij}^{(0)}(\mathbf{u}^{(0)}; r_c, \theta)n_j(\theta) = \sum_{j=1}^{3} \sigma_{ij}^{(1)}(\mathbf{u}^{(1)}; r_c, \theta)n_j(\theta), \quad i = 1, 2, 3 \qquad (2.4)$$

$$\mathbf{u}^{(0)}(r_c, \theta) = \mathbf{u}^{(1)}(r_c, \theta), \ 0 \leq \theta < 2\pi, \qquad (2.5)$$

where (r, θ) are the polar coordinates associated with the center of the cylinder. On the outer surface of the "coating" layer the conditions are

$$\sum_{j=1}^{3} \sigma_{ij}(\mathbf{u}; r_c + \varepsilon R, \theta)n_j(\theta) = \sum_{j=1}^{3} \sigma_{ij}^{(1)}(\mathbf{u}^{(1)}; r_c + \varepsilon R, \theta)n_j(\theta), \quad i = 1, 2, 3$$

$$\qquad (2.6)$$

$$\mathbf{u}(r_c + \varepsilon R, \theta) = \mathbf{u}^{(1)}(r_c + \varepsilon R, \theta), \ 0 \leq \theta < 2\pi. \qquad (2.7)$$

To solve the problem we require the so-called constitutive equations that describe what happens as the wave travels across the coating layer. We

employ the asymptotic technique of [1] leading to a set of conditions which specify continuity in tractions and a jump in displacements across the interface layer:

$$\sum_{j=1}^{3} \sigma_{ij}^{(0)}(\mathbf{u}^{(0)}; r_c, \theta)n_j(\theta) = \sum_{j=1}^{3} \sigma_{ij}(\mathbf{u}; r_c, \theta)n_j(\theta), \quad i = 1, 2, 3 \qquad (2.8)$$

$$u_r\Big|_{r=r_c} - u_r^{(0)}\Big|_{r=r_c} = \frac{R^2}{\lambda_1^* + 2\mu_1^*}\sigma_{rr}\Big|_{r=r_c}, \qquad (2.9)$$

$$u_\theta\Big|_{r=r_c} - u_\theta^{(0)}\Big|_{r=r_c} = \frac{R^2}{\mu_1^*}\sigma_{r\theta}\Big|_{r=r_c}, \qquad (2.10)$$

$$u_z\Big|_{r=r_c} - u_z^{(0)}\Big|_{r=r_c} = \frac{R^2}{\mu_1^*}\sigma_{zr}\Big|_{r=r_c}. \qquad (2.11)$$

Here we assume that the layer is thin and soft, that is, $\lambda_1 = \varepsilon\lambda_1^*$ and $\mu_1 = \varepsilon\mu_1^*$, where λ_1^* and μ_1^* are of the same order as λ_1 and μ_1. The conditions (2.8)-(2.11) characterise the so-called linear interface (see, for example, [1]).

For the out-of-plane shear problem, the Navier systems (2.1)-(2.2) simplify to the Helmholtz equations for the u_z and $u_z^{(0)}$ components of the displacements. The interface conditions for this problem are given by (2.8) and (2.11). The formulation for the out-of-plane shear problem is completed by specifying the incident wave and the quasi-periodicity condition in the x-direction, in the same way as in [3].

For the in-plane problem, we introduce scalar and vector potentials φ, φ_0 and $\boldsymbol{\psi}, \boldsymbol{\psi}_0$ such that

$$\mathbf{u}(\mathbf{r}) = \nabla\varphi + \nabla \times \boldsymbol{\psi}, \quad \mathbf{u}^{(0)}(\mathbf{r}) = \nabla\varphi_0 + \nabla \times \boldsymbol{\psi}_0, \qquad (2.12)$$

where $\boldsymbol{\psi} = (0, 0, \psi)$, $\boldsymbol{\psi}_0 = (0, 0, \psi_0)$. These potentials satisfy the Helmholtz equations (see, for example, [4]). The conditions (2.8)-(2.10) re-written in terms of the four potentials take the form:

$$\frac{R^2}{\lambda_1^* + 2\mu_1^*}\left[2\mu\left(\frac{1}{r}\frac{\partial^2\psi}{\partial\theta\partial r} - \frac{1}{r^2}\frac{\partial\psi}{\partial\theta} - \frac{1}{r}\frac{\partial\varphi}{\partial r} - \frac{1}{r^2}\frac{\partial^2\varphi}{\partial\theta^2}\right) - k_a^2(2\mu + \lambda)\varphi\right]$$

$$= \frac{\partial\varphi}{\partial r} + \frac{1}{r}\frac{\partial\psi}{\partial\theta} - \left(\frac{\partial\varphi_0}{\partial r} + \frac{1}{r}\frac{\partial\psi_0}{\partial\theta}\right), \quad r = r_c, \ 0 \le \theta < 2\pi,$$

$$\frac{R^2\mu}{\mu_1^*}\left[-\frac{2}{r^2}\frac{\partial\varphi}{\partial\theta} + \frac{2}{r}\frac{\partial^2\varphi}{\partial\theta\partial r} + k_b^2\psi + \frac{2}{r}\frac{\partial\psi}{\partial r} + \frac{2}{r^2}\frac{\partial^2\psi}{\partial\theta^2}\right] \qquad (2.13)$$

$$= \frac{1}{r}\frac{\partial\varphi}{\partial\theta} - \frac{\partial\psi}{\partial r} - \left(\frac{1}{r}\frac{\partial\varphi_0}{\partial\theta} - \frac{\partial\psi_0}{\partial r}\right),$$

$$\mu\left[-\frac{2}{r^2}\frac{\partial\varphi}{\partial\theta} + \frac{2}{r}\frac{\partial^2\varphi}{\partial\theta\partial r} + k_b^2\psi + \frac{2}{r}\frac{\partial\psi}{\partial r} + \frac{2}{r^2}\frac{\partial^2\psi}{\partial\theta^2}\right]$$

$$= \mu_0\left[-\frac{2}{r^2}\frac{\partial\varphi_0}{\partial\theta} + \frac{2}{r}\frac{\partial^2\varphi_0}{\partial\theta\partial r} + (k_b^{(0)})^2\psi_0 + \frac{2}{r}\frac{\partial\psi_0}{\partial r} + \frac{2}{r^2}\frac{\partial^2\psi_0}{\partial\theta^2}\right], \qquad (2.14)$$

$$\left[2\mu\left(\frac{1}{r}\frac{\partial^2\psi}{\partial\theta\partial r} - \frac{1}{r^2}\frac{\partial\psi}{\partial\theta} - \frac{1}{r}\frac{\partial\varphi}{\partial r} - \frac{1}{r^2}\frac{\partial^2\varphi}{\partial\theta^2}\right) - k_a^2(2\mu+\lambda)\varphi\right]$$

$$= \left[2\mu_0\left(\frac{1}{r}\frac{\partial^2\psi_0}{\partial\theta\partial r} - \frac{1}{r^2}\frac{\partial\psi_0}{\partial\theta} - \frac{1}{r}\frac{\partial\varphi_0}{\partial r} - \frac{1}{r^2}\frac{\partial^2\varphi_0}{\partial\theta^2}\right) - (k_a^{(0)})^2(2\mu_0+\lambda_0)\varphi_0\right].$$

The problem is finally completed by introducing the incident pressure (a-type) and shear (b-type) waves and the quasi-periodicity conditions for φ, φ_0 and ψ, ψ_0; see [3] for details.

3.   OUT-OF-PLANE SHEAR PROBLEM

The periodicity in the x-direction reduces the problem to a model problem for a unit cell (see [3] for details), which is solved using multipole expansions for u_z and $u_z^{(0)}$:

$$u_z(r,\theta) = \sum_{n=-\infty}^{\infty} \left[\mathcal{A}_n^b J_n(k_b r) + \mathcal{B}_n^b Y_n(k_b r)\right] e^{in\theta}, \qquad (3.1)$$

$$u_z^{(0)}(r,\theta) = \sum_{n=-\infty}^{\infty} \mathcal{C}_n^b J_n(k_b^{(0)} r) e^{in\theta}. \qquad (3.2)$$

The interface condition (2.11) is used to eliminate $\mathcal{C}_n^b$ from further calculations giving

$$\mathcal{C}_n^b = \frac{\mathcal{A}_n^b J_n(k_b r_c) + \mathcal{B}_n^b Y_n(k_b r_c)}{\alpha_b + \alpha^* k_b^{(0)} \alpha_b'}, \qquad (3.3)$$

where $\alpha^* = \mu_0 R/\mu_1^*$, $\alpha_b = J_n(k_b^{(0)} r_c)$, and prime denotes the derivative.

The continuity in tractions condition (2.8) implies

$$\mathcal{A}_n^b = -\mathcal{M}_n^b \mathcal{B}_n^b, \qquad (3.4)$$

where

$$\mathcal{M}_n^b = -\left(\frac{\mu k_b Y_n'(k_b r_c)(\alpha_b + \alpha^* k_b^{(0)} \alpha_b') - \mu_0 k_b^{(0)} \alpha_b' Y_n(k_b r_c)}{\mu_0 k_b^{(0)} \alpha_b' J_n(k_b r_c) - \mu k_b J_n'(k_b r_c)(\alpha_b - \alpha^* k_b^{(0)} \alpha_b')}\right). \qquad (3.5)$$

The problem is solved using Rayleigh's identity which, together with (3.4), gives a system of linear algebraic equations for the B coefficients. The reflection and transmission properties of a single grating are found from the reconstruction equations. The solution for a single grating is then employed in a recurrence procedure to calculate the overall scattering properties for a stack of gratings. An outline of the method and the reconstruction equations can be found in [3].

4. IN-PLANE PROPAGATION

The solution of the scattering problem for the vector case requires multipole expansions for φ, ψ and φ_0, ψ_0:

$$\varphi(r,\theta) = \sum_{n=-\infty}^{\infty} \left[A_n^a J_n(k_a r) + B_n^a Y_n(k_a r) \right] e^{in\theta}, \tag{4.1}$$

$$\psi(r,\theta) = \sum_{n=-\infty}^{\infty} \left[A_n^b J_n(k_b r) + B_n^b Y_n(k_b r) \right] e^{in\theta}, \tag{4.2}$$

$$\varphi_0(r,\theta) = \sum_{n=-\infty}^{\infty} C_n^a J_n(k_a^{(0)} r) \, e^{in\theta}, \quad \psi_0(r,\theta) = \sum_{n=-\infty}^{\infty} C_n^b J_n(k_b^{(0)} r) \, e^{in\theta}. \tag{4.3}$$

Substituting these expansions into (2.9) and (2.10) enables us to eliminate the coefficients C_n^a and C_n^b from further calculations. After rearranging we obtain

$$C_n^a \mathcal{D} = A_n^a(q_1 + \alpha E_5 - \beta E_1) + iA_n^b(q_2 + \alpha E_6 + \beta E_2)$$
$$+ B_n^a(q_3 + \alpha E_7 - \beta E_3) + iB_n^b(q_4 + \alpha E_8 + \beta E_4), \tag{4.4}$$
$$C_n^b \mathcal{D} = iA_n^a(q_5 + \gamma E_5 - \xi E_1) + A_n^b(q_6 - (\gamma E_6 + \xi E_2))$$
$$+ iB_n^a(q_7 + \gamma E_7 - \xi E_3) + B_n^b(q_8 - (\gamma E_8 + \xi E_4)), \tag{4.5}$$

where

$$\alpha = \frac{k_b^{(0)} R^2 \alpha_b'}{\lambda_1^* + 2\mu_1^*}, \quad \beta = \frac{lR^2 \alpha_b}{\mu_1^* r_c}, \tag{4.6}$$

$$\gamma = \frac{lR^2 \alpha_a}{r_c(\lambda_1^* + 2\mu_1^*)}, \quad \xi = \frac{k_a^{(0)} R^2 \alpha_a'}{\mu_1^*}, \quad \alpha_a = J_n(k_a^{(0)} r_c). \tag{4.7}$$

The expressions for $q_1 - q_8$, $E_1 - E_8$ and $\mathcal{D}$ are given in [4]. The multipole expansions (4.1)-(4.3) and the traction conditions (2.14) give us a matrix relation which connects the two sets of multipole coefficients A and B

$$\begin{pmatrix} A_n^a \\ A_n^b \end{pmatrix} = -\begin{pmatrix} M_n^{aa} & M_n^{ab} \\ M_n^{ba} & M_n^{bb} \end{pmatrix} \begin{pmatrix} B_n^a \\ B_n^b \end{pmatrix}. \tag{4.8}$$

The expressions for the M coefficients are similar to those in [4], with equations (4.4) and (4.5) replacing the original representations for the C coefficients.

To solve the problem we use a method similar to that of the out-of-plane shear problem; details can be found in [3].

5.   RESULTS

The diagrams in Figures 1 and 2 present the transmission efficiencies E_T^{aa}, E_T^{bb} defined by the formulae

$$E_T^{aa} = \sum_{p \in \Omega_a} |\tau_{pa}|^2, \; E_T^{bb} = \sum_{p \in \Omega_b} |\tau_{pb}|^2,$$

versus the normalised frequency $\tilde{\omega}$, where Ω_a, Ω_b denote the sets of indices corresponding to propagating orders of type a or b respectively, τ_{pa} and τ_{pb} are the transmission coefficients (see [3] for their representations). The normalised material parameters[1] for Figures 1(a)-(d) are $\rho = 1$, $\lambda = 2.3$ and $\mu = 1$ for the matrix, and $\rho_0 = 3.277$, $\lambda_0 = 1.916$, $\mu_0 = 1.642$ for the inclusions. (The choice of parameters corresponds to Cu as the inclusion material and Al as the matrix material, both having the same Poisson ratio of 0.35.) The results shown pertain to a stack of 20 gratings with $d = 1, \eta = 2$ and $r_c = 0.3$.

We study the effect of the "coating" layer on the transmission properties of the array by varying μ_1^* and λ_1^*, keeping the ratio λ_1^*/μ_1^* constant.

Figure 1(a) is for an array of perfectly bonded inclusions (given here for comparison), while Figs. 1(b)-(d) and Fig. 2(b) are for arrays of imperfectly bonded inclusions for different values of μ_1^* and λ_1^*. Fig. 1(b) for $\mu_1^* = 0.2$ exhibits a narrow common band gap in the low frequency range. Figs. 1(c)-(d) show that increasing the value of μ_1^* from 0.2 to 0.4 and 0.7 shifts this band gap to the higher frequency range.

In the higher frequency range the structures used in Figures 1(b)-(d) act as elastic filters (they reflect both types of waves) in the frequency range around 2.8 to 3.8 and as polarisers (reflect one type of wave and transmit the other) in the range $\tilde{\omega} = 4.2$ to $\tilde{\omega} = 5.0$.

Figure 2(b) is the transmission diagram for a square array of copper inclusions (of normalised radius $r_c = 0.1$) surrounded by a silicone layer in an epoxy matrix. The diagram shows a low frequency acoustic band gap. This can be attributed to the high density contrast between copper and epoxy which creates localised modes within the coating.

---

[1] We normalise the elastic constants by changing to non-dimensional coordinates $(x/d, y/d, z/d)$, dividing equations (2.1), (2.2) by μ/d^2 and taking $\tilde{\omega}^2 = \rho\omega^2 d/\mu$.
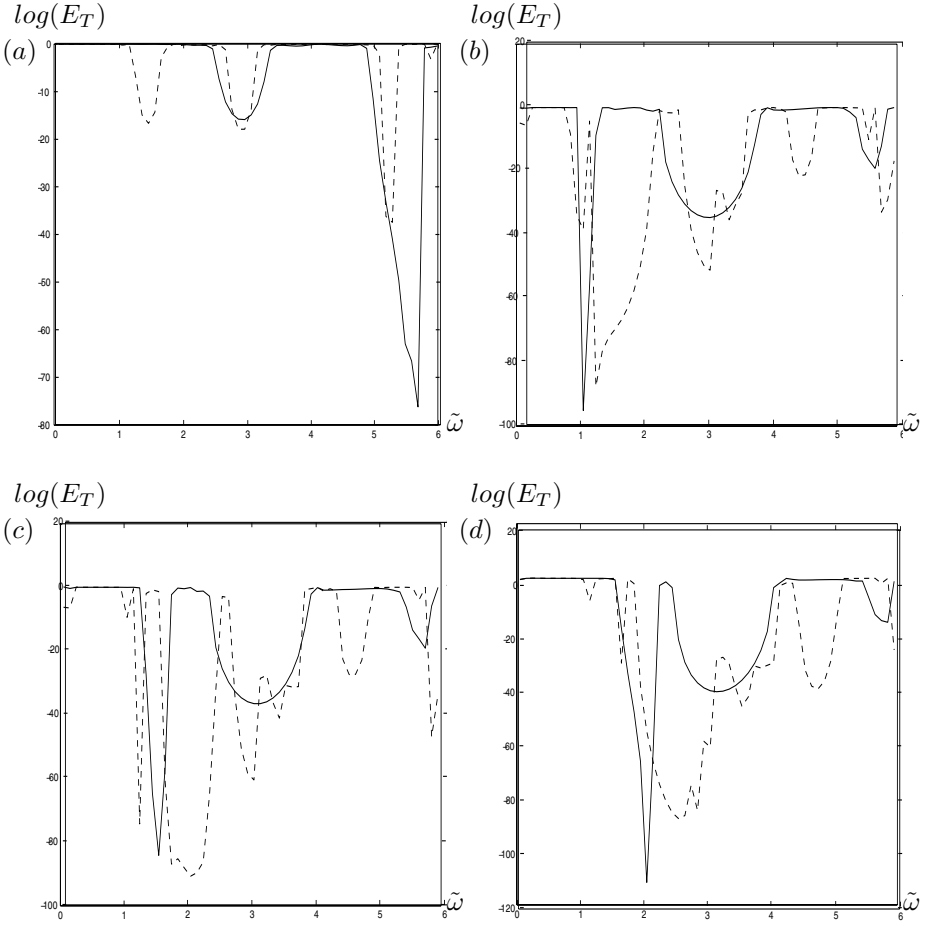
Figure 1 $Log(E_T^{(aa)})$ (solid line) and $Log(E_T^{(bb)})$ (dashed line) versus $\tilde{\omega} = (\rho\omega^2 d/\mu)^{1/2}$. Diagram (a) is for a regular array of perfectly bonded copper inclusions, (b)-(d) correspond to the same array of imperfectly bonded inclusions with $R = 1$, $\mu_1^* = 0.2, 0.4, 0.7$.
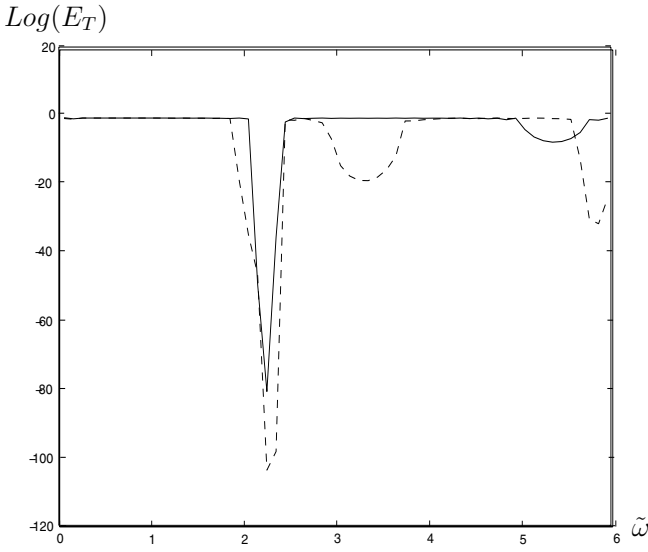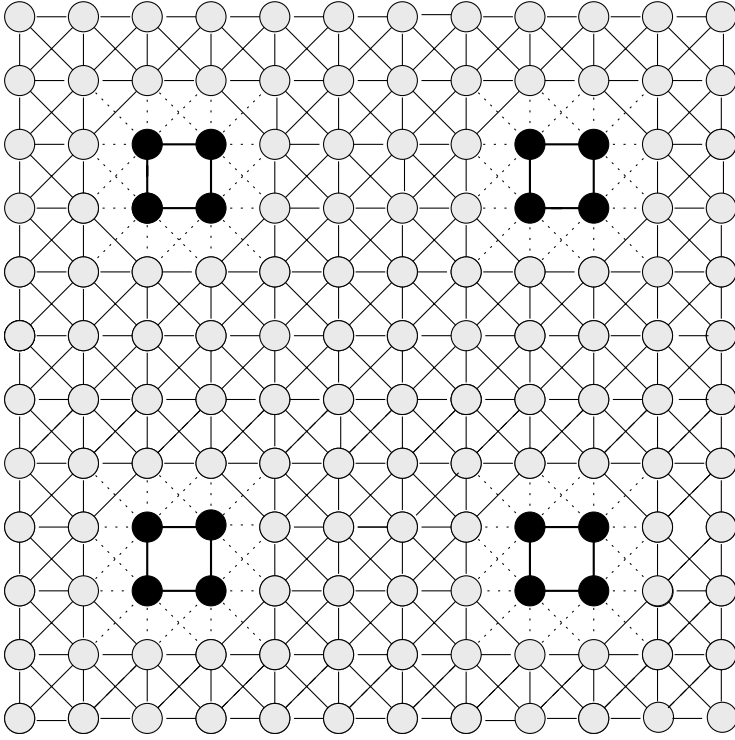
Figure 2 (a) is a schematic diagram of the discrete structure considered in [2], (b) is the transmission diagram for a square array of copper inclusions surrounded by a silicone layer in an epoxy matrix. $Log(E_T^{(aa)})$ is given by a solid line, and $Log(E_T^{(bb)})$ is given by a dashed line.

This is verified by comparing our result with that of [2], where a similar phenomenon has been observed for a discrete mass-spring model. The model consisted of an infinite array of 6×6 mass-spring unit cells, with each mass connected to its nearest neighbours by springs. Figure 2(a) shows schematically the discrete structure considered in [2]. The black circles connected by black lines represent the heavy inclusion, the dotted lines and solid lines correspond to the springs modelling the "coating" and the matrix material respectively.

The result for the discrete model (see Fig. 5(b) in [2]) is given in the form of a band gap diagram, which shows the propagating modes for all possible angles of incidence. It also shows a narrow band gap in a similar frequency range as the one in Figure 2(b).

6.   CONCLUSIONS

We have studied the propagation of waves through arrays of cylinders connected to an infinite elastic medium via a thin soft layer. Results show that these arrays exhibit good filtering and polarisation properties for elastic waves. We have demonstrated that the "coating" layer generates a narrow low frequency band gap corresponding to localised modes within the "coating".

Acknowledgment

References

[1] Bigoni, D., Serkov, S.K., Valentini, M. & Movchan, A.B. Asymptotic models of dilute composites with imperfectly bonded inclusions. *Int. J. Solids Structures*, **35**(1998), 3239-3258.

[2] Jensen, J.S. Phononic band gaps and vibrations in one- and two-dimensional mass-spring structures. (*to appear in Journal of Sound and Vibration*), 2003.

[3] Platts, S.B., Movchan, N.V., McPhedran, R.C. & Movchan, A.B. Two-dimensional phononic crystals and scattering of elastic waves by an array of voids. *Proc. R. Soc. Lond. A*, **458**(2002), 2327-2374.

[4] Platts, S.B., Movchan, N.V., McPhedran, R.C. & Movchan, A.B. Band gaps and elastic waves in disordered stacks: normal incidence. *Proc. R. Soc. Lond. A*, **459**(2003), 221-240.

[5] Platts, S.B. & Movchan, N.V. Scattering of elastic waves by a disorderd array of fluid filled cylinders: normal incidence. In: Applied Problems in Mechanics, 2002, St. Petersburg, Russia, 530-536.

PHONONIC BAND GAP STRUCTURES AS OPTIMAL DESIGNS

Jakob S. Jensen and Ole Sigmund

Department of Mechanical Engineering, Section for Solid Mechanics

Nils Koppels Allé, Building 404, Technical University of Denmark

DK-2800 Kgs. Lyngby, Denmark

jsj@mek.dtu.dk

Abstract   In this paper we use topology optimization to design phononic band gap structures. We consider 2D structures subjected to periodic loading and obtain the distribution of two materials with high contrast in material properties that gives the minimal vibrational response of the structure. Both in-plane and out-of-plane vibrations are considered.

1.   INTRODUCTION

In the last few decades the use of topology optimization methods has led to novel designs e.g. in compliant mechanisms, in MEMS applications, as well as in many other areas. An overview of theory and applications can be found in [1, 2]. This paper describes a new application of the method: the design of *phononic band gaps structures*.

Gaps may appear in the wave band structure for periodic materials implying that waves cannot propagate in certain frequency ranges. For propagation of electromagnetic waves the phenomenon is called photonic band gaps, see e.g. [3, 4], whereas for elastic waves we refer to phononic or acoustic band gaps. Much theoretical work has been done in the last decade dealing with the existence of band gaps for 2D and 3D periodic elastic materials, see e.g. [5, 6], and experimental support has been presented also, e.g. [7, 8].

Up to this point the work has mainly dealt with *prediction* and *observation* of band gaps for different materials and periodic configurations. In this work we show how topology optimization can be used to design periodic or near-periodic finite structures that are *optimal* with respect to a
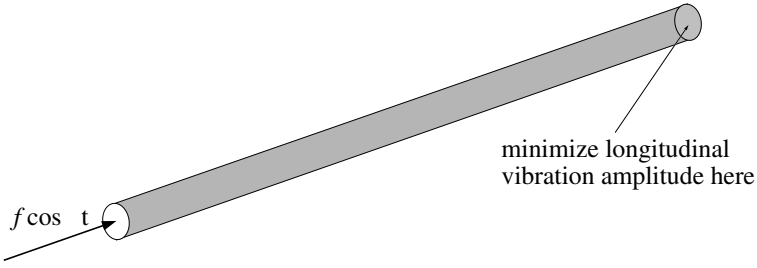
Figure 1 Simple optimization problem. Minimization of the longitudinal vibration amplitude in a thin rod subjected to a periodic force.

specific objective, e.g. minimization of the propagation of waves through a structure, minimization of the amplitude of vibration, or maximization of the output in certain structural areas (wave guiding). The method of topology optimization has already been successfully applied to the design of phononic band gap *materials* by maximizing the relative size of the band gaps [9], and optimization methods have been used also to enlarge the band gaps in photonic crystals, e.g. [10]. Some results regarding optimization of phononic band materials *and* structures have been obtained recently [11, 12].

The following example illustrates the basic idea. Figure 1 shows a model of a thin rod subjected to a periodic longitudinal force. The objective is now to distribute two materials, say PMMA and aluminum, so that the vibrational response at the end of the rod is minimized.

We model the longitudinal vibrations by the one-dimensional wave equation and discretize by dividing the rod into finite elements. A design variable x_e is now assigned to each element and this design variable is allowed to take values between 0 and 1, where 0 corresponds to material 1 (PMMA) and 1 to material 2 (aluminum). The optimal distribution of material is obtained by applying an iterative optimization algorithm utilizing e.g. Svanberg's MMA [13] and analytical sensitivities.

Figure 2 shows the optimized material distribution for minimal vibration amplitude for three rods of different lengths. The resulting structures are periodic-like with alternating sections of PMMA and aluminum with the number of sections and the relative distribution material in each section producing a band gap for $\Omega = 100\,\text{kHz}$. The designs are obtained without any *a priori* requirements to the solution, but band gap structures with a different number of alternating material sections can be obtained by changing the starting guess for the optimization algorithm. There seems to be no easy way to predict which of the possible band gap structures
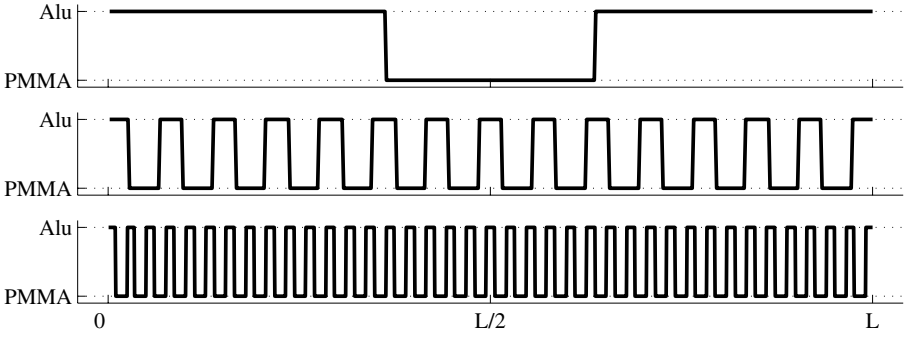
Figure 2 Optimal distribution of PMMA and aluminum in a thin rod subjected to a periodic force with frequency $\Omega = 100$ kHz for, top: $L = 0.02$ m, middle: $L = 0.15$ m, and bottom: $L = 0.4$ m.
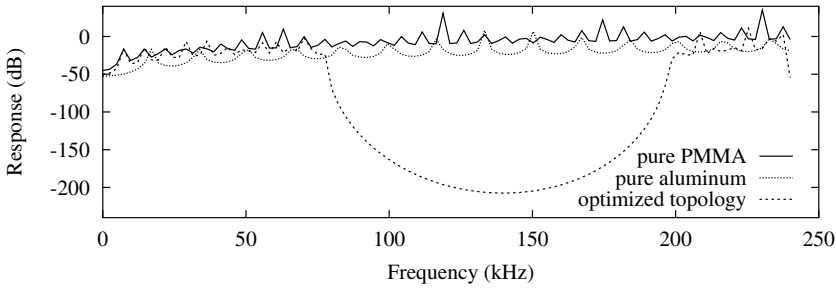
Figure 3 Frequency response for 15 cm rods of pure PMMA and aluminum and for the optimized rod for minimum response at $\Omega = 100$ kHz.

has the lowest response for the target frequency. It is also noted that the designs are purely "black-white", i.e. the design variables take only the values 0 and 1 meaning that no "intermediate materials" other than the two specified ones appear in the optimal design.

Figure 3 shows the corresponding response curves for the 15 cm rod. Shown are curves for the rods with pure PMMA and pure aluminum as well as for the rod optimized for a minimal response at $\Omega = 100$ kHz. A large reduction in the response is seen from $\Omega \approx 80$ kHz to $\Omega \approx 200$ kHz corresponding to the band gap frequency range for the periodic material. The response at the target frequency is reduced about 150 dB compared to the response for the homogeneous rods.

In the following, we will consider the more complex problem of minimizing the vibration amplitudes in 2D structures. In section 2 we define the basic equations and the finite element (FEM) model. In section 3

the topology optimization method is described and optimal structures are presented in section 4. Finally, in section 5 some conclusions are made.

2. WAVE PROPAGATION AND VIBRATIONS IN INHOMOGENEOUS ELASTIC MEDIA

The small-amplitude displacement of a 3D inhomogeneous elastic medium is governed by

$$\rho\frac{\partial^2 u}{\partial t^2} = \frac{\partial}{\partial x}\left(\lambda\nabla\cdot\mathbf{u}\right) + \nabla\cdot\left(\mu(\nabla u + \frac{\partial\mathbf{u}}{\partial x})\right) \tag{2.1}$$

$$\rho\frac{\partial^2 v}{\partial t^2} = \frac{\partial}{\partial y}\left(\lambda\nabla\cdot\mathbf{u}\right) + \nabla\cdot\left(\mu(\nabla v + \frac{\partial\mathbf{u}}{\partial y})\right) \tag{2.2}$$

$$\rho\frac{\partial^2 w}{\partial t^2} = \frac{\partial}{\partial z}\left(\lambda\nabla\cdot\mathbf{u}\right) + \nabla\cdot\left(\mu(\nabla w + \frac{\partial\mathbf{u}}{\partial z})\right) \tag{2.3}$$

where $\mathbf{u} = \{u\,v\,w\}^T$ is the displacement vector, (λ, μ) are Lamè's parameters, and ρ is the density.

In this paper we do not consider the full 3D problem. Instead we reduce the problem by considering waves that propagate in the xy-plane and allow the material to vary only in the xy-plane. The full problem (2.1)–(2.3) reduces into the coupled in-plane vector problem

$$\rho\frac{\partial^2 u}{\partial t^2} = \frac{\partial}{\partial x}\left((2\mu+\lambda)\frac{\partial u}{\partial x} + \lambda\frac{\partial v}{\partial y}\right) + \frac{\partial}{\partial y}\left(\mu(\frac{\partial u}{\partial y} + \frac{\partial v}{\partial x})\right) \tag{2.4}$$

$$\rho\frac{\partial^2 v}{\partial t^2} = \frac{\partial}{\partial x}\left(\mu(\frac{\partial v}{\partial x} + \frac{\partial u}{\partial y})\right) + \frac{\partial}{\partial y}\left((2\mu+\lambda)\frac{\partial v}{\partial y} + \lambda\frac{\partial u}{\partial x}\right) \tag{2.5}$$

and a scalar problem governing the out-of-plane motion

$$\rho\frac{\partial^2 w}{\partial t^2} = \frac{\partial}{\partial x}(\mu\frac{\partial w}{\partial x}) + \frac{\partial}{\partial y}(\mu\frac{\partial w}{\partial y}) \tag{2.6}$$

We apply external forcing with frequency Ω and analyze the time-reduced problem by expressing the displacement vector as

$$\mathbf{u} = \mathbf{a}e^{i\Omega t} \tag{2.7}$$

and insert (2.7) into either (2.4)–(2.5) or (2.6) depending on if the in-plane or out-of-plane problem is considered.

We now apply a standard finite element discretization and thereby recast the equations into matrix form

$$\left(\mathbf{K} + i\Omega\mathbf{C} - \Omega^2\mathbf{M}\right)\mathbf{a} = \mathbf{f} \tag{2.8}$$

where $\mathbf{f}$ is a force-amplitude vector, and where a damping matrix $\mathbf{C}$ has been added as well. As damping model is chosen a standard mass- and stiffness-proportional damping

$$\mathbf{C} = \alpha\mathbf{K} + \beta\mathbf{M} \tag{2.9}$$

where α and β are the two damping coefficients.

We now analyze two periodic structures made from band gap materials. In figure 4a,b are shown 10×10 cm structures consisting of an epoxy matrix with 5×5 aluminum inclusions of different shape placed in a 2D-quadratic array.[1]

Gaps in the band structure for aluminum inclusions in an epoxy matrix were previously considered, e.g. [7, 9]. In [9] it was shown that the *square* inclusions for some specific material properties were optimal for creating the widest band gap, but large band gaps exist for both periodic materials used in the structures in figure 4. Thus, with large band gaps forbidding the propagation of waves we can expect the vibrational response of the structure to be low in the corresponding frequency ranges.

The vibrational response is calculated for the structures subjected to in-plane periodic loading at the left boundary. The response is given as the average displacement at the right boundary and depicted in figure 4c. For the square inclusions a drop in the response appears between $\Omega \approx 53$ kHz and $\Omega \approx 79$ kHz except for a single resonance peak, and for the diamond-shaped inclusions a drop is seen between $\Omega \approx 56$ kHz and $\Omega \approx 74$ kHz also here with a resonance peak appearing in the frequency interval. For these frequency ranges band gaps exist for the corresponding periodic materials. For both structures a resonance peak appears inside the band gap. This is a local resonance involving the corners of the structure and it thus reflects an effect of the finite structural domain.

Thus, we can use a periodic material to create a structure that displays a significant decrease in the response in a certain frequency range. If we apply material optimization we can create a material with the largest possible band gap and consequently obtain a lower response. However, we cannot take into account effects due to the finite dimensions and the boundaries of the structure, and therefore structural optimization techniques are needed.

In figure 4c is also shown the response calculated for the square inclusions with mass-dependent damping included. With strong damping the resonance peaks have disappeared from the response. However, the response drop associated with the band gap is still seen in the response curve. This was also noticed in a recent study of the vibrational response of phononic

---

[1]Material data: $E_{alu} = 70$ GPa, $\rho_{alu} = 2700$ kg/m^3, $\nu_{alu} = 0.34$, $E_{epoxy} = 4.4$ GPa, $\rho_{epoxy} = 1200$ kg/m^3, $\nu_{epoxy} = 0.37$
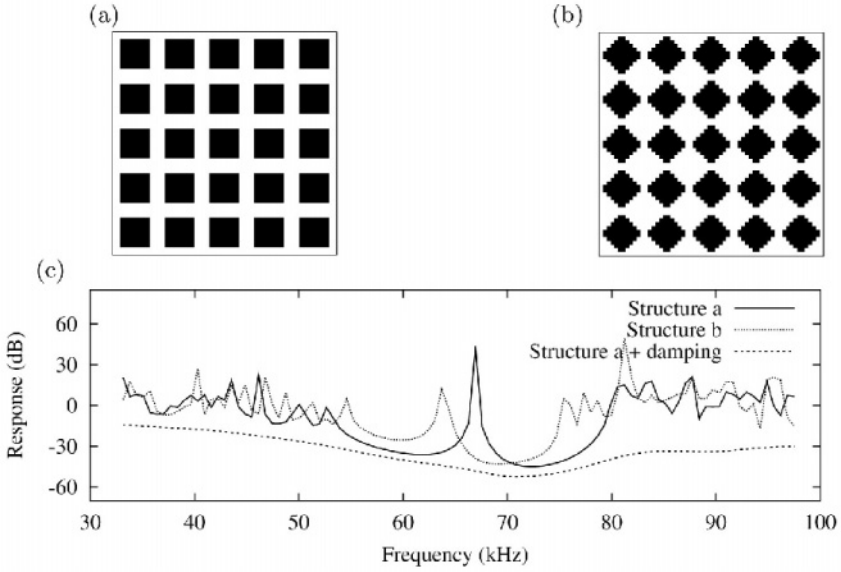
Figure 4 An epoxy matrix with 5×5 aluminum inclusions: (a) square inclusions, (b) diamond-shaped inclusions, and (c) the corresponding response of the two structures subjected to periodic loading at the left boundary, and the response of structure (a) with damping included ($\alpha = 0, \beta = 75000$).

band gap structures [14]. This important feature will be utilized in the optimization procedure to ensure convergence and avoid local minima.

3. TOPOLOGY OPTIMIZATION

In this section a short outline of the topology optimization method is presented.

We want to distribute two materials in the design domain and for this purpose introduce a design variable x_e in a number of structural elements, here conveniently chosen to coincide with the finite element discretization. The material properties in each element are now linearly interpolated as follows

$$\rho(x_e) = (1 - x_e)\rho_1 + x_e\rho_2 \tag{3.1}$$
$$\mu(x_e) = (1 - x_e)\mu_1 + x_e\mu_2 \tag{3.2}$$
$$\lambda(x_e) = (1 - x_e)\lambda_1 + x_e\lambda_2 \tag{3.3}$$

where the subscripts 1 and 2 correspond to the two materials.

With the objective of *minimizing* the structural response we can now formulate a topology optimization problem

$$\min_{\mathbf{x}} \quad c = |\mathbf{a}|^T \, \mathbf{L} \, |\mathbf{a}|$$

$$\text{s.t.}: \quad (\mathbf{K} + \mathrm{i}\Omega\mathbf{C} - \Omega^2\mathbf{M}) \, \mathbf{a} = \mathbf{f} \tag{3.4}$$

$$0 \le x_e \le 1, \quad e = 1, \ldots, N$$

where N is the number of finite elements and $\mathbf{L}$ is a zero matrix with ones at the diagonal elements corresponding to the degrees of freedom of the nodes, lines, or areas to be damped.

The optimization problem is solved using Svanberg's MMA [13]. We need to calculate the sensitivities of the objective function with respect to the design variables

$$\frac{\mathrm{d}c}{\mathrm{d}x_e} = 2\mathrm{Re}\left(\boldsymbol{\lambda}^T \left[\frac{\mathrm{d}\mathbf{K}}{\mathrm{d}x_e} + \mathrm{i}\Omega\frac{\mathrm{d}\mathbf{C}}{\mathrm{d}x_e} - \Omega^2\frac{\mathrm{d}\mathbf{M}}{\mathrm{d}x_e}\right] \mathbf{a}\right) \tag{3.5}$$

where $\boldsymbol{\lambda}$ is the solution to the adjoint problem

$$(\mathbf{K} + \mathrm{i}\Omega\mathbf{C} - \Omega^2\mathbf{M})^T \, \boldsymbol{\lambda} = -\mathbf{L}\bar{\mathbf{a}} \tag{3.6}$$

with the overbar denoting the complex conjugate. Thus, for each iteration step we need to solve the problem for only one extra load case in order to obtain the sensitivities.

4. RESULTS

We now apply the optimization method to design structures that have minimal vibrational response when they are subjected to periodic loading at the boundaries.

Consider the structures already analyzed in section 2 consisting of epoxy and aluminum. The periodic structure in figure 4a with square inclusions had low structural response in a large band gap frequency range. Thus, it can be expected that if we attempt to miminize the response for a frequency in this band gap frequency range we will obtain a topology close to the periodic one (also shown in figure 5a).

Figure 5b shows the result of the structural optimization: a topology with the optimal distribution of aluminum and epoxy for minimizing the response at $\Omega = 71\mathrm{kHz}$. In order to obtain the square symmetrical topology we solved a multi-load problem by applying the load a each boundary and minimizing the response at the opposite boundary for each load. The optimization was initially performed with mass-dependent damping included ($\alpha = 0$, $\beta = 75000$) in order to ensure convergence of the design but for the last few optimization iterations the damping was removed.
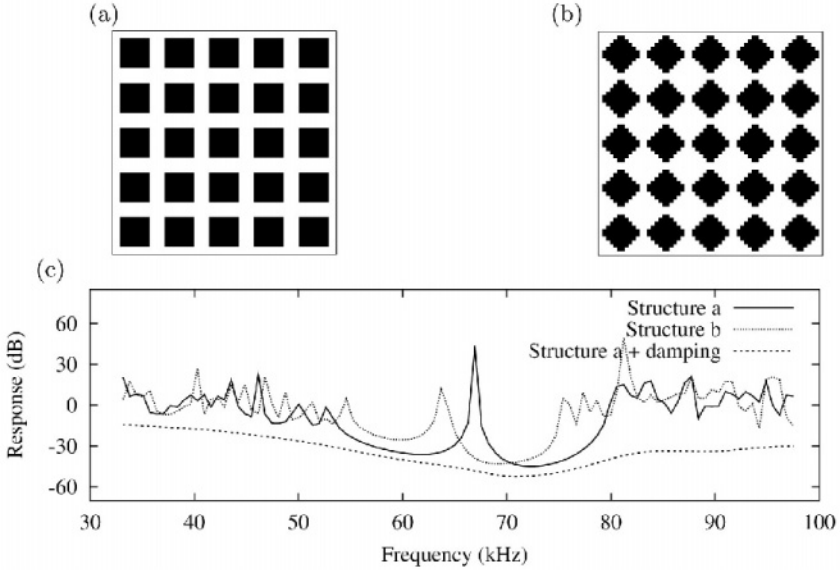
Figure 5 Optimization of a 10×10 cm structure subjected to in-plane loading, (a) periodic structure, (b) optimized topology for $\Omega = 71$ kHz, and (c) the response of the two structures to periodic loading.

We see that the optimal structure is near-periodic and resembles the periodic structure closely. It is noticed, when comparing to the periodic structure, that the largest difference is near the boundaries where aluminum inclusions have been moved to the rim. There is also some variation in size and shape of the inclusions due to the effect of boundaries. The reduction in response at the target frequency is ≈ 20 dB compared to the periodic structure.

We now consider the problem of out-of-plane vibrations. Figure 6a shows the 14×14 cm periodic structure and figure 6b the corresponding topology optimized structure obtained when optimizing for a minimal vibrational response at $\Omega \approx 45$ kHz.

The optimized topology in figure 6b is very close to being perfectly periodic, with the inclusions near the boundaries moved to the rim. It is also seen that the size of the inclusions are larger creating a larger gap in the response (figure 6c). For $\Omega = 45$ kHz the response of the optimized topology is ≈ 15 dB lower than for the periodic structure.

5. CONCLUSIONS

We have applied the topology optimization method to the design of phononic band gap structures.
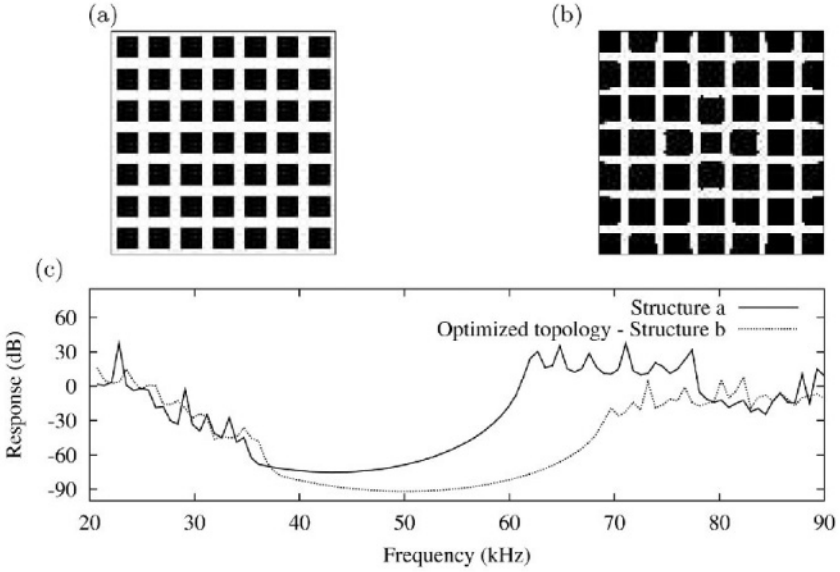
Figure 6   Optimization of a 14×14 cm structure subjected to out-of-plane loading, (a) periodic structure, (b) optimized topology for $\Omega = 45$ kHz, and (c) the response of the two structures to periodic loading.

The method provides a way to obtain the optimal distribution of two materials with different material properties, with the objective of e.g. minimizing the vibrational response of a structure subjected to a periodic force. In this paper we have shown that by using this method phononic band gap structures could be obtained that take into account the presence of the structural boundaries and finite dimensions.

It was discussed how damping in the computational model was important. We applied strong mass-dependent viscous damping and this was useful because it eliminated resonance peaks in the response but retained the band gap effect. In this way resonance-associated local minima were avoided and a better convergence of the optimization algorithm towards band gap structures was assured

A related application is in the design of wave guides [11, 12], where instead we *maximize* the response at certain structural points. The results obtained are promising with possible applications also in photonic wave guide structures.

All results presented in this paper were obtained with a relative coarse discretization in a Matlab code. An efficient Fortran code is currently being developed for treating larger problems, with the aim of also treating the full 3D problem.

Acknowledgments

References

[1] M. P. Bendsoe. *Optimization of Structural Topology, Shape and Material*. Springer Verlag, Berlin Heidelberg, 1995.

[2] M. P. Bendsoe and O. Sigmund. *Topology Optimization – Theory, Methods and Applications*. Springer Verlag, Berlin Heidelberg, 2003.

[3] J. D. Joannopoulos, R. D. Meade, and J. N. Winn. *Photonic Crystals*. Princeton University Press, New Jersey, 1995.

[4] E. Yablonovitch. Photonic crystals: semiconductors of light. *Scientific American*, 285(6):34–41, 2001.

[5] M. M. Sigalas and E. N. Economou. Elastic and acoustic wave band structure. *Journal of Sound and Vibration*, 158(2):377–382, 1992.

[6] M. S. Kushwaha. Classical band structure of periodic elastic composites. *International Journal of Modern Physics*, 10(9):977–1094, 1996.

[7] J. O. Vasseur, P. A. Deymier, G. Frantziskonis, G. Hong, B. Djafari-Rouhani, and L. Dobrzynski. Experimental evidence for the existence of absolute acoustic band gaps in two-dimensional periodic composite media. *J. Phys.: Condens. Matter*, 10:6051–6064, 1998.

[8] Z. Liu, X. Zhang, Y. Mao, Y. Y. Zhu, Z. Yang, C. T. Chan, and P. Sheng. Locally resonant sonic materials. *Science*, 289:1734–1736, 2000.

[9] O. Sigmund. Microstructural design of elastic band gap structures. In G. D. Cheng, Y. Gu, S. Liu, and Y. Wang, editors, *Proceedings of the Fourth World Congress of Structural and Multidisciplinary Optimization, on CD-rom*, Dalian, China, 2001. WCSMO-4.

[10] S. J. Cox and D. C. Dobson. Band structure optimization of two-dimensional photonic crystals in h-polarization. *Journal of Computational Physics*, 158(2):214–224, 2000.

[11] O. Sigmund and J. S. Jensen. Topology optimization of elastic band gap structures and waveguides. In H. A. Mang, F. G. Rammerstorfer, and J. Eberhardsteiner, editors, *Proceedings of the Fifth World Congress on Computational Mechanics, http://wccm.tuwien.ac.at*, Vienna, Austria, 2002. WCCM V.

[12] O. Sigmund and J. S. Jensen. Systematic design of phononic band gap materials and structures by topology optimization. *Phil. Trans. R. Soc. Lond. A,* **361***, 1001-1019*, 2003.

[13] K. Svanberg. The method of moving asymptotes - a new method for structural optimization. *International Journal for Numerical Methods in Engineering*, 24:359–373, 1987.

[14] J. S. Jensen. Phononic band gaps and vibrations in one- and two-dimensional mass-spring structures. *Journal of Sound and Vibration, to appear*, 2003.

A PARAMETRIC INVESTIGATION OF THE ACOUSTIC POWER IN A TWO-DIMENSIONAL WAVEGUIDE WITH MEMBRANE BOUNDED CAVITY

Idil M. Mohamed-Guled, Jane B. Lawrie

Department of Mathematical Sciences

Brunel University, Uxbridge UB8 3PH, UK

idil.mohamed@brunel.ac.uk, jane.lawrie@brunel.ac.uk

1.   INTRODUCTION

This investigation is concerned with acoustic scattering in a two dimensional waveguide with a membrane bounded cavity. The waveguide comprises rigid inlet and outlet ducts occupying the regions $0 \leq \bar{y} \leq \bar{a}$, $|\bar{x}| > \bar{\ell}$, together with a finite duct of height $\bar{b} > \bar{a}$ in the gap $|\bar{x}| \leq \bar{\ell}$. The structure is closed by two vertical rigid surfaces at $\bar{x} = \pm\bar{\ell}$, $\bar{a} \leq \bar{y} \leq \bar{b}$ forming a rectangular cavity. The interior region of the duct contains a compressible fluid of sound speed c and density ρ. The fluid in the cavity is, however, separated from the main body of fluid by a horizontal membrane which lies along $\bar{y} = \bar{a}$, $|\bar{x}| \leq \bar{\ell}$. A plane wave, of harmonic time dependence $e^{-i\omega\bar{t}}$, where ω is the radian frequency, is incident in the positive $\bar{x}$ direction through the fluid towards $\bar{x} = -\bar{\ell}$ and is scattered at the discontinuity. The time dependent fluid velocity potential, $\bar{\Phi}$, can be expressed as

$$\bar{\Phi}(\bar{x}, \bar{y}, \bar{t}) = \bar{\varphi}(\bar{x}, \bar{y})e^{-i\omega\bar{t}} \qquad (1.1)$$

and henceforth the time-independent potential $\bar{\varphi}$ will be used. It is convenient to non-dimensionalise the boundary value problem using typical length and time scales k^{-1} and ω^{-1}, where $k = \omega/c$. Thus, the non-dimensional quantities x, y etc. will henceforth be used. These are related to their dimensional counterparts by $x = k\bar{x}$, $y = k\bar{y}$ etc.

The fluid velocity potentials in the inlet and outlet ducts may be expressed in the form of standard Fourier cosine series. In contrast, due to the presence of high order spacial derivatives in the membrane boundary condition, the eigen-system of the cavity region is non Sturm-Liouville.
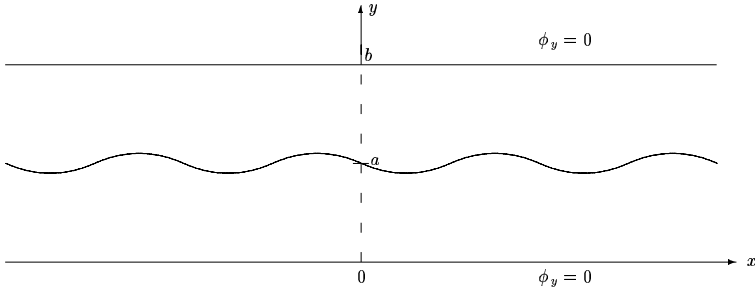
Figure 1   Infinite rigid duct divided horizontally by a membrane.

Further, the eigenfunctions are piece-wise continuous. Nevertheless, the system satisfies a known orthogonality relation, see [1]. This, together with the usual orthogonality property for $\{\cos(n\pi y/a)\}$, enables continuity of pressure/normal velocity to be imposed at the mouths of the inlet/outlet ducts and appropriate edge conditions to be applied where the membrane joins the structure. The two resulting systems of algebraic equations, formulated in terms of the amplitudes of the reflected and transmitted waves, are truncated and solved numerically. For brevity, neither the completeness of the eigenfunctions nor the regularity of these systems is proven here.

In section 2 the travelling wave forms for the cavity region are discussed. It is shown that they can be categorised as either fluid-membrane coupled or uncoupled. A general expression, encapsulating both types, is derived and the appropriate orthogonality relation is stated. These results are used in section 3 where the problem of acoustic scattering in an infinite duct with membrane bounded cavity is solved using the mode-matching technique outlined above. In section 4, numerical results are presented in the form of a parametric investigation of the power distributed in the membrane and various fluid regions.

2.   TRAVELLING WAVE SOLUTIONS

In this section a detailed discussion of the travelling wave forms for the cavity region is presented. It is appropriate, therefore, to consider the unforced boundary value problem governing the fluid velocity potential within an infinite rigid duct, of height b, in which a horizontal membrane is situated along $y = a$, $-\infty < x < \infty$ with $0 < a < b$, see figure 1.

The velocity potential satisfies Helmholtz's equation with unit wavenumber, that is

$$(\nabla^2 + 1)\varphi = 0. \tag{2.1}$$

At the rigid walls the normal component of velocity potential is zero:

$$\frac{\partial \varphi}{\partial y} = 0, \quad y = 0, b, \qquad -\infty < x < \infty. \tag{2.2}$$

The membrane at $y = a$, $-\infty < x < \infty$, is described by the condition

$$\left(\frac{\partial^2}{\partial x^2} + \mu^2 \right) \frac{\partial \varphi}{\partial y} - \alpha [\varphi(x, y)]_{a^-}^{a^+} = 0, \quad y = a, \tag{2.3}$$

where μ and α are the in vacuo wave number and fluid loading parameter respectively, see [1].

2.1.   FLUID-MEMBRANE COUPLED MODES

On using separation of variables, boundary condition (2.2) and continuity of normal velocity at $y = a$, it is found that φ has the form

$$\varphi = \begin{cases} \cosh(\gamma y)e^{\pm i\nu x}, & 0 < y \le a \\ -\dfrac{\sinh(\gamma a)}{\sinh[\gamma(b-a)]} \cosh[\gamma(b-y)]e^{\pm i\nu x}, & a < y \le b \end{cases}, \tag{2.4}$$

where γ and ν are as yet unspecified but are related by $\gamma^2 - \nu^2 + 1 = 0$. Admissible values of γ are determined by substituting (2.4) into the membrane equation (2.3). The resulting dispersion relation is

$$K(\gamma) = (\gamma^2 + 1 - \mu^2)\gamma \sinh(\gamma a) - \alpha \frac{\sinh(\gamma b)}{\sinh[\gamma(b-a)]} = 0. \tag{2.5}$$

Since $K(\gamma)$ is an even function of γ, it is convenient to denote the roots of (2.5) by $\pm\gamma_n$, $n = 0, 1, 2, \ldots$ and discuss only the positive roots. It is found that there is always one real root, $\gamma_0 > 0$, and an infinite number of imaginary roots, γ_n, $n = 2, 3, \ldots$, which are labelled with increasing distance up the imaginary axis.

2.2.   UNCOUPLED MODES

In addition to the fluid membrane modes discussed above there are other possible waves forms for the cavity region. Firstly, the plane acoustic wave e^{ix}. This is a trivial solution to (2.3) and it follows that this mode can always exist without interaction with the membrane. Other uncoupled modes exist only if the duct height b can be expressed in the form $b = pa/q$, for integer values of p and q. The modes of interest are a subset of the usual rigid duct modes: those that have zero velocity normal to the membrane

at $y = a$. These modes have the form

$$\varphi_j = \cos\left(\frac{j\pi q y}{pa}\right) e^{\pm i\tau_j x}, \tag{2.6}$$

where $\tau_j = (1 - j^2\pi^2/b^2)^{1/2}$ and $j = pm$, $m = 1, 2, 3, \ldots$. Equivalently,

$$\varphi_j = \begin{cases} \cosh(\gamma_j y)e^{\pm i\nu_j x}, & 0 < y \le a \\ (-1)^j \cosh[\gamma_j (b - y)]e^{\pm i\nu_j x}, & a < y \le b \end{cases}. \tag{2.7}$$

where $\gamma_j = ij\pi q/(pa)$ and $\nu_j = (\gamma_j^2 + 1)^{1/2} = \tau_j$. Thus, admissible wave numbers for the uncoupled modes are defined by $\gamma_1 = 0$ (always present) and $\gamma_j = ij\pi q/(pa)$, $j = p, 2p, 3p, \ldots$ (present only for $b = pa/q$).

2.3.   THE GENERAL CASE

For convenience the coupled and uncoupled duct modes are combined into one expression. It is found that,

$$\varphi_n = Y_n(y)e^{\pm i\nu_n x}, \quad 0 \le y \le b, \tag{2.8}$$

where

$$Y_n(y) = \begin{cases} \cosh(\gamma_n y), & 0 \le y \le a \\ \xi_n \cosh[\gamma_n (b - y)], & a < y \le b \end{cases}, \tag{2.9}$$

and

$$\xi_n = \begin{cases} -\dfrac{\sinh(\gamma_n a)}{\sinh[\gamma_n (b - a)]}, & n \ne 1 \quad \text{and} \quad \gamma_n \ne \frac{ij\pi q}{pa} \\ 1, & n = 1 \\ (-1)^j, & n \ne 1 \quad \text{and} \quad \gamma_n = \frac{ij\pi q}{pa} \end{cases}. \tag{2.10}$$

Note that the set of values, γ_n, $n = 0, 1, 2, \ldots$ now includes all admissible values for both fluid-membrane coupled and uncoupled modes, ordered γ_0, γ_1 and then by increasing imaginary part. The functions $Y_n(y)$ defined by (2.9) and (2.10) satisfy the following orthogonality relation:

$$Y_n'(a)Y_m'(a) + \alpha \int_0^b Y_n(y)Y_m(y)\, dy = E_n\delta_{mn} \tag{2.11}$$

where the prime indicates differentiation with respect to y and δ_{mn} is the usual Kronecker delta. For fluid coupled modes the quantity E_n is given by

$$E_n = \frac{Y_n'(a)}{2\gamma_n}\frac{d}{d\gamma}K(\gamma)\Big|_{\gamma=\gamma_n}. \tag{2.12}$$
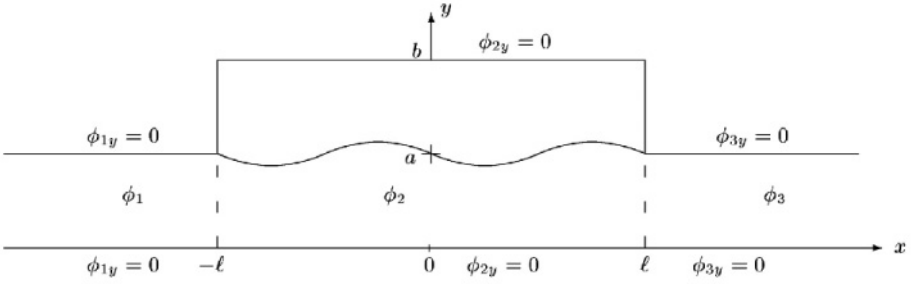
Figure 2   Infinite rigid duct with a membrane bounded cavity for $-\ell \leq x \leq \ell$.

For the uncoupled modes

$$E_n = \frac{\alpha b}{2} \varepsilon_{n-1} \tag{2.13}$$

where $\varepsilon_n = 2$ for $n = 0$ and 1 otherwise. Equations (2.12) and (2.13) can be rearranged for the general case as

$$E_n = \frac{\alpha}{2}[\beta_n(a) + \xi_n^2 \beta_n(b-a)], \tag{2.14}$$

where

$$\beta_n(x) = x + \frac{(3\gamma_n^2 + 1 - \mu^2)}{2\gamma_n(\gamma_n^2 + 1 - \mu^2)} \sinh(2\gamma_n x). \tag{2.15}$$

3.   THE BOUNDARY VALUE PROBLEM

The mode-matching solution for acoustic scattering in a waveguide with membrane bounded cavity is presented in this section. A detailed description of the waveguide has been given in the introduction. This is not repeated here, instead the reader is refered to figure 2 which clearly summarises the non-dimensional geometry.

A plane acoustic wave, of unit amplitude and harmonic time dependence, is incident in the positive x direction towards $x = -\ell$ where it is scattered. It is convenient to split the velocity potential into three parts corresponding to the regions $-\infty < x \leq -\ell$, $|x| < \ell$ and $\ell \leq x < \infty$. Thus,

$$\varphi(x, y) = \begin{cases} \varphi_1(x, y), & -\infty < x \leq -\ell \\ \varphi_2(x, y), & -\ell \leq x \leq \ell \\ \varphi_3(x, y), & \ell \leq x < \infty \end{cases}. \tag{3.1}$$

The velocity potential, φ, satisfies the non-dimensionalised Helmholtz's equation (2.1) with boundary conditions:

$$\frac{\partial \varphi_1}{\partial y} = 0, \quad y = 0, a, \quad -\infty < x \le -\ell, \tag{3.2}$$

$$\frac{\partial \varphi_2}{\partial y} = 0, \quad y = 0, b, \quad -\ell \le x \le \ell, \tag{3.3}$$

$$\frac{\partial \varphi_2}{\partial x} = 0, \quad x = \pm \ell, \quad a < y \le b, \tag{3.4}$$

$$\frac{\partial \varphi_3}{\partial y} = 0, \quad y = 0, a, \quad \ell \le x < \infty. \tag{3.5}$$

The membrane bounding the cavity has boundary condition

$$\left(\frac{\partial^2}{\partial x^2} - \mu^2 \right) \frac{\partial \varphi_2}{\partial y} - \alpha [\varphi_2(x, y)]_{a^-}^{a^+} = 0, \quad -\ell \le x \le \ell. \tag{3.6}$$

A suitable edge condition must be applied to both ends of the membrane. In this article zero displacement is assumed, that is

$$\varphi_{2y}(\pm \ell, a) = 0, \tag{3.7}$$

where the subscript y indicates differentiation. The eigen-function expansions for φ_j, $j = 1, 2, 3$ are

$$\varphi_1 = e^{ix} + \sum_{n=0}^{\infty} A_n \cos \left(\frac{n \pi y}{a} \right) e^{-i \eta_n x}; \tag{3.8}$$

$$\varphi_2 = \sum_{n=0}^{\infty} (B_n e^{i \nu_n x} + C_n e^{-i \nu_n x}) Y_n(y); \tag{3.9}$$

$$\varphi_3 = \sum_{n=0}^{\infty} D_n \cos \left(\frac{n \pi y}{a} \right) e^{i \eta_n x}, \tag{3.10}$$

where $Y_n(y)$ is given by (2.9). Here A_n and D_n are the complex amplitudes of the nth reflected and transmitted modes respectively, $\eta_n = (1 - n^2 \pi^2 / a^2)^{1/2}$ and $\nu_n = (\gamma_n^2 + 1)^{1/2}$, $n = 0, 1, 2, \ldots$.

The coefficients A_n, B_n, C_n and D_n are determined by matching the fluid pressure and the normal velocity at the interfaces $x = \pm \ell$, $0 \le y \le a$. Continuity of pressure can be expressed as

$$\varphi_1(-\ell, y) = \varphi_2(-\ell, y), \quad 0 \le y \le a, \tag{3.11}$$

and

$$\varphi_2(\ell, y) = \varphi_3(\ell, y), \quad 0 \le y \le a. \tag{3.12}$$

Similarly, continuity of normal velocity gives

$$\frac{\partial \varphi_2}{\partial x}(-\ell, y) = \begin{cases} \frac{\partial \varphi_1}{\partial x}(-\ell, y), & 0 \leq y \leq a \\ \\ 0, & a < y \leq b \end{cases}, \tag{3.13}$$

and

$$\frac{\partial \varphi_2}{\partial x}(\ell, y) = \begin{cases} \frac{\partial \varphi_3}{\partial x}(\ell, y), & 0 \leq y \leq a \\ \\ 0, & a < y \leq b \end{cases}. \tag{3.14}$$

On substituting (3.8)–(3.10) into (3.11)–(3.12) and making use of the orthogonality relation for $\{\cos(n\pi y/a)\}$, it is found that

$$A_n = \frac{-2e^{-i\eta_n \ell}}{a\epsilon_n} \left[e^{-i\ell} \delta_{0n} - \sum_{m=0}^{\infty} \left(B_m e^{-i\nu_m \ell} + C_m e^{i\nu_m \ell} \right) R_{nm} \right] \tag{3.15}$$

and

$$D_n = \frac{-2e^{i\eta_n \ell}}{a\epsilon_n} \sum_{m=0}^{\infty} \left(B_m e^{i\nu_m \ell} + C_m e^{-i\nu_m \ell} \right) R_{nm}, \tag{3.16}$$

where

$$R_{nm} = \int_0^a \cos\left(\frac{n\pi y}{a}\right) \cosh(\gamma_m y) dy = \frac{(-1)^n \gamma_m \sinh(\gamma_m a)}{\gamma_m^2 + \frac{n^2 \pi^2}{a^2}}. \tag{3.17}$$

Similarly, on substituting (3.8)–(3.10) into (3.13)–(3.14) and using the orthogonality relation (2.11) it is found, after a little rearrangement, that

$$B_n + C_n = \frac{i}{2E_n \nu_n \sin(\nu_n \ell)} \left[- iJY_n'(a) + \alpha e^{-i\ell} R_{0n} \right. \tag{3.18}$$

$$\left. - \alpha \sum_{m=0}^{\infty} (A_m + D_m) \eta_m e^{i\eta_m \ell} R_{mn} \right];$$

and

$$B_n - C_n = \frac{1}{2E_n \nu_n \cos(\nu_n \ell)} \left[- iHY_n'(a) + \alpha e^{-i\ell} R_{0n} \right. \tag{3.19}$$

$$\left. - \alpha \sum_{m=0}^{\infty} (A_m - D_m) \eta_m e^{i\eta_m \ell} R_{mn} \right].$$

It is straightforward to use (3.18) and (3.19) to eliminate B_m and C_m from (3.15) and (3.16). It is found that

$$\psi_n = -\frac{2}{\epsilon_n}e^{-i\ell}\delta_{0n} \tag{3.20}$$

$$-\frac{2}{\epsilon_n a}\sum_{m=0}^{\infty}\frac{\tan(\nu_m\ell)}{E_m\nu_m}R_{nm}\left[HY_m'(a) + i\alpha\left(e^{-i\ell}R_{0m} - \sum_{j=0}^{\infty}\psi_j\eta_j R_{jm}\right)\right]$$

and

$$\chi_n = -\frac{2}{\epsilon_n}e^{-i\ell}\delta_{0n} \tag{3.21}$$

$$+\frac{2}{\epsilon_n a}\sum_{m=0}^{\infty}\frac{\cot(\nu_m\ell)}{E_m\nu_m}R_{nm}\left[JY_m'(a) + i\alpha\left(e^{-i\ell}R_{0m} - \sum_{j=0}^{\infty}\chi_j\eta_j R_{jm}\right)\right],$$

where $\psi_n = (A_n - D_n)e^{i\eta_n\ell}$ and $\chi_n = (A_n + D_n)e^{i\eta_n\ell}$.

The constants H and J are determined via the edge condition, (3.7). It is found that

$$H = \frac{-i\alpha\sum_{n=0}^{\infty}\frac{\tan(\nu_n\ell)}{E_n\nu_n}Y_n'(a)[e^{-i\ell}R_{0n} - \sum_{m=0}^{\infty}\psi_m\eta_m R_{mn}]}{\sum_{j=0}^{\infty}\frac{\tan(\nu_j\ell)}{E_j\nu_j}[Y_j'(a)]^2} \tag{3.22}$$

and J may be obtained from (3.22) on replacing $\tan(\nu_{n(j)}\ell)$ with $\cot(\nu_{n(j)}\ell)$.

4. NUMERICAL RESULTS

In this investigation it is the power distribution between the various fluid regions and the membrane that is of interest. The appropriate expressions for the power can be found in [1]. In each of the graphs presented below the membrane mass is 0.67 kg/m the tension is 1333 N/m the inlet/outlet ducts are of height 0.25 m.

Figures 3 and 4 show power plotted against ℓ for frequency 560 Hz and with the cavity region of height 0.5 m. The reflected (bold line) and transmitted power (dashed line) are shown in figure 3. Although the two curves oscillate rapidly with ℓ there is a clear envelope bounding them. The power in the membrane (bold line) and the power flux in the fluid (dashed line) of the region $|x| < \ell$ are shown in figure 4. The vast majority of the power is in the fluid, however, there are a number of spikes where the membrane and the fluid both transmit significant power but in opposite directions. These spikes signify resonant-type behaviour but, even though the individual components have magnitudes greater than one, the power balance remains intact.
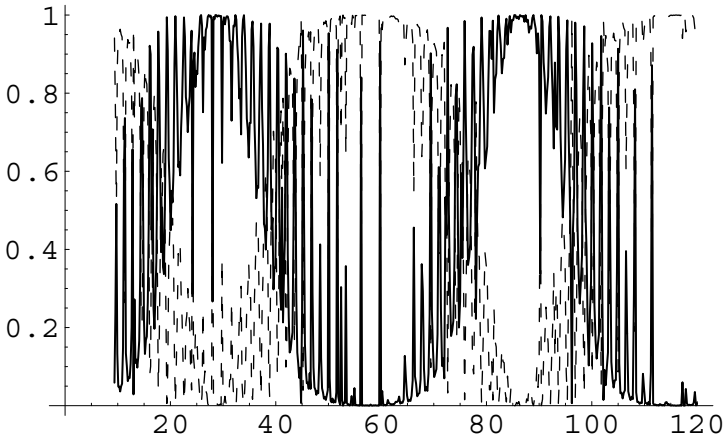
Figure 3   Reflected (bold) and transmitted (dashed) power against ℓ.
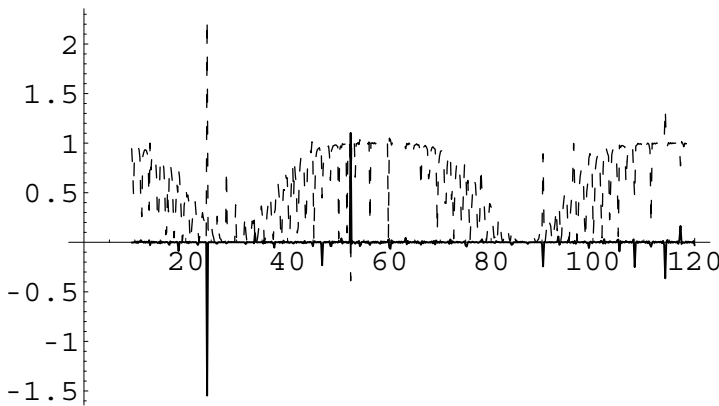
Figure 4   Fluid flux (dashed) and membrane (bold) power against ℓ.

When plotted against b the reflected (bold line) and transmitted (dashed line) powers show significantly less oscillation. This is shown in figure 5 for frequency 560 Hz and with cavity region half length 0.8 m. It is clear that for most values of b the power is almost entirely transmitted. At regular intervals, however, the transmitted power plummets whilst the reflected power peaks. This behaviour is consistent with a new mode "switching on" in the cavity region.

Figure 6 shows the reflected and transmitted powers plotted against frequency for cavity region half length 0.8 m and height 0.5 m. The two curves exhibit rapid oscillations with no bounding envelope for frequencies less than approximately 350 Hz. As frequency is increased the membrane
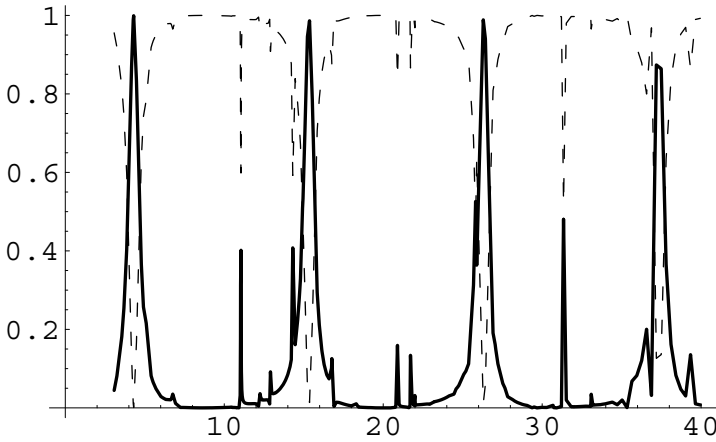
Figure 5   Reflected (bold) and transmitted power (dashed) against b.
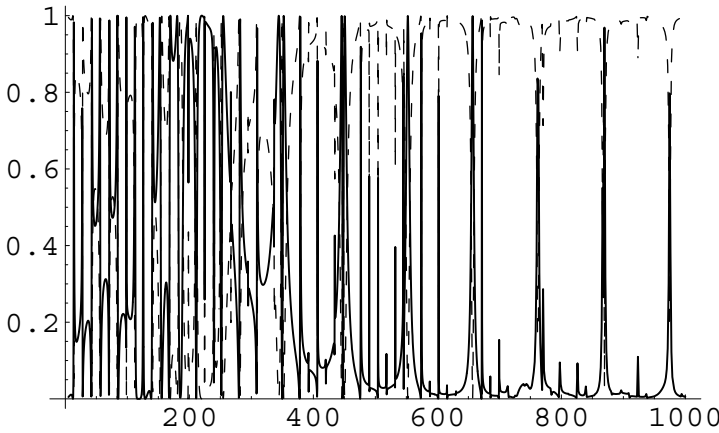
Figure 6   Reflected (bold) and transmitted (dashed) powers against frequency f.

response decreases and for frequencies above 350 Hz, the graph assumes a more regular form with the majority of the power being transmitted. Isolated spikes in the reflected power (with corresponding drops in the transmitted) are again evident and are indicative of modes being "cut-on" with the increasing frequency.

References

[1] Warren, D.P., Lawrie, J.B. & Mohamed, I.M. (2002) Acoustic scattering in waveguides that are discontinuous in geometry and material property. Wave Motion, **36(2)**, pp $119 - 142$.

VIBRATIONS OF A CIRCULAR CYLINDER IN OBLIQUE INCIDENCE REVISITED

J. Servant[†], S. Guenneau[‡1], A. B. Movchan[‡] and C. Poulton[⋆]

[†] *Ecole Supérieure de Mécanique de Marseille, IMT, technopôle de Château-Gombert, 13451 Marseille Cedex 20, France*

[‡] *Department of Mathematical Sciences, University of Liverpool, M & O Building, Liverpool L69 3BX, UK*

abm@liv.ac.uk

[⋆] *High Frequency and Quantum Electronics Laboratory, University of Kalrsruhe, 76128 Karlsruhe, Germany*

Keywords: Spectral analysis, elastic scattering, acoustic waveguides.

Abstract   In this paper, we analyse the propagation of elastodynamic waves in a circular cylinder in the case of oblique incidence. We use a scattering matrix approach and derive an algebraic linear system which allows us to get a complete picture of the dispersion curves. This derivation is of the foremost importance, since it provides the right form for the algebraic system associated to a singular cylinder, basis of its generalisation to a doubly periodic array of circular cylinders.

1.   INTRODUCTION

The study of phononic crystals has renewed the interest in physics of mechanical waveguides; they may form the basis of new sonic devices such as phasers, audio and light filters. Although the field of acoustic waveguides was developed since the 60's (see the classic book by Achenbach [1] for an overview), the mathematical formulations of these problems still have interesting and challenging issues. In this paper, we provide a complete analysis of the eigenvalue problem associated with an elastic cylinder of circular cross-section, by considering a representation of the displacement field in a suitable cylindrical basis consisting of *adequate* combination of

---

[1]Current address: Condensed Matter Theory Group, Blackett Laboratory, Imperial College, Prince Consort Rd., London SW7 2AZ, UK

96

Bessel functions. These analytical findings are accompanied by numerical simulations and analysis of dispersion diagrams. Also, we discuss inconsistencies in some classical articles on mechanical waveguides [6],[1],[3],[2] and compare our spectral analysis with [6],[1],[2]. By doing so, we provide a complete solution of the canonical problem of elastodynamics, which is required in analysis of oblique incidence of elastic waves propagating in an infinite array of circular cylinders (phononic crystal fibres). This paper has to be understood as the touchstone of this analysis [5].

2. GOVERNING EQUATIONS

To study the propagation of elastic waves in a circular cylinder, it is convenient to use a system of cylindrical coordinates, with respectively r, θ and z for radial, angular, and axial coordinates.

The motion of an isotropic and elastic medium with no body forces is then governed by the system of Navier equations:

$$\mu \nabla^2 \mathbf{u} + (\lambda + \mu) \nabla \nabla . \mathbf{u} = \rho \frac{\partial^2 \mathbf{u}}{\partial t^2} \tag{2.1}$$

where, $\mathbf{u}$ is the displacement vector, (λ, μ) are the two Lamé constants, and ρ is the density of the medium.

The displacement vector $\mathbf{u}$ can be written via a vector potential $\mathbf{\Psi}$ and a scalar potential φ in such a way that :

$$\mathbf{u} = \nabla \varphi + \nabla \times \mathbf{\Psi} \tag{2.2}$$

Taking (2.2) into account in (2.1), we are led on one hand to $\frac{\mu}{\rho} \nabla \times \nabla \times \mathbf{\Psi} + \frac{\partial^2 \mathbf{\Psi}}{\partial t^2} = -\nabla g$, where g is an arbitrary scalar potential that we set to $\frac{\mu}{\rho} \nabla . (\mathbf{\Psi})$, and on the other hand to $\nabla . \nabla \left[\frac{\lambda + 2\mu}{\rho} \nabla^2 \varphi - \frac{\partial^2 \varphi}{\partial t^2} \right] = 0$. Finally, we obtain that $\mathbf{\Psi}$ and φ are solutions of the two wave equations:

$$v_1^2 \nabla^2 \varphi = \frac{\partial^2 \varphi}{\partial t^2} \ , \ \ v_2^2 \nabla^2 \mathbf{\Psi} = \frac{\partial^2 \mathbf{\Psi}}{\partial t^2} \tag{2.3}$$

Where $v_1^2 = \frac{\lambda + 2\mu}{\rho}$ and $v_2^2 = \frac{\mu}{\rho}$.

Up to now, no assumption has been made on the geometry of the cylinder. If we consider a cylinder of circular cross-section, cylindrical coordinates can be used, and the differential equations for φ, Ψ_r, Ψ_θ and Ψ_z become :

$$\nabla^2 \varphi - \frac{1}{v_1^2} \frac{\partial^2 \varphi}{\partial t^2} = 0 \tag{2.4}$$

$$\nabla^2 \Psi_r - \frac{2}{r^2} \frac{\partial \Psi_\theta}{\partial \theta} - \frac{\Psi_r}{r^2} - \frac{1}{v_2^2} \frac{\partial^2 \Psi_r}{\partial t^2} = 0 \tag{2.5}$$

$$\nabla^2 \Psi_\theta + \frac{2}{r^2} \frac{\partial \Psi_r}{\partial \theta} - \frac{\Psi_\theta}{r^2} - \frac{1}{v_2^2} \frac{\partial^2 \Psi_\theta}{\partial t^2} = 0 \tag{2.6}$$

$$\nabla^2 \Psi_z - \frac{1}{v_2^2} \frac{\partial^2 \Psi_z}{\partial t^2} = 0 \tag{2.7}$$

3.   BOUNDARY CONDITIONS

The boundary conditions, for free motions are

$$\sigma_{rr} = \sigma_{r\theta} = \sigma_{rz} = 0 \tag{3.1}$$

for $r = r_c$, where r_c is the radius of the cylinder . The stress-displacement relations are given by

$$\epsilon_{rr} = \frac{\partial u_r}{\partial r} \; , \epsilon_{rz} = \frac{1}{2} \left(\frac{\partial u_r}{\partial z} + \frac{\partial u_z}{\partial r} \right)$$

$$\epsilon_{r\theta} = \frac{1}{2} \left(r \frac{\partial}{\partial r} \left(\frac{u_\theta}{r} \right) + \frac{1}{r} \frac{\partial u_r}{\partial \theta} \right) \; , \tag{3.2}$$

and the stress-strain relations are

$$\sigma_{rr} = \lambda \Delta + 2\mu\epsilon_{rr} \; , \sigma_{rz} = 2\mu\epsilon_{rz} \; , \sigma_{r\theta} = 2\mu\epsilon_{r\theta} \; . \tag{3.3}$$

Here Δ is the dilatation defined as: $\Delta = \dfrac{\partial u_r}{\partial r} + \dfrac{u_r}{r} + \dfrac{1}{r} \dfrac{\partial u_\theta}{\partial \theta} + \dfrac{\partial u_z}{\partial z} \; .$

4.   A CLASS OF NON-TRIVIAL SOLUTIONS

Consider the following forms for $\boldsymbol{\Psi}$ and φ, as solutions of the previous equations :

$$\varphi = f(r) \cos n\theta \cos(\omega t + \beta z) \tag{4.1}$$

$$\Psi_r = h_r(r) \sin n\theta \sin(\omega t + \beta z) \tag{4.2}$$

$$\Psi_\theta = h_\theta(r) \cos n\theta \sin(\omega t + \beta z) \tag{4.3}$$

$$\Psi_z = h_z(r) \sin n\theta \cos(\omega t + \beta z), \tag{4.4}$$

where $\beta > 0$ is the constant of propagation, and ω is the radian frequency of an eigenmode. Representations (4.1)-(4.4) [1] generate a complete orthonormal Fourier basis.

---

[1] We note that in the paper by Meeker and Meitzler [6] (formula (48), p. 130) and in the book by Achenbach [1] (formulae (6.107)-(6.110), p. 238), there are discrepancies in their choice of the exponential basis.

Using the previous basis for $\boldsymbol{\Psi}$ and φ, in the equations governing φ, Ψ_r, Ψ_θ and Ψ_z, differential equations for $f(r)$, $h_r(r)$, $h_\theta(r)$ and $h_z(r)$ are found. For $f(r)$ and $h_z(r)$ the differential equations are :

$$\frac{d^2 f(r)}{dr^2} + \frac{1}{r}\frac{df(r)}{dr} + (k_{\perp a}^2 - \frac{n^2}{r^2})f(r) = 0 \tag{4.5}$$

$$\frac{d^2 h_z(r)}{dr^2} + \frac{1}{r}\frac{dh_z(r)}{dr} + (k_{\perp b}^2 - \frac{n^2}{r^2})h_z(r) = 0 \tag{4.6}$$

where $k_{\perp a}^2 = \frac{\omega^2}{v_1^2} - \beta^2$ and $k_{\perp b}^2 = \frac{\omega^2}{v_2^2} - \beta^2$.

Considering the coupled equations with Ψ_r and Ψ_θ, the differential equations for $h_r(r)$ and $h_\theta(r)$ become

$$\frac{d^2 h_r(r)}{dr^2} + \frac{1}{r}\frac{dh_r(r)}{dr} + (k_{\perp b}^2 - \frac{n^2+1}{r^2})h_r(r) + \frac{2n}{r^2}h_\theta(r) = 0 \tag{4.7}$$

$$\frac{d^2 h_\theta(r)}{dr^2} + \frac{1}{r}\frac{dh_\theta(r)}{dr} + (k_{\perp b}^2 - \frac{n^2+1}{r^2})h_\theta(r) + \frac{2n}{r^2}h_r(r) = 0 \tag{4.8}$$

If we add and subtract (4.7) and (4.8), we end up with

$$\frac{d^2}{dr^2}(h_r(r) + h_\theta(r)) + \frac{1}{r}\frac{d}{dr}(h_r(r) + h_\theta(r))$$
$$+(k_{\perp b}^2 - \frac{(n-1)^2}{r^2})(h_r(r) + h_\theta(r)) = 0 \tag{4.9}$$

$$\frac{d^2}{dr^2}(h_r(r) - h_\theta(r)) + \frac{1}{r}\frac{d}{dr}(h_r(r) - h_\theta(r))$$
$$+(k_{\perp b}^2 - \frac{(n+1)^2}{r^2})(h_r(r) - h_\theta(r)) = 0 \tag{4.10}$$

Thus, $f(r)$, $h_z(r)$, $(h_r(r) + h_\theta(r))$ and $(h_r(r) - h_\theta(r))$ are solutions of the equations of Bessel type, and are given in terms of Bessel functions as follows:

$$f(r) = A_n^{(a)} \chi_n(k_{\perp a}r) \tag{4.11}$$

$$h_r(r) + h_\theta(r) = A_{n-1}^{(b_1)} X_{n-1}(k_{\perp b}r) \tag{4.12}$$

$$h_r(r) - h_\theta(r) = A_{n+1}^{(b_2)} X_{n+1}(k_{\perp b}r) \tag{4.13}$$

$$h_z(r) = A_n^{(b_3)} X_n(k_{\perp b}r) \tag{4.14}$$

where $\chi_n(z)$ (respectively X_n) is either $J_n(z)$, when z is real, or $I_n(z)$ if z is complex.

At this stage, one is to remember that we have an additional degree of freedom coming from the decomposition of $\mathbf{u}$ in terms of Lamé potentials. We

thus require a compatibility condition. In [4], a divergence free condition for $\mathbf{\Psi}$ was chosen, together with a full exponential basis for φ and $\mathbf{\Psi}$, leading to an intricate system of algebraic equations. Here, we take full account of the axial symmetry of the waveguide allowing us to take $h_r(r) = -h_\theta(r)$, thereby removing (4.12). Now, the displacement field becomes

$$u_r = \left(f'(r) + \frac{n}{r} h_z(r) + \beta h_r(r) \right) \cos n\theta \cos(\omega t + \beta z) \qquad (4.15)$$

$$u_\theta = \left(-\frac{n}{r} f(r) - h_z'(r) + \beta h_r(r) \right) \sin n\theta \cos(\omega t + \beta z) \qquad (4.16)$$

$$u_z = \left(-\beta f(r) - h_r'(r) - \frac{n+1}{r} h_r(r) \right) \cos n\theta \sin(\omega t + \beta z) \qquad (4.17)$$

We note that the dilatation expands as follows:

$$\Delta = \left\{ f''(r) + \frac{f'(r)}{r} - \frac{n^2}{r^2} f(r) - \beta^2 f(r) \right\} \cos(n\theta) \cos(\omega t + \beta z)$$
$$= -(k_{\perp a}^2 + \beta^2) f(r) \cos(n\theta) \cos(\omega t + \beta z) \qquad (4.18)$$

The tractions $(\sigma_{rr}, \sigma_{r\theta}, \sigma_{rz})$ can be represented in terms of the potentials $f(r)$, $h_z(r)$ and $h_r(r)$ as follows :

$$\sigma_{rr} = \left\{ -\lambda \left(\beta^2 + k_{\perp a}^2 \right) f(r) + 2\mu \left[f''(r) + \beta h_r'(r) \right. \right.$$
$$\left. \left. + \frac{n}{r} \left(h_z'(r) - \frac{h_z(r)}{r} \right) \right] \right\} \cos n\theta \cos(\omega t + \beta z) \qquad (4.19)$$

$$\sigma_{r\theta} = \mu \left\{ -\frac{2n}{r} (f'(r) - \frac{f(r)}{r}) - \beta \left(\frac{n+1}{r} h_r(r) - h_r'(r) \right) \right.$$
$$\left. - \left(2h_z''(r) + k_{\perp b}^2 h_z(r) \right) \right\} \sin n\theta \cos(\omega t + \beta z) \qquad (4.20)$$

$$\sigma_{rz} = \mu \left\{ -2\beta f'(r) - \frac{n}{r} \left[h_r'(r) + \frac{n+1}{r} h_r(r) \right] \right.$$
$$\left. - \left(\beta^2 - k_{\perp b}^2 \right) h_r(r) - \frac{n\beta}{r} h_z(r) \right\} \cos n\theta \sin(\omega t + \beta z) \qquad (4.21)$$

The boundary conditions [2] for free motions are : $\sigma_{rr} = \sigma_{r\theta} = \sigma_{rz} = 0$ for $r = r_c$, where r_c is the radius of the cylinder.

---

[2]We note the discrepancies in the expressions for the stress components $\sigma_{r\theta}$ and σ_{rz} in the papers by Gazis ([3], eq. 17, p. 570) and Armenákas ([2], eq. 14, p. 825), and in Meeker and Meitzler ([6], eq. 67, p. 132).

5.   FREQUENCY EQUATION

For given geometric and physical parameters, we can now derive a frequency equation which constitutes a relationship between the conical parameter β, the number of circumferential waves n, and the eigenfrequency. For any chosen values of the elastic constants λ, μ and ρ and of the wave parameters β and n, the frequency equation yields an infinite number of values of ω.

On the boundary conditions the stresses are depending on $A_n^{(a)}$, $A_{n+1}^{(b_2)}$ and $A_n^{(b_3)}$. The general frequency equation for a single cylinder can be obtained when the determinant of the algebraic system associated with (3.1) is set to zero:

$$
\begin{vmatrix}
[n^2 - \frac{r_c^2(k_{\perp b}^2 - \beta^2)}{2}]\chi_n(k_{\perp a}r_c) & -\{n^2 - r_c^2 k_{\perp b}^2\}X_n(k_{\perp b}r_c) + k_{\perp b}r_c X_n'(k_{\perp b}r_c) \\
\quad -k_{\perp a}r_c\chi_n'(k_{\perp a}r_c) & \quad +n\{k_{\perp b}r_c X_n'(k_{\perp b}r_c) - X_n(k_{\perp b}r_c)\}
\end{vmatrix}
$$

$$
n\{n\chi_n(k_{\perp a}r_c) - k_{\perp a}r_c\chi_n'(k_{\perp a}r_c)\} \quad [\frac{r_c^2 k_{\perp b}^2}{2} - n^2]X_n(k_{\perp b}r_c) + k_{\perp b}r_c X_n'(k_{\perp b}r_c)
$$
$$
+n\{k_{\perp b}r_c X_n'(k_{\perp b}r_c) - X_n(k_{\perp b}r_c)\}
$$

$$
-r_c k_{\perp a}\chi_n'(k_{\perp a}r_c) \qquad -\frac{n}{2}X_n(k_{\perp b}r_c) - \frac{k_{\perp b}^2 - \beta^2}{2\beta^2}k_{\perp b}r_c X_n'(k_{\perp b}r_c)
$$

$$
2n(k_{\perp b}r_c X_n'(k_{\perp b}r_c) - X_n(k_{\perp b}r_c))
$$

$$
-[2n^2 - r_c^2 k_{\perp b}^2]X_n(k_{\perp b}r_c) + 2k_{\perp b}r_c X_n'(k_{\perp b}r_c) \Bigg| = 0 \qquad (5.1)
$$

$$
-nX_n(k_{\perp b}r_c)
$$

This equation is written in terms of Bessel functions $\chi_n(k_{\perp a}r_c)$ and $X_n(k_{\perp b}r_c)$. One has to consider $\chi_n(z)$ and $X_n(z)$ as either the Bessel function $J_n(z)$ if its argument z is real, or the modified Bessel function $I_n(z)$ if its argument z is imaginary.

We note that the above determinant is real, which enables us to look for a change of sign in the determinant for two consecutive values of the eigenfrequency ω, as an evidence of root between these two values. One can also see that there is no shift in the indices of Bessel functions involved in the matrix, which indicates the advantage of the canonical basis (4.1)-(4.4).

6.   ANALYSIS OF THE FREQUENCY EQUATION AND NUMERICAL RESULTS

6.1.   AXISYMMETRIC MODES

If we consider the motion independent of θ (i.e. for n=0 in the general frequency equation), two kinds of modes occur, and these modes are uncoupled. First, there are torsional modes, which involve a displacement u_θ.

Second, there are longitudinal modes, which are governed by Pochammer's equation and involve displacements u_r and u_z .

The diagrams were plotted in the same conditions as in the paper by A. E. Armenákas [2] and as in the book of J. D. Achenbach [1] in dimensionless normalised frequency and angle of incidence $\frac{\omega r_c}{\pi v_2}$ and $\frac{\beta r_c}{\pi}$, for a given Poisson's ratio $\nu = 0.3$.

Torsional waves. The frequency equation for the torsional modes is given by :

$$r_c k_{\perp b} X_0(k_{\perp b} r_c) - 2X_1(k_{\perp b} r_c) = 0 \tag{6.1}$$

The cut-off frequency line : $k_{\perp b} = 0$ ($\frac{\omega}{v_2} = \beta$) is also plotted on the same diagram (Figure 1). On the Figure 1, we note that the line corresponding to the first root and the cut-off frequency line coincide. In comparison with the paper by A. E. Armenákas [2] (Figure 7, p. 830), we print an additional root for the frequency $\frac{\omega r_c}{\pi v_2} = 5.7$.
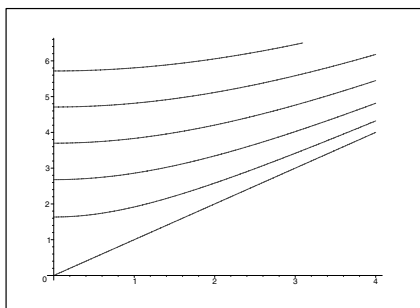
Figure 1 torsional waves : dispersion curves for normalised frequencies ($\frac{\omega r_c}{\pi v_2}$) versus normalised angles of incidence ($\frac{\beta r_c}{\pi}$)

Longitudinal waves. The frequency equation for the longitudinal modes is given by Pochammer's equation :

$$2k_{\perp a} r_c(k_{\perp b}^2 - \beta^2)\chi_1(k_{\perp a} r_c)X_1(k_{\perp b} r_c) - r_c^2(k_{\perp b}^2 - \beta^2)^2\chi_0(k_{\perp a} r_c)X_1(k_{\perp b} r_c)$$

$$-4r_c^2\beta^2 k_{\perp a}k_{\perp b}\chi_1(k_{\perp a} r_c)X_0(k_{\perp b} r_c) = 0 \tag{6.2}$$

where $(\chi, X) \in (I, I)$ when $k_{\perp,a}^2 \leq 0$ and $k_{\perp,b}^2 \leq 0$,
and $(\chi, X) \in (I, J)$ when $k_{\perp,a}^2 \leq 0$ and $k_{\perp,b}^2 \geq 0$,
and $(\chi, X) \in (J, J)$ when $k_{\perp,a}^2 \geq 0$ and $k_{\perp,b}^2 \geq 0$.
We note a discrepancy between our results given in Figure 2 and the work by Armenákas ([2], Figure 8, p. 831). Our results are consistent with Pao and Mindlin [7]. Here there are two cut-off frequencies associated to

different types of waves i.e. the first one for $k_{\perp a} = 0$ $(\frac{\omega}{v_1} = \beta)$ and the second one for $k_{\perp b} = 0$ $(\frac{\omega}{v_2} = \beta)$. These two cut-off frequencies are plotted on the left diagram of Figure 2.
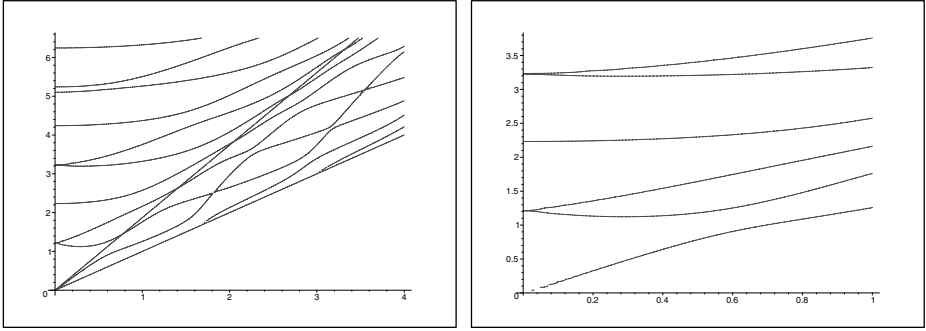
Figure 2 Longitudinal waves: dispersion curves for normalised frequencies $(\frac{\omega r_c}{\pi v_2})$ versus normalised angles of incidence $(\frac{\beta r_c}{\pi})$.

In comparison to the paper by Armenákas [2] (Figure 8, p. 831), for the range of frequencies $\frac{\omega r_c}{\pi v_2}$ between 0 and 6.5, four additional roots are found. For a large angle of incidence, new phenomena can be observed. We can see that the dispersion curves touch each other at different points (consistent with the work by Pao and Mindlin [7]), contrarily to the curves provided by Armenakas, which have an asymptotic linear behaviour. We also observe that new roots appear along the cut-off frequency's line $k_{\perp a} = 0$ $(\frac{\omega}{v_1} = \beta)$.

We have also plotted the dispersion curves for the lower ranges $(\frac{\beta r_c}{\pi} \in [0, 1]$ and $\frac{\omega r_c}{\pi v_2} \in [0, 4])$ (Figure 2, right), which is consistent with the work by Armenákas [2] (Figure 8, p. 831). In the second part of Figure 2, we observe that the slope of the curve representing the second root may be negative. This phenomenon cannot be obtained in a classical optical waveguide [9], but may arise for instance in similar problems for photonic crystal fibres.

6.2.   FLEXURAL MODES

To determine the frequency equation for flexural modes, one has to satisfy three homogeneous boundary conditions (3.1), which lead to equation (5.1). This frequency equation was studied in detail by Pao and Mindlin [7]. The low flexural modes (Figure 3, left) agree with Achenbach ([1], fig. 6.17, p. 248) and Armenákas ([2], fig. 10, p. 833) for a small angle of incidence. We note that for a large angle of incidence (Figure 3, right) our dispersion curves touch each other at different points: this is consistent

with the work by Pao and Mindlin [7], but differs from Armenákas ([2], fig. 10, p. 833).
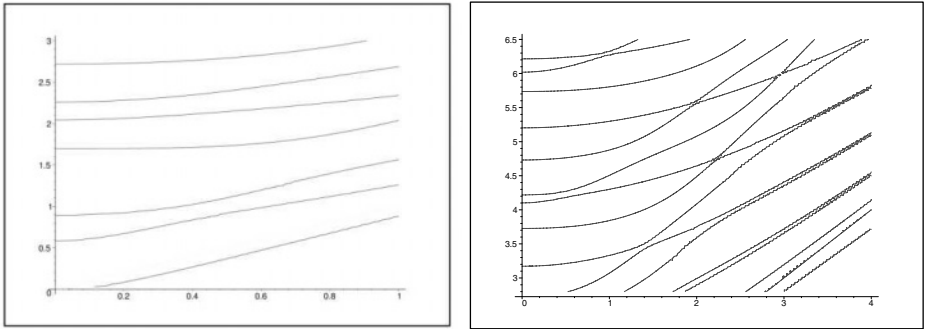
Figure 3 Flexural waves: dispersion curves for normalised frequencies ($\frac{\omega r_c}{\pi v_2}$) versus normalised angles of incidence ($\frac{\beta r_c}{\pi}$).

7. CONCLUSION

We have presented a model analysis of conically incident elastic waves on a single cylinder of circular cross-section. Our solution involving a canonical basis is used to generate dispersion diagrams for propagating modes. This study has been used to construct a rapidly convergent series representation for a solution of problem of oblique incidence of elastic waves on an array of circular cylindrical fibres via the multipole method [5].

Acknowledgments

References

[1] J. D. Achenbach, Harmonic waves in waveguides, in *Wave Propagation in Elastic Solids*, ed. by H. A. Lauwerier and W. T. Koiter . North-Holland Publishing Company (1973), p. 240.

[2] A. E. Armenákas, Propagation of harmonic waves in composite circular-cylindrical rods, *J. Acoust. Soc. Am.*, (1970), **47**, p. 822-837.

[3] D. C. Gazis, Three-dimensional investigation of the propagation of waves in hollow circular cylinders. I. Analytical Foundation II. Numerical results, *J. Acoust. Soc. Am.*, (1958), **31**, p. 568-578.

[4] S. Guenneau, C. Poulton and A.B. Movchan, A spectral problem for conically propagating elastic waves through an array of cylindrical channels, *C. R. Acad. Sci., series in Mechanics, Paris*, (2002), **330**, p. 491-497.

[5] S. Guenneau and A. B. Movchan, Analysis of elastic band structures for oblique incidence, *Archive for Rational Mechanics and Analysis*, (to appear).

[6] T. R. Meeker and A. H. Meitzler, Guided wave propagation in elongated cylinders and plates, in : *Physical Acoustics I PART A*, ed. by W. P. Mason. New York, Academic Press (1964), p. 130.

[7] Y.H. Pao, R.D. Mindlin, Dispersion of flexural waves in an elastic, circular cylinder, *Journal of Applied Mechanics*, (1960), p. 513-520.

[8] L. Pochammer, Ueber die Fortpflangzungsgeschwindigkeiten Kleiner Schwingungen in einem unbergrenzten isotropen Kreiscylinder, *Zeitschrift fur Mathematik*, (1876) **81**, p. 324-336.

[9] A.W Snyder, J.D. Love, Optical waveguide theory, *chapman and hall* (1983), New-York.

ASYMPTOTIC ANALYSIS OF A "CRACK" IN A LAYER OF FINITE THICKNESS

J.P. Bercial-Velez

Dept. of Mathematical Sciences, University of Liverpool L69 3BX, UK

jbercial@liv.ac.uk

Keywords: Wave equation, dynamic weight function.

Abstract   Rice *et al.* [1] studied a perturbation problem for the wave equation in a space containing a moving discontinuity surface. We analyse the solutions of the wave equation in a 3D layer, which contains a "crack" propagating dynamically, using the singular perturbation technique developed by Willis and Movchan [3]. The dynamic weight function is discussed for time-dependent Neumann boundary conditions on a semi-infinite "crack" extending at a constant speed V in a 3D layer. The Fourier transform of the weight function is constructed by solving a scalar Wiener-Hopf problem. In this case the weight function is no longer homogeneous (due to the geometry considered). Within the first order perturbation theory framework, a relationship between the intensity factor and a small time-dependent perturbation of the "crack" front is found; we also analyse the transfer function which relates the "crack" front position and the energy release rate.

1.   PROBLEM DESCRIPTION

Rice *et al.* [1] considered a crack propagating dynamically in an unbounded solid, and it was addressed within a model framework, involving a single "displacement variable" u satisfying a scalar wave equation. We consider a 3D layer bounded by the two planes $x_3 = \pm a$. The layer contains a "crack" extending dynamically, so that at time t it occupies the region $x_1 - Vt < 0$, $-\infty < x_2 < \infty$, $x_3 = 0$. The medium through which the "crack" propagates is isotropic, with the material constant μ and the mass density ρ. The problem we want to solve consists of the wave equation

$$\mu \nabla^2 u - \rho \frac{\partial^2 u}{\partial t^2} = 0, \tag{1.1}$$

and the Neumann boundary conditions on the "crack" surfaces

$$\mu \left.\frac{\partial u}{\partial x_3}\right|_{x_3=\pm 0} = -P(t, x_1, x_2), \quad x_1 < Vt,$$

where $P(t, x_1, x_2)$ is given. We also assume that $u = 0$ for $x_3 = \pm a$, and u and $\sigma \equiv \mu(\partial u/\partial x_3)$ are continuous ahead of the "crack", that is, for $x_3 = 0, x_1 > Vt$.

In what follows we shall use the method of [3] to analyse the associated σ field in the vicinity of the "crack". We shall begin by constructing the corresponding weight function which will then be used in the integral identity (see [3], formula (3.11))

$$[U] * \sigma - \Sigma * [u] = 0 \tag{1.2}$$

to evaluate the intensity factor at the "crack" tip. In (1.2) $[f]$ denotes the jump of f across the plane $x_3 = 0$, i.e., $[f] = f|_{x_3=0+} - f|_{x_3=0-}$. The quantities σ and Σ are evaluated for $x_3 = 0$.

2.   DYNAMIC WEIGHT FUNCTION FOR A 3D LAYER

To find the weight function, we consider the coordinate transformation $X = x_1 - Vt$, and define the weight function as a solution of equation (1.1) satisfying the following conditions:

(a) $[U] = 0$ for $X < 0$;

(b) $U = 0$ for $x_3 = \pm a$;

(c) $\Sigma \equiv \mu(\partial U/\partial x_3)$ is continuous and vanishes for $x_3 = 0$ and $X > 0$;

(d) $U \to kX^{-1/2}\delta(x_2)\delta(t)$ as $X \to 0^+$, where k is a constant.

We would like to emphasise that, due to the geometry considered, the weight function U is no longer homogeneous.

Taking the Fourier transform with respect to X, x_2, t,

$$\overline{U}(\omega', \xi_1, \xi_2, x_3) = \int_{-\infty}^{\infty} \int_{-\infty}^{\infty} \int_{-\infty}^{\infty} U(t, X + Vt, x_2, x_3)$$
$$\times e^{i(X\xi_1 + x_2\xi_2 + t\omega)} dX dx_2 dt,$$

we arrive at the equation

$$\frac{\partial^2 \overline{U}}{\partial x_3^2} = \gamma^2 \overline{U}, \tag{2.1}$$

where $\gamma^2 = \xi_1^2 + \xi_2^2 - (\omega'^2/c^2)$, $\omega' = \omega - V\xi_1$ and $c = \sqrt{\rho/\mu}$. Using the symmetry we find the solution $\overline{U}$ of (2.1) in the form

$$\overline{U} = A\cosh(\gamma x_3) + B\sinh(\gamma x_3), \quad x_3 \in (0, a), \tag{2.2}$$

where A and B are constants. The boundary conditions $(a) - (c)$ give

$$A = -B\tanh(\gamma a), \quad B = (\mu\gamma)^{-1}\overline{\Sigma}\big|_{x_3=0}. \tag{2.3}$$

Using (2.2) and (2.3) we derive the following relation

$$[\overline{U}] = -\frac{p(\omega', \xi_1, \xi_2)}{\mu\gamma(\omega', \xi_1, \xi_2)}\overline{\Sigma}\big|_{x_3=0}, \tag{2.4}$$

where $p(\omega', \xi_1, \xi_2) = \tanh(a\gamma(\omega', \xi_1, \xi_2))$. From the conditions (a) and (c), with ω, ξ_2 fixed, we deduce that $[\overline{U}](\xi_1)$ is analytic in the upper half-plane $Im(\xi_1) > -id_1$ (we shall call it a " $+$ " function and denote $[\overline{U}]^{(+)}$), and $\overline{\Sigma}(\xi_1)$ is analytic in the lower half-plane $Im(\xi_1) < id_2$ (we shall call it a " $-$ " function and denote $\overline{\Sigma}^{(-)}$); here $d_1, d_2 > 0$. In the strip $S = \{\xi_1 \in \mathbb{C} : -id_1 < Im(\xi_1) < id_2\}$ both functions are analytic.

The function $p(\xi_1)$ has infinitely many poles and zeros, which are given by

$$\xi_1^{p(n)} = -\frac{\omega V}{c^2 - V^2} \pm \frac{c}{c^2 - V^2}\left(\omega^2 - (c^2 - V^2)\xi_2^2 - \frac{(2n+1)^2\pi^2(c^2 - V^2)}{4a^2}\right)^{1/2} \quad \text{(poles)}$$

$$\xi_1^{z(n)} = -\frac{\omega V}{c^2 - V^2} \pm \frac{c}{c^2 - V^2}\left(\omega^2 - (c^2 - V^2)\xi_2^2 - \frac{n^2\pi^2(c^2 - V^2)}{a^2}\right)^{1/2} \quad \text{(zeros)}$$

Figure 1 illustrates the position of the poles and zeros of $p(\xi_1)$ for $a = 1$, $c = 1$, $\omega = 1 + 0.3i$ and $\xi_2 = 0$.

Since $p(\xi_1) \to 1$ as $\xi_1 \to \infty$, we can write it as a product p_+p_-, where p_+ is analytic in the upper half plane $Im(\xi_1) > -id_1$ and p_- is analytic in the lower half plane $Im(\xi_1) < id_2$; the functions p_+ and p_+ have the form

$$p_\pm = \exp\left\{\frac{1}{2\pi i}\int_{-\infty\mp\delta i}^{\infty\mp\delta i}\frac{\log p(\zeta)}{\zeta - \xi_1}d\zeta\right\}, \tag{2.5}$$

with $\delta > 0$ chosen in such a way that both contours of integration lie in the common strip of analyticity S. Since $p(\xi_1) - 1$ decays exponentially as $\xi_1 \to \infty$, both integrals in (2.5) converge. The remaining factor $\gamma(\xi_1)$ in (2.4) can be factorised as follows:

$$\gamma(\xi_1) = \alpha(\xi_1 - \xi_1^+)^{1/2}(\xi_1 - \xi_1^-)^{1/2},$$

where $\alpha = \left(1 - \dfrac{V^2}{c^2}\right)^{1/2}$, and

$$\xi_1^{\pm} = -\frac{\omega V}{c^2 - V^2} \pm \frac{1}{c^2 - V^2} c(\omega^2 - (c^2 - V^2)\xi_2^2)^{1/2}. \tag{2.6}$$

Equation (2.4) can then be written in the form

$$\frac{[\overline{U}]^{(+)}(\xi_1 - \xi_1^-)^{1/2}}{\sqrt{2i}p_+(\xi_1)} = -\frac{p_-(\xi_1)\overline{\Sigma}^{(-)}}{\sqrt{2i}\alpha\mu(\xi_1 - \xi_1^+)^{1/2}}. \tag{2.7}$$

Applying Liouville's theorem we obtain

$$[\overline{U}]^{(+)} = \frac{\sqrt{2i}p_+(\xi_1)}{(\xi_1 - \xi_1^-)^{1/2}}, \quad \overline{\Sigma}^{(-)} = -\frac{\sqrt{2i}\alpha\mu(\xi_1 - \xi_1^+)^{1/2}}{p_-(\xi_1)}. \tag{2.8}$$

As $\xi_1 \to \infty$,

$$p_{\pm} \sim \exp\left\{\frac{-1}{\xi_1 \pm i0}\frac{1}{2\pi i}\int_{-\infty \mp i\delta}^{\infty \mp i\delta} \log p(\zeta)d\zeta\right\}$$

$$\sim 1 - \frac{1}{\xi_1 \pm i0}\frac{1}{2\pi i}\int_{-\infty \mp i\delta}^{\infty \mp i\delta} \log p(\zeta)d\zeta,$$

and therefore,

$$[\overline{U}]^{(+)} \sim \frac{\sqrt{2i}}{(\xi_1 + 0i)^{1/2}}\left(1 + \frac{i\overline{Q}}{\xi_1 + 0i}\right), \tag{2.9}$$
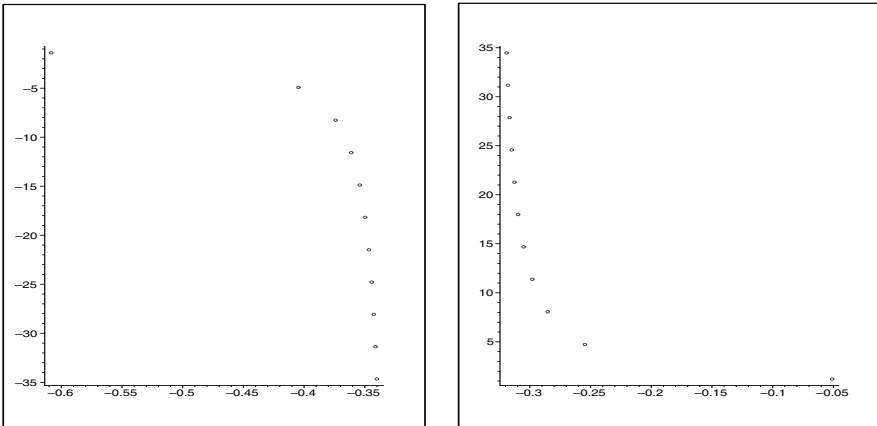
Figure 1   Poles of $p(\xi_1)$ for $a = 1$, $c = 1$, $\omega = 1 + 0.3i$ and $\xi_2 = 0$.

where

$$i\overline{Q}(\xi_2, \omega) = \frac{\xi_1^-}{2} - \frac{1}{2\pi i} \int_{-\infty-i\delta}^{\infty-i\delta} \log\tanh(\gamma(\zeta)a)d\zeta. \tag{2.10}$$

Numerical calculations show that

$$\lim_{a\to\infty} \int_{-\infty-i\delta}^{\infty-i\delta} \log\tanh(\gamma(\zeta)a)d\zeta = 0, \tag{2.11}$$

the latter agrees with the result of [3],[5] for the entire space.

3.   APPLICATION TO A WAVY "CRACK"

Assume now that the "crack" occupies the region $x_1 - Vt < \varepsilon\varphi(t, x_2)$, $-\infty < x_2 < \infty$, $x_3 = 0$, where $0 < \varepsilon \ll 1$ is a small parameter, and the function φ is bounded. A solution will be sought using first order perturbation theory, for small ε. The fields u and σ associated with the perturbed "crack" are represented as $u^0 + \Delta u$ and $\sigma^0 + \Delta\sigma$, where u^0 and σ^0 are the fields corresponding to the unperturbed configuration. The identity (1.2) applies to both the unperturbed and the perturbed fields. Subtracting one identity from the other gives

$$[U]^{(+)} * \Delta\sigma - \Sigma^{(-)} * [\Delta u] = 0. \tag{3.1}$$

We can write σ as $\sigma(t, X, x_2, 0) = -P(t, X, x_2)H(-X) + \sigma^{(+)}(t, X, x_2)$, where

$$\sigma^{(+)} \sim \left\{ \frac{K(t, x_2)}{\sqrt{2\pi X}} - P(t, 0, x_2) + AX^{1/2} \right\} H(X),$$

and using the result of [4] we have

$$[u] \sim \left\{ \frac{K\sqrt{(-X)}}{\mu\alpha\sqrt{2\pi}} - B(-X)^{3/2} \right\} H(-X).$$

Therefore, applying (1.2) we obtain

$$\overline{\Delta K} = \varepsilon \left[\overline{Q}\,\overline{\varphi K_0} + \left(\frac{\pi}{2}\right)^{1/2} \overline{\varphi A} \right]. \tag{3.2}$$

A and K_0 can be found from [2]

$$A = \frac{Pa}{4}\sqrt{\frac{\pi}{a^3\alpha}}, \quad K_0 = Pa\sqrt{\frac{2\alpha}{a}}. \tag{3.3}$$

4.   ENERGY RELEASE RATE AND TRANSFER FUNCTION

Let us define the energy release rate G as $G = \dfrac{K^2}{2\mu\alpha}$. We shall follow the method of [5] and find the transfer function h which relates the "crack" front position and the energy release rate. For the perturbation of the "crack" front described above, we can write $K = K_0 + \varepsilon K_1 \varphi$ and $V = V_0 + \varepsilon\dot\varphi$, where K_0 is the intensity factor for the unperturbed "crack". Since $K^2 B(V) = G(V)$, we obtain:

$$(K_0 + \varepsilon K_1 \varphi)^2 (B(V_0) + \varepsilon\dot\varphi B')V_0) = G,$$

where $B(V) = (2\mu\alpha)^{-1}$. Thus,

$$\frac{\Delta G}{G_0} = \varepsilon \left\{ 2\frac{K_1\varphi}{K_0} + \dot\varphi\frac{B'(V_0)}{B(V_0)} \right\}. \tag{4.1}$$

Taking the Fourier transform gives

$$\frac{\overline{\Delta G}}{\varepsilon G_0} = \left\{ 2\frac{\overline{K_1}}{\overline{K_0}} - \frac{iV_0\omega}{c^2\left(1 - V_0^2/c^2\right)} \right\}\overline\varphi.$$

Since $\dfrac{\overline{\Delta K}}{K_0} = \varepsilon\dfrac{\overline{K_1}}{\overline{K_0}}\overline\varphi$, we obtain

$$\frac{\overline{\Delta G}}{G_0} = \left\{ 2\frac{\overline{\Delta K}}{K_0} - \frac{iV_0\omega}{c^2 - V_0^2}\,\overline\varphi\varepsilon \right\}. \tag{4.2}$$

We can now use the expression (3.2) to derive

$$\frac{\overline{\Delta G}}{\varepsilon\,G_0} = \left[\frac{2}{K_0}(\overline{QK_0} + (\pi/2)^{1/2}A) - \frac{iV_0\omega}{c^2 - V_0^2} \right]\overline\varphi. \tag{4.3}$$

Thus, the relationship between "crack" front position and energy release rate has the form

$$\varepsilon\overline\varphi = \overline h\,\frac{\overline{\Delta G}}{G_0}, \tag{4.4}$$

where the transfer function $\overline h$ is given by

$$\overline h = \left[(2\pi)^{1/2}\frac{A}{K_0} + 2\overline Q - \frac{iV_0\omega}{c^2 - V_0^2} \right]^{-1}. \tag{4.5}$$

Since in (4.4) $\overline{\Delta G} \to 0$ at the "crack" front and $\varepsilon\overline\varphi$ remains finite, $\overline h$ should tend to infinity when we approach the perturbed "crack" front. Hence, to

determine the velocities of the "crack" front waves, we are looking for the poles of $\overline{h}$. The latter, considering the values for A, K_0 in (3.3) gives us the following

$$\frac{\pi^{3/2}}{4\alpha a} + 2\overline{Q} - \frac{iV_0\omega}{c^2 - V_0^2} = 0. \tag{4.6}$$

Taking into account the structure of $\overline{Q}(\xi_2, \omega)$ given by (2.10) and the representation (2.6) for ξ_1^- we arrive at the following equation

$$\frac{\pi^{3/2}}{4\alpha a} + ic\frac{(\omega^2 - (c^2 - V_0^2)\xi_2^2)^{1/2}}{c^2 - V_0^2} + \frac{1}{\pi}\int_{-\infty-i\delta}^{\infty-i\delta} \log\tanh(\gamma(\zeta)a)d\zeta = 0, \tag{4.7}$$

where $\gamma(\zeta) = \left(\left(1 - \frac{V_0^2}{c^2}\right)\zeta^2 + 2\frac{\omega V_0}{c^2}\zeta + \xi_2^2 - \frac{\omega^2}{c^2}\right)^{1/2}$.

We are going to analyse the structure of equation (4.7), for large a. The integrand in (4.7) is exponentially small for large a and therefore we obtain

$$\frac{\pi^{3/2}}{4\alpha a} + ic\frac{(\omega^2 - (c^2 - V_0^2)\xi_2^2)^{1/2}}{c^2 - V_0^2} = 0. \tag{4.8}$$

Writing $\omega^2 = v^2\xi_2^2$, we can solve (4.8) for v to obtain

$$v^2 = (c^2 - V_0^2)\left(\frac{16a^2\omega^2}{16a^2\omega^2 + (c^2 - V_0^2)\pi^3}\right). \tag{4.9}$$

As $a \gg 1$,

$$v^2 + V_0^2 \sim c^2 - \frac{(c^2 - V_0^2)^2\pi^3}{16a^2\omega^2},$$

which shows the presence of "crack" front waves for $0 < \sqrt{v^2 + V_0^2} < c$ for a "crack" propagating within a layer of finite thickness.

However, in the limit as $a \to \infty$ we obtain $v^2 + V_0^2 = c^2$. Therefore, for a "crack" propagating in an infinite space, there are no "crack" front waves whose total velocities satisfy $0 < \sqrt{v^2 + V_0^2} < c$.

Acknowledgments

References

[1] Rice, J.R., Ben-Zion, Y. and Kim, K.S., (1994) "Three-dimensional perturbation solution for a dynamic crack moving unsteadily in a model elastic solid", *J. Mech. Phys. Solids*, **Vol. 42**, No. 5, 814-843.

[2] Sih, G. C., Chen, E. P., (1970) "Moving cracks in a finite strip under tearing action" *Journal of the Franklin Institute* **Vol. 290**, No.1.

[3] Willis, J. R. and Movchan, A. B., (1995) "Dynamic weight functions for a moving crack. I. Mode I loading", *J. Mech. Phys. Solids*, **Vol. 43**, No. 3, 319-341.

[4] Freund, L. B., (1998) "Dynamic fracture mechanics", *Cambridge University Press.*

[5] Woolfries, S., Movchan, A. B., Willis, J. R., (2002) "Perturbation of a dynamic planar crack moving in a model viscoelastic solid" *Int. J. Solids Struct.* , **Vol. 39**, Nos. 21-22, 5409-5426.

SUMMATION OF GAUSSIAN BEAMS IN 3D PROBLEMS OF RADIATION AND SCATTERING OF ELASTIC WAVES

V. Zalipaev

Faculty of Mathematical Studies, University of Southampton

vvz@maths.soton.ac.uk

Abstract   The method of Gaussian Beams Summation is applied to the two important problems of the theory of elastic waves - the scattering of compressional wave from a planar crack embedded into a homogeneous and isotropic elastic medium and time-harmonic radiation of a normal transducer of arbitrary shape directly coupled to a homogeneous and isotropic elastic solid. The problems are studied in the case of high-frequency approximation. Moreover, the radiating near zone of transducer and the near zone of the field scattered from crack is analyzed. The radiated and scattered fields have the ray structure of main beam and edge diffracted rays. A family of the edge diffracted rays is singular near to caustics. A well-known ray asymptotic solution of the Geometrical Theory of Diffraction (GTD) is not valid near to caustics. Application of the method of Gaussian Beams Summation to both problems in the neighborhood of caustics has proved to be efficient from the point of view of asymptotic and computational analysis.

Introduction

One of the main methods to study radiation, propagation or scattering of elastic short waves is the application of the ray asymptotic method. The leading order of a ray asymptotic solution is represented as a product of rapidly oscillating function and slowly varying amplitude (see, for example, [1] and [2]). The amplitude involves a square root of geometrical spreading in the denominator. Derivation of the ray solution is based on so-called ray coordinates, which determine ray trajectories and wave front surfaces. The geometrical spreading characterizes divergence of rays and is calculated as a Jacobian of a transformation between the Cartesian and the ray coordinates. However, in practice a family of rays, the ray method solution is based on, frequently becomes singular. This means that the Jacobian of a transformation between the Cartesian and the so-called ray coordinates

vanishes at some manifolds called caustics (geometrical spreading is zero). These manifolds could be a surface, a line or a point. Thus the ray solution becomes singular. There are some methods to tackle the problem. One of them is the Gaussian beams summation method GBSM (see review [3]).

This talk describes the application GBSM to 3D problems of the scattering of compressional wave from a planar crack embedded into a homogeneous and isotropic elastic medium and time-harmonic radiation of a normal transducer of arbitrary shape directly coupled to a homogeneous and isotropic elastic solid studied before in [4] and [5]. The problems are considered in the case of high-frequency approximation (HFA). Both, the edge of a crack and the transducer rim, may have an arbitrary shape of smooth edge. For both problems the near zone of radiated or scattered field is considered. The ray structure of radiated or scattered fields has direct rays of main beams, radiated or reflected, surrounded by a geometrical shadow boundary (penumbra) as well as a family of edge diffracted rays emitted by the transducer rim or the crack edge.

The Geometrical Theory of Diffraction (GTD) asymptotic solution is applicable to both problems. However, it fails, firstly near the penumbra of the main beam, and then, near to caustics of diffracted rays of compressional and shear edge waves. The traditional recipe of GTD to treat singularity near to penumbra has been used. The main subject of the talk is the application of GBSM to treat singularity near to caustics in both problems . The unique property of Gaussian beam being regular, near to, or exactly on caustics of an arbitrary geometrical structure, is used to represent HFA of contribution of compressional and shear edge diffracted waves in the form of a double integral over Gaussian beams. This is based on a fan of rays covering the neighborhood of the observation point lying near caustics.

1.　SCATTERING OF A PLANE P-WAVE FROM A PLANAR CRACK

Consider the first time-harmonic problem in which the incident field illuminating the crack S is a plane compressional wave (see Fig. 1) given by

$$\mathbf{u}^{P(inc)} = \mathbf{n}_{inc}^{P} e^{ik_P \mathbf{n}_{inc}^{P} \cdot \mathbf{x}}, \tag{1.1}$$

where the unit displacement vector in the Cartesian coordinate system is

$$\mathbf{n}_{inc}^{P} = \sin\theta^{P}\cos\varphi_0\ \mathbf{e}_x + \sin\theta^{P}\sin\varphi_0\ \mathbf{e}_y - \cos\theta^{P}\ \mathbf{e}_z.$$

In the paper, $k_\alpha = \omega/c_\alpha$ is a wave number, ω is the frequency and c_α is the speed of the compressional wave if $\alpha = P$ and shear if $\alpha = S$. Then the time-harmonic displacement field $\mathbf{u} = \mathbf{u}^{P(inc)} + \mathbf{u}^{(scat)}$ inside the solid

Scattering of a plane P wave from crack
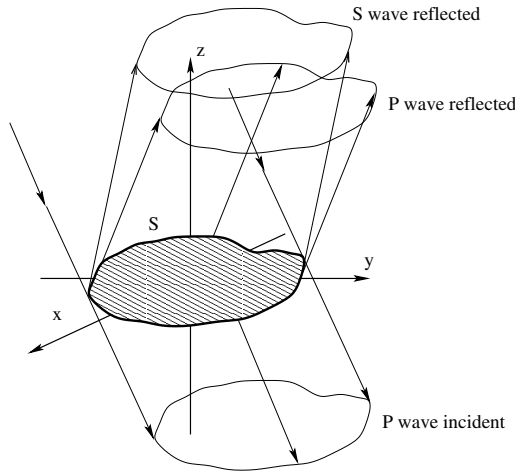
Figure 1 Scattering of compressional plane wave from crack S.

is described by the reduced elastodynamic equation

$$(c_P^2 - c_S^2)\nabla \mathrm{div}\mathbf{u} + c_S^2\Delta\mathbf{u} + \omega^2\mathbf{u} = 0, \qquad (1.2)$$

the total vector displacement of the scattered field $\mathbf{u}^{(scat)}$ decomposes into P and S waves $\mathbf{u}^{(scat)} = \mathbf{u}^{P(scat)} + \mathbf{u}^{S(scat)}$. The total displacement satisfies the zero surface traction boundary condition on the crack surface

$$(\sigma_{ij}^{(tot)} \cdot n_j)|_S = \sigma_{i3}^{(tot)}|_S = 0, \qquad (1.3)$$

where $\sigma_{ij}^{(tot)}$ are the components of the stress tensor of the total field. We are interested in the high-frequency approximation of the displacement of the scattered field $\mathbf{u}^{(scat)}$, namely, we assume that $k_P\rho \gg 1$, where ρ is the radius of curvature of the crack edge or transducer rim. Moreover, only the case of the near field is studied, that is, the distance between the observation point and transducer or crack is supposed to be comparable with their dimensions.

Let us assume that the observation point does not lie in the vicinity of the geometrical shadow boundary. Let $\mathbf{x}^{\alpha(GE)}$ denote so-called specular point which is the point of reflection of the incident ray from crack plane according to the law of geometrical optics (elastodynamics) or the point of intersection of the incident ray with crack plane. High-frequency asymptotic approach based on the uniform stationary phase method and Green formula which was developed in [4] yields the asymptotics of the scattered

filed in the form:

$$\mathbf{u}^{\alpha(scat)}(\mathbf{x}) = \mathbf{u}^{\alpha(GE)} + \mathbf{u}^{\alpha(dif)}(\mathbf{x}), \qquad (1.4)$$

where the first, geometric elastodynamic, term is

$$\mathbf{u}^{\alpha(GE)} = R_\alpha H_\alpha \mathbf{p}^{\alpha(ref)} e^{ik_\alpha \mathbf{n}_r^\alpha \cdot \mathbf{x}}, \ \ z > 0, \ \ \mathbf{u}^{P(GE)} = -\mathbf{n}_{inc}^P H_P e^{ik_P \mathbf{n}_{inc}^P \cdot \mathbf{x}}, \ \ z < 0,$$
$$(1.5)$$

where $H_\alpha = 1$ if $\mathbf{x}^{\alpha(GE)} \in S$ and $H_\alpha = 0$ if $\mathbf{x}^{\alpha(GE)} \notin S$. The polarization vector is given by

$$\mathbf{p}^{P(ref)} = \mathbf{n}_r^P, \qquad \mathbf{p}^{S(ref)} = \mathbf{n}_{r\perp}^S,$$

where the directional unit vectors for P and S reflected waves as well as the unit vector of particle motion for S wave (see, for example, [2]) are

$$\mathbf{n}_r^\alpha = \sin\theta^\alpha \cos\varphi_0 \ \mathbf{e}_x + \sin\theta^\alpha \sin\varphi_0 \ \mathbf{e}_y + \cos\theta^\alpha \ \mathbf{e}_z,$$

$$\mathbf{n}_{r\perp}^S = (-\cos\theta^S \cos\varphi_0, -\cos\theta^S \sin\varphi_0, \sin\theta^S),$$

where $\sin\theta^S = \sin\theta^P c_S/c_P$. The following are P and S plane wave reflection coefficients

$$R_P = \frac{\sin 2\theta^P \sin 2\theta^S - \cos^2 2\theta^S (k_S/k_P)^2}{\sin 2\theta^P \sin 2\theta^S + \cos^2 2\theta^S (k_S/k_P)^2},$$

$$R_S = \frac{-2\sin 2\theta^P \cos 2\theta^S k_S/k_P}{\sin 2\theta^P \sin 2\theta^S + \cos^2 2\theta^S (k_S/k_P)^2}.$$

The second term is the edge diffracted P or S waves. According to GTD, it is represented by contributions of two or four rays coming from the so-called edge flash points s_m^α, which obey the Snell's law for P wave

$$< \mathbf{e}_t(s), \mathbf{n}_{inc}^P > = < \mathbf{e}_t(s), \mathbf{n}(s) >,$$

and for S wave

$$k_P < \mathbf{e}_t(s), \mathbf{n}_{inc}^P > = k_S < \mathbf{e}_t(s), \mathbf{n}(s) >,$$

where $<,>$ stands for a scalar product, and s is the arc length along the edge, $\mathbf{e}_t(s)$ is the unit vector tangent to the edge, $\mathbf{n}(s)$ is the unit vector pointing direction from an edge point $\mathbf{x}(s)$ to the observation point $\mathbf{x}$. They are critical points of the phase function $\tau^\alpha(s)$ given by

$$k_\alpha \tau^\alpha(s) = k_P \mathbf{n}_{inc}^P \cdot \mathbf{x}(s) + k_\alpha d(s), \qquad d(s) = |\mathbf{x} - \mathbf{x}(s)|.$$

If all s_m^α are isolated from each other, we have the GTD contributions of the flash points given by

$$\mathbf{u}^{\alpha(dif)}(\mathbf{x}) = \sum_{m=1}^{M_\alpha} \mathbf{u}_m^{\alpha(dif)}(\mathbf{x}),$$

Keller's Diffraction Cone
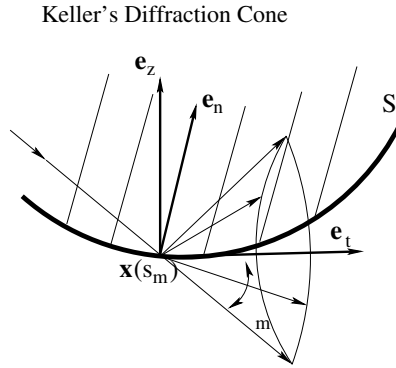
Figure 2 Keller's diffraction cone in scattering of a plane wave from edge

where

$$\mathbf{u}_m^{\alpha(dif)}(\mathbf{x}) = \frac{D^\alpha(s_m^\alpha, \varphi_m^\alpha)}{\sqrt{k_\alpha J_m^\alpha}} \mathbf{p}_m^\alpha \mathrm{e}^{ik_\alpha \tau^\alpha(s_m^\alpha) + i(-1)^m \pi/4} \cdot (1 + O(k_\alpha^{-1})), \quad (1.6)$$

and M_α, which equals 2 or 4, is the number of flash points. The Keller's diffraction coefficients $D^\alpha(s_m^\alpha, \varphi_m^\alpha)$ and the components of the polarization vector $\mathbf{p}_m^\alpha$ can be found in [4]. This is a ray asymptotic solution. In accordance with GTD, an incident ray that hits a flash point $\mathbf{x}(s_m^\alpha)$ generates two cones of the edge diffracted rays of P and S waves. The corresponding ray coordinates are $(s_m^\alpha, \varphi_m^\alpha, \tau_m^\alpha)$ (see [1, 2]), where $\tau_m^\alpha = \tau^\alpha(s_m^\alpha)$, and φ_m^α is the polar angle (see Fig. 2), so that the unit directional vector lying on the cone surface is given by

$$\mathbf{n}_m^\alpha = \mathbf{e}_t(s_m^\alpha) \cos \Omega_m^\alpha + \mathbf{e}_n(s_m^\alpha) \sin \Omega_m^\alpha \cos \varphi_m^\alpha + \mathbf{e}_z \sin \Omega_m^\alpha \sin \varphi_m^\alpha. \quad (1.7)$$

The geometrical spreading is

$$J_m^\alpha = \frac{\partial(x, y, z)}{\partial(s_m^\alpha, \varphi_m^\alpha, \tau_m^\alpha)}.$$

It is known that the GTD ray asymptotics of edge waves described above (nonuniform asymptotics) are singular, first, in the vicinity of geometrical shadow boundary (penumbra). Geometrically, the specular point $\mathbf{x}^{\alpha(GE)}$ gets very close to one of the flash points $\mathbf{x}(s_n^\alpha)$. In this case, applying the uniform GTD, to two leading order we obtain

$$\mathbf{u}^{\alpha(scat)}(\mathbf{x}) = \mathbf{u}_n^{\alpha(pen)}(\mathbf{x}) + \sum_{m=1}^{M_\alpha} \mathbf{u}_m^{\alpha(dif)}(\mathbf{x}), \quad (1.8)$$

where the extra term cancelling the singularity looks like this

$$\mathbf{u}_n^{\alpha(pen)}(\mathbf{x}) = R_\alpha F(v_n^\alpha)\mathbf{p}^{\alpha(ref)}e^{ik_\alpha \mathbf{n}_r^\alpha \cdot \mathbf{x}}, \quad z > 0,$$

$$\mathbf{u}_n^{P(pen)} = -\mathbf{n}_{inc}^P F(v_n^P)e^{i\mathbf{k}^{P(inc)} \cdot \mathbf{x}}, \quad z < 0. \tag{1.9}$$

The function $F(v)$ is expressed via the Fresnel integral

$$F(v) = \frac{1}{\sqrt{\pi i}}\left[\int_v^\infty e^{it^2}dt + \frac{e^{iv^2}}{2iv}\right], \tag{1.10}$$

$$(v_n^\alpha)^2 = k_\alpha(\tau_n^\alpha - \mathbf{n}_r^\alpha \cdot \mathbf{x}), \quad z > 0, \qquad (v_n^P)^2 = k_P(\tau_n^P - \mathbf{n}_{inc}^P \cdot \mathbf{x}), \quad z < 0.$$

2.   SUMMATION OF GAUSSIAN BEAMS. CAUSTICS OF THE SCATTERED FIELD

The GTD ray asymptotics of edge waves (1.6) (nonuniform asymptotics) are singular in the vicinity of caustic surface as the geometrical spreading in the denominator of the amplitude vanishes. This corresponds to a coalescence of two or three flash points. One of alternative methods to replace the GTD asymptotic solution in this case is Gaussian beams summation method (GBSM) (see review [3] and there cited references as well as the history of the method). If the observation point crosses a smooth part of the caustic surface, two flash points coalesce. If three flash points coalesce, that means that the observation point comes near caustic cusp. In the Fig. 3 (a), you can see the caustics of the edge diffracted P wave in the case of normal incidence and elliptic crack with $a = 4\lambda_S$ and $b = 2\lambda_S$. This is a vertical cylinder based on astroid. In case of oblique incidence with $\theta^P = 30^0$ and $\varphi_0 = 45^0$, a piece of caustic surface of the edge diffracted P wave is shown in Fig. 3 (b). We have approximately the same picture of the P edge wave caustics for the case of a circular crack and oblique incidence. In all cases four edge cusps can be seen clearly if the edge curve is convex. Thus, it is obvious that the caustics is a closed surface located near the main incident or reflected beam. If the observation point is inside caustics we have four flash points and, consequently, four incoming edge rays. If the observation point is outside caustic surface we have two flash points and two incoming rays.

Consider first the scalar 3D case of acoustic wave propagation describing by the Helmholtz equation $(\Delta + \omega^2/c^2(\mathbf{x}))u(\mathbf{x}) = 0$, where frequency ω is a large parameter. Let l be a ray of a ray asymptotic solution. Then, the equality

$$\mathbf{x} = \mathbf{x}(\sigma) + \mathbf{e}_1(\sigma)q_1 + \mathbf{e}_2(\sigma)q_2$$

represents an orthogonal coordinate system (σ, q_1, q_2) describing the neighborhood of the ray l given by $\mathbf{x} = \mathbf{x}(\sigma)$, where σ is the arc length along the
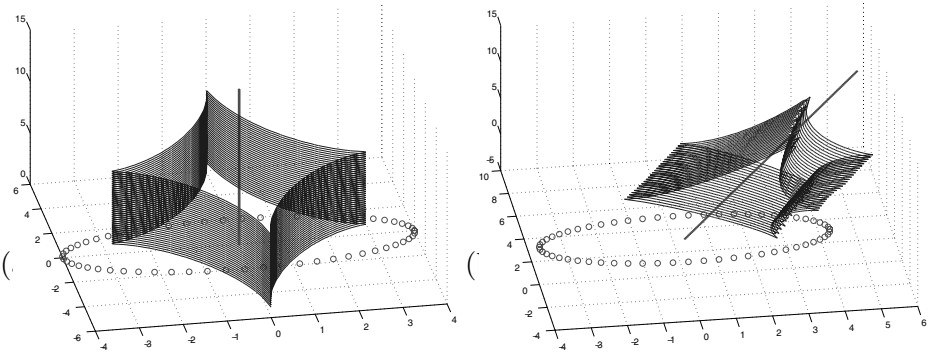
Figure 3 Parts of P edge wave caustics in the case of normal incidence - a, and in case of oblique incidence with $\theta^P = 30^0$, $\varphi_0 = 45^0$ - b, and elliptic crack with $a = 4\lambda_S$ and $b = 2\lambda_S$. The crack is illuminated from above.

ray. Here $\mathbf{e}_1$ and $\mathbf{e}_2$ are mutually orthogonal unit vectors lying in the plane orthogonal to l for arbitrary σ. This coordinate system is always regular within asymptotically small neighborhood of the ray. A solitary Gaussian beam as a localized asymptotic solution to the Helmholtz equation calculated at the point M with coordinates σ, q_1, q_2 inside asymptotically small neighborhood of the ray l is given by

$$u(M) = \sqrt{\frac{c_0(\sigma)}{\det Q}} \exp\{i\omega(\tau_0(M) + \frac{1}{2} < \Gamma q, q >)\}(1 + O(\omega^{-1/2})), \quad (2.1)$$

where $q = (q_1, q_2)$, and $c_0(\sigma)$ is the speed of wave propagation calculated along the ray l. The eikonal $\tau_0(M)$ is determined by

$$\tau_0(M) = \int_{\sigma_0}^{\sigma} \frac{d\sigma}{c_0(\sigma)}. \quad (2.2)$$

The symbol $< \Gamma q, q >$ means a quadratic form with a complex symmetric 2×2 matrix $\Gamma = PQ^{-1}$. The 2x2 matrices Q and P satisfy the system ODE in variations

$$\dot{Q} = c_0(\sigma)P, \quad \dot{P} = -\frac{1}{c_0^2(\sigma)}\Phi(\sigma)Q, \quad \Phi_{ij} = \left(\frac{\partial^2 c}{\partial q_i \partial q_j}\right)\Big|_{g_1=q_2=0}.$$

It is important that this solution is always regular whatever a geometrical structure of caustics takes place as the $\det Q$ never vanishes. This is an asymptotically localized solution as the matrix Γ has definite positive imaginary part $\text{Im}\{< \Gamma q, q >\} > 0$. It decays exponentially away from the fixed ray l.

The desired form of asymptotic solution which is regular near caustics is the integral over Gaussian beams (GBS) with a weight where the integration proceeds over a domain such that the corresponding rays totally cover the neighborhood of the observation point lying near to caustics.

Thus, for displacement representing contributions of compressional and shear diffracted edge waves, namely, for the part corresponding coalescing flash points, to the leading order we have the following GBS integral

$$\mathbf{u}^{\alpha(dif)} = \int_{\delta s} \int_{\delta \varphi} \frac{\mathbf{A}^{\alpha}(s, \varphi)}{\sqrt{\det Q^{\alpha}}} \exp\{ik_{\alpha}(\tau_0^{\alpha}(s, \varphi) + \frac{1}{2} < \Gamma^{\alpha} q, q >)\} ds d\varphi$$

$$\cdot (1 + O(k_{\alpha}^{-1/2})), \tag{2.3}$$

where the eikonal is

$$\tau_0^{\alpha}(s, \varphi) = k_P/k_{\alpha} \mathbf{n}_{inc}^P \cdot \mathbf{x}(s) + d(s).$$

The complex solutions of $\dot{Q}^{\alpha} = P$, $\dot{P}^{\alpha} = 0$ are chosen in the following way

$$Q^{\alpha}(\sigma) = \begin{pmatrix} a_1 + ia_2\sigma & 0 \\ 0 & a_1 + ia_2\sigma \end{pmatrix}, \qquad P^{\alpha} = \begin{pmatrix} ia_2 & 0 \\ 0 & ia_2 \end{pmatrix}, \tag{2.4}$$

so that we have

$$\Gamma^{\alpha}(\sigma) = P^{\alpha} Q^{\alpha-1} = \begin{pmatrix} \frac{ia_2}{a_1+ia_2\sigma} & 0 \\ 0 & \frac{ia_2}{a_1+ia_2\sigma} \end{pmatrix}. \tag{2.5}$$

Parameters a_1, a_2 are positive numbers which must be chosen in such a way that the width of Gaussian beams is as small as possible. The domain of integration in the GBS integral must be chosen in such a way so that discretising the GBS integral using, for example, the rectangular formula, we have a rather dense fan of rays totally covering the neighborhood of the observation point.

Away from the caustic surface, where the family of rays are regular, the GBS integral may be evaluated asymptotically using the saddle-point method. Thus, this result must coincides with the ray asymptotic solution. Matching both asymptotic expansions we can determine the unknown amplitude $\mathbf{A}^{\alpha}(s, \varphi)$

$$\mathbf{A}^{\alpha}(s, \varphi) = \frac{e^{-i\pi/4}}{2\pi} \sqrt{k_{\alpha} \det(P^{\alpha} G_q^{\alpha} - G_p^{\alpha} Q^{\alpha})} D^{\alpha}(s, \varphi) \mathbf{p}^{\alpha}, \tag{2.6}$$

where

$$G_q^{\alpha}(s, \varphi) = \begin{pmatrix} d(s) \sin \Omega^{\alpha} & -d(s) \cos \Omega^{\alpha} \sin \varphi / \rho(s) \\ 0 & \sin \Omega^{\alpha} - d(s)(\dot{\Omega}^{\alpha} + \cos \varphi / \rho(s)) \end{pmatrix}$$

$$G_p^\alpha(s,\varphi) = \begin{pmatrix} \sin\Omega^\alpha & -\cos\Omega^\alpha \sin\varphi/\rho(s) \\ 0 & -(\dot{\Omega}^\alpha + \cos\varphi/\rho(s)) \end{pmatrix}$$

Symbol $\dot{\Omega}^\alpha$ means a derivative with respect to s. Inside a smooth caustic boundary layer if two flash points with s_1^α and s_2^α coalesce, the P and S wave component of the scattered field is

$$\mathbf{u}^{\alpha(scat)}(\mathbf{x}) = \mathbf{u}^{\alpha(GE)} + \mathbf{u}_{1,2}^{\alpha(caus)} + \sum_{m=3}^{4} \mathbf{u}_m^{\alpha(dif)}(\mathbf{x}), \qquad (2.7)$$

where $\mathbf{u}_{1,2}^{\alpha(caus)}$ is represented by the GBS integral in (2.3).

3.   RADIATION BY NORMAL TRANSDUCER

Let us consider the radiating field of a time-harmonic normal transducer of arbitrary convex shape (domain S). It is directly coupled to an elastic homogeneous half-space. We seek solution which satisfies the reduced elastodynamic equations and the following boundary conditions for the component of the stress tensor

$$\sigma_{zx}|_{z=0} = \sigma_{zy}|_{z=0} = 0, \sigma_{zz}|_{z=0} = -Q, \text{ if } \mathbf{x} \in S, \text{ and } \sigma_{zz}|_{z=0} = 0, \text{ if } \mathbf{x} \notin S,$$

where Q is the amplitude of the load per unit square element of S. In the Kirchhoff approximation offered in [5], in which the near zone of the radiating field was studied, each point of the transducer treated as a point source. Thus, the radiating field is the integral over S of HFA of the Green function of the Lamb problem. Using this model, in the radiating near zone of HFA the compressional edge diffracted wave of a solution is represented in the form of the following curvilinear integral (for the shear edge wave we have similar result)

$$\mathbf{u}^{P(dif)} = \frac{1}{ik_P} \int_0^L \frac{\exp(ik_P d(s))}{d(s) < \mathbf{e}_n(s), \mathbf{n}(s) >} f^P(\theta(s))\mathbf{n}(s)ds + ...,$$

$$f^P(\theta) = \frac{Q}{2\pi\mu}(2\sin^2\theta - \gamma^{-2})\cos\theta[(2\sin^2\theta - \gamma^{-2})^2 + \sin^2 2\theta\sqrt{\gamma^{-2} - \sin^2\theta}]^{-1},$$

$$\gamma = c_s/c_p, \quad \theta = \cos^{-1}\frac{d(s)}{z},$$

where $\mathbf{e}_n(s)$ is the unit vector in the plane $z = 0$ normal to the edge, and $\mathbf{n}(s), d(s)$ have the same meaning as in section 1. Evaluating this integral with the aide of the phase stationary method (see, for example, [6]), if all critical points s_m are isolated, we obtain the GTD ray asymptotics

$$\mathbf{u}^{P(dif)} = \frac{1}{ik_P} \sum_{m=1}^{M} \exp(ik_P R(s_m) + i\frac{\pi}{4}(-1)^m) \frac{f^P(\theta(s_m))\mathbf{n}(s_m)}{< \mathbf{e}_n(s_m), \mathbf{n}(s_m) >}\sqrt{\frac{2\pi}{k_P J_m}} + ...,$$

where geometrical spreading is given by $J_m = d(s_m)(1 - d(s_m)\cos\varphi_m\rho_m^{-1})$, and the number M of edge diffracted rays is equal to 2 or 4. As the critical
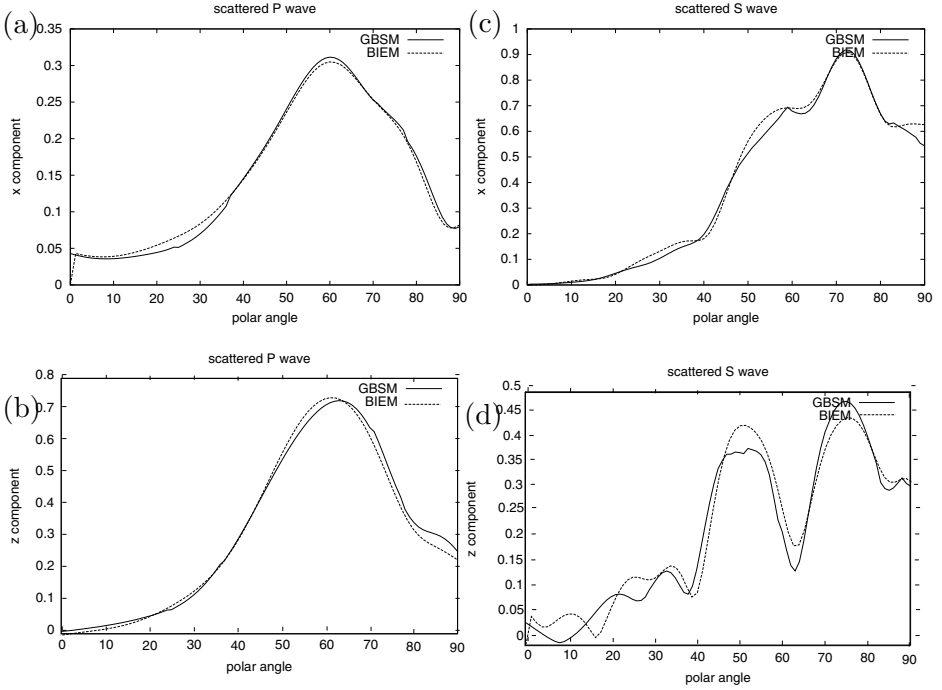
Figure 4 Absolute values of x and z components of P and S waves are given in the case of oblique incidence $\theta^P = 30^o$, $\varphi_0 = 45^o$ scattered from elliptic crack with $a = 4\lambda_S$, $b = 2\lambda_S$ calculated at the points of the vertical cut with $R = 5\lambda_S$, $\varphi = 45^o$, using GBSM and BIEM.

points are found from $< \mathbf{e}_t(s_m), \mathbf{n}(s_m) >= 0$ (see the section 1 in the case of the normal incidence), we have

$$\mathbf{n}(s_m) = \mathbf{e}_n(s_m) \cos \varphi_m + \mathbf{e}_z \sin \varphi_m, \qquad \theta_m = \pi/2 - \varphi_m.$$

If two or more critical points coalesce, the observation point gets near to caustics of the edge diffracted rays and J_m vanishes. Applying the GBSM in a similar way as it was done for the scattering from crack, we come to the GBS integral representing a contribution of coalescing critical points

$$\mathbf{u}^{P(dif)} = \int_{\delta s} \int_{\delta \varphi} \frac{\mathbf{A}^P(s, \varphi)}{\sqrt{\det \mathrm{Q^P}}} \exp\{ik_P(\tau^P(s, \varphi) + \frac{1}{2} < \Gamma^P q, q >)\}dsd\varphi + ...,$$

$$\mathbf{A}^P(s, \varphi) = \frac{e^{-i\pi/4}}{2\pi} \sqrt{k_P \det(P^P G_q^P - G_p^P Q^P)} \frac{\sqrt{2\pi}}{ik_P} \frac{f^P(\theta(s))\mathbf{n}(s)}{< \mathbf{e}_n(s), \mathbf{n}(s) >}.$$

4.   NUMERICAL RESULTS

The computer code was implemented on the basis of the above time-harmonic uniform asymptotic solution to the problem of scattering from

crack, which includes ray asymptotics, penumbra term and GBSM contribution. This has been tested against the code based on the boundary integral equation method (BIEM) and made by Glushkovs Eugene and Natalia. We present results for the scattering from elliptic crack with semi-axes $a = 4\lambda_S$ and $b = 2\lambda_S$ in upper half-space, $\lambda_S = 2\pi/k_S$. The direction of the incident P wave is given by $\theta^P = 30^o$ and $\varphi_0 = 45^o$. We show the magnitudes of scattered P and S waves components $|u_x^{P(scat)}|$, $|u_z^{P(scat)}|$, $|u_x^{S(scat)}|$ and $|u_z^{S(scat)}|$ in Fig. 4 (a), (b), (c) and (d), correspondingly, calculated at the points of the vertical cut defined in the spherical coordinates by $\varphi = 45^o$ and $R = 5\lambda_S$, and polar angle θ varies from 0° and 90°. In this case the observation point crosses the penumbra surface and smooth part of caustics. As it can be seen clearly there is a good agreement between both results as the problem parameters suit the domain where applicability regions of both approaches overlap.

5.　　CONCLUSION

Application of GBSM to describe HFA of contribution of edge diffracted waves in the problem of scattering from cracks and radiation by transducer was considered. This method is independent of the type of singularity of caustics, which makes the method universal. The code based on GTD and GBSM computing the diagram of radiated or scattered field proved to be fast and quite accurate. The present realization of this method does not need caustics to be constructed.

References

[1] Borovikov, V A and Kinber, B Ye (1994). *Geometrical Theory of Diffraction*, IEE, London.

[2] Achenbach, J D, Gautesen, A K and McMaken, H (1982). *Ray Methods for Waves in Elastic Solids; With Applications to Scattering by Cracks*, Pitman, N.Y.

[3] Babich, V M and Popov, M M (1990) *Gaussian Summation Method (review)*, Radiphysics and Quantum Electrinics. **32**(12), 1063–1081.

[4] Fradkin, L J, Zalipaev, V V and Gridin, D (2001) *Mathematical Modelling of NDT*, J. Appl. Math. and Decision Sci., **5**(3), 165–180.

[5] Fradkin, L Yu, Kiselev, A P and Krylova, Eu (1998) *The radiating near-field asymptotics of a normal time-harmonic circular ultrasonic transducer in an elastic half-space*, J. Acoust. Soc. Am. **104**(3), 1178–1187.

[6] Borovikov, V A (1994). *Uniform Stationary Phase Method*, IEE, London.

Chapter 2
Asymptotics
for eigenvalue problems

ASYMPTOTICS FOR THE FIRST SIX EIGENFREQUENCIES OF A 1D-3D MULTI-STRUCTURE

A.G. Aslanyan[1], A.B. Movchan[2] and Ö. Selsil[2]

[1] *MIREA, Moscow, Russia*
aslanian@aha.ru

[2] *Department of Mathematical Sciences, University of Liverpool, UK*
abm@liv.ac.uk, oselsil@liv.ac.uk

Keywords: Multi-structures, asymptotic analysis, eigenvalue problems.

Abstract   We consider vibrations of a massive three-dimensional body Ω^* supported by thin cylindrical rods which are parallel to each other. We assume that the number of rods, say K, is greater than three and the junction points (where the rods are attached to Ω^*) do not belong to the same straight line. We present comparisons between explicit asymptotic formulae and finite element computations to prove the efficiency of the approach.

Background and structure of the paper

This work is based on the results of the spectral analysis included in the book by Kozlov, Maz'ya & Movchan [1] and is developed for elasticity problems posed in parameter dependent domains containing subsets of different limit dimensions (multi-structures). Multi-structures may involve large three-dimensional bodies as well as thin rods, thin plates or thin shells. In the present paper we consider a multi-structure which consists of a finite size body Ω^* connected to a set of parallel thin elastic rods. It is assumed that one of the ends of each rod is connected to Ω^* and the other end is fixed (clamped). The objective of this work is to derive explicit asymptotic formulae for the first six eigenfrequencies of vibration of the multi-structure.

In the earlier papers by Aslanyan, Movchan and Selsil [2], [3], [4], we performed the analysis for 2D-3D multi-structures involving three dimensional bodies and axi-symmetric thin shells. The formal asymptotic procedure

is accompanied by explicit formulae for the eigenfrequencies of vibrating multi-structure; these formulae are new and were not derived elsewhere.

The structure of this paper can be outlined as follows: In Section 1 we formulate the problem and introduce main notations. The skeleton of the multi-structure and the albegraic relations for forces and moments are described in Section 2. Finally, we give explicit asymptotic formulae for the first six eigenfrequencies and present comparisons with the results of finite element simulations.

1. FORMULATION OF THE PROBLEM

Let us consider a multi-structure Ω_ε^* which consists of a three-dimensional body and a number of thin cylinders that are parallel to each other; the superscript $*$ is used to indicate that the multi-structure is defined in dimensional coordinates. Here, ε is a small non-dimensional parameter, which denotes the normalised thickness of the thin rods.

We assume that a three-dimensional body Ω^* has the Lipschitz boundary $\partial\Omega^*$ such that part of its boundary is located in the plane $x_3^* = 0$. We also assume that the axis Ox_3^* is directed downwards and the centre of mass of the body Ω^* belongs to this axis, i.e.

$$\int_\Omega x_j^* dx_1^* dx_2^* dx_3^* = 0, \quad j = 1, 2. \tag{1.1}$$

Here $\mathbf{x}^* = (x_1^*, x_2^*, x_3^*)$ are dimensional coordinates. We introduce a two-dimensional bounded Lipschitz domain $\tilde{g}^*$ whose closure belongs to the disk of radius r_0^*, with the centre at the origin. Then, we can define the multi-structure Ω_ε^* as

$$\Omega_\varepsilon^* = \Omega^* \cup \Pi_\varepsilon^{*\ (1)} \cup \cdots \cup \Pi_\varepsilon^{*\ (K)}, \quad K \geq 3, \tag{1.2}$$

where

$$\Pi_\varepsilon^{*\ (j)} = \left\{ \mathbf{x}^* : 0 \leq x_3^* < \tilde{l}^{*\ (j)}, \left((x_1^* - a_1^{*\ (j)}), (x_2^* - a_2^{*\ (j)}) \right) \in \tilde{g}^* \right\}, \tag{1.3}$$

$j = 1, \ldots, K$ are thin cylinders connected to the flat part of the surface $\partial\Omega^*$ at the points $(a_1^{*\ (j)}, a_2^{*\ (j)}, 0)$, $j = 1, \ldots, K$. We require that these "junction points" do not lie on the same straight line. We also assume, for the sake of simplicity, that all the rods have the same cross-sectional shape.

In the text below we use the following dimensional normalisation constants

$$\kappa_0 = 1 \text{ cm}, \quad \kappa_1 = 1 \text{ g}, \quad \kappa_2 = 1 \text{ sec},$$

and we define the non-dimensional system of coordinates by $\mathbf{x} = \kappa_0^{-1}\mathbf{x}^*$.

The vibrating multi-structure is described by the characteristic linear size $a^* = \kappa_0 a$ of the rigid body Ω^*, the characteristic length $l_0^* = \kappa_0 l_0$ of the thin rods, the characteristic size of cross-section $r_0^* = \kappa_0 r_0$ of the thin rods, Young's modulus $E^* = \kappa_1 E/(\kappa_0 \kappa_2^2)$, the density $\rho^* = \kappa_1 \rho/\kappa_0^3$, Poisson's ratio ν of the material of the multi-structure and the frequency of the vibrations $\omega^* = \omega/\kappa_2$.

We also need the scaled dimensionless coordinates

$$\mathbf{y} = \frac{\mathbf{x}}{l_0} = (y_1, y_2, y_3). \tag{1.4}$$

Now, we can define the thin cylinders as

$$\Pi_\varepsilon^{(j)} = g_j(\varepsilon) \times [0, l^{(j)}), \tag{1.5}$$

where

$$g_j(\varepsilon) = \left\{ (y_1, y_2) : \varepsilon^{-1} \left((y_1 - b_1^{(j)}), (y_2 - b_2^{(j)}) \right) \in g \right\}, \tag{1.6}$$

$$\varepsilon = \frac{r_0}{l_0}, \quad b_k^{(j)} = \frac{a_k^{(j)}}{l_0}, \quad l^{(j)} = \frac{\tilde{l}^{(j)}}{l_0}, \quad k = 1, 2, \ j = 1, \ldots, K. \tag{1.7}$$

Here, g is a two-dimensional bounded Lipschitz domain independent of ε, whose closure belongs to the unit disk, with the centre at the origin.

We denote the part of the boundary corresponding to the base region of the thin rod $\Pi_\varepsilon^{(j)}$ by $S_\varepsilon^{(j)}$, so that

$$S_\varepsilon = \cup_{j=1}^K S_\varepsilon^{(j)}. $$

Now, let us consider the spectral problem

$$-\mathbf{L}\mathbf{u} = \Lambda\mathbf{u}, \quad \mathbf{y} \in \Omega_\varepsilon, \tag{1.8}$$

$$\boldsymbol{\sigma}^{(\mathbf{n})}(\mathbf{u}) = \mathbf{0}, \quad \mathbf{y} \in \partial\Omega_\varepsilon \setminus \bar{S}_\varepsilon, \tag{1.9}$$

$$\mathbf{u} = \mathbf{0}, \quad \mathbf{y} \in S_\varepsilon^{(j)}, \ j = 1, \ldots, K, \tag{1.10}$$

where $\mathbf{u} = (u_1, u_2, u_3)^T$ is the displacement vector, $\mathbf{n}$ is the unit outward normal on $\partial\Omega_\varepsilon$, and $\mathbf{L}, \boldsymbol{\sigma}^{(\mathbf{n})}$ are defined by

$$\mathbf{L} := \Delta + \frac{1}{1 - 2\nu} \, \text{grad div}, \tag{1.11}$$

$$\sigma_i^{(\mathbf{n})} := \sum_{j=1}^3 \sigma_{ij} n_j, \tag{1.12}$$

respectively. Here, σ_{ij} are dimensionless components of the stress tensor

$$\sigma_{ij} := \left(\frac{\partial u_i}{\partial y_j} + \frac{\partial u_j}{\partial y_i}\right) + \frac{2\nu}{1 - 2\nu}\left(\delta_{ij}\sum_{i,j=1}^{3}\frac{\partial u_i}{\partial y_j}\right), \qquad (1.13)$$

and

$$\Lambda = 2(1 + \nu)\frac{\rho\omega^2}{E}l_0^2, \qquad (1.14)$$

is the dimensionless spectral parameter.

The problem (1.8)-(1.10) has a non-negative discrete spectrum which consists of isolated eigenvalues of finite multiplicity (see, for example, Birman & Solomyak, Chapter 10, Section 1 [5]). Let us enumarate these eigenvalues (taking into account multiplicities) in non-decreasing order as

$$0 \leq \Lambda_1 \leq \Lambda_2 \leq \cdots \leq \Lambda_n \leq \dots. \qquad (1.15)$$

A rigorous mathematical analysis of this problem can be found in Kozlov, Maz'ya & Movchan [1]. In particular, they have shown that (see Theorem 6.3 on page 264 in Kozlov, Maz'ya & Movchan [1])

$$\Lambda_j = q_j\varepsilon^4 + O(\varepsilon^5), \quad j = 1, 2, 3, \qquad (1.16)$$
$$\Lambda \geq C_0\varepsilon^2, \quad (C_0 > 0). \qquad (1.17)$$

Here, q_j, $j = 1, 2, 3$ are the roots of the equation (6.3.24) in Kozlov, Maz'ya & Movchan [1]. In the present work, using the results from Kozlov, Maz'ya & Movchan [1], we extend the investigation of the spectrum of the problem (1.8)-(1.10).

2.   SKELETON OF THE MULTI-STRUCTURE

Let us now consider the balance of principal forces and moments within the multi-structure following Aslanyan, Movchan & Selsil [3]. The interaction between the rigid body Ω^* and the thin elastic rods is characterised by lock forces $\mathbf{F}^{*(k)}$ and lock moments $\mathbf{M}^{*(k)}$ which are applied at the junction points. We assume that the force $\mathbf{F}^*$ and the moment $\mathbf{M}^*$ are applied to Ω^*. Then, the equilibrium equations have the form

$$\mathbf{F}^* + \sum_{k=1}^{K}\mathbf{F}^{*(k)} = \mathbf{0}, \qquad (2.1)$$

$$\mathbf{M}^* + \sum_{k=1}^{K}\left\{\mathbf{M}^{*(k)} + \mathbf{a}^{*(k)} \times \mathbf{F}^{*(k)}\right\} = \mathbf{0}. \qquad (2.2)$$

Let

$$F_i^* = \frac{\kappa_0 \kappa_1}{\kappa_2^2} F_i, \quad M_i^* = \frac{\kappa_0^2 \kappa_1}{\kappa_2^2} l_0 M_i, \quad i = 1, 2, 3. \qquad (2.3)$$

We define the rigid-body displacements of Ω^* as

$$\boldsymbol{\alpha}^* + \tilde{\boldsymbol{\beta}} \times \mathbf{x}^*, \qquad (2.4)$$

where $\boldsymbol{\alpha}$ and $\tilde{\boldsymbol{\beta}}$ are constant vectors. We use the notations

$$\alpha_i^* = \kappa_0 \alpha_i, \quad \tilde{\beta} = \beta_i / l_0, \quad i = 1, 2, 3, \qquad (2.5)$$
$$\boldsymbol{\alpha\beta} = (\alpha_1, \alpha_2, \beta_3, \alpha_3, \beta_1, \beta_2)^T, \qquad (2.6)$$
$$\mathbf{FM} = (F_1, F_2, M_3, F_3, M_1, M_2)^T, \qquad (2.7)$$
$$\boldsymbol{\Psi}^* = \frac{\kappa_1}{\kappa_0^2 \kappa_2^2} \{\mathbf{a} + \mathbf{b} \times \mathbf{y}\}, \qquad (2.8)$$
$$\mathbf{ab} = (a_1, a_2, b_3, a_3, b_1, b_2)^T. \qquad (2.9)$$

We refer to Kozlov, Maz'ya & Movchan p.178, [1] for the representation of the vector $\mathbf{FM}$:

$$\mathbf{FM} = \begin{pmatrix} \varepsilon^4 A & \varepsilon^4 D^T \\ \varepsilon^4 D & \varepsilon^2 B + \varepsilon^4 E \end{pmatrix} \boldsymbol{\alpha\beta}, \qquad (2.10)$$

where the dimensionless matrices A, B, D and E are given by

$$A = \sum_{k=1}^K \frac{12}{l^{(k)3}} \begin{pmatrix} D_1 & 0 & -D_1 b_2^{(k)} \\ 0 & D_2 & D_2 b_1^{(k)} \\ -D_1 b_2^{(k)} & D_2 b_1^{(k)} & b_1^{(k)2} D_2 + b_2^{(k)2} D_1 + l^{(k)2} D_4/12 \end{pmatrix}, \qquad (2.11)$$

$$B = \sum_{k=1}^K \frac{D_3}{l^{(k)}} \begin{pmatrix} 1 & b_2^{(k)} & -b_1^{(k)} \\ b_2^{(k)} & b_2^{(k)2} & -b_1^{(k)} b_2^{(k)} \\ -b_1^{(k)} & -b_1^{(k)} b_2^{(k)} & b_1^{(k)2} \end{pmatrix}, \qquad (2.12)$$

$$D = \sum_{k=1}^K \frac{6}{l^{(k)2}} \begin{pmatrix} 0 & 0 & 0 \\ 0 & -D_2 & -D_2 b_1^{(k)} \\ D_1 & 0 & -D_1 b_2^{(k)} \end{pmatrix}, \quad E = \sum_{k=1}^K \frac{4}{l^{(k)}} \begin{pmatrix} 0 & 0 & 0 \\ 0 & D_2 & 0 \\ 0 & 0 & D_1 \end{pmatrix}. \qquad (2.13)$$

Here, D_i, $i = 1, 2, 3, 4$ are the normalised stiffness coefficients defined as

$$D_k = El_0 \int_g y_k^2 dy_1 dy_2, \quad k = 1, 2, \qquad D_3 = El_0 \text{mes}_2 g, \qquad (2.14)$$

$$D_4 = \frac{El_0}{2(1+\nu)} \int_g ||\nabla \varphi - y_2 \mathbf{e}^{(1)} + y_1 \mathbf{e}^{(2)}||^2 dy_1 dy_2, \qquad (2.15)$$

where the function φ is a solution of the Neumann boundary value problem

$$\Delta\varphi = 0, \quad \mathbf{y} \in g, \tag{2.16}$$

$$\frac{\partial\varphi}{\partial\mathbf{n}} = y_2 n_1 - y_1 n_2, \quad \mathbf{y} \in \partial g, \tag{2.17}$$

and n_i, $i = 1, 2$ are components of the unit outward normal $\mathbf{n}$ on the boundary ∂g.

We note that the matrices A and B are non-singular (see Kozlov, Maz'ya & Movchan, p.175 [1]) since the junction points are not located on the same straight line.

On the other hand, we have (see Aslanyan, Movchan & Selsil [3])

$$\mathbf{FM} = l_0^3 \begin{pmatrix} G_1 & G_2 \\ G_3 & G_4 \end{pmatrix} \mathbf{ab}, \tag{2.18}$$

where

$$G_1 = \mathrm{diag}\{\Omega_0, \Omega_0, I_3\}, \quad G_2 = G_3^T = \begin{pmatrix} 0 & 0 & K_0 \\ 0 & -K_0 & 0 \\ 0 & -R_{13} & -R_{23} \end{pmatrix},$$

$$G_4 = \begin{pmatrix} \Omega_0 & 0 & 0 \\ 0 & I_1 & -R_{12} \\ 0 & -R_{12} & I_2 \end{pmatrix}, \tag{2.19}$$

$$\Omega_0 = \int_\Omega dy_1 dy_2 dy_3, \quad K_0 = \int_\Omega y_3 dy_1 dy_2 dy_3,$$

$$I_k = \int_\Omega (y_1^2 + y_2^2 + y_3^2 - y_k^2)\, dy_1 dy_2 dy_3, \quad k = 1, 2, 3,$$

$$R_{ij} = \int_\Omega y_i y_j dy_1 dy_2 dy_3, \quad i, j = 1, 2, 3, \quad i \neq j.$$

It follows that the characteristic equation can be written as

$$\det \begin{pmatrix} \varepsilon^4 A - t G_1 & \varepsilon^4 D^T - t G_2 \\ \varepsilon^4 D - t G_3 & \varepsilon^2 B + \varepsilon^4 E - t G_4 \end{pmatrix} = 0, \tag{2.20}$$

where $t = \rho\omega^2 l_0^3$ is a dimensionless spectral parameter.

At this point, we consider two cases:

(a) Let $t = \varepsilon^4 q$, $q > 0$. In this case, the equation (2.20) takes the form

$$\det \begin{pmatrix} A - q G_1 & D^T - q G_2 \\ O(\varepsilon^2) & B + O(\varepsilon^2) \end{pmatrix} = 0. \tag{2.21}$$

Since the matrix B is non-degenerate, equation (2.21) can be reduced to the form

$$\det(A - qG_1) = 0, \tag{2.22}$$

which coincides with equation (6.3.24) from Kozlov, Maz'ya & Movchan [1].

Let us now denote the roots of the equation (2.22) by q_j, $j = 1, 2, 3$. From (2.19) and (2.20) it follows that

$$t_j = \varepsilon^4 q_j + O(\varepsilon^5), \quad j = 1, 2, 3. \tag{2.23}$$

The matrix A, defined in (2.11) is symmetric and positive definite (see Kozlov, Maz'ya & Movchan p.174-175 [1]). Hence the roots q_j, $j = 1, 2, 3$ are positive.

(b) Let

$$t = \varepsilon^2 q. \tag{2.24}$$

In this case, equation (2.20) takes the form

$$\det \begin{pmatrix} -qG_1 + O(\varepsilon^2) & -qG_2 + O(\varepsilon^2) \\ -qG_3 + O(\varepsilon^2) & B - qG_4 + O(\varepsilon^2) \end{pmatrix} = 0,$$

or neglecting higher order terms we obtain

$$\det \begin{pmatrix} -qG_1 & -qG_2 \\ -qG_3 & B - qG_4 \end{pmatrix} = 0. \tag{2.25}$$

We denote the first positive roots of equation (2.25) by q_j, $j = 4, 5, 6$. From (2.20), (2.24) and (2.25) it follows that

$$t_j = \varepsilon^2 q_j + O(\varepsilon^3), \quad j = 4, 5, 6. \tag{2.26}$$

Assuming that the junction points $b^{(k)}$, $k = 1, 2, \ldots, K$ are not located on the same straight line we conclude that the matrix B, defined in (2.12), is symmetric positive definite (see Kozlov, Maz'ya & Movchan p.175 [1]). Hence the roots q_j, $j = 4, 5, 6$ are positive.

3.   EXPLICIT FORMULAE FOR THE EIGENFREQUENCIES

In this section we consider the multi-structure Ω_ε^* (see (1.2)) where Ω^* is the cube $\mathbf{a}^* \otimes \mathbf{a}^* \otimes \mathbf{a}^*$. The four parallel thin rods $\Pi_\varepsilon^{*(j)}$, $j = 1, 2, 3, 4$ $(K = 4)$ have the same cross-sectional shape. We define this shape as the square $-(r_0^*/2) \le x_1, x_2 \le (r_0^*/2)$. The thin rods $\Pi_\varepsilon^{*(j)}$ are assumed to have the lengths $\tilde{l}^{*(j)} = \tilde{l}^*$, $j = 1, 2, 3, 4$ independent of j. The points $a^{*(j)}$ where

the thin rods are connected to the body (the junction points) have the coordinates:

$$a^{*(1)} = (a_1^*, a_1^*, 0), \quad a^{*(2)} = (-a_1^*, a_1^*, 0),$$
$$a^{*(3)} = (-a_1^*, -a_1^*, 0), \quad a^{*(4)} = (a_1^*, -a_1^*, 0),$$

where $0 < a_1^* < (a^*/2)$. We note that the characteristic length of the thin rods is equal to $l_0^* = \tilde{l}^* = \kappa_0 l_0$.

Let us denote the density of the material by ρ_0^*, the Young's modulus and the Poisson's ratio by E and ν respectively.

Remembering that $\mathbf{y} = \mathbf{x}/l_0$ (see (1.4)) we obtain

$$a = \frac{\tilde{a}}{l_0}, \quad l^{(j)} = 1, \ j = 1, 2, 3, 4, \quad b_k^{(j)} = \frac{1}{l_0} a_k^{(j)}, \ k = 1, 2, \ j = 1, 2, 3, 4,$$

$$\varepsilon = \frac{r_0}{l_0}, \quad g = \{(y_1, y_2) : -(1/2) \leq y_1, y_2 \leq (1/2)\},$$

$$D_1 = D_2 = \frac{1}{12} E l_0, \quad D_3 = E l_0, \quad D_4 = \frac{E l_0}{2(1+\nu)} D_{4,0},$$

where $D_{4,0} \approx 0.1414$.

The matrices $A, B, G_k, \ k = 1, 2, 3, 4$ have the form

$$A = \mathrm{diag}\{4El_0, 4El_0, 8a_1^2 \frac{E}{l_0} + \frac{2El_0}{1+\nu} D_{4,0}\}, \quad B = \mathrm{diag}\{4El_0, 4E\frac{a_1^2}{l_0}, 4E\frac{a_1^2}{l_0}\},$$

$$G_1 = \mathrm{diag}\{\frac{\tilde{a}^3}{l_0^3}, \frac{\tilde{a}^3}{l_0^3}, \frac{\tilde{a}^5}{6l_0^5}\}, \quad G_2 = G_3^T = \begin{pmatrix} 0 & 0 & -\frac{\tilde{a}^4}{2l_0^4} \\ 0 & \frac{\tilde{a}^4}{2l_0^4} & 0 \\ 0 & 0 & 0 \end{pmatrix},$$

$$G_4 = \mathrm{diag}\{\frac{\tilde{a}^3}{l_0^3}, \frac{5\tilde{a}^5}{12l_0^5}, \frac{5\tilde{a}^5}{12l_0^5}\}.$$

Using these formulae we derive

$$f_1 = f_2 \approx \frac{1}{\pi} \sqrt{\frac{E}{\rho_0}} \frac{r_0^2}{(l_0 \tilde{a}^{3/2})}, \tag{3.1}$$

$$f_3 \approx \frac{1}{\pi} \sqrt{\frac{E}{\rho_0}} \frac{r_0^2}{\tilde{a}^2 \sqrt{l_0 \tilde{a}}} \sqrt{12 \left(\frac{a_1}{l_0}\right)^2 + \frac{3D_{4,0}}{1+\nu}}, \tag{3.2}$$

$$f_4 = f_5 \approx \frac{1}{\pi} \sqrt{\frac{E}{\rho_0}} \frac{a_1 r_0}{\tilde{a}^2} \sqrt{\frac{6}{\tilde{a} l_0}}, \tag{3.3}$$

$$f_6 \approx \frac{1}{\pi} \sqrt{\frac{E}{\rho_0}} \frac{r}{\tilde{a}} \frac{1}{\sqrt{\tilde{a} l_0}}. \tag{3.4}$$

Now, we consider the following particular values:

$$\tilde{a}^* = 100 \text{ cm}, \quad \tilde{l}^{*(j)} = 200 \text{ cm}, \ j = 1, 2, 3, 4,$$

$$r_0^* = 4 \text{ cm}, \quad a_1^* = 25 \text{ cm},$$

$$E^* = 2.1 \ 10^{12} \ \frac{\text{g}}{\text{cms}^2}, \quad \rho_0^* = 7.8 \frac{\text{g}}{\text{cm}^3}, \quad \nu = 0.3.$$

We note that $\varepsilon = (1/50) \ll 1$ in this particular case, and

$$D_{4,0} = \frac{1}{3} - \frac{64}{\pi^5} \sum_{k=0}^{\infty} \frac{\tanh(\pi(2k+1)/2)}{(2k+1)^5)} \tag{3.5}$$

Using (3.1)-(3.4) we obtain

$$f_1 = f_2 \approx 0.93, \quad f_3 \approx 1.34, \quad f_4 = f_5 \approx 28.58, \quad f_6 \approx 46.67.$$

The numerical results (using the finite element package COSMOS/M) give

$$f_1 = f_2 \approx 0.93, \quad f_3 \approx 1.4, \quad f_4 = f_5 \approx 28.14, \quad f_6 \approx 46.31.$$

Comparing these numerical results with the results of our analytical formulae we see an almost perfect agreement.

References

[1] Kozlov, V A, Maz'ya, V G, Movchan A B (1999) *Asymptotic analysis of fields in multi-structures,* Oxford Science Publications, Clarendon Press, Oxford.

[2] Aslanyan, A G, Movchan, A B, Selsil, Ö (2000) *A universal asymptotic algorithm for elastic thin shells,* Euro. Jnl of Applied Mathematics, **11**(6), 573–594.

[3] Aslanyan, A G, Movchan, A B, Selsil, Ö (2002) *Vibrations of multi-structures including elastic shells: asymptotic analysis,* Euro. Jnl of Applied Mathematics, **13**, 109–128.

[4] Aslanyan, A G, Movchan, A B, Selsil, Ö *Estimates for the low eigenfrequencies of a multi-structure including an elastic shell,* to be published in Euro. Jnl of Applied Mathematics.

[5] Birman, M S, Solomyak, M Z (1987) *Spectral theory of self-adjoint operators in Hilbert space,* D. Reidel, Dodrecht.

THE TWO-TERM INTERIOR ASYMPTOTIC EXPANSION IN THE CASE OF LOW-FREQUENCY LONGITUDINAL VIBRATIONS OF AN ELONGATED ELASTIC RECTANGLE

E. Babenkova and J. Kaplunov

Department of Mathematics, The University of Manchester,
Manchester M13 9PL, UK

elena@ma.man.ac.uk, kaplunov@ma.man.ac.uk

Keywords: Low-frequency, asymptotic, elastic, Saint-Venant, rectangle.

Abstract   The two-term interior asymptotic expansion is derived for low-frequency longitudinal vibrations of an elongated elastic rectangle. The consideration starts from the second-order theory of plate extension with the second-order boundary conditions involving a dynamic correction.
A multi-parametric nature of the associated stress state is emphasized. The contribution of the self-equilibrated component of end data is investigated.

INTRODUCTION

It is well known (see for example [2, 3, 6]) that the compound asymptotic expansions for thin plates and shells include both interior components and boundary layers localized near edges. As a rule, the former are of a greater interest for structural analysis. In fact, all the applied engineering theories for plates and shells refer only to the interior stress state. At the same time asymptotic considerations can not ignore boundary layers. The point is that they affect the boundary conditions for the interior equations. Consistent boundary conditions in asymptotic structural theories have to be treated as decay relations for boundary layers (e.g. see [4]). In the leading order these usually agree with the Saint-Venant principle stating static self-equilibrium of external loads. In this case, the relevant interior govern-

ing equations follow from the Kirchhoff plate theory or the Kirchhoff-Love shell theory.

Higher-order asymptotic theories have to start both from refined interior equations and boundary conditions. Higher-order equations derived by asymptotic integration of the 3D equations in elasticity may be found in [5, 10]. Higher-order boundary conditions should utilize advanced decay relations incorporating possible deviations from the traditional formulation of the Saint-Venant principle. To our best knowledge, improved boundary conditions have been developed only for static problems (see also [8]).

In this paper we introduce the second-order decay condition for longitudinal motion of a semi-infinite elastic strip taking into account a dynamic correction. The associated boundary conditions are combined with the second-order dynamic theory of plate extension to establish the two-term interior expansion for forced harmonic vibrations of an elongated rectangular strip. The proposed expansion allows a further insight into structural dynamic response. In particular, it takes into consideration low-frequency motions induced by statically self-equilibrated end data.

1.   STATEMENT OF THE PROBLEM

Let us consider the harmonic motion of an elongated elastic rectangular strip $0 \leq x_1 \leq l$, $-h \leq x_2 \leq h$; $\eta = h/l \ll 1$ (see Fig 1).
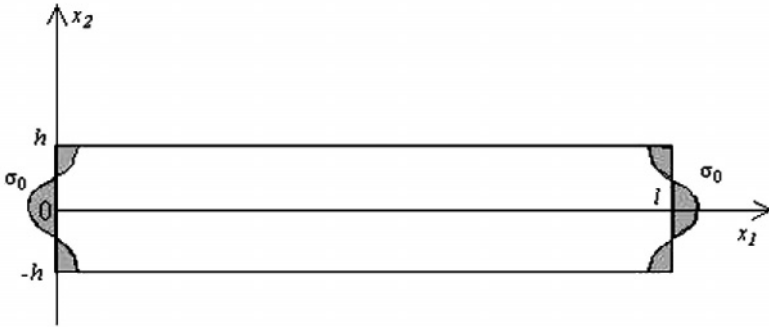
Figure 1   Elongated rectangular strip under end loading

In the case of plane strain, the equations of motion can be written as

$$\frac{E}{2(1+\nu)}\left(\frac{\partial^2 v_i}{\partial x_i^2} + \frac{\partial^2 v_i}{\partial x_j^2}\right) + \frac{E}{2(1+\nu)(1-2\nu)}\left(\frac{\partial^2 v_i}{\partial x_i^2} + \frac{\partial^2 v_j}{\partial x_i \partial x_j}\right) + \rho\omega^2 v_i = 0,$$

(1.1)

$(i \neq j = 1, 2)$,

where $v_i = v_i(x_1, x_2)$ are displacements, E is Young's modulus, ν is Poisson's ratio, ρ is the mass density, ω is the circular frequency.

The formulae expressing the stresses σ_{11}, σ_{21} and σ_{22} in terms of displacements become

$$\sigma_{11} = \frac{E(1-\nu)}{(1+\nu)(1-2\nu)} \left(\frac{\partial v_1}{\partial x_1} + \frac{\nu}{1-\nu} \frac{\partial v_2}{\partial x_2} \right),$$

$$\sigma_{22} = \frac{E(1-\nu)}{(1+\nu)(1-2\nu)} \left(\frac{\nu}{1-\nu} \frac{\partial v_1}{\partial x_1} + \frac{\partial v_2}{\partial x_2} \right), \tag{1.2}$$

$$\sigma_{21} = \frac{E}{2(1+\nu)} \left(\frac{\partial v_2}{\partial x_1} + \frac{\partial v_1}{\partial x_2} \right).$$

Below we restrict ourselves to boundary conditions corresponding to the traction-free faces $x_2 = \pm h$ and the edges $x_1 = 0$ and $x_1 = l$ both loaded by the stress of magnitude $\sigma_0(x_2)$ exciting low-frequency vibrations. Thus we assume:

$$\sigma_{21}(x_1, \pm h) = 0, \qquad \sigma_{22}(x_1, \pm h) = 0,$$

$$\sigma_{21}\big|_{x_1=0} = \sigma_{21}\big|_{x_1=l} = 0, \tag{1.3}$$

$$\sigma_{11}\big|_{x_1=0} = \sigma_{11}\big|_{x_1=l} = \sigma_0(x_2),$$

and

$$\lambda = \omega l \sqrt{\frac{2(1+\nu)\rho}{E}} \ll \eta^{-1} \quad or \quad \Lambda = \lambda\eta \ll 1. \tag{1.4}$$

It is well known that the leading order low-frequency approximation for the *interior* rectangular domain, i.e. outside the end zones of the width $O(\eta)$ affected by boundary layers, corresponds to the elementary plate theories. In particular, we arrive at the equation for plate extension $(\sigma_0(x_2) = \sigma_0(-x_2))$ in terms of the leading order longitudinal displacement

$$\frac{d^2V}{d\xi^2} + \frac{\lambda^2(1-\nu)}{2}V = 0 \tag{1.5}$$

where

$$v_1(\xi, \zeta) = lV(\xi) + \dots$$

The boundary conditions become

$$\frac{dV}{d\xi}\bigg|_{\xi=0} = \frac{dV}{d\xi}\bigg|_{\xi=1} = \frac{1-\nu^2}{E} \int_0^1 \sigma_0(\zeta)d\zeta, \tag{1.6}$$

where

$$\xi = \frac{x_1}{l}, \qquad \zeta = \frac{x_2}{h}. \tag{1.7}$$

The 1D equation (1.5) represents the leading order approximation of the 2D initial equations of motion (1.1) in the case of the homogeneous face

conditions $(1.3)_1$-$(1.3)_2$, whereas the boundary conditions (1.6) follow from the static Saint-Venant principle applied to the end stress $\sigma_0(x_2)$. This states that the interior solution depends only on the non-self-equilibrium component of the end data, while the self-equilibrated one forms boundary layers localized near ends.

To establish a two-term asymptotic expansion for the interior domain we should refine both the leading-order equation of motion (1.5) as well as the boundary conditions (1.6).

2. SECOND-ORDER EQUATION OF MOTION AND SECOND-ORDER BOUNDARY CONDITIONS

The asymptotic procedure for deriving higher order dynamic plate theories has been established in [5, 10]. In the case under consideration the second-order equation of motion can be written as

$$\frac{d^2V}{d\xi^2} + \lambda^2 \left(\frac{1-\nu}{2} + \frac{\nu^2\Lambda^2}{12} \right) V = 0. \tag{2.1}$$

It is clear that the correction to the elementary theory of plate extension (the second term within the brackets of (2.1)) is of order $O(\Lambda^2)$.

Below we also exploit the two-term asymptotic expansion for the longitudinal stress $\sigma_{11}(\xi, \zeta)$ expressed in terms of $V(\xi)$. It is

$$\sigma_{11}(\xi, \zeta) = E \left(\sigma_{11}^{(0)}(\xi) + \Lambda^2 \zeta^2 \sigma_{11}^{(2)}(\xi) \right), \tag{2.2}$$

with

$$\sigma_{11}^{(0)}(\xi) = \frac{1}{1-\nu^2} \left(1 - \frac{\nu^2\Lambda^2}{4(1-\nu)} \right) \frac{dV}{d\xi},$$

$$\sigma_{11}^{(2)}(\xi) = \frac{\nu(2\nu-1)}{4(1-\nu)(1-\nu^2)} \frac{dV}{d\xi}. \tag{2.3}$$

To refine the classical boundary conditions (1.6) we need to improve the static decay conditions for a semi-infinite strip [7, 9] by incorporating a low-frequency correction.

Below we start from the formula

$$\int_0^1 \left(1 - \frac{\nu\Lambda^2}{4} \zeta^2 \right) \Sigma_0(\zeta) d\zeta = 0, \tag{2.4}$$

where $\Sigma_0(\zeta)$ is a prescribed end longitudinal stress $(\Sigma_0(\zeta) = \Sigma_0(-\zeta))$.

The condition (2.4) involves a correction of order $O(\Lambda^2)$ (the second term within the brackets of (2.4)) to the traditional formulation of the Saint-Venant principle requiring self-equilibrium of the end data $\Sigma_0(\zeta)$.

The derivation of a second order decay condition may be based, for example, on the Laplace transform technique similar to that developed in [9] for the static equilibrium of an elastic semi-infinite strip. In this case, the condition (2.4) does not allow asymptotically small poles ($\lambda \ll 1$) associated with low-frequency propagating modes (see author's forthcoming publication [1] for more detail). It is essential that, as it is demonstrated in Appendix, all the decaying Lamb modes (e.g. see [10]) satisfy to the proposed decay condition to within the error $O(\Lambda^4)$. Such a test proves the validity of the latter.

As usual, we utilize then the substitution

$$\Sigma_0(\zeta) = \sigma_0(\zeta) - \sigma_{11}(\xi, \zeta) \tag{2.5}$$

with $\xi = 0$ or $\xi = 1$.

By introducing the two-term expansion (2.2)-(2.3) for $\sigma(\xi, \zeta)$ into the decay condition (2.4) we obtain the second-order boundary conditions

$$\left.\frac{dV}{d\xi}\right|_{\xi=0} = \left.\frac{dV}{d\xi}\right|_{\xi=1} = \frac{1-\nu^2}{E}\left(1 + a\Lambda^2\right)\int_0^1 \sigma_0(\zeta)d\zeta \tag{2.6}$$

with

$$a = -\frac{\nu}{2}\left(\frac{b}{2} - \frac{1}{3(1-\nu)}\right), \tag{2.7}$$

where

$$b = \frac{\displaystyle\int_0^1 \zeta^2 \sigma_0(\zeta)d\zeta}{\displaystyle\int_0^1 \sigma_0(\zeta)d\zeta}. \tag{2.8}$$

3. TWO-TERM INTERIOR ASYMPTOTIC EXPANSION

The sought for two-term expansion follows immediately from the formulae of Section 2. In particular, for the longitudinal stress along the centre-line it becomes ($\sigma(\xi) = \sigma_{11}(\xi, 0)$)

$$\sigma(\xi) = A\cos\left[\frac{(2\xi - 1)\lambda}{4}\sqrt{2(1-\nu) + \frac{\nu^2\Lambda^2}{3}}\right], \tag{3.1}$$

where

$$A = \sqrt{1 + \frac{\nu^2\Lambda^2}{6(1-\nu)}\left(1 - \frac{\nu^2\Lambda^2}{4(1-\nu)}\right)}\sec\left[\frac{\lambda}{4}\sqrt{2(1-\nu) + \frac{\nu^2\Lambda^2}{3}}\right] \times$$
$$\left(1 - \frac{\nu\Lambda^2}{4}\left(b - \frac{(2-\nu)}{3(1-\nu)}\right)\right)\int_0^1 \sigma_0(\zeta)d\zeta. \tag{3.2}$$

As it might be expected the last formula depends on two parameters η and λ. Only for $\lambda \sim 1$ it takes an one-parametric form involving the single parameter $\Lambda = \lambda\eta$. For higher frequencies $(1 \ll \lambda \ll \eta^{-1})$ the contribution of secondary terms entering trigonometric functions exceed that for algebraic ones. The first of them is of order $O(\lambda^3\eta^2)$ and corresponds to the second-order equation of motion (2.1), while the second one is of order $O(\lambda^2\eta^2)$ and associated with the second-order boundary conditions (2.6). It is also follows from this that the elementary plate solution

$$\sigma(\xi) = A_0 \cos\left[\frac{(2\xi - 1)\lambda}{4}\sqrt{2(1 - \nu)}\right], \qquad (3.3)$$

where

$$A_0 = \sec\left[\frac{\lambda}{4}\sqrt{2(1 - \nu)}\right]\int_0^1 \sigma_0(\zeta)d\zeta \qquad (3.4)$$

is justified only for $\lambda \ll \eta^{-2/3}$, i.e. not over the whole low-frequency band $\lambda \ll \eta^{-1}$ $(\Lambda \ll 1)$. These observations fully agree with general conclusions in [5, 10].

Numerical results are presented in Fig.2 and Fig.3 (T=σ/E). The nearly self-equilibrated load $\sigma_0(\zeta) = E(cos\pi\zeta + \varepsilon)$ $(\varepsilon \ll 1)$ is studied. The two-term expansion (3.1) (continuous lines) is compared with the elementary solution (3.3) (dash lines) for $\nu = 0.4$, $\eta = 0.05$ and $E = 1$. The figures clearly demonstrate an increasing contribution of the self-equilibrated cos-sinusoidal component for small ε and moderate λ. It is interesting that even a quasi-static distribution along the longitudinal direction depends considerably on the self-equilibrated component (see Fig.2).

4.   CONCLUDING REMARKS

The proposed two-parametric formula (3.1) (which depends on the geometric parameter η and the dimensionless frequency λ) is based on the second-order theory of plate extension as well as the second-order boundary conditions incorporating a dynamic correction. It confirms that for higher frequencies $(1 \ll \lambda \ll \eta^{-1})$ the effect of higher order terms in the boundary conditions (2.6) becomes negligible compared with those in the equation of motion (2.1). Another interesting feature is that the second-order boundary conditions allow investigation of vibrations excited by self-equilibrated end data. It should be also mentioned that the developed methodology might be adapted for more general problems in structural mechanics.

Acknowledgments

(a)

(b)

(c)
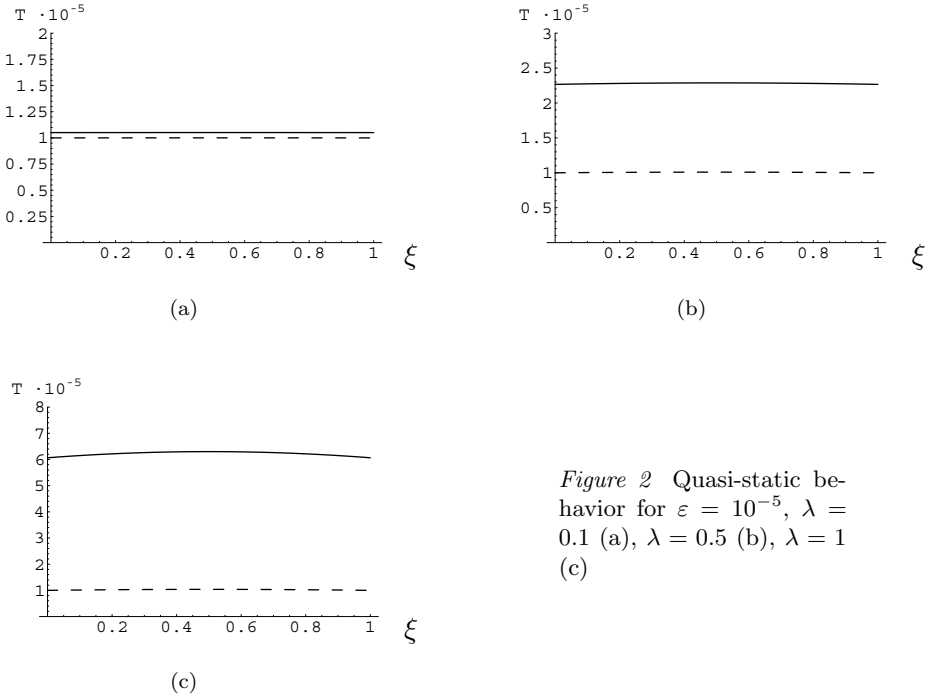
Figure 2 Quasi-static behavior for $\varepsilon = 10^{-5}$, $\lambda = 0.1$ (a), $\lambda = 0.5$ (b), $\lambda = 1$ (c)

Appendix: Testing of decay condition

Symmetric Lamb modes can be written as (e.g. see [10])

$$
\sigma_{11}(\chi, \zeta) = C e^{im\chi} \frac{E}{1 + \nu} \Big[m^2 \alpha \beta \sinh \alpha \cosh(\beta\zeta) -
$$
$$
\gamma^2 \left(m^2 + \frac{\nu\Lambda^2}{2(1 - \nu)} \right) \sinh \beta \cosh(\alpha\zeta) \Big], \tag{A.1}
$$

with

$$
\alpha^2 = m^2 - \frac{1 - 2\nu}{2(1 - \nu)}\Lambda^2, \qquad \beta^2 = m^2 - \Lambda^2, \qquad \gamma^2 = m^2 - \frac{\Lambda^2}{2},
$$

where $\chi = x_1/h$, C is an arbitrary constant and m is a root of the Rayleigh-Lamb dispersion equation

$$
\gamma^4 \cosh \alpha \frac{\sinh \beta}{\beta} - \alpha^2 m^2 \frac{\sinh \alpha}{\alpha} \cosh \beta = 0 \tag{A.2}
$$

For the decaying low-frequency modes $(A.1)$ $(\Lambda \ll 1)$ we have $m \sim 1$.

(a)

(b)

(c)
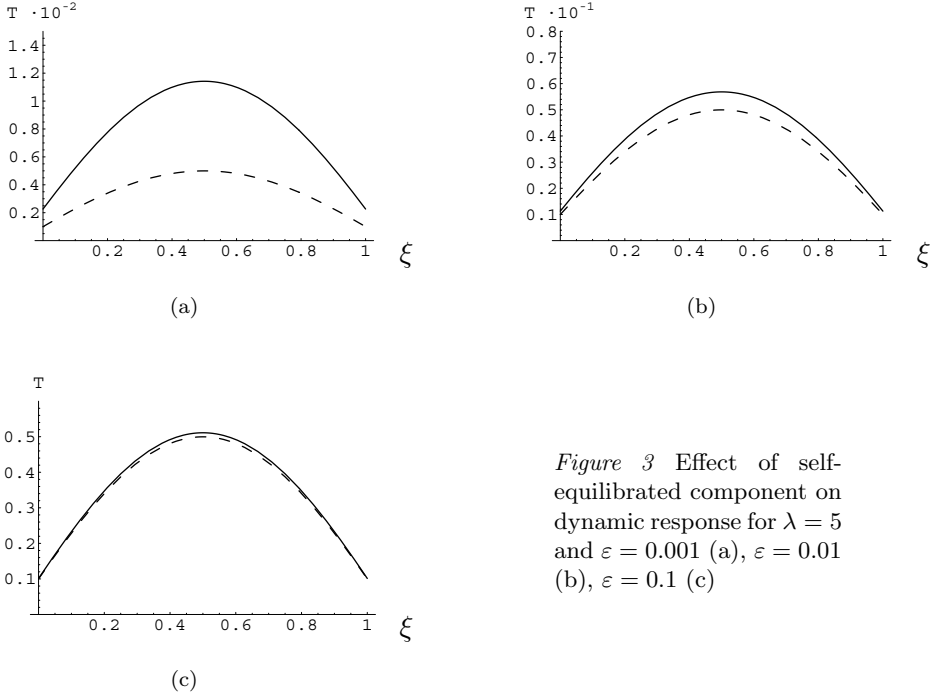
Figure 3 Effect of self-equilibrated component on dynamic response for $\lambda = 5$ and $\varepsilon = 0.001$ (a), $\varepsilon = 0.01$ (b), $\varepsilon = 0.1$ (c)

The substitution of this into the static decay condition, expressing the Saint-Venant principle, yields

$$\int_0^1 \sigma_{11}(0,\zeta)d\zeta = -\frac{CE\nu\Lambda^2\sinh^2 m}{4m(\nu^2-1)}[1+O(\Lambda^2)]. \qquad (A.3)$$

At the same time the refined decay condition (2.4) provides higher accuracy. In the latter case we get

$$\int_0^1 \left(1 - \frac{\nu\Lambda^2}{4}\zeta^2\right)\sigma_{11}(0,\zeta)d\zeta \sim \Lambda^4. \qquad (A.4)$$

References

[1] Babenkova, E V and Kaplunov, J D (submitted for publication), *Low-frequency decay conditions for a semi-infinite elastic strip.*

[2] Friedrichs, K O and Dressler, R F (1961), *A boundary-layer theory for elastic plates*, Comm. Pure Appl. Math. **14**(1), 1–33.

[3] Goldenveiser, A L (1962), *An application of asymptotic integration of the equations of elasticity to derive an approximate theory for plate bending*, PMM (Appl. Math. Mech.) **26**, 668–686.

[4] Goldenveiser, A L (1998), *The boundary conditions in the two-dimensional theory of shells. The mathematical aspect of the problem*, PMM (Appl. Math. Mech.) **62**, 617–629.

[5] Goldenveizer, A L, Kaplunov, J D and Nolde, E V (1993), *On Timoshenko-Reissner Type Theories of Plates and Shells*, Int. J. Solids Structures **30**(5), 675–694.

[6] Green, A E (1963), *Boundary layer equations in the linear theory of thin elastic shells*, Proc. R. Soc. **A269**(1339), 481–491.

[7] Gregory, R D and Wan, F Y M (1984), *Decaying states of plane strain in a semi-infinite strip and boundary conditions for plate theory*, J. Elasticity **14**, 27–64.

[8] Gregory, R D and Wan, F Y M (1985), *On plate theories and Saint-Venant principle*, Int. J. Solids Structures **21**, 1005–1024.

[9] Gusein-Zade, M I (1965), *On the conditions of existence of decaying solutions of the two-dimensional problem of the elasticity for a semi-infinite strip*, PMM (Appl. Math. Mech.) **29**(2), 393–399.

[10] Kaplunov, J D, Kossovich, L Yu and Nolde, E V (1998), *Dynamics of Thin Walled Elastic Bodies*. San-Diego: Academic Press.

TRANSVERSE PROPAGATING WAVES IN PERTURBED PERIODIC STRUCTURES

C. G. Poulton[†], S. Guenneau[‡1], A. B. Movchan[‡] and A. Nicolet[⋆]

[†]*High Frequency and Quantum Electronics Laboratory, University of Kalrsruhe, 76128 Karlsruhe, Germany*

[‡]*Department of Mathematical Sciences, University of Liverpool, Liverpool L69 3BX, UK*

[⋆]*Institut Fresnel, UMR 6133, Faculté de St. Jérôme case 162, F13397 Marseille Cedex 20, France*

Keywords: Bloch waves, perturbation method, eigenvalue problem, photonic crystals, finite element method.

Abstract   We present here an analysis of electromagnetic waves propagating through a doubly periodic array of inclusions which are not necessarily circular. A small perturbation to a circular boundary is introduced, and this can be used to derive the effective boundary conditions for the perturbed inclusion. We examine the effect of this perturbation on the dispersion curves for the material, and compare this with a finite element modelling of the perturbed structure.

1.   INTRODUCTION

The problem of waves propagating in a photonic crystal is well known, however most studies of this make simplifying assumptions about the structure under consideration. We study here the effect of perturbation of the boundary of the cylinders in the array. This perturbation may be inherent in the structure, resulting from the manufacturing process of the photonic crystal, or it may be the result of a sound wave moving through the array. In this way the perturbation could be used to model the coupling between light and sound in photonic crystals, and also to examine the behaviour of light in such an array when the photonic crystal is 'squashed'.

---

[1]Current address: Condensed Matter Theory Group, Blackett Laboratory, Imperial College, Prince Consort Rd., London SW7 2AZ, UK

In this paper we examine the case when the perturbation of the boundary of each cylinder is small in comparison to the cylinder's radius. In this way the solution for this perturbed problem can be calculated directly from the solution of an array of unperturbed cylinders, in terms of a correction term which is on the order of the size of the perturbation.

There are several methods available to solve the classical (unperturbed) problem; these can be loosely categorized into plane-wave methods, multipole methods and transfer matrix methods [5, 6, 9]. In this case it is most appropriate to use a multipole method known as the generalised method of Rayleigh, since this gives a semi-analytic expansion of the solution around each circular inclusion. The method itself will not be given here, and can be found discussed at length elsewhere [6, 8].

As a means of comparison, and being of no small interest itself, we also compare the results derived using the asymptotic method with a direct calculation using finite elements. This combination of finite elements and the Bloch condition is new and is interesting enough to warrant additional attention, because highly accurate results can be obtained quickly for inclusions of arbitrary shape.

2.   OUTLINE OF THE PROBLEM

We consider an array of 'squashed' cylinders. By this, we mean cylinders whose original circular cross-section has been slightly perturbed. We impose here the restrictions that the spacing between the cylinders should not vary and that the perturbation for each cylinder be exactly the same; in this way the problem is strictly doubly periodic. A time-harmonic electromagnetic wave propagating through this material can be represented by a scalar function $u(r, \theta)$, which obeys everywhere the Helmholtz equation

$$(\Delta + k^2)u = 0 , \tag{2.1}$$

where k is the spectral parameter (in this case, the frequency divided by the wave-speed) and Δ is the Laplace operator in two dimensions. The doubly-periodic nature of the problem requires that the Bloch-Floquet condition be satisfied throughout the unit cell[3], thus:

$$u(\mathbf{x} + \mathbf{d}) = u(\mathbf{x})e^{i\mathbf{k}_{\text{Bloch}} \cdot \mathbf{d}} , \tag{2.2}$$

where $\mathbf{x} = (r, \theta)$ and $\mathbf{d}$ is any vector which can be drawn from the centre of one elementary cell to the centre of another. The vector $\mathbf{k}_{\text{Bloch}}$ is commonly known as the Bloch vector, and the relationship between k and $\mathbf{k}_{Bloch}$ is known as the dispersion relation for the array.

3. PERTURBATION FOR THE TE MODE WITH PERFECTLY CONDUCTING CYLINDERS

We begin with a single, unperturbed, cell of the array, as shown in Figure 1, and consider the exterior region Ω_0, with a boundary $\partial C_0 \cup B$, where $C_0 = \{(r, \theta) : r \leq a\}$ is the circular region which corresponds to the body of the central inclusion, and B is the outer boundary of the central unit cell.
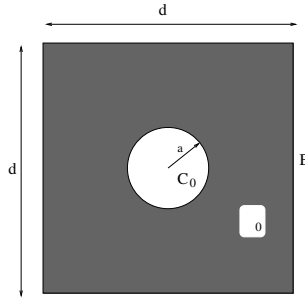
Figure 1 The geometry for the unperturbed problem.

Within the region Ω_0 we introduce the unperturbed field $u_0(r, \theta)$, which satisfies

$$(\Delta + k_0^2)u_0 = 0, \tag{3.1}$$

where k_0 is the unperturbed spectral parameter. On the boundary of the inclusion we specify, for the purpose of this demonstration, homogeneous Neumann conditions

$$\left.\frac{\partial u_0}{\partial n}\right|_{\partial C_0} = 0, \tag{3.2}$$

which are appropriate for a Transverse Electric wave incident on a perfectly conducting cylinder. As mentioned previously, the periodicity of the problem requires that the Bloch-Floquet condition be satisfied throughout the unit cell i.e. u_0 satisfies (2.2). In particular this condition can be used to prescribe the boundary conditions on the exterior edge of the unit cell B, and so completely determine the problem for u_0, to within a multiplicative factor. The solution u_0 can be normalised with respect to the energy, and so we specify that

$$\int\int_{\Omega_0} |u_0|^2 dA = 1. \tag{3.3}$$

We now note that this problem for circular cylinders is very well studied, and there are at least three different methods available by which the solu-

tion can be constructed [5, 6, 9]. This solution can be used to construct the solution for the perturbed array.

We now perturb the boundary, so that $\partial C_0 \to \partial C_1$. The new boundary of the inclusion can be described by the curve r_1, where

$$r_1(\theta) = a + \epsilon h(\theta), \tag{3.4}$$

where $h(\theta)$ is a smooth function and ϵ is a small parameter such that $\varepsilon h(\theta) \ll a$. The region of the perturbed inclusion is $C_1 = \{(r, \theta) : r \leq a + \epsilon h(\theta)\}$ and the region Ω_1 is the remaining region within the unit cell. Without loss of generality, we specify that $h(\theta) \geq 0$, so that the unperturbed inclusion C_0 lies entirely within C_1.
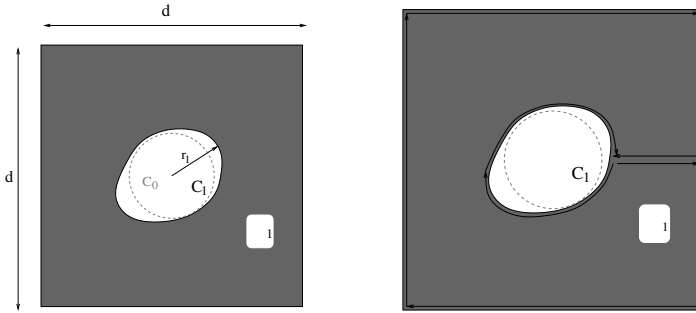
Figure 2 Left: the geometry for the perturbed problem. The dashed line shows the unperturbed circular boundary. Right: the contour to be used for the application of Green's theorem.

The solution to the perturbed problem is denoted by u_1, with the perturbed spectral parameter k_1, and it satisfies

$$(\Delta + k_1^2)u_1 = 0, \tag{3.5}$$

with the boundary condition

$$\left. \frac{\partial u_1}{\partial n} \right|_{\partial C_1} = 0. \tag{3.6}$$

The function u_1 also satisfies the Bloch-Floquet condition (2.2).

We would like to examine the effect of the perturbation of the boundary on the spectral parameter k_0. To do this, we apply Green's theorem within the region Ω_1, using the perturbed field u_1 and a function which is the complex conjugate of u_0, which we designate $\overline{u}_0$. Using the contour depicted in Figure 2, we obtain

$$\int\int_{\Omega_1} (\overline{u}_0 \Delta u_1 - u_1 \Delta \overline{u}_0) dA = \int_{\partial C_1 \cup B} (u_1 \frac{\partial \overline{u}_0}{\partial n} - \overline{u}_0 \frac{\partial u_1}{\partial n}) d\ell. \tag{3.7}$$

We now take into account the fact that the function $\overline{u}_0$ satisfies a conjugate quasiperiodicity condition to (2.2), specifically:

$$\overline{u}_0(\mathbf{x} + \mathbf{d}) = \overline{u}_0(\mathbf{x})e^{-i\mathbf{k}_{\text{bloch}} \cdot \mathbf{d}}. \tag{3.8}$$

This causes the integral around the outer boundary B to be zero in (3.7). In addition, we know that the function $\overline{u}_0$ and u_1 satisfy the Helmholtz equations (3.1) and (3.5) respectively, and so we deduce that

$$(-k_1^2 + k_0^2) \int \int_{\Omega_1} u_1 \overline{u}_0 dA = \int_{\partial C_1} (u_1 \frac{\partial \overline{u}_0}{\partial n} - \overline{u}_0 \frac{\partial u_1}{\partial n}) d\ell . \tag{3.9}$$

The problem is regularly perturbed, and so we know that the field will behave 'reasonably' in response to the perturbation of the boundary [1]. Specifically, we can say that

$$u_1 = u_0 + \mathcal{O}(\epsilon)$$
$$\frac{\partial u_1}{\partial n} = \frac{\partial u_0}{\partial n} + \mathcal{O}(\epsilon) \quad \text{in } \Omega_1 \tag{3.10}$$

In this case the eigenvalues will also behave reasonably, and we can write

$$k_1 = k_0 + \delta k \tag{3.11}$$

where δk is of order $O(\epsilon)$. With this in mind, we can write equation (3.9) as

$$-2k_0 \delta k \int \int_{\Omega_1} |u_0|^2 dA = \int_{\partial C_1} (u_1 \frac{\partial \overline{u}_0}{\partial n} - \overline{u}_0 \frac{\partial u_1}{\partial n}) d\ell + \mathcal{O}(\epsilon^2) . \tag{3.12}$$

Because of equations (3.3) and (3.10), we also know that

$$\int \int_{\Omega_1} |u_0|^2 dA = \int \int_{\Omega_0} |u_0|^2 dA + \mathcal{O}(\epsilon)$$
$$= 1 + \mathcal{O}(\epsilon) \tag{3.13}$$

and so, regardless of the boundary conditions on ∂C, we can write

$$\delta k = -\frac{1}{2k_0} \int_{\partial C_1} (u_1 \frac{\partial \overline{u}_0}{\partial n} - \overline{u}_0 \frac{\partial u_1}{\partial n}) d\ell + \mathcal{O}(\epsilon^2) . \tag{3.14}$$

We will now evaluate the integral on the right-hand side. Firstly we note that for the Neumann problem we have $\partial u_1/\partial n = 0$ on ∂C_1, and so

$$\delta k = -\frac{1}{2k_0} \int_{\partial C_1} u_1 \frac{\partial \overline{u}_0}{\partial n} d\ell + \mathcal{O}(\epsilon^2) . \tag{3.15}$$

Next, we would like to obtain a representation of $\partial \overline{u}_0 / \partial n$ in terms of the values of the function u_0 on the unperturbed boundary. We represent the curve ∂C_1 as being a level curve of Φ, where

$$\Phi(r, \theta) = r - \epsilon h(\theta) \tag{3.16}$$

The unit normal vector at each point is then given by $\hat{\mathbf{n}} = \nabla \Phi / |\nabla \Phi|$. The gradient of Φ is

$$\nabla \Phi |_{\partial C_1} = \left[\frac{\partial \Phi}{\partial r} \hat{\mathbf{r}} + \frac{1}{r} \frac{\partial \Phi}{\partial \theta} \hat{\theta} \right]_{\partial C_1} \tag{3.17}$$

and therefore

$$\hat{\mathbf{n}}|_{\partial C_1} = \hat{\mathbf{r}} - \frac{\epsilon h'(\theta)}{a} \hat{\theta} + \mathcal{O}(\epsilon^2) . \tag{3.18}$$

Now:

$$\frac{\partial \overline{u}_0}{\partial n} \bigg|_{\partial C_1} = \frac{\partial \overline{u}_0}{\partial r} \bigg|_{\partial C_1} - \frac{\epsilon h'(\theta)}{a^2} \frac{\partial \overline{u}_0}{\partial \theta} \bigg|_{\partial C_1} + \mathcal{O}(\epsilon^2) . \tag{3.19}$$

Thanks to the Helmholtz equation (3.1) we deduce

$$\frac{\partial \overline{u}_0}{\partial n} \bigg|_{\partial C_1} = - \epsilon h(\theta) k_0^2 \overline{u}_0 |_{\partial C_0} - \frac{\epsilon h(\theta)}{a^2} \frac{\partial^2 \overline{u}_0}{\partial \theta^2} \bigg|_{\partial C_0} - \frac{\epsilon h'(\theta)}{a^2} \frac{\partial \overline{u}_0}{\partial \theta} \bigg|_{\partial C_0}$$
$$+ \mathcal{O}(\epsilon^2) \tag{3.20}$$

Noting that $u_1|_{\partial C_1} = u_0|_{\partial C_0} + \mathcal{O}(\epsilon)$, we then substitute (3.20) into the integral (3.15) to yield

$$\delta k = - \frac{1}{2 k_0} \int_{\partial C_0} u_0 \left(-\epsilon h(\theta) k_0^2 \overline{u}_0 - \frac{\epsilon h(\theta)}{a^2} \frac{\partial^2 \overline{u}_0}{\partial \theta^2} - \frac{\epsilon h'(\theta)}{a^2} \frac{\partial \overline{u}_0}{\partial \theta} \right) d\ell + \mathcal{O}(\epsilon^2)$$
$$= \frac{\epsilon k_0}{2} \int_{\partial C_0} \left(h(\theta) |u_0|^2 + \frac{h(\theta)}{(k_0 a)^2} u_0 \frac{\partial^2 \overline{u}_0}{\partial \theta^2} + \frac{h'(\theta)}{(k_0 a)^2} u_0 \frac{\partial \overline{u}_0}{\partial \theta} \right) d\ell + \mathcal{O}(\epsilon^2) \tag{3.21}$$

This can be evaluated if the function u_0 and its derivative on the boundary are known. Let us now expand the function u_0 on the boundary in a Fourier series, so that

$$u_0|_{\partial C_0} = \sum_{\ell=-\infty}^{\infty} \alpha_\ell e^{i\ell\theta} , \tag{3.22}$$

where the coefficients α_m are known. We will also specify that the function $h(\theta)$ which controls the perturbation can be written in a similar manner,

so that

$$h(\theta) = \sum_{n=-\infty}^{\infty} h_n e^{in\theta} \ . \tag{3.23}$$

The expression for the perturbation can then be written explicitly in terms of these values. Substituting into (3.21),

$$\delta k = \frac{\epsilon k_0 a}{2} \int_0^{2\pi} \left(\sum_{\ell,m,n=\infty}^{\infty} (1 + \tfrac{(-m)^2}{(k_0 a)^2} + \tfrac{-nm}{(k_0 a)^2}) \alpha_\ell h_n \overline{\alpha_m} \ e^{i(\ell+n-m)\theta} \right) d\theta$$

$$= \epsilon \pi k_0 a \sum_{\ell,n=-\infty}^{\infty} (1 - \tfrac{(n+\ell)^2}{(k_0 a)^2} + \tfrac{n(n+\ell)}{(k_0 a)^2}) \alpha_\ell h_n \overline{\alpha_{\ell+n}} \tag{3.24}$$

Here the complex conjugate is denoted by the overline. Shuffling the sum indices, we obtain the formula

$$\delta k = \epsilon \pi k_0 a \sum_{\ell,m=-\infty}^{\infty} h_{m-\ell} \alpha_\ell \overline{\alpha_m} (1 - \frac{\ell m}{(k_0 a)^2}) \ . \tag{3.25}$$

4.   FINITE ELEMENT MODELLING

Since we want to use a variational approach, let us reformulate (2.1) as:

$$-\nabla \cdot (\nabla u) = k^2 u \text{ in } Y \setminus \bar{C} \ , \ \frac{\partial u}{\partial n} = 0 \text{ on } \partial C \tag{4.1}$$

where C is the metallic inclusion and $Y = \,]0;1[^2$ denotes the elementary cell of the previous section (for the sake of simplicity, we take $d = 1$ in this section).

As for the weak formulation, the condition of zero normal derivative of u on the metallic boundary (homogeneous Neumann boundary conditions) is naturally fulfilled and one just has to exclude C from the basic cell Y:

$$\mathcal{R}(u, u') = \int_{Y \setminus \bar{C}} \nabla u \cdot \nabla \overline{u'} \, dx dy - k_0^2 \int_{Y \setminus \bar{C}} u \overline{u'} \, dx dy \tag{4.2}$$

Existence and uniqueness of the solution is ensured by the Lax-Milgram lemma applied to the function u and its conjugate $\bar{u}$ in the Hilbert space

$$H^1_\sharp(\mathbf{k}_{Bloch}, Y) = \left\{ u \in H^1_{loc}(\mathbb{R}^2, \mathbb{C}) \ , \ u \text{ is } (\mathbf{k}_{Bloch}, Y)\text{-periodic} \right\} \tag{4.3}$$

of $(\mathbf{k}_{Bloch}, Y)$-periodic functions (i.e. satisfying (2.2)) which are square integrable on every compact subset of $\mathbb{R}^2$, with values in $\mathbb{C}$ and with locally square integrable gradients.

The discrete formulation is set up with nodal elements (first order triangular elements). In order to find Bloch modes with the finite element method, some changes have to be performed with respect to classical boundary value problems that will be named *discrete Bloch conditions* [4]. A scalar discrete field $U(x, y)$ on the square cell Y with Bloch conditions relates the left and the right sides. The set of nodes is separated in three subsets: the nodes on the left side, i.e. with $x = 0$, corresponding to the column array of unknowns $\mathbf{u_l}$, the nodes on the right side, i.e. with $x = 1$, corresponding to the column array of unknowns $\mathbf{u_r}$, and the internal nodes, i.e. with $x \in]0, 1[$, corresponding to the column array of unknowns $\mathbf{u}$. One has the following structure for the matrix problem (corresponding in fact to natural boundary conditions i.e. Neumann homogeneous boundary conditions):

$$\mathbf{A} \begin{pmatrix} \mathbf{u} \\ \mathbf{u_l} \\ \mathbf{u_r} \end{pmatrix} = \mathbf{b} \tag{4.4}$$

where $\mathbf{A}$ is the (square Hermitian) matrix of the system and $\mathbf{b}$ a column array. The solution to be approximated by the numerical method is a discrete Bloch function $U(x, y) = U_\sharp(x, y) e^{i(k_{Bloch}^x x + k_{Bloch}^y y)}$, $U_\sharp$ being Y-periodic and in particular $U_\sharp(x + 1, y) = U_\sharp(x, y)$. Therefore,

$$U(1, y) = U_\sharp(1, y) e^{i(k_{Bloch}^x + k_{Bloch}^y y)} = U(0, y) e^{i k_{Bloch}^x} \tag{4.5}$$

and the relation between the left and the right side is:

$$\mathbf{u_r} = \mathbf{u_l} e^{i k_{Bloch}^x} \tag{4.6}$$

Consequently, the set of unknowns can be expressed in function of the reduced set $\mathbf{u}$ and $\mathbf{u_l}$ thanks to:

$$\begin{pmatrix} \mathbf{u} \\ \mathbf{u_l} \\ \mathbf{u_r} \end{pmatrix} = \mathbf{P} \begin{pmatrix} \mathbf{u} \\ \mathbf{u_l} \end{pmatrix} \quad \text{with } \mathbf{P} = \begin{pmatrix} \mathbf{I} & \mathbf{0} \\ \mathbf{0} & \mathbf{I} \\ \mathbf{0} & \mathbf{I} e^{i k_{Bloch}^x} \end{pmatrix} \tag{4.7}$$

where $\mathbf{I}$ and $\mathbf{0}$ are identity and null matrices respectively with suitable dimensions. The finite element equations related to the eliminated nodes have now to be taken into account. Thanks to periodicity of the structure, an element sitting on the left of the right side of the basic cell Y corresponds to an element on the left of the left side of the basic cell. Therefore their contributions (i.e. equations corresponding $\mathbf{u_r}$) must be added to the equations corresponding to $\mathbf{u_l}$ with the correct phase factor $e^{-i k_{Bloch}^x}$. This amounts to multiplying the system matrix by $\mathbf{P}^*$ i.e. the Hermitian conjugate of $\mathbf{P}$. Finally, the linear system to be solved is:

$$\mathbf{P}^* \mathbf{A} \mathbf{P} \begin{pmatrix} \mathbf{u} \\ \mathbf{u_l} \end{pmatrix} = \mathbf{P}^* \mathbf{b} \tag{4.8}$$

where it is worth noting that the system matrix is still Hermitian which is important for numerical computation. Now a generalized eigenvalue problem (with natural boundary conditions) $\mathbf{Au} = \lambda\mathbf{Bu}$ is transformed to an eigenvalue problem with Floquet-Bloch boundary conditions according to $\mathbf{P}^*\mathbf{APu}' = \lambda\mathbf{P}^*\mathbf{BPu}'$. Such problems involving large sparse Hermitian matrices can be solved using Lanczos algorithm that gives the largest eigenvalues [7]. Physically we are in fact interested in the smallest eigenvalues and therefore $\mathbf{A}^{-1}$, the inverse of $\mathbf{A}$, instead of $\mathbf{A}$ itself must be used in the iterations. Of course, the inverse is never computed explicitly but the matrix-vector products are replaced by system solutions thanks to a Generalized Minimal Residual method (GMRES) [7]. method. It is therefore obvious that the numerical efficiency of the process relies strongly on Krylov space techniques and the Arnoldi iteration algorithm [10]. The practical implementation of the model has been performed thanks to the *GetDP* software [2].

5.   NUMERICAL RESULTS

Using the generalised method of Rayleigh, we were able to solve the unperturbed problem for u_0 and were able directly to extract the coefficients α_ℓ from the Fourier expansion of the boundary. Using the formula (3.25) we were then in a position to calculate the correction δk for an arbitrary perturbation.

In Figure 3(a) we can see the dispersion curves for an array of elliptical inclusions, where the major and minor axes are 0.25 and 0.20 respectively and the axes of the ellipses are oriented along the y axis. A diagram showing the path taken in the Brillouin zone is included in Figure 3(b).

It is interesting to note that, for waves travelling in the y-direction, the elliptical array behaves almost identically to an array of cylinders with the same cross section in x. The difference in the dispersion relation for waves travelling in the y-direction is more apparent.

In Figure 4 we can see the dispersion curves for an array of elliptical inclusions, with major and minor axes $0.2d$ and $0.3d$ respectively. Here we have compared the results with the finite element calculation. One can see that the asymptotic formula gives quite good results even when the perturbation is no longer small: in this case, $\epsilon/a = 0.5$. In the case when the eccentricity is higher (e.g. elongated ellipsis of major and minor axes $0.1d$ and $0.4d$), we have numerically checked that the asymptotic approximation fails. It is also apparent on Figure 4 that the asymptotic formula breaks down for higher values of k. For higher frequencies the second order approximation (involving terms of order ϵ^2) would be required to obtain an accurate solution.

(a)
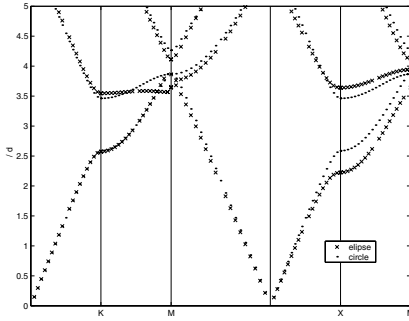
(b)
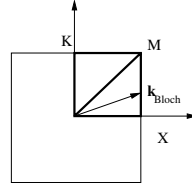
Figure 3 (a) Dispersion curves for a TE wave moving through an array of perfectly conducting cylinders. The crosses represent the dispersion diagram for an ellipse elongated in the y direction, with minor (x) axis $0.20d$ and major (y) axis $0.25d$. Also shown is the curve for the unperturbed problem, which is an array of circular cylinders of radius $0.20d$. (b) The path traversed by $\mathbf{k}_{\text{Bloch}}$ within the first irreducible segment of the Brillouin zone.
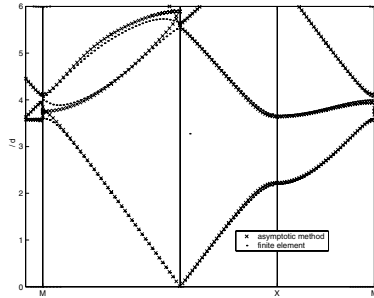
Figure 4 Dispersion curves for a TE wave moving through an array of elliptical inclusions, with major and minor axes $0.2d$ and $0.3d$. A comparison with the results from a finite element method is shown.

6. CONCLUSIONS

We have used an asymptotic approach to calculate the effect on the dispersion relations for a medium in response to the perturbation of the boundary of the included material. The formula which results could be used to optimise the shape of the cylinders for some desired property of the dispersion relation, for example, to increase the band-gap in a certain direction. In addition this technique could be used, in conjunction with

elasticity theory, to calculate the opto-acoustic properties of structured materials.

Acknowledgments

References

[1] S. Agmon, A. Douglis, L. Nirenberg, Estimates near the boundary for solutions of elliptic partial differential equations satisfying general boundary conditions, I, *Comm. Pure Appl. Math.*, **12** (1959), 623-727; II, *Comm. Pure Appl. Math.*, **17** (1964), 35-92

[2] P. Dular, C. Geuzaine, F. Henrotte and W. Legros, A general environment for the treatment of discrete problems and its application to the finite element method, *IEEE Transactions on Magnetics* **34** No. 5 (1998) 3395–3398, and see also the Internet address `http:\\www.geuz.org` .

[3] C. Kittel, *Introduction to solid state physics*, John Wiley and Sons, Seventh edition, (1996), 185.

[4] Ph. Langlet, A.-C. Hladky-Hennion, J.-N. Decarpigny, Analysis of the propagation of plane acoustic waves in passive periodic materials using the finite element method, *J. Acoust. Soc. Am.*,**98**, No.5, Pt. 1(1995), 2792-2800.

[5] K. M. Leung and Y.F. Liu, Full vector wave calculation of photonic band structures in face-centred cubic dielectric media, *Phys. Rev. Lett.*,**65**, (1990), 2646-2649.

[6] R. C. McPhedran and N. A. Nicorovici and L. C. Botten and Ke-Da Bao, Green's function, lattice sums and Rayleigh's identity for a dynamic scattering problem, *IMA Volumes in Mathematics and its Applications*, **96**, Springer-Verlag, New York, (1997), 155-186.

[7] B. Meys, *Ph.D. Thesis*, Université de Liège, (1999).

[8] N. A. Nicorovici and R. C. McPhedran and L. C. Botten, Photonic band gaps for arrays of perfectly conducting cylinders, *Phys. Rev. E*, **52**, (1995b), 1135-1145.

[9] J. B. Pendry and P. M. Bell, Transfer matrix techniques for electromagnetic waves, *NATO ASI Series E:Applied Sciences*, **315**, Kluwer Dordrecht, (1996), 153.

[10] L. N. Trefethen, D. Bau III, *Numerical Linear Algebra*, SIAM, Philadelphia, (1997).

ANTI-PLANE HARMONIC PROBLEMS FOR A CLASS OF ELASTIC MATERIALS WITH FUNCTIONAL INHOMOGENEITY

D.J. Hasanyan[1], G.T. Piliposian[2], A.H. Kamalyan[3] and M.I. Karakhanyan[3]

[1] *Dept. of Engineering Sci. and Mechanics,*
Virginia Polytechnic Institute and State University,
118 Norris Hall, MC 0219, Blacksburg,
Virginia 24061, USA
dhasanya@vt.edu

[2] *The University of Liverpool,*
Department of Mathematical Sciences, Liverpool, L69 3BX, UK
gayane@liv.ac.uk

[3] *Dept. of Mathematics, Yerevan State University,*
1 Aleg Manoogian st, Yerevan, Armenia

Keywords: Wave propagation, stress deformation state, semi-infinite crack, inhomogeneity.

Abstract   Two dynamical (harmonic) problems for an isotropic elastic media with spatially varying functional inhomogeneity are considered: the propagation of surface anti-plane shear SH waves, and the stress deformation state of an anti-plane vibrating medium with a semi-infinite crack. The shear modulus and mass density are assumed to be functions of depth into a half-space. In the shear wave problem the existence conditions and the speed of propagation of surface shear waves has been found. In the crack problem the asymptotic expression for the stress near the crack tip is analysed, which leads to a closed form solution of the dynamic stress intensity factor.

Introduction

There is currently considerable interest in the problem of the propagation of elastic anti-plane waves in functionally graded inhomogeneous materials [1-6]. Such materials have a number of important applications in coating technology. For example, high-temperature-resistant ceramic

thermal barrier coatings are used in jet engines to improve turbine efficiency, component durability, and fuel economy. Cutting tools coated with wear-resistant ceramic layers have higher cutting performance and longer life. In functionally graded coatings, the composition and microstructure vary continuously with distance into the material, eliminating any mismatch of material properties at the interface between the coating and the substrate [7]. This enhances the bonding strength, reduces the residual thermal stresses, and significantly improves the durability of the coating.

Shear surface waves in a half-space with a slight surface inhomogeneity are considered in [1]. In [2] it is shown that the existence conditions for surface wave propagation essentially depend on the parameters describing the inhomogeneity. The problems of diffraction, propagation and reflection of elastic waves in piecewise homogeneous and functionally inhomogeneous media are discussed in [3-6]. Also of great interest is the problem of finding the stress-strain state of inhomogeneous media that include defects such as cracks and inclusions. By choosing the inhomogeneity in an appropriate way, one can control the stress-strain state (SSS) of the material. The problem of the definition of the SSS of piecewise homogeneous and functionally inhomogeneous elastic bodies and containing a crack has been considered by many authors [7-11]. In the present paper we investigate the problem of anti-plane shear waves in materials with a spatially varying functional inhomogeneity, and the definition of the SSS in such materials with a semi-infinite crack. The speed of surface waves, and dynamic stress intensity factor near the edge of the crack, are determined analytically, and from this it is possible to demonstrate how the values of these quantities are influenced by the parameters characterising the inhomogeneity.

1.　THE EQUATION OF MOTION

Consider the propagation of an anti-plane deformation

$$\mathbf{u} = (0, 0, u_z(x, y, t)) \tag{1.1}$$

in an isotropic inhomogeneous linearly elastic body. Assuming that the shear modulus μ and mass density ρ are functions of the depth y, the equation of motion for $u_z(x, y, t)$ has the form [3]

$$\frac{\partial^2 u_z}{\partial x^2} + \frac{1}{\mu(y)} \frac{\partial}{\partial y} \left[\mu(y) \frac{\partial u_z}{\partial y} \right] - \frac{\rho(y)}{\mu(y)} \frac{\partial^2 u_z}{\partial t^2} = 0. \tag{1.2}$$

Considering solutions of the type

$$u_z(x, y, t) = [\mu(y)]^{-1/2} \, \Psi(x, y) e^{i\omega t}, \tag{1.3}$$

we get

$$\Delta \Psi + k^2(y) \Psi = 0, \tag{1.4}$$

where

$$k^2(y) = \frac{\rho(y)}{\mu(y)}\omega^2 - \frac{1}{2}\frac{\mu''}{\mu} + \frac{1}{4}\frac{\mu'^2}{\mu^2}. \tag{1.5}$$

2.   PROPAGATION OF ANTI-PLANE SHEAR SURFACE WAVES IN AN INHOMOGENEOUS SOLID

In considering the propagation of anti-plane shear waves in the elastic half-space $D = \{|x| < \infty, y > 0\}$, we consider a solution of equation (1.4) of the type

$$\Psi(x, y) = \Phi(y)e^{i\alpha x}, \tag{2.1}$$

where α is the wave number, and Φ is the amplitude of the waves. Substituting in (1.4) we obtain

$$\frac{d^2\Phi}{dy^2} - [\alpha^2 - k^2(y)]\Phi = 0. \tag{2.2}$$

Assuming that the boundary $\partial D = \{y = 0, |x| < \infty\}$ is traction-free, so that

$$\sigma_{yz} = \mu\frac{\partial u_z}{\partial y} = 0, \qquad \text{when} \quad y = 0,$$

over $y = 0$ the function Φ must satisfy the boundary condition

$$\frac{\mu'(0)}{\mu(0)}\Phi(0) - 2\Phi'(0) = 0. \tag{2.3}$$

We further assume that the displacement vanishes at infinity, whence

$$\Phi(y) \to 0, \quad \text{when} \quad y \to \infty. \tag{2.4}$$

As can be seen from (1.5), equation (2.2) has a simple solution when $k^2(y) = k_0^2 = $ const, see [3-5, 7, 11]. We consider the case when $k^2(y) \neq$ const, and show analytically that surface wave propagation is possible in this case. Consider an inhomogeneity of the following type:

$$\mu(y) = \mu_0 = \text{const}, \quad \rho(y) = \rho_0 + \frac{2\rho_1}{\cosh^2(\beta y)}, \tag{2.5}$$

where μ_0, ρ_0, and ρ_1 are constants characterizing the inhomogeneity. In this case

$$\alpha^2 - k^2(y) = \alpha^2 - k_0^2 - \frac{2\beta^2}{\cosh^2(\beta y)}, \tag{2.6}$$

where

$$k_0^2 = \frac{\omega^2 \rho_0}{\mu_0} = \frac{\omega^2}{V_0^2}, \quad \beta^2 = \frac{\rho_1 \omega^2}{\mu_0} = \frac{\omega^2}{V_1^2}, \quad V_0 = \sqrt{\frac{\mu_0}{\rho_0}}, \quad V_1 = \sqrt{\frac{\mu_0}{\rho_1}}.$$

The solution of equation (2.2) subject to the attenuation condition (2.4) can then be presented in the following way:

$$\Phi(y) = \Phi_0 e^{-\sqrt{\alpha^2 - \frac{\omega^2}{V_0^2}} y} \left[\sqrt{\alpha^2 - \frac{\omega^2}{V_0^2}} + \frac{\omega}{V_1} \tanh\left(\frac{\omega}{V_1} y\right) \right], \quad (2.7)$$

where

$$\alpha^2 - \frac{\omega^2}{V_0^2} > 0, \quad \text{or} \quad \text{equivalently} \quad \frac{V}{V_0} < 1, \quad (2.8)$$

and $V = \omega/\alpha$ is the relative speed of the surface wave. Substituting the solution (2.7) into the boundary condition (2.3) we obtain

$$\frac{V}{V_0} = \sqrt{\frac{V_1^2}{V_0^2 + V_1^2}} = \sqrt{\frac{\rho_0}{\rho_0 + \rho_1}}. \quad (2.9)$$

The solution (2.9) satisfies the condition (2.8). In other words, inhomogeneities of type (2.5) lead to the existence of SH waves on the free surface of the half space. Note that when $\beta = 0$ (homogeneous material) it follows from (2.9) that $V/V_0 = 1$ and the condition (2.8) is not satisfied. This means, that SH waves do not propagate over the free surface of a homogeneous half-space.

3.   VIBRATION OF AN INHOMOGENEOUS MEDIUM WITH A CRACK

Consider an elastic isotropic inhomogeneous infinite body with an inner "tunnel" crack $x < 0, \quad y = 0$, subject to an anti-plane force $q(x)e^{i\omega t}$. For this case the boundary conditions are:

$$\begin{cases} \sigma_{yz}(x, 0, t) = -q(x)e^{i\omega t}, \ x \leq 0, \\[2mm] u_z(x, 0) = 0, \qquad x > 0. \end{cases} \quad (3.1)$$

In addition to the conditions (3.1), we require that $u_z(x, y, t) \to 0$ as $|y| \to \infty$.

Applying a Fourier transform with respect to x, the solution of (1.2) can be represented in the following way:

$$u_z(x, y, t) = e^{i\omega t} \int_{-\infty}^{\infty} D(\alpha) (\nu_0(\alpha) + \beta \tanh(\beta y)) e^{-\nu_0(\alpha)y} e^{-i\alpha x} d\alpha, \quad (3.2)$$

$$\sigma_{yz} = \mu_0 e^{i\omega t} \times$$

$$\int\limits_{-\infty}^{\infty} D(\alpha) \left[-\nu_0^2(\alpha) + \frac{\beta^2}{\cosh^2(\beta y)} - \nu_0(\alpha)\beta\tanh(\beta y) \right] e^{-i\alpha x} e^{-\nu_0(\alpha)y} d\alpha,$$

$$(3.3)$$

where $D(\alpha)$ is an unknown function which will be found from the boundary conditions (3.1), and the function ν_0 is chosen in the form

$$\nu_0(\alpha) = \begin{cases} (\alpha^2 - \aleph^2)^{\frac{1}{2}}, & |\alpha| > \aleph, \\ -i(\aleph^2 - \alpha^2)^{\frac{1}{2}}, & |\alpha| < \aleph, \end{cases} \quad (3.4)$$

where $\aleph^2 = \dfrac{\omega^2}{V_0^2}$.

Using boundary conditions (3.1) we get the following system of integral equations for $D(\alpha)$;

$$\begin{cases} \int\limits_{-\infty}^{\infty} \nu_0(\alpha)D(\alpha)e^{-i\alpha x}d\alpha = 0, & x > 0, \\ \int\limits_{-\infty}^{\infty} (\nu_0^2(\alpha) - \beta^2)D(\alpha)e^{-i\alpha x}d\alpha = -\dfrac{q(x)}{\mu_0}, & x < 0. \end{cases} \quad (3.5)$$

For simplicity we assume that $q(x) = q_0 = \text{const.}$ (The case $q \neq \text{const}$ can be considered in an analogous way.) To determine $D(\alpha)$, the inverse Fourier transform should be applied to both equations (3.5). Two unknown functions are introduced, one of which is defined for $x < 0$, the other for $x > 0$. A Wiener-Hopf problem is then obtained by eliminating $D(\alpha)$ [12-15]. The path of integration in equations (3.5) has to be indented so as to avoid the points $\alpha = -\aleph$, $\alpha = \aleph$ and $\alpha = 0$. The branch points $\alpha = \pm\aleph$ will not be part of the path of integration along the real axis as shown in Figure 1.

Contour integration around a path from $-\infty$ to ∞ connected by a semi-circle of infinite radius in the upper α plane and application of the residue theorem and Jordan's Lemma show that the second equation in (3.5) would be satisfied if

$$\left(\nu_0^2(\alpha) - \beta^2\right)D(\alpha) = -\frac{q_0}{\mu_0} \frac{1}{2\pi i} \frac{M(\alpha)}{M(0)} \frac{1}{\alpha}, \quad (3.6)$$

where $M(\alpha)$ is an undetermined function, analytic above the path of integration, with $|M(\alpha)/\alpha| \to 0$ as $|\alpha| \to \infty$ in the upper half-plane.
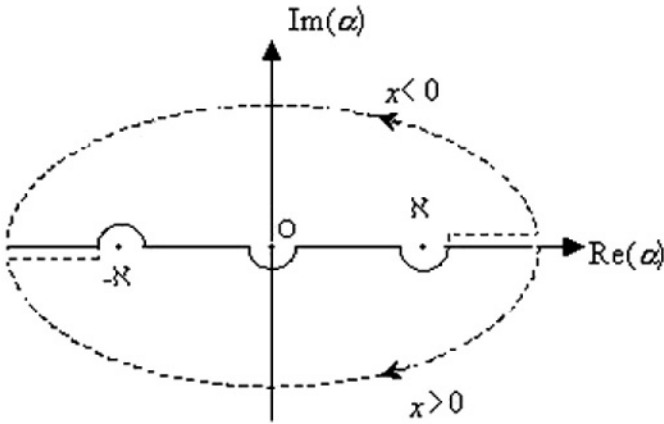
Figure 1   The α plane with cuts

Similarly, the first equation in (3.5) can be satisfied if

$$\nu_0(\alpha)D(\alpha) = N(\alpha) \tag{3.7}$$

is viewed as the transform of a function, which is zero for $x > 0$, so that $N(\alpha)$ is analytic in the lower half-plane and $|N(\alpha)| \to 0$ as $|\alpha| \to \infty$.

Eliminating $D(\alpha)$ from equations (3.6) and (3.7) we get

$$\frac{N(\alpha)}{M(\alpha)} = -\frac{q_0}{\mu_0} \frac{1}{2\pi i} \frac{\sqrt{\alpha^2 - \aleph^2}}{\alpha^2 - (\aleph^2 + \beta^2)} \frac{1}{M(0)} \frac{1}{\alpha}. \tag{3.8}$$

One of the essential steps encountered in the Wiener-Hopf technique is the decomposition of the function $E(\alpha) = \sqrt{\alpha^2 - \aleph^2}/(\alpha^2 - (\aleph^2 + \beta^2))$ in the form of a product

$$E(\alpha) = E_+(\alpha)E_-(\alpha), \tag{3.9}$$

in which $E_+(\alpha)$ and $E_-(\alpha)$ are analytic and non-zero in the upper and lower half-planes, respectively.

It is easy to check that $E_\pm(\alpha) = \sqrt{\alpha \pm \aleph}/(\alpha \pm \sqrt{(\aleph^2 + \beta^2)})$, and from equation (3.8) we obtain

$$N(\alpha) = -\frac{q_0}{\mu_0} \frac{1}{2\pi i} \frac{1}{\alpha} \frac{1}{M(0)} \frac{\sqrt{\alpha - \aleph}}{\alpha - \sqrt{(\aleph^2 + \beta^2)}},$$

$$M(\alpha) = \frac{\alpha + \sqrt{\aleph^2 + \beta^2}}{\sqrt{\alpha + \aleph}}, \qquad M(0) = \frac{\sqrt{\aleph^2 + \beta^2}}{\sqrt{\aleph}}. \qquad (3.10)$$

The function $D(\alpha)$ can be determined from equation (3.6) or (3.7) and can be represented in the form

$$D(\alpha) = -\frac{q_0}{\mu_0} \frac{1}{2\pi i} \frac{\sqrt{\omega_0}}{\omega_2} \frac{1}{\alpha(\alpha - \omega_2)\sqrt{\alpha + \omega_0}},$$

$$\omega_0 = \frac{\omega}{V_0}, \qquad \omega_2 = \sqrt{\frac{\omega^2}{V_0^2} + \frac{\omega^2}{V_1^2}}. \qquad (3.11)$$

From (3.3) we now obtain the following expression

$$\sigma_{yz} = \mu_0 \frac{\partial u_z}{\partial y} = q_0 \frac{\sqrt{\dfrac{\omega}{V_0}}}{\sqrt{\dfrac{\omega^2}{V_0^2} + \dfrac{\omega^2}{V_1^2}}} \times$$

$$\int_{-\infty}^{\infty} \frac{\left(-\nu_0^2(\alpha) + \dfrac{\beta^2}{\cosh^2(\beta y)} - \nu_0(\alpha)\beta\tanh(\beta y)\right) e^{-\nu_0(\alpha)y}}{\alpha(\alpha - \omega_2)(\alpha + \omega_0)^{1/2}} e^{i\omega t} e^{-i\alpha x} d\alpha \qquad (3.12)$$

for the stress.

As a result, from the Abel theorem [12] relating asymptotic properties of transforms, on the line $y = 0$ we have

$$\sigma_{yz} \to q_0 \frac{\sqrt{\dfrac{\omega}{V_0}}}{\sqrt{\dfrac{\omega^2}{V_0^2} + \beta^2}} (1 - i)e^{i\omega t} x^{-\frac{1}{2}}, \qquad x \to +0, \qquad (3.13)$$

or

$$K_3 = \lim_{x \to +0} x^{\frac{1}{2}} \sigma_{yz}(x, 0, t) = q_0 \frac{\sqrt{\dfrac{\omega}{V_0}}}{\sqrt{\dfrac{\omega^2}{V_0^2} + \beta^2}} (1 - i)e^{i\omega t}. \qquad (3.14)$$

When the parameter β characterising the inhomogeneity of the media is zero, formula (3.14) coincides with the formula for the stress intensity factor

obtained in [14,15] for homogeneous media, namely,

$K_3^{hom} = (1-i)q_0\sqrt{\dfrac{V_0}{\omega}}e^{i\omega t}$. From (3.14),

$$\frac{K_3}{K_3^{hom}} = \frac{\sqrt{\dfrac{\omega^2}{V_0^2}}}{\sqrt{\dfrac{\omega^2}{V_0^2}+\beta^2}} \leq 1, \tag{3.15}$$

which means that the inhomogeneities of the type considered decrease the coefficient of intensity compared to the homogeneous case. From (3.12) the elastic stress near the top of the crack has a singularity of the form $x^{-1/2}$ (i.e. $x^{1/2}\sigma_{yz}(x,0,t) \to A = $ const, when $x \to +0$). This means that the inhomogeneity considered does not change the character of the singularity of the elastic stress near the crack tip compared with the homogeneous case.

4.   CONCLUSION

Some dynamic (harmonic) problems for functional inhomogeneity of elastic media are considered. Inhomogeneity of the media is given by spatially varying continuous differentiable function. It is assumed that the media is in anti-plane stress deformation state. The following two problems are considered :

1. propagation of surface anti-plane SH waves,

2. the stress-deformation state of vibrating medium with semi infinite crack.

It is shown that

a) a surface SH wave can propagate through free surface of half space and the speed of propagation is determined,

b) when $|x| \to 0$, the elastic stress near the crack tip has a singularity $\sigma \sim x^{-1/2}$, i.e. the considered inhomogeneity does not change the character of singularity compared with the homogeneous case.

c) inhomogeneities of the type considered decrease the stress intensity factor compared with that of homogeneous case.

References

[1] Viktorov, I A (1978) Surface Waves Induced by an Inhomogeneity in a Solid (in Russian), Proc. of the 10th All-Union Conference on Quantum Acoustics and Acoustoelectronics, pp.101-103, Tashkent, USSR.

[2] Belubekyan, M V & Mukhsikhachoyan, A R (1996) Anti-Plane Shear Surface Wave in Weakly Inhomogeneous Elastic Bodies, Acoustic Journal Vol.42, No.2, pp.179-182.

[3] Maugin, G A (1988) Elastic Surface Waves with Transverse Horizontal Polarization, Advances in Applied Mechanics, New-York Vol.23, pp.373-434.

[4] Brekhovskikh, L M (1980) Waves in Layered Media. Academic Press.

[5] Mukhsikhachoyan, A R (1999) On the Shear Surface Waves in a Inhomogeneous Solid, Proc. of National Academy of Science of Armenia, ser. Mechanics Vol.52, No.1, pp.12-16.

[6] Naifeh, A H & Nemat-Naser, S (1972) Elastic Waves in a Inhomogeneous Elastic Media, Journal of Applied Mechanics, ASME, ser.E, Vol.39, No.3, pp. 696-702.

[7] Jin , Z H & Batra, R C (1996) Interface Cracking Between Functionally graded Coating and a Substrate Under Antiplane Shear, International Journal of Engineering Science Vol.34, No.15, pp.1705-1716.

[8] Babaei, R & Lukasiewicz, S A (1998) Dynamic Response of a Crack in a Functionally Graded Material Between Two Dissimilar Half Planes Under Antiplane Shear Impact Load, Engineering Fracture Mechanics Vol.60, No.4, pp.479-487.

[9] Sih, G C& Chen, E P (1981) Cracks in Composites Materials. In: Sih, G.C. (Ed), Mechanics of Fracture Vol.6, Noordhoff International Publishing, Leyden.

[10] Erdogan, F (1995) Fracture Mechanics of Functional Graded Materials, Composites Engineering Vol.5, pp.753-770.

[11] Atkinson, C (1975) Some Results on Crack Propagation in Media With Spatially Varying Elastic Moduli, International Journal of Fracture, Vol. 11, No. 4, pp.619-628.

[12] Noble, B (1988) Methods Based on Wiener-Hopf Technique for the Solution of Partial Differential Equations, Chelsea publishing company, New York.

[13] Antipov, Y A, Avila-Pozos O, Kolaczkowski S T & Movchan A B (2001) Mathematical Model of Delamination Cracks on Imperfect Interfaces, International Journal of Solids and Structures, Vol. 38, pp. 6665-6697.

[14] Parton, B Z & Boriskovski, V G (1985) Dynamic Mechanics of Fracture. Moscow, Mashinostroenie.

[15] Chen, E P, Sih, G C (1977) Scattering waves about stationary and moving cracks. Mechanics of Fracture, 4, Elastodynamics crack problems (Edited by G. C. Sih), Noordhoff Int. Publishing, Leyden, pp.119-212.

ON ANALYSING THE PERFORMANCE OF A DISSIPATIVE SILENCER: A MODE-MATCHING APPROACH

Jane B. Lawrie and Ray Kirby
Department of Mathematical Sciences
Brunel University, Uxbridge UB8 3PH, UK
jane.lawrie@brunel.ac.uk, ray.kirby@brunel.ac.uk

1.   INTRODUCTION

Dissipative silencers are widely used to attenuate broad-band noise in heating, ventilation and air-conditioning (HVAC) ducts. In general a ducting system of this class is of rectangular cross-section and consists of several sections of duct and a variety of components. A typical silencer comprises a finite section of duct with layers of porous material positioned parallel to one of the duct walls. In the simplest configuration a section of the duct is "lined", that is, two layers of porous material are positioned in contact with opposite duct walls. Further layers may be inserted, each one positioned centrally and parallel to the duct lining, to form what is commonly is referred to as a "splitter silencer".

For engineers wishing to determine the efficiency of such devices, a pragmatic model for the porous material is required and the usual choice is an "equivalent fluid". In this formulation the porous material is replaced with a fluid in which the speed of propagation, c_p, and density, ρ_p, are considered to be complex. Much experimental work has been done on relating c_p and ρ_p to the bulk acoustic properties of real porous materials and the complex values of these parameters are known in principle (see [1]). The major advantage of such a model is that it permits the use of modal analysis. To date, however, design techniques commonly rely on quantifying the attenuation of the fundamental acoustic mode and possibly the first-order mode. Whilst this approach will provide some insight into silencer performance, it necessarily suppresses the complex multi-modal behaviour present in larger ducts and/or at higher frequencies, and omits the influence of the outlet/inlet planes of the silencer.

The eigensystem for a silencer is Sturm-Liouville in type. Yet industrial application of mode-matching techniques for analysing the performance of a dissipative silencer is, at best, rare. This is due, in part, to the difficulty of reliably locating the roots of the dispersion relation which contains complex parameters. As the imaginary parts of these increase (corresponding to low frequency and/or highly absorbent materials) the problem of root location intensifies. As the number of layers of porous material in the silencer increases, the algebraic complexity of the dispersion relation further compounds the problem. Not only is it difficult to locate all the roots in a given region of the complex plane, but there are few reliable techniques for determining if any roots are missing. Although the effect of a missing root on the results obtained through mode-matching depends on the location of the root, it is always undesirable and often the cause of significant inaccuracies.

In this article it is shown that, if the transmission loss is the physical quantity of interest, it is not necessary to solve the dispersion relation. An exact system of equations, by which to determine the reflection and transmission coefficients, is derived using the analytic properties of the eigensystem in the silencer region but without explicit knowledge of the eigenvalues. In section 2 the method is demonstrated for a simple silencer comprising a finite length lined duct inserted into an otherwise infinite rigid duct. Numerical results are presented and the implications of this approach for analysing the splitter silencer are discussed in section 3.

2.   A SIMPLE DISSIPATIVE SILENCER

A typical HVAC duct can be modelled as a three-dimensional, infinite, rigid duct occupying, say, the region $|\bar{y}| \leq \bar{b}$, $|\bar{z}| \leq \bar{c}$, $-\infty < \bar{x} < \infty$ of a Cartesian frame of reference. The section of duct lying in the region $0 < \bar{x} \leq 2\bar{\ell}$ is lined, on two opposite walls, with a porous material which occupies the space $\bar{a} \leq |\bar{y}| \leq \bar{b}$, $|\bar{z}| \leq \bar{c}$, $\bar{b} > \bar{a}$. A compressible fluid of sound speed c and density ρ fills the interior of the duct. The porous media is modelled as an equivalent fluid with complex speed of propagation c_p and complex density $\rho_p = Z_a/c_p$ where Z_a is the impedance of the material.

A plane wave, of unit amplitude and harmonic time dependence $e^{+i\omega\bar{t}}$, where $\omega = ck$, is incident through the fluid in the positive $\bar{x}$ direction towards $\bar{x} = 0$. Since the forcing is independent of z and there is no change of geometry or material property in the $\bar{z}$ direction, the two-dimensional version of the model problem is considered. Further, since the $\bar{x}$-axis is a line of symmetry, it is sufficient to consider only the upper half of the duct $(0 \leq \bar{y} \leq \bar{b})$ with a rigid surface at $\bar{y} = 0$ (see figure 1).
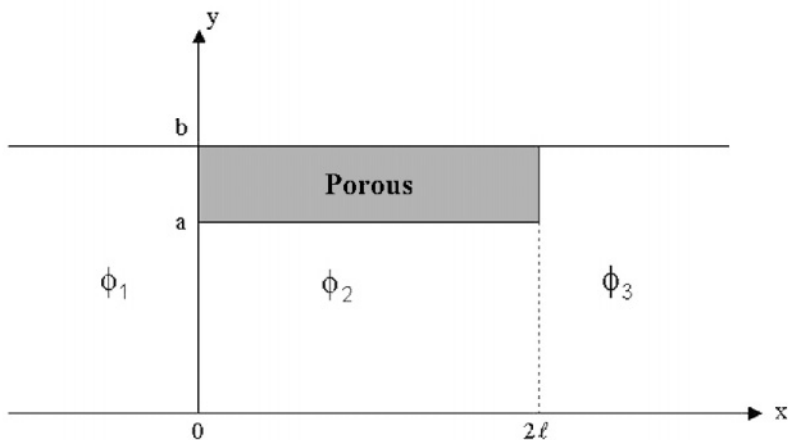
Figure 1 Infinite rigid duct with finite length dissipative silencer.

2.1.   THE BOUNDARY VALUE PROBLEM

It is convenient to non-dimensionalise the boundary value problem using typical length and time scales k^{-1} and ω^{-1}. Thus, $x = k\bar{x}$, $y = k\bar{y}$ etc. where the "barred" quantities are dimensional. The time-independent fluid velocity potential is defined for each duct region in figure 1. For the inlet and outlet ducts ($x < 0$ and $x > 2\ell$ respectively) the velocity potentials are governed by Helmholtz's equation and must satisfy the rigid wall conditions at $y = 0$ and $y = b$. Thus,

$$(\nabla^2 + 1)\varphi_j(x, y) = 0, \quad 0 \le y \le b, \quad j = 1, 3 \tag{2.1}$$

and

$$\frac{\partial \varphi_j}{\partial y} = 0, \quad y = 0, b, \quad j = 1, 3. \tag{2.2}$$

The velocity potential in the silencer region ($0 \le x \le 2\ell$) must satisfy Helmholtz's equation with unit wavenumber in the central passage, $0 \le y < a$ and with wavenumber c/c_p in the porous media $a < y \le b$. At the interface between the porous media and the fluid ($y = a$) it is assumed that the pressure and normal velocity are continuous whilst at the rigid duct walls the normal velocity is zero. It follows that the potential φ_2 must satisfy the following:

$$(\nabla^2 + 1)\varphi_2(x, y) = 0, \quad 0 \le y < a, \tag{2.3}$$
$$(\nabla^2 - \Gamma^2)\varphi_2(x, y) = 0, \quad a \le y \le b, \tag{2.4}$$

where $\Gamma = ic/c_p$, together with

$$\varphi_2(x, a^-) = \beta\varphi_2(x, a^+), \tag{2.5}$$

$$\frac{\partial\varphi_2}{\partial y}(x, a^-) = \frac{\partial\varphi_2}{\partial y}(x, a^+), \tag{2.6}$$

where $\beta = \rho_p/\rho$, and

$$\frac{\partial\varphi_2}{\partial y} = 0, \quad y = 0, b. \tag{2.7}$$

At the interfaces between the inlet/outlet duct and the silencer the conditions of continuity of pressure and normal velocity are applied. Thus, at $x = 0$

$$\varphi_1(0, y) = \begin{cases} \varphi_2(0, y), & 0 \le y < a \\ \beta\varphi_2(0, y), & a < y \le b \end{cases} \tag{2.8}$$

$$\frac{\partial\varphi_1}{\partial x}(0, y) = \frac{\partial\varphi_2}{\partial x}(0, y), \quad 0 \le y \le b \tag{2.9}$$

whilst at $x = 2\ell$

$$\varphi_3(2\ell, y) = \begin{cases} \varphi_2(2\ell, y), & 0 \le y < a \\ \beta\varphi_2(2\ell, y), & a < y \le b \end{cases}, \tag{2.10}$$

$$\frac{\partial\varphi_3}{\partial x}(2\ell, y) = \frac{\partial\varphi_2}{\partial x}(2\ell, y), \quad 0 \le y \le b. \tag{2.11}$$

2.2.   EIGENSYSTEM FOR THE SILENCER

Equations (2.3)–(2.7) describe the unforced boundary value problem for a lined duct of any length. The travelling wave forms in a duct of this type are easily determined by separation of variables. A typical mode travelling in the positive x direction has the form $\varphi_{2n}(x, y) = Y_n(y)e^{s_n x}$ where

$$Y_n(y) = \begin{cases} Y_{1n}(y), & 0 \le y < a \\ Y_{2n}(y), & a \le y \le b \end{cases} \tag{2.12}$$

and the wavenumber s_n is defined below as a root of (2.20). The eigenfunctions $Y_n(y)$, $n = 0, 1, 2, \ldots$ are the solutions to the eigensystem:

$$Y_1'' - \gamma^2 Y_1 = 0, \quad 0 \le y < a; \tag{2.13}$$

$$Y_1'(0) = 0; \tag{2.14}$$

$$Y_2'' - \lambda^2 Y_2 = 0, \quad a \le y < b; \tag{2.15}$$

$$Y_2'(b) = 0; \tag{2.16}$$

$$Y_1(a) = \beta Y_2(a); \tag{2.17}$$

$$Y_1'(a) = Y_2'(a) \tag{2.18}$$

where $\gamma(s) = (-1 - s^2)^{1/2}$ and $\lambda(s) = (\Gamma^2 - s^2)^{1/2}$ the branches being chosen such that $\gamma(0) = +i$ and $\lambda(0) = +\Gamma$.

It is easily shown that

$$Y_n(y) = \begin{cases} \cosh(\gamma_n y), & 0 \leq y < a \\ -\dfrac{\gamma_n \sinh(\gamma_n a)}{\lambda_n \sinh[\lambda_n(b-a)]} \cosh[\lambda_n(b-y)], & a \leq y \leq b \end{cases}. \tag{2.19}$$

Here $\gamma_n = \gamma(s_n), \lambda_n = \lambda(s_n)$ and s_n, $n = 0, 1, 2, \ldots$ are those roots of the dispersion relation $K(s) = 0$ with $\mathrm{Re}(s_n) \geq 0$ where

$$K(s) = \cosh(\gamma a) + \frac{\beta\gamma \sinh(\gamma a)}{\lambda \sinh[\lambda(b-a)]} \cosh[\lambda(b-a)]. \tag{2.20}$$

Note that the roots s_n, $n = 0, 1, 2, \ldots$ are numbered by increasing real part. Thus, the mode with wavenumber s_0 is the least attenuated.

The orthogonality relation for this set of eigenfunctions (c.f. [2]) is

$$\int_0^a Y_{1n}Y_{1m} \, dy + \beta \int_a^b Y_{2n}Y_{2m} \, dy = \delta_{mn}E_n \tag{2.21}$$

where δ_{mn} is the usual Kronecker delta and

$$E_n = \frac{Y_{1n}'(a)}{2s_n} \frac{d}{ds}K(s)\bigg|_{s=s_n}, \tag{2.22}$$

the prime indicating differentiation with respect to y.

2.3.   MODE-MATCHING SOLUTION

The velocity potentials φ_j, $j = 1, 2, 3$ can be written as eigenfunction expansions in the form:

$$\varphi_1 = e^{-ix} + \sum_{j=0}^{\infty} \frac{A_j}{\varepsilon_j} \cos(\frac{j\pi y}{b})e^{\eta_j x}; \tag{2.23}$$

$$\varphi_2 = \sum_{j=0}^{\infty}(B_j e^{-s_j x} + C_j e^{s_j x})Y_j(y); \tag{2.24}$$

$$\varphi_3 = \sum_{j=0}^{\infty} \frac{D_j}{\varepsilon_j} \cos(\frac{j\pi y}{b})e^{-\eta_j x} \tag{2.25}$$

where $\varepsilon_j = 2$ for $j = 0$ and 1 otherwise. Note that the incident wave takes the form e^{-ix} and $\eta_j = (j^2\pi^2/b^2 - 1)^{1/2}$ with $\eta_0 = i$, these definitions being appropriate for the choice of time dependence. The orthogonality property for $\{\cos(n\pi y/b)\}$ together with (2.21) enable conditions (2.8)–(2.11) to be enforced at the interfaces $x = 0$ and $x = 2\ell$, $0 \leq y \leq b$.

Two linear systems of equations are obtained, the solutions of which yield the complex amplitudes A_j, and D_j. For brevity the details are omitted, however, the first system is

$$\chi_n = \frac{2i}{\eta_n^{1/2}}\delta_{0n} - \frac{2}{b\eta_n^{1/2}}\Lambda_{0n} - \frac{2}{b\eta_n^{1/2}}\sum_{j=0}^{\infty}\chi_j\frac{\Lambda_{jn}}{\varepsilon_j\eta_j^{1/2}} \qquad (2.26)$$

where $\chi_n = (A_n + D_n e^{-2\eta_n\ell})\eta_n^{1/2}$ and

$$\Lambda_{jn} = \sum_{m=0}^{\infty}\frac{s_m}{E_m}\tanh(s_m\ell)R_{jm}R_{nm} \qquad (2.27)$$

with

$$\begin{aligned} R_{jm} = {}& \cos(\frac{j\pi a}{b})Y'_{1m}(a)\left\{\frac{1}{\gamma_m^2 + (j\pi/b)^2} - \frac{1}{\lambda_m^2 + (j\pi/b)^2}\right\} \qquad (2.28)\\ & + \frac{j\pi}{\beta b}\sin(\frac{j\pi a}{b})Y_{1m}(a)\left\{\frac{\beta}{\gamma_m^2 + (j\pi/b)^2} - \frac{1}{\lambda_m^2 + (j\pi/b)^2}\right\}. \end{aligned}$$

The second system of equations, for $\psi_n = (A_n - D_n e^{-2\eta_n\ell})\eta_n^{1/2}$, is identical in structure to (2.26) but with Λ_{jn} replaced with $\Omega(j,n)$. The quantity Ω_{jn} is obtained from (2.27) by replacing $\tanh(s_m\ell)$ with $\coth(s_m\ell)$.

Equation (2.26) (and the equivalent for ψ_n) many be solved by truncation and numerical inversion of the matrix. Crucial to this process is accurate knowledge of sufficient roots, s_m, of (2.20). As previously discussed, missing roots are often the source of significant inaccuracies and, due to the complex nature of these roots, the Argument Principle is the only reliable method of ascertaining whether all the roots in a specified area of the complex plane have been found. If, however, one or more are missing it is of limited help in locating them. The question arises then: is it possible to solve equation (2.26) without knowledge of s_n, $n = 0, 1, 2, \ldots$?

2.4.   RECASTING THE MATRIX ELEMENTS

Expression (2.27) can be recast in a form where the summation takes place over eigenvalues that can be expressed in closed form. (This is not the case with s_n, $n = 0, 1, 2, \ldots$ which, although well defined, must be determined numerically.) The key is expression (2.22) which relates the quantity E_n to the derivative of the dispersion relation. This enables (2.27) to be recognised as the sum over a family of poles for a carefully selected integral. The appropriate integral is

$$I_{jm} = \frac{-1}{2\pi i}\int_{-i\infty}^{i\infty}\frac{s^2\gamma\sinh(\gamma a)}{K(s)\coth(s\ell)}L_j(s)L_m(s)\,ds \qquad (2.29)$$

where

$$L_j(s) = \frac{P_j(s)}{\gamma^2 + (j\pi/b)^2} - \frac{Q_j(s)}{\lambda^2 + (j\pi/b)^2}, \tag{2.30}$$

with $\gamma = (-1 - s^2)^{1/2}$ and $\lambda = (\Gamma^2 - s^2)^{1/2}$, and

$$P_j(s) = \cos(\frac{j\pi a}{b}) - \frac{j\pi}{b}\sin(\frac{j\pi a}{b})\frac{\beta\cosh[\lambda(b-a)]}{\lambda\sinh[\lambda(b-a)]}; \tag{2.31}$$

$$Q_j(s) = \cos(\frac{j\pi a}{b}) - \frac{j\pi}{b}\sin(\frac{j\pi a}{b})\frac{\cosh[\lambda(b-a)]}{\lambda\sinh[\lambda(b-a)]}. \tag{2.32}$$

The path of integration in (2.29) lies along the imaginary axis and is indented to the left(right) of any poles on the upper(lower) half of the imaginary axis. Therefore, since the integrand is an odd function of s, $I_{jm} = 0$. The integrand has poles at $s = \eta_j$ and $s = \eta_m$ (which produce a double pole when $m = j = 0$) and families of poles when

i) $K(s) = 0$, i.e. $s = s_n$, ;

ii) $\cosh(s\ell) = 0$, i.e. $s = \sigma_n = (2n+1)i\pi/(2\ell)$;

iii) $\sinh[\lambda(b-a)] = 0$, i.e. $s = \nu_n = [\Gamma^2 + n^2\pi^2/(b-a)^2]^{1/2}$,

where in each case $n = 0, 1, 2, \ldots$. The first family of poles yields Λ_{jm} and, on evaluating all the other pole contributions, it is found that

$$\begin{aligned}
\Lambda_{jm} = {}& -\frac{2}{\ell}U_{jm} + (1 - \delta_{j0})(1 - \delta_{m0})\frac{2}{\beta d}V_{jm} \\
& - (1 - \delta_{jm})\{(1 - \delta_{j0})f_{jm} + (1 - \delta_{m0})f_{mj}\} \\
& + \delta_{jm}(1 - \delta_{m0})g_m + \delta_{m0}\delta_{j0}\{\frac{d}{\beta}\nu_0\tanh(\nu_0\ell) - a\tan(\ell)\} \\
& + \frac{\nu_0}{\beta}\tanh(\nu_0\ell)\{\delta_{m0}(1 - \delta_{j0})h_j + \delta_{j0}(1 - \delta_{m0})h_m\}
\end{aligned} \tag{2.33}$$

where $d = b - a$ and U_{jm}, V_{jm} are given by:

$$U_{jm} = \sum_{n=0}^{\infty} \frac{\sigma_n^2\gamma(\sigma_n)\sinh[\gamma(\sigma_n)a]}{K(\sigma_n)}L_j(\sigma_n)L_m(\sigma_n); \tag{2.34}$$

$$\begin{aligned}
V_{jm} = {}& \frac{j\pi}{b}\sin(\frac{j\pi a}{b})\frac{m\pi}{b}\sin(\frac{m\pi a}{b})\sum_{n=0}^{\infty}\frac{\nu_n}{\varepsilon_n}\tanh(\nu_n\ell) \\
& \times \left\{\frac{\beta}{(j\pi/b)^2 + \gamma^2(\nu_n)} - \frac{1}{(j\pi/b)^2 + \lambda^2(\nu_n)}\right\} \\
& \times \left\{\frac{\beta}{(m\pi/b)^2 + \gamma^2(\nu_n)} - \frac{1}{(m\pi/b)^2 + \lambda^2(\nu_n)}\right\}.
\end{aligned} \tag{2.35}$$

The functions f_{jm}, h_j and g_m are defined by:

$$f_{jm} = \eta_j \tanh(\eta_j \ell) \frac{j\pi}{b} \sin(\frac{j\pi a}{b}) L_m(\eta_j), \qquad (2.36)$$

$$h_j = \frac{j\pi}{b} \sin(\frac{j\pi a}{b}) \left\{ \frac{\beta}{\gamma^2(\nu_0) + (j\pi/b)^2} - \frac{b^2}{j^2\pi^2} \right\} \qquad (2.37)$$

and

$$g_m = \eta_m \tanh(\eta_m \ell) \left\{ \frac{a}{2} + \frac{b\sin(2m\pi a/b)}{4m\pi} + \frac{2m\pi}{b} \sin(\frac{m\pi a}{b}) \frac{Q_m(\eta_m)}{\Gamma^2 + 1} \right\}$$

$$+ \frac{m\pi}{2b} \sin(\frac{m\pi a}{b}) \left\{ \ell\operatorname{sech}^2(\eta_m\ell) + \frac{\tanh(\eta_m\ell)}{\eta_m} \right\} P_m(\eta_m) \qquad (2.38)$$

$$- \frac{\beta}{2} \eta_m \tanh(\eta_m\ell) \left[\frac{(m\pi/b)\sin(m\pi a/b)}{\lambda(\eta_m)\sinh[\lambda(\eta_m)d]} \right]^2 \left\{ d + \frac{\sinh[2\lambda(\eta_m)d]}{2\lambda(\eta_m)} \right\}.$$

It should be noted that expressions (2.33)–(2.38) hold provided $\gamma^2(\sigma_n)$+ $(j\pi/b) \neq 0$ for any n or j. At the discrete frequencies, or duct configurations, for which this is zero the analysis is altered slightly due to the presence of an isolated higher order pole in the integrand of (2.29).

A similar expression for Ω_{jm} can be obtained using the integral (2.29) but with the term $\coth(s\ell)$ in the denominator of the integrand replaced with $\tanh(s\ell)$. The result is obtained from equations (2.33)–(2.38) by:

i) redefining the eigenvalues σ_n as $\sigma_n = n\pi i/\ell$, $n = 0, 1, 2, \dots$;

ii) replacing every occurrence of tanh with coth;

iii) replacing, in g_m, the term $\ell\operatorname{sech}^2(\eta_m\ell)$ with $-\ell/\sinh^2(\eta_m\ell)$;

iv) replacing, in the fifth term of (2.33), $-a\tan(\ell)$ with $a\cot(\ell)$.

Then, having recast the matrix elements into a form that is independent of the roots of (2.20), equation (2.26) (and the equivalent for ψ_n) many be truncated and solved numerically. The results presented below were obtained by truncating the systems to 40 terms.

3. RESULTS AND DISCUSSION

The usual measure of performance for a dissipative silencer is transmission loss $\mathcal{L} = -20\log_{10}(T)$ where T is the ratio of transmitted to incident power given, for this problem, by

$$T = \frac{1}{2}\operatorname{Re}\{i \sum_{n=0}^{\infty} \frac{|D_n|^2}{\varepsilon_n} \eta_n^* \} \qquad (3.1)$$
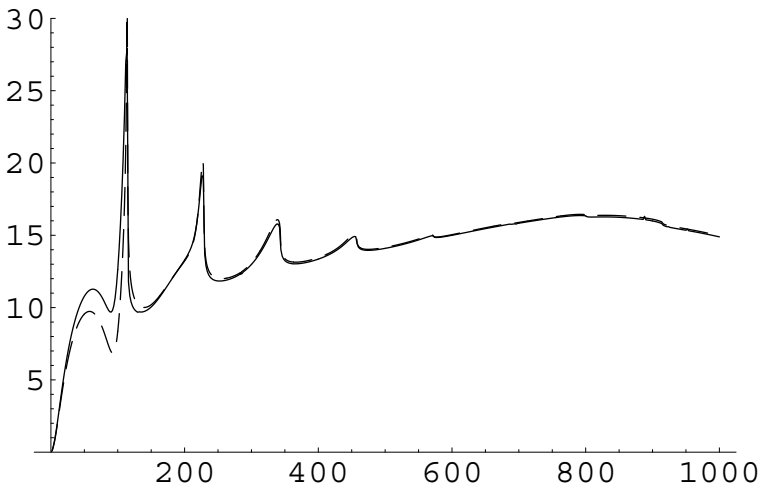
Figure 2   Transmission loss against frequency for E-glass; the plot of $\mathcal{L}$ versus f.

where $\eta_n = (n^2\pi^2/b^2 - 1)^{1/2}$. In this section two graphs of the transmission loss against frequency are presented. In both cases the duct height is 1.5 m, the lining is 1.25 m thick and the silencer half-length is 0.5 m. The spikes, apparent on both graphs, correspond to the "cut-on" frequencies for modes in the inlet/outlet ducts.

In figure 2 the duct lining comprises E-glass. This is an acoustically dense material with flow resistivity 30716 rayl/m (where 1 rayl is 1 Nsm^{-4}) and thus, for low frequencies, $|\beta| >> 1$ with $\mathrm{Re}(\beta) > 0$ and $Im(\beta) < 0$. The dashed line is the transmission loss obtained using (2.27) to calculate Λ_{jm} (and Ω_{jm}) with an inefficient rootfinder. The solid curve is the transmission loss using (2.33) for Λ_{jm} and the analogous expression for Ω_{jm}. The inaccuracy caused by missing modes is clear. For frequencies of 60–153 Hz the second mode is missing, for 154–600 Hz, the third mode is missing and for frequencies above 600 Hz the fourth mode is missing. Clearly, for this configuration, the lower the mode that is missed the bigger the inaccuracy.

Figure 3 shows the transmission loss for a "Delany and Bazley" material with flow resistivity of 4000 rayl/m. As in the previous figure, the solid curve is the transmission loss calculated using the recast forms for Λ_{jm} and Ω_{jm}. The dashed curve is the transmission loss obtained using an inefficient rootfinder. In this case, the second mode is missing for frequencies in the range 50–160 Hz, the third mode is missing for 161–172 Hz and the second and/or third is missing for higher frequencies.

This article has demonstrated that it is possible to calculate transmission loss for a simple dissipative silencer without solving the dispersion relation. For the lined silencer considered here the method provides only
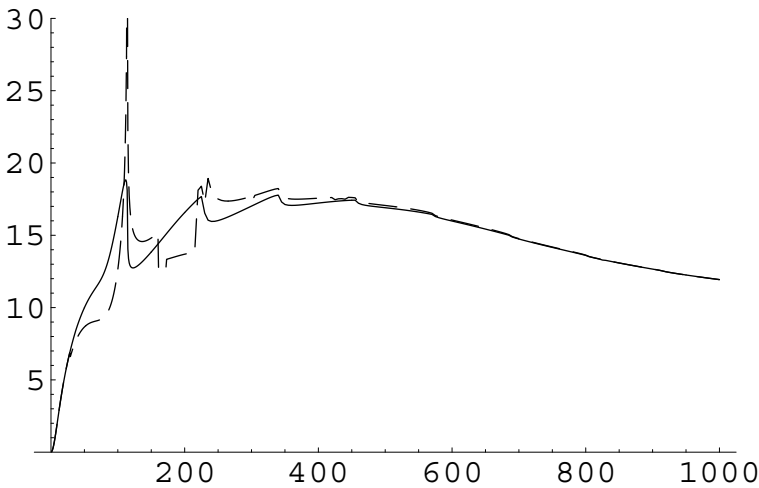
Figure 3   Transmission loss for a Delany and Bazley material; the plot of $\mathcal{L}$ versus f.

an alternative approach as the wavenumbers can be determined if reasonable care is taken. For a splitter silencer, however, the dispersion relation is more complicated and reliable location of the eigenvalues for all frequencies presents significant problems. Under such circumstances it is clearly an advantage to re-express the problem in terms of eigenvalues that are explicitly defined.

References

[1] Kirby, R. & Cummings, A. (1999) Prediction of the bulk acoustic properties of fibrous materials at low frequencies. Applied Acoustics,**56**, 101 –125.

[2] Glav, R. (1996) The point-matching method on dissipative silencers of arbitrary cross-section. J. Sound Vib. **189**, 123–135.

Chapter 3
Green's functions and defect modes

LOCALIZED GREEN'S FUNCTIONS FOR A TWO-DIMENSIONAL PERIODIC MATERIAL

C. G. Poulton[1], R. C. McPhedran[2], N. A. Nicorovici[2] and L. C. Botten[3]

[1] *High Frequency and Quantum Electronics Laboratory, University of Karlsruhe, 76128 Karlsruhe, Germany*
[2] *School of Physics, University of Sydney, New South Wales 2006, Australia*
[3] *School of Mathematical Sciences, University of Technology, Sydney, NSW 2007, Australia*

Keywords: Green's functions, photonic crystals, defects, Bloch functions.

Abstract   We describe a method for the calculation of Green's functions for an array of dielectric cylinders. The method is to first construct quasi-periodic Green's functions, with Bloch vector $\boldsymbol{k}_{\mathrm{B}}$. This function also obeys the appropriate electromagnetic boundary conditions on the surface of each cylinder. The Green's function for a single source in the array can then be calculated by averaging the quasi-periodic result over the Brillouin zone.

1.   INTRODUCTION

Photonic band gap materials are the focus of intensive research and development, with the aim of providing the analogue of semiconductors for photons [1]. The first phase of their development was to produce structures with an optical band gap in which the only waves which exist are evanescent. An example of a structure that achieves this is a stack of gratings composed of high refractive index cylinders, which can now be fabricated routinely using lithographic methods from the semiconductor industry. Much current research is focused on the creation and exploitation of defects in regular arrays, which act as the equivalent of doping [2]. It is our purpose here to present a new and accurate technique for the generation of localized Green's functions which may be used to model the electromagnetic fields around defects in two-dimensional photonic crystals.

Many previous authors have studied defects in photonic crystals [1]. For two-dimensional structures, one common method [3] uses transmittance

through a slab of the crystal structure of finite thickness to indicate the locations of defects. Their field structures may also be calculated. A second approach [4] is to embed the defect in a supercell, and then replicate the supercell periodically, calculating the modes of the resultant structure using plane wave expansions of fields. A popular approach is to use the finite difference time domain method (FDTD) [5], in which a dispersion behaviour is assumed for the rod material, enabling Fourier representations in a temporal solution of the field problem. Figotin et al [6] use a resolvent method, leading to an iterative procedure for constructing defect states.

The method we describe here is designed to permit easy generalization to provide a complete basis of localized functions with a source at a prescribed point in a two-dimensional photonic crystal. The functions obey boundary conditions on the surfaces of all cylinders in the infinite crystal, and the method works well even with cylinders made of material having a high (or complex) dielectric constant ratio with the matrix material, unlike plane wave methods. It deals with each frequency separately, unlike FDTD methods, and so does not need to assume dispersion models for dielectric or lossy cylinders. It starts off by assuming a quasiperiodicity, rather like the supercell method, but then by averaging over different quasiperidocity factors, succeeds in constructing a Green's function which corresponds to a single source term- i.e., corresponds to the solution in an infinite domain with no periodicity property.This characteristic would also render the solution difficult or impossible to obtain with finite element techniques . Furthermore, the numerical technique is well adapted to parallel computer implementation, if large scale numerics are needed.

2.   THE PHASED ARRAY OF SOURCES

We consider first the problem depicted in Figure 1, which depicts a phased array of point sources placed in a doubly-periodic lattice of circular inclusions. We would like to find a function which has the correct behaviour at the source points and also which satisfies the appropriate boundary conditions on the perimeter of each inclusion. Such a function can be thought of as a quasiperiodic Green's function for the lattice.

The inclusions have a radius of r_c and are separated by a distance d, and possess transport properties which are different from the matrix material which surrounds them. The geometry of the array is represented by the lattice vector $\boldsymbol{R}_p$, where $p = (md, nd) \in \mathcal{R}^2$ is a multi-index which points to the centre of the $p - th$ cylinder.

We assume that the material is strictly periodic, so if we represent the wave by a scalar field $u(r, \theta)$ then it must obey the Bloch-Floquet condition

$$u(\boldsymbol{r} + \boldsymbol{R}_p) = u(\boldsymbol{r})e^{i\boldsymbol{k}_{\mathrm{B}} \cdot \boldsymbol{R}_p} \qquad (2.1)$$
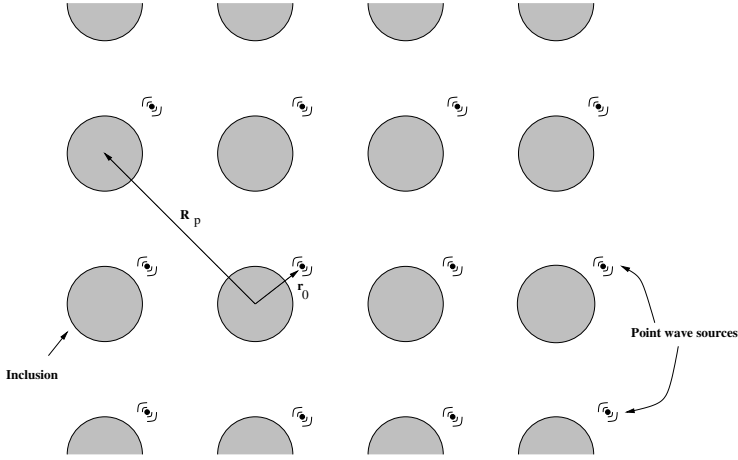
Figure 1   The two-dimensional array of inclusions, with regularly spaced sources of outgoing waves.

where $\boldsymbol{k}_{\mathrm{B}}$ is the Bloch wavevector. Within the matrix material, external to the circular inclusions, the field u satisfies the Helmholtz equation

$$(\Delta + k^2)u = \sum_p \delta(\boldsymbol{r} - \boldsymbol{r}_0 - \boldsymbol{R}_p)e^{i\boldsymbol{k}_{\mathrm{B}}\cdot\boldsymbol{R}_p} \ . \qquad (2.2)$$

Here k is the characteristic frequency of the wave. Within the inclusions themselves we have

$$(\Delta + n^2 k^2)u = 0 \qquad (2.3)$$

where n is the refractive index of the inclusions, relative to the surrounding material.

On the surface of every cylinder we can specify the appropriate boundary conditions; for purpose of illustration we consider the TM mode where the cylinder material is non-magnetic. The boundary conditions in this case are:

$$u = u^{int} \qquad (2.4)$$

$$\frac{\partial u}{\partial r} = \frac{\partial u^{int}}{\partial r} \qquad (2.5)$$

We note that it would be possible to study the TE polarisation by setting the second boundary condition to be $\partial u/\partial r = 1/n^2 \partial u^{int}/\partial r$.

The problem is now determined uniquely. In order to solve it we follow [7] and expand the total field in terms of multipoles around the origin:

$$u(r, \theta) = \sum_{m=-\infty}^{\infty} \left(A_m J_m(kr) + B_m Y_m(kr)\right) e^{im\theta} \qquad (2.6)$$

Here A_m and B_m are coefficients which we seek to determine. It should be noted that the expansion (2.6) is applied around the boundary of the central inclusion (It's radius of convergence, in fact, extends out to the source point). From the boundary conditions (2.4), (2.5) we can immediately write

$$A_m = -M_m B_m, \tag{2.7}$$

where

$$M_m = \frac{n J_m'(nkr_c)Y_m(kr_c) - J_m(nkr_c)Y_m'(kr_c)}{n J_m'(nkr_c)J_m(kr_c) - J_m(nkr_c)J_m'(kr_c)} \tag{2.8}$$

for the TM mode. In order to solve the problem we must have an additional relation between the coefficients A_m and B_m. By identifying the part of the field which is singular at the origin as coming from the contribution of the central cylinder, while the regular part arises from all the effect of all the sources external to the central cylinder, one can derive the identity:

$$\sum_{m=-\infty}^{\infty} A_m J_m(kr)e^{im\theta} = \sum_{m=-\infty}^{\infty} \sum_{\ell=-\infty}^{\infty} B_\ell (-1)^{\ell+m} S_{\ell-m}^Y J_m(kr)e^{im\theta}$$
$$+ u_s(r,\theta) , \tag{2.9}$$

where $u_s(r,\theta)$ is the field arising from all the sources in the array, and the coefficients S_ℓ^Y are the lattice sums

$$S_\ell^Y = \sum_{p \neq \{0,0\}} Y_\ell(kR_p)e^{i\ell\theta_p}e^{i\boldsymbol{k}_B \cdot \boldsymbol{R}_p} . \tag{2.10}$$

We can write the total source field as

$$u_s(r,\theta) = -\frac{i}{4}\sum_p e^{i\boldsymbol{k}_B \cdot \boldsymbol{R}_p} H_0^{(1)}(k|\boldsymbol{r} - \boldsymbol{r}_0 - \boldsymbol{R}_p|)$$
$$= -\frac{i}{4}H_0^{(1)}(k|\boldsymbol{r} - \boldsymbol{r}_0|) - \frac{i}{4}\sum_{p \neq \{0,0\}} e^{i\boldsymbol{k}_B \cdot \boldsymbol{R}_p} H_0^{(1)}(k|\boldsymbol{r} - \boldsymbol{r}_0 - \boldsymbol{R}_p|)$$

$$\tag{2.11}$$

We can now use Graf's addition theorem [8] in order to re-expand this field in coordinates based in the central unit cell:

$$u_s(r, \theta) = -\frac{i}{4} H_0^{(1)}(k|\boldsymbol{r} - \boldsymbol{r}_0|)$$

$$-\frac{i}{4} \sum_{p \neq \{0,0\}} e^{i\boldsymbol{k}_{\mathrm{B}} \cdot \boldsymbol{R}_p} \left(\sum_{\ell=-\infty}^{\infty} J_\ell(k|\boldsymbol{r} - \boldsymbol{r}_0|) e^{-i\ell\theta_{\boldsymbol{r}-\boldsymbol{r}_0}} H_\ell^{(1)}(kR_p) e^{i\ell\theta_p} \right)$$

$$-\frac{i}{4} H_0^{(1)}(k|\boldsymbol{r} - \boldsymbol{r}_0|) - \frac{i}{4} \sum_{\ell=-\infty}^{\infty} [S_\ell^J + i S_\ell^Y] J_\ell(k|\boldsymbol{r} - \boldsymbol{r}_0|) e^{-i\ell\theta_{\boldsymbol{r}-\boldsymbol{r}_0}} \ ,$$

$$(2.12)$$

where the coefficients S_ℓ^J are defined to be

$$S_\ell^J = \sum_{p \neq \{0,0\}} J_\ell(kR_p) e^{i\ell\theta_p} e^{i\boldsymbol{k}_{\mathrm{B}} \cdot \boldsymbol{R}_p} \tag{2.13}$$

$$(2.14)$$

Using the convenient result [9] that

$$S_\ell^J = -\delta_{\ell,0} \ , \tag{2.15}$$

it can be seen that

$$u_s(r, \theta) = \frac{1}{4} Y_0(k|\boldsymbol{r} - \boldsymbol{r}_0|) + \frac{1}{4} \sum_{\ell=-\infty}^{\infty} S_\ell^Y J_\ell(k|\boldsymbol{r} - \boldsymbol{r}_0|) e^{-i\ell\theta_{\boldsymbol{r}-\boldsymbol{r}_0}} \tag{2.16}$$

The first term in equation (2.16) comes from the presence of the source in the central unit cell; the second term arises due to the sources in all the other cells of the lattice.

We now re-expand the field about the origin. Taking into account the fact that $r < r_0$:

$$Y_0(k|\boldsymbol{r} - \boldsymbol{r}_0|) = \sum_\ell Y_\ell(kr_0) J_\ell(kr) e^{i\ell(\theta - \theta_0)} \ . \tag{2.17}$$

Also,

$$J_\ell(k|\boldsymbol{r} - \boldsymbol{r}_0|) e^{-i\ell\theta_{\boldsymbol{r}-\boldsymbol{r}_0}} = \sum_m (-1)^m J_{\ell-m}(kr_0) J_m(kr) e^{im\theta} e^{i(\ell-m)\theta_0} \ .$$

$$(2.18)$$

Therefore the source field, expanded around the origin, is:

$$u_s(r,\theta) = \frac{1}{4}\sum_m \left(Y_m(kr_0)e^{-im\theta_0}\right)J_m(kr)e^{im\theta}$$

$$+\frac{1}{4}\sum_m \left(\sum_\ell(-1)^{m+\ell}S^Y_{\ell-m}J_\ell(kr_0)e^{-i\ell\theta_0}\right)J_m(kr)e^{im\theta} \ .$$

$$(2.19)$$

The Rayleigh identity (2.9) is then

$$\sum_{m=-\infty}^\infty A_m J_m(kr)e^{im\theta} = \sum_{m=-\infty}^\infty \sum_{\ell=-\infty}^\infty B_\ell(-1)^{\ell+m}S^Y_{\ell-m}J_m(kr)e^{im\theta}$$

$$+\frac{1}{4}\sum_m \left(Y_m(kr_0)e^{-im\theta_0}\right)J_m(kr)e^{im\theta} \qquad (2.20)$$

$$+\frac{1}{4}\sum_m \left(\sum_\ell(-1)^{m+\ell}S^Y_{\ell-m}J_\ell(kr_0)e^{-i\ell\theta_0}\right)J_m(kr)e^{im\theta} \ .$$

By equating coefficients of $J_m(kr)e^{im\theta}$, we conclude that

$$A_m = \sum_\ell(-1)^{m+\ell}S^Y_{\ell-m}B_\ell \qquad (2.21)$$

$$+\frac{1}{4}Y_m(kr_0)e^{-im\theta_0} + \frac{1}{4}\sum_\ell(-1)^{m+\ell}S^Y_{\ell-m}J_\ell(kr_0)e^{-i\ell\theta_0} \ ,$$

or, by using $A_m = -M_m B_m$,

$$M_m B_m + \sum_\ell(-1)^{m+\ell}S^Y_{\ell-m}B_\ell = \qquad (2.22)$$

$$-\frac{1}{4}Y_m(kr_0)e^{-im\theta_0} - \frac{1}{4}\sum_\ell(-1)^{m+\ell}S^Y_{\ell-m}J_\ell(kr_0)e^{-i\ell\theta_0} \ .$$

We can put this linear identity into a more compact form by re-writing it as

$$M_m B_m + \sum_\ell(-1)^{m+\ell}S^Y_{\ell-m}[B_\ell + \frac{1}{4}J_\ell(kr_0)e^{i\ell\theta_0}] = -\frac{1}{4}Y_m(kr_0)e^{-im\theta_0} \ , \quad (2.23)$$

and then we define

$$\widetilde{B}_\ell = B_\ell + \frac{1}{4}J_\ell(kr_0)e^{i\ell\theta_0} \ . \qquad (2.24)$$

The linear system (2.23) can then be re-written as

$$M_m\widetilde{B}_m + \sum_\ell(-1)^{m+\ell}S^Y_{\ell-m}\widetilde{B}_m$$

$$= -\frac{1}{4}(Y_m(kr_0)e^{-im\theta_0} + M_m J_m(kr_0)e^{-im\theta_0}) \ . \qquad (2.25)$$

This is an infinite linear system which can be solved for the coefficients $\widetilde{B}_m$, from which the original coefficients A_m and B_m in the field expansion

(2.6) can be deduced. The system is not very well conditioned and solving directly for large values of the truncation order can be problematic. For the purpose of solving the system numerically we can follow [10] and define a new variable $x_m = \sqrt{M_m}\widetilde{B}_m$ and then solve for the unknown coefficients x_m. The new system is then well-behaved and the $\widetilde{B}_m$ coefficients can be immediately recovered.

The expansion of the field about the central cylinder is

$$u(r,\theta) = \sum_{m=-\infty}^{\infty} \left(A_m J_m(kr) + B_m Y_m(kr)\right) e^{im\theta} \qquad (2.26)$$

with the coefficients A_m and B_m given by the solution to the system (2.25), together with the boundary condition equation (2.7). If we require the function to be expanded about the pth cylinder then we take advantage of the quasiperiodicity of the field u and write

$$u(r',\theta') = \sum_{m=-\infty}^{\infty} \left(A_m^p J_m(kr') + B_m^p Y_m(kr')\right) e^{im\theta'} \qquad (2.27)$$

where $(r',\theta') = \boldsymbol{r} + \boldsymbol{R}_p$ are the local coordinates in the pth cell, and

$$A_m^p = A_m e^{i\boldsymbol{k}_{\text{B}}\cdot\boldsymbol{R}_p}, \quad B_m^p = B_m e^{i\boldsymbol{k}_{\text{B}}\cdot\boldsymbol{R}_p} \ . \qquad (2.28)$$

3.   THE DEFECT GREEN'S FUNCTION

The field due to the phased array of sources constructed in the previous section satisfies the differential equation

$$(\Delta + k^2)u = \sum_p \delta(\boldsymbol{r} - \boldsymbol{r}_0 - \boldsymbol{R}_p)e^{i\boldsymbol{k}_{\text{B}}\cdot\boldsymbol{R}_p} \ , \qquad (3.1)$$

when expanded about the central cylinder. It has been mentioned that this represents a quasi-periodic Green's function which also satisfies the right boundary conditions; we would now like to use $u(r,\theta)$ to construct a *defect Green's function*, which has a single source placed somewhere in the unit cell and still satisfies the appropriate boundary conditions on all the cylinders in the array.

We first denote $\langle f(r,\theta)\rangle_{\text{BZ}}$ to be the average of a function f over all values of $\boldsymbol{k}_{\text{B}}$ in the first Brillouin zone. In particular, we define a new function $g_d(r,\theta)$ as

$$g_d(r,\theta) = \langle u(r,\theta)\rangle_{\text{BZ}}$$
$$= \int_{-\pi/d}^{\pi/d}\int_{-\pi/d}^{\pi/d} u(r,\theta,k,\boldsymbol{k}_{\text{B}})d\boldsymbol{k}_{\text{B}} \ . \qquad (3.2)$$

Expanded about the central cylinder we can write this new averaged function as

$$g_d(r, \theta) = \sum_{m=-\infty}^{\infty} \left(A_m J_m(kr) + B_m Y_m(kr) \right) e^{im\theta} \tag{3.3}$$

¿From equation (2.2) the new function satisfies

$$(\Delta + k^2)g_d = \sum_p \delta(\boldsymbol{r} - \boldsymbol{r}_0 - \boldsymbol{R}_p) \left\langle e^{i\boldsymbol{k}_{\mathrm{B}} \cdot \boldsymbol{R}_p} \right\rangle_{\mathrm{BZ}}$$
$$= \delta(\boldsymbol{r} - \boldsymbol{r}_0) \tag{3.4}$$

This last step we have taken because

$$\left\langle e^{i\boldsymbol{k}_{\mathrm{B}} \cdot \boldsymbol{R}_p} \right\rangle_{\mathrm{BZ}} = \delta_{p, \{0,0\}} . \tag{3.5}$$

In addition the averaged function will still satisfy the boundary conditions required on the edge of each cylinder.

We can now identify $g_d(r, \theta)$ as a defect Green's function for the array. The expansion about the pth cylinder is

$$g_d(r', \theta') = \sum_{m=-\infty}^{\infty} \left(\langle A_m^p \rangle_{\mathrm{BZ}} J_m(kr') + \langle B_m^p \rangle_{\mathrm{BZ}} Y_m(kr') \right) e^{im\theta'} \tag{3.6}$$

where (r', θ') are again the coordinates in the local cell, and

$$\langle A_m^p \rangle_{\mathrm{BZ}} = \left\langle A_m e^{i\boldsymbol{k}_{\mathrm{B}} \cdot \boldsymbol{R}_p} \right\rangle_{\mathrm{BZ}}, \quad \langle B_m^p \rangle_{\mathrm{BZ}} = \left\langle B_m e^{i\boldsymbol{k}_{\mathrm{B}} \cdot \boldsymbol{R}_p} \right\rangle_{\mathrm{BZ}}. \tag{3.7}$$

We can also see that the boundary conditions in the pth cell are satisfied, because

$$\langle A_m^p \rangle_{\mathrm{BZ}} = \left\langle -M_m B_m e^{i\boldsymbol{k}_{\mathrm{B}} \cdot \boldsymbol{R}_p} \right\rangle_{\mathrm{BZ}}$$
$$= -M_m \langle B_m^p \rangle_{\mathrm{BZ}} . \tag{3.8}$$

This last step is possible because the boundary coefficients M_m do not depend on the Bloch vector $\boldsymbol{k}_{\mathrm{B}}$.

4.   NUMERICAL RESULTS

In Figure 2 we show the response of an array of cylinders due to a single source located at the very centre of the central cylinder. The cylinders each possess a radius of $r_c = 0.374$ and a refractive index of 3.0. The source radiates into the TM mode, at a frequency of $kd/\pi = 1.7931$. This is outside the band gap, which extends in this case between 1.548 and 1.708, as can be seen in Figure 2(b).

(a)

(b)
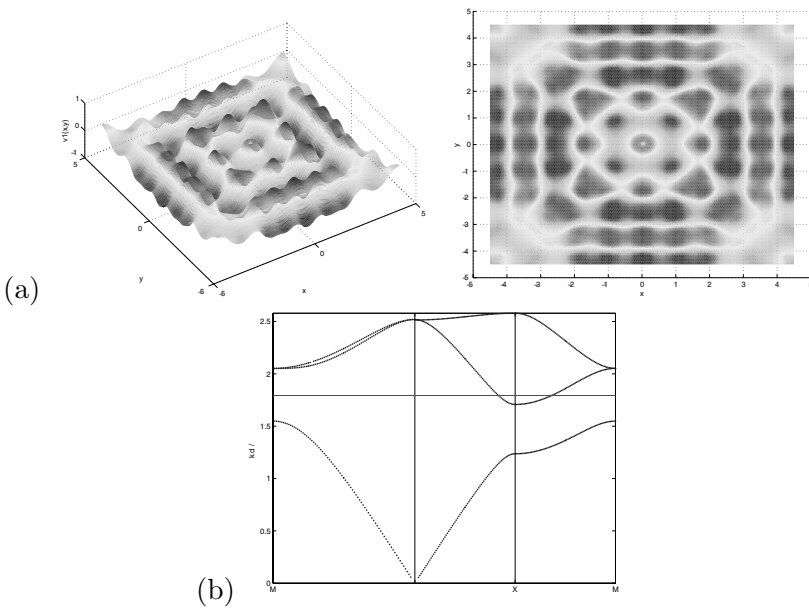
Figure 2   (a) Plot of the response field to a source located in the middle of the central inclusion, outside band-gap. (b) The dispersion relation for the material, showing the frequency of the source.

In Figure 3 we can see the response if the frequency of the source is shifted so that it lies just within the first band-gap, at a frequency of $kd/\pi = 1.5862$. It can be seen that the fields are strongly localized around the central source; this can be attributed to the fact that the waves are not permitted to propagate outwards due to the presence of the band-gap.

Acknowledgments

References

[1] J. Dowling, H. Everitt, and E. Yablonovitch, 2002. Photonic & Acoustic Band-Gap Bibliography (http://home.earthlink.net/j̃pdowling).

[2] J. D. Joannopoulos, R. D. Meade, and J. N. Winn. *Photonic Crystals: Molding the Flow of Light.* Princeton University, New Jersey, 1995.

[3] M. Agio and C.M. Soukoulis. Ministop bands in single-defect photonic crystal waveguides. *Phys. Rev. E*, 64:056603:1–056603:4, 2001.

190

(a)

(b)
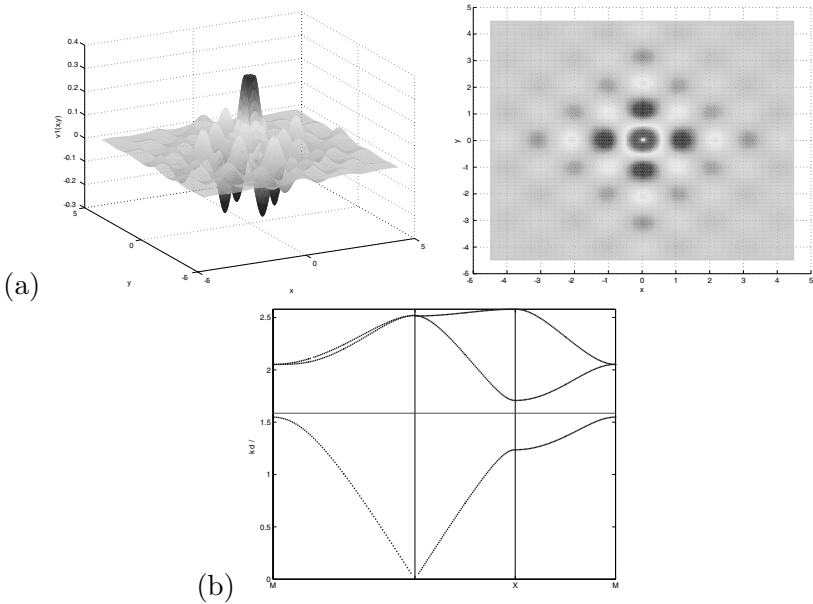
Figure 3   (a) Plot of the response field to a source located in the middle of the central inclusion, with frequency within the band-gap. (b) Dispersion relation for the material, showing the frequency of the point source.

[4] D. Cassagne, A. Barra, and C. Jouanin. Defects and diffraction in photonic crystals. *Superlattices and microstructures*, 25:343–346, 1999.

[5] S. S. M. Cheng, L.M. Li, C.T. Chan, and Z.Q. Zhang. Defect and transmission properties of two-dimensional quasiperiodic photonic band-gap sytems. *Phys. Rev. B*, 59:4091–4099, 1999.

[6] A. Figotin and V. Goren. Resolvent method for computation of localized defect modes of h-polarization in two-dimensional photonic crystals. *Phys. Rev. E*, 64:056623:1–056623:16, 2001.

[7] R. C. McPhedran, N. A. Nicorovici, L. C. Botten, and Ke-Da Bao. *Green's function, lattice sum and Rayleigh's identity for a dynamic scattering problem*, volume 96 of *IMA Volumes in Mathematics and its Applications*, pages 155–186. Springer-Verlag, New York, 1997.

[8] M. Abramowitz and I. A. Stegun, editors. *Handbook of Mathematical Functions*, pages 355–433. Dover, New York, 1972.

[9] R. C. McPhedran and D. H. Dawes. Lattice sums for an electromagnetic scattering problem. *J. Electromagn. Waves Appl.*, 6:1327–1340, 1992.

[10] V.V. V.V. Zalipaev, N.A. Movchan, C.G. Poulton, and R.C. McPhedran. Elastic waves and homogenization in oblique periodic structures. *Proc. Roy. Soc. A*, 458:1887–1912, 2002.

BOUNDARY ALGEBRAIC EQUATIONS FOR LATTICE PROBLEMS

P.G. Martinsson[1], G.J. Rodin[2]

[1] *Department of Mathematics, Yale University, 10 Hillhouse Ave, New Haven, CT 06511, USA*

per-gunnar.martinsson@yale.edu

[2] *Texas Institute for Computational and Applied Mathematics, The University of Texas at Austin, Austin TX 78712, USA*

gjr@ices.utexas.edu

Abstract Boundary algebraic equations corresponding to Dirichlet boundary-value problems on lattices are introduced. These equations are based on the lattice Green's function, from which discrete single- and double-layer potentials are derived. Structurally, the boundary algebraic equations are similar to the boundary integral equations of classical potential theory. Numerical experiments indicate that boundary algebraic equations possess excellent spectral properties.

1. INTRODUCTION

In this paper, we present a new method for solving conduction problems defined on periodic lattices of finite extent. Conceptually, the new method is similar to the boundary integral equation methods of classical potential theory (Mikhlin, 1957). In particular, in the new method, the discrete boundary-value problems defined on lattices are re-formulated in terms of equivalent boundary algebraic (as opposed to integral) equations that involve lattice Green's functions as the kernels. As a result one replaces sparse algebraic problems defined on the entire domain with dense algebraic problems defined on the domain boundary only. This replacement is particularly useful for very large problems because (i) the dense algebraic problems involve less unknowns, (ii) they can be solved using

$\mathcal{O}(N)$ summation methods, and (iii) they involve much smaller condition numbers than the sparse algebraic problems defined on the entire domain.

Due to the space constraints, we restrict our attention to Dirichlet problems defined for two-dimensional structures made of square lattices. For these problems, we develop boundary equations involving the discrete single- and double-layer kernels and present several example problems which support the notion that boundary algebraic equations posses superior spectral properties. For further details, we refer to Martinsson (2002), who also provides a detailed treatment of lattice Green's functions and the corresponding $\mathcal{O}(N)$ summation methods.

The paper is organized as follows. In Section 2, we introduce the notation and define the discrete Dirichlet boundary-value problem. In Section 3, we introduce the discrete single- and double-layer kernels and construct the boundary algebraic equations for the homogeneous Dirichlet boundary-value problem. In Section 4, we generalize the boundary algebraic equations to inhomogeneous problems and irregular lattices. In Section 5, we present numerical examples that demonstrate the superior spectral properties of the boundary algebraic equations.

2.   PROBLEM STATEMENT

Consider the lattice obtained by connecting each node in $\mathbb{Z}^2$ to its four nearest neighbors by links of conductivity one. Poisson's equation for heat conduction on this lattice reads

$$[\mathfrak{A}\mathfrak{u}](m) = \mathfrak{f}(m), \qquad \forall\, m \in \mathbb{Z}^2, \tag{2.1}$$

where $\mathfrak{u}(m)$ is the unknown temperature and $\mathfrak{f}(m)$ is a prescribed heat source. The discrete Laplace operator is defined by

$$[\mathfrak{A}\mathfrak{u}](m) = 4\mathfrak{u}(m) - \mathfrak{u}(m + e_1) - \mathfrak{u}(m - e_1) - \mathfrak{u}(m + e_2) - \mathfrak{u}(m - e_2),$$

where $e_1 = [1,\, 0]$ and $e_2 = [0,\, 1]$.

Next we consider heat conduction on the finite lattice obtained by connecting the nodes in a finite subset $\Omega \subset \mathbb{Z}^2$, see Fig. 1a. The boundary of Ω is denoted by Γ and is defined as the set of points with less than four neighbors in Ω. With the introduction of the set of interior nodes $\Omega_- := \Omega \backslash \Gamma$, the discrete homogeneous Dirichlet problem reads

$$\begin{cases} [\mathfrak{A}\mathfrak{u}](m) = 0, & m \in \Omega_-, \\ \mathfrak{u}(m) = \mathfrak{g}(m), & m \in \Gamma, \end{cases} \tag{2.2}$$

where $\mathfrak{g}(m)$ are prescribed nodal temperatures.
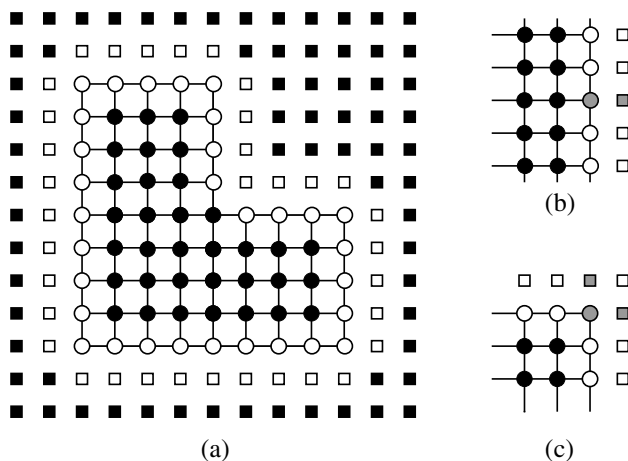
Figure 1   (a) An example of a lattice domain, $\Omega = \Gamma \cup \Omega_-$. The black circles form the interior Ω_- and the white circles form the boundary Γ. (b) Illustration of the set $\mathbb{D}_n$ (the grey square) for a boundary node n (grey circle) along a straight edge. (c) Illustration of $\mathbb{D}_n$ for a corner node.

3.   SINGLE AND DOUBLE LAYER KERNELS

Using Fourier analysis, it is possible to derive a fundamental solution of (2.1) in the form

$$\mathfrak{G}(m,n) = \frac{1}{(2\pi)^2} \int_{(-\pi,\pi)^2} \frac{e^{-\mathbf{i}(m-n)\cdot\xi} - 1}{4\sin^2 \frac{\xi_1}{2} + 4\sin^2 \frac{\xi_2}{2}} \, d\xi.$$

This function satisfies the following equation

$$[\mathfrak{A}\mathfrak{G}](m,n) = \begin{cases} 1 & \text{if } m = n \\ 0 & \text{if } m \neq n \end{cases} \qquad m,n \in \mathbb{Z}^2. \qquad (3.1)$$

When $|m-n|$ is large, the function $\mathfrak{G}$ closely approximates the fundamental solution of the Laplace operator, in fact $\mathfrak{G}(m,n) = -(2\pi)^{-1}\log|m-n| + O(|m-n|^{-2})$ as $|m-n| \to \infty$, see Duffin (1953). However, the behavior is quite different when $|m-n|$ is small, for instance, $\mathfrak{G}(m,m)$ is finite. As far as boundary algebraic equations are concerned, $\mathfrak{G}(m,n)$ is the single-layer kernel.

In order to define a discrete analogue of the double layer potential, we envision Ω to be embedded in the infinite lattice $\mathbb{Z}^2$. The double layer kernel $\mathfrak{G}_\nu(m,n)$ is then defined as the flux through the boundary Γ at the boundary node n that is induced by a point charge at node m. Letting $\mathbb{D}_n$ denote the nodes in $\mathbb{Z}^2 \setminus \Omega$ that connect to the node n (see Fig. 1b,c), we

can write

$$\mathfrak{G}_\nu(m,n) = \sum_{k\in\mathbb{D}_n} \mathfrak{G}(m,k) - \mathfrak{G}(m,n).$$

The double layer kernel could alternatively be defined by first introducing an exterior difference operator ∂_ν by setting $\partial_\nu\mathfrak{u}(n) = \sum_{k\in\mathbb{D}_n}\big(\mathfrak{u}(k) - \mathfrak{u}(n)\big)$ and then defining $\mathfrak{G}_\nu(m,n) = \partial_{\nu_n}\mathfrak{G}(m,n)$.

4. BOUNDARY ALGEBRAIC EQUATIONS

4.1. INDIRECT BOUNDARY ALGEBRAIC EQUATIONS

In order to construct an indirect boundary algebraic equation corresponding to (2.2) we make the ansatz

$$\mathfrak{u}(m) = \sum_{n\in\Gamma} \mathfrak{G}(m,n)\varphi(n).$$

Then automatically, $[\mathfrak{Au}](m) = 0$ for $m \in \Omega_-$. The boundary condition is satisfied if the sources $\varphi(n)$ are chosen so that

$$\sum_{n\in\Gamma} \mathfrak{G}(m,n)\varphi(n) = \mathfrak{g}(m) \quad \forall m \in \Gamma. \tag{4.1}$$

This formulation is characterized by a positive definite matrix (Martinsson, 2002) and therefore has a unique solution for any $\mathfrak{g}$. In contrast, the integral equation corresponding to (4.1) is of the first kind, and uniqueness of its solution is not generally guaranteed.

Alternatively, we can use the double layer kernel in the ansatz,

$$\mathfrak{u}(m) = \sum_{n\in\Gamma} \mathfrak{G}_\nu(m,n)\varphi(n),$$

which leads to the algebraic equation

$$\sum_{n\in\Gamma} \mathfrak{G}_\nu(m,n)\varphi(n) = \mathfrak{g}(m) \quad \forall m \in \Gamma. \tag{4.2}$$

Here $\varphi(n)$ represents a layer of dipoles formed by placing couples of heat sources of opposite signs on the boundary of Ω and the boundary of Ω^c (the white nodes in Fig. 1a). The spectral properties of (4.2) are similar to those of the discretization of the corresponding second kind integral equation.

4.2. DIRECT BOUNDARY ALGEBRAIC EQUATIONS

To formulate a direct boundary algebraic equation corresponding to (2.2), let us consider two thermal states of Ω. The first state involves

the nodal temperatures $\mathfrak{u}$ and boundary fluxes $\mathfrak{u}_\nu$ corresponding to the solution of (2.2); of course at this stage only the nodal temperatures on Γ are known. The second state involves the nodal temperatures and fluxes generated by imbedding Ω within an infinite lattice and placing a unit heat source at a point m on Γ. These nodal temperatures and fluxes are $\mathfrak{G}(n, m)$ and $\mathfrak{G}_\nu(m, n)$, respectively. Then by applying the reciprocity theorem to these two states we obtain:

$$\mathfrak{u}(m) + \sum_{n\in\Gamma} \mathfrak{G}_\nu(m, n)\mathfrak{u}(n) = \sum_{n\in\Gamma} \mathfrak{G}(n, m)\mathfrak{u}_\nu(n) \,.$$

By imposing the boundary condition and replacing $\mathfrak{G}(n, m)$ with $\mathfrak{G}(m, n)$, we obtain a direct boundary algebraic equation

$$\sum_{n\in\Gamma} \mathfrak{G}(m, n)\mathfrak{u}_\nu(n) = \mathfrak{g}(m) + \sum_{n\in\Gamma} \mathfrak{G}_\nu(m, n)\mathfrak{g}(n) \quad \forall m \in \Gamma \,. \tag{4.3}$$

As expected, this equation is similar to the indirect equation based on the single-layer kernel.

Remark: We defined the boundary is such a way that it does not include a vertex node at a 270° angle, such as the re-entrant corner node in Fig. 1a. If it is desired to prescribe boundary conditions at such a node, this can easily be done by including an additional unknown for each such node in the system of boundary equation. We have found that such en enrichment of the system does not significantly change the conditioning.

5.   INCLUSIONS

The methods presented in Section 4.1 can be extended to analysis of lattices with inclusions. To this end, let us consider the perturbed Dirichlet problem

$$\begin{cases} [(\mathfrak{A} - \mathfrak{A}_\mathrm{r})\mathfrak{u}](m) = 0, & m \in \Omega_-, \\ \mathfrak{u}(m) = \mathfrak{g}(m), & m \in \Gamma, \end{cases} \tag{5.1}$$

where $\mathfrak{A}_\mathrm{r}$ represents a (typically local) perturbation due to inclusions. The first step is to reformulate (5.1) as an unperturbed problem

$$\begin{cases} [\mathfrak{A}\mathfrak{u}](m) = \mathfrak{f}_\mathrm{r}, & m \in \Omega_-, \\ \mathfrak{u}(m) = \mathfrak{g}(m), & m \in \Gamma, \end{cases} \tag{5.2}$$

where $\mathfrak{f}_\mathrm{r} = \mathfrak{A}_\mathrm{r}\mathfrak{u}$ are fictitious heat sources applied to the unperturbed lattice. For concreteness, let us suppose that $\mathfrak{A}_\mathrm{r}$ represents J removed bars. The nodes of the j-th bar are denoted $k_-^{(j)}$ and $k_+^{(j)}$. Now, there exists a $\psi(j)$ (to be determined), such that the effect of removing the bar j is

identical to adding charges $-\psi(j)$ and $+\psi(j)$ at the nodes $k_-^{(j)}$ and $k_+^{(j)}$ to the unperturbed lattice. Thus

$$\mathfrak{f_r}(m) = \sum_{j=1}^{J} \psi(j) \left[\delta(m, k_+^{(j)}) - \delta(m, k_-^{(j)}) \right],$$

where δ is the Kronecker symbol. With a single layer potential on the boundary, the ansatz is now

$$\mathfrak{u}(m) = \sum_{n \in \Gamma} \mathfrak{G}(m, n) \varphi(n) + \sum_{j=1}^{J} \left[\mathfrak{G}(m, k_+^{(j)}) - \mathfrak{G}(m, k_-^{(j)}) \right] \psi(j). \qquad (5.3)$$

To determine φ and ψ we first invoke the boundary condition,

$$\mathfrak{g}(m) = \sum_{n \in \Gamma} \mathfrak{G}(m, n) \varphi(n) + \sum_{j=1}^{J} \left[\mathfrak{G}(m, k_+^{(j)}) - \mathfrak{G}(m, k_-^{(j)}) \right] \psi(j), \qquad m \in \Gamma.$$

$$(5.4)$$

Then we get J additional conditions by requiring that the flux through the removed bar i equals $\psi(i)$, which is to say that $\psi(i) = \mathfrak{u}(k_+^{(i)}) - \mathfrak{u}(k_-^{(i)})$, or

$$\psi(i) = \sum_{n \in \Gamma} \left[\mathfrak{G}(k_+^{(i)}, n) - \mathfrak{G}(k_-^{(i)}, n) \right] \varphi(n) +$$

$$\sum_{j=1}^{J} \left[\mathfrak{G}(k_+^{(i)}, k_+^{(j)}) - \mathfrak{G}(k_+^{(i)}, k_-^{(j)}) - \mathfrak{G}(k_-^{(i)}, k_+^{(j)}) + \mathfrak{G}(k_-^{(i)}, k_-^{(j)}) \right] \psi(j). \quad (5.5)$$

Combined, equations (5.4) and (5.5) uniquely determine the heat sources φ and ψ.

A double layer equation can be obtained by simply replacing $\mathfrak{G}(m, n)$ in (5.3) by the double layer kernel $\mathfrak{G}_\nu(m, n)$. An alternative technique for deriving equations that govern lattices with inclusions is to use the direct methods of Section 4.2. One will find that the sums in the reciprocity theorems will include the nodes $k_\pm^{(j)}$ and that the resulting equations are very similar to the ones derived above.

6. CONDITIONING OF THE BOUNDARY EQUATIONS

In this section we will present several examples that indicate that the conditioning of the boundary algebraic equations is superior to that of the difference equation (2.1). Furthermore, as far as conditioning is concerned, we show that the boundary algebraic equations are at least as good as
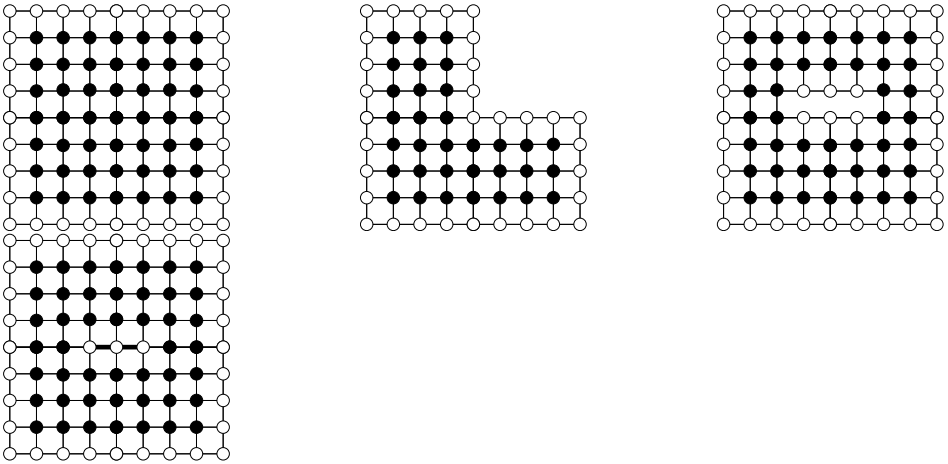
Figure 2   The geometries we used to estimate the condition numbers. Reading from left to right, first row first, we label them: "the square", "the L-shape", "the slit" and "the shortcut". The long side of the square has $2N + 1$ nodes.

discretized integral equations. To this end we consider Dirichlet problems on the four domains shown in Figure 2, namely:

- A square with $(2N + 1) \times (2N + 1)$ nodes.

- A square with one quadrant removed, *i.e.* an L-shaped domain.

- A square with a horizontal slit extending along the middle third of the middle row.

- A square with a horizontal shortcut extending along the middle third of the middle row.

We let K, K_S and K_D denote the matrices associated with the original difference equation, the single formulation, and the double layer formulation, respectively. For each geometry, we computed the condition numbers for these matrices for N in the range between 2 and 50. Results of the computation are summarized in Table 1.

The numbers in the table lend support to our belief that the conditioning of boundary algebraic equations is superior to that of the original difference equations. Further, the condition numbers for the square are consistent with the condition numbers for discretized integral equations, see Atkinson (1997). Remarkably, the condition numbers for the L-shaped domain are essentially the same as for the square. The results for the last two problems indicate that the double-layer formulation possess good spectral properties even for more challenging problems in which periodicity is locally violated.

	Square	L-shape	Slit	Shortcut
cond(K)	$1.6N^2$	$0.83N^2$	$1.6N^2$	$0.28N^3$
cond(K_{S})	$40N$	$40N$	$4N^2$	$4.2N^2$
cond(K_{D})	7.0	7.3	$0.63N$	$0.68N$

Table 1   Asymptotic estimates of the condition numbers for different boundary equations and different geometries.

However, at this stage our understanding of the spectral properties for such problems is incomplete.

In passing, we note that although the condition numbers for the single layer potential perform somewhat poorly, the estimates in the tables can be improved by a factor of 10 using Wieland's deflation technique.

References

[1] K. E. Atkinson. *The numerical solution of integral equations of the second kind.* Cambridge University Press, Cambridge, 1997.

[2] R. J. Duffin. Discrete potential theory. *Duke Mathematical Journal*, 20:233–251, 1953.

[3] P. G. Martinsson. *Fast multiscale methods for lattice equations.* Ph.D. thesis, The University of Texas at Austin, Computational and Applied Mathematics, 2002.

[4] S. G. Mikhlin. *Integral equations and their applications to certain problems in mechanics, mathematical physics and technology.* Pergamon Press, New York, 1957. Translated from the Russian by A. H. Armstrong.

Chapter 4
Mathematical models
of cracks

DYNAMIC PERTURBATION OF
A PROPAGATING CRACK:
IMPLICATIONS FOR CRACK STABILITY

John R. Willis

Department of Applied Mathematics and Theoretical Physics,
University of Cambridge Cambridge, U.K.

J.R.Willis@damtp.cam.ac.uk

Abstract   A general perturbation solution for the stress-intensity factors at the edge
of a propagating crack whose surface is slightly undulating and whose edge
is not quite straight is briefly reviewed, in the case that the medium through
which the crack propagates is viscoelastic. This solution (which was gen-
erated in collaboration with A B Movchan) has already been exploited to
demonstrate the persistence of "crack front waves" in the high-frequency
limit, as well as to find the lowest-order corrections (which induce disper-
sion and attenuation) when the frequency is large but not infinite. So far,
crack front waves have been studied, allowing only in-plane perturbation
of the crack edge. Here, the corresponding formulae are summarised for a
general three-dimensional perturbation, together with the forms to which
they reduce in the high-frequency limit. Such formulae are expected to
form the basis for an explanation of "Wallner lines". At finite frequency,
they provide a base for conducting a general study of the linear stability
of a rectilinear propagating crack. Such a study has been completed in the
special case of two-dimensional perturbation (plane strain), reported by O
Obrezanova in these Proceedings.

1.   INTRODUCTION

The problem to be studied concerns a crack whose configuration at time
t is

$$S_\varepsilon(t) = \{\mathbf{x} : -\infty < x_1 < Vt + \varepsilon\varphi(x_2, t),$$
$$-\infty < x_2 < \infty, x_3 = \varepsilon\psi(x_1, x_2)\}. \qquad (1.1)$$

The functions φ and ψ are smooth and bounded and $0 \leq \varepsilon \ll 1$; the case $\varepsilon = 0$ defines the configuration of the crack without perturbation. The medium is loaded so that stress $\boldsymbol{\sigma}^{\mathrm{nc}}$ and displacement $\mathbf{u}^{\mathrm{nc}}$ would be generated in the absence of the crack. The crack induces *additional* fields $\boldsymbol{\sigma}$, $\mathbf{u}$. The medium through which the crack propagates is linearly viscoelastic (including elastic as a special case).

Having found the solution for the perturbed crack, the objective is then to develop equations that define the perturbation functions $\varphi(x_2, t)$ and $\psi(x_1, x_2)$, given that the crack propagates in such a way as to respect the Griffith energy balance, and also a condition of "local symmetry" (made more precise later). When specialised to Mode I loading and restricted to a perturbation in the plane $x_3 = 0$, so that $\psi(x_1, x_2) = 0$, these equations deliver the "crack front wave", first found during a computation by Morrissey and Rice [1] and confirmed analytically by Ramanathan and Fisher [2], using formulae for the perturbed crack which were originally derived by Willis and Movchan [3]. Subsequently, the more general development of Willis and Movchan [4] extended the analysis to propagation through a viscoelastic medium and, in the process, demonstrated that the solution of Ramanathan and Fisher was strictly valid only asymptotically, as frequency tends to infinity. The solution of Ramanathan and Fisher is valid (asymptotically) even when the medium is viscoelastic; this was demonstrated in [4] and, in addition, the lowest-order "correction" when the frequency is large but finite was found, for a general isotropic viscoelastic medium.

Here, a similar path is followed for the case of an out-of-plane perturbation ($\varphi(x_2, t) = 0$, $\psi(x_1, x_2) \neq 0$). The general formulae for the perturbation are summarised and then simplified in the high-frequency limit. It appears that, in this limit at least, the dispersion relation has no root that is exactly real, but there is a root with small imaginary part if the crack is running sufficiently fast. Conceivably, the inclusion of nonlinear terms and allowance for linear dispersion might give rise to a persistent nonlinear wave, as observed experimentally by Sharon, Cohen and Fineberg [5]. At this stage, however, this is no more than speculation. A more thorough study is planned.

The basic perturbation formulae, specialised to plane strain (no dependence on the coordinate x_2), have been employed by Obrezanova, Movchan and Willis [6] in a general study of the stability of rectilinear propagation; a summary of this work appears in [7] in this volume.

2.   FUNDAMENTAL IDENTITY

In this section an identity which is fundamental to the subsequent development is derived, in a form that applies for a general viscoelastic medium.

Note first the relation

$$\mathbf{u} = -\mathbf{G} * \boldsymbol{\sigma}, \tag{2.1}$$

where $\mathbf{u}$ and $\boldsymbol{\sigma}$ denote the values of the displacement vector (with components u_i) and the traction vector (with components σ_{i3}) on the surface $x_3 = 0$ of the half-space $x_3 > 0$. $\mathbf{G}$ is the Green's function that relates them.

The symbol $*$ denotes convolution over x_1, x_2 and t. It is assumed that all waves emanate from the surface $x_3 = 0$. A similar identity applies to the half-space $x_3 < 0$: replace $\mathbf{G}$ by minus its transpose, $-\mathbf{G}^T$.

Now, write three column vectors like $\mathbf{u}$ side by side to form a matrix $\mathbf{U}(+0)$, and let $\boldsymbol{\Sigma}(+0)$ represent the matrix formed from the three corresponding vectors $\boldsymbol{\sigma}$. Then

$$\mathbf{U}(+0) = -\mathbf{G} * \boldsymbol{\Sigma}(+0). \tag{2.2}$$

The argument $(+0)$ signifies values on the boundary of the upper half-space.

Next, apply similar reasoning to the identity for the lower half-space $x_3 < 0$, to get

$$\mathbf{U}(-0) = \mathbf{G}^T * \boldsymbol{\Sigma}(-0). \tag{2.3}$$

Now note that

$$\begin{aligned}
\{\mathbf{U}(+0)\}^T * \boldsymbol{\sigma}(-0) &= -\{\boldsymbol{\Sigma}(+0)\}^T * \mathbf{G}^T * \boldsymbol{\sigma}(-0) \\
&= -\{\boldsymbol{\Sigma}(+0)\}^T * \mathbf{u}(-0), \tag{2.4}
\end{aligned}$$

$$\begin{aligned}
\{\mathbf{U}(-0)\}^T * \boldsymbol{\sigma}(+0) &= \{\boldsymbol{\Sigma}(-0)\}^T * \mathbf{G}^T * \boldsymbol{\sigma}(+0) \\
&= -\{\boldsymbol{\Sigma}(-0)\}^T * \mathbf{u}(+0). \tag{2.5}
\end{aligned}$$

Subtracting the second line from the first and rearranging gives the identity

$$[\mathbf{U}]^T * \langle \boldsymbol{\sigma} \rangle - \langle \mathbf{U} \rangle^T * [\boldsymbol{\sigma}] = -[\boldsymbol{\Sigma}]^T * \langle \mathbf{u} \rangle + \langle \boldsymbol{\Sigma} \rangle^T * [\mathbf{u}], \tag{2.6}$$

where $\langle f \rangle = \frac{1}{2}(f(+0) + f(-0))$ and $[f] = f(+0) - f(-0)$.

It is helpful to employ coordinates that move with the crack: replace x_1 by $X = x_1 - Vt$. The operation of convolution survives, with functions regarded as functions of X, x_2, t and the convolutions taken over these new variables.

Now revert to the crack problem. For the unperturbed crack problem,

$$[\boldsymbol{\sigma}] \equiv 0, \quad [\mathbf{u}] = 0 \text{ when } X > 0, \quad \boldsymbol{\sigma} \equiv \langle \boldsymbol{\sigma} \rangle = -\boldsymbol{\sigma}^{\text{nc}} \text{ when } X < 0. \tag{2.7}$$

Interpret Eq. (2.6) relative to the moving frame, and perform factorizations of the Green's function so that $\mathbf{U}$ and $\boldsymbol{\Sigma}$ display the related properties

$$[\boldsymbol{\Sigma}] \equiv 0, \quad [\mathbf{U}] = 0 \text{ when } X < 0, \quad \boldsymbol{\Sigma} \equiv \langle \boldsymbol{\Sigma} \rangle = 0 \text{ when } X > 0. \tag{2.8}$$

This is fairly straightforward because the conditions (2.8) imply

$$[\mathbf{U}] = -(\mathbf{G} + \mathbf{G}^T) * \langle \boldsymbol{\Sigma} \rangle, \quad \langle \mathbf{U} \rangle = -\tfrac{1}{2}(\mathbf{G} - \mathbf{G}^T) * \langle \boldsymbol{\Sigma} \rangle. \tag{2.9}$$

The first of these relations defines a Wiener–Hopf problem; the second then gives $\langle \mathbf{U} \rangle$ directly. The Wiener–Hopf problem uncouples into two sub-problems. One, associated with the opening mode I of the crack, is a scalar problem. It was solved in the case of elasticity in [3], and for a viscoelastic medium in [9]. The remaining problem involves modes II and III, coupled. It was solved in the case of elasticity in [8]; the method is equally applicable to the viscoelastic problem.

The field $[\mathbf{U}]$ has a singularity proportional to $X^{-1/2}H(X)\delta(x_2)\delta(t)$ as $X \to 0$. Choose the constant of proportionality to be $(2/\pi)^{1/2}\mathbf{I}$. Then, call $[\mathbf{U}]$ the *dynamic weight function* for the crack problem. With this choice, letting $X \to +0$ in the identity (2.6) generates

$$\mathbf{K} = \lim_{X \to +0}[\mathbf{U}]^T * \boldsymbol{\sigma}^{\mathrm{nc}}, \tag{2.10}$$

where $\mathbf{K}$ denotes the vector of stress-intensity factors $(K_{II}, K_{III}, K_I)^T$. The right side of this equation involves the known (effective) loading on the crack faces. For a more general problem, with different loading applied to each face, a convolution with $\langle \mathbf{U} \rangle$ would also participate. The function $\langle \mathbf{U} \rangle$ thus represents a dynamical version of Bueckner's non-symmetric weight function [10].

3.   THE PERTURBATION SOLUTION

The asymptotic solution (as $\varepsilon \to 0$) will be non-uniform, on account of the singularity at the crack tip, whose position is perturbed. The problem can be approached via matched asymptotic expansions: away from the crack (i.e. for any fixed $x_3 \neq 0$ and also $X = x_1 - Vt \neq 0$), the additional stress field will have expansion

$$\sigma_{ij} \sim \sigma_{ij}^0 + \varepsilon\sigma_{ij}^1. \tag{3.1}$$

The field σ_{ij}^0 is the field generated by the unperturbed crack. The perturbation σ_{ij}^1 has to be such that

$$\sigma_{ij}n_j + \sigma_{ij}^{\mathrm{nc}}n_j = 0 \text{ on the crack faces} \tag{3.2}$$

is satisfied, correct to order ε. In addition, σ_{ij}^1 may have a singularity of order $(X^2 + x_3^2)^{-3/4}$, since the shifted crack edge appears as a singularity in the "outer" region.

Close to the crack edge ($(X^2 + x_3^2)^{1/2} = O(\varepsilon)$), introduce a new coordinate system:

$$\mathbf{x}' = \begin{pmatrix} x_1' \\ x_2' \\ x_3' \end{pmatrix} = \begin{pmatrix} 1 & -\varepsilon\varphi_{,2} & \varepsilon\psi_{,1} \\ \varepsilon\varphi_{,2} & 1 & \varepsilon\psi_{,2} \\ -\varepsilon\psi_{,1} & -\varepsilon\psi_{,2} & 1 \end{pmatrix} \begin{pmatrix} X - \varepsilon\varphi \\ x_2 \\ x_3 - \varepsilon\psi \end{pmatrix} \quad (3.3)$$

Relative to this frame, the stresses (σ_{ij}') have an asymptotic form so that

$$\sigma_{i3}'(x_1, 0, 0) \sim (K_i^0 + \varepsilon K_i^1)/(2\pi x_1')^{1/2} + (P_i^0 + \varepsilon P_i^1) + (A_i^0 + \varepsilon A_i^1)(x_1')^{1/2}. \quad (3.4)$$

Formally, now, apply the identity (2.6), using the weight function fields discussed above, and take $\boldsymbol{\sigma}$ as the *outer expansion* (3.1). Mathematically, it is possible to consider the relation in the limit as $X \to 0$. Then, the convolution of the stress ahead of the crack with $[\mathbf{U}]$ involves the *inner limit* of the outer expansion. This can be identified with the *outer limit* (to order ε) of the inner expansion, which contains the parameters introduced in Eq. (3.4). The relation that emerges gives an explicit representation for the stress-intensity factor perturbation $\mathbf{K}^1$. It is necessary to expand the weight function $[\mathbf{U}]$ as far as its second term. To this order,

$$[\mathbf{U}](X, x_2, t) \sim \left(\frac{2}{\pi}\right)^{1/2} \mathbf{I} X^{-1/2} H(X)\delta(x_2)\delta(t) + X^{1/2} H(X)\mathbf{Q}(x_2, t). \quad (3.5)$$

The convolution of $X^{-1/2}$ with the term proportional to $X^{-3/2}$ in the outer expansion makes no contribution because it is proportional to $\delta(X)$, which is zero for any $X > 0$. However, the convolution of $X^{1/2}\mathbf{Q}$ with this term does make a finite contribution, involving the unperturbed stress intensity factor $\mathbf{K}^0$. The term proportional to $\mathbf{A}^0$ in (3.4) contributes, after expansion, a term of order $X^{-1/2}$ which participates in the final expression. In the case of elasticity, the function $\mathbf{Q}$ is a homogeneous generalized function (or distribution) of degree -3; in the case of viscoelasticity it is not homogeneous, but its high-frequency component reduces to the corresponding elastic form. The function $[\mathbf{U}]$ has no simple form, but its Fourier transform can be found explicitly; similarly, the Fourier transform of the term $\mathbf{Q}$ can be found immediately from the large-argument expansion of the Fourier transform of $[\mathbf{U}]$.

Now here is the formula, taken from [11], as corrected in [12][1]:

---

[1]Strictly speaking, these formulae have been derived only for the case of elasticity; their modification for viscoelasticity would require allowance for the frequency-dependence of the speeds a and b of dilatational and shear waves. Only the case of Mode I loading has so far received explicit treatment in the case of viscoelasticity [9].

$$\mathbf{K} \sim \mathbf{K}^0 + \varepsilon \mathbf{K}^1, \tag{3.6}$$

where

$$
\begin{aligned}
K_{II}^1 &= -Q_{11} * \psi \Theta_{13} K_I^0 - \psi_{,1} \omega_{13} K_I^0 - \psi \left(\Sigma_{11} + \frac{V^2}{2b^2} \Sigma_{12} \right) A_3^0 \\
&\quad + [U]_{11} * \langle P_1^{(1)} \rangle + [U]_{21} * \langle P_2^{(1)} \rangle - \langle U \rangle_{31} * [P_3^{(1)}], \tag{3.7}
\end{aligned}
$$

$$
\begin{aligned}
K_{III}^1 &= -Q_{12} * \psi \Theta_{13} K_I^0 - \psi_{,2} \omega_{23} K_I^0 + [U]_{12} * \langle P_1^{(1)} \rangle \\
&\quad + [U]_{12} * \langle P_1^{(1)} \rangle + [U]_{22} * \langle P_2^{(1)} \rangle - \langle U \rangle_{32} * [P_3^{(1)}], \tag{3.8}
\end{aligned}
$$

$$
K_I^1 = Q_{33} * \varphi K_I^0 + \left(\frac{\pi}{2} \right)^{1/2} \varphi A_3^0 + [U]_{13} * \langle P_1^{(1)} \rangle + [U]_{23} * \langle P_2^{(1)} \rangle
\tag{3.9}
$$

The functions that appear in these equations are as follows:

$$
\begin{aligned}
\Theta_{13} &= \Sigma_{11} + \frac{V^2}{2b^2} \Sigma_{12}, \\
\omega_{13} &= \frac{\alpha - \beta}{R(V)} (1 + \beta^2)(\alpha + 2\beta) - 2, \\
\omega_{23} &= \frac{2\nu}{R(V)} (1 + \beta^2)(\alpha^2 - \beta^2) - 1, \\
\Sigma_{11} &= \frac{4\alpha\beta - (1 + 2\alpha^2 - \beta^2)(1 + \beta^2)}{R(V)}, \\
\Sigma_{12} &= \frac{-2(1 + \beta^2 - 2\alpha\beta)}{R(V)}, \\
\alpha^2 &= 1 - V^2/a^2, \quad \beta^2 = 1 - V^2/b^2, \\
R(V) &= 4\alpha\beta - (1 + \beta^2)^2, \\
\langle P_1^{(1)} \rangle &= -\psi \{ \sigma_{11,1}^0 + \sigma_{11,1}^{\mathrm{nc}} - \rho V^2 (u_{1,11}^0 + u_{1,11}^{\mathrm{nc}}) \} - \psi_{,1}(\sigma_{11}^0 + \sigma_{11}^{\mathrm{nc}}), \\
\langle P_2^{(1)} \rangle &= -\psi_{,2}(\sigma_{22}^0 + \sigma_{22}^{\mathrm{nc}}), \\
[P_3^{(1)}] &= \psi \rho V^2 (u_{3,11}^0 + u_{3,11}^{\mathrm{nc}}). \tag{3.10}
\end{aligned}
$$

Here, a, b denote, respectively, the speeds of longitudinal and shear waves

Now consider the preceding equations, Fourier transformed (equivalently, take sinusoidal perturbations):

$$\overline{K}^1_{II} = -\overline{Q}_{11}\overline{\psi}\Theta_{13}K^0_I + \mathrm{i}k_1\overline{\psi}\omega_{13}K^0_I - \overline{\psi}\left(\Sigma_{11} + \frac{V^2}{2b^2}\Sigma_{12}\right)A^0_3$$

$$+ \overline{[U]_{11} * \langle P^{(1)}_1\rangle} + \overline{[U]_{21} * \langle P^{(1)}_2\rangle} - \overline{\langle U\rangle_{31} * [P^{(1)}_3]}, \quad (3.11)$$

$$\overline{K}^1_{III} = -\overline{Q}_{12}\overline{\psi}\Theta_{13}K^0_I + \mathrm{i}k_2\overline{\psi}\omega_{23}K^0_I$$

$$+ \overline{[U]_{12} * \langle P^{(1)}_1\rangle} + \overline{[U]_{22} * \langle P^{(1)}_2\rangle} - \overline{\langle U\rangle_{32} * [P^{(1)}_3]}, \quad (3.12)$$

$$\overline{K}^1_I = \overline{Q}_{33}\overline{\varphi}K^0_I + \left(\frac{\pi}{2}\right)^{1/2}\overline{\varphi}A^0_3 + \overline{[U]_{13} * \langle P^{(1)}_1\rangle} + \overline{[U]_{23} * \langle P^{(1)}_2\rangle}$$

$$(3.13)$$

The transforms of convolutions that appear in the above equations can be written more explicitly; a generic term has the form

$$\overline{U * P} = \int_{-\infty}^0 \tilde{U}(-X', k_2, k_1 V)P(X')\mathrm{e}^{-\mathrm{i}k_1 X'}\,\mathrm{d}X', \quad (3.14)$$

where $\tilde{(.)}$ denotes the Fourier transform with respect to X, x_2 and t.

4.   CRACK FRONT WAVES

So far, crack front waves have only been studied in the case of pure Mode I loading, and for in-plane perturbation, so that $\psi = 0$. The only non-zero stress intensity factor is K_I, and the perturbation formula discussed above reduces to

$$K^1_I = Q * \varphi K^0_I + \left(\frac{\pi}{2}\right)^{1/2}\varphi A^0_I, \quad (4.1)$$

where $Q = Q_{33}$ and A^0_I has been written for A^0_3, since it is relevant to Mode I.

Now apply the Griffith energy balance, that the energy flux $\mathcal{G}$ into the crack edge is a constant, $\mathcal{G}_c$:

$$\mathcal{G} \equiv f(v)K^2_I = \mathcal{G}_c. \quad (4.2)$$

Here, v is local crack speed and $f(v)$ is a known function (e.g., [13]):

$$f(v) = \frac{v^2\alpha(v)}{2\rho b^4_0\{4\alpha(v)\beta(v) - [1 + \beta^2(v)]^2\}}. \quad (4.3)$$

This applies even in the case of viscoelasticity, since the strain-rates are large close to the crack edge so that the material responds as though it is elastic, with wave speeds a_0, b_0 corresponding to high-frequency response.

Expanding the Griffith energy balance (4.2) to order ε, using the relation (4.1) and $v \sim V + \varepsilon\dot{\varphi}$, yields the requirement that

$$2Q * \varphi + \frac{f'(V)}{f(V)}\dot{\varphi} + 2m\varphi = 0, \tag{4.4}$$

where $m = (\pi/2)^{1/2}A_I^0/K_I^0$. Now seek a solution for which $\varphi = \overline{\varphi}e^{-i(\omega t + kx_2)}$. A non-zero solution is possible only if the dispersion relation

$$2\overline{Q}(\omega, k) - i\omega\frac{f'(V)}{f(V)} + 2m = 0 \tag{4.5}$$

is satisfied.

In the case of elasticity, $\overline{Q}$ is a homogeneous function of degree 1 in (ω, k): call it $\overline{Q}_0(\omega, k)$. At high frequency and large wavenumber, therefore,

$$2\overline{Q}_0(\omega, k) - i\omega\frac{f'(V)}{f(V)} = 0. \tag{4.6}$$

This equation was solved for the (real) wave speed ω/k by Ramanathan and Fisher [2].

Exactly the same relation applies, at high frequency and wavenumber, in the case of viscoelasticity [4]: $\overline{Q}$ has the asymptotic form

$$\overline{Q} \sim \overline{Q}_0 + \frac{1}{\omega\tau}\overline{Q}_1, \tag{4.7}$$

where τ is a characteristic relaxation time and $\overline{Q}_1$ is also homogeneous of degree 1. Equation (4.6) has a real solution, $\omega/k = u_0$, for all V up to the speed of Rayleigh waves. The solution of Eq. (4.7) can be solved iteratively [4], to give a correction of order $1/\omega\tau$.

5. STABILITY AGAINST OUT-OF-PLANE PERTURBATION

Stability can be studied, once a fracture criterion is identified. There is not as yet general agreement as to the form that this should take, for general three-dimensional motion of the crack. It is known that cracks do not like Mode II *and* they do not like Mode III. If, however, an undulation occurs, the crack *must* have tolerated some amount of K_{III}. The proposition that the crack propagates so as to maintain $K_{II} = 0$ together with the Griffith energy balance has recently received theoretical support, on the basis of a version of Hamilton's principle [14]. Adopting this criterion then, to lowest order, ψ must satisfy $K_{II}^1 = 0$, where K_{II}^1 is given by (3.7) and its transform is given by (3.11). The relation simplifies (analogous to crack front waves)

if it is assumed that $\omega \equiv k_1 V$ and k_2 are large. The leading-order term in (3.11) gives

$$\overline{K}^1_{II} = \{-\overline{Q}_{11}\Theta_{13} + \mathrm{i}(\omega/V)\omega_{13}\}K^0_I\overline{\psi} = 0. \tag{5.1}$$

This relation is homogeneous of degree 1 in ω and k_2, and so is non-dispersive. In contrast to the dispersion relation (4.6), the relation (5.1) is not exactly satisfied for any real value of ω/k_2, but for crack speeds V greater than a critical value V_c, there is a value of ω/k_2 with small, negative, imaginary part that satisfies (5.1). The critical speed V_c depends weakly on Poisson's ratio of the material, and is close to 0.6 of the Rayleigh wave speed. This corresponds to a "corrugation wave" which suffers slow attenuation as it propagates, consistent with an as-yet unpublished result of Ramanathan and Fisher, described qualitatively in [15]. It is claimed in [15] that such a wave exists for all crack speeds but the evidence for this is apparently not conclusive[2]. A more complete study, allowing for large but finite frequency, is in progress.

References

[1] Morrissey, J W and Rice, J R (1998) *Crack front waves*, J. Mech. Phys. Solids **46**, 467–487.

[2] Ramanathan, S and Fisher, D S (1997) *Dynamics and instabilities of planar tensile cracks in heterogeneous media*, Phy. Rev. Lett. **79**, 877–880.

[3] Willis, J R and Movchan, A B (1995) *Dynamic weight functions for a moving crack. I. Mode I loading*, J. Mech. Phys. Solids **43**, 319–341.

[4] Willis, J R and Movchan, A B (2002) *Theory of crack front waves*, Diffraction and Scattering in Fluid Mechanics and Elasticity, edited by I. D. Abrahams, P. A. Martin and M. J. Simons, pp. 235-250. Kluwer, Dordrecht.

[5] Sharon, E and Cohen, G and Fineberg, J (2002) *Propagating solitary waves along a rapidly moving crack front*, Nature **410**, 68–71.

[6] Obrezanova, O and Movchan, A B and Willis, J R (2002) *Dynamic stability of a propagating crack*, J. Mech. Phys. Solids, **50**, 2637–2668.

[7] Obrezanova, O and Movchan, A B and Willis, J R (2003) *Dynamic crack stability*, Asymptotics, Singularities and Homogenization in Problems of Mechanics, edited by A. B. Movchan, Kluwer, Dordrecht, 211-220.

[8] Movchan, A B and Willis, J R (1995) *Dynamic weight functions for a moving crack. II. Shear loading*, J. Mech. Phys. Solids **43**, 1369–1383.

---

[2]Personal communication from S. Ramanathan.

[9] Woolfries, S and Movchan, A B and Willis, J R (2002) *Perturbation of a dynamic planar crack moving in a model viscoelastic solid*, Int. J. Solids Struct., accepted for publication.

[10] Bueckner, H F (1987) *Weight functions and fundamental solutions for the penny shaped and half-plane crack in three space*, Int. J. Solids Struct. **23**, 57–93.

[11] Willis, J R and Movchan, A B (1997) *Three-dimensional dynamic perturbation of a propagating crack*, J. Mech. Phys. Solids **45**, 591–610.

[12] Willis, J R (1999) *Asymptotic analysis in fracture: An update*, Int. J. Fract. **100**, 85–103.

[13] Freund, L B (1990) *Dynamic Fracture Mechanics.* Cambridge: Cambridge University Press.

[14] Oleaga, G (2003) *On the dynamics of cracks in three dimensions*, J. Mech. Phys. Solids, accepted for publication.

[15] Bouchaud, E and Bouchaud, J P and Fisher, D S and Ramanathan, S and Rice, J R (2002) *Can crack front waves explain the roughness of cracks?* J. Mech. Phys. Solids **50**, 1703–1725.

DYNAMIC CRACK STABILITY

Olga Obrezanova[1], Alexander B. Movchan[2] and John R. Willis[1]

[1] *Department of Applied Mathematics and Theoretical Physics,*
University of Cambridge Cambridge, U.K.
O.Obrezanova@damtp.cam.ac.uk, J.R.Willis@damtp.cam.ac.uk
[2] *Department of Mathematical Sciences,*
University of Liverpool, Liverpool, U.K.
abm@maths.liv.ac.uk

Keywords: Dynamic stress intensity factors, asymptotic analysis, crack stability.

Abstract   This work is a study of the stability of a straight dynamically propagating crack to small perturbation of its path. Obrezanova et al. in [1] investigated stability of a crack propagating through an infinite elastic medium loaded by remote body forces following the crack as it advances. Here we extend the study to the case when the crack faces are subjected to given tractions in addition to a remote loading. We present formulae for the general case and consider a particular example when the crack is loaded by point force tractions on the crack faces.

INTRODUCTION

The work presented here is an extension to the case of surface loading of the study [1] of stability of the crack loaded by remote forces. Also we consider a particular example — a dynamic crack subjected to point force tractions on its faces — the corresponding quasistatic case for which was investigated in [2].

We investigate the linearized stability of the crack against small in-plane perturbation (i.e. the crack remains straight, but the crack speed is perturbed) and out-of-plane perturbation (the crack can take a wavy path). The unperturbed configuration whose stability is investigated is as follows. A straight crack propagates at uniform speed under conditions of plane strain, through an infinite elastic medium which is loaded so that the crack propagates in pure opening mode ("Mode I"). The crack is driven by a com-

bination of remote body force and surface tractions which travel with the crack and are symmetric about the crack.

We use the technique presented in [1]. Specialising to the case of two dimensions formulae for the perturbations of the stress intensity factors induced by a small three-dimensional dynamic perturbation of a nominally plane crack obtained in [3, 4] and using the Griffith fracture criterion and the principle of "local symmetry" (i.e the crack path adjusts itself so that the local shear stress intensity factor K_{II} is maintained at the value zero) we derive equations for the in-plane and out-of-plane perturbations of the crack path. The equation for the out-of-plane perturbation function has a "convolution" structure, which reduces the study of stability to locating singularities of a "transfer function". The formulae for the case of general loading are presented in Section 1.

We apply the formulae to the case when the crack is loaded by a pair of opposite point forces on its faces and subjected to a remote uniaxial stress, aligned with the direction of the unperturbed crack. In Section 2 we present equations for the perturbation functions and numerical results on crack stability comparing those with corresponding results for the quasistatic crack obtained in [2]. The numerical results show that in the case of this particular loading the crack is unstable to out-of-plane perturbation, for either compressive or tensile stress applied parallel to the crack. We have found a variety of oscillatory instability modes. This suggests a possibility that the crack can develop a complex fracture surface as one or more of the available instability modes are triggered.

1.   GENERAL FORMULAE

Formulation of the problem

We consider the crack extending dynamically in an elastic isotropic infinite two-dimensional body which is characterized by the speeds of dilatational and shear waves a and b, and density ρ. Thus, at time t say, the crack's position is

$$C_\varepsilon(t) = \{\mathbf{X} : X_2 = \varepsilon\psi(X_1), -\infty < X_1 < Vt + \varepsilon\varphi(t)\},$$

where $0 \leq \varepsilon \ll 1$, ψ defines the shape of the out-of-plane perturbation of the crack path and φ defines the in-plane perturbation. The unperturbed crack, whose stability is to be investigated, corresponds to $\varepsilon = 0$; it is straight and extends with uniform velocity V along the axis $X_2 = 0$.

The crack is driven by a combination of body forces and surface tractions which travel with the crack. The body force $\mathbf{F}$, which is assumed to be symmetric about the X_1-axis, depends on $\mathbf{X}$ and t in the combination $(X_1 - Vt, X_2)$. The surface tractions $\mathbf{P}$ are taken in the form of pure

"pressure loading", that is, $\mathbf{P} = P\mathbf{n}$, where $\mathbf{n}$ is the outer normal to the crack and the function P depends on $X_1 - Vt$ only. In addition, loading at infinity is allowed, which produces a uniform tensile stress σ_{11}^∞ parallel to the unperturbed crack. Thus, the unperturbed crack ($\varepsilon = 0$) is subjected to Mode I loading.

In the absence of the crack, the given loading would generate stress and displacement fields $\boldsymbol{\sigma}^{(nc)}(X_1 - Vt, X_2)$, $\mathbf{u}^{(nc)}(X_1 - Vt, X_2)$; the only non-zero component of $\boldsymbol{\sigma}^{(nc)}$ as $|\mathbf{X}| \to \infty$ is σ_{11}^∞, constant. Let the *additional* stress and displacement fields, created by the presence of the crack, be $\boldsymbol{\sigma}$, $\mathbf{u}$. These satisfy the homogeneous equations of elastodynamics together with the boundary conditions

$$\sigma_{ij}n_j + \sigma_{ij}^{(nc)}n_j + Pn_i = 0 \quad \text{on } C_\varepsilon^\pm. \tag{1.1}$$

It is convenient to express the problem in terms of a moving coordinate system (x_1, x_2, t), where $x_1 = X_1 - Vt$, $x_2 = X_2$, which we will use in the remainder of the text.

Unperturbed problem

When $\varepsilon = 0$, the unperturbed crack is straight. The corresponding stress and displacement fields $\boldsymbol{\sigma}^{(0)}$, $\mathbf{u}^{(0)}$ satisfy the homogeneous equations of elastodynamics and boundary conditions

$$\sigma_{12}^{(0)} = 0, \quad \sigma_{22}^{(0)} = -\sigma_{22}^{(nc)} - P(x_1), \quad x_2 = \pm 0, \; x_1 < 0. \tag{1.2}$$

Due to the special type of loading which follows the extending crack tip, $\boldsymbol{\sigma}^{(0)}$, $\mathbf{u}^{(0)}$ do not depend on t, that is $\boldsymbol{\sigma}^{(0)} = \boldsymbol{\sigma}^{(0)}(x_1, x_2)$, $\mathbf{u}^{(0)} = \mathbf{u}^{(0)}(x_1, x_2)$. This is a steady-state problem; the solution of problems of this type is well-known (e.g. [5]).

At the extension of the crack near its tip the following asymptotic approximation holds for $x_1 > 0$

$$\sigma_{22}^{(0)}(x_1, 0) \sim \frac{K_I^{(0)}}{(2\pi x_1)^{1/2}} - \sigma_{22}^{(nc)}(0, 0) - P(0) + A_I^{(0)}\sqrt{x_1}, \tag{1.3}$$

where the Mode I stress intensity factor $K_I^{(0)}$ and the next coefficient $A_I^{(0)}$ depend on the applied loading.

Stress intensity factors for perturbed problem

For general three-dimensional perturbation of the crack the perturbed stress intensity factors were obtained in [3, 4] to first order in ε. In the present two-dimensional case, specialising also to symmetric loading, these

formulae reduce to

$$K_I = K_I^{(0)} + \varepsilon K_I^{(1)} + O(\varepsilon^2), \tag{1.4}$$

$$K_{II} = \varepsilon K_{II}^{(1)} + O(\varepsilon^2), \tag{1.5}$$

where

$$K_I^{(1)}(t) = -\dot{\varphi}(t)q_I K_I^{(0)} + \sqrt{\frac{\pi}{2}}\varphi(t)A_I^{(0)}, \tag{1.6}$$

$$K_{II}^{(1)}(Vt) = \psi'(Vt)(Vl_1 q_{II} - l_2)K_I^{(0)} - \sqrt{\frac{\pi}{2}}\psi(Vt)l_1 A_I^{(0)} + B(\psi), \tag{1.7}$$

$$B(\psi) = \left([U]_{11} * \langle P_1^{eff} \rangle - \langle U \rangle_{31} * [P_2^{eff}]\right)|_{x_1=0}. \tag{1.8}$$

Here, $*$ denotes convolution with respect to the variables x_1 and t; square and angular brackets denote jump and average of a function across the line $x_2 = 0$; $[U]_{11}$ and $\langle U \rangle_{31}$ are components of dynamic weight functions which were constructed in [3, 4]; q_I, q_{II}, l_1, l_2 are constants depending on the velocity V. Because of limitations on the length of the article we are not able to give formulae for the weight functions and the constants but refer to [1], Appendix A. The vector $\mathbf{P}^{eff} = (P_1^{eff}, P_2^{eff})$ represents the effective traction components:

$$\langle P_1^{eff} \rangle(x_1, t) = -\left(\psi'(x_1 + Vt)P(x_1) - \psi(x_1 + Vt)T^{(1)}(x_1) \right.$$

$$\left. + \frac{\partial}{\partial x_1}\left\{ \psi(x_1 + Vt)T^{(0)}(x_1) \right\} \right), \tag{1.9}$$

$$\left[P_2^{eff} \right](x_1, t) = \psi(x_1 + Vt)\rho V^2 [u_{2,11}^{(0)}](x_1), \tag{1.10}$$

where

$$T^{(0)}(x_1) = \sigma_{11}^{(0)}(x_1, 0) + \sigma_{11}^{(nc)}(x_1, 0), \tag{1.11}$$

$$T^{(1)}(x_1) = \rho V^2 \left(u_{1,11}^{(0)}(x_1, 0) + u_{1,11}^{(nc)}(x_1, 0) \right). \tag{1.12}$$

Here, $u_{i,jk} = \partial^2 u_i / \partial x_j \partial x_k$.

Crack instability

We assume that the crack will extend in such a way as to maintain "local symmetry" (i.e. local $K_{II} = 0$), and to satisfy the Griffith energy criterion. The Griffith energy balance with constant surface energy implies that the local crack speed v must adjust itself so that (see [6])

$$K_I^2 = \mathcal{F}(v)K_{Ic}^2, \tag{1.13}$$

where $\mathcal{F}(v)$ is a known function of crack speed, and K_{Ic} is the static plane-strain fracture toughness. To be consistent with the unperturbed motion we assume that $K_I^{(0)2} = \mathcal{F}(V)K_{Ic}^2$.

Using this criterion and formulae (1.4), (1.6) for the stress intensity factor K_I we obtain the differential equation for the perturbation function $\varphi(t)$. For the derivation and analysis of this equation we refer to [1]. Note that the introduction of surface tractions on the crack faces did not affect K_I, therefore the equation for $\varphi(t)$ remains the same.

It was found that the crack is stable to in-plane perturbation if $A_I^{(0)} < 0$, unstable if $A_I^{(0)} > 0$ (function $\varphi(t)$ is growing exponentially); $A_I^{(0)} = 0$ defines the boundary of stability.

The criterion $K_{II} = 0$ implies, to first order in ε, that

$$K_{II}^{(1)}(Vt) = 0. \tag{1.14}$$

It was shown in [1] that the equation for the out-of-plane perturbation function has a "convolution" structure, which reduces the study of stability to locating singularities of a "transfer function". The equation defining singularities of the transfer function has the form:

$$-\mathrm{i}k(Vl_1q_{II} - l_2)K_I^{(0)} - \sqrt{\frac{\pi}{2}}l_1A_I^{(0)} + \int_0^\infty \widehat{[U]}_{11}(s, kV)\tau_1(s,k)ds$$

$$-\int_0^\infty \widehat{\langle U\rangle}_{31}(s, kV)\tau_2(s,k)ds = 0, \tag{1.15}$$

where $\widehat{[U]}_{11}$, $\widehat{\langle U\rangle}_{31}$ are Fourier transforms of $[U]_{11}$, $\langle U\rangle_{31}$ with respect to the time variable,

$$\tau_1(s, k) = \exp(\mathrm{i}ks)\,[T^{(1)}(-s) - T^{(0)'}(-s)$$
$$+ \mathrm{i}kT^{(0)}(-s) + \mathrm{i}kP(-s)], \tag{1.16}$$
$$\tau_2(s, k) = \exp(\mathrm{i}ks)\,\rho V^2[u_{2,11}^{(0)}](-s). \tag{1.17}$$

Complex roots of this equation such that $\mathbf{Im}\,k > 0$ correspond to singularities of the transfer function at $-\mathrm{i}k$.

Equation (1.15) could be equally obtained by seeking a perturbation of the form

$$\psi(x_1 + Vt) = \exp(-\mathrm{i}kx_1)\,\exp(-\mathrm{i}kVt) = \exp(-\mathrm{i}kX_1). \tag{1.18}$$

This implies a perturbation of the crack edge ($X_1 = Vt$) of $\exp(-\mathrm{i}kVt)$; the shape $\exp(-\mathrm{i}kX_1)$ for all $X_1 < Vt$ follows because the crack, once formed, remains unchanged.

A root of the equation such that $\mathbf{Im}\,k > 0$ gives the crack path which deviates increasingly from the path $x_2 = 0$ as the crack advances, implying instability.

2.　　LOADING BY POINT FORCE TRACTIONS

We now consider the case when the body forces are absent and the crack faces are loaded by a pair of opposing point forces of magnitude A acting in the direction normal to the perturbed crack, together with the remotely applied tension or compression σ_{11}^{∞}. Let d (> 0) be a distance from the crack tip to the point of force application. In the moving coordinate system we have

$$\mathbf{F} = 0, \qquad \mathbf{P} = P\mathbf{n}, \ P = A\delta(x_1 + d). \qquad (2.1)$$

Stress and displacement components for the unperturbed problem

The solution of a steady-state problem with a straight crack under general Mode I loading was given in [5], for example. For the present case of point force tractions the components of the stress and displacement fields have the following form at the crack faces ($x_2 = 0$, $x_1 < 0$):

$$\sigma_{11}^{(0)}(x_1, \pm 0) = \mathcal{M}(V)\sigma_{22}^{(0)}(x_1, \pm 0) = -A\,\mathcal{M}(V)\delta(x_1 + d), \qquad (2.2)$$

$$u_{1,11}^{(0)}(x_1, 0) = A\,\frac{2\beta\alpha - (1 + \beta^2)}{\mu R(V)}\,\delta'(x_1 + d), \qquad (2.3)$$

$$\left[u_{2,11}^{(0)}\right](x_1) = 2u_{2,11}^{(0)}(x_1, +0) = -\frac{A\alpha V^2}{\pi\mu d^{1/2}b^2 R(V)}$$

$$\times (-x_1)^{-3/2}\left(1 + \frac{x_1(d - x_1)}{(d + x_1)^2}\right), \qquad (2.4)$$

where $\mu = \rho b^2$ is the shear modulus,

$$\mathcal{M}(V) = \frac{2(1 + \beta^2)(\alpha^2 - \beta^2)}{R(V)} - 1,$$

$$\alpha = \sqrt{1 - V^2/a^2}, \qquad \beta = \sqrt{1 - V^2/b^2}, \qquad R(V) = 4\alpha\beta - (1 + \beta^2)^2.$$

The stress intensity factor and coefficient $A_I^{(0)}$ are

$$K_I^{(0)} = A\sqrt{\frac{2}{\pi d}}, \qquad A_I^{(0)} = -\frac{A}{\pi d^{3/2}}. \qquad (2.5)$$

The only non-zero component of $\boldsymbol{\sigma}^{(nc)}$ is σ_{11}^{∞}, constant.

Crack path instability

As we pointed out in Section 1 the stability of the crack to in-plane perturbation depends on the sign of $A_I^{(0)}$. For the present case $A_I^{(0)} < 0$ and therefore the crack is stable to in-plane perturbation.

To obtain the algebraic equation for investigation of out-of-plane insta-
bility of the crack we substitute formulae (2.2)–(2.5), (1.11), (1.12) into
(1.15)–(1.17). We have

$$\tau_1(s,k) = e^{iks}\Big[Al_1\delta^{'}(d-s) - ikA(\mathcal{M}(V)-1)\delta(d-s) + ik\sigma_{11}^\infty\Big]. \quad (2.6)$$

Obviously the convolution of this function with the weight function
$[\widehat{U}]_{11}(s,-kV)$ will give the values of the weight function and of its deriva-
tive with respect to s at $s = d$.

It is convenient to give the final equation in dimensionless form. Let $\lambda = kd$ be a new dimensionless variable. Then the equation defining instabilities
of the crack path takes the form:

$$\sqrt{\frac{l_1}{2\pi}} + i\lambda\sqrt{\frac{2}{\pi}}\,(l_2 - Vl_1q_{II}) + \mathcal{J}_1(\lambda) - \mathcal{J}_2(\lambda) + (i-1)m_1\sqrt{\lambda}M = 0, \quad (2.7)$$

where

$$\mathcal{J}_1(\lambda) = e^{i\lambda}\Big[l_1d^{3/2}\frac{\partial}{\partial x_1} + i\lambda\, l_3d^{1/2}\Big][\widehat{U}]_{11}(d, \lambda V/d), \qquad (2.8)$$

$$\mathcal{J}_2(\lambda) = \int_0^\infty d^{1/2}\langle\widehat{U}\rangle_{31}(yd, \lambda V/d)\,\bar{\tau}_2(y,\lambda)dy, \qquad (2.9)$$

$$\bar{\tau}_2(y,\lambda) = -\frac{\alpha(1-\beta^2)^2}{\pi R(V)}\,e^{i\lambda y}y^{-3/2}\Big(1 - \frac{y(1+y)}{(1-y)^2}\Big). \qquad (2.10)$$

The parameter

$$M = \sigma_{11}^\infty d/A$$

can be positive (tensile stress is applied along the x_1-axis) or negative
(compressive stress).

Here $l_3 = l_1 - \mathcal{M}(V) + 1$; q_{II}, l_1, l_2, m_1 are known functions of the crack
speed (see [1]).

Equation (2.7) depends on the crack speed V and the parameter M. We
will seek roots of equation (2.7) such that **Im** $\lambda > 0$. If such roots exist the
crack is unstable to out-of-plane perturbations. As we have mentioned in
Section 1 the existence of such roots means that the perturbation function
ψ may have the form (1.18) with $k = \lambda/d$.

It is easy to see from the expression (2.10) that the integrand function
in (2.9) has singularities at $y = 0$ and $y = d$. The integral should be
interpreted in the sense of generalized functions and regularized in the
following way:

$$\int_0^\infty f(y)y^{-3/2}dy = \int_0^\infty (f(y) - f(0))y^{-3/2}dy,$$
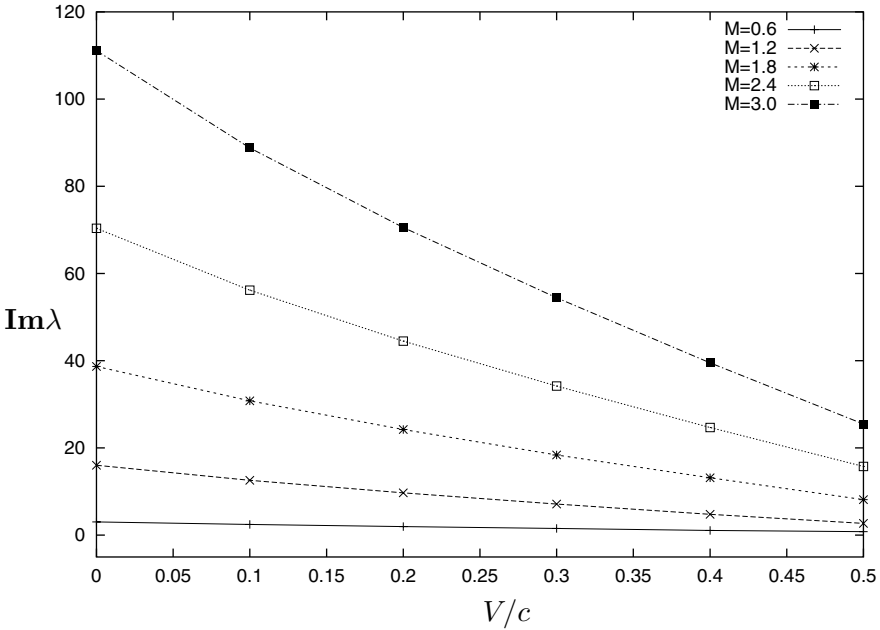
Figure 1 Pure imaginary root of equation (2.7) versus V/c for different values of M.

$$\int_{-1}^{1} \frac{f(y)}{y^2} dy = \mathbf{Re} \lim_{\epsilon \to 0} \int_{-1}^{1} \frac{f(y)}{(y - i\epsilon)^2} dy$$

$$= \mathbf{Re}\left[\int_{-1}^{1} \frac{f(y) - f(0) - yf'(0)}{y^2} dy - 2f(0) + i\pi f'(0)\right].$$

Numerical results on out-of-plane instability of the crack

As $V \to 0$ equation (2.7) coincides with the equation for the quasistatic case which was studied in [2]. The corresponding quasistatic equation has a pure imaginary root if $M > 0$, which corresponds to pure exponential departure of the crack path from the straight line, and an infinite number of roots with non-zero real part for any M, which correspond to oscillating crack paths.

In the present dynamic case equation (2.7) has the same root structure. We have found that (2.7) has an imaginary root for $M > 0$. Thus, if the crack is subjected to tensile stress along the x_1-axis, the crack is unstable and its path departs exponentially from the straight line. In Fig. 1 this root is plotted versus V/c for different values of the parameter M. Here c
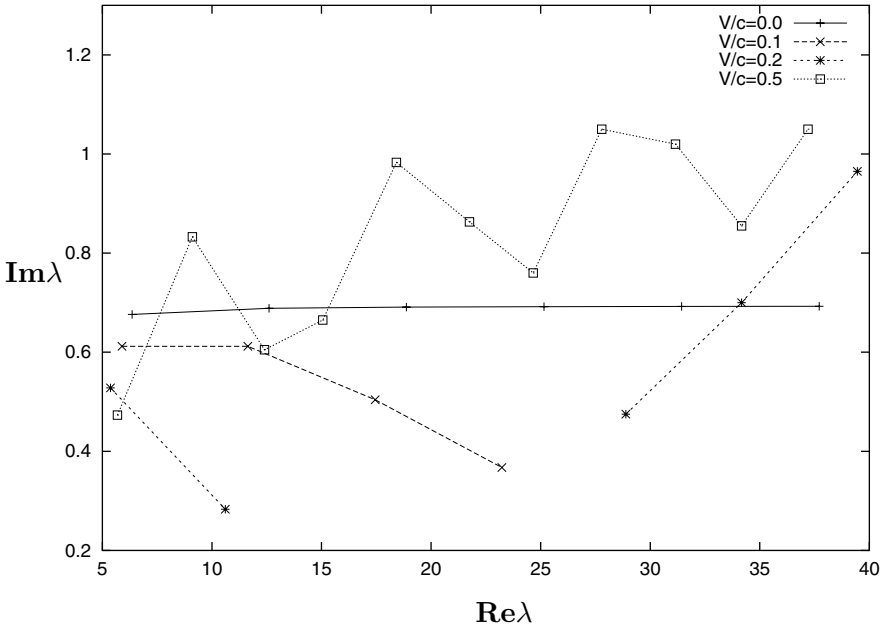
Figure 2   Distribution of roots with non-zero real part for different values of V/c; $M = 0$. The picture shows discrete sets of roots; they are connected to show that they are associated with a common value of V/c.

is the Rayleigh wave speed. Quasistatic results are included in the graph for comparison.

It seems that, similarly to the quasistatic case, equation (2.7) has an infinite number of roots with non-zero real part for any value of M. We were, however, limited to study the equation for $\mathbf{Re}\,\lambda < 40$; further calculations could be prone to loss of accuracy. Thus, the crack is unstable for either compressive or tensile stress along the x_1-axis and can develop an oscillating path. In Fig. 2 the distribution of roots is shown for $M = 0$ for four different values of the crack speed. The density of the roots increases as the crack speed V increases. Our calculations do not allow us to conclude whether or not the magnitude of the imaginary part of a root saturates as its real part increases, nor whether the number of roots for any given V is finite or infinite. However, the calculations have shown that the crack subjected to point force tractions at the crack faces is unstable to out-of-plane perturbation for any loading configuration, for either compressive or tensile stress applied parallel to the crack, and suggest that the crack may develop a complicated fracture surface if more than one instability mode is triggered.

Acknowledgments

References

[1] Obrezanova, O and Movchan, A B and Willis, J R (2002) *Dynamic stability of a propagating crack*, J. Mech. Phys. Solids, **50**, 2637–2668.

[2] Obrezanova, O and Movchan, A B and Willis, J R (2002) *Stability of an advancing crack to small perturbation of its path*, J. Mech. Phys. Solids **50**, 57–80.

[3] Willis, J R and Movchan, A B (1995) *Dynamic weight functions for a moving crack. I. Mode I loading*, J. Mech. Phys. Solids **43**, 319–341.

[4] Willis, J R and Movchan, A B (1997) *Three-dimensional dynamic perturbation of a propagating crack*, J. Mech. Phys. Solids **45**, 591–610.

[5] Craggs, J W (1960) *On the propagation of a crack in an elastic-brittle material*, J. Mech. Phys. Solids **8**, 66–75.

[6] Freund, L B (1990) *Dynamic Fracture Mechanics.* Cambridge: Cambridge University Press.

A THERMOELASTICITY PROBLEM IN A DOMAIN WITH AN EDGE CRACK: ASYMPTOTIC ANALYSIS

Ö. Selsil[1], I.S. Jones[2] and A.B. Movchan[1]

[1] *Department of Mathematical Sciences, University of Liverpool, UK*

oselsil@liv.ac.uk, abm@liv.ac.uk

[2] *School of Engineering, John Moores University, Liverpool, UK*

i.s.jones@livjm.ac.uk

Abstract   We consider a quasi-static problem of uncoupled thermoelasticity posed in a domain with a small edge crack perpendicular to the boundary. Real life examples leading to our problem arise naturally in, for example, fast breeder reactors, pressurised water reactor nozzles, etc. The effect of rapid changes or fluctuations on the surface of these structures is known as thermal striping and is considered as the origin of thermal fatigue damage.

Introduction

In this paper we propose a simple asymptotic algorithm for evaluation of the upper bound for the stress-intensity factor (SIF) at the vertex of a small edge crack placed in a finite size elastic body subjected to a time-dependent thermal load.

The motivation for this work stemmed from the study of "thermal striping" problems studied in Jones & Lewis [1], [2], [3]. These problems are important in a number of applications involving time-dependent thermal loads imposed on cracked surfaces of elastic solids. As the size of the crack is small, compared to the size of the whole elastic body, the domain is said to be "singularly perturbed". Technically, this would create certain complications in direct numerical methods, e.g. one would need to construct a very fine mesh around the crack to be able to treat the problem by means of finite difference or finite element method.
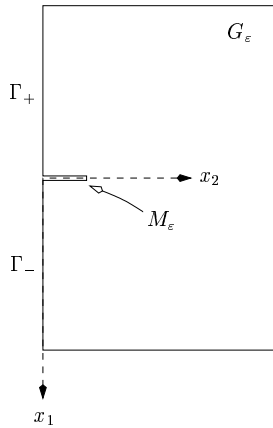
Figure 1 A domain with a small perpendicular edge crack.

We construct a "boundary layer" in a neighbourhood of the crack. This boundary layer is defined as a solution of a certain model problem in a half-plane. The stress-intensity factor (SIF) corresponding to the boundary layer is given in explicit analytical form following Koiter [4] and Stallybras [5]. The only numerical calculation we need to perform is for the uncracked body which is a straightforward task.

The asymptotic estimate is sufficiently accurate and the asymptotic formulae are easy to implement in numerical examples.

In Section 1 we give the formulation of the problem. Section 2 includes a general description of the asymptotic algorithm. Section 3 and 4 deal with a particular case of time-periodic thermal loading and give an illustrative example characterising the solution of boundary layer type. Finally, Section 5 presents results of comparison of asymptotic estimates with finite element computations produced by COSMOS/M [6].

1.   FORMULATION OF THE PROBLEM

Let the displacement vector $\mathbf{u} = (u_1, u_2)^T$ and the temperature T satisfy the following boundary value problem in a domain G_ε (see Fig.1) with a small edge crack M_ε (see Boley & Weiner [7]):

$$\mathbf{Lu} = \gamma \nabla T, \quad (\mathbf{x}, t) \in G_\varepsilon \times [0, \infty), \qquad (1.1)$$

$$\kappa \nabla^2 T = \frac{\partial T}{\partial t}, \quad (\mathbf{x}, t) \in G_\varepsilon \times [0, \infty), \qquad (1.2)$$

where

$$\mathbf{L} = \mu \nabla^2 + (\lambda + \mu) \text{ grad div}, \qquad (1.3)$$

with the boundary conditions

$$\left\{ \mu \left(\frac{\partial u_i}{\partial x_j} + \frac{\partial u_j}{\partial x_i} \right) + (\lambda \nabla \cdot \mathbf{u} - \gamma T) \delta_{ij} \right\} n_j = \mathbf{p}(\mathbf{x}), \qquad (1.4)$$

$$T = \tau(\mathbf{x}, t), \qquad (1.5)$$

$(\mathbf{x}, t) \in \partial G_0 \times [0, \infty)$. Here $\gamma = \alpha(3\lambda + 2\mu)$, where α is the linear thermal expansion coefficient, λ and μ are Lamè constants and κ is the thermal diffusivity. $\mathbf{p}(\mathbf{x})$ corresponds to a self balanced external load and τ denotes the behaviour of the temperature, both on the surface $\partial G_0 = \Gamma_+ \cup \Gamma_- \cup M_\varepsilon$. We also prescribe an ideal contact on the faces of the crack M_ε. We note that it is essential in our work to introduce a dimensionless parameter $\varepsilon \ll 1$ denoting the ratio of the crack length to the thickness.

2.   ASYMPTOTIC ALGORITHM

We decompose our original problem into two model problems, for which the small parameter ε is not involved. The first one corresponds to a plane strain problem for an homogeneous elastic body without a crack. The principal term, say $\mathbf{v}^0$, of the solution can be expanded into its Taylor series in a neighbourhood of the origin as

$$v_i^0 = v_i^0(\mathbf{0}) + \mathbf{x} \cdot \nabla v_i^0(\mathbf{0}) + O(|\mathbf{x}|^2). \qquad (2.1)$$

We can see that the vector function $\mathbf{v}^0$ does not satisfy the boundary condition (1.4) on the crack faces. Hence we define the principal term of the discrepancy by the linear term in (2.1). Following the conventional approach, we can compensate the discrepancy by means of a solution of a boundary layer type. For this purpose, we introduce new scaled coordinates

$$\boldsymbol{\xi} = (\xi_1, \xi_2) = \varepsilon^{-1}(x_1, x_2). \qquad (2.2)$$

Remembering that $\partial G_0 = \Gamma_+ \cup \Gamma_- \cup M_\varepsilon$ is free of external loading we can see that the strain components ε_{kl}, $k, l = 1, 2$, are identically zero when $x_2 = 0$. Therefore

$$\varepsilon_{12}(0, x_2) \sim \varepsilon_{12}(0, 0) + x_2 \frac{\partial \varepsilon_{12}}{\partial x_2}(0, 0) = \varepsilon \xi_2 \frac{\partial \varepsilon_{12}}{\partial x_2}(0, 0),$$

$$\varepsilon_{22}(0, x_2) \sim \varepsilon_{22}(0, 0) + x_2 \frac{\partial \varepsilon_{22}}{\partial x_2}(0, 0) = \varepsilon \xi_2 \frac{\partial \varepsilon_{22}}{\partial x_2}(0, 0), \qquad (2.3)$$

$$\varepsilon_{11}(0, x_2) \sim \varepsilon_{11}(0, 0) + x_2 \frac{\partial \varepsilon_{11}}{\partial x_2}(0, 0) = \varepsilon_{11}(0, 0) + \varepsilon \xi_2 \frac{\partial \varepsilon_{11}}{\partial x_2}(0, 0),$$

leading us to solve the second model problem posed in a linearly elastic half-plane with an edge crack:

$$\mathbf{L}\mathbf{w}(\boldsymbol{\xi},t) = \mathbf{0}, \quad (\boldsymbol{\xi},t) \in \mathbb{R}_2^+ \times [0,\infty), \tag{2.4}$$

$$\frac{\partial w_1}{\partial \xi_2} + \frac{\partial w_2}{\partial \xi_1} = 0, \quad (\lambda+2\mu)\frac{\partial w_1}{\partial \xi_1} + \lambda\frac{\partial w_2}{\partial \xi_2} = -\mathbb{C} + \gamma T(\xi_2,t), \quad \boldsymbol{\xi} \in M_\pm,$$
$$\tag{2.5}$$

$$\frac{\partial w_1}{\partial \xi_2} + \frac{\partial w_2}{\partial \xi_1} = 0, \quad (\lambda+2\mu)\frac{\partial w_2}{\partial \xi_2} + \lambda\frac{\partial w_1}{\partial \xi_1} = 0, \quad \xi_1 \in \mathbb{R}, \ \xi_2 = 0, \tag{2.6}$$

where $\mathbf{L}$ is the Lamè operator defined in (1.3) and $\mathbb{C}$ is a constant to be clarified in the following section. In addition we require that $|\mathbf{w}| \to \mathbf{0}$ as $\xi_2 \to 0$.

We emphasise that the time has the role of a parameter in the right-hand sides of boundary conditions. Thus, the asymptotic behaviour of the solution in a neighbourhood of the origin can be described by means of the following relationship

$$\mathbf{u}(\mathbf{x},t) \sim \mathbf{v}^0(\mathbf{x},t) + \varepsilon\mathbf{w}(\frac{\mathbf{x}}{\varepsilon},t). \tag{2.7}$$

Note that the function $\mathbf{v}^0$ is a regular function, and, therefore, the SIF K at the tip of the crack is defined by the term $\varepsilon\mathbf{w}$ of a boundary layer type.

3. TIME PERIODIC TEMPERATURE LOADING

Let us consider the case of a periodic temperature loading on the boundary of the half-plane. Under the ideal heat contact assumption on the crack faces the temperature satisfies the following problem

$$\kappa\frac{\partial^2 T}{\partial \xi_2^2}(\xi_2,t) = \frac{\partial T}{\partial t}, \quad \xi_2 > 0, \ t > 0, \tag{3.1}$$

$$T(0,t) = T_0 e^{i\omega t}, \quad t > 0, \tag{3.2}$$

which has the solution

$$T(\xi_2,t) = T_0 \operatorname{Re}\left\{\exp\{-(1+i)\sqrt{\frac{\omega}{2\kappa}}\xi_2 + i\omega t\}\right\}, \tag{3.3}$$

that decays as $\xi_2 \to \infty$.

4.   STRESS SINGULARITY AND THE SIF

We assume that a small crack, perpendicular to the surface, exists in the elastic body (see Fig.1). The stress is singular at the crack tip

$$\sigma_{11} \sim \frac{K_I(\mathbf{u})}{\sqrt{2\pi(x_2 - l)}},$$

where $K_I(\mathbf{u})$ is known as Mode-I SIF. We note that K_I is a linear functional, and

$$K_I\left(\mathbf{v}^0(\mathbf{x}) + \varepsilon\mathbf{w}(\mathbf{x}/\varepsilon)\right) = K_I(\varepsilon\mathbf{w}(\mathbf{x}/\varepsilon)),$$

which means that the leading term in the approximation of the SIF is determined by the boundary layer existing near the small crack that can be evaluated in closed form, since it solves the model problem (2.4)-(2.6) in a half-plane.

The exact solution for an elastic half-plane containing a crack perpendicular to the free surface and loaded by polynomial tractions is obtained in Stallybras [5].

The term γT in the right-hand side of (2.5) can be approximated by a polynomial

$$\gamma T \sim \sum_{k=0}^{\infty} p_k \, x_2{}^k,$$

over the crack length. If $\sigma_{11} = \gamma T$, $\sigma_{12} = 0$, on the crack surface, then for this model problem the Stallybras solution delivers (for a polynomial of degree 10)

$$\begin{aligned}
K_I{}^{(1)} = -\sqrt{2\pi l} \; \big(&0.793 \; p_0 + 0.4829 \; p_1 l + 0.3716 \; p_2 l^2 \\
&+ 0.3118 \; p_3 l^3 + 0.2735 \; p_4 l^4 + 0.2464 \; p_5 l^5 + 0.2260 \; p_6 l^6 \\
&+ 0.2099 \; p_7 l^7 + 0.1968 \; p_8 l^8 + 0.1858 \; p_9 l^9 + 0.1765 \; p_{10} l^{10}\big).
\end{aligned}$$

$$(4.1)$$

The first term $\mathbb{C}$ in the right-hand side of (2.5) is defined by the formula:

$$\mathbb{C} = (\lambda + 2\mu)\frac{\partial v_1^0}{\partial x_1}(\mathbf{0}) + \lambda\frac{\partial v_2^0}{\partial x_2}(\mathbf{0}). \tag{4.2}$$

Its contribution to the SIF is given by (see Koiter [4])

$$K_I{}^{(2)} = 1.12147 \, \mathbb{C} \, \sqrt{\pi l}. \tag{4.3}$$

The stress-intensity is time-dependent but we look for an upper bound, so that

$$|K_I(l, t)| < K_I{}^*,$$
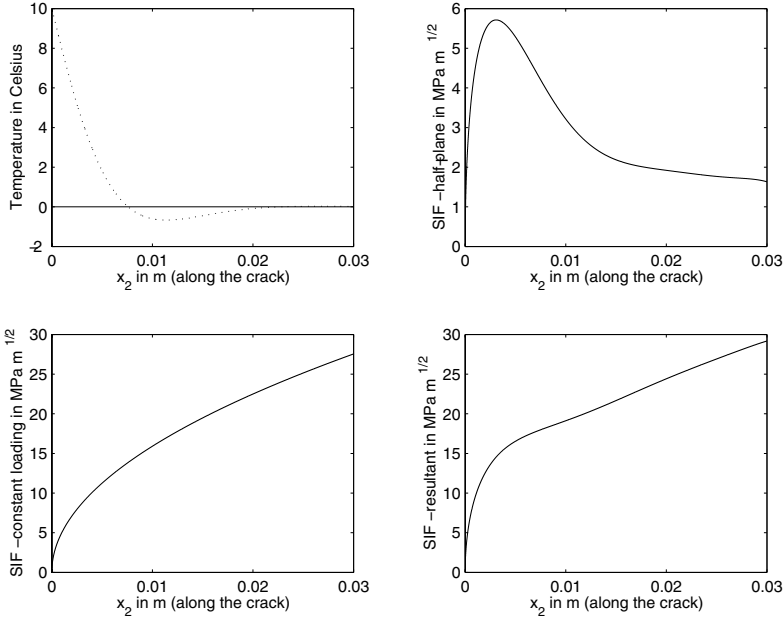
Figure 2 The temperature field described in (3.3) for fixed time and graphs for Mode-I SIF. The following values of parameters are used for the computation: $T_0 = 10°$C, $\omega = 0.0625$Hz, $\kappa \approx 4.6 \times 10^{-6}$m^2/sec, $\alpha = 20 \times 10^{-6}$ $°$C^{-1}, $\rho = 7760$ kg/m^3, $E = 1.63 \times 10^{11}$ N/m^2, $\nu = 0.3$.

where $K_I{}^* = \max_{t \in (0,t^0)} \left(|K_I^{(1)}| + |K_I^{(2)}| \right)$, t^0 is the period of oscillations of temperature.

We note that the SIF $K_I^{(2)}$ increases with the increase of l, whereas $K_I^{(1)}$ decreases as the crack length grows. As a result, the sum $K_I^{(1)} + K_I^{(2)}$ is not necessarily monotonic. The illustrative diagrams are given in Fig.2.

5. ILLUSTRATIVE NUMERICAL EXAMPLES

Here, we give a comparison between the asymptotic estimates and the finite element method. We consider a thin plate, clamped at the ends, under thermal load applied to one of the sides, the other side of the surface is traction free. A small surface crack is introduced in the middle of the beam, perpendicular to its surface. We consider two cases:

(a) the surface temperature oscillates with the frequency of 0.0625 Hz,

(b) the temperature oscillates with the frequency of 1 Hz.
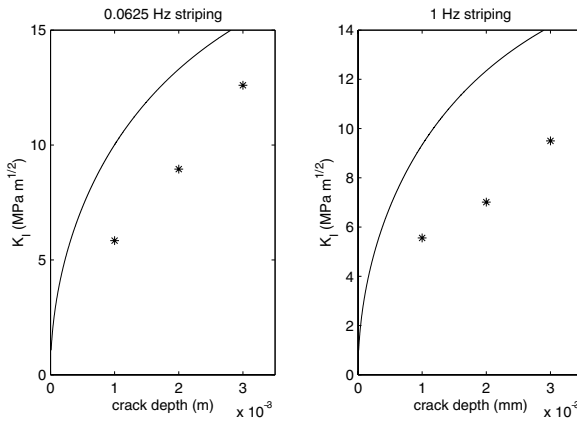
Figure 3 The upper bounds (asymptotic results in solid line) and the finite element computations of SIF (denoted by *) based on COSMOS/M. The upper bound for $|K_I|$ is sufficiently accurately predicted by the asymptotic method.

Thermal and mechanical characteristics of the system are defined as follows:

$$T_0 = 10 \text{ °C}, \quad \alpha = 20 \times 10^{-6} \text{ °C}^{-1}, \quad \kappa \approx 4.6 \times 10^{-6} \text{ m}^2/\text{sec},$$
$$\rho = 7760 \text{ kg/m}^3, \ E = 1.63 \times 10^{11} \text{ N/m}^2, \quad \nu = 0.3.$$

Here, E is the Young's modulus and ν is the Poisson's ratio.

We perform finite element computations for three different crack length for each case (a) and (b). In both cases, we pose zero displacement at the ends of the plate and periodic temperature distribution on the free surface where the small crack is located, whereas the rest of the boundary is adiabatic. The FE results are taken after a certain number of cycles to allow for settling.

The total computation time is high even for the case of lower frequency due to the fact that it requires computations for thermal as well as stress analysis. The region where the crack exists demands very fine meshing and is another cause of long computation time. On the other hand, the asymptotic algorithm uses a straightforward finite element computation for the uncracked body to compute the constant stress at the origin (see (4.2) and (4.3)). The results presented in Fig.3 are sufficiently accurate and easy to obtain following the asymptotic algorithm. For further comparison between finite element and weight function method in the assessment of thermal striping damage we refer the reader to [8].

Future work lies along the line of generalising the solution for any smooth load on the crack surface. Also, uncoupled thermoelasticity problems posed

domains containing a set of parallel small edge cracks or a small oblique edge crack are interesting to investigate. The effects of posing non-ideal heat contact on the crack faces is another direction to take our problem a step forward.

References

[1] Jones, I S, Lewis M W J (1994) *A frequency response method for calculating stress intensity factor due to thermal striping loads,* Fatigue Fract. Engng Mater. Struct. **17** (6), 709–720.

[2] Jones, I S, Lewis M W J (1995) *The effect of various constraint conditions in the frequency response model of thermal striping,* Fatigue Fract. Engng Mater. Struct. **18** (4), 489–502.

[3] Jones, I S, Lewis M W J (1997) *An impulse response method for the prediction of thermal striping damage,* Engineering Fracture Mechanics, **55** (5), 795–812.

[4] Koiter, W T (1956) *On the flexural rigidity of a beam weakened by transverse saw cuts,* Proc. Royal Neth. Acad. of Sciences **B59**, 354–374.

[5] Stallybras, M P (1970) *A crack perpendicular to an elastic half-plane,* Int. J. Engng Sci. **8**, 351–362.

[6] COSMOS/M 2.0 (1997), *A complete finite element analysis system,* Structural Research & Analysis Corp.

[7] Boley, B A, Weiner, J H (1960) *Theory of thermal stresses,* John Wiley & Sons, Inc. Press.

[8] Galwin, S B J, Graham, I D, Jones I S, Rothwell G (1997) *A comparison between the finite element and frequency response methods in the assesment of thermal striping damage,* Int. J. Pres. Ves. & Piping, **74**, 205–212.

METHODS OF ASSESSMENT OF THERMAL STRIPING FATIGUE DAMAGE

Ian S. Jones

School of Engineering, John Moores University, Byrom St., Liverpool, L3 3AF, UK

i.s.jones@livjm.ac.uk

Abstract   The phenomenon of high-cycle fatigue crack growth, caused by thermal striping on metallic components, is examined. A general outline of the mathematical models used for the assessment of thermal striping damage will be presented. Comparisons between all of these models and the finite element method will also be given for the calculation of stress intensity factors.

1.   INTRODUCTION

Thermal striping is random temperature fluctuation produced by the incomplete mixing of fluid streams at different temperatures. Structures exposed to such temperature fluctuations can suffer thermal fatigue damage. This problem has been discussed in [1]-[8]. For an engineering component containing a defect and situated in such a flow, the stress intensity factor (SIF), associated with the defect, will fluctuate in response to the imposed component surface temperature fluctuations. For a component of a given material under specified external loading, it is necessary to ascertain the maximum allowable surface temperature fluctuation amplitude before growth of the defect will occur.

Thermal striping fatigue damage has the potential to occur in a number of areas where there is good heat transfer between fluid and component. It can arise in certain liquid metal-cooled fast breeder reactor (LMFBR) structures, notably those situated above the core, because of the large temperature differences (up to about 100^0C) which exist between liquid sodium emerging from both the core and the breeder sub-assemblies. Other areas of potential occurrence include piping systems in pressurised and boiling water reactors where hot and cold flows meet.

Apart from the finite element method, three approaches have been developed to assess the thermal fatigue damage caused by such temperature fluctuations. These have been implemented in the computer codes TBL [2], [3], [6]-[8] , CLOUDBURST [5], [7] and STRIPE [1]. The analysis of realistic, temporally random striping is possible only in TBL and CLOUDBURST whereas all of the codes are able to analyse the results for the special case of sinusoidal patterns of striping. The methods underlying these approaches will be outlined and comparisons made between them and the finite element method. The methods are based on the weight function approach [9] for the calculation of SIF's. An appropriate weight function for displacement-controlled loading has been developed specifically for thermal striping in [10].

2. PROBLEM FORMULATION

Consider an isotropic, elastic body G with boundary ∂G containing an edge crack of length a. Assuming plane strain linear elasticity, this may be considered as a problem of uncoupled thermoelasticity in which the displacement vector $\mathbf{u} = [u_1(x_1, x_2, t),\ u_2(x_1, x_2, t)]$ and the temperature $T(x_1, x_2, t)$ satisfy the following equations in the absence of body forces:

$$\mu \nabla^2 u_i + (\lambda + \mu)\frac{\partial}{\partial x_i}\left(\frac{\partial u_j}{\partial x_j}\right) = \beta\frac{\partial T}{\partial x_i}, \qquad (\mathbf{x} \in G) \qquad (2.1)$$

$$\frac{\partial T}{\partial t} = \kappa \nabla^2 T \qquad (\mathbf{x}, t) \in G \times [0, \infty) \qquad (2.2)$$

with boundary conditions

$$\left\{ \mu\left(\frac{\partial u_i}{\partial x_j} + \frac{\partial u_j}{\partial x_i}\right) + \delta_{ij}\left[\lambda\left(\frac{\partial u_k}{\partial x_k}\right) - \beta T\right]\right\} n_j = p_i(x_1, x_2) \qquad (\mathbf{x} \in \partial G)$$
$$(2.3)$$

$$\frac{\partial T}{\partial x_j} n_j = h\left[T(x_1, x_2, t) - \varphi(x_1, x_2, t)\right] \qquad (\mathbf{x} \in \partial G) \qquad (2.4)$$

and initial conditions

$$T(x_1, x_2, 0) = f(x_1, x_2) \qquad (\mathbf{x} \in G), \qquad (2.5)$$

$$u_i(x_1, x_2, 0) = u_i^0(x_1, x_2) \qquad (\mathbf{x} \in G) \qquad (2.6)$$

$$\frac{\partial u_i}{\partial t}(x_1, x_2, 0) = 0 \qquad (\mathbf{x} \in G) \qquad (2.7)$$

Here λ and μ are the Lamé constants, κ the thermal diffusivity, (x_1, x_2) the plane spatial coordinates, t time, n the outward normal to the surface, h is a convective heat transfer coefficient between the body and the

surrounding fluid which is at a temperature $\varphi(x_1, x_2, t)$, p the external surface loading, $f(x_1, x_2)$, $u^0(x_1, x_2)$ the prescribed initial temperature and displacement distributions respectively within the body. In addition, $\beta = \alpha(3\lambda + 2\mu)$ where α is the linear expansion coefficient.

3.   THE FREQUENCY RESPONSE METHOD

Further details of this method are given in [2],[3],[6]-[8]. Consideration will now be restricted to a component such as a slab containing a single edge crack or an infinitely long cylinder containing a circumferential crack, with various restraint conditions. The cracked face is thermally striped by a temporally sinusoidal, surface temperature variation, the unstriped surface having the general radiation boundary condition (2.4). The striping on the cracked face is considered to be spatially uniform. Thus heat is assumed to flow in the x direction only, where x is the co-ordinate through the plate or cylinder wall with origin on the striped face (see Fig. 1).
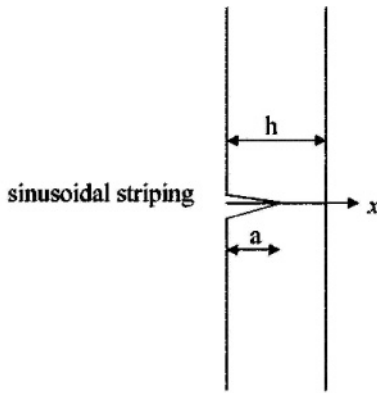
Figure 1   Parameters of the slab.

If the temporal, sinusoidal surface striping frequency is ω then the quasi-steady state solution will be of the form

$$T(x, t) = T_0 e^{i\omega t} [P(x, \omega) + iQ(x, \omega)] \tag{3.1}$$

where T_0 is the surface striping amplitude. The spatial variation functions $P(x, \omega)$ and $Q(x, \omega)$ will depend on the thermal boundary conditions. The temperature profile will induce stress in the component. For the calculation of the mode I SIF for an edge crack in a plate or a circumferential crack in a cylinder, the axial stress will be the relevant component to be considered. The axial stress is dependent on the geometry and restraint conditions

and further details are given in [2],[3],[6] for the edge cracked plate and circumferentially cracked cylinder under various restraint conditions. For illustration purposes, the case of the fully restrained edge cracked plate [2], where the stress is proportional to the temperature field, will be considered. For the fully restrained edge cracked plate, the axial stress $\sigma(x,t)$ will be given by

$$\sigma(x,t) = -\frac{\alpha E}{(1-\nu)}T(x,t) \tag{3.2}$$

where E is Young's modulus and ν is Poisson's ratio. The SIF $K(a,t)$ can be derived from this thermal stress using the weight function method [9] as

$$K(a,t) = \int_0^a \sigma(x,t)\,M(x,a)\,dx \tag{3.3}$$

where $M(x,a)$ is the weight function which depends on the component geometry but not on the loading. Thus for the fully restrained edge cracked plate, the SIF is given by

$$K(a,t) = \frac{\alpha E T_0}{(1-\nu)}e^{i\omega t}\left[\int_0^a P(x)\,M(x,a)\,dx + i\int_0^a Q(x)\,M(x,a)\,dx\right] \tag{3.4}$$

Hence the peak-to-peak SIF fluctuation $\Delta K(a)$ is

$$\Delta K(a) = \frac{\alpha E \Delta T}{(1-\nu)}\sqrt{I_1^2 + I_2^2} \tag{3.5}$$

where ΔT is the peak to peak surface temperature fluctuation and

$$I_1 = \int_0^a P(x)\,M(x,a)\,dx \tag{3.6}$$

and

$$I_2 = \int_0^a Q(x)\,M(x,a)\,dx \tag{3.7}$$

The calculation of $\Delta K(a)$ from ΔT is a frequency response calculation with modulus of the transfer function $H(\omega,a)$ given by

$$|H(\omega,a)| = \frac{\alpha E}{(1-\nu)}\sqrt{I_1^2 + I_2^2} \tag{3.8}$$

The above analysis is based on a single sinusoidal surface temperature variation. In practical situations, the surface temperature variation will be

random. The general surface temperature time signal may be characterised by its power spectral density (PSD) $S_T(\omega)$.

The root mean square (rms) value of the SIF is then given by

$$K_{rms}(a) = \frac{\alpha E}{(1-\nu)} \left[\int\limits_{-\infty}^{\infty} S_T(\omega) \left(I_1^2 + I_2^2 \right) d\omega \right]^{1/2} \tag{3.9}$$

The measure of practical interest in this fatigue process is the maximum fluctuation in the SIF $\Delta K_{\max}(a)$ since this may be compared with the material threshold SIF fluctuation in order to ascertain the behaviour of existing defects. In [2], a conservative approximation of this quantity, derived from the rms value, is discussed. It may be summarised as

$$\frac{\Delta K_{\max}(a)}{K_{rms}(a)} = \frac{\Delta T_{\max}}{T_{rms}} \tag{3.10}$$

where $\Delta T_{\max}$ and T_{rms} are the maximum fluctuation and rms values of the surface temperature signal. This gives the maximum SIF fluctuation as

$$\Delta K_{\max}(a) = \frac{\alpha E \Delta T_{\max}}{(1-\nu)T_{rms}} \left[\int\limits_{-\infty}^{\infty} S_T(\omega) \left(I_1^2 + I_2^2 \right) d\omega \right]^{1/2} \tag{3.11}$$

A variety of PSD's have been examined in [2], based on an experimental thirty-minute real time sample taken from an experimental rig at AEA Technology. This is a 0.2-scale air model of the Prototype Fast Reactor above core region at Dounreay. The bulk of the energy was found to be concentrated below 5Hz with a steady fall off above this frequency. It was found that the results were not particularly sensitive to differing PSD models of this sample. A 'white' PSD with upper frequency ω_0 will be taken as

$$S_T(\omega) = \begin{cases} T_{rms}^2/2\omega_0 & \omega \leq \omega_0 \\ 0 & \omega > \omega_0 \end{cases} \tag{3.12}$$

With this particular PSD, the maximum SIF fluctuation becomes

$$\Delta K_{\max}(a) = \frac{\alpha E \Delta T_{\max}}{(1-\nu)\sqrt{\omega_0}} \left[\int\limits_{0}^{\omega_0} \left(I_1^2 + I_2^2 \right) d\omega \right]^{1/2} \tag{3.13}$$

4.   THE IMPULSE RESPONSE METHOD

A general outline of the CLOUDBURST method will now be given. Further details of the refinements of the method are given in [5] and [7].

Consider the plate, initially at a uniform temperature, which is subjected to a spatially uniform unit temperature pulse on the striped edge lasting a time δt with the back face being, for example, an adiabatic surface. The temperature response through the plate $G(x,t)$ can be found from (2.2) as

$$G(x,t) = \frac{4}{\pi} \sum_{n=0}^{\infty} \frac{(-1)^{n-1}}{2n-1} \cos(\lambda_n(h-x)) \exp\left(-\lambda_n^2 \kappa t\right) \left[\exp\left(\lambda_n^2 \kappa \delta t\right) - 1\right]$$

(4.1)

where

$$\lambda_n = \frac{\pi(2n-1)}{2h}$$

(4.2)

Now consider a situation where the striped face is subjected to a general temperature time history and, in digitised form, let $\theta_i(t_i)$ be the magnitude of the temperature signal at time $t_i = i\delta t$. The temperature response $\theta_s(t_i)$ to this general signal will be given by the convolution

$$\theta_s(x,t) = \sum_{i=1}^{\infty} G(x,t_i)\theta_i(t-t_i)$$

(4.3)

Let the temperature response be partitioned as

$$\theta_s(x,t) = \theta_M(t) + \theta_B(t)(1 - \frac{2x}{h}) + \vartheta_P(x,t)$$

(4.4)

Then

$$\theta_M(t) = \sum_{i=1}^{\infty} M(t_i)\theta_i(t-t_i)$$

(4.5)

$$\theta_B(t) = \sum_{i=1}^{\infty} \theta_i(t-t_i) \left[3M(t_i) - B(t_i)\right]$$

(4.6)

$$\theta_P(x,t) = \sum_{i=1}^{\infty} \theta_i(t-t_i) \left[G(x,t_i) - \left(4 - \frac{6x}{h}\right)M(t_i) + \left(1 - \frac{2x}{h}\right)B(t_i)\right]$$

(4.7)

where

$$M(t_i) = \frac{1}{h} \int_0^h G(x,t_i)\, dx$$

(4.8)

$$B(t_i) = \frac{6}{h^2} \int_0^h x\, G(x,t_i)\, dx$$

(4.9)

Thus the temperature response can be found from the digitised surface temperature and the impulse response function $G(x,t)$. This temperature distribution will induce a thermal stress field. For the plate, this can be related to the temperature as

$$\sigma(x,t) = -g_m\theta_M(t) - g_b\theta_B(t)\left(1 - \frac{2x}{h}\right) - g_p\vartheta_P(x,t) \tag{4.10}$$

The constants g depend on the restraint conditions of the plate [3]. For a fully restrained plate

$$g_m = g_b = g_p = \frac{\alpha E}{(1-\nu)} \tag{4.11}$$

The SIF may be calculated using (3.3) with, for example, the Bueckner form [9] of weight function

$$M(x,a) = \frac{1}{\sqrt{a-x}}\left[1 + m_1\left(1 - \frac{x}{a}\right) + m_2\left(1 - \frac{x}{a}\right)^2\right] \tag{4.12}$$

where m_1 and m_2 are polynomials [9] in (a/h).

Thus the convolution for the SIF is

$$K(a,t) = -g_m\sum_{i=1}^{\infty}\theta_i(t-t_i)I_m(t_i) \; - \; g_b\sum_{i=1}^{\infty}\theta_i(t-t_i)I_b(t_i)$$

$$- g_p\sum_{i=1}^{\infty}\theta_i(t-t_i)I_p(t_i) \tag{4.13}$$

where the impulse response functions I are given by

$$I_m(t_i) = \frac{16}{\pi^2}\sqrt{\frac{2a}{\pi}}\left(1 + \frac{m_1}{3} + \frac{m_2}{5}\right)\sum_{n=1}^{\infty}\frac{\exp\left(-\kappa\lambda_n^2 t_i\right)\left\{\exp\left(\kappa\lambda_n^2\delta t\right) - 1\right\}}{(2n-1)^2} \tag{4.14}$$

$$I_b(t_i) = \frac{48}{\pi^2}\sqrt{\frac{2a}{\pi}}\left[\left(1 + \frac{m_1}{3} + \frac{m_2}{5}\right) - \frac{4a}{h}\left(\frac{1}{3} + \frac{m_1}{15} + \frac{m_2}{35}\right)\right]$$
$$\times \sum_{n=1}^{\infty}\left[1 - \frac{4(-1)^{n-1}}{\pi(2n-1)}\right]\frac{\exp\left(-\kappa\lambda_n^2 t_i\right)\left\{\exp\left(\kappa\lambda_n^2\delta t\right) - 1\right\}}{(2n-1)^2} \tag{4.15}$$

$$I_p(t_i) = \frac{2}{ah}\sqrt{\frac{2a}{\pi}}\sum_{n=1}^{\infty}\frac{\exp\left(-\kappa\lambda_n^2 t_i\right)\left\{\exp\left(\kappa\lambda_n^2\delta t\right) - 1\right\}}{\lambda_n^2}$$
$$\times\Bigg[m_1 + m_2$$
$$+ \frac{(4a^2\lambda_n^2 - 3m_2)}{2a\lambda_n}\sqrt{\frac{\pi}{2a\lambda_n}}\left\{\sin(a\lambda_n)C(a\lambda_n) - \cos(a\lambda_n)S(a\lambda_n)\right\}$$
$$- m_1\sqrt{\frac{\pi}{2a\lambda_n}}\left\{\sin(a\lambda_n)S(a\lambda_n) + \cos(a\lambda_n)C(a\lambda_n)\right\}\Bigg]$$
$$- I_m(t_i) - I_b(t_i) \tag{4.16}$$

The functions $C(x)$ and $S(x)$ are Fresnel integrals.

Thus (4.13) can be used to find the SIF time history at a particular crack depth based on a digitised temperature time history and the three impulse response functions (4.14)-(4.16). Further details and corresponding results for other thermal backface conditions are given in [5]. Maximum fluctuations in the SIF, $\Delta K_{\max}(a)$, may then be found from this SIF time history.

5.   NUMERICAL RESULTS

Some comparisons between the codes have been made [5],[7] when applied to an edge-cracked slab and an infinitely long cylinder containing an internal circumferential crack. The material composition of components found above the core in LMFBR's is typically Type 321 stainless steel. The material properties are given in [5]. The components were analysed using TBL, CLOUDBURST, STRIPE and the finite element code ABAQUS [11] for three representative sinusoidal striping frequencies, 0.0625Hz, 1.0Hz and 6.25Hz, with a peak to peak temperature fluctuation of 20^0C. The plate was fully restrained and two different restraint conditions were examined for the cylinder: (a) the ends were restrained against expansion/contraction and (b) the cylinder was free standing. For the purposes of this comparison of methods, only crack growth due to thermal striping is considered. In a structural integrity assessment of a component at such a temperature, other potential causes of failure would need to be acknowledged. Further details are given in [7].

The variation of the ΔK values with crack depth is shown in Figs. 2-3(a) for the three striping frequencies applied to the fully restrained plate, the cylinder with axial restraint and the freestanding cylinder. For each frequency, results from TBL, CLOUDBURST, STRIPE and the finite element method are shown for the plate with TBL and finite element results given for the two cylinder restraint conditions. The plate results for all of the methods for the three frequencies are in good agreement with the finite element results. The differences become larger with increasing crack depth for all frequencies. This is because the limitations of the Bueckner form of the weight function. The TBL results for the cylinder also show good agreement with the FE results.

At the lowest frequency, there are no severe temperature gradients through the plate thickness. The monotonic increase in ΔK with crack depth occurs because of the influence of the weight function i.e. deep cracks are more likely to become deeper. At the highest frequency, there is a local minimum in the SIF curve for a plate. This is because of two opposing effects. At this high frequency, there is considerable scope for temperature
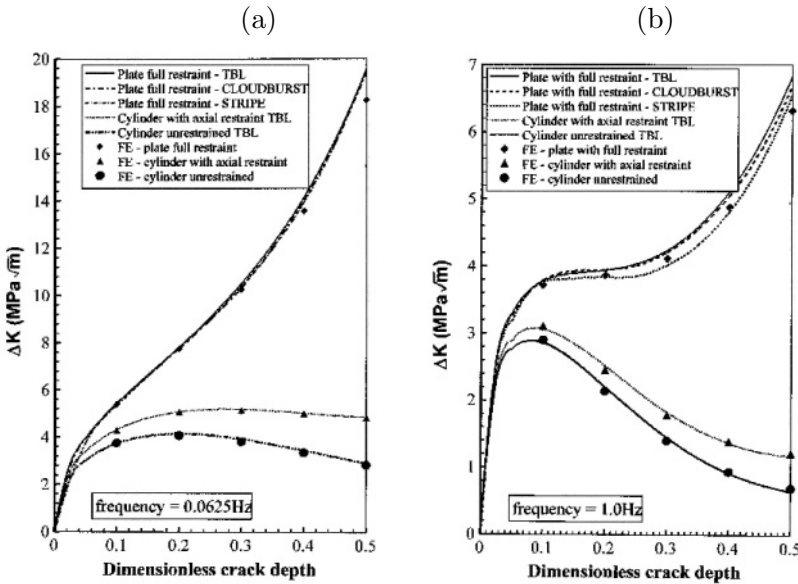
Figure 2   The variation of the peak to peak stress intensity factor fluctuation with crack depth for the plate and cylinder. Comparison of TBL, CLOUDBURST, STRIPE and the finite element method. Striping frequency (a) 0.0625Hz; (b) 1.0Hz.

attenuation, particularly near the striped surface of the plate, and this leads to a reducing SIF with crack depth. At greater crack depths, the geometry effect dominates resulting in increasing SIF with crack depth. Thus there is the possibility of crack arrest in situations where the striping signal contains a high frequency component as the ΔK value reduces, with increasing crack depth, to a value below ΔK_{th}, the material threshold value.

As an example, consider a 2mm deep defect in both the fully restrained plate and the axially restrained cylinder. The ΔK_{th} value for the material will be taken as $5\text{MPa}\sqrt{\text{m}}$. If the components are striped with a frequency of 0.625Hz, then the ΔK values are shown in Fig. 2 and, more accurately, are $7.82\text{MPa}\sqrt{\text{m}}$ (plate) and $5.07\text{MPa}\sqrt{\text{m}}$ (cylinder). Thus the allowable peak-to-peak surface striping temperature is 13^0C (plate) and 19^0C (cylinder). For the case when the striping frequency is 1Hz, the corresponding ΔK values are $3.94\text{ MPa}\sqrt{\text{m}}$ (plate) and $2.52\text{ MPa}\sqrt{\text{m}}$ (cylinder). This leads to allowable striping temperatures of 25^0C (plate) and 40^0C(cylinder). At the frequency of 6.25Hz, the allowable temperature ranges increase to 68^0C (plate) and 125^0C (cylinder). This illustrates how the lower frequency striping may be more damaging. Comparisons have been made when a general temperature time profile is used to stripe a

(a)   (b)
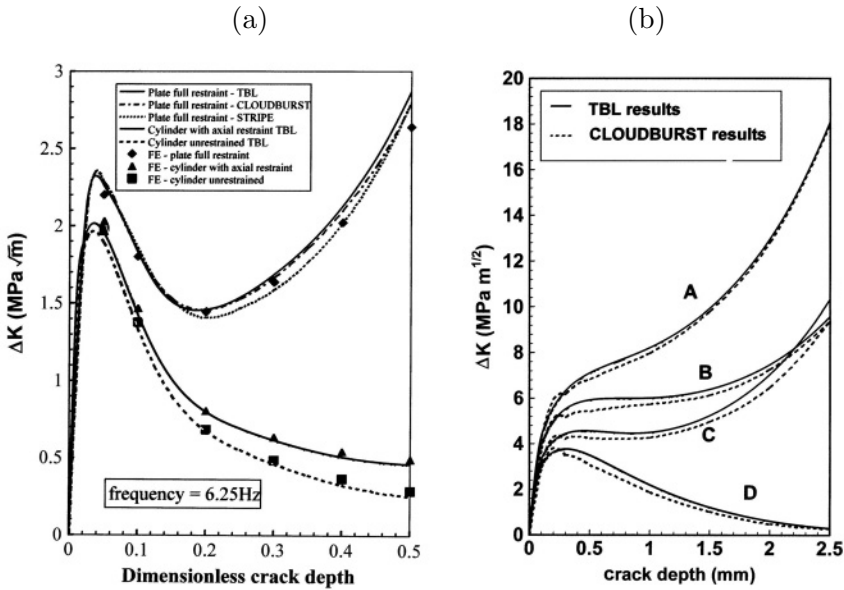
Figure 3 (a) The variation of the peak to peak stress intensity factor fluctuation with crack depth for the plate and cylinder. Comparison of TBL, CLOUDBURST, STRIPE and the finite element method. Striping frequency 6.25Hz.
(b) The variation of the maximum peak to peak stress intensity factor fluctuation with crack depth for the PFR shroud tube. (A) Full restraint (B) Restraint against bending only (C) Restraint against expansion/contraction (D) No restraint condition

LMFBR shroud tube [3],[5]. The thin shroud tube is a component in the above core region and, for illustration, is modelled as a plate. The material properties and other conditions used here are given in [3]. For the input to CLOUDBURST, a digitised recording of temperature fluctuations obtained from the AEA Technology 0.2 scale air model of the Dounreay prototype fast reactor above core region was used. For TBL, a white PSD was used with maximum frequency component of 10Hz. The results for maximum ΔK values as a function of crack depth are shown in Figure 3(b). TBL and CLOUDBURST results are shown for a variety of restraint conditions. Again, good agreement is obtained between the two methods.

6.   CONCLUSION

A review has been given of some of the methods available for the assessment of thermal striping damage. Good agreement between all of the methods has been demonstrated in the calculation of the SIF.

References

[1] Green, D (1985) *Crack growth under constant amplitude rapid thermal striping.*. Thermal Fatigue and Thermal Striping ASME Pressure Vessel and Piping Conference. New Orleans.

[2] Jones I S and Lewis M W J (1994) *A frequency response method for calculating stress intensity factors due to thermal striping loads.*, Fatigue and Fracture of Eng. Mater. and Struct. **17**(6) 709 - 720.

[3] Jones I S and Lewis M W J (1995) *The effect of various constraint conditions in the frequency response model of thermal striping.*, Fatigue and Fracture of Eng. Mater. and Struct. **18**(4) 489 - 502.

[4] Jones I S and Lewis M W J (1995) *The effect of spatial incoherence in surface temperature fluctuations on the stress intensity factor in thermal striping.*, Int. J. Pres. Ves. and Piping. **62**(3) 227 -247.

[5] Jones I S and Lewis M W J (1996) *An impulse response model for the prediction of thermal striping damage.*, Engineering Fracture Mechanics. **55**(5) 795 - 812.

[6] Jones I S (1996) *The frequency response model of thermal striping for cylindrical geometries.*, Fatigue and Fracture of Eng. Mater. and Struct. **20**(6) 871 - 882.

[7] Galvin S B J, Graham I D, Jones I S, and Rothwell G. (1996) *A comparison between the finite element and frequency response methods in the assessment of thermal striping damage.*, Int. J. Pres. Ves. and Piping. **74** 205 - 212.

[8] Jones I S (1999) *The application of a displacement controlled weight function for a single edge cracked plate to thermal fatigue damage assessment.*, Engineering Fracture Mechanics. **63** 325 - 343

[9] Bueckner H F. (1973) *Methods of Analysis of Solutions of Crack Problems.* Vol 1 (Edited by G. C. Sih.), Nordhoff International, Leyden. Page 239

[10] Jones I S (1998) *A wide range weight function for a single edge cracked geometry with clamped ends.*, Int J. Fracture. **89** 1 - 18.

[11] ABAQUS/Standard. Hibbit, Karlson and Sorensen, Providence, RI, USA

NEAR-TIP FIELDS OF MODE III STEADY-STATE CRACK PROPAGATION IN ELASTIC-PLASTIC STRAIN GRADIENT SOLIDS

Massimiliano Gei[1] and Enrico Radi[2]

[1] *Department of Mechanical and Structural Engineering,*
University of Trento, Italy
mgei@ing.unitn.it

[2] *Department of Engineering Sciences and Methods,*
University of Modena and Reggio Emilia, Italy
eradi@unimore.it

Keywords: Strain-gradient plasticity, mode-III crack propagation, elastic-plastic solids.

Abstract   The mode III asymptotic fields near a steadily propagating crack tip are investigated by employing the flow-theory version of the couple-stress strain gradient plasticity. Compared to classical plasticity results, an increase of the stress singularity is observed, also for small hardening. The performed asymptotic analysis can provide useful predictions about the increase of the traction level ahead of the crack tip due to the strain gradient effects, which have been found relevant and non negligible at the micron scale.

1.   INTRODUCTION

Strain gradient plasticity theories have been proposed in order to capture the size effect exhibited by ductile materials when subject to non-uniform plastic deformation at the micron scale [1]. A key point is the incorporation in the model of characteristic lengths which specify the range when strain gradients are dominant. These theories may also improve considerably the estimate of the stress traction level ahead of the crack tip required for the occurring of cleavage or atomic decohesion during crack growth processes, experimentally observed in ductile metals in [2]. Indeed, conventional plasticity theories are unable to predict such stress intensity which is of the order of ten times the tensile yield stress [3, 4].

In this note, the effects of strain rotation gradient on mode III crack propagation are investigated by performing an asymptotic analysis of the crack-tip fields, within the framework of the flow theory of couple-stress strain gradient plasticity [5]. By contrast with the Mode I and Mode II problems [6], a qualitative analysis shows that the leading order term of the velocity field turns out to be rotational. Moreover, it is found that the skew-symmetric stress field dominates the asymptotic crack-tip field. In particular, if the elastic strain gradients are kept sufficiently small, the singularity of the stress fields significantly increases with respect to the classical J$_2$-flow theory due only to the skew-symmetric stress term, with no need to invoke additional stretch gradient contributions.

2. CRACK GROWTH PROBLEM

The problem of a plane crack propagating at constant velocity V along a rectilinear path in an infinite medium under mode III condition in a couple-stress elastic-plastic medium is addressed. A cylindrical co-ordinate system (r, θ, x_3) moving with the crack tip towards the $\theta = 0$ direction is considered, where the x_3-axis coincides with the straight crack front. The condition of steady-state crack propagation yields the following time derivative rule, which holds for any scalar function φ

$$\dot{\varphi} = \frac{V}{r}(\varphi_{,\theta} \sin\theta - r\varphi_{,r} \cos\theta). \tag{2.1}$$

The considered constitutive model refers to the flow theory version of the strain gradient plasticity presented by Fleck and Hutchinson [5]. This model fits within the general framework of couple-stress theory and involves a single material length scale ℓ, which specifies the order of non-uniform deformation at which the effects of strain gradients become significant, and thus being generally small (about 4 μm for copper and 6 μm for nickel).

According to the couple-stress model [7, 8], a surface element of a body with unit area can transmit a force traction vector $\mathbf{p}$ and a couple-stress traction vector $\mathbf{q}$. These surface forces $\mathbf{p}$ and $\mathbf{q}$ can be expressed in terms of the non-symmetrical Cauchy stress tensor $\mathbf{t}$ and of the couple-stress tensor $\boldsymbol{\mu}$ as

$$\mathbf{p} = \mathbf{t}^T\mathbf{n} + \nabla\mu_{nn} \times \mathbf{n}, \quad \mathbf{q} = (\mathbf{I} - \mathbf{n}\otimes\mathbf{n})\boldsymbol{\mu}^T\mathbf{n}. \tag{2.2}$$

In the following the Cauchy stress $\mathbf{t}$ will be decomposed into the symmetric part $\boldsymbol{\sigma}$ and the skew-symmetric part $\boldsymbol{\tau}$.

For an antiplane problem, the non-vanishing stress and couple-stress components in polar coordinates are σ_{r3}, $\sigma_{\theta 3}$, τ_{r3}, $\tau_{\theta 3}$, $\mu_{r\theta}$, $\mu_{\theta r}$ and $\mu_{\theta\theta} = -\mu_{rr}$ (since $\boldsymbol{\mu}$ is a purely deviatoric tensor), and the equilibrium equations are

$$(rt_{r3})_{,r} + t_{\theta 3,\theta} = 0, \tag{2.3}$$

$$(r\mu_{rr})_{,r} + \mu_{\theta r,\theta} - \mu_{\theta\theta} + 2r\tau_{\theta 3} = 0, \quad (r\mu_{r\theta})_{,r} + \mu_{\theta\theta,\theta} + \mu_{\theta r} - 2r\tau_{r3} = 0. \quad (2.4)$$

Moreover, the only non-vanishing component of the velocity vector $\mathbf{v}$ is v_3. Therefore, the kinematic compatibility conditions for the strain and deformation curvature rate tensors, respectively $\dot{\boldsymbol{\varepsilon}}$ and $\dot{\boldsymbol{\chi}}$, namely $\dot{\boldsymbol{\varepsilon}} = (\nabla\mathbf{v} + \nabla\mathbf{v}^T)/2$ and $\dot{\boldsymbol{\chi}} = \text{curl}\,\dot{\boldsymbol{\varepsilon}}$, specialise in

$$\dot{\varepsilon}_{r3} = v_{3,r}/2, \quad r\dot{\varepsilon}_{\theta 3} = v_{3,\theta}/2, \quad (2.5)$$

$$\dot{\chi}_{rr} = \dot{\varepsilon}_{3\theta,r}, \quad \dot{\chi}_{r\theta} = \dot{\varepsilon}_{3\theta,\theta} + \dot{\varepsilon}_{3r}/r, \quad \dot{\chi}_{\theta r} = -\dot{\varepsilon}_{3r,r}, \quad (2.6)$$

where $\dot{\chi}_{\theta\theta} = -\dot{\chi}_{rr}$.

Within the context of small deformations incremental theory, the total strain rate $\dot{\boldsymbol{\varepsilon}}$ is the sum of elastic $\dot{\boldsymbol{\varepsilon}}^e$ and plastic $\dot{\boldsymbol{\varepsilon}}^p$ parts. Similarly, the total deformation curvature rate $\dot{\boldsymbol{\chi}}$ is the sum of elastic $\dot{\boldsymbol{\chi}}^e$ and plastic $\dot{\boldsymbol{\chi}}^p$ contributions. Both elastic parts are related to stress and couple-stress rates through the incremental relations

$$\dot{\boldsymbol{\varepsilon}}^e = \frac{1}{E}[(1+\nu)\dot{\boldsymbol{\sigma}} - \nu(\text{tr}\dot{\boldsymbol{\sigma}})\,\mathbf{I}], \quad \dot{\boldsymbol{\chi}}^{eT} = \frac{1+\nu}{E\,\ell_e^2}\dot{\boldsymbol{\mu}}, \quad (2.7)$$

where E denotes the elastic Young modulus, ν the Poisson ratio and ℓ_e is the elastic length scale introduced in [5] in order to divide the deformation curvature rate tensor into its elastic part $\dot{\boldsymbol{\chi}}^e$ and plastic part $\dot{\boldsymbol{\chi}}^p$, being $\ell_e < \ell$.

The fundamental relationships of the constitutive model are briefly summarised below.

- Yield condition

$$f(\Sigma, Y) = \Sigma - Y = 0, \quad (2.8)$$

  where Σ is the overall effective stress defined as

$$\Sigma^2 = 3\,(\boldsymbol{\sigma}_{\text{dev}} \cdot \boldsymbol{\sigma}_{\text{dev}} + \ell^{-2}\boldsymbol{\mu} \cdot \boldsymbol{\mu})/2, \quad (2.9)$$

  and Y denotes the uniaxial flow stress defining isotropic hardening behaviour. Linear isotropic hardening is introduced below.

- Associative flow rule

$$\dot{\boldsymbol{\varepsilon}}^p = \Lambda\frac{\partial f}{\partial\boldsymbol{\sigma}} = \frac{3\Lambda}{2\,\Sigma}\,\boldsymbol{\sigma}_{\text{dev}}, \quad \dot{\boldsymbol{\chi}}^{pT} = \Lambda\frac{\partial f}{\partial\boldsymbol{\mu}} = \frac{3\Lambda}{2\,\Sigma\,\ell^2}\,\boldsymbol{\mu}, \quad (2.10)$$

  where Λ is the plastic multiplier.

- Linear isotropic hardening rule

$$\dot{Y} = \Lambda H, \quad (2.11)$$

where $H = \alpha E/(1 - \alpha)$ is the hardening modulus and $\alpha = E_t/E$ $(0 < \alpha < 1)$ is the ratio between the tangent modulus and the Young modulus for a bilinear stress-strain curve obtained by a uniaxial tension test.

- Prager consistency condition

$$\dot{f} = 0 \quad \text{or equivalently} \quad \dot{\Sigma} = \dot{Y}, \tag{2.12}$$

which gives the non-negative plastic multiplier Λ as

$$\Lambda = \begin{cases} \langle \dot{\Sigma} \rangle / H & \text{if} \quad f(\Sigma, Y) = 0 \\ 0 & \text{if} \quad f(\Sigma, Y) < 0, \end{cases} \tag{2.13}$$

where $\langle x \rangle = (|x| + x)/2$ and

$$\dot{\Sigma} = 3 \left(\boldsymbol{\sigma}_{\text{dev}} \cdot \dot{\boldsymbol{\sigma}} + \ell^{-2} \boldsymbol{\mu} \cdot \dot{\boldsymbol{\mu}} \right) / (2\,\Sigma). \tag{2.14}$$

From (2.7) the elastic-plastic incremental constitutive equations for the stress and couple-stress tensors, $\boldsymbol{\sigma}$ and $\boldsymbol{\mu}$, turn out to be

$$\dot{\boldsymbol{\varepsilon}} = \frac{1}{E} \left[(1 + \nu)\,\dot{\boldsymbol{\sigma}} - \nu (\text{tr}\dot{\boldsymbol{\sigma}})\,\mathbf{I} \right] + \frac{3}{2\,\Sigma}\,\Lambda\,\boldsymbol{\sigma}_{\text{dev}}, \tag{2.15}$$

$$\ell^2 \dot{\boldsymbol{\chi}}^T = \frac{1 + \nu}{E\,\xi^2}\,\dot{\boldsymbol{\mu}} + \frac{3}{2\,\Sigma}\,\Lambda\,\boldsymbol{\mu}, \tag{2.16}$$

where $\xi = \ell_e/\ell < 1$ is a non-dimensional parameter. Equations (2.15)-(2.16) hold when the yield condition (2.8) is satisfied. Otherwise, the incremental constitutive relationship reduces to the couple-stress isotropic elasticity, recovered when $\Lambda = 0$. Note that strain gradient effects occur also for a purely elastic response. However, their magnitude may be made arbitrarily small by choosing a sufficiently small ξ. Finally, it can be observed that the resulting constitutive equations (2.15)-(2.16) represent a generalization of the widely used J_2-flow theory of plasticity, and reduce to that model when the strain gradients are vanishing small.

3.   ASYMPTOTIC CRACK-TIP FIELDS

Equations (2.3)-(2.6) together with the constitutive incremental equations (2.11), (2.15) and (2.16) form a system of first order PDEs that governs the problem of mode III crack propagation. The solution is sought in a separable variable form, by considering the most singular terms in the asymptotic expansion of near-tip fields. In particular, within the zone of radius ℓ about the crack tip, namely, where strain gradients are supposed

to be dominant, the velocity, stress and couple-stress asymptotic fields are assumed in the following form

$$v_3(r,\theta) = V\left(\frac{r}{R}\right)^s w(\theta), \qquad \sigma_{\alpha 3}(r,\theta) = E\left(\frac{r}{R}\right)^s s_\alpha(\theta),$$

$$\tau_{\alpha 3}(r,\theta) = E\frac{\ell^2}{r^2}\left(\frac{r}{R}\right)^s t_\alpha(\theta), \quad \mu_{\alpha\beta}(r,\theta) = E\frac{\ell^2}{r}\left(\frac{r}{R}\right)^s M_{\alpha\beta}(\theta),$$

(3.1)

where $w(\theta)$, $s_\alpha(\theta)$, $t_\alpha(\theta)$, $M_{\alpha\beta}(\theta)$ are scalar functions and the Greek indices α and β stand for r and θ. The exponent s defines the radial dependence of the symmetric stress and velocity fields. Moreover, R denotes a characteristic dimension of the plastic zone which defines the amplitude of the leading order asymptotic fields. Note that the condition $M_{\theta\theta} = -M_{rr}$ holds true since $\boldsymbol{\mu}$, and thus $\mathbf{M}$, must be deviatoric. According to the stress and couple-stress crack-tip fields $(3.1)_{1,4}$ the overall effective stress and flow stress fields near the crack tip assume the following asymptotic representations

$$\Sigma(r,\theta) = E\frac{\ell}{r}\left(\frac{r}{R}\right)^s \Gamma(\theta), \quad Y(r,\theta) = E\frac{\ell}{r}\left(\frac{r}{R}\right)^s \gamma(\theta), \qquad (3.2)$$

respectively. From (2.9) and $(3.1)_{2,4}$ the function Γ may be defined as

$$\Gamma = (1.5\,\mathbf{M}\cdot\mathbf{M})^{1/2}, \qquad (3.3)$$

and thus the leading asymptotic term of the effective stress is given by the sole contribution of the couple-stress field.

By using the steady-state derivative (2.1), the rates of the fields $\boldsymbol{\sigma}$, $\boldsymbol{\mu}$ and Y in $(3.1)_{2,4}$ and $(3.2)_2$ can be written in the form

$$\dot\sigma_{\alpha 3}(r,\theta) = E\frac{V}{r}\left(\frac{r}{R}\right)^s h_\alpha(\theta), \quad \dot\mu_{\alpha\beta}(r,\theta) = EV\frac{\ell^2}{r^2}\left(\frac{r}{R}\right)^s H_{\alpha\beta}(\theta), \quad (3.4)$$

$$\dot Y(r,\theta) = EV\frac{\ell}{r^2}\left(\frac{r}{R}\right)^s \kappa(\theta). \qquad (3.5)$$

The constitutive relations (2.15)-(2.16) imply that the strain and deformation curvature rates must have the same radial dependence assumed for the stress and couple-stress rates in (3.4). Therefore, the strain and deformation curvature rates assume the following asymptotic representations

$$\dot\varepsilon_{\alpha 3}(r,\theta) = \frac{V}{r}\left(\frac{r}{R}\right)^s d_\alpha(\theta), \quad \dot\chi_{\alpha\beta}(r,\theta) = \frac{V}{r^2}\left(\frac{r}{R}\right)^s X_{\alpha\beta}(\theta). \qquad (3.6)$$

By substituting the above expressions in the governing equations a system of nine first order ODEs is attained. Appropriate boundary conditions

may be obtained from the skew-symmetric character of the problem along the plane $\theta = 0$, and by imposing null tractions at the crack flanks through a specialisation of (2.2), namely

$$t_{\theta 3} + \mu_{\theta\theta,r}/2 = 0, \quad \mu_{\theta r} = 0. \tag{3.7}$$

An eigenvalue problem is therefore formulated in term of the exponent s. Details of the procedure are given in [6, 9].

4.   RESULTS

The results here reported are for $\nu = 0.3$. The variation of the exponent s with the ratio $\xi = \ell_e/\ell$ is plotted in Fig. 1a for $\alpha = 0.01, 0.1, 0.45$. For the same crack growth problem the classical J_2-flow theory predicts an extremely weak stress singularity [4], $s \sim -\alpha^{0.5}$. The results here obtained for couple-stress elastoplasticity show that the exponent s of the stress fields ranges between 0.5 and 0.94, (depending on α) so that, even if the symmetric stress components are not singular at the crack tip, the couple-stress and the skew-symmetric stress fields display strong singularities $(3.1)_{2,4}$, respectively of order $s - 1$ and $s - 2$. In particular, when the ratio ξ is reduced, the exponent s tends to decrease and for vanishing elastic characteristic length the exponent of the stress fields s approaches the value 0.5, correspondingly the couple-stress and the skew-symmetric stress fields display the singularities -0.5 and -1.5, respectively. As ξ tends to zero the limit value for s is found to be almost independent of the hardening coefficient α, so that the strength of the stress singularity increases with respect to the classical J_2-flow theory also for low hardening, mainly due to the contribution of the non-symmetric stress components. Although the skew-symmetric stresses dominate the asymptotic solution, only the couple-stress field contributes to the effective stress Σ and to the strain-energy density, so that the high stress singularity does not violate the boundedness of the flux of energy toward the crack tip.

The variation of the elastic unloading and reloading angles, θ_1 and θ_2, with ξ is then reported in Fig. 1b. Sectors $0 < \theta < \theta_1$ and – possible– $\theta_2 < \theta < \pi$ are plastic zones, while in the intermediate region $\theta_1 < \theta < \min\{\theta_2, \pi\}$, elastic unloading occurs. As ξ tends to vanish, an elastic unloading sector starts at $\theta_1 = 95.6°$ and extends up to the crack flanks for each α. For $\xi = 0.1, 0.35$ a plastic reloading sector appears for $\alpha = 0.01, 0.1$ respectively and the elastic unloading sector rapidly reduces in size and tends to vanish for $\xi = 0.18, 0.6$ for the two cases. For higher values of ξ the crack-tip zone is fully plastic. As noted in [5], the considered constitutive model may give reasonable predictions for small values of ξ, namely $\xi \ll 1$, in view of the fact that the magnitude of the couple stress in the elastic sector turns out to be proportional to ξ. As the strain gra-
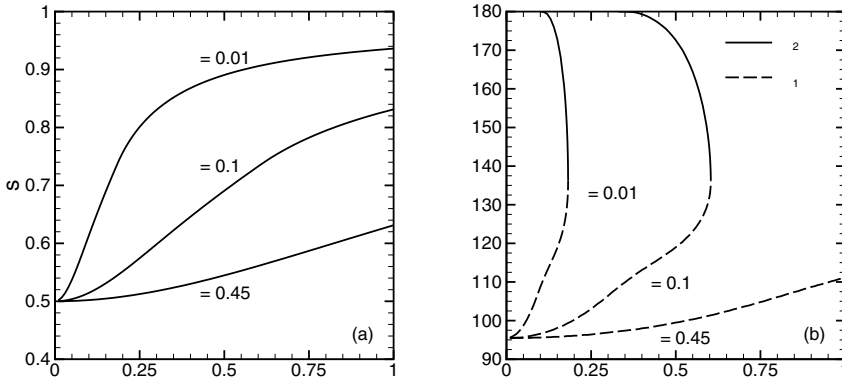
Figure 1   Exponent of the stress fields (a), elastic unloading and plastic reloading angles (b) as functions of ratio ξ, for $\nu = 0.3$.

dient effects are associated with the occurrence of geometrically necessary dislocations, they scarcely influence the elastic behaviour. Therefore, the results obtained for small values of ξ are expected to be more realistic.

In Fig. 2 the angular distributions of the asymptotic crack-tip fields for $\alpha = 0.01$, which are meaningful for $r < \ell$, are plotted for $\xi = 0.15$ ($\theta_1 = 118.9°, \theta_2 = 172.8°$). All functions are normalised by condition $s_\theta(0) = 1$. In detail, Fig. 2a shows that the symmetric stress components s_r and s_θ largely increase within the elastic unloading sector and are almost vanishing within the plastic loading sector. The angular variation of the out-of-plane velocity is also reported in Fig. 2a. In Fig. 2b the angular variations of the couple-stress field $\mathbf{M}$ and the current flow stress γ are shown. Note that the current flow stress, which is given by the single contribution of the couple-stress field, rapidly increases at the crack flanks as is usual for crack propagation problems in elastic-plastic materials displaying linear isotropic hardening [4]. The angular variations of the skew-symmetric stress components are plotted in Fig. 2c. Note that the shear stress t_θ ahead of the crack tip is negative and, thus, opposite to its counterpart in the mode III solution for classical J_2-flow theory [4] and also the radial shear stress component t_r displays negative values in a small sector ahead of the crack tip. The reason for the switch in the shear directions is unclear but certainly related to the strain gradient effects for the antiplane problem, since it agrees with the findings of Zhang et al. [10] obtained for a stationary mode III crack in couple-stress elasticity. Finally,
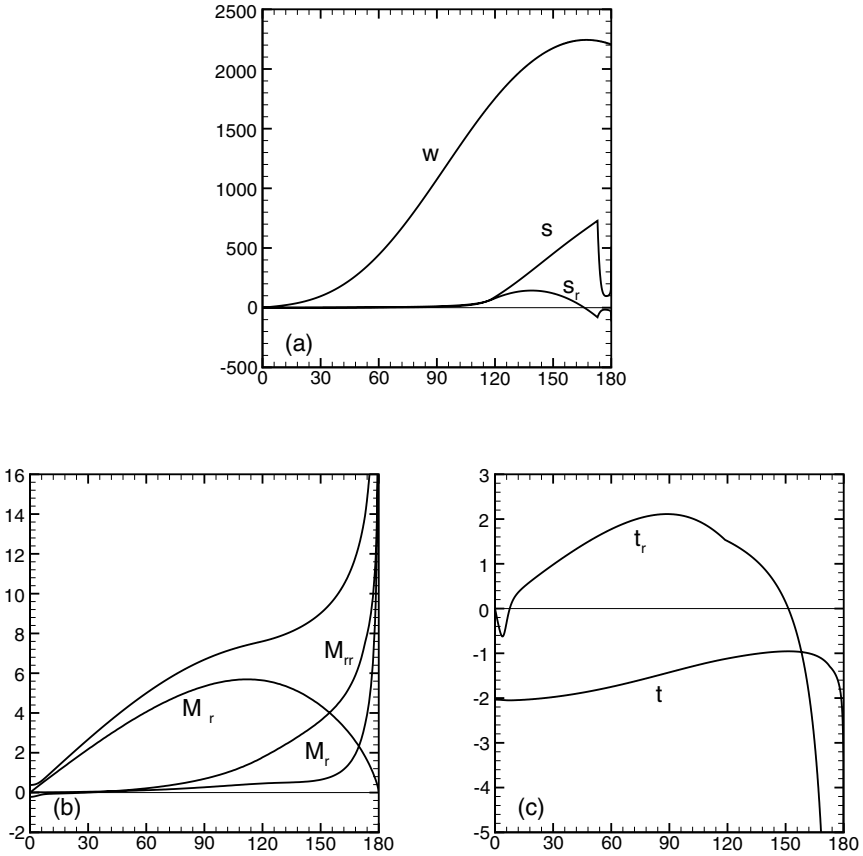
Figure 2 Angular variations of the asymptotic crack-tip fields of velocity and symmetric stress (*a*), couple-stress (*b*) and skew-symmetric stress (*c*) for $\alpha = 0.01$, $\xi = 0.15$ and $\nu = 0.3$.

note that t_θ and M_{rr} tend to large but opposite values on the crack faces, as required by $(3.7)_1$.

In conclusion, the obtained results show that the use of the strain gradient plasticity model for the analysis of the stress field in the vicinity of a propagating crack tip gives more realistic predictions on the level of traction ahead of the crack tip, allowing the detailed mechanisms by which fracture may grow and propagate in ductile metals to be understood in more depth.

Acknowledgments

References

[1] Hutchinson, J.W. (2000) *Plasticity at the micron scale, Int. J. Solids Structures* **37**, 225–238.

[2] Elssner, G., Korn D. and Ruehle M. (1994) *The influence of interface impurities on fracture energy of UHV diffusion bonded metal-ceramic bicrystals*, Scripta Metall. Mater. **31**, 1037–1042.

[3] Drugan, W.J., Rice, J.R. and Sham, T.L. (1982) *Asymptotic analysis of growing plane strain tensile cracks in elastic-ideally plastic solids*, J. Mech. Phys. Solids **30**, 447–473.

[4] Ponte Castañeda, P. (1987) *Asymptotic fields in steady crack growth with linear strain-hardening, J. Mech. Phys. Solids* **35**, 227–268.

[5] Fleck, N.A. and Hutchinson, J.W. (1993) *A phenomenological theory for strain gradient effects in plasticity, J. Mech. Phys. Solids* **41**, 1825–1857.

[6] Radi, E. (2003) *Strain-gradient effects on steady-state crack growth in linear hardening materials, J. Mech. Phys. Solids* **51**, 547–577.

[7] Toupin, R.A. (1962) *Elastic materials with couple-stresses, Arch. Rat. Mech. Analysis* **11**, 385–414.

[8] Mindlin, R.D. and Tiersten, H.F. (1962) *Effects of couple-stresses in linear elasticity, Arch. Rat. Mech. Analysis* **11**, 415–448.

[9] Radi, E. and Gei, M. (2002) *Mode III crack growth in linear hardening materials with strain gradient effects*, Submitted.

[10] Zhang, L., Huang, Y., Chen, J.Y. and Hwang, K.C. (1998) *The mode III full-field solution in elastic materials with strain gradient effects*, Int. J. Fract. **92**, 325–348.

MODE III INTERFACE CRACK LYING AT THIN NONHOMOGENEOUS ANISOTROPIC INTERFACE. ASYMPTOTICS NEAR THE CRACK TIP

Gennady S. Mishuris

Department of Mathematics, Rzeszów University of Technology,
W. Pola 2, 35-959, Rzeszów, Poland

miszuris@prz.rzeszow.pl

Keywords: Nonclassical transmission conditions, interface crack, singularities

Abstract   Mode III problem for the interface crack tip lying at various nonideal (imperfect) interfaces in dissimilar elastic body is investigated. Nonclassical transmission conditions described by features of thin nonhomogeneous anisotropic elastic layer situated between the matched materials are discussed. For this aim, an accurate asymptotic technique is applied. Asymptoptic expansions of elastic solutions in three different cases (soft, stiff and comparable in values interphases) are obtained. It is shown that the asymptotic approximation depends essentially on types of the interface as well as its local geometrical and mechanical properties.

Introduction

Interfacial crack problem is the classical problem of fracture mechanics and has been investigated by many researchers (e.g. [1, 2, 3, 4]). Within the ideal (perfect) interface approach the vectors of displacements and tractions are assumed to be continuous across the interface of zero thickness. In particular, it has been shown that the classic stress singularity appears under Mode III condition, while such physical inconsistencies as stress oscillation and interpenetration of the crack surfaces near the crack tip present in elastic solutions for the plane problems. Both the effects, however, disappear if a contact zone is introduced in the model (e.g. [3, 4]). Nevertheless, the classical interface model is not able to incorporate in the analysis any features of real interfaces at least at stage of finding distribution of the

displacement and stress fields. In order to take into account geometrical and mechanical properties of the interface, it can be considered as an additional structure with a crack situated within the intermediate zone or lying at interphase boundary (see a review in [5]). Other approach to investigate a nonideal (imperfect) interface consists of modelling the interface by non-classical transmission conditions. For this purpose, various techniques can be used. First, it is possible to directly choose a phenomenological relationship between the displacement and stress fields having some information about interphase properties. Then parameters of the interfacial model have to be found experimentally. Other way is to evaluate the transmission conditions as a result of passage to the limit with respect to the interphase thickness. However, from our best knowledge, the only first attempts have been independently done in [6, 7, 8] to investigate asymptotic behaviour of elastic field near the tip of the interface crack lying at imperfect interfaces.

1.   TRANSMISSION CONDITIONS

In this section we briefly discuss evaluation of nonclassical bimaterial transmission conditions by asymptotic analysis. Here and everywhere further $0 < \varepsilon \ll 1$ is a small dimensionless parameter.
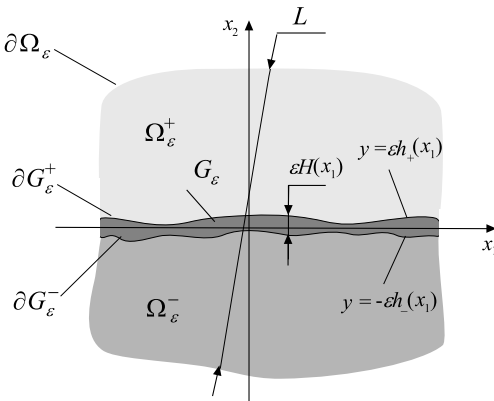
Figure 1 Dissimilar elastic solid Ω_ε containing a thin slightly curved and weakly anisotropic elastic intermediate layer G_ε of thickness εH.

Let us consider a bimaterial structure Ω_ε consisted of two elastic parts $\Omega_\varepsilon^\pm$ matched by a thin nonhomogeneous anisotropic elastic layer $G_\varepsilon = \{(x_1, x_2), \; x_1 \in (a, b), -\varepsilon h_-(x_1) < x_2 < \varepsilon h_+(x_1)\}$ (see Figure 1). The shear moduli of the bonded materials and the anisotropic interphase are $\mu_\pm$ and $\mu_1(\mathbf{x})$, $\mu_2(\mathbf{x})$, respectively. The following boundary value problem can be formulated for the Mode III deformation.

In the corresponding domains equations:

$$\Delta u^\pm = 0, \;\; \mathbf{x} \in \Omega_\varepsilon^\pm, \qquad \nabla \cdot [\mu_1 D_1, \mu_2 D_2] u = 0, \;\; \mathbf{x} \in G_\varepsilon, \qquad (1.1)$$

have to be satisfied, where D_j is the derivative along the variable x_j.

Along $\partial\Omega_\varepsilon^\pm$ some boundary conditions are given:

$$B^\pm u^\pm = 0, \quad \mathbf{x} \in \partial\Omega_\varepsilon^\pm. \tag{1.2}$$

Operator $B^\pm$ can define Dirichlet, Neumann or mixed boundary conditions. Finally, along the bimaterial interfaces $\partial G_\varepsilon^\pm$ the perfect bonding are assumed:

$$\mathbf{B}[u^\pm, u] = 0, \quad \mathbf{x} \in \partial G_\varepsilon^\pm, \tag{1.3}$$

where the components of the classic transmission operator $\mathbf{B}$ are

$$B_1[u^\pm, u] \equiv u^\pm - u, \qquad B_2[u^\pm, u] \equiv \sigma_{nz}^\pm - \sigma_{nz}. \tag{1.4}$$

For geometrical and mechanical parameters of the problem we assume that $\mu_j \in C^\infty(G_\varepsilon)$, $h_\pm \in C^\infty(a,b)$ are positive functions and:

$$H/L = O(1), \quad h'_\pm = O(1), \quad \mu_1/\mu_2 = O(1), \quad \mu_+/\mu_- = O(1), \tag{1.5}$$

with respect to the small parameter ε. Here $H(x_1) = h_+(x_1) + h_-(x_1)$ and L is a characteristic size of the dissimilar body. Let us note that estimates $(1.5)_{1-3}$ mean, in fact, that we consider, in a specific sense, thin slightly curved and weakly anisotropic elastic layer G_ε. Three different cases can be considered:

$$\mu_j/\mu_\pm = O(\varepsilon^k), \quad k = -1, 0, 1, \tag{1.6}$$

where $k = -1$ corresponds to the soft interphase, $k = 1$ defines the stiff one and in case $k = 0$ all material parameters are comparable in value.

Following for the asymptotic procedure [9] let us rescale the problem by introducing a new variable ξ instead of x_2 in the layer G_ε:

$$\xi = \big(2x_2 + \varepsilon[h_-(x_1) - h_+(x_1)]\big)\{2\varepsilon H(x_1)\}^{-1}, \quad \xi \in (-1/2, 1/2). \tag{1.7}$$

Then equation $(1.1)_2$ and transmission conditions (1.3) can be rewritten in term of a new function $w(x_1, \xi) = u(\mathbf{x})$, respectively:

$$P(x_1, \xi, D)\big(\nu_1 P(x_1, \xi, D)\big)w + \{\varepsilon H(x_1)\}^{-2}D_\xi\big(\nu_2 D_\xi\big)w = 0 \tag{1.8}$$
$$w(x_1, \pm 1/2) = u^\pm(x_1, \pm\varepsilon h_\pm(x_1)), \tag{1.9}$$

$$\varepsilon^k \mathbf{n}^\pm \cdot [\nu_1 P(x_1, \xi, D), \frac{\nu_2}{\varepsilon H}D_\xi]w(x_1, \pm 1/2) = \mu_\pm \mathbf{n}^\pm \cdot \nabla u^\pm(x_1, \pm\varepsilon h_\pm(x_1)).$$

Here we have also introduced the notations:

$$\mu_j(\mathbf{x}) = \varepsilon^k \nu_j(x_1, \xi), \quad \mathbf{n}^\pm(x_1) = \big\{1 + [\varepsilon h'_\pm(x_1)]^2\big\}^{-1/2}\big[-\varepsilon h'_\pm(x_1), \pm 1\big],$$
$$\tag{1.10}$$
$$P(x_1, \xi, D) = D_1 + \big[h'_-(x_1) - h'_+(x_1) - 2\xi H'(x_1)\big]\{2H(x_1)\}^{-1}D_\xi.$$

Finally, representation of the solution in each domain can be sought in form of series with respect to the small parameter ε:

$$w(\varepsilon, x_1, \xi) = \sum_{j=0}^{\infty} \varepsilon^j w_j(x_1, \xi), \quad u^{\pm}(\varepsilon, \mathbf{x}) = \sum_{j=0}^{\infty} \varepsilon^j u_j^{\pm}(\mathbf{x}). \qquad (1.11)$$

Then sequential terms in the representation $(1.11)_1$ are obtained from equation (1.8) by simple integration $(w_{-2} = w_{-1} \equiv 0)$:

$$w_j(x_1, \xi) = c_j(x_1) \int_{-1/2}^{\xi} \frac{dt}{\nu_2(x_1, t)} + d_j(x_1) -$$
$$\int_{-1/2}^{\xi} \frac{H^2(x_1)dt}{\nu_2(x_1, t)} \int_{-1/2}^{t} P(x_1, y, D) \Big(\nu_1(x_1, y) P(x_1, y, D) \Big) w_{j-2}(x_1, y) dy. \qquad (1.12)$$

Unknown functions c_j and d_j have to be chosen in such a way to satisfy the transmission conditions (1.9) and three possibilities (1.6) have to be considered separately. However, the cases $k = 1, 0$ have been considered in [9], so we concentrate our interest on the stiff interface $(k = -1)$ only. Because in this case the left-hand side of transmission condition $(1.9)_2$ exhibits the order $O(\varepsilon^{-2})$, one can conclude from (1.12) that:

$$D_\xi w_j(x_1, \pm 1/2) = 0 \quad \Rightarrow \quad w_j(x_1, \xi) = d_j(x_1), \quad j = 0, 1. \qquad (1.13)$$

As a result, a solvability condition for the first external boundary value problem for the functions $u_0^{\pm}(\mathbf{x})$ in domains $\Omega_0^{\pm}$ follows from $(1.9)_1$:

$$u_0^+(x_1, 0) = u_0^-(x_1, 0) = w_0(x_1) \quad \Rightarrow \quad [u_0]_{x_2=0} = 0. \qquad (1.14)$$

To obtain the second solvability condition for functions $u_0^{\pm}(\mathbf{x})$ let us compare the terms of $O(1)$ in the transmission condition $(1.9)_2$:

$$\mu_{\pm} D_2 u_0^{\pm}(x_1, 0) = \nu_2 H^{-1} D_\xi w_2(x_1, \xi) \mp h'_{\pm} \nu_1 D_1 w_0(x_1), \quad \xi = \pm 1/2, \quad (1.15)$$

where function $w_2(x_1, \xi)$ is defined in (1.12) by the known function $w_0(x_1)$. Eliminating from two equations (1.15) the only unknown function $c_2(x_1)$ one can show that:

$$[\mu D_2 u_0]_{x_2=0} + H(x_1) \int_{-1/2}^{1/2} P(x_1, \xi, D) \nu_1(x_1, \xi) D_1 w_0(x_1) d\xi +$$
$$\Big(h'_+(x_1) \nu_1(x_1, 1/2) + h'_-(x_1) \nu_1(x_1, -1/2) \Big) D_1 w_0(x_1) = 0.$$

Finally, after some algebra this equation can be simplified to obtain the second sought-for transmission condition along the interface $x_2 = 0$:

$$[\mu D_2 u_0]_{|x_2=0} + D_1 \big(\tau^*(x_1) D_1 \big) u_0^{\pm}(x_1, 0) = 0, \qquad (1.16)$$

which together with $(1.14)_2$ constitutes corresponding transmission conditions for the stiff nonideal interface. For a comparison, in case of the soft nonideal interface ($k = 1$ in equation $(1.10)_1$), respective nonclassical transmission conditions take the following form:

$$[\mu D_2 u_0]_{|x_2=0} = 0, \quad [u_0]_{|x_2=0} - \tau_*(x_1)\mu_{\pm}D_2u_0^{\pm}(x_1,0) = 0. \qquad (1.17)$$

Here functions $\tau_*(x_1)$ and $\tau^*(x_1)$ are defined by equations:

$$\tau^* = H(x_1) \int\limits_{-1/2}^{1/2} \nu_1(x_1,\xi)d\xi, \quad \tau_* = H(x_1) \int\limits_{-1/2}^{1/2} \nu_2^{-1}(x_1,\xi)d\xi. \qquad (1.18)$$

In case when all materials constants are comparable in value ($k = 0$) the classic transmission conditions with the operator from (1.3)-(1.4) can be justified. If the shear moduli of the interphase are constant as well as it thickness then the functions $\tau_*(x_1)$ and $\tau^*(x_1)$ are also constants. It is interesting to note that in case when the coefficients τ_* and τ^* in (1.16), $(1.17)_2$ vanish, both the respective transmission conditions converge to the classical one. On the other hand, when the coefficients become very large in value, the transmission conditions change to those corresponding to the rigid interface and to the free boundary, respectively. However, all mentioned passages to limit provide singular perturbations in the problems.

Further we are going to investigate solutions of the interface crack problems for the stiff and soft imperfect interfaces. For this purpose, we need to know the behaviour of the functions $\tau_*(x_1)$ and $\tau^*(x_1)$ near the crack tip. However, such information is not always available a priori. When specific imperfect interface problem is under consideration, behaviour of the functions near the crack tip depends on two factors. Because surfaces of the matched materials are not identical and contain various roughnesses and asperities, the interphase thickness can vary from its maximal value even to zero. On the other hand, mechanical properties of the intermediate material can change during the process, for example, due to a damage accumulation near the crack tip. To analyze a sufficiently general case we assume that local behaviour of the functions (1.18) near the crack has a power low character:

$$\tau^*(x_1) = \tau^* x_1^{\beta}, \quad \tau_*(x_1) = \tau_* x_1^{\alpha}. \qquad (1.19)$$

Actually, the cases $\alpha, \beta \geq 0$ have been considered in papers [6, 7] and for the soft interface in particular case $\alpha = 0$ in [13]. However, it is important to investigate also negative values of the exponents. In fact, let us assume that the soft nonideal interface is under consideration and due to the damage accumulation the shear moduli of the interface decrease and tend to zero

near the crack tip. From $(1.18)_2$ and $(1.19)_2$ it immediately follows that $\alpha < 0$. On the other hand, if one can consider the stiff nonideal interface then condition (1.6) with $k = -1$ has to be satisfied or that is equivalent: $\mu_\pm/\mu_j = O(\varepsilon)$. Let us note that condition $\mu_j(x_1) \to \infty$ as $x_1 \to 0$ is compatible with the mentioned necessary assumption and gives $\tau_*(x_1) \to \infty$ as $x_1 \to 0$ ($\beta < 0$ in $(1.19)_1$).

2.   ASYMPTOTICS NEAR THE CRACK TIP

Second part of the paper deals with investigation of asymptotic behaviour of the solution for the interface crack lying at the nonideal interfaces discussed above. For this purpose we need to solve respective modelling problems in the bimaterial plane with semi-infinite interfacial crack. Both mentioned stiff and soft nonideal interface models will be considered independently.
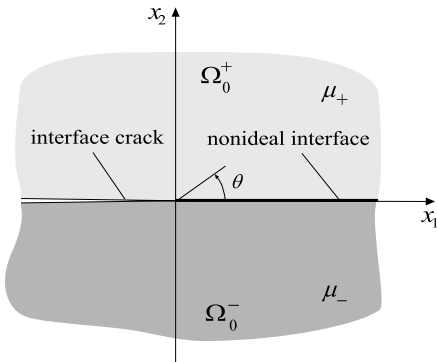

Figure 2 Semi-infinite interface crack ($x_2 = 0, x_1 < 0$) situated at the imperfect interface ($x_2 = 0, x_1 > 0$) between two different elastic materials in the infinite plane

We will find two harmonic functions $u^\pm$ in respective half-planes $\Omega_0^\pm$. Along the crack surfaces ($x_2 = 0, x_1 < 0$) tractions are given:

$$\mu_\pm D_2 u^\pm_{|x_2=0} = \pm g_\pm(-x_1), \quad -\infty < x_1 < 0. \tag{2.1}$$

Such conditions correspond to the initial stage of the crack propagation. They can always be used to model slow quasi static crack growth with complete destruction of the interface at the crack tip. As usual we assume that the functions $g_\pm$ have a compact support and

$$\int_0^\infty g_+(r)dr = \int_0^\infty g_-(r)dr. \tag{2.2}$$

The sought-for functions $u^\pm$ have to satisfy additional conditions at singular points with unknown constants $\omega_0, \omega_\infty \geq 0$, $\gamma_0, \gamma_\infty > 0$:

$$u^\pm = \begin{cases} O(r^{\omega_0}), & r \to 0, \\ O(r^{-\omega_\infty}), & r \to \infty, \end{cases} \quad \nabla u^\pm = \begin{cases} O(r^{\gamma_0-1}), & r \to 0, \\ O(r^{-\gamma_\infty-1}), & r \to \infty. \end{cases} \tag{2.3}$$

Here the second estimate guarantees a finite elastic energy, while the first one makes us possible to choose a unique solution of the problem.

2.1.   SOFT IMPERFECT INTERFACE

To complete the problem (2.1)-(2.3) we assume that transmission conditions (1.17) are satisfied on the crack line ahead ($x_2 = 0, x_1 > 0$) with function τ_* from (1.19)$_2$. Then applying Mellin transform technique according to [6] one obtains a functional equation:

$$\bar{\tau}_* F_*(s + \alpha - 1) - \frac{1 + \mu_*}{s\mu_*} F_*(s) \cot \pi s = -\frac{\tilde{g}_+(s) + \mu_* \tilde{g}_-(s)}{s\mu_* \sin \pi s}, \quad (2.4)$$

in a strip: $\max\{-\gamma_0 + 1 - \alpha, -\omega_0\} < \mathrm{Re}s < \min\{\gamma_\infty + 1 - \alpha, \omega_\infty\}$. Here $F_*(s) = \tilde{\sigma}_{\theta z}^\pm(s, 0)$ is the Mellin transform of the traction, $\sigma_{\theta z} = \mu u'_\theta$, along the crack line ahead. Due to the assumptions (2.3), $F_*(s)$ is analytic in the strip $-\gamma_0 < \mathrm{Re}s < \gamma_\infty$ and satisfies an additional condition $F_*(0) = \tilde{g}_\pm(0)$. Here we have introduced parameters: $\bar{\tau}_* = \tau_*\mu_-$, $\mu_* = \mu_+/\mu_-$.

When function $F_*(s)$ is known, asymptotics of the solution near the crack tip will be found from the inverse Mellin transform:

$$u^\pm(r, \theta) = \frac{\pm 1}{2\pi i \mu_\pm} \int_{-i\infty+\delta}^{i\infty+\delta} \left[F_*(s) \cos[s(\pi \mp \theta)] - \tilde{g}_\pm(s) \cos \theta s \right] \frac{r^{-s} ds}{s \sin \pi s}. \quad (2.5)$$

Repeating the same line of reasoning as in [6], we can prove that in case $\alpha < 0$ the sought-for function $F_*(s)$ is analytic in the strip $\alpha - 1 < \mathrm{Re}s < 1/2$ and has simple poles at points $s = \alpha - 1$, $s = 1/2$. As a result, $\omega_0 = 0$, $\gamma_0 = 1$, $\omega_\infty = \gamma_\infty = 1/2$ and the asymptotic behaviour of the solution near the crack tip ($r \to 0$) follows from (2.5):

$$u^\pm(r, \theta) = \frac{\pm 1}{\pi \mu_\pm} \left[v_0^\pm - v_1^\pm r \cos \theta + v_\alpha r^{1-\alpha} \cos[(\alpha - 1)(\pi \mp \theta)] \right] + O(r^2), \quad (2.6)$$

where the constants are $v_0^\pm = F'_*(0) - \tilde{g}'_\pm(0)$, $v_1^\pm = F_*(-1) + \tilde{g}_\pm(-1)$ and $v_\alpha = (v_0^+ + \mu_* v_0^-)[\mu_* \bar{\tau}_*(1 - \alpha) \sin \pi\alpha]^{-1}$. It is easy to calculate the displacement discontinuity and the traction near the crack tip on the crack line ahead from (2.6):

$$[u]_{\theta=0} = \delta_u + O(r), \quad \sigma_{\theta z}^\pm(r, 0) = \tau_*^{-1}\delta_u r^{-\alpha} + O(r^{1-\alpha}), \quad r \to 0, \quad (2.7)$$

where we have introduce a notation: $\delta_u \equiv (v_0^+ + \mu_* v_0^-)[\pi\mu_+]^{-1}$. To obtain the estimation of the second terms in (2.7) one can note that the second pole of the function $F_*(s)$ situated at point $s = \alpha - 2$. In order to calculate the constants $v_0^\pm$, $v_1^\pm$ and v_α functional equation should be transformed to a

singular integral equation with fixed point singularities as it has been done in Appendix [6]. It is important to note that the representations (2.7) are naturally compatible with the transmission condition $(1.17)_2$. Thus, if the displacement discontinuity δ_u near the crack tip is calculated then the constant in asymptotics of the traction along the interface will be immediately known.

REMARK 1. In case $\alpha < -1$ the third term in the asymptotics (2.6) becomes of the higher degree than $O(r^2)$ and has to be removed. In an intermediate case $\alpha = -1$ it should be also removed from (2.6), however, the estimate will change to give $O(r^2 \ln r)$.

REMARK 2. Although in case $\alpha < 0$ the traction along the soft nonideal interface disappears near the crack tip, the constant in term $O(r^{-\alpha})$ (see (2.7)) can be sufficiently large. Thus, if the value of the parameter $\bar{\tau}_*$ vanishes then direct numerical calculations show that $\delta_u = O(\bar{\tau}_*^{\alpha-1/2})$. This means, in fact, that the following estimate for the traction is true: $\sigma_{\theta z}^{\pm}(d, 0) = O(d^{-1/2})$ on a distance d from the crack tip comparable with $\bar{\tau}_*$ $(d \sim \bar{\tau}_*)$, that could be expected.

2.2.   STIFF IMPERFECT INTERFACE

Now let us consider the modelling problem (2.1)-(2.3) with the transmission conditions $(1.14)_2$ and (1.16) on the crack line ahead with function τ^* from $(1.19)_1$. By the same Mellin transform technique one obtains other functional equation for unknown function $F^*(s) = s\tilde{u}^{\pm}(s, 0)$:

$$\tau^* F^*(s + \beta - 1) - \frac{\mu_+ + \mu_-}{s} F^*(s) \tan \pi s = -\frac{\tilde{g}_+(s) - \tilde{g}_-(s)}{s \cos \pi s}, \qquad (2.8)$$

in a strip: $\max\{-\gamma_0 + 1 - \beta, -\omega_0\} < \mathrm{Re}\, s < \min\{\gamma_\infty + 1 - \beta, \omega_\infty\}$, while $F^*(s)$ is analytic in the strip $-\omega_0 < \mathrm{Re}\, s < \omega_\infty$ and $F^*(0) = 0$. Finally, asymptotic approximation of the solution is found from the inverse Mellin transform:

$$u^{\pm}(r, \theta) = \frac{1}{2\pi i} \int_{-i\infty}^{i\infty} \left[F^*(s) \cos[s(\pi \mp \theta)] + \frac{\tilde{g}_{\pm}(s)}{\mu_{\pm}} \sin \theta s \right] \frac{r^{-s} ds}{s \cos \pi s}. \qquad (2.9)$$

When $\beta < 0$ the sought-for function $F^*(s)$ is analytic in the strip $\beta - 3/2 < \mathrm{Re}\, s < 1$ and has a simple pole at point $s = \beta - 3/2$ and the next pole in the half-plane $\mathrm{Re}\, s < 0$ situated at point $s = \beta - 5/2$. Then from (2.9) one can conclude that in this case $\omega_0 = \gamma_0 = \omega_\infty = \gamma_\infty = 1/2$ and the asymptotic behaviour of the solution near the crack tip takes form:

$$u^{\pm}(r, \theta) = \frac{K_{\pm}^*}{\mu_{\pm}} \sqrt{r} \sin \frac{\theta}{2} - \frac{k_{\pm}^*}{\mu_{\pm}} r\sqrt{r} \sin \frac{3\theta}{2} + O(r^{3/2-\beta}), \quad r \to 0, \qquad (2.10)$$

$$K^*_\pm = \frac{2}{\pi}[\tilde{g}_\pm(-1/2) - \mu_\pm F^*(-1/2)], \quad k^*_\pm = \frac{2}{3\pi}[\tilde{g}_\pm(-3/2) + \mu_\pm F^*(-3/2)].$$

REMARK 3. In the limiting case $\beta = 0$, the second term in the asymptotics (2.9) depends also on $\ln r$. Namely, in this case $F^*(s) = f_0(s + 3/2)^{-1} + f_1 + O(s + 3/2)$, and $s \to -3/2$ and to obtain the respective formula one should substitute in (2.10) a function

$$k^*_\pm(\ln r, \theta) = \frac{2}{3\pi}\left[\tilde{g}_\pm\left(-\frac{3}{2}\right) + \mu_\pm f_0\left(\ln r \pm (\pi \mp \theta)\cot\frac{3\theta}{2} + \frac{2}{3} + \frac{f_1}{f_0}\right)\right]$$

instead of the constant $k^*_\pm$ and replace the estimate by $O(r^{5/2}\ln^2 r)$.

REMARK 4. Let us note, that in case of symmetrical loading $(g_+ \equiv g_-)$ function $F^*(s)$ is identically equal to zero and the solution of the interface crack problem for the stiff nonideal interface completely coincides with the solution for the ideal interface.

Conclusions

This paper completes the analysis of asymptotic behaviour of the solution for Mode III interface crack lying at various nonideal interfaces starting in papers [6, 7, 13]. Distribution of all arising stress singularities $\lambda_k \leq 0$ $(\sigma(r, \theta) \sim \sum_k c_k f_k(\theta) r^{\lambda_k}, \; r \to 0)$ are presented in schematic forms in Figures 3,4. Along the horizontal axis the value of power exponents α and β in
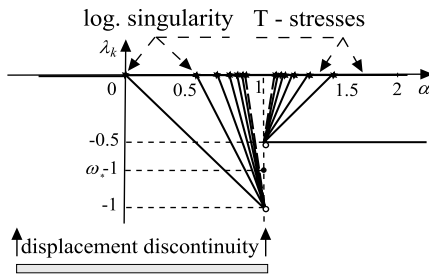
Figure 3   Variation of the stress singularity exponents λ_k, $k = 1, 2, \ldots$ (solid lines) with parameter $\alpha \in (-\infty, \infty)$ in case of the soft nonideal interface.
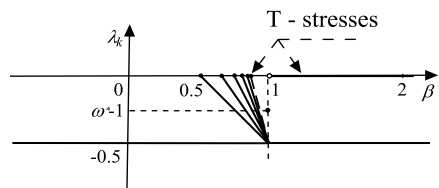
Figure 4   Distribution of the stress singularities for different values of parameter $\beta \in (-\infty, \infty)$ in case of the stiff nonideal interface.

rules (1.19) are shown. As it follows from the schemes, asymptotics for the stiff nonideal interface looks similar to that for the ideal interface. However, even in this case a number of singular terms of stresses appears near point $\beta = 1$. Moreover, although the main singularity is always the same as in the classic case, SIFs in asymptotics from the different half-planes are not the same! In case of the soft nonideal interface, asymptotic behaviour of solution takes essentially more complicated character and coincides with

the ideal interface only when $\alpha > 1.5$ (but with other SIF then for the ideal interface). In a very important for applications case, $\alpha = 0$, (local nonzero thickness near the crack tip and nonvanishing interphase shear moduli) stresses exhibit logarithmic singularity near the crack tip. The main stress singularity for the soft interface model has a gap at point $\alpha = 1$ and a number of singular terms appears in interval $|\alpha - 1| < 0.5$. Moreover, the number tends to infinity as $\alpha, \beta \to 1$! This strange unstable behaviour of the asymptotics still need a clear explanation. Accurate asymptotic expansions for the cases $0 \leq \alpha < \infty$ and $0 < \beta < \infty$ which have not been discussed in this paper can be found in [6, 7, 8].

Acknowledgments

References

[1] Willis, J R (1971) *Fracture mechanics of interfacial crack*, Int. J. Mech. Phys. Solids. **19**, 353-368.

[2] Cherepanov, G P (1979) *Mechanics of Brittle Fracture*. New York: Mc Graw-Hill

[3] Comninou, M (1979) *An overview of interface crack*, Engng Fract. Mech. **37**, 197-208.

[4] Rice, J R (1988) *Elastic fracture mechanics concepts for interfacial cracks*, J. Appl. Mech (ASME) **55**, 98-103.

[5] Erdogan, F (1997) *Fracture mechanics of interfaces*, in: Proc. of First Int. Conf. on Damage and Failure of Interfaces, ed: Rossmanith, Rotterdam-Brookfield: A.A. Balkoma , 3-36.

[6] Mishuris, G S (2001) *Interface crack and nonideal interface concept (Mode III)*, Int. J. Fract., **107**, 279-296.

[7] Mishuris, G S and Kuhn, G (2001) *Asymptotic behaviour of the elastic solution near the tip of a crack situated at a nonideal interface*, in Proc. of IUTAM Symp. on Anal. and Comp. Fract. Mech. of Non-Homogeneous Materials, ed.: Karihaloo, Kluwer Publishers, 57-62.

[8] Antipov, Y A, Avila-Pozos, O, Kolaczkowski, S T and Movchan, A B (2001) *Mathematical model of delamination cracks on imperfect interfaces*, Int. J. Solids and Strictures **38**, 6665-6697.

[9] Movchan, A B and Movhan, N V (1995) Mathematical Modelling of Solids of with Nonregular Boundaries, CRC Press.

FRACTURE CRITERION FOR CRACKS WITH BRIDGED ZONE

Mikhail N. Perelmuter[*]

Institute for Problems in Mechanics of RAS

Pr. Vernadskogo 101-1, 119526, Moscow, Russia

perelm@ipmnet.ru

Keywords: Fracture criterion, crack growth, bridged end zone.

Abstract   The application of two-parametric fracture criterion to the problem of cracks limit equilibrium is considered. The necessary condition of the crack tip limit equilibrium is the equality of the energy release rate and the rate of the energy absorbed by the bonds (the first condition of fracture). The second condition of fracture is the condition of the bond limit stretching at the trailing edge of the bridge zone. Based on these two fracture conditions the regimes of the bridged zone and the crack tip equilibrium and growth are considered.

1.   PROBLEM FORMULATION

Let us consider a straight crack of length 2ℓ at an interface of two dissimilar elastic half-planes such that the crack is placed at $|x| \leq \ell, y = 0$. Assume that the uniform tensile stresses, σ_o, are applied at infinity normal to the interface. Consider segments of length d (end zones) adjacent to the tips of the crack $(\ell - d) \leq |x| \leq \ell$. In these zones the surfaces of the crack interact with each other, which suppresses the crack opening. The physical nature of the crack surfaces interaction is generally changed depending on the crack scale and distance from the crack tip. The interatomic and intermolecular forces are the limiting mechanisms of the surfaces interaction at the small distances from the crack tips (where the crack opening does not exceed the size of the region of the molecular forces action) while "mechanical" forces prevail at relatively larger distances. These mechanical forces can be caused by reinforcing action of fibers in composites or

---

© 2003 *Kluwer Academic Publishers. Printed in the Netherlands.*

polymer chains connecting the crack surfaces in polymer-polymer joints or polymer joints with other materials (metals, ceramics etc.). To describe mathematically the interaction between the surfaces of the crack, we assume that there exist bonds between the surfaces of the crack at the end zone. The law of deformation of these bonds, which is generally nonlinear, is given.

Under the action of external loads, σ_0, the stresses $Q(x)$ appear in the bonds between the surface of the interface crack at the boundary between different materials. These stresses have the normal $q_y(x)$ and tangential $q_x(x)$ components

$$Q(x) = q_y(x) - iq_x(x), \; i^2 = -1 \tag{1}$$

The surfaces of the crack are loaded by the normal and tangential stresses which are numerically equal to these components.

The opening of the interface crack, $u(x)$ at $|x| \leq \ell, y = 0$, can be written as follows

$$u(x) = u_y(x) - iu_x(x) \tag{2}$$

where $u_y(x) = u_y^+(x) - u_y^-(x)$ and $u_x(x) = u_x^+(x) - u_x^-(x)$ are the projections of the crack opening on the coordinate axes, u_x^+, u_y^+ and u_x^-, u_y^- denote the components of the displacements of the upper and lower crack surfaces.

The relation between the crack opening and the bond tractions (the bond deformation law) depends on the physical origin of the bonds and their properties. In the case of spring-like bonds the deformation law can be written as follows [1, 2]

$$u_i(x) = c_0(x, \sigma)q_i(x) \, , c_0(x, \sigma) = \gamma_0(x, \sigma)\frac{H}{E_B} \tag{3}$$

where γ_0 is a dimensionless function, H is a linear scale proportional to the bonding zone thickness, E_B is the effective Young modulus of the bonds and the function c_0 can be considered as the effective bond compliance, $\sigma = \sqrt{q_x^2 + q_y^2}$ is the modulus of the traction vector.

For the bond deformation law similar to (3) (displacements depends on bonds stresses) the bonds stresses and the crack opening along the crack end zone can be determined from solution of the singular integral-differential equations system [1, 2].

2. TWO PARAMETRIC FRACTURE CRITERION

Supposing that the bonds stresses and the crack opening along the crack end zone are known, the total potential energy of a body containing a crack

with bridged zone (in the absence of body forces) is

$$\Pi = \int_v w(\varepsilon_{ij})dv - \int_{s_e} t_i u_i ds + \int_{s_i} \Phi(u)ds, \tag{4}$$

where $w(\varepsilon_{ij})$ is the density of the deformation energy in the body volume v, ε_{ij} are the components of the strain tensor; t_i, u_i are the tractions and displacements at the body boundary and (or) crack surfaces s_e; $\Phi(u)$ is the density of the strain energy of the bonds in the crack end zones, u is the crack opening in the end zones of area s_i.

The crack limit equilibrium corresponds to the following condition

$$-\frac{\partial \Pi}{\partial \ell} = -\frac{\partial}{\partial \ell}\left[\int_v w(\varepsilon_{ij})dv - \int_{s_e} t_i u_i ds\right] - \frac{\partial}{\partial \ell}\int_{s_i}\Phi(u)ds = 0 \tag{5}$$

The terms in the brackets represent the strain energy release rate at creation of a new crack surface and the last term is the rate of the energy absorption in the crack end zone and is associated with the energy necessary to create a unit of its new surface. Note, that within the framework of the model the rate of the energy absorption depends on the end zone size and bond characteristics. The equilibrium end zone size is not assumed to be constant. It can be determined from condition (5) while searching for the critical load needs additional conditions of the bond rupture.

The strain energy release rate in the case of an interface crack under the external load σ_0 and the stresses $-Q(x)$ applied to the crack surfaces in the bridged zone can be written as follows [3]

$$G_{tip}(d, \ell) = \left(\frac{k_1 + 1}{\mu_1} + \frac{k_2 + 1}{\mu_2}\right)\frac{K_B^2}{16 \cosh^2(\pi\beta)}, \tag{6}$$

where $k_{1,2} = 3 - 4\nu_{1,2}$ or $k_{1,2} = (3 - \nu_{1,2})/(1 + \nu_{1,2})$ for the plane strain or plane stress states, respectively; $\nu_{1,2}$, $\mu_{1,2}$ are the Poisson ratios and shear moduli of the materials $1(y > 0)$ and $2(y < 0)$, $\alpha = (\mu_2 k_1 + \mu_1)/(\mu_1 k_2 + \mu_2)$, $\beta = \ln\alpha/2\pi$ and $K_B = \sqrt{K_I^2 + K_{II}^2}$ is the modulus of the stress intensity factors due to the external loads and the stresses in the crack end zone.

The stress intensity factors (SIF) $K_{I,II}$ are determined by [1]

$$K_I + iK_{II} = \frac{\sigma_0\sqrt{\pi\ell}}{(2\ell)^{i\beta}}\left[\left(1 - \frac{2\cosh(\pi\beta)}{\pi}\int\limits_{1-d/\ell}^{1}\frac{p_y(t)}{\sqrt{1-t^2}}dt\right) + \right.$$

$$+ i \left(2\beta - \frac{2\cosh(\pi\beta)}{\pi} \int\limits_{1-d/\ell}^{1} \frac{t p_x(t)}{\sqrt{1-t^2}} dt \right) \Bigg] \tag{7a}$$

$$p_y(x) - i p_x(x) = Q(x) \left(\frac{\ell - x}{\ell + x} \right)^{i\beta} \tag{7b}$$

Let us calculate the rate of the energy absorption for the interface crack with bonding. Denote by $U_{bond}(d, \ell)$ the work of the deformation of bonds and by $G_{bond}(d, \ell)$ the rate of the energy absorption per unit thickness of the body. Then

$$U_{bond}(d, \ell) = b \int\limits_{\ell-d}^{\ell} \Phi(u) dx , \quad G_{bond}(d, \ell) = \frac{\partial U_{bond}(d, \ell)}{b \, \partial \ell} \tag{8}$$

where b is the body thickness.

The density of the strain energy of the bonds is equal to

$$\Phi(u) = \int\limits_{0}^{u(x)} \sigma(u) du , \quad u(x) = \sqrt{u_x^2(x) + u_y^2(x)}, \quad \sigma = \sqrt{q_x^2 + q_y^2} \tag{9}$$

After differentiation in formula (8) with respect to the upper and the bottom limits of the integral we can get

$$\frac{\partial U_{bond}(d, \ell)}{b \partial \ell} = \int\limits_{\ell-d}^{\ell} \left(\frac{\partial u(x)}{\partial \ell} \sigma(u) \right) dx + G_c - G_b, \tag{10}$$

where

$$G_c = \int\limits_{0}^{u(\ell)} \sigma(u) du; , \quad G_b = \int\limits_{0}^{u(\ell-d)} \sigma(u) du \tag{11}$$

If we consider the model of the crack with zero opening at the crack tip $(u(\ell) = 0)$ then $G_c = 0$ and it is necessary to add in the left part of (10) the value of the intrinsic toughness of the matrix material

$$G_c = 2 c_m \gamma_m$$

where c_m is the volume fraction of the matrix material and $2\gamma_m$ is the matrix toughness.

Finally, we obtain the following expression for the rate of the energy absorption

$$G_{bond}(d, \ell) = \int\limits_{\ell-d}^{\ell} \left(\frac{\partial u_y(x)}{\partial \ell} q_y(u) + \frac{\partial u_x(x)}{\partial \ell} q_x(u) \right) dx - \int\limits_{0}^{u(\ell-d)} \sigma(u)du + G_c$$

(12)

where the second term is the density of deformation energy allocated at break of the bond at the trailing edge of the crack end zone.

For a homogeneous material or an adhesion layer connecting different materials the following relations are held

$$G_c = G_b = \int\limits_{0}^{u(\ell-d)} \sigma(u)du$$

(13)

In this case the expression (12) completely coincides with similar expression from [1, 2].

For a weak matrix material ($G_c \ll G_b$) we suppose $G_c = 0$ in (12). In this case $G_{bond}(d, \ell) \to 0$ if $d/\ell \to 0$ and therefore this approach coincide with Barenblatt's model in this limit [1].

The condition of the crack tip limit equilibrium (5) can be rewritten as follows taking into account formulae (6) and (12)

$$G_{tip}(d, \ell) = G_{bond}(d, \ell)$$

(14a)

Condition (14a) is necessary but insufficient for searching for a limit equilibrium state of the crack tip and the end zone. This condition enables us to determine the end zone size, d_{cr}, such that the crack tip is in an equilibrium at the given level of the external loads. To search for the limit state of both the crack tip and end zone within the framework of the model one should introduce an additional condition, e.g., the condition of bond limit stretching at the trailing edge of the end zone $x_0 = \ell - d_{cr}$

$$u(x_0) = ([u_x(x_0)]^2 + [u_y(x_0)]^2)^{1/2} = \delta_{cr}$$

(14b)

where δ_{cr} is the bond rupture length.

If

$$G_{tip}(d, \ell) \geq G_{bond}(d, \ell)$$

(15)

at a certain end zone size, d, and

$$u(\ell - d) < \delta_{cr}$$

(16)

then the crack length increases with the end zone growth up to the size d_{cr} without bond rupture. This stage of the crack growth can be treated as

the system shakedown to the given level of the external loads (subcritical crack growth).

The crack tip advance with simultaneous bond rupture at the trailing edge of the end zone occurs if both conditions

$$u(\ell - d) \geq \delta_{cr} \qquad (17)$$

and (15) are fulfilled.

The regime of bond rupture at the trailing edge of the end zone without the crack tip advance is observed then conditions

$$G_{tip}(d, \ell) < G_{bond}(d, \ell) \qquad (18)$$

and (17) are fulfilled. In this case the size of the end zone decreases and tends to the limit value d_{cr} at the given load.

The end zone size and crack length are reserved within the framework of the model if the inequalities (16) and (18) hold. Thus, the bond rupture characteristics and load level determine the fracture regimes: the crack tip advance with the end zone growth; end zone shortening without the crack tip advance; the crack tip advance and bond rupture at the trailing edge of the end zone.

Solving simultaneously eqs. (14a)–(14b) we can determine the critical external loads σ_0, the end zone size d_{cr} and the adhesion fracture resistance at the crack limit equilibrium state for given crack length and bond characteristics.

3. CRACK WITH UNIFORM BRIDGED STRESSES

Analytical consideration of the proposed criterion is performed for the problem of the straight crack in a homogeneous plane with the rectilinear law of the bond stress. In this very simple case the normal bridged stresses in the crack end zone are prescribed, uniformly distributed along the end zone and independent of the crack opening. The normal displacements of an upper crack surface are given by (plane stress state) [4]

$$u_0(x) = \frac{1}{E} \left(2\sigma_0 - \frac{4P_0}{\pi} \arccos \frac{h}{\ell} \right) \sqrt{\ell^2 - x^2} +$$

$$+ \frac{P_0}{\pi E} \left[(x - h) F(\ell, x, h) - (x + h) F(\ell, x, -h) \right] \qquad (19)$$

where $h = \ell - d$, E is Young modulus of material, σ_0 is an external stress applied normal to the crack plane, P_0 is the normal bridge stress in the

crack end zone of the size d and $F(\ell, x, h)$ is the source function given by [4]

$$F(\ell, x, \xi) = \ln \frac{\ell^2 - x\xi - \sqrt{(\ell^2 - x^2)(\ell^2 - \xi^2)}}{\ell^2 - x\xi + \sqrt{(\ell^2 - x^2)(\ell^2 - \xi^2)}} \quad (20)$$

Taking into account that in this case $Q(x) = P_0, \beta = 0$ (see (7b)), substituting these values into statement (7) and the crack opening from (19) $u_y(x) = 2u_0(x)$, $u_x(x) = 0$ into statement (12), we obtain, after some tedious calculations, the following relationships for the strain energy release rate and for the rate of the energy absorption $(t = d/\ell)$

$$G_{tip}(d, \ell) = G_f \left(1 - Z_0 A(t)\right)^2, \quad G_{bond}(d, \ell) = 2G_f \varphi(t) + G_c \quad (21)$$

where

$$Z_0 = \frac{2P_0}{\pi \sigma_0}, \quad G_f = \frac{\sigma_0^2 \pi \ell}{E} \quad (22)$$

$$A(t) = \arccos(1 - t), \quad B(t) = \sqrt{2t - t^2}, \quad C(t) = (1 - t)\ln(1 - t) \quad (23)$$

and

$$\varphi(t) = Z_0 \left\{A(t) - B(t) - Z_0 \left[A(t)\left[A(t) - 2B(t)\right] - 2C(t)\right]\right\} \quad (24)$$

The first fracture condition (14a) can be written using the equations (21)–(24) as follows

$$2Z_0 \left\{[2A(t) - B(t)] - Z_0 \left[1.5A^2(t) - 2A(t)B(t) - 2C(t)\right]\right\} +$$

$$+ 2\eta R_0 Z_0^2 - 1 = 0 \quad (25)$$

where

$$\eta = \frac{G_c}{G_b}, \quad G_b = P_0 \delta_{cr}, \quad R_0 = \frac{\pi E \delta_{cr}}{8P_0 \ell} \quad (26)$$

The second fracture condition (14b) in this case is

$$\frac{B(t)}{Z_0} - [A(t)B(t) + C(t)] = R_0 \quad (27)$$

The equations (25) and (27) is the nonlinear algebraic system and the solution of this system (if it exists) gives us the external critical stress and the size of the crack end zone in the crack limit equilibrium state. The nonlinear algebraic system is solved numerically and the main parameters governing the solution of the system are η and R_0. At the fixed value of η the solution of the system exists if $R_0 < R_f$, where R_f is the critical value of R_0 (see section 3.1). If the solution of the system does not exist (under the fixed values of E, P_0, δ_{cr}) then, from mechanical point of view,

the size of the crack is less than the crack size associated with initiation of the quasistatic crack growth. In this case the subcritical crack growth is observed (see conditions (15)-(16)).

We shall consider further subcritical growth of a crack with the end zone, assuming that an initial slit of the size $2\ell_0 \geq 0$ without bonds and the crack end zone of the size $2d$ is formed as the external loading monotonically increases. Then $t = d/(\ell_0 + d)$. Let the external load change in such a manner that at each current size of the crack end zone the condition (14a) is satisfied, and the crack opening at the edge of the end zone does not exceed the critical value (condition (16)). The dependence of the external loading on the size of the crack end zone in this case can be obtained from the equation (25) (a quadratic equation with respect to Z_0)

$$\frac{\sigma_0}{P_0} = \frac{2}{\pi}\left[2A(t) - B(t) + \sqrt{A^2(t) + B^2(t) + 4C(t) + 2\eta R_0}\right] \qquad (28)$$

As the external load increases, a subcritical growth of the crack occurs (see (28)), and the size of the crack end zone reaches its critical value, provided the condition (14b) holds. To maintain a further quasistatic crack growth, it is necessary to reduce the external loading; in this case the equations (14a) and (14b) are considered simultaneously.

Next, we shall consider two asymptotic cases for a crack totally occupied by bonds (region of weak material bonds) and a crack with a small end zone (the small scale bridging limit).

3.1. CRACK TOTALLY OCCUPIED BY BONDS

Consider a crack totally occupied by bonds, $t = (d/\ell) = 1$, see eqs. (21)–(27) under a monotonically increasing external load. The condition (27) in this case is reduced to the expression determining the value of the critical external loading, at which the failure of bonds at the center of the crack is initiated

$$\frac{\sigma_{cr}}{P_0} = 1 + \frac{2R_0}{\pi} \qquad (29)$$

In this problem at monotonic loading the value (12) increases faster than the value (6) and these quantities become equal when the external load σ_m satisfies the condition (14a). Using the equations (21) for the crack totally occupied by bonds, together with the condition (14a), we obtain

$$\frac{\sigma_m}{P_0} = 2\left(1 - \frac{1}{\pi}\right) + \sqrt{1 + \frac{4}{\pi^2}(1 + 2\eta R_0)} \qquad (30)$$

The values σ_{cr} and σ_m depend on the values $\eta = const$ and R_0 (this parameter decreases as the crack grows). If $\sigma_{cr} > \sigma_m$ and the condition

(30) holds, then with the increase of the external loading the crack tip will advance without breaking the bonds. The condition (14b) corresponds to a failure of bonds at the center of the crack and formation of a free zone, without bonds. We would like to determine the critical value of the parameter $R_0 = R_f$, at which $\sigma_{cr} = \sigma_m = \sigma_f$. The relationships (29)–(30) imply

$$R_f^2 - R_f \left[\pi + 2(\eta - 1)\right] - \pi = 0$$

and, hence,

$$R_f = \frac{\pi}{2} \left[\left(1 + \frac{2(\eta - 1)}{\pi}\right) + \sqrt{\left(1 + \frac{2(\eta - 1)}{\pi}\right)^2 + \frac{4}{\pi}}\right] \tag{31}$$

Note, that in the case considered above the crack represents a zone of the weakened bonds in a material. Thus, the expressions (30) gives an estimate of strength of an uncracked material.

For fixed parameters (E, P_0, δ_{cr}), characterising the elastic matrix and bonds, the expressions (26) and (31) yield an estimate of the length of an initial crack (ℓ_f) (the quasistatic growth of a crack occurs in accordance with (14a)–(14b))

$$\ell_f = \frac{\pi E \delta_{cr}}{8 P_0 R_f} \tag{32}$$

and the numerical calculations show that the solution of the nonlinear algebraic system (the equations (25) and (27)) exists if $R_0 < R_f$. On the other hand, it is possible to choose parameters (P_0, δ_{cr}) in such a way that condition (32) is satisfied for a crack of a given size.

3.2.   SMALL SIZE OF A CRACK END ZONE

Next, we consider a crack subject to the small scale bridging condition [5]. In this case $t \to 0$ and the equations (25) and (27) can be written as follows

$$(Z_0 \xi)^2 - 2 Z_0 \xi - 2\eta R_0 Z_0^2 + 1 = 0, \quad Z_0(0.5\xi^2 + R_0) - \xi = 0 \tag{33}$$

where $\xi = \sqrt{2d/\ell}$. From eqs.(33) we obtain the critical end zone size which is independent of the crack size in a small scale bridging limit

$$d_{cr} = d_\infty = \frac{\pi E \delta_{cr}}{8 P_0} \left(\sqrt{\eta + 1} - \sqrt{\eta}\right)^2 \tag{34}$$

and the critical external stress

$$\sigma_{cr} = \sqrt{(1 + \eta) \frac{E P_0 \delta_{cr}}{\pi \ell}} = \sqrt{\frac{E(G_b + G_c)}{\pi \ell}} \tag{35}$$

The size and shape of the crack end zone do not change in the case of small scale bridging, and therefore, the condition of an autonomy of the end zone is satisfied, and the energy absorbed to bonds in the end zone is equal to the energy released while breaking the bonds at the edge of the end zone. Thus, the total flow of the energy to the crack tip is spent on formation of a new surface of the crack. For this reason relationships (34)–(35) coincide with formulae obtained in [5, 6] on the basis of the two-parametric fracture criterion; $K_0 - K_b = K_{Ic}$, where K_0 is the SIF due to an external loading, K_b is the SIF due to bonds and K_{Ic} is the matrix toughness.

The expression (28) for subcritical crack growth in the small scale bridging limit is

$$\frac{\sigma_0}{P_0} = \frac{2}{\pi} \left[\sqrt{2t} + \sqrt{2\eta R_0} \right], \quad t = \frac{d}{\ell} \tag{36}$$

and this expression agrees with the results in [7] for a material with zero matrix toughness $\eta = 0$.

References

[1] Goldstein, R V and Perelmuter M N (1999) *Modelling of bonding at an interface crack*, International J. of Fracture, **99** (1-2), 53-79.

[2] Perelmuter, M N (1998) *Polymer interface crack and adhesion resistance* In: Proc. of Workshop 'Mechanical Reliability of Polymeric Materials and Plastic Packages of IC Devices', 231-236, Paris, France.

[3] Salganik, R L (1963) *Brittle fracture of glued bodies*, Appl. Math. Mech. (PMM), **27**(5), 957-965.

[4] Panasyuk, V V (1971) *Limiting Equilibrium of Brittle Solids with Fractures*. Michigan Information Service, Detroit, 284 pp.

[5] Cox B N and Marshall D B (1994) *Concepts for bridged cracks in fracture and fatigue*, Acta metal mater. **42**(2), 341-363.

[6] Massabo R and Cox B N (1999) *Concepts for Bridged Mode II Delamination Cracks*, J. Mech. Phys. Solids, **47**, 1265-1300.

[7] Ungsuwarungsri T and Knauss W G (1988) *A nonlinear analysis of an equilibrium craze: Part II - Simulation of craze and crack growth*, Trans. ASME, J. of Appl. Mech. **55**, 52-58.

Chapter 5
Models of damage
in solids

DYNAMICS OF DAMAGE
IN TWO-DIMENSIONAL STRUCTURES
WITH WAITING LINKS

Andrej Cherkaev and Liya Zhornitskaya

Department of Mathematics, University of Utah, Salt Lake City, Utah 84112, USA

Keywords: Dynamics of damage, Failure, Structures.

Abstract   The paper deals with simulation of damage spread in special structures with "waiting links." These structures are stable against dynamic impacts due to their morphology. They are able to transform "partial damage" through a large region, thereby dissipating the energy of the impact. We simulate various structures with waiting links and compare their characteristics with conventional designs.

1.   INTRODUCTION

This paper describes protective structures that exhibit an unusually high dissipation when they are subject to a concentrated (ballistic) impact. Such a structure is defined as an assembly (network) of rods connected in knots and submerged into a viscous substance.

During the impact (hit), the kinetic energy of the projectile must be absorbed in the structure; the structure fails if it is unable to absorb the energy. While theoretically a material can absorb energy until it melts, real structures are destroyed by a tiny fraction of this energy due to material instabilities and an uneven distribution of the stresses throughout the structure.

We want to find a structure that absorbs maximal kinetic energy of the projectile without rupturing or breaking. The increase of the stability is achieved due to special structural elements, "waiting links," see [1]. These elements contain parts that are initially inactive and start to resist when the strain is large enough; they lead to large but stable pseudo-plastic strains. Structures with "waiting links" distribute the strain over a large

area, in contrast to conventional unstructured solids in which the strain is concentrated near the zone of an impact.

2.   EQUATIONS AND ALGORITHMS

2.1.   WAITING ELEMENTS

Brittle-elastic bar.   Consider a stretched rod made from a homogeneous elastic-brittle material. If loaded, this material behaves as linear elastic, unless the length z reaches a critical value z_f, and fails (becomes damaged) after this. The critical value z_f is proportional to the length L of the rod at equilibrium

$$z_f = L(1 + \epsilon_f), \tag{2.1}$$

where the critical strain ϵ_f is a material constant. If the rod is monotonically elongated, the force $F_{monotone}$ depends on its length z as

$$F_{monotone}(z) = \begin{cases} ks(z/L - 1) & \text{if } z < z_f, \\ 0 & \text{if } z \geq z_f, \end{cases} \tag{2.2}$$

where k is an elastic modulus and s is the cross-section of the rod.

Damage parameter.   Generally, the elongation of an element is nonmonotone. In order to model the state of damageable rods, we add a principle: *Once damaged, the rod stays damaged forever.*   Namely, we assume that the force F in a rod depends on its length z and on the *damage parameter c*:

$$F(z, c) = ks(1 - c)(z/L - 1), \tag{2.3}$$

where K is the elastic modulus. Damage parameter c is equal to zero if the rod is not damaged and is equal to one if the rod is destroyed. Development of the damage is described as the increase of the damage parameter $c(z, t)$ from zero to one. The damage parameter can only increase in time; the increase occurs only when the length of the rod exceeds the critical value. The damage parameter stops increasing when the element is completely damaged. This formalism is similar to the description of damage suggested in [2] for brittle-elastic continuum.

We suggest describing the increase of the damage parameter by the simple differential equation

$$\frac{d\,c(z, t)}{d\,t} = \begin{cases} v_d & \text{if } z \geq z_f \text{ and } c < 1 \\ 0 & \text{otherwise} \end{cases}, \quad c(0) = 0, \tag{2.4}$$

where z_f is the maximal elongation that the element can sustain without being damaged, and v_d is the speed of damage. The speed v_d can be chosen as large as needed.

Remark 1. *The dependence (2.2) corresponds to the discontinuous damage parameter c_H that is equal to zero if the element is undamaged and to one if it is damaged:*

$$c_H(z,t) = \lim_{v_d \to \infty} c(z,t).$$

Consideration of continuously varying damage parameter instead of a discontinuous one increases stability of the computational scheme.

One can argue about the behavior of the rod with an intermediate value of the damage parameter. We do not think that these states need a special justification: they simply express the fact that stiffness rapidly deteriorates to zero when the sample is over-strained.

Waiting links. Let us introduce special structural elements – waiting links – that significantly increase the resistivity of the structure due to their morphology. These elements and their quasistatic behavior are described in [1]. The link is an assembly of two elastic-brittle rods, lengths L and Δ ($\Delta > L$) joined by their ends. The longer bar is initially slightly curved to fit. When an increasing external elongation stretches the link, only the shortest rod resists in the beginning. If the elongation exceeds the critical value, this rod breaks and the next (longer) rod then assumes the load replacing the broken one (see Figure 1, left).
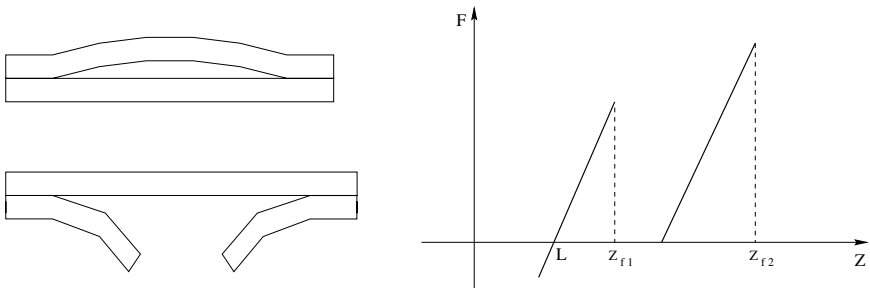

Figure 1 Left above: the waiting link in the initial state. Left below: the waiting link after the first rod is broken. Right: the force-versus-length dependence for a monotone elongation.

Assume that a unit amount of material is used for both rods. This amount is divided between the shorter and longer rod: the amount α is used for the shorter (first) rod and the amount $1 - \alpha$ is used for the longer (second) one. The cross-sections s_1 and s_2 of rods are:

$$s_1(\alpha) = \frac{\alpha}{L} \quad \text{and} \quad s_2(\alpha) = \frac{1 - \alpha}{\Delta}, \tag{2.5}$$

The force-versus-elongation dependence in the shorter rod is:

$$F_1(z) = ks_1(\alpha)\left(\frac{z}{L} - 1\right)(1 - c_1), \tag{2.6}$$

where $c_1 = c_1(z,t)$ is the damage parameter for this rod; it satisfies the equation similar to (2.4)

$$\frac{d\,c_1(z,t)}{d\,t} = \begin{cases} v_d \text{ if } z \geq z_{f_1} \text{ and } c_1(z,t) < 1, \\ 0 \quad \text{otherwise,} \end{cases} \qquad c_1(z,0) = 0, \tag{2.7}$$

where $z_{f_1} = L(1 + \epsilon_f)$.

The longer rod starts to resist when the elongation z is large enough to straighten this rod. After the rod is straight, the force-versus-elongation dependence is similar to that for the shorter rod:

$$F_2(z) = \begin{cases} ks_2(\alpha)\left(\frac{z}{\Delta} - 1\right)(1 - c_2), & \text{if } z \geq \Delta \\ 0, & \text{if } z < \Delta \end{cases}. \tag{2.8}$$

Here F_2 is the resistance force and $c_2 = c_2(z,t)$ is the damage parameter for the second rod:

$$\frac{d\,c_2(z,t)}{d\,t} = \begin{cases} v_d \text{ if } z \geq z_{f_2} \text{ and } c_2(z,t) < 1, \\ 0 \quad \text{otherwise,} \end{cases} \qquad c_2(z,0) = 0. \tag{2.9}$$

These equations are similar to (2.6), (2.7), where the cross-section $s_1(\alpha)$ is replaced by $s_2(\alpha)$ and the critical elongation z_{f_1} by $z_{f_2} = \Delta(1 + \epsilon_f)$. The difference between the two rods is that the longer (slack) rod starts to resist only when the elongation is large enough.

The total resistance force $F(z)$ in the waiting link is the sum of $F_1(z)$ and $F_2(z)$:

$$F(z) = F_1(z) + F_2(z). \tag{2.10}$$

The graph of this force-versus-elongation dependence for the monotone external elongation is shown on Figure 1 where the damage parameters jump from zero to one at the critical point z_{f_1}.

One observes that the constitutive relation is nonmonotone. Therefore one should expect that the dynamics of an assembly of such elements is characterized by abrupt motions and waves (similar systems but without damage parameter were investigated in [5, 6]).

2.2. STRUCTURES

Now we describe the model structure: a two-dimensional assembly of the waiting links. Consider a equilateral triangular grid: each inner point has six equally distant neighbors. The distance between neighboring knots

is equal to L. The knots in the boundary (including corners) have lower number of neighbors. The waiting links connect the neighboring knots. Initially, the system is in equilibrium and does not have any inner stress.

If the strain is small everywhere and each link is strained less than the critical value z_f, the system is linear and it models a linear elastic material. After the first rod in a link breaks and is replaced with a longer one, the net experiences an "irreversible phase transition."

After each break, the network changes its elastic properties and its equilibrium position. The dynamics of the damage and failure of the net can be viewed as a series of these transitions. In contrast with the conventional structure, the waiting links become stronger after first break. Another advantage is that the additional slackness that is added after the break helps to spread the damage across the structure.

Remark 2. *In our model, an assembly of a finite number of heavy concentrated masses and weightless damageable springs is studied instead of a continuous structure. The model does not require any a priori assumptions on the thermodynamics or mechanical properties of the modeled media. On the contrary, the properties of equivalent media can be derived by homogenization of the finite model, as the elasticity equation can be derived from the mass-spring model (see, for example, [3]). From this viewpoint, the model is similar to the model by Slepyan [4] of crack dynamics.*

Dynamics and viscosity.   It is assumed that the inertial masses m_i are concentrated in the knots, joined by the inertialess waiting links (nonlinear springs), therefore the dynamics of the structure is described by ordinary differential equations of motion of the knots. We assume that the links are elastic-brittle, as described above.

Additionally, we assume that the space between the knots is filled with a viscous substance with the dissipation coefficient γ. Without the viscosity, the system never reaches a steady state. On the other hand, even a slow external excitation leads to intensive waves in the system caused by breaking of the links. These waves, reflected from the boundaries, cause intensive vibration of the structure and the viscosity eventually absorbs the energy.

The motion of the ith knot satisfies the equation

$$m_i \ddot{\mathbf{z}}_i + \gamma \dot{\mathbf{z}}_\mathbf{i} = \sum_{j \in N(i)} \frac{F_{ij}(|\mathbf{z_i} - \mathbf{z_j}|)}{|\mathbf{z_i} - \mathbf{z_j}|} (\mathbf{z_i} - \mathbf{z_j}), \qquad (2.11)$$

where $\mathbf{z_i}$ is the vector of coordinates of the ith knot, $|.|$ is length of the vector, $N(i)$ is the set of knots neighboring the knot i and m_i is the mass of the ith knot. The force F_{ij} in the ijth link depends on the damage

parameters $c_{ij,1}$ and $c_{ij,2}$ as in (2.10). The set of neighbor knots depends on the geometric configuration.

Remark 3. *In this model, the masses are permitted to travel as far as the elastic links permit. In particular, when these links are completely broken, the concentrated mass can move "between" other masses without interaction with them. Below in Section 3.1, we discuss a special model for a projectile that is "large enough" so that it does not slip through the rows of linked masses.*

Waves of damage.   The speed of waves in a structure is of the order of the speed of sound in the material which the structure is made of (approximately 2,000 m/s for steel). In our numerical experiments, we assume that the speed of the impact is much smaller (recall that the speed of sound in the air is 336 m/s). A slow-moving projectile does not excite intensive waves in stable structures, but it does excite mighty waves of damage in waiting structures. The reason is that the energy stored in the elastic links suddenly releases when the links are broken. This phenomenon explains the superb resistance of the waiting structure: The energy of the projectile is spent to excite the waves of damage which are spread upon a large area and dissipate.

2.3.   NUMERICAL ALGORITHM

Solving the system (2.11) numerically, we rewrite it as an autonomous system of first order differential equations:

$$\dot{\mathbf{z_i}} = \mathbf{p_i}, \tag{2.12}$$

$$\dot{\mathbf{p_i}} = \frac{1}{m_i}(\varphi_i - \gamma \mathbf{p_i}), \tag{2.13}$$

where

$$\varphi_i = \sum_{j \in N(i)} \frac{F_{ij}(|\mathbf{z_i} - \mathbf{z_j}|)}{|\mathbf{z_i} - \mathbf{z_j}|}(\mathbf{z_i} - \mathbf{z_j}). \tag{2.14}$$

Introducing the notation

$$\vec{\mathbf{x}} = \{\mathbf{z_i}, \mathbf{p_i}\}, \quad \vec{\mathbf{f}} = \left\{\mathbf{p_i}, \frac{1}{m_i}(\varphi_i - \gamma \mathbf{p_i})\right\},$$

we get

$$\dot{\vec{\mathbf{x}}} = \tilde{\mathbf{f}}(\tilde{\mathbf{x}}).$$

We solve the resulting system via the second order Runge-Kutta method

$$\vec{\mathbf{x}}_{n+1} = \vec{\mathbf{x}}_n + \frac{k}{2}\left(\vec{\mathbf{f}}(\vec{\mathbf{x}}_n) + \vec{\mathbf{f}}(\vec{\mathbf{x}}_n + h\vec{\mathbf{f}}(\vec{\mathbf{x}}_n))\right), \tag{2.15}$$

where k denotes the time step. The stability condition of the numerical method depends on the speed v_d from (2.7), (2.9) of damage propagation and on the dissipation coefficient γ. In all numerical experiments that follow we establish convergence empirically via time step refinement.

3.   STRUCTURES UNDER A CONCENTRATED IMPACT

In this section, we describe the resistance and failure of structures from waiting links impacted by a massive concentrated projectile. The kinetic energy of the projectile must be absorbed in the structure without its total failure.

3.1.   MODEL OF THE PROJECTILE

The model takes into account penetration of the projectile through the structure and does not allow "slipping through" the line on knots. One cannot simply model the projectile as another "heavy knot" in the structure with an initial kinetic energy: In such a model the projectile would not be connected with the knots but the immediate neighbors; the projectile would slip through the net after the failure of the neighboring links.

In our simulation, the projectile is modeled as an "elastic ball" of mass M_p centered at the position z_p. Motion of the mass satisfies the equation

$$M_p \ddot{\mathbf{z}}_p = \sum_j \frac{F_{pj}(|\mathbf{z_p} - \mathbf{z_j}|)}{|\mathbf{z_p} - \mathbf{z_j}|}(\mathbf{z_p} - \mathbf{z_j}), \qquad (3.1)$$

where j is the number of the knot in the structure. Equation (3.1) is similar to (2.11), but the force F_{pj} is found from a different equation

$$F_{pj}(z) = \begin{cases} 0 & \text{if } z > B, \\ \ln\left(\frac{B-A}{z-A}\right) & \text{if } A < z \le B, \\ +\infty & \text{if } z \le A. \end{cases} \qquad (3.2)$$

In the numerical experiments that follow $A = 0.5L$, $B = 2L$.

This model states that the repulsive force $F_{pj}(z)$ is applied to the knots when the distance between them and the center $\mathbf{z_p}$ of the projectile is smaller than a threshold B. This force grows when the distance decreases and becomes infinite when the distance is smaller than A. This model describes the projectile as a nonlinear elastic ball with a rigid nucleus. When it slips through the structure, the knots are repulsed from its path causing strain and/or breaking of the links.

3.2.   EFFECTIVENESS OF A DESIGN

Comparing the history of damage of several designs, we need to work out a quantitative criterion of the effectiveness of the structure. This task is nontrivial, since different designs are differently damaged after the collision.

Effectiveness criterion.   We use an integral criterion that is not sensitive to the details of the damage; all we are measuring is the variation of the impulse of the projectile. It is assumed here that the projectile hits the structure falling down into it. To evaluate the effectiveness of the protective structure, we compute the *scaled impulse d* – the ratio in the vertical component $p_v = \mathbf{p} \cdot (0,1)$ of the impulse $\mathbf{p}$ of the projectile before and after the impact:

$$d = \frac{p_v(T_{final})}{|p_v(T_0)|}, \tag{3.3}$$

where T_0 and T_{final} are the initial and final moments of the observation, respectively. Notice that scaled impulse d does not vary when the projectile is not in contact with the structure; in this sense it is insensitive to the exact value of T_{final}.

Scaled impulse d shows what portion of the impulse is passed to the structure from the projectile. It evaluates the structure's performance using the projectile as the measuring device. An elastic impact with a rigid body corresponds to the final impulse being opposite to the initial one ($d = -1$). The absence of the structure corresponds to $d = 1$, because the impulse of the projectile does not change. If the projectile stops then $d = 0$, if it breaks through the structure then $0 < d \leq 1$, and if it is repulsed then $-1 \leq d < 0$. The smaller d is, the more effective the structure is.

Other criteria.   Other criteria compare the state of the structure before and after the collision. These criteria are applicable only if the structure (or its pieces) after the collision reaches a steady state. We register (i) the percentage of partially damaged links; (ii) the percentage of destroyed links. The first number shows how much damage spreads, and the second shows what percent of the structure is destroyed. Ideally, we wish to have a structure in which all elements are partially damaged, but no element is completely destroyed.

Remark 4. *The percentage of destroyed links is a rough criterion: It ignores the positions of the destroyed links.*

3.3.   BRIDGE-LIKE DESIGNS

Finally, we discuss the simulation of damage of a bridge-like truss structure made from waiting links. We assume that the vertical sides of the
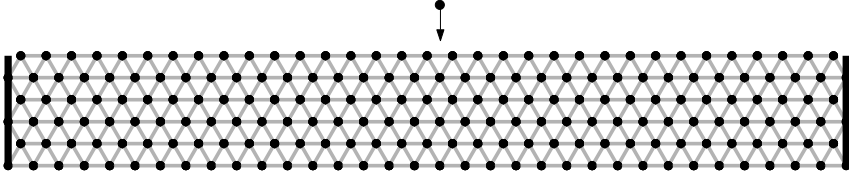
Figure 2   The bridge is supported from the sides. It is impacted by a projectile moving downward.

structure are supported and the horizontal sides are free. A projectile that is modeled as "elastic ball" (section 3.1) impacts the center of the upper side of the structure moving vertically down with an initial speed v_0 (Figure 2).

The difference in the impulse of the projectile before and after impact shows the effectiveness of the structure. The number of destroyed links also represents the effectiveness showing how much the damage is spread. If the speed is small, the projectile is repulsed; otherwise it penetrates through the structure.
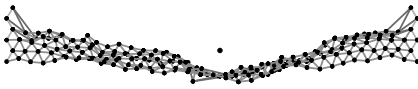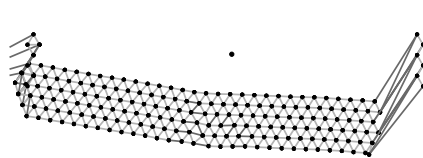

(a) $\alpha = 0.10, T_{final} = 500$, projectile is repulsed.
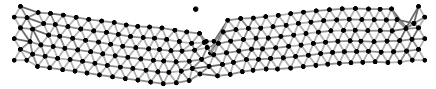
(b) $\alpha = 0.25, T_{final} = 500$, projectile is repulsed.
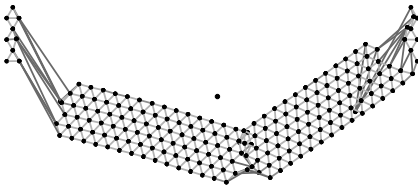
(d) $\alpha = 1.00, T_{final} = 250$, projectile goes through.

(c) $\alpha = 0.50, T_{final} = 250$, projectile goes through.

Figure 3   The final stages of the impacted bridges. The designs use the same amount of the materials, but differ in the parameter α: percentage of material used for the first (shorter) rod in the waiting link.

We simulate the damage process of the bridge by varying the parameter α (the fraction of material put into the shorter link) while keeping the other parameters ($L, \Delta, z_{f_1}, z_{f_2}$, total amount of material, etc.) the same

for all runs. The results are summarized in Table 1 and Figure 3. One can see from Table 1 that as α decreases from 1.00 (conventional structure) to 0.10 the percentage of partially damaged links increases as the percentage of destroyed links decreases making the structure more resistant. Table 1 also shows that $\alpha = 0.25$ is optimal for both minimizing the number of destroyed links and minimizing the scaled final impulse d (see the discussion in Section 3.2).

Figure 3 shows the final stages of the impacted bridges. Intact waiting elements (both links are undamaged) are aquamarine; partially damaged elements (the short link is destroyed, the longer one is undamaged) are blue; destroyed elements (both links are damaged) are purple. The structures with $\alpha = .50$ and $\alpha = 1.00$ (conventional structure) soon develop cracks and fall apart allowing the projectile to go through (see Figures 3(c), 3(d)) while the structures with $\alpha = 0.10$ and $\alpha = 0.25$ preserve the *structural integrity* by dissipating energy and taking the stress away from the point of impact; this results in the rejection of the projectile (see Figures 3(a), 3(b)). Notice that the final time T_{final} is twice as small in the last two examples.

The propagation of the damage in the bridge is due to several factors: (i) local instabilities of the part of the network that contains a damaged link; (ii) the increase of force on neighboring links which allows the damage to spread; (iii) the waves that propagate through the network and initiate damage in areas remote from the point of collision.

Acknowledgments

Figure	α	% of damaged links	% of destroyed links	Scaled final impulse d
Figure 3(a)	0.10	94%	3.8%	-0.26
Figure 3(b)	0.25	42%	3.8%	-0.32
Figure 3(c)	0.50	4.6%	6.3%	0.54
Figure 3(d)	1.00	0%	8.6%	0.46

Table 1 Damage and/or destruction of a bridge.

References

[1] A. Cherkaev, and L. Slepyan. Waiting Element Structures and Stability under Extension. Int. J. Damage Mechanics, 1955, 4, No 1, 58-82.

[2] G. A. Francfort and J.-J. Marigo, Stable damage evolution in a brittle continuous medium. European J. Mech. A Solids **12** (1993), no. 2, 149–189

[3] Timoshenko, S.P; Goodier, J. N. Theory of Elasticity. 2d ed. McGraw-Hill Book Company, Inc., New York, Toronto, London, 1951.

[4] L.I. Slepyan, L.I. Mechanics of Cracks, Sudostroenie, Leningrad, 1990 (in Russian)

[5] Balk, A., Cherkaev, A. and Slepyan, L. Dynamics of Chains with Non-monotone Stress-strain Relations. I. Model and numerical experiments. J. Mech. Phys. Solids, 49, 2001, 131-148.

[6] Balk, A., Cherkaev, A. and Slepyan, L. Dynamics of Chains with Non-monotone Stress-strain Relations. II. Nonlinear Waves and Wave of Phase Transition. J. Mech. Phys. Solids, 49, 2001, 149-171.

LOCAL AND NON-LOCAL APPROACHES TO FATIGUE CRACK INITIATION AND PROPAGATION

S.E. Mikhailov and I.V. Namestnikova

Div. of Mathematics, Glasgow Caledonian University, Glasgow, G4 0BA, UK

s.mikhailov@gcal.ac.uk, i.namestnikova@gcal.ac.uk

Keywords: Non-local strength conditions; Durability; Cyclic loading; Crack initiation; Crack propagation; Volterra equations.

Abstract   A functional form of local strength conditions under fatigue loading is introduced and employed to formulation and analysis of fatigue crack initiation and propagation. For the strength conditions associated with the Palmgren-Miner linear damage accumulation rule and the power-type S–N diagram, the problem is reduced to a non-linear integral Volterra equation, which can be transformed to a linear one for the case of a single crack. An analytical solution of some simple problems are presented for the latter case and shortcomings of the local approach are pointed out. A non-local approach free from the shortcomings is presented along with an example of its implementation.

1.   INTRODUCTION

Let us consider a cyclic process in a body Ω represented as a temporal sequence $\{\sigma_{ij}^c(m, x)\}_{m=1,2,...}$ of connected closed but generally non-coinciding loops (cycles) $\sigma_{ij}^c(m, x) = [\sigma_{ij}(\tau, x); \tau_{m-1} \leq \tau \leq \tau_m]$ in the stress space, $\sigma_{ij}(x, \tau_m) = \sigma_{ij}(x, \tau_{m-1})$, where $m = 1, 2, ...$ is the cycle number and $x \in \Omega$. The pure fatigue is a dependence of material mechanical properties, and particularly material strength, on the loading process history, considered as a sequence of events, but no explicit dependence on time or the process rate is supposed. Then the cyclic fatigue can be described in terms of the cycle number n (instant n) as a discrete or continuous time-like parameter.

A common practice of a body fatigue life local analysis includes usually two steps. First, a crack initiation cycle number $n^*\{\sigma\}$ is determined from a fatigue strength condition expressed in terms of a damage measure based

on a cycle stress range $\Delta\sigma_{ij}(n, y)$. A crack of a length a_0 is supposed to appear at a point y^* in a body Ω where and when the fatigue strength condition is violated. Then the Paris type equation for the crack propagation rate, based on the stress intensity factor ranges, with the initial condition $a(n^*\{\sigma\}) = a_0$ is used for evaluation of the cycle number $n^*(\{\sigma\}; \Omega)$ to separation of the body Ω into pieces or to unstable crack growth. However the value a_0 being a key issue for the fatigue crack propagation prediction is often not clearly fixed or is connected with the measuring ability of available equipment. On the other hand, the Paris type equation using the stress intensity factor ranges, which are characteristics of the stress field only at the crack tip y, can describe neither the scale effect for short cracks nor the influence of the fatigue damage during the previous cycles on the crack propagation rate. Moreover, the material parameters of the strength condition of the first step seem to be completely unrelated to the Paris law parameters.

Trying to avoid the shortcomings, we first describe in this paper a local united approach based on an extension of the classical fatigue strength conditions to the crack propagation stage, and show its limitations. To overcome the limitations, we then give a non-local modification of that approach merging a special form of the general static non-local strength analysis [1] with the functional description of cyclic strength [3] (see also [2]). This allows to analyse strength and durability under oscillating in time homogeneous as well as highly inhomogeneous stress fields and predict both the crack initiation in a virgin material without cracks and its propagation through the damaged material as a united process. Note that some other particular non-local approaches were used for predicting fatigue life in [6]-[9].

Considered examples of the local and non-local approaches applications lead to linear or non-linear Volterra equations of the first or the second kind and some results of their solutions are presented.

2.   LOCAL CYCLIC BRITTLE STRENGTH AND DURABILITY CONDITIONS

To describe cyclic fracture, i.e. crack initiation and propagation under cycling loading, we will analyse the brittle strength, that is strength at a particular point y along a particular infinitesimal plane (with a normal vector) $\vec{\zeta}$ at that point.

The local brittle cyclic strength condition *for a plane $\vec{\zeta}$ at a point $y \in \Omega$* can be taken in the form

$$\underline{\Lambda}(\{\sigma^c(\cdot, y)\}; n, y, \vec{\zeta}) < 1, \qquad (2.1)$$

where $\underline{\Delta}(\{\sigma^c(\cdot, y)\}; n, y, \vec{\zeta})$ is a local brittle *cyclic normalised equivalent stress functional* (CNESF) defined similar to [3] on the sequence $\{\sigma_{ij}^c(m, y)\}_{m=1,2,...}$ and being positively homogeneous in $\{\sigma_{ij}^c\}$ non-decreasing in n material characteristics.

An example of the CNESF associated with the power S–N durability diagram and the Palmgren–Miner linear accumulation rule can be taken in the following form similar to [3],

$$\underline{\Delta}(\{\sigma^c(\cdot, y)\}; n, y, \vec{\zeta}) = \left\{ \int_0^n \frac{\|\vec{\sigma}^c(m, y, \vec{\zeta})\|^b}{[\sigma_1^{c*}(\tilde{\sigma}^c(m, y, \vec{\zeta}); y, \vec{\zeta})]^b} dm \right\}^{\frac{1}{b}}, \quad (2.2)$$

where $\vec{\sigma}^c(m, y, \vec{\zeta})$ is the loop of the traction vector $\sigma_{ij}\zeta_j$ on the plane $\vec{\zeta}$ at the point y during the cycle m; $\|\vec{\sigma}^c(m, y, \vec{\zeta})\|$ is a norm of the m−th loop of the vector function $\vec{\sigma}^c(m, y, \vec{\zeta})$, e.g., $\|\vec{\sigma}^c(m, y, \vec{\zeta})\| = \sup_{\vec{\sigma} \in \vec{\sigma}^c(m,y,\vec{\zeta})} |\vec{\sigma}|$; b is a non-negative material constant, and $\sigma_1^{c*}(\tilde{\sigma}^c(m, y, \vec{\zeta}); y, \vec{\zeta})$ is a non-negative material function of the normalised loop shape $\tilde{\sigma}^c(m, y, \vec{\zeta}) = \vec{\sigma}^c(m, y, \vec{\zeta})/\|\vec{\sigma}^c(m, y, \vec{\zeta})\|$ depending also on y and $\vec{\zeta}$ for inhomogeneous and anisotropic materials.

One can further assume in the example that the fatigue strength of the plane $\vec{\zeta}$ is determined only by the loops of the normal stress $\sigma_{\zeta\zeta}^c$, and the normalised loop shape $\tilde{\sigma}_{\zeta\zeta}^c$ does not vary with m (self-similar process). If $\sigma_{\zeta\zeta}(\tau, y)$ has not more than one internal local maximum and local minimum on each cycle, then $\sigma_1^{c*}(\tilde{\sigma}_{\zeta\zeta}^c(y); y, \vec{\zeta}) = \sigma_{R1}^*(y, \vec{\zeta})$ is a material parameter depending only on the asymmetry ratio $R(y, \vec{\zeta}) = \sigma_{\zeta\zeta min}(y, \vec{\zeta})/ \sigma_{\zeta\zeta max}(y, \vec{\zeta})$ for a material point y and plane $\vec{\zeta}$. Then CNESF (2.2) can be rewritten in terms of the stress range $\Delta\sigma_{\zeta\zeta}(m, y) = \sigma_{\zeta\zeta max}(m, y) - \sigma_{\zeta\zeta min}(m, y)$,

$$\underline{\Delta}(\{\sigma^c(\cdot, y)\}; n, y, \vec{\zeta}) = \frac{1}{\sigma_{R1}^{*\Delta}(y, \vec{\zeta})} \left\{ \int_0^n [\Delta\sigma_{\zeta\zeta}(m, y)]^b dm \right\}^{\frac{1}{b}}, \quad (2.3)$$

where $\sigma_{R1}^{*\Delta} = (1 - R)\sigma_{R1}^*$ if $|R| \leq 1$ and $\sigma_{R1}^{*\Delta} = (1 - 1/R)\sigma_{R1}^*$ if $|R| > 1$.

Let us return to the general case. Let a body occupy at an instant n an open domain $\Omega(n)$. Its boundary $\Gamma(n) = \Gamma(0) \cup Y^*(n)$ consists of an initial body boundary $\Gamma(0)$ and a new crack surface $Y^*(n)$ occurring and growing during the loading process. Let $q(\tau, x)$ denote applied multi-axial in-phase cyclic regular volume and boundary loading. Under the assumption that the material is elastic, the stress tensor field is $\sigma_{ij}(\tau, y) = \sigma_{ij}(\tau; \Gamma(\tau), y) = \sigma_{ij}(q(\tau, \cdot), \Gamma(\tau), y)$. Consequently, the m−th stress tensor loop $\sigma_{ij}^c(m, y) = \sigma_{ij}^c(m, \Gamma^c(m), y) = \sigma_{ij}^c(q^c(m, \cdot), \Gamma^c(m), y)$ at a body point y depends on the changing body shape $\Gamma^c(m)$, as well as on the applied cyclic load loop $q^c(m, x)$ on the same cycle m only.

We will consider further the cycle number m as a continuous variable attributing some loops $\sigma^c(m; \Gamma(m), y)$ also to the non-integer values of m. Generally, using a brittle non-local CNESF $\underline{\Lambda}(\{\sigma^c(\cdot, y)\}; n, y, \vec{\zeta})$, the cyclic fracture process (the cyclic crack initiation and its propagation through the damaged material) can be described as follows. First, there is no fracture in a body $\Omega(0)$ if inequality (2.1) is satisfied on all infinitesimal planes $\vec{\zeta}$ at all points $y \in \Omega$. Then a crack or cracks appear on a cycle n_0^* at the points y^* on the planes $\vec{\zeta}^*(y^*)$, where inequality (2.1) is violated and becomes equality, that is, the points y^* constitute a crack set $Y^*(n_0^*)$, which becomes a part of the body boundary $\Gamma(n_0^*) = \Gamma(0) \cup Y^*(n_0^*)$, with the normal vector $\vec{\zeta}^*(y^*)$ and with zero boundary tractions. Taking into account that $\underline{\Lambda}$ is non-decreasing in n, we have that the crack initiation instant (cycle number) n_0^*, the crack initiation set $Y^*(n_0^*) \ni y^*(n_0^*)$ and the crack initiation planes $Z^*(n_0^*) \ni \vec{\zeta}^*(y_0^*)$ are determined from the following equation and inequality,

$$n_0^* = \sup\{n : \sup_{y} \sup_{\vec{\zeta}} \underline{\Lambda}(\{\sigma^c(\cdot; \Gamma(0), y)\}; n, y, \vec{\zeta}) < 1\}, \qquad (2.4)$$

$$\underline{\Lambda}(\{\sigma^c(\cdot; \Gamma(0), y)\}; n_0^*, y_0^*, \vec{\zeta}_0^*(y_0^*)) \geq 1,$$

$$\underline{\Lambda}(\{\sigma^c(\cdot; \Gamma(\cdot), y\}; n, y, \vec{\zeta}(y)) = 1, \quad \forall n > n_0^*, \quad y \in \Gamma(n). \qquad (2.5)$$

If the sets $Y^*(n_0^*)$ and $Z^*(n_0^*)$ are empty, then n_0^* is an instability instant and $Y^*(n)$ and $Z^*(n)$ will be not empty for any $n > n_0^*$. If there is an analytical or numerical method of the stress field calculation for any crack set $Y^*(n)$, relations (2.4)-(2.5) allow to describe the crack propagation for any cycle n.

Assuming a smooth dependence of $\underline{\Lambda}(\{\sigma^c(\cdot; \Gamma(\cdot), y)\}; n, y, \vec{\zeta})$ on $\vec{\zeta}$ and using (2.5), the fracture plane with a unit normal $\vec{\zeta}^*(y)$ can be determined also from the equations

$$\left. \frac{\partial \underline{\Lambda}(\{\sigma^c(\cdot; \Gamma(\cdot), y)\}; n, y, \vec{\zeta})}{\partial \zeta_j} \right|_{\vec{\zeta} = \vec{\zeta}^*(y)} = 0, \quad |\vec{\zeta}^*(y)| = 1 \quad \forall n \ \forall y \in Y^*(n).$$

If the direction of crack growth is a priori known then there is no need to determine $\vec{\zeta}^*$.

3. EXAMPLE OF LOCAL DURABILITY ANALYSIS

3.1 Symmetric plane problem for fatigue crack initiation and propagation

Let us consider a plane problem for an elastic homogeneous body symmetric

with respect to axis x_1 and symmetrically loaded. Let the body have one edge crack of a length $a(m)$ or one central crack of a length $2a(m)$ or two symmetric edge cracks of a length $a(m)$ each along the x_1 axis (in the last two cases the symmetry with respect the axis orthogonal to x_1 is also supposed), already existing or appearing during the process. Thus the geometry change is described by only one parameter $a(m)$, i.e. $\Gamma(m) = \Gamma(a(m))$, and the fatigue crack propagation path is straight with a normal vector $\vec{\zeta}^* = \{0, 1\}$.

Let an external multi-axial self-similar cyclic loading be represented in the form $q(\tau, x) = q_0(\tau)\hat{q}(x)$, where $q_0(\tau)$ is a scalar cyclic function with a constant asymmetry ratio R, and consequently $\Delta q(m, x) = \Delta q_0(m)|\hat{q}(x)|$. Assuming the crack growth during a cycle is small, we can neglect its influence on the stress cycle shape distortion during one cycle and write $\Delta\sigma_{ij}(m, y) = \Delta q_0(m)|\hat{\sigma}_{ij}(a(m), y)|$ for this case.

Let us take CNESF (2.3). Then the equation for finding the crack initiation instant n_0^* according to (2.4) is

$$|\hat{\sigma}_{22}(a_0, y^*)|^b \int_0^{n_0^*} [\Delta q_0(m)]^b dm = (\sigma_{R1}^{*\Delta})^b, \tag{3.1}$$

where $a_0 = 0$ if there is no crack initially in the body, y^* is the tip of an already existing crack or the stress concentration point where the crack will initiate. If there exists an initial crack, $a_0 \neq 0$, then (3.1) implies $n_0^* = 0$ due to the stress singularity at the crack tip, $|\hat{\sigma}_{22}(a_0, a_0)| = \infty$.

Let the origin of the coordinate system be in the middle of the central crack or at the open end of the edge crack or at the point where the crack will appear. Then (2.5) leads to a non-linear Volterra equation for $a(n)$. However, we can change variables similar to Zobnin and Rabotnov (see [4] where a solution of the *creep* durability problem analogous to problem 3.2 below is presented for $b = 1$). Then the dependence $a(m)$ for the developing crack length is to be obtained from the following non-convolution *linear* Volterra integral equation of the first kind given by (2.5) for $g(a) = \left[\Delta q_0(m(a))/\sigma_{R1}^{*\Delta}\right]^b dm(a)/da$,

$$\int_{a_0}^{a(n)} |\hat{\sigma}_{22}(a, a(n))|^b g(a)da = 1 - \frac{|\hat{\sigma}_{22}(a_0, a(n))|^b}{|\hat{\sigma}_{22}(a_0, a_0)|^b}. \tag{3.2}$$

3.2 Crack in an infinite plane under uniform loading

Consider now a more particular example of a straight crack with a length $2a(m)$ in an infinite plate. The origin of the Cartesian coordinate system $\{x_1, x_2\}$ coincides with the centre of the crack. Let a uniform cyclic traction with a range $\Delta q(m, x) = \Delta q_0(m)$ and with a constant asymmetry ratio R is applied parallel to the x_2-axis at infinity.

An exact expression for $\Delta\sigma_{22}(m; x_1)$ ahead of the crack in an infinite isotropic or anisotropic plate has the form (e.g. [5])

$$\Delta\sigma_{22}(m; y_1) = \frac{\Delta K_1(m, a(m))y_1}{\sqrt{\pi a(m)(y_1^2 - a^2(m))}}, \qquad (3.3)$$

$$\Delta K_1(m, a(m)) = \Delta q(m)\sqrt{\pi a(m)}, \qquad (3.4)$$

where $\Delta K_1(m)$ is the mode 1 stress intensity factor range.

For periodic tensile cyclic traction $\Delta q(m) = \Delta q_0 = const$, the problem can be solved analytically. Equation (3.1) implies the fracture cycle number for an infinite plane without crack is $n_\infty^* = \left(\sigma_{R1}^{*\Delta}/\Delta q_0\right)^b$ under such loading. As was mentioned above, $n_0^* = 0$ if there exists an initial crack.

Let $\tilde{n} = n/n_\infty^*$ be the normalised cycle number. After substituting stress (3.3) into (3.2), the equation can be solved using the Laplace transform *under the assumption $b < 2$*, giving

$$\frac{da(\tilde{n})}{d\tilde{n}} = \frac{\Delta K_1^2(a(\tilde{n}))}{\Delta q_0^2 2\sin(b\pi/2)}\left[\frac{\Delta K_1^4(a(\tilde{n}))}{\Delta K_1^4(a_0)} - 1\right]^{1-b/2}. \qquad (3.5)$$

The results are presented on Fig. 1 and 2 for different b by solid lines.

On the other hand, the normal stress range $\Delta\sigma_{22}(m; y_1)$ (3.3)-(3.4) near the crack tip can be approximated asymptotically (e.g. [5]) by the expression $\Delta\sigma_{22}(m; a(m), y_1) = \frac{\Delta K_1(m, a(m))}{\sqrt{2\pi(y_1 - a(m))}}$. If we use the asymptotic stress distribution, after solving the corresponding Volterra equation we arrive at the results presented on Fig. 1 and 2 by dashed lines.
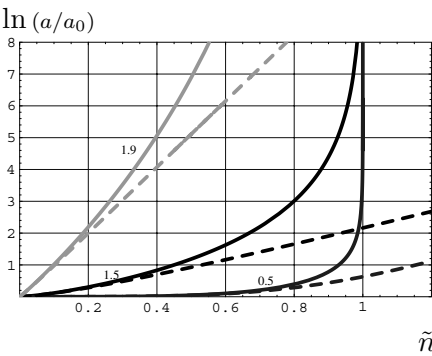

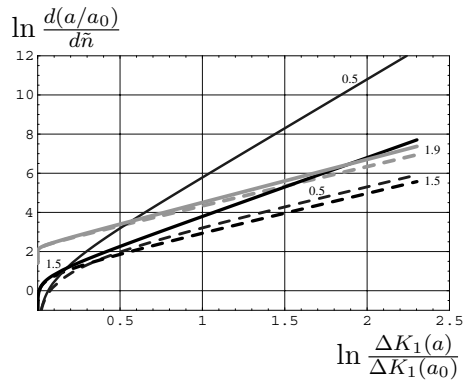*Figure 1* Fatigue crack length vs. cycle number for different b (local approach).

Figure 2 Fatigue crack growth rate vs. stress intensity factor range for different b (local approach).

One can see from Fig. 1 that the durability of the *infinite* plane with any crack is the same as its durability n_∞^* without crack. On the contrary, ex-

pression based on approximate (asymptotic) stress representation predicts unrealistic infinite durability for the infinite plane with a crack. The crack growth rate equations for both stress distributions look like the Paris type law given however not by a material functions of ΔK_1 but highly dependent on the initial crack size a_0 and applied loading q_0. They tend to the Paris law $da/dn = C\Delta K_1^k$ as $a(n)$ grows, see also Fig. 2, where the exponent $k = 2$ for employing the asymptotic stress distribution) and $k = 6 - 2b$ for the exact one (3.3), however C is again not a material constant but depends on the initial crack and applied loading.

The both solutions are valid only for $b < 2$ and blow up when $b \to 2$, that is, they are not able to describe the fatigue crack propagation for common structural materials with experimentally determined values for S–N diagram constants (usually $b \geq 4$). The local approach does not also predict the fatigue crack start delay observed experimentally. A way to overcome those shortcomings is an application of a non-local approach.

4. NON-LOCAL CYCLIC BRITTLE STRENGTH AND DURABILITY CONDITIONS

We will suppose that cyclic strength at a point $y \in \Omega$ on a plane $\vec{\zeta}$ depends not only on the cyclic stress history at that point, $\{\sigma_{ij}^c(m, y)\}_{m=1,2,\dots}$ but also on the stress history in its neighbourhood and generally, in the whole of the body, $\{\sigma^c(m, x)\}_{m=1,2,\dots}$, $x \in \Omega$.

A non-local brittle cyclic normalised equivalent stress functional $\underline{\Lambda}^{\odot}(\{\sigma\}; n, \Gamma, y, \vec{\zeta})$, which is positively homogeneous in σ and non-decreasing in n, can be introduced. It is considered as a material characteristics implicitly reflecting influence of material microstructure. Then the non-local cyclic strength condition *for a plane $\vec{\zeta}$ at a point $y \in \Omega$* takes the form $\underline{\Lambda}^{\odot}(\{\sigma\}; n, \Gamma, y, \vec{\zeta}) < 1$.

The simplest examples of the non-local brittle CNESFs and strength conditions are obtained by replacing the local stress $\sigma_{ij}(\tau, x)$ by its non-local counterpart $\sigma_{ij}^{\odot}(\tau; \Gamma, y, \vec{\zeta})$ in the corresponding local brittle CNESFs described in Section 2,

$$\underline{\Lambda}^{\odot}(\{\sigma^c\}; n, \Gamma, y, \vec{\zeta}) = \underline{\Lambda}(\{\sigma^{c\odot}(\cdot, \Gamma(\cdot), y, \vec{\zeta})\}; n, y, \vec{\zeta}), \qquad (4.1)$$

Similar to the non-local analysis of non-cyclic ([1] and references therein) and cyclic [6]–[9] strength, the non-local stress can be taken particularly as a weighted average of $\sigma_{ij}(\tau, x)$

$$\sigma_{ij}^{\odot}(\tau; \Gamma(\tau), y, \vec{\zeta}) = \int_{\Omega^{\odot}(y, \vec{\zeta}; \Gamma)} w(y, x)\sigma_{ij}(\tau; \Gamma(\tau), x, \vec{\zeta})dx, \qquad (4.2)$$

where the weight function $w(y, x)$ and the non-locality zone $\Omega^{\odot}$ (some neighbourhood of y) are characteristics of material point and plane and generally of the body shape Γ.

Using the introduced brittle non-local CNESF, the cyclic fracture process can be described as in Section 2 after replacement there the stress tensor σ by its non-local counterpart $\sigma^{\odot}$.

5. EXAMPLE OF NON-LOCAL DURABILITY ANALYSIS

5.1 Let us consider the 2D problem from Section 3.1 using the non-local durability analysis with the particular non-local CNESF (4.1)-(4.2), where the crack propagation plane $\vec{\zeta}^*$ is prescribed by the problem symmetry, $\Omega^{\odot}(\Gamma, y, \vec{\zeta}^*)$ is the interval $(y_1 - \delta_-(y_1), y_1 + \delta)$ for y ahead of the crack $a(n)$ and not close to an opposite body boundary, $\delta_-(y_1) = \min(\delta, |y_1 - a(n)|)$ and δ is a material constant. As possible approximations, one can choose $w(y, x)$ as a constant w.r.t $x \in \Omega^{\odot}(y)$ and arrive at the Neuber stress averaging, cf [1], or as a piece-wise linear or as a more smooth hat-shaped function of x.

Repeating the same reasoning as in Section 3.1 but now for the non-local stress range $\Delta\sigma_{22}^{\odot}(m; a, y_1)$, we arrive at the same equations (3.1)-(3.2) where $\hat{\sigma}_{22}(a, y_1)$ must be replaced by $\hat{\sigma}_{22}^{\odot}(a, y_1) = \int_{y_1 - \delta_-(y_1)}^{y_1 + \delta} w(y_1, x_1)\hat{\sigma}_{22}(a, x_1)dx_1$. For a problem with initially existing crack, the crack propagation start instant n_0^* obtained from the non-local counterpart of (3.1) is non-zero since $|\hat{\sigma}_{22}^{\odot}(a_0, a_0)| < \infty$ at the crack tip in spite $|\hat{\sigma}_{22}(a_0, a_0)| = \infty$. For example, the start delay for a constant Δq_0 is $n_0^* = n_{\infty}^* |\hat{\sigma}_{22}^{\odot}(a_0, a_0)|^{-b}$.

Since $|\hat{\sigma}_{22}^{\odot}(a(n), a(n))| < \infty$, we can differentiate the non-local counterpart of (3.2) w.r.t. $a(n)$ and arrive at the following linear non-convolution Volterra equation of the second kind for the unknown function $g(a)$

$$g(a(n)) + \int_{a_0}^{a(n)} \mathcal{K}(a(n), a)g(a)da = -|\hat{\sigma}_{22}^{\odot}(a_0, a_0)|^{-b}\mathcal{K}(a(n), a_0), \quad (5.1)$$

where $\mathcal{K}(a(n), a) = |\hat{\sigma}_{22}^{\odot}(a(n), a(n))|^{-b}\frac{\partial}{\partial a(n)}|\hat{\sigma}_{22}^{\odot}(a, a(n))|^{b}$.

5.2 Let us consider the non-local version of the particular problem from Section 3.2, and choose the piece-wise linear weight

$$w(y_1, x_1) = \frac{2(\delta - |y_1 - x_1|)}{\delta^2 + 2\delta\delta_-(y_1) - \delta_-^2(y_1)},$$

$x_1 \in (y_1 - \delta_-(y_1), y_1 + \delta)$. Using (3.3) for $y_1 = a_0$ and $\delta_-(y_1) = 0$, we obtain the corresponding non-local stress at the crack tip. It can be used

to estimate the material parameter $\delta = \frac{32}{9\pi} \left(\frac{K_{1c}}{\sigma_r} \right)^2$ from the experimental data on the monotonous tensile strength σ_r for a smooth sample and the critical stress intensity factor K_{1c} for a sample with a long crack. The non-local stress can be also used in the above formula for n_0^* to calculate the crack start delay

$$n_0^* = n_\infty^* \left[\frac{(a_0+\delta)\sqrt{2a_0+\delta}}{\delta^{3/2}} + \frac{a_0^2}{\delta^2} \ln \frac{a_0}{a_0+\delta+\sqrt{\delta(2a_0+\delta)}} \right]^{-b}$$

under a uniform tensile periodic traction $\Delta q(m, x) = \Delta q_0$.

Results of the numerical solution of Volterra equation (5.1) with $\delta = 0.5a_0$ are presented on Fig. 3 and Fig. 4 for different b. The specific non-
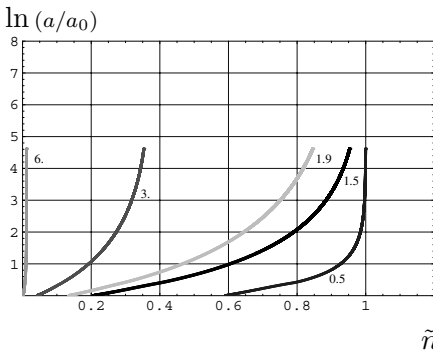

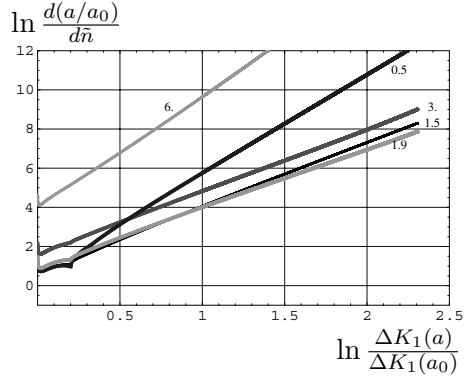*Figure 3*   Fatigue crack length vs. cycle number for different b (non-local approach).

Figure 4   Fatigue crack growth rate vs. stress intensity factor range for different b (non-local approach).

monotonous and non-smooth dependence of the crack growth rate $\frac{d(a/a_0)}{d\tilde{n}}$ on the stress intensity factor range $\frac{\Delta K_1(a)}{\Delta K_1(a_0)}$ at the beginning, Fig. 4, can be perceived as a signature of the particular weight $w(y, x)$ and employed for simulation of the short crack retardation near inter-grain boundaries. Such curves may be useful for experimental identification of $w(y, x)$.

6.   CONCLUSIONS

A united description of fatigue crack initiation and propagation is principally possible using the local as well as the non-local approach, however the local approach in the considered examples can be applied only for a limited range of material fatigue parameters and cannot describe the crack start delay. The non-local approach seems to be free of the drawbacks. When the stress fields are available analytically or numerically and the strength conditions are associated with the linear accumulation rule, the 2D problem in both approaches can be reduced to non-linear Volterra equation(s) for the unknown crack geometry. It can be transformed for a single crack

to a linear non-convolution Volterra equation in the case of a material with a power-type S–N diagram.

Acknowledgments

References

[1] Mikhailov S.E., (1995-I,II). A functional approach to non–local strength conditions and fracture criteria – I. Body and point fracture. II. Discrete fracture. Engng Fracture Mech. **52**, p. 731-754.

[2] Mikhailov, S.E., (2003) Theoretical Backgrounds of Durability Analysis by Normalized Equivalent Stress Functionals, *Mathematics and Mechanics of Solids*, **8**, p. 105–142.

[3] Mikhailov, S.E., Namestnikova I.V., (2001) *Normalised Equivalent Stress Functionals for Cyclic Fatigue*, Preprint PP/MAT/SEM/0102-005, Glasgow Caledonian University, 53 p.

[4] Rabotnov Yu.N., (1980) Elements of hereditary solid mechanics, Moscow, Mir Publishers, 387 p.

[5] Savin G.N., (1961) Stress concentration around holes, Oxford, Pergamon Press.

[6] Seweryn A. and Mróz Z., (1996) A non-local stress failure and fatigue damage accumulation condition, In *Multiaxial Fatigue and Design*, ESIS 21 (Edited by A.Pineau, G.Cailletaud, and T.C.Lindley), Mechanical Engineering Publications, London, p.261-282.

[7] Shang D.G., Wang D.K., Li M., Yao W.X., (2001) Local stress-strain field intensity approach to fatigue life prediction under random cyclic loading, *International Journal of Fatigue*, **23**, p. 903-910.

[8] Sheppard S.D., (1989) Field effects in fatigue crack initiation long life fatigue strength, In *Failure Prevention and Reliability - 89*, ASME, New York, p. 119-127.

[9] Taylor D., (2001) A mechanistic approach to critical-distance methods in notch fatigue, *Fatigue and Fracture of Engineering Materials and Structures*, **24**(4), p. 215-224.

A VARIATIONAL APPROACH TO MODELLING INITIATION OF FRACTURE IN NONLINEAR ELASTICITY

J. Sivaloganathan[1] and S. J. Spector[2]

[1] *Department of Mathematical Sciences, University of Bath, Bath BA2 7AY, U.K.*
js@maths.bath.ac.uk

[2] *Department of Mathematics, Southern Illinois University, Carbondale IL 62901, U.S.A.*
sspector@math.siu.edu

Keywords: Nonlinear elasticity, cavitation, energy momentum tensor.

Abstract   In this paper we present an overview of a variational approach to modelling the initiation of fracture in a nonlinearly elastic material. The work is motivated by experiments on polymers in which cracks initiate at cavities that form in the polymer sample under sufficiently severe loading.

1.   INTRODUCTION

This work is motivated in part by interesting experiments of Gent and Park [6]. Gent and Park took samples of transparent polymers and bonded a rigid bead within each sample. They then subjected the samples to uniaxial tension. The beads acted as stress concentrators and Gent and Park observed that, as the loading increased, small cavities (not previously evident in the sample) would form near the poles of the bead along the axis of tension. These would then enlarge and elongate into a crack-like shape in the direction of loading leading eventually to failure/fracture of the sample (see figure 1).

In this paper we give an overview of new results on a variational approach to modelling such phenomenon that has recently been developed (see e.g. [13], [14], [15]).

The experiments of Gent & Park
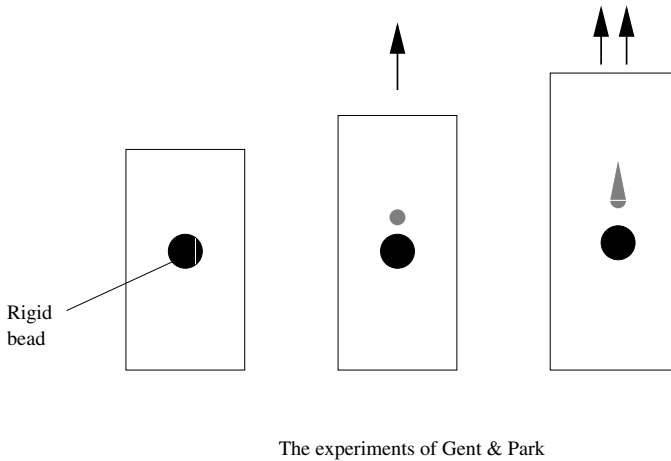
Figure 1   Formation of a cavity leading to a crack.

It is known that, under suitable hypotheses, minimisers of variational problems in elasticity may develop discontinuities which can be interpreted as cavities forming in an initially perfect material. (See [1], [12], [17], [8] for the radial cavitation problem and subsequent development of [10], [13], [14] for general boundary value problems with no assumption of symmetry.) Alternatively, such singular minimisers can be interpreted as the limiting deformation of a body containing a small pre-existing cavity in the reference configuration of diameter $\varepsilon > 0$, centred at the cavitation point, in the limit as $\varepsilon \to 0$ (see [12], [7], [18]).

In elastomers, such as used in the Gent and Park experiments, one expects that the cavities observed result from the expansion of pre-existing (initially non-visible) holes in the material. Thus, in the theoretical variational approach of [10] cavities can form anywhere whereas, in an actual material sample, the cavities are formed by the expansion of tiny pre-existing voids which were created during the manufacturing process.

In this paper both the above viewpoints are adopted simultaneously: the theoretical material is modelled as initially perfect using a homogeneous stored energy function but the flaws in the actual material are incorporated by using deformations whose point discontinuities are constrained to be at pre-specified points (the flaws in the material). If pre-existing voids (flaws) are widespread then one anticipates both approaches should yield similar results. However, we show that if a flaw is not located at an energetically optimal point then this gives rise to a configurational force. Hence, if flaw points are sparse and all such points are located sufficiently far from

energetically optimal points, then we conjecture that cavitation will first occur at one of these flaws and that the resulting configurational force may be sufficient to produce a fracture/crack in the material initiating from the cavity.

We would like to acknowledge the fundamental work of Ball [1] on radial cavitation which has motivated our current approach. Our aim in this paper is to give the underlying ideas whilst, for the most part, suppressing technical details.

2. MATHEMATICAL PRELIMINARIES

Let $\Omega \subset \mathbb{R}^3$ denote the region occupied by a nonlinear elastic body in its reference (undeformed) state. By a deformation of the body we mean a map $\mathbf{u} : \Omega \to \mathbb{R}^3$ belonging to the Sobolev space $W^{1,1}(\Omega)$, which is one-to-one (almost everywhere), and which satisfies the local invertibility condition

$$\det \nabla \mathbf{u} > 0. \tag{2.1}$$

As we shall see, this class of deformations includes discontinuous maps. In nonlinear hyper-elasticity we associate with each such deformation of the body an energy given by

$$E(\mathbf{u}) = \int_\Omega W(\nabla \mathbf{u}(\mathbf{x})) \, d\mathbf{x}, \tag{2.2}$$

where $W : \mathrm{M}_+^{3 \times 3} \to \mathbb{R}^+$ is the stored energy function of the material and $\mathrm{M}_+^{3 \times 3}$ denotes the 3×3 matrices with positive determinant. (See e.g. [4], [2] for further background.) In this paper we consider the displacement boundary value problem in which we require that

$$\mathbf{u}|_{\partial \Omega} = \mathbf{A}\mathbf{x}, \tag{2.3}$$

where $\mathbf{A} \in \mathrm{M}_+^{3 \times 3}$ is fixed.

The equilibrium equations of nonlinear elasticity are formally given by the Euler-Lagrange equations for (2.2):

$$\mathrm{Div}\left(\frac{\partial W}{\partial \mathbf{F}}(\nabla \mathbf{u})\right)_i = \frac{\partial}{\partial x^\alpha}\left[\frac{\partial W}{\partial F_\alpha^i}(\nabla \mathbf{u}(\mathbf{x}))\right] = 0, \ \mathbf{x} \in \Omega, \ i = 1, 2, 3. \tag{2.4}$$

An alternative form of the equilibrium equations is the so called energy-momentum form given by

$$\mathrm{Div}\, \mathbf{M}(\nabla \mathbf{u}) = \mathbf{0}, \tag{2.5}$$

where

$$\mathbf{M}(\nabla \mathbf{u}) := W(\nabla \mathbf{u})\mathbf{I} - (\nabla \mathbf{u})^{\mathrm{T}}\frac{\partial W}{\partial \mathbf{F}}(\nabla \mathbf{u})$$

is the energy-momentum tensor. (See Eshelby [5], and Ball [3] for a rigorous derivation of (2.5) as a necessary condition for a minimiser.) For smooth, invertible equilibria the two forms are equivalent but, for singular/discontinuous equilibria, weak solutions of (2.4) and (2.5) may differ. In the variational approach we seek weak solutions of (2.4), (2.5) by minimising the energy among deformations satisfying (2.1) and (2.3).

Notice that an immediate solution of (2.4), (2.3) is the homogeneous map

$$\mathbf{u}^h(\mathbf{x}) \equiv \mathbf{A}\mathbf{x}.$$

A central question we will address is whether there exist discontinuous deformations satisfying (2.3) with less energy than $\mathbf{u}^h$. The next remark shows that, far from being special, the homogeneous deformations $\mathbf{u}^h$ and the class of boundary conditions (2.3) play an important role in studying local minimisers of the energy (2.2).

Remark. If $\mathbf{u}_0 \in W^{1,1}(\Omega)$ is a strong local minimiser of (2.2) (i.e. for some $\epsilon > 0$, $E(\mathbf{u}) \geq E(\mathbf{u}_0)$ for any $\mathbf{u}$ with $||\mathbf{u} - \mathbf{u}_0||_{L^\infty} < \epsilon$) subject to the conditions (2.1),(2.3) and if $\mathbf{u}_0$ is C^1 at $\mathbf{x}_0 \in \Omega$ then it follows that, for any domain D, the stored energy function satisfies

$$E(\tilde{\mathbf{u}}) = \int_D W(\mathbf{A}_0 + \nabla\mathbf{v}(\mathbf{y}))\, d\mathbf{y} \geq \int_D W(\mathbf{A}_0)\, d\mathbf{y} = E(\mathbf{u}_0^h)$$

for all $\mathbf{v} \in W_0^{1,1}(\Omega)$, where $\tilde{\mathbf{u}}_0(\mathbf{y}) = \mathbf{A}_0\mathbf{y} + \mathbf{v}(\mathbf{y})$, $\mathbf{u}_0^h(\mathbf{y}) = \mathbf{A}_0\mathbf{y}$ and $\mathbf{A}_0 := \nabla\mathbf{u}_0(\mathbf{x}_0)$. In other words the homogeneous deformation $\mathbf{u}_0^h$ has least energy amongst all deformations of $\Omega = D$ satisfying the boundary condition (2.3) with $\mathbf{A} = \mathbf{A}_0$ or, equivalently, the stored energy function W is $W^{1,1}$-quasiconvex at $\mathbf{A}_0$. (See James and Spector [9] for further details.)

Example. A simple class of stored energy functions we will consider is given by

$$W(\mathbf{F}) = \kappa|\mathbf{F}|^p + h(\det \mathbf{F}), \quad \mathbf{F} \in M_+^{3\times3}, \quad p \geq 1, \tag{2.6}$$

where $\kappa > 0$, $|\cdot|$ denotes the Euclidean norm ($|\mathbf{A}|^2 = \text{trace}(\mathbf{A}^T\mathbf{A})$), and $h : (0,\infty) \to [0,\infty)$ is C^1, convex and satisfies $h(d) \to +\infty$ as $d \to 0^+$ and $\frac{h(d)}{d} \to +\infty$ as $d \to +\infty$. Such energy functions are examples of polyconvex stored energies introduced by Ball (see e.g. [2]) and include examples of energies proposed by Ogden [11] to fit observed experimental data. For ease of exposition we state the results in this paper for stored energy functions of the form (2.6) (though our methods apply to much more general polyconvex stored energy functions, including those with explicit dependence on the adjugate of $\mathbf{F}$, $\text{Adj}\,\mathbf{F}$).

It is a mathematical fact that, for stored energy functions of the form (2.6), if $p > 3$ and $E(\mathbf{u}) < +\infty$ then $\mathbf{u} \in W^{1,p}(\Omega)$ and is continuous by the Sobolev embedding theorem (a more sophisticated argument yields the same result under condition (2.1) in the case $p = 3$). Hence to model the formation of discontinuities we work in the regime $p < 3$.

The Distributional Jacobian. The key to modelling the formation of discontinuities lies in the use of the distributional Jacobian; first note that, for C^2 maps, $\det \nabla \mathbf{u}$ is expressible as a divergence:

$$\det \nabla \mathbf{u} = \frac{\partial}{\partial x^\alpha} \left(\frac{1}{3} (\mathrm{Adj} \nabla \mathbf{u})_i^\alpha u^i \right) = \mathrm{div} \left(\tfrac{1}{3} (\mathrm{Adj} \nabla \mathbf{u}) \mathbf{u} \right). \qquad (2.7)$$

where $\mathrm{Adj} \nabla \mathbf{u}$ denotes the adjugate matrix of $\nabla \mathbf{u}$. Next let $\varphi \in C_0^\infty(\Omega)$ (the infinity differentiable functions on Ω with compact support), multiply (2.7) by φ and integrate by parts to obtain

$$\int_\Omega \varphi \det \nabla \mathbf{u} \, d\mathbf{x} = - \int_\Omega \nabla \varphi \cdot \left[\frac{1}{3} (\mathrm{Adj} \nabla \mathbf{u}) \mathbf{u} \right] d\mathbf{x}. \qquad (2.8)$$

This motivates the definition of the distributional Jacobian, $\mathrm{Det}\, \nabla \mathbf{u}$, which is the functional defined by

$$(\mathrm{Det}\, \nabla \mathbf{u})(\varphi) := -\frac{1}{3} \int_\Omega \nabla \varphi \cdot [(\mathrm{Adj} \nabla \mathbf{u}) \mathbf{u}] \, d\mathbf{x}, \quad \forall \varphi \in C_0^\infty(\Omega). \qquad (2.9)$$

It follows from (2.8) that for C^2 maps $\mathbf{u}$

$$(\mathrm{Det}\, \nabla \mathbf{u})(\varphi) = \int_\Omega \varphi \det \nabla \mathbf{u} \, d\mathbf{x}, \quad \forall \varphi \in C_0^\infty(\Omega),$$

and we denote this by

$$\mathrm{Det}\, \nabla \mathbf{u} = (\det \nabla \mathbf{u}) \mathcal{L}^3, \qquad (2.10)$$

where $\mathcal{L}^3$ denotes 3-dimensional Lebesgue measure. For discontinuous deformations $\mathbf{u} \in W^{1,1}(\Omega)$ the distributional Jacobian is not in general given by (2.10) as illustrated by the next example.

Example. Let $\Omega = B$ the unit ball in $\mathbb{R}^3$ and let $\mathbf{u} : \Omega \longrightarrow \mathbb{R}^3$ be given by $\mathbf{u}(\mathbf{x}) = \mathbf{x} + c \frac{\mathbf{x}}{|\mathbf{x}|}$ where $c > 0$. Then $\det \nabla \mathbf{u}(\mathbf{x}) > 0$ for $\mathbf{x} \neq \mathbf{0}$ and $\mathbf{u}$ produces a hole of radius c at the centre of B. The distributional Jacobian of this map is given by

$$\mathrm{Det}\, \nabla \mathbf{u} = (\det \nabla \mathbf{u}) \mathcal{L}^3 + \frac{4}{3} \pi c^3 \delta_{\mathbf{0}} , \qquad (2.11)$$

where $\delta_{\mathbf{0}}$ denotes the Dirac measure supported at the origin. In analogy with (2.10), (2.11) is to be interpreted in the sense (of distributions) that

$$(\text{Det } \nabla \mathbf{u})(\varphi) = \int_\Omega \varphi \det \nabla \mathbf{u}\, d\mathbf{x} + \frac{4}{3}\pi c^3 \varphi(0), \quad \forall \varphi \in C_0^\infty(\Omega).$$

Modelling flaws in a material. The above discussion motivates our modelling of (initially non-visible) flaws in a material by restricting attention to maps satisfying

$$\text{Det } \nabla \mathbf{u} = (\det \nabla \mathbf{u})\mathcal{L}^3 + \sum_{i=1}^m \alpha_i \delta_{\mathbf{x}_i}, \tag{2.12}$$

where $\alpha_i \geq 0$. Hence if $\alpha_k > 0$ for some k, then the map $\mathbf{u}$ produces a hole of volume α_k at $\mathbf{x}_k \in \Omega$. (Note that the holes produced need not be spherical.)

Condition INV. It turns out that maps $\mathbf{u} \in W^{1,1}(\Omega)$ satisfying (2.1) and (2.3) need not be one-to-one almost everywhere. Take, for example, the discontinuous deformation of B given above and this time let $-1 < c < 0$ (a hole of "negative radius"). It is easily verified that the corresponding deformation $\mathbf{u}$ still satisfies $\det \nabla \mathbf{u} > 0$ almost everywhere, however, $\mathbf{u}$ is no longer one-to-one in a neighbourhood of the origin. Moreover, in this case

$$\int_B \det \nabla \mathbf{u}\, d\mathbf{x} = \frac{4}{3}\pi((1+c)^3 - c^3) > \text{vol}(\mathbf{u}(B)),$$

so the classical change of variables formula clearly fails.

The (invertibility) condition INV introduced by Müller and Spector [10] in particular excludes the last example and is well suited for proving the existence of minimisers of (2.2) in classes of deformations that allow cavitation to occur. Essentially, INV is the requirement that holes produced within one part of the body are not filled by material from other parts (see [10] for further details).

Remark. In particular, it is shown in [10] that if $\mathbf{u}$ satisfies INV on Ω and $\mathbf{u}|_{\partial\Omega} = \mathbf{h}$, where $\mathbf{h} : \bar{\Omega} \to \mathbb{R}^3$ is a homeomorphism then $\text{vol}(\mathbf{h}(\Omega)) = (\text{Det } \nabla \mathbf{u})(\Omega)$.

Theorem 1 (Existence of minimisers [13]). *Let* $\mathbf{x}_1, \mathbf{x}_2, \ldots, \mathbf{x}_m \in \Omega$, $p > 2$, $\alpha_1, \alpha_2, \ldots, \alpha_m \geq 0$, *and define the set of admissible deformations*

$\mathcal{A} = \mathcal{A}(\mathbf{x}_1, \mathbf{x}_2, \ldots, \mathbf{x}_m)$ *by*

$$\mathcal{A} := \{\mathbf{u} \in W^{1,p}(\Omega) : \mathbf{u}|_{\partial\Omega} = \mathbf{A}\mathbf{x}, \; \mathbf{u}^e \text{ satisfies INV on } \Omega_0,$$

$$\text{Det } \nabla\mathbf{u} = (\det \nabla\mathbf{u})\mathcal{L}^3 + \sum_{i=1}^{m} \alpha_i \delta_{\mathbf{x}_i}, \; \det \nabla\mathbf{u} > 0 \; a.e.\},$$

where Ω_0 is a bounded domain with $\Omega_0 \supset \bar{\Omega}$ and $\mathbf{u}^e$ is the homogeneous extension to Ω_0 of $\mathbf{u}$ defined by[1]

$$\mathbf{u}^e(\mathbf{x}) := \begin{cases} \mathbf{u}(\mathbf{x}), & \text{if } \mathbf{x} \in \bar{\Omega}, \\ \mathbf{A}\mathbf{x}, & \text{if } \mathbf{x} \notin \bar{\Omega}. \end{cases}$$

Let E be defined by (2.2) and (2.6). Then E has a minimum on $\mathcal{A}$.

The next result shows that any minimiser given by the above theorem must produce a discontinuity if the boundary condition (2.3) is sufficiently severe.

Theorem 2. *Let $\tilde{\mathbf{A}} \in \mathrm{M}_+^{3\times3}$ be fixed and define $\mathbf{A} = t\tilde{\mathbf{A}}$ where $t > 0$. Then for sufficiently large t any minimiser of E on $\mathcal{A}$ (whose existence is given by the last theorem) must satisfy $\alpha_i > 0$ for some i.*

Proof. The proof proceeds in two stages.

Step 1. We first prove that if the deformation $\mathbf{u}$ is such that $\alpha_i = 0$, $i = 1, 2, \ldots, m$, then
$$E(\mathbf{u}) \geq E(\mathbf{u}^h),$$
where $\mathbf{u}^h$ is the homogeneous deformation. This follows easily from the definition of E and the convexity of h in (2.6) since

$$E(\mathbf{u}) = \int_\Omega [\kappa|\nabla\mathbf{u}|^p + h(\det \nabla\mathbf{u})] \, d\mathbf{x}$$

$$\geq \int_\Omega \left[\kappa|\nabla\mathbf{u}|^p + h(\det \mathbf{A}) + h'(\det \mathbf{A})(\det \nabla\mathbf{u} - \det \mathbf{A})\right] d\mathbf{x}.$$

It follows from our assumptions that $\text{Det } \nabla\mathbf{u} = (\det \nabla\mathbf{u})\mathcal{L}^3$ and hence, by an earlier remark (see discussion on condition INV), it follows that

$$\int_\Omega \det \nabla\mathbf{u} \, d\mathbf{x} = \text{vol}(\mathbf{u}^h(\Omega)) = \int_\Omega \det \mathbf{A} \, d\mathbf{x}.$$

---

[1] The use of $\mathbf{u}^e$ is a technical requirement which prevents the formation of cavities at the boundary of Ω.

Thus

$$E(\mathbf{u}) \geq \int_\Omega \kappa |\nabla \mathbf{u}|^p + h(\det \mathbf{A})\, d\mathbf{x} \geq \int_\Omega \kappa |\mathbf{A}|^p + h(\det \mathbf{A})\, d\mathbf{x} = E(\mathbf{u}^h),$$

where the last inequality is a result of Jensen's inequality.

Step 2. It now suffices to demonstrate that for sufficiently large t, there exists a deformation $\tilde{\mathbf{u}} \in \mathcal{A}$ satisfying

$$E(\tilde{\mathbf{u}}) < E(\mathbf{u}^h).$$

It will then follow that any minimiser must satisfy $\alpha_i > 0$ for some i (i.e. the minimiser must be discontinuous). We first assume that $\Omega = B$ and define

$$\tilde{\mathbf{u}}(\mathbf{x}) = \tilde{\mathbf{A}}(d|\mathbf{x}|^3 + (1-d))^{\frac{1}{3}} \frac{\mathbf{x}}{|\mathbf{x}|}, \tag{2.13}$$

where $d \in (0,1)$ is a constant. An easy calculation yields

$$\det \nabla \tilde{\mathbf{u}} = (\det \tilde{\mathbf{A}})\, d$$

and clearly

$$\tilde{\mathbf{u}}|_{\partial B} = \tilde{\mathbf{A}}\mathbf{x}.$$

For $t > 0$ we next compare the energies of the maps

$$\mathbf{u} = t\tilde{\mathbf{u}}, \qquad \mathbf{u}^h = t\tilde{\mathbf{u}}^h,$$

where $\tilde{\mathbf{u}}^h(\mathbf{x}) \equiv \tilde{\mathbf{A}}\mathbf{x}$. Define $\triangle E := E(\mathbf{u}) - E(\mathbf{u}^h)$. Then

$$\triangle E = \int_\Omega \left[t^p [|\nabla \tilde{\mathbf{u}}|^p - |\tilde{\mathbf{A}}|^p] + h(t^3 \det \nabla \tilde{\mathbf{u}}) - h(t^3 \det \tilde{\mathbf{A}}) \right] d\mathbf{x}$$

$$= t^p \int_\Omega \left[|\nabla \tilde{\mathbf{u}}|^p - |\tilde{\mathbf{A}}|^p \right] d\mathbf{x} + |\Omega| \left[h(t^3 d \det \tilde{\mathbf{A}}) - h(t^3 \det \tilde{\mathbf{A}}) \right]$$

$$= t^p \int_\Omega \left[|\nabla \tilde{\mathbf{u}}|^p - |\tilde{\mathbf{A}}|^p \right] d\mathbf{x} + |\Omega| \left[\int_{t^3 d \det \tilde{\mathbf{A}}}^{t^3 \det \tilde{\mathbf{A}}} -h'(s)\, ds \right]$$

$$\leq t^p \int_\Omega \left[|\nabla \tilde{\mathbf{u}}|^p - |\tilde{\mathbf{A}}|^p \right] d\mathbf{x} - |\Omega| t^3 (1-d)(\det \tilde{\mathbf{A}}) h'(t^3 d \det \tilde{\mathbf{A}}).$$

Next note that, since $\frac{h(s)}{s} \to \infty$ by assumption, it follows that $h'(s) \to \infty$ as $s \to \infty$ and thus, since $p < 3$, it follows that $\triangle E < 0$ for all sufficiently large t. This completes the proof in the case $\Omega = B$. If $\Omega \neq B$ then we simply rescale and translate the deformation (2.13) onto a small ball centred at one of the flaw points and then extend it to $\Omega \backslash B$ by the homogeneous

deformation $\tilde{\mathbf{A}}\mathbf{x}$. Then exactly analogous arguments yield the same result.

Remark. It is a consequence of arguments in [16] that if $\mathbf{A} \in \mathrm{M}_+^{3\times3}$ is such that $h'(\det \mathbf{A}) \leq 0$ then

$$E(\mathbf{u}^h) \leq E(\mathbf{u}) \text{ for all } \mathbf{u} \in \mathcal{A}.$$

So discontinuous deformations satisfying (2.3) do not have less energy than the homogeneous deformation $\mathbf{u}^h$ if this condition holds.

3.   OPTIMAL LOCATION FOR A DISCONTINUITY

We next consider the case where there is only one flaw point in the material (so that deformations satisfy (2.12) with $m = 1$, i.e. there is only one flaw at $\mathbf{x}_1 \in \Omega$). It is a consequence of a simple scaling argument that if there exists a deformation $\mathbf{u} \in \mathcal{A}(\mathbf{x}_1)$ with a discontinuity at $\mathbf{x}_1 \in \Omega$ and such that $E(\mathbf{u}) < E(\mathbf{u}^h)$ then given *any* point $\mathbf{x}_2 \in \Omega$ there exists a map $\tilde{\mathbf{u}} \in \mathcal{A}(\mathbf{x}_2)$ with discontinuity at $\mathbf{x}_2$ and with $E(\tilde{\mathbf{u}}) < E(\mathbf{u}^h)$ (see [14]). We now address the problem of determining the energetically optimal location for the flaw point.

Inner variations; moving a flaw; the energy momentum tensor. Let $\mathbf{u} = \mathbf{u}(\cdot, \mathbf{x}_1, \mathbf{A})$ denote a minimiser of E on $\mathcal{A}(\mathbf{x}_1)$. We consider an inner variation of $\mathbf{u}$ i.e. a variation of $\mathbf{u}$ of the form:

$$\mathbf{u}_\varepsilon(\mathbf{x}) = \mathbf{u}(\mathbf{x} + \varepsilon\mathbf{v}(\mathbf{x})), \quad \varepsilon \in \mathbb{R},$$

where $\mathbf{v} \in C_0^1(\Omega)$ satisfies $\mathbf{v} \equiv -\mathbf{m}$ (a constant vector in a neighbourhood $B_\delta(\mathbf{x}_1)$ of $\mathbf{x}_1$). Note that the variations move the potential discontinuity point $\mathbf{x}_1$ in the direction of $\mathbf{m}$. It follows from arguments of, for example, Ball [3] that if h satisfies $|sh'(s)| \leq const[h(s) + 1] \ \forall s$ then

$$\delta E := \frac{d}{d\varepsilon} E(\mathbf{u}_\varepsilon)\Big|_{\varepsilon=0} = \int_{\Omega\backslash B_\delta(\mathbf{x}_1)} \nabla\mathbf{v} : \mathbf{M}(\nabla\mathbf{u}) \, d\mathbf{x},$$

where

$$\mathbf{M}(\mathbf{F}) = \left[W(\mathbf{F})\mathbf{I} - \mathbf{F}^{\mathrm{T}}\frac{\partial W}{\partial \mathbf{F}}(\mathbf{F})\right]$$

is the energy-momentum tensor.

Next assume that $\mathbf{u}(\cdot, \mathbf{x}_1, \mathbf{A})$ is smooth in $\Omega\backslash B_\delta(x_1)$ (so that (2.5) holds in this region) to obtain

$$\delta E = \int_{\Omega\backslash B_\delta(\mathbf{x}_1)} \mathrm{div}[\mathbf{M}(\nabla\mathbf{u})^{\mathrm{T}}\mathbf{v}] \, d\mathbf{x} = \int_{\partial B_\delta(x_1)} \mathbf{v} \cdot \mathbf{M}(\nabla\mathbf{u})\mathbf{n} \, ds$$

$$= \int_{\partial B_\delta(\mathbf{x}_1)} -\mathbf{m} \cdot \mathbf{M}(\nabla \mathbf{u})\mathbf{n} \, ds = \int_{\partial\Omega} \mathbf{m} \cdot \mathbf{M}(\nabla \mathbf{u})\mathbf{n} \, ds. \tag{3.1}$$

To continue with our analysis we need to make assumptions on the regularity of minimisers given by Theorem 1. These are motivated by corresponding results that are known to hold in the case of radial cavitation.

Hypotheses. We assume that for each $\mathbf{x}_1 \in \Omega$ there is a unique minimiser of E on $\mathcal{A}(\mathbf{x}_1)$ denoted $\mathbf{u}(\cdot, \mathbf{x}_1, \mathbf{A})$. We further assume that $\mathbf{A}(t)$, $t \in \mathbb{R}$ is a smooth one-parameter family of matrices such that for $t > 0$ the minimiser $\mathbf{u}(\cdot, \mathbf{x}_1, \mathbf{A}) \in \mathcal{A}(\mathbf{x}_1)$ is discontinuous and for $t \le 0$ the minimiser is $\mathbf{u}(\mathbf{x}, \mathbf{x}_1, \mathbf{A}) \equiv \mathbf{A}\mathbf{x}$. We define $\mathbf{A}_{crit} = \mathbf{A}(0)$. Finally we assume that for any $\delta > 0$, $\mathbf{u}(\cdot, \mathbf{x}_1, \mathbf{A}) \to \mathbf{u}_{crit}^h \equiv \mathbf{A}_{crit}\mathbf{x}$ in $C^2(\bar{\Omega} \backslash B_\delta(\mathbf{x}_1))$ as $t \to 0$.

We write

$$\mathbf{u}(\mathbf{x}, \mathbf{x}_1, \mathbf{A}) = \mathbf{A}\mathbf{x} + \mathbf{w}(\mathbf{x}, \mathbf{x}_1, \mathbf{A}), \tag{3.2}$$

where $\mathbf{w} = \mathbf{0}$ for $\mathbf{x} \in \partial\Omega$, and expand (3.1) as a series for $t > 0$ at $t = 0$. First, we rewrite the right hand side of (3.1) using (3.2) as

$$\mathbf{m} \cdot \int_{\partial\Omega} \left[(W(\mathbf{A} + \nabla_{\mathbf{x}}\mathbf{w}) - W(\mathbf{A}))\mathbf{I} - (\nabla_{\mathbf{x}}\mathbf{w})^{\mathrm{T}} \frac{\partial W}{\partial \mathbf{F}}(\mathbf{A} + \nabla_{\mathbf{x}}\mathbf{w}) \right] \mathbf{n} \, ds, \tag{3.3}$$

where we have used the fact that

$$\int_{\partial\Omega} \mathbf{A}^{\mathrm{T}} \frac{\partial W}{\partial \mathbf{F}}(\mathbf{A} + \nabla_{\mathbf{x}}\mathbf{w})\mathbf{n} \, ds = \mathbf{0}$$

since $\mathbf{u}(\cdot, \mathbf{x}_1, \mathbf{A})$ is a minimiser of E on $\mathcal{A}(\mathbf{x}_1)$ (see [14] for details) and also that

$$\int_{\partial\Omega} W(\mathbf{A})\mathbf{n} \, ds = \mathbf{0}.$$

Expanding (3.3) as a series in t for $t > 0$ now yields

$$\delta E = -\frac{t^2}{2} \mathbf{m} \cdot \int_{\partial\Omega} \mathbf{n} \left(\nabla_{\mathbf{x}} \dot{\mathbf{w}} : \frac{\partial^2 W}{\partial \mathbf{F}^2}(\mathbf{A}_{crit})[\nabla_{\mathbf{x}}\dot{\mathbf{w}}] \right) ds + o(t^2)$$

$$= -\frac{t^2}{2} \int_{\partial\Omega} m^\gamma n^\gamma \frac{\partial \dot{w}^i}{\partial x^\alpha} \frac{\partial^2 W}{\partial F_\alpha^i \partial F_\beta^j}(\mathbf{A}_{crit}) \frac{\partial \dot{w}^j}{\partial x^\beta} \, ds + o(t^2), \tag{3.4}$$

where $\dot{\mathbf{w}} = \frac{d}{dt}\mathbf{w}(\mathbf{x}, \mathbf{x}_1, \mathbf{A}(t))\big|_{t=0}$ is the right derivative of $\mathbf{w}$ at $t = 0$. The next lemma shows that $\dot{\mathbf{w}}$ solves a linear system.

Lemma 1. $\dot{\mathbf{w}}$ *is a (singular) solution of the linear system*

$$\frac{\partial}{\partial x^\gamma} \left[\frac{\partial^2 W}{\partial F_\gamma^i \partial F_\beta^j}(\mathbf{A}_{crit}) \frac{\partial \dot{w}^j}{\partial x^\beta} \right] = 0 \text{ in } \Omega \backslash \{\mathbf{x}_1\}, \ i = 1, 2, 3, \tag{3.5}$$

and satisfies the boundary condition $\dot{\mathbf{w}} = \mathbf{0}$ *on* $\partial\Omega$.

The proof of this follows from the assumptions on $\mathbf{w}$: in particular $\mathbf{w}$ satisfies

$$\frac{\partial}{\partial x^\alpha}\left[\frac{\partial W}{\partial F_\alpha^i}(\mathbf{A} + \nabla\mathbf{w})\right] = 0 \text{ in } \Omega\backslash\{\mathbf{x}_1\}, \ i = 1, 2, 3$$

and $\mathbf{w} = \mathbf{0}$ on $\partial\Omega$. Then, taking a right hand derivative with respect to t at $t = 0$ yields the required result.

Remark. To evaluate the integral in (3.4) it is helpful to first note that $\dot{\mathbf{w}} = 0$ on $\partial\Omega$ and to then rewrite it in the form

$$\int_{\partial\Omega} m^\gamma n^\gamma \frac{\partial \dot{w}^i}{\partial x^\alpha} \Lambda_{\alpha\beta}^{ij} \frac{\partial \dot{w}^j}{\partial x^\beta} - 2\dot{w}^i \Lambda_{\alpha\beta}^{ij} \frac{\partial^2 \dot{w}^j}{\partial x^\beta \partial x^\gamma} m^\gamma n^\alpha \, ds, \tag{3.6}$$

where $\Lambda_{\alpha\beta}^{ij} = \frac{\partial^2 W}{\partial F_\alpha^i \partial F_\beta^j}(\mathbf{A}_{crit})$. The second term is included since, by lemma 1, the corresponding integrand is then divergence free in $\Omega\backslash\{\mathbf{x}_1\}$ i.e. we have the quadratic conservation law

$$\frac{\partial}{\partial x^\gamma}\left(m^\gamma \frac{\partial \dot{w}^i}{\partial x^\alpha} \Lambda_{\alpha\beta}^{ij} \frac{\partial \dot{w}^j}{\partial x^\beta}\right) - \frac{\partial}{\partial x^\alpha}\left(2\dot{w}^i \Lambda_{\alpha\beta}^{ij} \frac{\partial^2 \dot{w}^j}{\partial x^\beta \partial x^\gamma} m^\gamma\right) = 0. \tag{3.7}$$

in $\Omega\backslash\{x_1\}$. In evaluating the integral (3.6) it is sometimes helpful to use (3.7) to transform it to an integral on $\partial B_\varepsilon(x_1)$ (see [15]).

Concluding Remarks. Our approach is to next derive an expansion on $\partial\Omega$ for the singular solution $\dot{\mathbf{w}}$ of the system (3.5) and hence calculate the sign of δE given by (3.1). If $\delta E \neq 0$ then we can conclude in particular that the location of the flaw point is not optimal. This procedure has been carried out in [15] in the case when $\Omega = B$, $\mathbf{A} = \lambda\mathbf{I}$ and it is shown that $\delta E \neq 0$ unless $\mathbf{x}_1$ is located at the centre of the ball B. Hence a cavity forming at a non-central location in the ball induces a non-zero configurational force (which is in fact directed towards the centre of the ball). We conjecture that this may be sufficient to cause the formation of a crack initiated from the cavity and directed towards the centre of the ball. For further details and a discussion of related issues we refer the interested reader to [13], [14], [15].

306

References

[1] J. M. Ball, "Discontinuous equilibrium solution and cavitation in nonlinear elasticity", Phil. Trans. Roy. Soc. London A **306** (1982), 557–611.

[2] J. M. Ball, "Constitutive inequalities and existence theorems in nonlinear elastostatics" in Nonlinear Analysis and Mechanics, Heriot-Watt Symposium Vol. 1, 187–241, Ed. R. J. Knops, Pitman, 1977.

[3] J. M. Ball, "Minimisers and the Euler-Lagrange equations" in Trends and Applications of Pure Mathematics to Mechanics, 1–4, Eds. P. G. Ciarlet and M. Roseau, Springer, 1984.

[4] P. G. Ciarlet, Mathematical Elasticity Vol. 1: Three-Dimensional Elasticity, North Holland, Amsterdam, 1988.

[5] J. D. Eshelby, "The elastic energy-momentum tensor", J. Elasticity **5** (1975), 321–335.

[6] A. Gent and B. Park, "Failure processes in elastomers at or near a rigid spherical inclusion", J. Materials Sci. **19** (1984), 1947–1956.

[7] C. O. Horgan and R. Abeyaratne, "A bifurcation problem for a compressible nonlinearly elastic medium: growth of a microvoid", J. Elasticity **16** (1986), 189–200.

[8] C. O. Horgan and D. A. Polignone, "Cavitation in nonlinearly elastic solids: A review", Appl. Mech. Rev. **48** (1995), 471–485

[9] R. D. James and S. J. Spector, "Remarks on $W^{1,p}$-quasiconvexity, interpenetration of matter, and function spaces for elasticity", Anal. non linéaire **9** (1992), 263–280.

[10] S. Müller and S. J. Spector, "An existence theorem for nonlinear elasticity that allows for cavitation" Arch. Rational Mech. Anal. **131** (1995), 1–66.

[11] R. Ogden, "Large deformation isotropic elasticity: on the correlation of theory and experiment for compressible rubberlike solids", Proc. Roy. Soc. London, A**328** (1972), 567–583.

[12] J. Sivaloganathan, "Uniqueness of regular and singular equilibria for spherically symmetric problems of nonlinear elasticity", Arch. Rational Mech. Anal. **96** (1986), 97–136.

[13] J. Sivaloganathan and S. J. Spector, "On the existence of minimisers with prescribed singular points in nonlinear elasticity", J. Elasticity **59** (2000), 83–113

[14] J. Sivaloganathan and S. J. Spector, "On the optimal location of singularities arising in variational problems of nonlinear elasticity", J. Elasticity **58** (2000), 191–224.

[15] J. Sivaloganathan and S. J. Spector, "On cavitation, configurational forces and implications for fracture in a nonlinearly elastic material", J. Elasticity, **67** (2002), 25-49.

[16] S. J. Spector, "Linear deformations as global minimisers in nonlinear elasticity", Q. Appl. Math. **52** (1994), 59–64.

[17] C. A. Stuart, "Radially symmetric cavitation for hyperelastic materials", Analyse Nonlineaire **2** (1985), 33–66.

[18] J. Sivaloganathan, S. J. Spector, and V. Tilakraj, "On the convergence of regularised minimisers of variational problems in nonlinear elasticity", preprint (2003).

MODELING FRACTURE IN NANO MATERIALS

Huajian Gao and Baohua Ji

Max Planck Institute for Metals Research
Heisenbergstrasse 3, D-70569, Stuttgart
Germany

hjgao@mf.mpg.de, ji@mf.mpg.de

Abstract   The recent surging interest in nanotechnology is providing a strong impetus to understanding fracture processes in nanoscale materials. There are open challenges because many classical concepts of fracture mechanics are no longer applicable as the characteristic dimension of a structure at nanoscale becomes comparable to or smaller than the size of the cohesive zone near a crack tip. In this paper, we apply a top down approach, the recently developed Virtual-Internal-Bond (VIB) method to investigating fracture of such nano-materials. We demonstrate that, at a critical length scale typically on the order of nanometer scale, the fracture mechanism changes from the classical Griffith fracture to one of homogeneous failure near the theoretical strength of solids.

Keywords: Nanomaterial, size effect, fracture modeling, cohesive zone

1.   INTRODUCTION

We are now entering the era of nano-technology. More and more nano-sized devices and nano-structured materials have or will come into our life, e.g. nanotubes, nanowires, nanobelts, biomolecular motors and nano bio-composites, etc. As the dimension of a structure approaches the fundamental length scale of a physical property, new mechanical, optical, and electrical properties arise that are not present in a macroscopic bulk material. Many classical concepts of fracture mechanics will no longer be applicable as the characteristic size of a structure becomes comparable to or smaller than the size of the cohesive zone near a crack tip. The failure mechanisms of materials become drastically different as the characteristic dimension decreases to nanoscale. For example, no well-defined crack front was observed in the molecular dynamics (MD) simulation of nanowire frac-

ture [1]. The effects of surfaces and interfaces are expected to dominate at nanoscale. In nanocomposites, the interfacial region, which is usually an imperceptible region of the matrix in a traditional filled polymer, becomes the dominant phase [2]. Biomolecular systems exhibit strong entropic effects at nanoscale [3, 4].

Atomistic methods for modeling nanoscale phenomena are often referred to as the "bottom up" approach, starting from electrons and atoms and reaching the scale of large molecular clusters. This is represented by various MD or *ab inito* calculations for simulating the mechanical behavior of nanostructures. The bottom up methods could accurately model the atomic nature of materials, but they are still subject to severe length and time scale limitations. On the other hand, continuum methods for nanoscale modeling and simulation can be called the "top down" approach. Such methods often start with extending the range of applicability of proven engineering methodologies to nanoscale phenomena. The continuum models are not subject to length and time scale limitations, but for obvious reasons they are phenomenological and can be quite inaccurate for nanoscale modeling.

Continuum models incorporating the atomic structure of solids can be traced back to the 19th century. An example was the Cauchy-Born rule that was described by Born as a means to estimate the theoretical strength and to assess the stability of cubic crystals subject to simple deformation. Attempts to make connections between atomistic and continuum descriptions of materials quickly followed [5, 6, 7]. Recently [8], the Cauchy-Born rule was used to derive nonlinear, hyperelastic constitutive models for use in numerical simulations to predict stress and deformation under physically realistic loading conditions. Gao and Klein [9, 10, 11] extended the concepts of Cauchy-Born rule and developed a Virtual-Internal-Bond method (VIB) to model crack nucleation, propagation and instability. The VIB model could describe the fracture process as a localization zone near a crack tip which is related to the virtual bond potential and fracture energy. In this paper, we apply the VIB method to investigating fracture in a nanoscale material. We focus on the features that are unique at the nanoscale such as transition of fracture mode from the classical Griffith fracture to homogeneous failure at the cohesive strength.

2. FRACTURE LOCALIZATION ZONE MODELED BY THE VIRTUAL INTERNAL BOND METHOD

The Virtual-Internal-Bond model was developed based on an extension of the Cauchy-Born concept which is a multiscale assumption about how

the motion of atoms can be related to continuum deformation measures. It attempts to reproduce the behavior of a homogeneous, hyperelastic solid, which has a microstructure consisting of internal cohesive bonds between a network of material particles which are not necessary atoms [9, 10, 11]. It had been demonstrated in the previous work [10] that the onset of fracture predicted by the VIB model is not determined solely by the choice of bond potential, but also depends on the state of deformation in the localization zone. The size of this localization zone could be evaluated via a J-integral analysis as [10]

$$h = -\frac{G}{\pi D_0 U(l_0)} \tag{2.1}$$

where D_0 is the constant in bond density function [9, 10], U is virtual bond potential, and l_0 is the length of the unstretched bond.

The dimension of h is a measure of the fracture localization zone. We see that the size of the localization zone is correlated with the fracture energy G and the virtual bond potential of the VIB model. The failure process of material described by the VIB model is illustrated in Fig.1, from point A of maximum traction force at the crack tip to the traction free point B where a pair of new surfaces are created. During the fracture simulation using a VIB-based finite element method (VIB-FEM), crack growth and nucleation is represented by a separation of two adjacent nodes at the crack tip, and the localization zone of fracture is represented by one overstretched sheet of mesh. In contrast to a conventional FEM calculation where the mesh size is a numerical concept which is selected only to achieve a desired computational accuracy, the mesh size of VIB-FEM has specific physical meaning in the sense that it is directly related to the J-integral and the fracture surface energy of the material. This is an important difference between VIB-FEM and conventional FEM calculations.

3.   FRACTURE STRENGTH OF NANOMATERIALS

According to the discussion of the last section, we know that the VIB model could describe fracture in a material via a localization zone whose width is determined from the fracture energy and the virtual bond potential. This will be the theoretical basis for our probing the size dependent fracture behavior of a nanomaterial. To illustrate the basic concept of nanoscale fracture, we start with a simple model involving an infinite nanostrip containing a semi-infinite crack along the midline of the strip, as shown in Fig.2. For simplicity we consider loading by constant vertical displacements along the strip boundaries. The height of the strip is H. We

can calculate the energy release rate of crack extension by J integral (plane stress) on the dashed–line contour Γ.

$$G = \Phi H = \frac{\sigma^2}{2E} H \tag{3.1}$$

where Φ is the strain energy density, E is the Young's modulus, and σ is the vertical normal stress far ahead of the crack tip in the strip. If we apply the Griffith criterion (i.e. the energy release rate equals twice the fracture surface energy γ for brittle fracture),

$$G = 2\gamma \tag{3.2}$$

the fracture strength and strain of strip can be obtained as

$$\sigma_f = 2\sqrt{\frac{\gamma E}{H}} \tag{3.3}$$

which corresponds to a fracture strain of

$$\varepsilon_f = 2\sqrt{\frac{\gamma}{EH}} \tag{3.4}$$

On the other hand, assuming the theoretical strength of solid is $\sigma_{th} = E/30$, we could write the following relation

$$\frac{\sigma_f}{\sigma_{th}} = 60\sqrt{\frac{\gamma}{EH}} \tag{3.5}$$

According to eqs. (3.4) and (3.5), the fracture strength has a simple relation with a dimensionless number $\sqrt{\frac{\gamma}{EH}}$, described in Fig.3 as the dashed-lines. There is a cross point between the dashed-line and the horizontal line measuring the cohesive strength on both Fig.3(a) and (b), beyond which the fracture strength predicted from the Griffith criterion would exceed the theoretical strength (This is physically impossible! See discussions below). This point corresponds to a critical thickness

$$H^* = \frac{4E\gamma}{\sigma_{th}^2} \tag{3.6}$$

Taking Young's modulus of the strip as 100 GPa, the fracture surface energy as 1 J/m^2, we obtain a value of H^* being around 40nm.

The Griffith criterion predicts a fracture strength exceeding the theoretical strength of solids is a physical contradiction and indicates that linear elastic fracture mechanics (LEFM) is not applicable at sufficiently small length scales. In fact, the critical length in eq. (3.6) measures the size of

the cohesive zone near a crack tip. As the structure size approaches this critical length which is on the nanometer scale, the small scale yielding concept, which is the basis for LEFM, is no longer valid and the hyperelastic material properties play a dominating role on fracture behavior. The implication is that in nanomaterials, the elastic softening behavior near the cohesive limit of materials, which is normally restricted to within the cohesive zone near a crack tip, now controls the fracture process. The conventional elasticity and FEM methods do not include the cohesive behaviors of solids and therefore can not be used to model the fracture behaviors of nanomaterials. One would need to develop new methods capable of modeling both the linear elastic and cohesive elastic material behaviors. VIB model is one of such examples and can be used to model nanoscale fracture.

In the following we use the VIB model to analyze the fracture strength of the same strip problem shown in Fig.2. The strain energy density in the nano-strip can be expressed with VIB model as [9, 10, 11]

$$\Phi(E_{IJ}) = D_0 \int_{-\pi}^{\pi} U\left(l_0\sqrt{1 + 2\xi_I E_{IJ}\xi_J}\right) d\varphi \tag{3.7}$$

where E_{IJ} and ξ_I denotes the Green-Lagrange strain tensor and the bond orientation, respectively. For two dimensional problem, $\xi = (\cos\varphi, \sin\varphi)$. The deformation gradient in this case is

$$\mathbf{F} = \begin{bmatrix} 1 & 0 \\ 0 & 1 + \varepsilon \end{bmatrix} \tag{3.8}$$

where ε is the uniform normal strain in the nano-strip far from the crack tip caused by the uniform load acted on the top side of the strip (see Fig. 2). From $E_{IJ} = \frac{1}{2}(F_{iI}F_{iJ} - \delta_{IJ})$, we have $E_{22} = \varepsilon + \varepsilon^2/2$, and eq. (3.7) becomes

$$\Phi(E_{IJ}) = \Phi(\varepsilon) = D_0 \int_{-\pi}^{\pi} U\left(l_0\sqrt{1 + (2\varepsilon + \varepsilon^2)\sin^2\varphi}\right) d\varphi \tag{3.9}$$

Solving the following equation

$$\Phi(\varepsilon_f) = \frac{2\gamma}{H} \tag{3.10}$$

yields a relation between ε_f and $\sqrt{\frac{\gamma}{EH}}$, where E is the Young's modulus of the VIB model. The P-K stress in normal direction is

$$S_{22}^f = D_0 \int_{-\pi}^{\pi} \frac{l_0^2 U'\left(l_0\sqrt{1 + (2\varepsilon_f + \varepsilon_f^2)\sin^2\varphi}\right)}{l_0\sqrt{1 + (2\varepsilon_f + \varepsilon_f^2)\sin^2\varphi}} \sin^2\varphi \, d\varphi \tag{3.11}$$

The Cauchy stress can be evaluated to be,

$$\sigma_f = (1 + \varepsilon_f)S_{22}^f \tag{3.12}$$

and the relation between σ_f and $\sqrt{\frac{\gamma}{EH}}$ can be further calculated. The predictions of the VIB model are described in Fig.3 as the solid lines. Note that the VIB predictions (solid curves) coincide with those of LEFM at large values of H but start to deviate from classical predictions for sufficiently small values of H. The critical thickness predicted by VIB is

$$H^* = \frac{2\gamma}{\Phi_{max}} \tag{3.13}$$

where Φ_{max} is the strain energy density when the stress is exactly equal to the theoretical strength. We emphasize that for hyperelastic material, $\Phi_{max} \neq \sigma^2/2E$. If we use the same material parameters as those used in the previous calculations based on LEFM, the critical thickness of strip is estimated to be about 10nm. The VIB model predicts that, as the strip height reduces to below this critical material length, the fracture strength no longer depends on the structure size and remains at the theoretical strength level.

What is the stress distribution near the crack tip near the critical length? What is the characteristic stress field associated with nanoscale fracture? How does the stress field near a crack tip changes from the classical K-field as the structural dimension decreases to nanoscale? To answer these questions and visualize the theoretical predictions, we use VIB-based finite element method to calculate the stress in the strip as a function of the strip height. The VIB-FEM method could model crack initiation and propagation according to the associated constitutive law without a presumed fracture criterion. The simulation results (marked by scattered data points) are compared with those of theoretical analysis in Fig.3(a) and (b). The stress field near the state of emergent crack growth at different values of strip height is plotted as color maps in Fig.3(c). Attached to each stress color map is a curve describing the distribution of stress concentration ahead of the crack tip. When the height of the strip is large (P1), there is distinct stress concentration with a kidney shaped stress field in front of the crack tip, is consistency with the classical K-field. With decreasing the height of strip (P2, P3), the stress concentration becomes weaker and weaker. As the strip height reaches the critical point (P4), the stress concentration completely disappears, and the stress distribution in the strip becomes uniform and equal to the cohesive strength of the material. This picture demonstrates that materials become insensitive to pre-existing flaws at nanoscale and can maintain theoretical strength despite of defects. The stress con-

centration vanishes at a critical structural size. This is very different from the macroscopic engineering concepts that failure always occurs by stress concentration near materials flaws and the severe stress concentration at a crack tip can cause catastrophic structure failure under applied stresses much lower than theoretical strength.

4. CONCLUSIONS

We extend the recently developed VIB model [9, 10, 11] to modeling fracture of nanomaterials. By analytical VIB modeling and VIB-FEM simulation, we showed that, as the structural size shrinks to the nanometer scale, there is a transition of fracture mechanism from the classical Griffith linear elastic fracture mechanics to one of homogeneous failure with no stress concentration at the crack tip. The unique feature of nanoscale fracture stems from the fact that material strength is limited by theoretical strength of solid. At nanoscale, the background stress in a cracked specimen will approach the theoretical strength. When this occurs, the stress concentration near the crack tip disappears and the structure becomes insensitive to pre-existing flaws.

Acknowledgments

References

[1] Walsh P, Li W, Kalia R K, Nakano A, Vashishta P, Saini S (2001) *Structural transformation, amorphization, and fracture in nanowires: A multimillion-atom molecular dynamics study,* Applied Physics Letters. **78**(21), 3328-3330.

[2] Vaia R A, Giannelis E P. (2001) *Polymer nanocomposites: status and opportunities,* MRS Bulletin. **26**, 394-401.

[3] Stoneham A M (2003) *The challenges of nanostructures for theory,* Materials Science and Engineering: C. **23**, 235-241.

[4] Bao G (2002) *Mechanics of biomolecules,* Journal of Mechanics and Physics of Solids. **50**(11), 2237-2274

[5] Born M and Huang K (1956) *Dynamical theories of crystal lattices,* Clarendon, Oxford Press.

[6] Huang K (1950) *On the atomic theory of elasticity,* Proceedings of the Royal Society of London. **A203**, 178-194.

[7] Stakgold I (1950) *The Cauchy relations in a molecular theory of elasticity,* Quarterly of Applied Mechanics. **8**, 169-186.

[8] Tadmor E B, Ortiz M, Phillips R (1996) *Quasicontinuum analysis of defects in solids,* Phil. Mag. A. **73**, 1529-63.

[9] Gao H, Klein P (1998) *Numerical simulation of crack growth in an isotropic solid with randomized internal cohesive bonds,* J. Mech. Phys. Solids. **46**,187-218.

[10] Klein P, Gao H (1998) *Crack nucleation and growth as strain localization in a virtual-bond continuum,* Engineering fracture mechanics. **61**, 21-48.

[11] Klein P, Foulk J W, Chen E P, Wimmer S A, Gao H (2001) *Physics-based modeling of brittle fracture: cohesive formulations and the application of meshfree methods,* Theoretical and Applied Fracture Mechanics. **37**, 99-166.
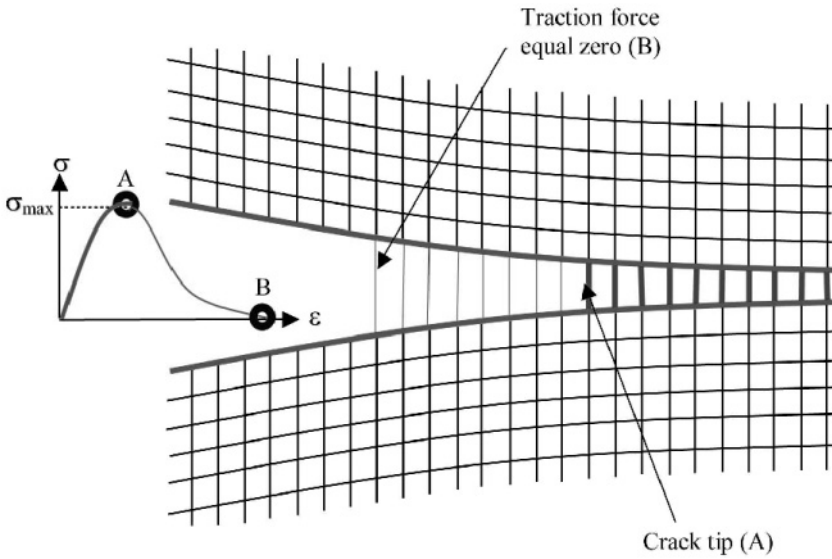
Figure 1   Illustration of crack nucleation in VIB-FEM including a stress (σ) strain (ε) curve showing the stress softening process at the crack tip.
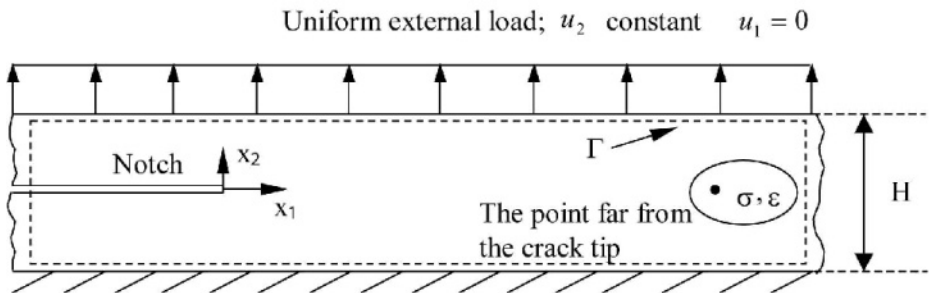
Figure 2   Illustration of a notched nano-strip under uniform external load. Γ is the J integral contour. σ and ε are the uniform stress and strain, respectively, in the strip far ahead of the crack tip.

(a)

(b)

(c)
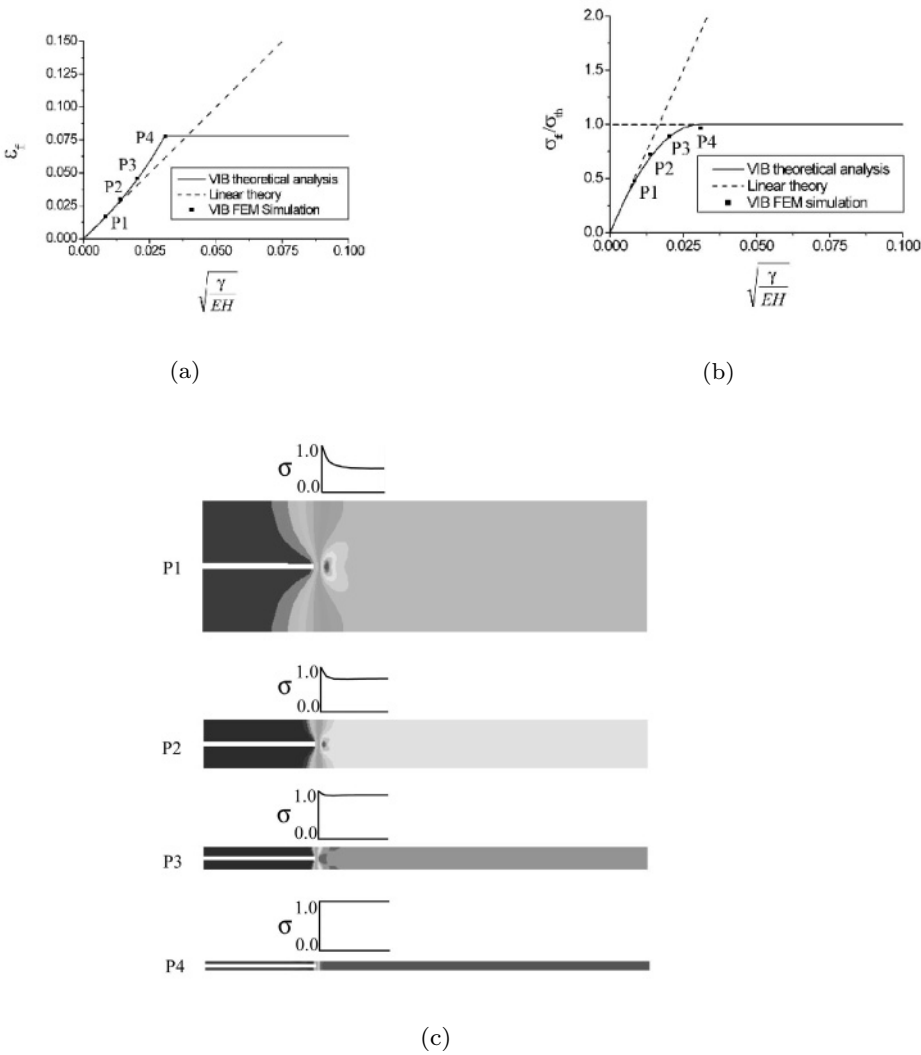
Figure 3 The prediction of the fracture strength and the critical thickness of a notched strip. (a) The curves for the fracture strain of the strip versus the dimensionless number $\sqrt{\frac{\gamma}{EH}}$, and the discrepancy between the VIB prediction and that of LEFM. (b) The fracture strength of the strip versus the dimensionless number $\sqrt{\frac{\gamma}{EH}}$, and comparison of VIB prediction with LEFM. (c) The VIB-FEM calculated color maps of the stress field at different widths of the strip; the size dependent stress distribution ahead of the crack tip. At the critical thickness, the stress concentration disappears and the fracture strength approaches the theoretical strength of solid.

BOUNDARY ELEMENTS AND SHEAR BANDS IN INCREMENTAL ELASTICITY

Michele Brun[1], Davide Bigoni[1] and Domenico Capuani[2]

[1] *Dipartimento di Ingegneria Meccanica e Strutturale, Università di Trento,*
Via Mesiano 77-38050 Povo, Trento, Italia
michele.brun@ing.unitn.it, bigoni@ing.unitn.it

[2] *Dipartimento di Ingegneria, Università di Ferrara,*
Via Saragat 1 - 44100 Ferrara, Italia
cpd@dns.unife.it

Abstract Perturbations in terms of small elastic deformations superimposed upon a given homogeneous strain are analysed within a boundary element framework. This is based on a recently-developed Green's function and boundary integral equations for non-linear incremental elastic deformations. Plane strain deformations are considered of an incompressible hyperelastic solid within the elliptic range. The proposed approach is shown to yield bifurcation loads and modes via a perturbative approach. Numerical treatment of the problem is detailed and applications to multilayers are shown. Relations between shear band formation and global instabilities are given evidence.

1. INTRODUCTION

The response to perturbations of a pre-stressed, non-linear elastic solid is an important issue in a broad spectrum of mechanical problems including the modelling of biological tissues, the analysis of geological formations and the behaviour of seismic insulators and rubber bearings.

With reference to plane strain deformations of incompressible materials, Biot [1] has shown that the incremental elastic response is governed by two incremental moduli, functions of the current stretch. Biot's constitutive framework was assumed in [2] to obtain a Green's function and a boundary integral formulation for incremental deformations superimposed upon a given, homogeneous strain. Both Green's function and integral formulation

pave the way for constructing a boundary element technique (BEM) suitable to analyse incremental problems of non-linear elasticity. This is the purpose of the present article, where a general numerical scheme is formulated to handle generic boundary value problems with prescribed nominal tractions or displacement boundary conditions.

It should be mentioned that several attempts have been presented to analyse non-linear problems using boundary element techniques. In these cases, in addition to the usual boundary integrals, a domain integral is introduced, leading to the so-called 'field-boundary element method'. The introduction of this term nullifies a main advantage of BEM and originates from the discrepancy between the nonlinear character of the equations governing the problem and the employed fundamental solution (usually pertinent to linear, isotropic elasticity). Although restricted to perturbations of homogeneously deformed, elastic solids, the proposed boundary element technique retains all the well-known advantages of the small strain formulation, like: discretization limited to the domain boundary; automatic satisfaction of the incompressibility constraint; description of singularities near corner points of the boundary.

The method is shown to be particularly suitable to analyse bifurcation problems even involving surface and localized modes.

2. INCREMENTAL CONSTITUTIVE EQUATIONS

Constitutive equation given by Biot [1] for incompressible materials incrementally deformed in plane strain is adopted. The constitutive framework embraces a broad class of material behaviours including hyper and hypo elasticity, and the loading branch of associated elastoplasticity. In a Lagrangian formulation of field equations, with the current state taken as reference, the constitutive equations for the nominal stress tensor rate $\dot{t}_{ij}$ can be written in the form

$$\dot{t}_{ij} = \mathbb{K}_{ijkl}v_{l,k} + \dot{p}\delta_{ij} = \tilde{\mathbb{K}}_{ijkl}v_{l,k} + \dot{\pi}\delta_{ij}, \quad v_{i,i} = 0, \qquad (2.1)$$

where v_i is the velocity, δ_{ij} is the Kronecker delta and

$$\dot{p} = \frac{\dot{\sigma}_1 + \dot{\sigma}_2}{2}, \qquad \dot{\pi} = \frac{\dot{t}_{11} + \dot{t}_{22}}{2} = \dot{p} - \frac{\sigma_1 - \sigma_2}{2}v_{1,1}, \qquad (2.2)$$

are the in plane hydrostatic stress rates (positive in tension), related to the principal components σ_1, σ_2 of the Cauchy stress and to the nominal stress. The tensor $\mathbb{K}_{ijkl}$ represents the instantaneous stiffness, characterised by the

major symmetry $\mathbb{K}_{ijkl} = \mathbb{K}_{klij}$ and having the form [3]

$$\mathbb{K}_{1111} = \mu_* - \frac{\sigma}{2} - p, \ \mathbb{K}_{1122} = -\mu_*, \qquad \mathbb{K}_{1112} = \mathbb{K}_{1121} = 0,$$

$$\mathbb{K}_{2211} = -\mu_*, \qquad \mathbb{K}_{2222} = \mu_* + \frac{\sigma}{2} - p, \qquad \mathbb{K}_{2212} = \mathbb{K}_{2221} = 0,$$

$$\mathbb{K}_{1212} = \mu + \frac{\sigma}{2}, \qquad \mathbb{K}_{1221} = \mathbb{K}_{2112} = \mu - p, \ \mathbb{K}_{2121} = \mu - \frac{\sigma}{2},$$

where

$$\sigma = \sigma_1 - \sigma_2, \qquad p = \frac{\sigma_1 + \sigma_2}{2}, \tag{2.3}$$

and μ, μ_* are two incremental moduli corresponding respectively to shearing parallel to, and at 45° to, the Eulerian principal axes.

The formulation is restricted to the elliptic range (E), corresponding to negative or complex coefficients γ_1 and γ_2:

$$\left.\begin{array}{c} \gamma_1 \\ \gamma_2 \end{array}\right\} = \frac{1 - 2\dfrac{\mu_*}{\mu} \pm \sqrt{\Delta}}{1 + k}, \quad \Delta = k^2 - 4\frac{\mu_*}{\mu} + 4\left(\frac{\mu_*}{\mu}\right)^2, \tag{2.4}$$

where $k = \sigma/(2\mu)$ is a parameter characterising the pre-stress. The elliptic range may be further sub-divided into elliptic-imaginary (EI: $\Delta > 0$, so that γ_1 and γ_2 are both negative) and elliptic-complex (EC: $\Delta < 0$, so that γ_1 and γ_2 are a conjugate pair) regimes.

Discontinuous strain rates corresponding to shear bands are possible at the boundary of the elliptic range. Elliptic imaginary/parabolic (EI/P) boundary is attained when $k = 1$ ($\gamma_1 = 0$) whereas elliptic complex/hyperbolic (EC/H) boundary is attained when $\Delta = 0$ ($\gamma_1 = \gamma_2$).

3.   THE FUNDAMENTAL SOLUTION

In the framework described by the constitutive eqns. (2.1), the Green's function set $\{v_i^g; \dot{\pi}^g\}$ for an infinite and uniformly deformed medium can be written in the form [2]:

$$v_i^g = \frac{1}{2\pi^2\mu(1+k)} \left\{ \frac{\pi\,\delta_{ig}\,\log r}{[(2-i)\,\gamma_2 + 1 - i]\,\sqrt{-\gamma_1} + [(2-i)\,\gamma_1 + 1 - i]\,\sqrt{-\gamma_2}} \right.$$
$$\left. - \int_0^{\frac{\pi}{2}} [K_i^g(\alpha + \theta) + (3 - 2i)\,(3 - 2g)\,K_i^g(\alpha - \theta)]\log(\cos\alpha)\,d\alpha \right\},$$

$$\tag{3.1}$$

$$\dot{\pi}^g = -\frac{1}{2\pi r} \left\{ \cos\left[\theta - (g-1)\frac{\pi}{2}\right] + \frac{1}{\pi(1+k)}\int_0^\pi \frac{\tilde{K}_g(\alpha+\theta)}{\cos\alpha}\,d\alpha \right\}, \tag{3.2}$$

where r and θ are the polar coordinates singling out the generic point with respect to the position $\mathbf{y}$ of the concentrated force, indices i and g range between 1 and 2 and

$$K_i^g(\alpha) = \frac{\sin\left[\alpha + (i-1)\frac{\pi}{2}\right]\sin\left[\alpha + (g-1)\frac{\pi}{2}\right]}{\Lambda(\alpha)}, \tag{3.3}$$

$$\Lambda(\alpha) = \sin^4 \alpha(\cot^2 \alpha - \gamma_1)(\cot^2 \alpha - \gamma_2) > 0, \tag{3.4}$$

$$\tilde{K}_g(\alpha) = K_g^g(\alpha)\cos\left[\alpha + (g-1)\frac{\pi}{2}\right]\Gamma(\alpha), \quad (g \text{ not summed}) \tag{3.5}$$

$$\Gamma(\alpha) = 2\left(\frac{\mu_*}{\mu} - 1\right)(2\cos^2\alpha - 1) - k. \tag{3.6}$$

From the Green's velocity v_i^g and pressure rate $\dot{\pi}^g$, the in-plane hydrostatic stress rate $\dot{p}^g$ and the associated incremental nominal stress $\dot{t}_{ij}^g$ can be obtained by using constitutive equations (2.1).

4.   BOUNDARY ELEMENT FORMULATION

We refer to mixed boundary value problems in which velocities and incremental nominal tractions $\dot{\tau}$ are prescribed functions

$$v_i = \bar{v}_i, \text{ on } \partial B_v, \qquad \dot{t}_{ij}n_i = \dot{\bar{\tau}}_j \text{ on } \partial B_\tau, \quad \partial B = \partial B_v \cup \partial B\tau, \tag{4.1}$$

defined on separate portions ∂B_v and ∂B_τ of the boundary ∂B of a solid B, currently in a state of homogeneous, finite deformation.

In this context, an integral representation exists relating the velocity at interior points of the body to the boundary values of nominal traction rates and velocities [2]:

$$v_g(\mathbf{y}) = \int_{\partial B}\left[\dot{t}_{ij}(\mathbf{x})\,n_i(\mathbf{x})\,v_j^g(\mathbf{x},\mathbf{y}) - \dot{t}_{ij}^g(\mathbf{x},\mathbf{y})\,n_i(\mathbf{x})\,v_j(\mathbf{x})\right]dl_x. \tag{4.2}$$

If the point $\mathbf{y}$ is at the boundary, eqn.(4.2) becomes [2]

$$C_j^g v_j(\mathbf{y}) = \int_{\partial B}\dot{\tau}_j(\mathbf{x})\,v_j^g(\mathbf{x},\mathbf{y})\,dl_x - \fint_{\partial B}\dot{\tau}_j^g(\mathbf{x},\mathbf{y})\,v_j(\mathbf{x})\,dl_x, \tag{4.3}$$

where

$$C_i^g = \lim_{\varepsilon \to 0}\int_{\partial C_\varepsilon}\dot{\tau}_i^g(\mathbf{x},\mathbf{y})\,dl_x, \tag{4.4}$$

is the so-called **C**-matrix, depending on the material parameters, state of pre-stress and the geometry of the boundary (in the case of a smooth boundary, $C_i^g = \frac{1}{2}\delta_{gi}$). Note that symbol ∂C_ε introduced in (4.4) denotes

the intersection between a circle of radius ε centred at $\mathbf{y}$ and the domain B.

The boundary equation (4.3) is the starting point to derive the *collocation boundary element method*. To this purpose, the boundary ∂B is divided into m elements Γ^e ($e = 1, \cdots, m$), with subsets m_u and m_τ belonging respectively to ∂B_u and ∂B_τ (clearly $m = m_u + m_\tau$).

Inside each boundary element Γ^e, the following discretization for velocities and nominal tractions is introduced

$$v_i(\mathbf{x}) = \varphi_\alpha(\mathbf{x})\, \bar{v}_{i\alpha},$$

$$\dot{\tau}_i(\mathbf{x}) = \varphi_\alpha(\mathbf{x})\, \dot{\bar{\tau}}_{i\alpha}, \qquad\qquad \alpha = 0, \cdots, \Theta, \tag{4.5}$$

where $\bar{v}_{i\alpha}$, $\dot{\bar{\tau}}_{i\alpha}$ are the nodal values of velocities and nominal traction rates, respectively, and φ_α are the relevant shape functions, selected as polynomials of degree Θ.

The discretized form of eqn. (4.3), collocating the point $\mathbf{y}$ at $\mathbf{y}^{(\bar{e}, \bar{\alpha})}$, corresponding to the node $\bar{\alpha}$ of the element $\bar{e}$ is:

$$C_i^g \bar{v}_{i\bar{\alpha}} + \sum_{e=1}^{m} \left(\bar{v}_{i\alpha}^e \int_{\Gamma^e} \varphi_\alpha(\mathbf{x})\, \dot{\tau}_i^g(\mathbf{x}, \mathbf{y}) dl_x - \dot{\bar{\tau}}_{i\beta}^e \int_{\Gamma^e} \psi_\beta(\mathbf{x})\, v_i^g(\mathbf{x}, \mathbf{y}) dl_x \right) = 0, \tag{4.6}$$

where indices α and i are summed and range between $0 - \Theta$ and $1 - 2$, respectively.

Collocating eqn. (4.6) at each node along the two directions x_1 and x_2 yields an algebraic system that can be written in a form

$$\mathbf{H}\hat{\mathbf{v}} = \mathbf{G}\dot{\hat{\tau}}, \tag{4.7}$$

where $\hat{\mathbf{v}}$ and $\dot{\hat{\tau}}$ are the vectorial expressions for $\bar{v}_{i\alpha}^e$ and $\dot{\bar{\tau}}_{i\beta}^e$, defined as:

$$\hat{v}_{2\Theta(e-1)+2\alpha+i} = \bar{v}_{i\alpha}^e, \qquad\qquad \dot{\hat{\tau}}_{2\Theta(e-1)+2\alpha+i} = \dot{\bar{\tau}}_{i\alpha}^e, \tag{4.8}$$

where Θ is not a free index, but the fixed number specifying the degree of the interpolating functions.

Solution of system (4.7), after re-arrangement of data and unknowns, gives the nodal velocities $\bar{v}_{i\alpha}$ on ∂B_τ, and the nominal traction rates $\dot{\bar{\tau}}_{i\beta}$ on ∂B_v.

We limit the presentation to discretization of the boundary into linear elements and linear shape functions, so that the singular integrals in eqn. (4.6) relative to elements adjacent to the collocation node e can be evaluated analytically. In particular, the strongly singular integral on the left hand side of eqn. (4.6), after change of variable, takes the form

$$I_{strong}^{(ig,e)} = \int_0^{l_{e-1}} \left(1 - \frac{\eta}{l_{e-1}} \right) \dot{\tau}_i^g(\eta, \theta_1)\, d\eta + \int_0^{l_e} \left(1 - \frac{\eta}{l_e} \right) \dot{\tau}_i^g(\eta, \theta_2)\, d\eta. \tag{4.9}$$

322

As far as the two elements $e-1$ and e are concerned, the incremental Green's tractions can be computed as:

$$\tau_i^g(r) = (-1)^e \frac{\chi_{ig}(k, \frac{\mu_*}{\mu})}{r}, \tag{4.10}$$

which are independent of θ. Introducing eqn. (4.10) into eqn. (4.9), we obtain

$$I_{strong}^{(ig,e)} = (-1)^e \chi_{ig} \log\left(\frac{l_e}{l_{e-1}}\right). \tag{4.11}$$

Analogously, the weakly singular integral on the right hand side of eqn. (4.6) is equal to

$$I_{weak}^{(ig,e)} = \int_0^{l_{e-1}} \left(1 - \frac{\eta}{l_{e-1}}\right) v_i^g(\eta, \theta_1)\, d\eta + \int_0^{l_e} \left(1 - \frac{\eta}{l_e}\right) v_i^g(\eta, \theta_2)\, d\eta. \tag{4.12}$$

Taking in account the expression of v_i^g given in eqn.(3.1) the integral (4.12) can be analytically evaluated and the resulting four components are listed in Table (1).

Table 1 Analytic expressions for the weakly singular integrals (4.12)

i	g	Integral $I_{weak}^{(ig,e)}$
1	1	$\frac{l_{e-1}}{2}\left[\frac{2\log(l_{e-1})-3}{D_{11}} + v_1^1(1,\theta_1)\right] + \frac{l_e}{2}\left[\frac{2\log(l_e)-3}{D_{11}} + v_1^1(1,\theta_2)\right]$
1	2	$\frac{l_{e-1}}{2}v_1^2(\theta_1) + \frac{l_e}{2}v_1^2(\theta_2)$
2	1	$\frac{l_{e-1}}{2}v_2^1(\theta_1) + \frac{l_e}{2}v_2^1(\theta_2)$
2	2	$\frac{l_{e-1}}{2}\left[-\frac{2\log(l_{e-1})-3}{D_{22}} + v_2^2(1,\theta_1)\right] + \frac{l_e}{2}\left[-\frac{2\log(l_e)-3}{D_{22}} + v_2^2(1,\theta_2)\right]$

$D_{11} = 4\mu\pi(1+k)(\gamma_2\sqrt{-\gamma_1}+\gamma_1\sqrt{-\gamma_2})$, $D_{22} = 4\mu\pi(1+k)(\sqrt{-\gamma_1}+\sqrt{-\gamma_2})$

5. NUMERICAL EXAMPLES

As a first example, the response of a multilayered elastic block to an incremental, skew-symmetric loading $\dot\tau$, (see the detail in Fig. 1) is investigated. The block is formed by three layers perfectly bonded to each other. Material (1) constituting the external layers is supposed to be different from material (2) of the inner layer. All layers are supposed to undergo

the same homogeneous, plane strain deformation with the principal directions of deformation aligned normal and parallel to the layers. Therefore, a uniaxial state of traction or compression prevails in the laminate, with different values for materials 1 and 2. Starting from this pre-stressed state, the incremental load $\dot{\tau}$ is applied. The loaded zone has been chosen to be equal to $2/15\ b$ (b is the half-length of the edges) and a regular boundary mesh for each layer has been adopted.

Three ratios of incremental shear moduli $(\mu_*/\mu)_1$, $(\mu_*/\mu)_2$ and μ_1/μ_2 have been considered for the two materials (Tab. 2) and the relevant results are shown in Fig. 1, where the velocity [normalized through multiplication by $\mu_1/(b\dot{\tau})$] is plotted versus the pre-stress k. It can be seen that trac-

Table 2   Bifurcation stress k for a three-layered elastic structure

Example	Shear moduli ratios			Bifurcation stress k	
	$(\mu_*/\mu)_1$	$(\mu_*/\mu)_2$	μ_1/μ_2	*Analytical*	*Numerical*
1	1.0	0.5	0.5	0.4722	$0.4852 \div 0.4859$
2	0.5	1.0	2.0	0.3714	$0.3789 \div 0.3797$
3	2/3	1.0	1.5	0.4386	$0.4469 \div 0.4477$

tion increases stiffness whereas compression induces stiffness degradation, which becomes dramatic when critical values of k are approached. Tab. 2 compares numerical estimates of the bifurcation values of k with those evaluated analytically by Bigoni and Gei [4], though for slightly different boundary conditions. It is worth noting that the value of k is independent of the material, but depends only on the maximum in-plane stretch.

A second example concerns the so-called 'van Hove condition', where the solid is subjected to prescribed displacements over the entire boundary and the current deformation (and stress) is homogeneous [5, 6]. In these conditions, starting from an unloaded configuration, shear bands occur as the first possible bifurcation. We analyse this situation for the square elastic block shown in Fig. 2, characterised by $\mu_*/\mu = 0.25$ (corresponding to the elliptic complex regime) and homogeneously deformed in a state of uniaxial tension and compression. All displacements are prescribed on the boundary, so that the solution is known unless an arbitrary value of homogeneous pressure. A perturbation is given by prescribing the triangular distribution of velocity sketched in Fig. 2. The level sets of the modulus of the velocity are reported in Fig. 3 and 4, for three different values of pre-stress $k = \{-0.859, 0, 0.859\}$. The values ± 0.859 are close to the boundary of loss of ellipticity (± 0.866), where shear bands become possible, inclined at an angle $\eta = 27.367°$, with respect to the direction of tensile stress.
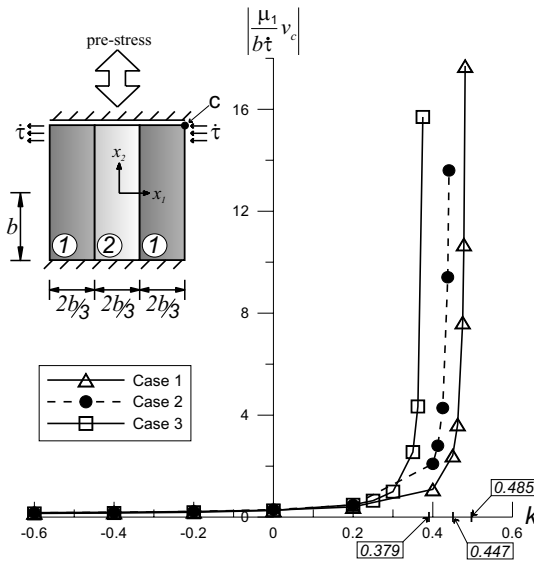
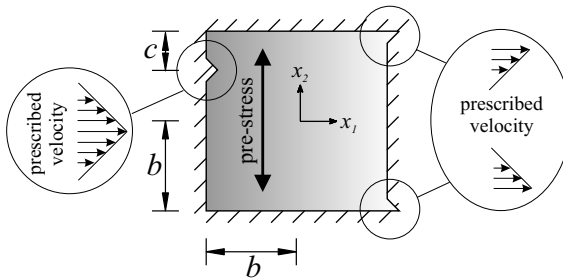*Figure 1* Non-dimensionalized velocity of the corner point c versus pre-stress k.

Figure 2 Loading geometry in van Hove conditions.

The fact that strain localization can be observed within the elliptic range — employing a perturbation approach — agrees with previous findings [2, 7]. This approach may provide an explanation of the fact that shear banding is a preferred instability when compared to other diffuse bifurcations, possible at loss of ellipticity under van Hove conditions [8].

The van Hove setting is very peculiar and provides the maximum possible 'confinement' to a material sample. A relaxation of this severe configuration was proposed by Ryzhak [9] and will be called 'weak van Hove' conditions in the following. In particular, the material must be homoge-
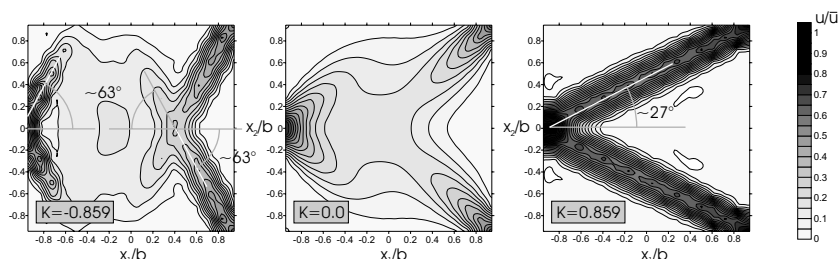
Figure 3 Level sets of modulus of velocity at different values of pre-stress k. Loading geometry is sketched in Fig. 2, with $c/b = 1/2$. Note the shear bands emerging at $k = \pm 0.859$.
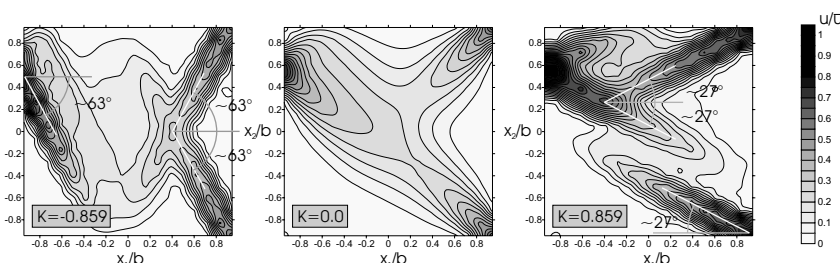
Figure 4 Level sets of modulus of velocity at different values of pre-stress k. Loading geometry is sketched in Fig. 2, with $c/b = 4/9$. Note the shear bands emerging at $k = \pm 0.859$.

neous and orthotropic, with orthotropy axes parallel and orthogonal to the given loading direction. Two parallel edges of the material element must be in smooth (bilateral) contact with a rigid constraint. The current configuration, sketched in Fig. 5, is perturbed with two assigned, triangular velocity distributions. For weak van Hove conditions, level sets of the modulus of the velocity are plotted in Figs. 6 and 7, for different values of pre-stress $k = \{0, 0.7, 0.857\}$, corresponding to compression parallel to x_2.

It can be seen that shear banding is not evident until $k = 0.7$ but it appears clearly for $k = 0.857$, which is close to the boundary of ellipticity. 'Reflection' of shear bands at the boundary emerges as a peculiar deformation pattern. Similar deformation mechanisms have been also observed in different contexts (porous plastic materials [10]; dynamics of visco-plastic solids [11, 12]), and may explain pattern formation in biological system or geological structures. The localization of deformation may also suggest possible technological applications. For instance, the highly strained regions could be employed to transmit signals so that the pre-stress could become a parameter controlling special types of delay lines.
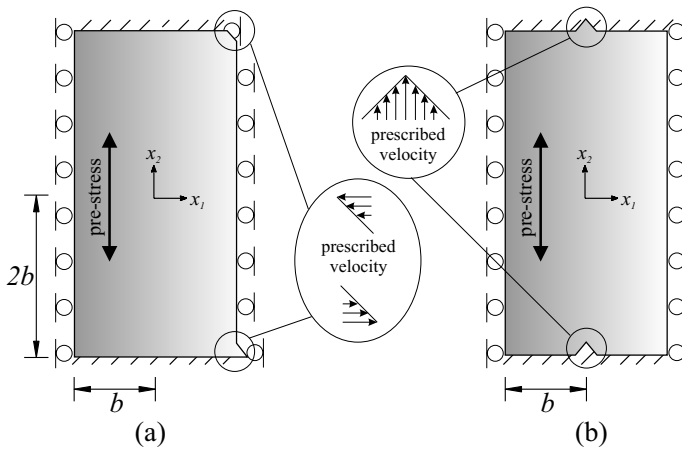
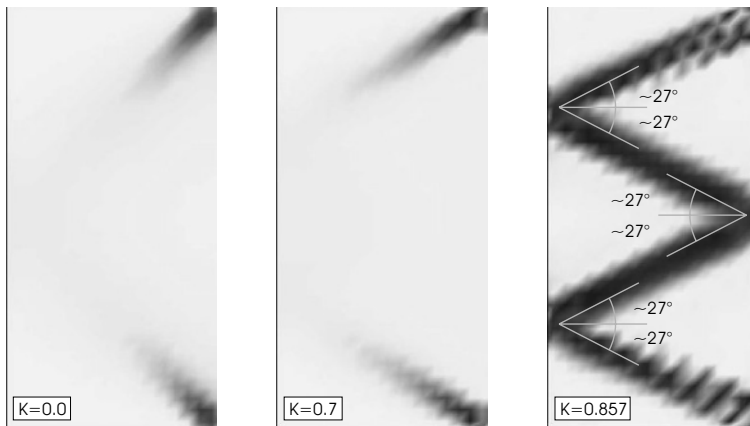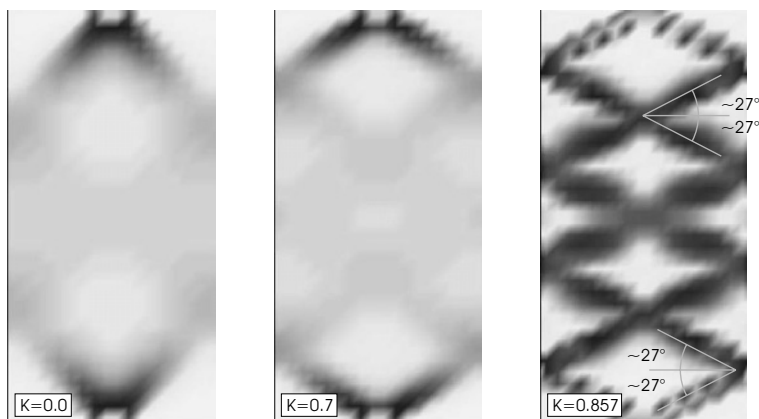*Figure 5*   Loading geometries in weak van Hove conditions.

Figure 6   Level sets of modulus of velocity at different values of pre-stress k. Loading geometry is sketched in Fig. 5(a). Note the shear bands emerging at $k = 0.857$.

Acknowledgments

References

[1] Biot, M A (1965) *Mechanics of incremental deformations.* J. Wiley and Sons, New York.

Figure 7 Level sets of modulus of velocity at different values of pre-stress k. Loading geometry is sketched in Fig. 5(b). Note the shear bands emerging at $k = 0.857$.

[2] Bigoni, D and Capuani, D (2002) *J. Mech. Phys. Solids* **50**, 471-500.

[3] Hill, R and Hutchinson, J W (1975) *J. Mech. Phys. Solids* **23**, 239-264.

[4] Bigoni, D and Gei, M (1999) On bifurcation of a layered, orthotropic, elastic medium. XXVIII AIAS National Congress, Vicenza, Italy, 8-11 September 1999.

[5] van Hove, L (1947) *Proc. Sect. Sci. K. Akad. van Wetenschappen*, Amsterdam **50**, 18-23.

[6] Bigoni, D (2000) Bifurcation and instability of non-associative elastic-plastic solids. *CISM Lecture Notes No. 414 "Material Instabilities in Elastic and Plastic Solids", H. Petryk,* Ed. Springer-Verlag, Wien-New York.

[7] Radi, E, Bigoni, D and Capuani, D (2002) *Int. J. Solids Structures* **39**, 3971-3996.

[8] Ryzhak, E I (1999) *Int. J. Solids Structures* **36**, pp. 4669-4691.

[9] Ryzhak, E I (1993) *J. Mech. Phys. Solids* **41**, 1345-1356.

[10] Tvergaard, V (1982) *J. Mech. Phys. Solids* **30**, 399-425.

[11] Deb, A, Prevost, J H and Loret, B (1996) *Comput. Meth. Appl. Mech. Engrg.* **137**, 285-306.

[12] Deb, A, Loret, B and Prevost, J H (1996) *Comput. Meth. Appl. Mech. Engrg.* **137**, 307-330.

Chapter 6
Homogenisation analysis and models of composite media

SPECTRAL COUPLING OF EFFECTIVE PROPERTIES OF A RANDOM MIXTURE

Elena Cherkaev

Department of Mathematics
The University of Utah
155 South 1400 East, JWB 233
Salt Lake City, UT, 84112, U.S.A.
elena@math.utah.edu

Abstract The paper deals with the problem of coupling of various effective properties of a random mixture. It is shown that effective properties of a random stationary composite formed of two different materials are coupled through the spectral measure in the Stieltjes representation of the effective properties. This gives an approach to indirect evaluation of the effective thermal or hydraulic conductivity of a random material from known effective complex permittivity of the same mixture. The spectral measure is reconstructed from effective complex permittivity measurements and used to estimate other effective properties of the same material.

1.   INTRODUCTION

Different effective properties of a finely-structured heterogeneous mixture are related or coupled through its microgeometry. The problem of formalizing this coupling of the properties is very important for predicting properties of composite materials in material design, as well as for indirect evaluation of the effective properties, when direct measurements are difficult to make. Implicit accounting for the geometry of the composite was exploited starting from the pioneering work of Prager [1] in deriving coupled bounds on the effective material properties. Coupled or cross-property bounds use measurements of one effective property to improve bounds on other effective properties. The work of Prager was followed by a number of papers by Avellaneda, Berryman, Cherkaev, Gibiansky, Milton, Torquato,

and others (see references in monographs [2, 3, 4]). Various empirical relations or relations derived for specific geometries are used in practice, such as for instance, Kozeny-Carman or Katz-Tompson relations providing an estimate for permeability of a porous material [5, 6]. Geometric characterization of the medium is often introduced through the "formation factor" F which relates properties of one phase in the mixture to the effective properties of the material: $F = \sigma/\sigma^*$, where σ is the conductivity of a fluid filling in the porous material, and σ^* is the effective conductivity.

The present work uses explicit analytic representation of various effective properties of a composite [7] through its geometric structural function associated with the spectral measure μ in the Stieltjes analytic integral representation of the effective complex permittivity ϵ^*. This analytic integral representation of the effective permittivity ϵ^* of a mixture of two materials with permittivities ϵ_1 and ϵ_2 was developed by Bergman, Milton, and Golden and Papanicolaou [8, 9, 10, 11] in the course of computing bounds for the effective permittivity of an arbitrary two component mixture. The integral representation gives a function $F(s)$ as an analytic function off $[0, 1]$-interval in the complex $s-$plane:

$$F(s) = 1 - \frac{\epsilon^*}{\epsilon_2} = \int_0^1 \frac{d\mu(z)}{s - z}, \qquad s = \frac{1}{1 - \epsilon_1/\epsilon_2} \qquad (1.1)$$

Here the positive measure μ is the spectral measure of a self-adjoint operator $\Gamma\chi$, with χ being the characteristic function of the domain occupied by one material, and

$$\Gamma = \nabla(-\Delta)^{-1}(\nabla\cdot), \qquad (1.2)$$

where $-\Delta$ is the Laplacian operator, and ∇ denotes the gradient, so that $(\nabla\cdot)$ is the divergence operator. The spectral function μ was used to derive microstructural information about the composite [12, 13, 14, 15], to bound the effective permittivity [16, 17, 18], to appraise the accuracy of the permittivity measurements [19], and to model the effective complex conductivity of geological mixtures [20, 21] or of random resistor networks [22]; it was calculated from reflectivity measurements at different temperatures in [23].

The paper discusses coupling of different properties of a stationary random mixture through the spectral function μ. It is demonstrated in [7] that different properties of a random mixture admit representations similar to (1.1) with the same function μ, and that the effective response of the random medium for a range of different parameters of the applied field determines the function μ. Hence, when computed from measurements of one effective property (say, from measurements of ϵ^*), the function μ can be used to evaluate the effective response of the same medium for

other applied fields as well. From the computational point of view, the problem of reconstruction of the spectral measure μ is extremely ill-posed: It is equivalent to the inverse potential problem and is well studied in the mathematical literature (see, for instance, the monograph on inverse source problems [24] and on regularization of ill-posed problems [25]). The last section shows computational results of recovering the spectral function μ from numerically simulated effective measurements of the complex permittivity of a composite using regularized algorithms developed in [7, 26]. As an example, the thermal conductivity of St-Peters sandstone is estimated using the reconstructed function μ [27]. Computed values of the thermal conductivity are in good agreement with measured values in [28].

2. COUPLING THROUGH THE SPECTRAL FUNCTION

We assume that the medium in a domain $\mathcal{O}$ is a fine scale mixture of two materials with the values of the complex permittivities ϵ_j and the thermal conductivities γ_j in regions $\mathcal{O}_j$, $j = 1, 2$, with $\mathcal{O} = \mathcal{O}_1 \cup \mathcal{O}_2$. Let χ be the characteristic function of the region $\mathcal{O}_1$ occupied by the first material for a realization $\eta \in \Omega$, where Ω is the set of all realizations of the random medium,

$$\chi(x, \eta) = \begin{cases} 1, & x \in \mathcal{O}_1, \\ 0, & \text{otherwise} \end{cases} \tag{2.1}$$

We assume that the characteristic size of the inhomogeneities is microscopic in comparison with the size of the region $\mathcal{O}$, hence χ is a finely oscillating function.

Suppose that two different fields are applied in this random medium, the electric field, E_ϵ, and the temperature gradient field, E_γ. The complex permittivity of the medium is modeled by a (spatially) stationary random field $\epsilon(x, \eta)$, $x \in R^d$ and $\eta \in \Omega$, $\epsilon(x, \eta) = \epsilon_1 \chi(x, \eta) + \epsilon_2(1 - \chi(x, \eta))$. Similarly, the thermal conductivity is $\gamma(x, \eta) = \gamma_1 \chi(x, \eta) + \gamma_2(1 - \chi(x, \eta))$. Since the stationary fields are governed by similar equations, we will use the notation σ to describe both properties. The stationary random fields $E_\sigma(x, \eta)$ and $J_\sigma(x, \eta)$ are related by $J_\sigma(x, \eta) = \sigma(x, \eta) E_\sigma(x, \eta)$ and satisfy the equations

$$\nabla \cdot J_\sigma = 0, \qquad \nabla \times E_\sigma = 0, \qquad \langle E_\sigma(x, \eta) \rangle = e_k, \qquad \sigma = \epsilon, \gamma. \tag{2.2}$$

Here e_k is a unit vector in the kth direction, for some $k = 1, \ldots, d$, and $\langle \cdot \rangle$ means ensemble average over Ω or spatial average over all of $\mathbf{R}^d$. The effective tensor σ^* is defined as a coefficient of proportionality between the averaged fields: $\langle J_\sigma \rangle = \sigma^* \langle E_\sigma \rangle$. Hence the effective property tensors ϵ^*

and γ^* are such that

$$\langle J_\epsilon \rangle = \epsilon^* \langle E_\epsilon \rangle \qquad \text{and} \qquad \langle J_\gamma \rangle = \gamma^* \langle E_\gamma \rangle \qquad (2.3)$$

We notice that both problems are coupled through the same function χ:

$$\nabla \cdot (\epsilon_1 \chi(x, \eta) + \epsilon_2(1 - \chi(x, \eta))) \, E_\epsilon = 0, \qquad \epsilon^* = \langle \epsilon E_\epsilon \rangle \qquad (2.4)$$

and

$$\nabla \cdot (\gamma_1 \chi(x, \eta) + \gamma_2(1 - \chi(x, \eta))) \, E_\gamma = 0 \qquad \gamma^* = \langle \gamma E_\gamma \rangle \qquad (2.5)$$

Suppose that one of the effective properties, ϵ^* (see 2.4), can be measured. The problem is to find the other effective property γ^* using (2.5). We consider here isotropic mixtures and focus on one diagonal coefficient $\epsilon^* = \epsilon_{kk}^*$ and $\gamma^* = \gamma_{kk}^*$.

Let the complex permittivities $\epsilon_i, i = 1, 2$, depend on a parameter p that can be varied, with the microstructure remaining the same. This means that variation of the parameter p does not change the function χ. The temperature dependent complex permittivity of sea ice provides an example of a medium which does not fall into this consideration, since induced by temperature variations, melting changes the structure of brine pockets.

Theorem. Assuming the known properties $\epsilon_i = \epsilon_i(p)$, $i = 1$ or $i = 2$, of materials in a stationary random mixture depend on a parameter p, measurements of the effective complex permittivity $\epsilon^*(p)$ (2.4) in an interval $p \in (p_1, p_2)$ uniquely determine the effective thermal conductivity γ^* (2.5) of the mixture for given values of the components $\gamma_i, i = 1, 2$.

The key observation is that the effective properties ϵ^* and γ^* are coupled through the function μ in their integral representation [7]:

$$\epsilon^*(s) = \epsilon_2 - \epsilon_2 \int_0^1 \frac{d\mu(z)}{s - z}, \qquad s = \frac{1}{1 - \epsilon_1/\epsilon_2} \qquad (2.6)$$

$$\gamma^*(s') = \gamma_2 - \gamma_2 \int_0^1 \frac{d\mu(z)}{s' - z}, \qquad s' = \frac{1}{1 - \gamma_1/\gamma_2} \qquad (2.7)$$

To demonstrate this, we consider a model problem for a random mixture of two materials with conductivity $\sigma_1 = h$ and $\sigma_2 = 1$, and derive the spectral integral representation for the effective property following [11]. The conductivity $\sigma(x, \eta)$ of the mixture is $\sigma(x, \eta) = h \chi(x, \eta) + (1 - \chi(x, \eta))$. The field E satisfies

$$\nabla \cdot (h\chi + 1 - \chi) \, E = 0 \qquad (2.8)$$

Introducing $s = 1/(1 - h)$, the last expression can be written as

$$\nabla \cdot \chi E = s \, \nabla \cdot E \,, \qquad s = \frac{1}{1 - h} \tag{2.9}$$

Let $\nabla \varphi$ be a perturbation of the constant field e_k , so that $E = e_k + \nabla \varphi$. Then,

$$\nabla \cdot \chi \, (\nabla \varphi + e_k) = s \, \Delta \varphi \tag{2.10}$$

Applying $(-\Delta)^{-1}$ to both sides of this equation, then taking gradient, and introducing the operator Γ as in (1.2), $\Gamma = \nabla(-\Delta)^{-1}(\nabla \cdot)$, we can express E as a function of $\Gamma \chi$,

$$E = s(sI + \Gamma \chi)^{-1} e_k. \tag{2.11}$$

The spectral resolution of $\Gamma \chi$ with the projection valued measure Q results in the representation

$$E(s) = \int_0^1 \frac{s}{s - z} \, dQ(z) \, e_k \tag{2.12}$$

The integral representation for the function $F(s)$ is obtained using (2.12). Indeed,

$$F(s) = 1 - \sigma^*(s) = \langle \, s^{-1} \chi \, E, \, e_k \, \rangle \tag{2.13}$$

and hence,

$$F(s) = \langle \chi \, (\, sI + \Gamma \, \chi \,)^{-1} e_k, e_k \rangle = \int_0^1 \frac{\langle \chi \, dQ(z) \, e_k, \, e_k \rangle}{s - z} \tag{2.14}$$

If a function μ is a positive function of bounded variation, corresponding to the spectral measure Q, $d\mu(z) = \langle \chi \, dQ(z) e_k, e_k \rangle$, then

$$F(s) = \int_0^1 \frac{d\mu(z)}{s - z} \tag{2.15}$$

Substituting now in this model problem the value of h as $h = \epsilon_1/\epsilon_2$ and $h = \gamma_1/\gamma_2$, we end up with representations (2.6) and (2.7).

It is shown in [7] that the spectral function μ in the Stieltjes integral representation can be uniquely reconstructed if measurements of the effective permittivity of the mixture ϵ^* are available on an arc in a complex plane. Provided the properties of the constituents are dependent on a parameter p, variation of p in an interval $p \in (p_1, p_2)$ gives the required set of data.

If the properties of the constituents depend on the frequency of the applied electromagnetic field, frequency can be taken as such a parameter

which variation does not change the structure of the mixture. The spectral measure μ is determined by the structure of the mixture, hence, it is quite natural that it is the same for different effective properties. Having reconstructed this function from one set of data, we can use it to compute other effective properties such as thermal or hydraulic conductivity of the same mixture. Practically, if the function μ is known from the measurements of ϵ^*, evaluation of the effective thermal conductivity γ^* reduces to a calculation of the integral in (2.7).

Similarly, we could consider other stationary problems for:

- diffusion coefficient with concentration gradient and mass flux

- hydraulic conductivity with pressure gradient and fluid velocity

- magnetic permeability with magnetic field and magnetic induction

3.   REGULARIZATION

The problem of reconstruction of the spectral measure μ can be reduced to an inverse potential problem. It is shown that the function $F(s)$ admits a representation as a logarithmic potential of the measure μ [7]

$$F(s) = \frac{\partial}{\partial s} \int \ln |s - z| \, d\mu(z), \qquad \partial/\partial s = (\partial/\partial x - i \, \partial/\partial y) \qquad (3.1)$$

The reconstruction problem for the logarithmic potential is extremely ill-posed and requires regularization to develop a stable numerical algorithm. The potential function u is a solution to the Poisson equation $-\Delta u = \psi$, $\quad \mathrm{supp}(\psi) \subset \Omega$, where ψ is the density of the mass distribution in Ω. Solution of the problem is given by the Newtonian potential with $d\mu(z) = \psi \, dz$, $\quad z \in \Omega$. The inverse problem is to find ψ given values of $\partial u / \partial n$, or ∇u.

Let A be an operator in (3.1) mapping the set of measures $\mathcal{M}[0,1]$ on the unit interval onto the set of complex potentials defined on a curve $\mathcal{C}$: $\zeta(s) = 0$:

$$A\mu(s) = f(s) + ig(s) = \frac{\partial}{\partial s} \int_0^1 \ln |s - z| \, d\mu(z), \qquad s \in \mathcal{C}. \qquad (3.2)$$

To construct the solution we formulate the minimization problem:

$$||A\mu - F|| \to \min_{\mu \in \mathcal{M}}, \qquad (3.3)$$

where $|| \cdot ||$ is the $L^2(\mathcal{C})$−norm, F is the function of the measured data, $F(s) = 1 - \epsilon^*(s)/\epsilon_2$, $s \in \mathcal{C}$. The solution of the problem does not continuously depend on the data: Unboundness of the operator A^{-1} leads

to arbitrarily large variations in the solution, and the problem requires a regularization technique.

A regularization algorithm developed in [7] is based on constrained minimization: It introduces a stabilization functional $J(\mu)$ which constrains the set of minimizers. As a result, the solution depends continuously on the input data. Instead of minimizing (3.3) over all functions in $\mathcal{M}$, minimization is performed over a convex subset of functions which satisfy $J(\mu) \leq \beta$, for some scalar $\beta > 0$. The functional $J(\mu)$ was chosen as a quadratic stabilization functional and a total variation functional.
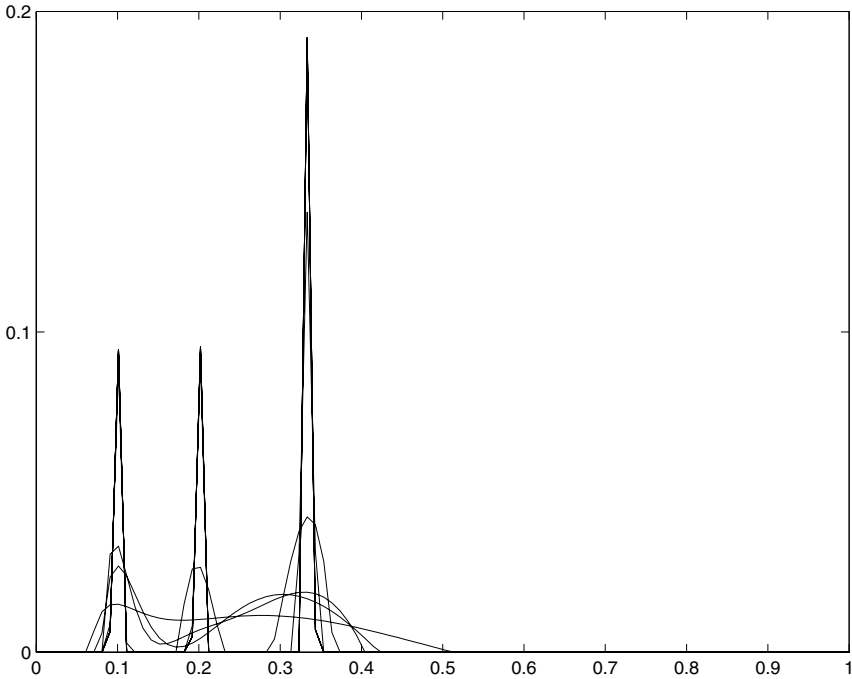
Figure 1 Reconstruction of a three-resonance structural function. Smooth functions are reconstructed using Tikhonov regularization with different regularization parameters α. The three delta-functions are recovered (almost identically to the true solution) using non-negatively constrained minimization [26].

The advantage of using a quadratic stabilization functional $J(\mu) = \|L\mu\|^2$, is the linearity of the corresponding Euler equation resulting in efficiency of the numerical schemes: $\mu_\alpha = (A^*A + \alpha L^*L)^{-1} A^*F^\delta$. However, the reconstructed solution necessarily possesses a certain smoothness. The alternative nonquadratic stabilization functional imposes constraint on the variation of the solution in the domain. The total variation penalization, as well as the regularization based on the non-negativity constraint [26], does

not impose smoothness on the solution, which permits recovering blocky and contrast structures.

Accurate reconstruction of the function μ is especially important when the initial materials' constants are in the vicinity of the spectral interval, say as in the case of percolation. In [26], we assume that the medium formed as a mixture of sandgrains and water, has three resonances. The corresponding structural function μ is shown in Figure 1 as a sum of three delta functions. Numerically simulated multi-frequency values of the imaginary part of the effective complex permittivity were used to recover the structural function μ. The functions μ reconstructed using Tikhonov and non-negatively constrained regularization, are also shown in the same figure. While the Tikhonov regularization gives oversmoothed curves, the non-negatively constrained solution practically exactly reconstructs the true function: The difference is indistinguishable on the given scale.

4.   COMPARISON WITH EXPERIMENT

For appraisal of the suggested indirect method of computation of the effective properties of the composite from known effective complex permittivity, the approach was applied in [27] to the data for St-Peters sandstone, which is composed of sandgrains and has 11% porosity. Assuming porous space filled with water, with known dependence of ϵ_{water} on frequency, measurements of the effective $\epsilon^*(\omega)$ were simulated using the Maxwell-Garnett model. These simulated data of ϵ^* were used to compute the spectral func-

Table 1   Thermal conductivity of St-Peters sandstone

	Wet sandstone	*Dry sandstone*
Measured	6.36	3.56
Computed	6.63	3.55

tion μ, which was used then to calculate the thermal conductivity of the rock. Computed and measured data for wet (sandgrains and 11 % of water) and dry (sandgrains and 11 % of air) sandstone are summarized in Table 1. Values of the thermal conductivity computed using the suggested algorithm are in good agreement with experimental data taken for comparison from [28].

5.   CONCLUSION

It is shown that various effective properties of a stationary random mixture are coupled through the spectral function. The spectral function can be found from measurements of effective complex permittivity and used to calculate other effective properties. The approach is applicable to porous media, biological materials, artificial composites, and other heterogeneous materials in which the scale of the microstructure is much smaller than the wavelength of the electromagnetic signal.

References

[1] Prager, S (1969) *Improved variational bounds on some bulk properties of a two-phase random medium*, J. Chem. Phys. **50**(10), 4305–4312.

[2] Cherkaev, A (2000) *Variational methods for structural optimization*, New York: Springer-Verlag.

[3] Milton, G W (2002) *Theory of composites*, Cambridge Press.

[4] Torquato, S (2002) *Random heterogeneous materials. Microstructure and macroscopic properties*, New York: Springer-Verlag.

[5] Avellaneda, M and Torquato, S (1991) *Rigorous link between fluid permeability, electrical conductivity, and relaxation times*, Phys. Fluids A **3**(11), 2529–2540.

[6] Berryman, J G and Blair, S C (1987) *Kozeny-Carman relations and image processing methods for estimating Darcy's constant*, J. Appl. Phys. **62**, 2221-2228.

[7] Cherkaev, E (2001) *Inverse homogenization for evaluation of effective properties of a mixture*, Inverse Problems **17**, 1203–1218.

[8] Bergman, D J (1978) *The dielectric constant of a composite material - A problem in classical physics*, Phys. Rep. C **43**, 377–407.

[9] Bergman, D J (1980) *Exactly solvable microscopic geometries and rigorous bounds for the complex dielectric constant of a two-component composite material*, Phys. Rev. Lett. **44**, 1285.

[10] Milton, G W (1980) *Bounds on the complex dielectric constant of a composite material*, Appl. Phys. Lett. **37**(3), 300–302.

[11] Golden, K and Papanicolaou, G (1983) *Bounds on effective parameters of heterogeneous media by analytic continuation*, Comm. Math. Phys. **90**, 473–491.

[12] McPhedran, R C, McKenzie, D R and Milton, G W (1982) *Extraction of structural information from measured transport properties of composites*, Appl. Phys. A **29**, 19–27.

[13] Gajdardziska-Josifovska, M, McPhedran, R C, McKenzie, D R and Collins, R E (1989) *Silver-magnesium fluoride cermet films. 2: Optical and electrical properties*, Applied Optics **28**(14), 2744–2753.

[14] McPhedran, R C and Milton, G W (1990) *Inverse transport problems for composite media*, Mat. Res. Soc. Symp. Proc. **195**, 257–274.

[15] Cherkaeva, E and Golden, K M (1998) *Inverse bounds for microstructural parameters of a composite media derived from complex permittivity measurements*, Waves in Random Media **8**, 437–450.

[16] Milton, G W (1981) *Bounds on the complex permittivity of a two component composite material*, J. Appl. Phys. **52**(8), 5286–5293.

[17] Bergman, D J (1982) *Rigorous bounds for the dielectric constant of a two-component composite*, Ann. Phys. **138**, 78.

[18] Bergman, D J (1993) *Hierarchies of Stieltjes functions and their application to the calculation of bounds for the dielectric constant*, SIAM, J. Appl. Math. **53**(4), 915–930.

[19] Eyre, D, Milton, G W and Mantese, J V (1997) *Finite frequency range Kramers Kronig relations: Bounds on the dispersion*, Phys. Rev. Lett. **79**, 3062–3064.

[20] Cherkaeva, E and Tripp, A C (1996) *Bounds on porosity for dielectric logging*, ECMI96, 9th Conference of the European Consortium for Mathematics in Industry, Denmark, 304–306.

[21] Tripp, A C, Cherkaeva, E and Hulen, J (1998) *Bounds on the complex conductivity of geophysical mixtures*, Geophysical Prospecting **46**(6), 589–601.

[22] Day, A R and Thorpe, M F (1996) *The spectral function of random resistor networks*, J. Phys. Condens. Matter **8**, 4389–4409.

[23] Day, A R, Thorpe, M F, Grant, A R and Sievers, A J (2000) *The spectral function of a composite from reflectance data*, Physica B, **279**, 17–20.

[24] Isakov, V (1990) *Inverse source problems*, Providence: AMS, Math. Surveys and Monographs, 34.

[25] Tikhonov, A N and Arsenin, V Y (1977) Solutions of ill-posed problems, New York: Willey.

[26] Cherkaev, E , Hansen, P C and Berglund, A (2003) *Regularization using non-negativity constraints.* to be submitted.

[27] Cherkaev, E and Zhang, D (2003) *Coupling of the effective properties of a random mixture through the reconstructed spectral representation*, Physica B: Physics of Condensed Matter, in print.

[28] Woodside, W and Messmer, J H (1961) *Thermal conductivity of porous media II: Consolidated rocks*, J Appl. Phys. **43**(9), 1699–1706.

HOMOGENIZATION TECHNIQUES APPLIED TO EARTHQUAKE PROBLEMS

M. Hori, T. Ichimura and H. Nakagawa
Earthquake Research Institute,
University of Tokyo, Yayoi, Bunkyo,
Tokyo 113-0032, Japan
hori@eri.u-tokyo.ac.jp

Abstract   The limitation of modeling complicated crust structures is one cause of difficulty in studying earthquake phenomena. When a stochastic model is used, the homogenization techniques based on the bounding medium theory, which constructs two deterministic models that bound the mean behavior of the stochastic model, enables us to efficiently analyze the model with the evaluation of variability of the earthquake processes. This paper presents the application of the homogenization techniques to two earthquake problems, the earthquake wave propagation and the surface earthquake fault formation. Numerical simulation is made and the results are compared with available data.

1.   INTRODUCTION

Earthquakes are mechanical phenomena which involve fracture and wave propagation processes; see, for instance, [1, 2]. While a simple homogeneous model is sufficient for qualitative analysis, a more detailed model is required to reproduce or predict earthquake more qualitatively. However, it is not possible to construct a reliable model, since measuring underground structures is difficult. Modeling is one bottleneck in studying earthquake.

An alternative of a deterministic model is a stochastic model, i.e., mean, variance or covariance is given to parameters for properties and configurations of the crust structures; see [3]. Variance or covariance corresponds to the uncertainty due to the limitation of measurement. The analysis of such a stochastic model is more laborious than a deterministic model; the

behaviour of the stochastic model becomes stochastic as well. A Monte-Carlo simulation is not a realistic solution for earthquake problems since one simulation requires huge numerical computation.

Homogenization techniques have been developed for the analysis of spatially heterogeneous materials; see [4] for a list of related references. Some techniques dealing with the spatial distribution of heterogeneity are applicable to problems which have both spatial and probabilistic distribution of heterogeneities. The authors are applying such techniques to analyze the stochastic model, and the techniques based on the *bounding medium theory*[5] is presented in this paper. The theory is an extension of computing bounds for the effective moduli of heterogeneous materials, and constructs two fictitious but deterministic models that provide optimistic and pessimistic estimate for the mean behaviour of the stochastic model, in the sense that these models give upper and lower bounds for the mean of the total strain energy stored in the stochastic model.

In this paper, we briefly summarize our recent studies on two earthquake problems, namely, the earthquake wave propagation and the surface earthquake fault formation. Presenting the bounding medium theory in Section 2, we show the results of numerical computation of these two problems in Sections 3.

Cartesian coordinates, denoted by x_i, are used. Index notation is used for a vector or tensor quantity, the summation convention is employed, and indices following a comma denote partial differentiation with respect to the corresponding coordinates.

2. FORMULATION OF HOMOGENIZATION TECHNIQUES

For simplicity, we present the bounding medium theory considering a two-dimensional anti-plane shear problem. For an isotropic but heterogeneous elastic body B, we denote displacement and an elastic modulus by u and c ($u = u_3$ and $c = c_{1313} = c_{2323}$). For given c, the governing equation of u is

$$(c(\mathbf{x})u_{,i}(\mathbf{x}))_{,i} = 0 \quad \text{for } \mathbf{x} \text{ in } B. \tag{2.1}$$

The boundary condition is, say, $u = \overline{u}$ on ∂B. This boundary value problem is transformed to a variational problem of

$$J(u,c) = \int_B \frac{1}{2}c(\mathbf{x})u_{,i}(\mathbf{x})u_{,i}(\mathbf{x})\mathrm{d}s_{\mathbf{x}}, \tag{2.2}$$

for u satisfying $u = \overline{u}$ on ∂B. Since c is positive, the solution of the boundary value problem, denoted by u^{e}, minimizes J.

We consider a case when the elastic moduli is given in a stochastic manner, i.e., the mean, variance or covariance is given to c. We regard

c as a random field in $(\Omega, \mathcal{F}, P)$, where ω represents a stochastic event, $\mathcal{F}$ is Borel set of Ω and P is the probability measure that gives the realization of B with a particular elastic moduli. An argument ω emphasizes that c is a random field. The displacement that satisfies Eq. (2.1) for such a stochastic c is regarded as a random field as well.

Our first interest is to evaluate the mean of the stochastic displacement; the mean behaviour is not the displacement when B has the mean of the stochastic elastic moduli. Computing the mean behaviour is difficult since the joint probability of the displacement and the elastic moduli need to be evaluated. Instead of directly computing the mean behaviour, we seek to find displacement fields which bound the mean behaviour. As mentioned, the bounding medium theory determines two fictitious but deterministic media which provide such bounding displacement fields[5]. While various bounding media can be determined for a given stochastic model, the simplest bounding medium is easily defined by using Eq. (2.2). For one realization of c, due to $c > 0$, the following inequality holds for displacement satisfying boundary conditions:

$$J(u^{\mathrm{e}}(\omega), c(\omega)) \leq J(u, c(\omega)) \quad \text{for } u \text{ satisfying } u = \overline{u} \text{ on } \partial B.$$

Here, $u^{\mathrm{e}}(\omega)$ is a yet-unknown solution of the boundary value problem when $c(\omega)$ is realized in B. The left side is the total strain energy stored in B. Denoting this energy by $E(\omega)$, we have

$$E(\omega) \leq J(u, c(\omega)).$$

Since c is a random field but u is deterministic, taking the mean for both sides of the above equation, we arrive at

$$\langle E \rangle \leq J(u, \langle c \rangle) \quad \text{for } u \text{ satisfying } u = \overline{u} \text{ on } \partial B, \tag{2.3}$$

where $\langle (.) \rangle = \int_{\Omega} (.) P(\mathrm{d}\omega)$ stands for the mean of $(.)$. The sharpest bound for the mean elastic energy $\langle E \rangle$ is given by the solution of the variational problem of $J(u, \langle c \rangle)$, i.e., displacement in a fictitious but deterministic body whose elastic moduli is $\langle c \rangle$. Thus, in the sense that an upper bound for the mean elastic strain energy is obtained, this body is a *bounding medium* for the stochastic body.

Another bounding medium is determined by considering the complementary strain energy. Denoting the compliance modulus by $d = 1/c$, we define a functional for stress σ_i as

$$I(\sigma, d) = - \int_B \tfrac{1}{2} d(\mathbf{x}) \sigma_i(\mathbf{x}) \sigma_i(\mathbf{x}) + \lambda(\mathbf{x})(\sigma_{i,i}(\mathbf{x})) \mathrm{d}s_{\mathbf{x}}$$
$$+ \int_{\partial B} n_i(\mathbf{x}) \sigma_i(\mathbf{x}) \overline{u}(\mathbf{x}) \mathrm{d}\ell_{\mathbf{x}}, \tag{2.4}$$

where λ is a Lagrange multiplier enforcing the equilibrium ($\sigma_{i,i} = 0$ in B) and n_i is outer unit normal of the boundary. In the same manner as shown above, the following inequality is derived for I:

$$\langle E \rangle \geq I(\sigma, \langle d \rangle) \quad \text{for } \sigma. \tag{2.5}$$

The exact solution, $\sigma_i^{\mathrm{e}}(\omega)$, gives the maximum value of I as $I(\sigma^{\mathrm{e}}, d(\omega)) = E(\omega)$, since σ_i^{e} is given as $\sigma_i^{\mathrm{e}} = c\, u_{,i}^{\mathrm{e}}$. Equation (2.5) shows that a fictitious but deterministic body with $d = \langle d \rangle$ (or $c = 1/\langle 1/c \rangle$) underestimates the mean strain energy. Thus, this body is another bounding medium for the stochastic model.

It is shown that the upper or lower bounding medium for the stochastic model is given by B with $\langle c \rangle$ or $1/\langle 1/c \rangle$, respectively. They correspond to the Voigt and Reuss bounds for the effective moduli of heterogeneous materials. It is known that the Hashin-Shtrikman bounds are always shaper than the Voigt and Reuss bounds; see, for instance, [4]. For stochastic models which are stochastically uniform and isotropic, we can determine shaper bounding media by making use of the (generalized) Hashin-Shtrikman variational principle instead of the variational problem of J or I; see [5].

3. APPLICATION TO TWO EARTHQUAKE PROBLEMS

We apply the homogenization techniques to two earthquake problems, the earthquake wave propagation and the surface earthquake fault formation. Curst structure is modelled as a three-dimensional isotropic body, with Young's modulus being stochastic and Poisson's ratio being deterministic. Symbol c is now used to denote Young's modulus, and elasticity tensor is given as ch_{ijkl} with h_{ijkl} being a constant tensor given by Poisson's ratio. The bounding media are determined by using available geological or ground data with uncertainties, and the elasticity tensor of the media are $\langle c \rangle h_{ijkl}$ and $(1/\langle 1/c \rangle))h_{ijkl}$.

3.1. EARTHQUAKE WAVE PROPAGATION

An earthquake wave is transmitted from a source fault, propagates in crust which consists of several geological layers[2], and is amplified in surface ground structures. For a given focal mechanism, we compute the earthquake wave propagation using the bounding media of the stochastic underground structure model. It should be emphasized that the spatial resolution in modeling near the ground surface must be much smaller than the length scale of the wave path, in order to compute higher frequency wave components which shake buildings and structures. The underground structure model becomes quite complicated in such a high spatial resolu-

tion, and huge computational resources will be required to solve the wave propagation in the highly heterogeneous body.

To efficiently solve the wave propagation in the underground structure, we apply the *homogenization method* or the multi-scale analysis based on the singular perturbation expansion[6, 7]. Denoting by ε the ratio of the two length scales of modeling and the wave path, this method introduces a fast spatial variable $\mathbf{y} = 1/\varepsilon \mathbf{x}$ and regards c as a function of $\mathbf{x}$ and $\mathbf{y}$; the dependence of c on $\mathbf{y}$ expresses the change in c in the modeling length scale. For a point $\mathbf{x}$, therefore, a region of the modeling length scale, denoted by $S_{\mathbf{x}}$, is used as a domain for $\mathbf{y}$. In this setting, the homogenization method takes the following expansion of u_i:

$$u_i(\mathbf{x}) = u_i^{(0)}(\mathbf{x}) + \varepsilon u_i^{(1)}(\mathbf{x}, \mathbf{y}) + \cdots . \tag{3.1}$$

In applying the homogenization method, we have to pay attentions to the boundary conditions for $S_{\mathbf{x}}$. The homogenization theory assumes periodic boundary conditions since it is aimed at analyzing composite materials of more or less uniform microstructures. Such periodicity, however, cannot be assumed for the underground structure. We use the uniform stress boundary conditions ($t_j = n_i \overline{\sigma}_{ij}$ with constant $\overline{\sigma}_{ij}$) for the upper bounding medium or uniform strain boundary conditions ($u_i = y_j \overline{\epsilon}_{ij}$ with constant $\overline{\epsilon}_{ij}$) for the lower bounding medium. This is because these boundary conditions, respectively, give the maximum and minimum strain energy among all boundary conditions that produce the same average strain, i.e., denoting the strain energy density by e, we have

$$\int_{S_{\mathbf{x}}} e^{\sigma} \mathrm{d} v_{\mathbf{y}} < \int_{S_{\mathbf{x}}} e^{g} \mathrm{d} v_{\mathbf{y}} < \int_{S_{\mathbf{x}}} e^{\epsilon} \mathrm{d} v_{\mathbf{y}}, \tag{3.2}$$

where superscript σ or ϵ stands for the uniform stress or strain boundary conditions and g for general (possibly mixed) boundary conditions; all of these boundary conditions produce the same average strain taken over $S_{\mathbf{x}}$. Inequality (3.2) is called the *universal bounds*[4] since it holds for any arbitrary linearly elastic bodies.

In the present analysis, the homogenization method is applied to the bounding media in static state. This treatment is not suitable for computing higher frequency wave components that have short wave length, which is smaller than the wave path length scale and comparable with the modeling length scale. Such components accompany larger acceleration even though they have smaller amplitudes. Lower accuracy is expected for the higher frequency components, which is the limitation of the present analysis.

We carry out numerical simulation of the earthquake wave propagation using the bounding media of the stochastic model. Two earthquakes which
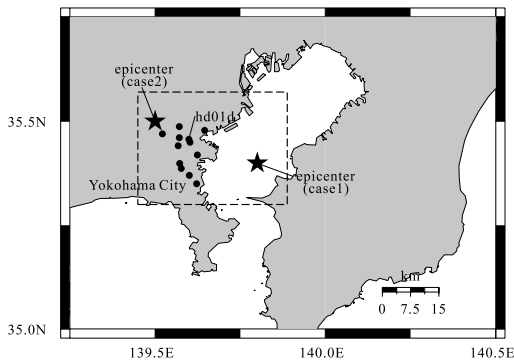
Figure 1   Epicenter of simulated earthquakes and location of measurement sites.

Table 1   Characteristics of target earthquake.

	Date	Lat.	Long.	Depth	Strike	Dip	Rake	Mag.
case1	08/11/1999	35.4N	139.8E	53km	62°	85°	73°	4.0Mw
case2	05/28/1999	35.5N	139.5E	38km	283°	70°	112°	3.5Mw

occurred near Tokyo are simulated; see Fig. 1. The characteristics of the target earthquakes are shown in Table 1. The two bounding models are constructed for the crust. While the difference of the two models is negligible in the geological length scale, they are quite different in the length scale of the surface soil layers. The numerical computation uses the spatial discretization of 2[m], and hence frequency components up to 2[Hz] are accurately computed. The target earthquake was measured at several sites; see Fig. 1. The results of the numerical simulation are compared with the measured data. Figures 2 and 3 show the comparison of the velocity wave at one site and the peak ground velocity at various sites; frequency components higher than 2[Hz] are filtered out in the measured data. The overall waveform of the waves that are synthesized by using the bounding media is similar to that of the measured wave, although the synthesized waveforms do not bound the measured one. For the estimation of the peak ground velocity, the bounding media provide bounds for the measured data at most sites. However, the estimation is quite different from the measured one at two sites (site 4 and 10). This is mainly due to the local topographical effects which the stochastic model fails to capture.
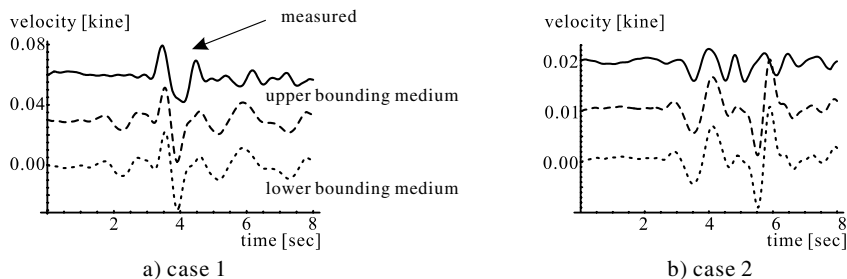
Figure 2   Comparison of velocity wave form.
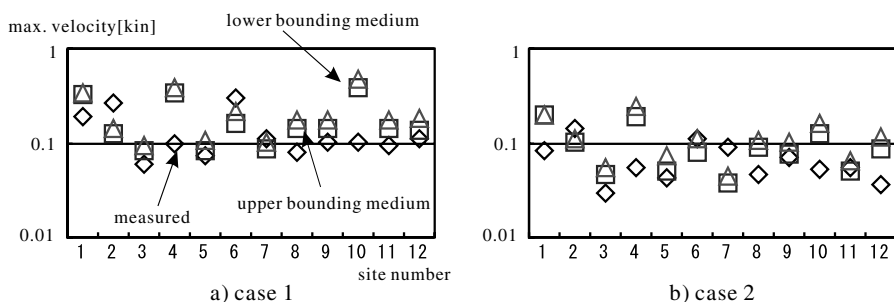
Figure 3   Comparison of peak ground velocity.

3.2.   SURFACE EARTHQUAKE FAULT FORMULATION

For a large earthquake, rupture process on the source fault reaches the ground surface, forming a surface earthquake fault. Echelon fault, a periodic array of oblique cracks caused by lateral sliding, is a typical example of the surface earthquake fault. Large variability in fault displacement is often observed for echelon faults, which is mainly due to the complicated soil layers and the bifurcation during the formation processes. We seek to evaluate the variability using the stochastic model of surface layers, by computing the echelon fault formation in soil layers when the base rock layer slides.

An elasto-plastic material with a yield function f of the Mohr-Column type is used for soil layers. Fault is modelled as the accumulation of plastic shear strain. A stochastic model is constructed by giving a stochastic description for Young's modulus c; Poisson's ratio and plastic material parameters are deterministic. For the evaluation of the variability, we seek to find a random field u in this stochastic and non-linear elasto-plastic

Table 2 Comparison of echelon fault configuration.

	experiment	simulation
orientation of fault direction	26cm	27.9cm
base slip causing failure	5cm	5.2cm
interval between adjacent fault	11cm	11±1cm

body. In incremental form, the governing equation is

$$(c^{ep}_{ijkl}(\mathbf{x},\omega)\dot{u}_{k,l}(\mathbf{x},\omega))_{,i} = 0, \tag{3.3}$$

where $\dot{u}_i$ is displacement increment and c^{ep}_{ijkl} is instantaneous moduli defined as

$$c^{ep}_{ijkl}(\mathbf{x},\omega) = \begin{cases} c(\mathbf{x},\omega)\left(h_{ijkl} - \frac{h_{ijpq}\nabla f_{pq}h_{klrs}\nabla f_{rs}}{\nabla f_{pq}h_{pqrs}\nabla f_{rs}}\right) & f = 0 \ \& \ \dot{f} = 0, \\ c(\mathbf{x},\omega)h_{ijkl} & \text{otherwise,} \end{cases} \tag{3.4}$$

Here, the yield function f is a function of stress and ∇f_{pq} is the gradient ($\nabla f_{pq} = \partial f/\partial \sigma_{pq}$) and h_{ijkl} is the deterministic tensor given by Poisson's ratio.

We approximately compute f using stress in the bounding medium[8]. This approximation means taking the perturbation of f at the mean stress and then approximating it with stress in the bounding medium. Hence, the approximate solution approaches the exact one as the variability of c decreases. For given f, Eq. (3.3) yields a linear stochastic problem for $\dot{u}_i$. This linear stochastic problem is solved by applying the spectral method[3], and the stochastic behaviour of the non-linear elasto-plastic body is evaluated. We carry out numerical simulation of model experiments of echelon faults. Figure 4 summarizes the characteristics of the model experiment and the numerical simulations. In Fig. 5, the distribution of the maximum shear strain on the top surface is presented. Oblique faults are well reproduced even though uniform sliding is applied on the bottom surface. The configuration of these faults is compared with the observed ones in Table 2. The agreement is satisfactory. The probability of failure with respect to the base slip is computed in Fig. 6; the failure is defined as the formation of echelon fault. The probability density function is not Gaussian nor Poisson distribution. The mean and standard deviation of the experimental data are shown. While the variability given by the standard deviation is underestimated, the mean is well reproduced in the simulation.

material properties	
mean of c (kgf/cm²)	12.5
Poisson's ratio	0.25
friction angle (degree)	51
standard deviation of c (kgf/cm²)	0.15
corelation length of c (cm)	50

model dimension and boundary conditions
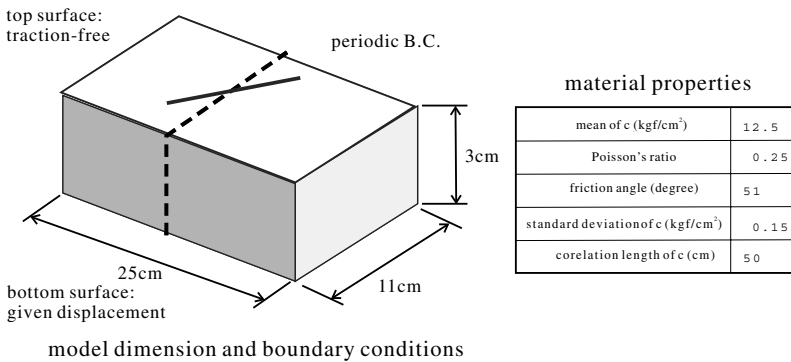
Figure 4 Characteristics of model experiment and numerical simulation.

4.   CONCLUDING REMARKS

The homogenization techniques based on the bounding medium theory enable us to efficiently analyze the stochastic model. While only limited comparison is made, the numerical simulation shows that the earthquake wave propagation and the surface earthquake fault formation can be reproduced to some extent by analyzing the stochastic models, and the variability due to the uncertainty of the underground structures is evaluated. Since it is not expected to fully measure the underground structure, stochastic modeling is a realistic choice for analyzing earthquake phenomena. A sophisticated analysis method of the stochastic model is needed.

Acknowledgments

References

[1] J. Rice: New perspectives on crack and fault dynamics, in *Mechanics for a New Millennium* (Proceedings of the 20th International Congress of Theoretical and Applied Mechanics, 27 Aug - 2 Sept 2000, Chicago), eds. H. Aref and J. W. Phillips, Kluwer, pp. 1-23, 2001.

[2] Lay, T. and C. Wallace: *Modern Global Seismology*, Academic press, 1995.

[3] R.G. Ghanem and P.D. Spanos: *Stochastic finite elements: a spectral approach*, Springer, 1991.

[4] S. Nemat-Nasser and M. Hori: *Micromechanics: overall properties of heterogeneous materials*, 2nd edition, North-Holland, 1998.

a) mean

b) standard deviation
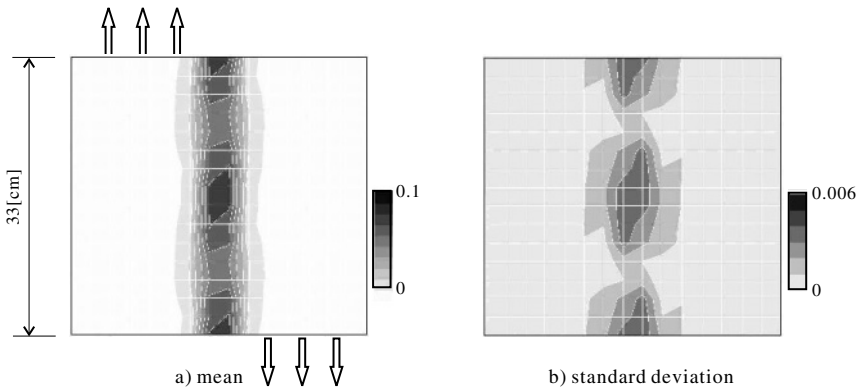
Figure 5   Examples of echelon fault formation on surface with its variability: distribution of maximum shear strain on surface.
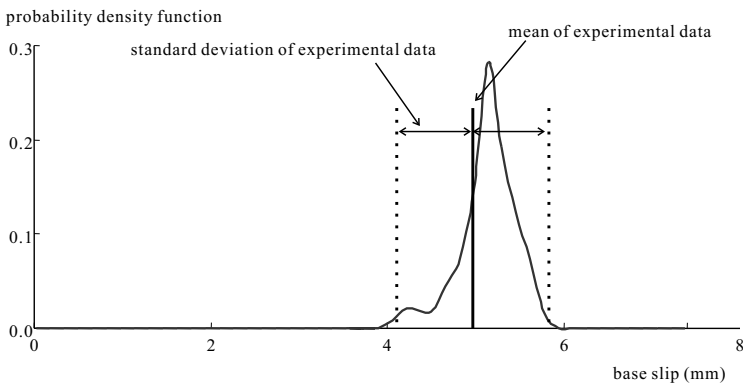
Figure 6   Probability density function of failure with respect to base slip.

[5] M. Hori and S. Munashinge: Generalized Hashin-Shtrikman variational principle for boundary-value problem of linear and non-linear heterogeneous body, *Mechanics of Materials*, Vol. 31, pp. 471-486, 1999.

[6] D.R. Smith: *Singular-perturbation theory*, Cambridge University Press, 1985.

[7] M. Hori and T. Ichimura: Macro-micro analysis for wave propagation in highly heterogeneous media - prediction of strong motion distributions in metropolis -, in *Proceedings of the International Workshop, Wave 2000* (ed. by N. Chouw and G. Schmid), Bochum, Germany, Dec. 13-15, Balkema, pp. 379-398, 2000.

[8] M. Anders and M. Hori: Stochastic finite element method for elasto- plastic body, *Int. J. Numer. Meth. Engng.*, Vol. 46, 1897-1916, 1999.

STOCHASTIC HOMOGENISATION OF FLUID FLOWS IN HETEROGENEOUS POROUS MEDIA

Ali Fadili, Philippe M.J. Tardy, and J.R. Anthony Pearson

Schlumberger Cambridge Research

Cambridge CB3 0EL, UK

afadili@cambridge.oilfield.slb.com

tardy@cambridge.oilfield.slb.com

pearson@cambridge.oilfield.slb.com

Abstract We present here a general methodology for using homogenisation technique, based on a stochastically stationary description of heterogeneities in porous media, to provide an overall pressure drop/flow rate relation valid at scales larger than those of the correlation lengths for heterogeneity. A dual formulation arises depending on whether flow rate or pressure gradient are treated as the independent variable. The homogenisation technique combines perturbation of the local variables with stochastic linearisation of the fluctuation equations. Closure problems are solved by means of spectral Stieltjes-Fourier decomposition under the statistical stationarity assumption. We then require the dual formulation to be consistent in form. The methodology is illustrated on generalized Newtonian single phase flow.

1.   INTRODUCTION

In the context of fluid flow in heterogeneous porous material, engineers are often interested in the mean response of the system in terms of flow rate and pressure drop, rather than in the details of the flow pattern at scales small compared with the flow field. In this paper we give a general methodology for solving the homogenisation problem, which aims at correctly transferring the hydrodynamical description between different scales. The mathematical flow model used at the local Darcy scale is an extension

of Darcy's law, and may be written as

$$\mathbf{F}(\mathbf{x}, n_i) = -\mathbf{K}(\mathbf{x}, P, \|\nabla P\|, n_i).\nabla P, \qquad (1.1)$$

where $\mathbf{F}$ is the volumetric flux density, and P the (pressure) potential. The generalised conductivity $\mathbf{K}$ is, in the general case, a positive second rank tensor which may depend P (unsaturated flows), $\|\nabla P\|$ (non-Newtonian fluid flows) and other parameters n_i describing the rheological behaviour of the fluid. Simplified versions of (1.1) are widely used for modelling Newtonian [1] and non-Newtonian [2] fluid flows in porous media. Here, we consider the formulation for non-Newtonian fluids flowing in isotropic heterogeneous porous media given by

$$\mathbf{F}(\mathbf{x}, n_i) = -K(\mathbf{x}, \|\nabla P\|, n_i)\nabla P. \qquad (1.2)$$

For a fixed pressure gradient, the spatial variation of K comes from its dependence on petrophysical parameters such as the rock permeability and porosity. The spatial variability of these parameters is modelled by a correlated stationary random field. At some larger scale, we are interested in deriving the relationship between the mean flux $\langle \mathbf{F} \rangle$ and the mean pressure gradient $\langle \nabla P \rangle$ by averaging (1.2). This requires the derivation of the cross-correlation between the heterogeneity of the porous medium and flux or pressure gradient fluctuations. It is worth noting that information is lost through approximations and linearisation used in the homogenisation procedure. We attempt to estimate, then reduce this error, and hence extend the domain of applicability of our homogenised results, by a dual homogenisation. This involves carrying out the procedure from the view point of using first volume flux and second pressure gradient as primitive variables. In each case, closure problems are solved using the Stieltjes-Fourier spectral representation of the fluctuations in the context of a stochastically stationary formulation for these fluctuations. Closed analytical expression of the macro-conductivity tensor $\mathbf{K}_e$ is then obtained.

2.   ASSUMPTIONS AND RESULTS

In this section we summarise the main assumptions and results obtained for generalized Newtonian fluids flowing in heterogeneous porous media. The local mathematical model is given by (1.2). We assume that K depends on geometrical parameters, which are spatially distributed and modelled by correlated stationary random fields, and that $A = \ln K$ admits continuous second order derivatives with respect to the norm of the pressure gradient $\|\nabla P\|$. Then, as we shall show below, the macro-scale relationship between the mean flux and the mean pressure gradient takes the following tensorial form

$$\langle F_i \rangle \approx -(K_e)_{ij} \langle (\nabla P)_j \rangle, \qquad (2.1)$$

where the generalised macro-conductivity $(K_e)_{ij}$ is given by

$$(K_e)_{ij} = \overline{K} \exp\left\{\frac{\sigma^2}{2} \int_{R^d} \frac{\mathbf{w}.\mathbf{w}[\mathbf{w}.\mathbf{w}\delta_{ij} - 2k_i k_j]}{[\mathbf{w}.\mathbf{w} + A_0^1 \frac{(\langle\nabla P\rangle.\mathbf{w})^2}{\|\langle\nabla P\rangle\|}]^2} S_{a^0 a^0}(\mathbf{w}) d\mathbf{w}\right\}. \quad (2.2)$$

Here $\mathbf{w}$ is the wave vector, $S_{a^0 a^0}$ is the spectral density of the fluctuation of the generalised log-conductivity, and $\overline{K}$ is given by

$$\overline{K} = \exp\{A_0^0 - \sigma^2 \frac{1}{\|\langle\nabla P\rangle\|} \int_{R^d} \frac{(\langle\nabla P\rangle.\mathbf{w})^2}{\mathbf{w}.\mathbf{w} + A_0^1 \frac{(\langle\nabla P\rangle.\mathbf{w})^2}{\|\langle\nabla P\rangle\|}} S_{a^0 a^1}(\mathbf{w}) d\mathbf{w}$$

$$+ \frac{\sigma^2}{2} \frac{A_0^1}{\|\langle\nabla P\rangle\|} \int_{R^d} \frac{(\langle\nabla P\rangle.\mathbf{w})^2 \mathbf{w}.\mathbf{w}}{[\mathbf{w}.\mathbf{w} + A_0^1 \frac{(\langle\nabla P\rangle.\mathbf{w})^2}{\|\langle\nabla P\rangle\|}]^2} S_{a^0 a^0}(\mathbf{w}) d\mathbf{w}$$

$$+ \frac{\sigma^2}{2} \frac{1}{\|\langle\nabla P\rangle\|^2} \left(A_0^2 - \frac{A_0^1}{\|\langle\nabla P\rangle\|}\right) \times$$

$$\int_{R^d} \frac{(\langle\nabla P\rangle.\mathbf{w})^4}{[\mathbf{w}.\mathbf{w} + A_0^1 \frac{(\langle\nabla P\rangle.\mathbf{w})^2}{\|\langle\nabla P\rangle\|}]^2} S_{a^0 a^0}(\mathbf{w}) d\mathbf{w}\}. \quad (2.3)$$

We have denoted by $S_{a^0 a^1}$ the cross spectral density between the fluctuations a^0 of the generalised log-conductivity and the fluctuation a^1 of its derivative with respect to the pressure gradient. All these quantities and others appearing in (2.3) are defined in Section 3, equation (3.7).

3.   DUAL HOMOGENISATION

Here, we apply the dual homogenisation described in the introduction to non-Newtonian fluid flows. We start with the dual formulations:

- Conductivity formulation (K-approach)

$$\mathbf{F}(\mathbf{x}) = -K(\mathbf{x}, \|\nabla P(\mathbf{x})\|, n_i) \nabla P(\mathbf{x}); \quad \nabla.\mathbf{F}(\mathbf{x}) = 0. \quad (3.1)$$

- Resistivity formulation (R-approach)

$$\nabla P(\mathbf{x}) = -R(\mathbf{x}, \|\mathbf{F}(\mathbf{x})\|, n_i) \mathbf{F}(\mathbf{x}); \quad \nabla.\mathbf{F}(\mathbf{x}) = 0. \quad (3.2)$$

Here R is the generalised resistivity. At this scale we require the relations between the flux and the pressure gradient to be pointwise reciprocal one of each other. Hence

$$K(\mathbf{x}, \|\nabla P(\mathbf{x})\|, n_i) R(\mathbf{x}, \|\mathbf{F}(\mathbf{x})\|, n_i) = 1. \quad (3.3)$$

Based on previous studies [3], we introduce new variables: $A = \ln K$ and $B = \ln R$. Then the reciprocal condition (3.3) becomes

$$A(\mathbf{x}, \|\nabla P\|, n_i) = -B(\mathbf{x}, \|\mathbf{F}\|, n_i). \quad (3.4)$$

The corresponding macro-scale equation (3.28) is used to justify an exponential correction. Last, we assume that the parameters of the rheological models are not spatially distributed.

3.1.   PERTURBATIONS

We introduce an expansion parameter σ for convenience only. For $\mathbf{V} = \mathbf{V}_0 + \sigma \mathbf{v}$, the second order approximation of the norm towards the mean value $\mathbf{V}_0$ is $\|\mathbf{V}\| \approx \|\mathbf{V}_0\| + \sigma \frac{\mathbf{V}_0 . \mathbf{v}}{\|\mathbf{V}_0\|} + \frac{\sigma^2}{2} \left[\frac{\mathbf{v} . \mathbf{v}}{\|\mathbf{V}_0\|} - \frac{(\mathbf{V}_0 . \mathbf{v})^2}{\|\mathbf{V}_0\|^3} \right]$. Then for any smooth function f, we have

$$f(\mathbf{x}, \|\mathbf{V}\|) \approx f(\mathbf{x}, \|\mathbf{V}_0\|) + \sigma f'(\mathbf{x}, \|\mathbf{V}_0\|) \frac{\mathbf{V}_0 . \mathbf{v}}{\|\mathbf{V}_0\|} + \frac{\sigma^2}{2} f''(\mathbf{x}, \|\mathbf{V}_0\|) \frac{(\mathbf{V}_0 . \mathbf{v})^2}{\|\mathbf{V}_0\|^2}$$
$$+ \frac{\sigma^2}{2} f'(\mathbf{x}, \|\mathbf{V}_0\|) \left[\frac{\mathbf{v} . \mathbf{v}}{\|\mathbf{V}_0\|} - \frac{(\mathbf{V}_0 . \mathbf{v})^2}{\|\mathbf{V}_0\|^3} \right], \tag{3.5}$$

where the prime denotes the derivation with respect to $\|\mathbf{V}\|$. We then decompose the different derivatives of f as a sum of a mean value and a fluctuation. Using perturbation of the pressure gradient and flux as

$$\nabla P = \nabla P_0 + \sigma \nabla p, \quad \langle \nabla p \rangle = 0 ; \qquad \mathbf{F} = \mathbf{F}_0 + \sigma \mathbf{f}, \quad \langle \mathbf{f} \rangle = 0, \tag{3.6}$$

the previous results lead us to define

$$A^0 \equiv \ln K(\mathbf{x}, \|\nabla P_0\|) = A_0^0 + \sigma a^0 ; \quad \langle a^0 \rangle = 0,$$
$$A^1 \equiv \frac{\partial \ln K}{\partial \|\nabla P\|}(\mathbf{x}, \|\nabla P_0\|) = A_0^1 + \sigma a^1 ; \quad \langle a^1 \rangle = 0, \tag{3.7}$$
$$A^2 \equiv \frac{\partial^2 \ln K}{\partial \|\nabla P\|^2}(\mathbf{x}, \|\nabla P_0\|) = A_0^2 + \sigma a^2 ; \quad \langle a^2 \rangle = 0,$$

and a similar decomposition for the log-resistivity $B(\mathbf{x}, \|\mathbf{F}\|)$. The upper index denotes the order of the derivative, and the lower index 0 denotes the ensemble average, *e.g.* $A_0^0 = \langle A^0 \rangle$. Rearranging the terms and taking ensemble average we obtain

$$A \approx \bar{A} + \sigma a \quad \text{and} \quad B \approx \bar{B} + \sigma b, \tag{3.8}$$

with

$$\begin{cases} \bar{A} = A_0^0 + \frac{\sigma^2}{2} \left(2 \frac{\nabla P_0 . \langle \nabla p \, a^1 \rangle}{\|\nabla P_0\|} + A_0^1 \frac{\langle \nabla p . \nabla p \rangle}{\|\nabla P_0\|} + \left(A_0^2 - \frac{A_0^1}{\|\nabla P_0\|} \right) \frac{\langle (\nabla P_0 . \nabla p)^2 \rangle}{\|\nabla P_0\|^2} \right), \\ a \approx a^0 + A_0^1 \frac{\nabla P_0 . \nabla p}{\|\nabla P_0\|}. \end{cases}$$
$$\tag{3.9}$$

A similar expression for $\bar{B}$ and b holds with $\mathbf{F}_0$ replacing ∇P_0, $\mathbf{f}$ replacing ∇p, B_0^d replacing A_0^d ($d = 0, 1, 2$), and b^d replacing a^d ($d = 1, 2$).

3.2.   MEAN EQUATIONS AND CLOSURE

Inserting the previous perturbations and approximations into (3.1), and taking the ensemble average, we obtain an *approximation* of the true mean flux, as function of the *true* mean pressure gradient

$$\mathbf{F}_0 \approx -\bar{K}\{[1 + \frac{\sigma^2}{2}\langle a^2\rangle]\nabla P_0 + \sigma^2\langle a\nabla p\rangle\}, \tag{3.10}$$

where $\bar{K} = \exp(\bar{A})$. Similarly with(3.2), we obtain an *approximation* of the true pressure gradient as function of the *true* mean flux

$$\nabla P_0 \approx -\bar{R}\{[1 + \frac{\sigma^2}{2}\langle b^2\rangle]\mathbf{F}_0 + \sigma^2\langle b\mathbf{f}\rangle\}, \tag{3.11}$$

where $\bar{R} = \exp(\bar{B})$. The linearised fluctuations can be written

$$\mathbf{f} \approx -\bar{K}\{\nabla p + a\nabla P_0\} \; ; \qquad \nabla p \approx -\bar{R}\{\mathbf{f} + b\mathbf{F}_0\}. \tag{3.12}$$

From (3.9) and (3.10) and similar expressions for the R-approach the following *closure terms* must be obtained:

Conductivity approach: $\langle a^0\,(\nabla p)_i\rangle; \langle a^1\,(\nabla p)_i\rangle; \langle (\nabla p)_i\,(\nabla p)_j\rangle,$
Resistivity approach: $\langle b^0\,f_i\rangle; \langle b^1\,f_i\rangle; \langle f_i\,f_j\rangle.$ $\tag{3.13}$

To do this, we use the mass conservation equation $\nabla.\mathbf{F}(\mathbf{x}) = 0$ which leads exactly to

$$\nabla.\mathbf{F}_0 = 0 \qquad \text{and} \qquad \nabla.\mathbf{f} = 0. \tag{3.14}$$

Taking the divergence of (3.12), using (3.14) with (3.9), freezing the mean terms, we obtain the following linearised equations for the pressure fluctuations (and similarly for the R-approach):

$$\text{Conductivity approach: } p_{,ii} + a^0_{,i}P_{0,i} + A^1_0\frac{P_{0,j}P_{0,i}}{\|P_0\|}\,p_{,ij} \approx 0, \tag{3.15}$$

$$\text{Resistivity approach: } p_{,ii} + \bar{R}\{b^0_{,i}F_{0i} + B^1_0\frac{F_{0j}F_{0i}}{\|\mathbf{F}_0\|}\,f_{j,i}\} \approx 0, \tag{3.16}$$

where indicial notation is used, and where the comma, *e.g.* $p_{,ii}$ or $f_{j,i}$, denotes the space derivative with respect to the ith spatial coordinate.

3.3.   SPECTRAL SOLUTION

Using the Stieltjes-Fourier spectral representation and the properties linking the spectral increments [4] [5], the partial differential equations (3.15) and (3.16) are transformed into algebraic equations between the spectral increments $d\widehat{a^0}$, $d\widehat{b^0}$, $d\widehat{p}$, $d\widehat{f_i}$, and the closure problems are transformed

into the determination of spectral densities through the Wiener-Khinchine theorem:

- conductivity approach: $S_{p_i\,a^0}$, $S_{p_i\,a^1}$, and $S_{p_i\,p_j}$

- resistivity approach: $S_{f_i\,b^0}$, $S_{f_i\,b^1}$ and $S_{f_i\,f_j}$

The main properties of the spectral increments used here are given in the Appendix. The basic algebraic equations between the spectral increments are thus

$$d\widehat{p} \approx i\frac{(\nabla P_0.\mathbf{w})}{\mathbf{w}.\mathbf{w} + A_0^1 \frac{(\nabla P_0.\mathbf{w})^2}{\|\nabla P_0\|}}\, d\widehat{a^0}, \tag{3.17}$$

$$d\widehat{f_i} \approx -\frac{1}{1 + B_0^1\|\mathbf{F}_0\|}\frac{\mathbf{w}.\mathbf{w}\,\delta_{ij} - w_i w_j}{\mathbf{w}.\mathbf{w} - \frac{B_0^1}{\|\mathbf{F}_0\|}\frac{(\mathbf{F}_0.\mathbf{w})^2}{1 + B_0^1\|\mathbf{F}_0\|}}\, F_{0j}\, d\widehat{b^0}. \tag{3.18}$$

These equations are used to calculate the spectral densities associated with the closure problems (3.13). For the K-approach, we obtain

$$S_{a^0 p,i} = -\frac{(\nabla P_0.\mathbf{w})\,w_i}{D_K(\mathbf{w})}\, S_{a^0 a^0} S_{a^1 p,i} = -\frac{(\nabla P_0.\mathbf{w})\,w_i}{D_K(\mathbf{w})}\, S_{a^0 a^1} \tag{3.19}$$

$$S_{p,i p,j} = \frac{(\nabla P_0.\mathbf{w})^2\,w_i w_j}{[D_K(\mathbf{w})]^2}\, S_{a^0 a^0}, \tag{3.20}$$

where, for convenience, we have put $D_K(\mathbf{w}) = \mathbf{w}.\mathbf{w} + A_0^1\frac{(\nabla P_0.\mathbf{w})^2}{\|\nabla P_0\|}$. Similarly, for the R-approach, we obtain

$$S_{b^0 f_i} = -\frac{1}{1 + B_0^1\|\mathbf{F}_0\|}\left[\frac{(\mathbf{w}.\mathbf{w})\,\delta_{ij} - w_i w_j}{D_R(\mathbf{w})}\right] F_{0j}\, S_{b^0 b^0}, \tag{3.21}$$

$$S_{b^1 f_i} = -\frac{1}{1 + B_0^1\|\mathbf{F}_0\|}\left[\frac{(\mathbf{w}.\mathbf{w})\,\delta_{ij} - w_i w_j}{D_R(\mathbf{w})}\right] F_{0j}\, S_{b^0 b^1}, \tag{3.22}$$

$$S_{f_i f_j} = \left(\frac{1}{1 + B_0^1\|\mathbf{F}_0\|}\right)^2 \left[\frac{(\mathbf{w}.\mathbf{w})\,\delta_{im} - w_i w_m}{D_R(\mathbf{w})}\right] \times$$
$$\left[\frac{(\mathbf{w}.\mathbf{w})\,\delta_{jn} - w_j w_n}{D_R(\mathbf{w})}\right] F_{0m} F_{0n}\, S_{b^0 b^0}, \tag{3.23}$$

where, for convenience, we have put $D_R(\mathbf{w}) = \mathbf{w}.\mathbf{w} - \frac{B_0^1}{\|\mathbf{F}_0\|}\frac{(\mathbf{F}_0.\mathbf{w})^2}{1 + B_0^1\|\mathbf{F}_0\|}$.

3.4.   MACRO-SCALE EQUATIONS

Going back to (3.10) we obtain the macro-scale relations

$$F_{0i} \approx \bar{F}_i = -(K_e)_{ij}(\nabla P_0)_j, \tag{3.24}$$

where the generalised macro-conductivity $(K_e)_{ij}$ is given by

$$(K_e)_{ij} = \overline{K} \left\{ \delta_{ij} + \frac{\sigma^2}{2} \int_{R^d} \frac{\mathbf{w}.\mathbf{w}[\mathbf{w}.\mathbf{w}\delta_{ij} - 2w_i w_j]}{[D_K(\mathbf{w})]^2} S_{a^0 a^0}(\mathbf{w}) d\mathbf{w} \right\}. \quad (3.25)$$

Similarly for (3.11) we obtain

$$(\nabla P_0)_i \approx \overline{\nabla P}_i = -(R_e)_{ij} F_{0j}, \quad (3.26)$$

where the generalised macro-resistivity $(R_e)_{ij}$ is given by

$$(R_e)_{ij} = \overline{R} \left\{ \delta_{ij} - \frac{\sigma^2}{2} \frac{1}{(1 + B_0^1 \|\mathbf{F}_0\|)^2} \int_{R^d} \frac{\mathbf{w}.\mathbf{w}[\mathbf{w}.\mathbf{w}\delta_{ij} - 2w_i w_j]}{[D_R(\mathbf{w})]^2} S_{b^0 b^0}(\mathbf{w}) d\mathbf{w} \right\}. \quad (3.27)$$

The perturbation results (3.25) and (3.27) may become negative for high values of σ, resulting in unphysical relations between the mean pressure gradient and the mean flux. In order to recover more robust results, we follow the procedure already used in [3] and [5], by imposing the following two constraints to (3.25) and (3.27):

$$\mathbf{K}_e.\mathbf{R}_e = \mathbf{R}_e.\mathbf{K}_e = \mathbf{I} \; ; \quad \mathbf{K}_e \geq 0 \quad \mathbf{R}_e \geq 0 \quad (3.28)$$

The first constraint states that the permeability and the resistivity approach have to be equivalent. For the K-approach, the positivity constraint requires that $\overline{\nabla P}.\mathbf{F}_0 \leq 0$ (a similar relation holds for the R-approach). From these constraints it can be seen that an exponential extrapolation of the macro-scale tensors $(K_e)_{ij}$ and $(R_e)_{ij}$ preserves their symmetry, and satisfy both criteria. This correction leads to (2.2)-(2.3). If the mean flow is not aligned with the anisotropy of the medium, these effective coefficients are full second rank tensor [5].

4. NUMERICAL TESTS AND CONCLUSION

This methodology has been recently applied to power-law fluids in [5, 6], and a general case may be found in [7, 8]. Here, we further investigate the power-law fluid and also study a visco-elastic fluid as modelled by Wissler [9]. The local resistivities of these fluids may be written as

$$R = \frac{\mu}{k} \left(\alpha_1 + \alpha_2 \left(\frac{\|\mathbf{F}\|}{F_c} \right)^m \right), \quad (4.1)$$

where μ is interpreted as a reference viscosity, k is the rock permeability, α_i are dimensionless functions depending on the fluid model, F_c is a critical flux, and m is a power-law index. For power-law fluid, $\mu = \chi$ is

the consistency index, $\alpha_1 = 0$, $\alpha_2 = ((3n + 1)/4n)^n)$ where n is power-law exponent, $F_c = (1/\sqrt{c})\sqrt{k\varphi/c}$, with c the shape factor and φ the porosity, last $m = n - 1$. For Wissler fluid, $\mu = \mu_0$ is zero flow-rate viscosity, $\alpha_1 = \alpha_2 = 1$, $F_c = (1/\lambda)\sqrt{k\varphi/c}$, with λ the relaxation time, and $m = 2$. We denote by R^{pl} and R^W the local resistivities of these fluids respectively. Four 2D isotropic media are considered, all with the same φ, c, and same correlation function. The different media are characterised by their permeability $k(\mathbf{x})$, with the same geometrical mean k_G. We generated twelve media by increasing the standard deviation of $\ln k$ as $\sigma_{\ln k}^2 = 0.1, 1.0, 10$. The numerical model used to solve flow in these media is described in [5, 8]. By analogy to the local Darcy law, we define the macro-viscosities $\mu_e^{pl} = \chi R_e^{pl}(n, \chi, \|\mathbf{F}_0\|)/R_e^{pl}(1, \chi, \|\mathbf{F}_0\|)$ for the power-law fluid, and $\mu_e^W = \mu_0 R_e^W(\mu_0, \lambda, \|\mathbf{F}_0\|)/R_e^W(\mu_0, \lambda, 0)$ for the Wissler fluid. For 2D exponential correlation function, we obtain [5, 6]

$$\mu_e^{pl} = \chi_e \|\mathbf{F}_0\|^{n-1}; \; \chi_e = \left(\tfrac{3n+1}{4n}\right)^n \left(\tfrac{c}{\sqrt{k_G\varphi}}\right)^{n-1} e^{\tfrac{\sigma_{\ln k}^2}{2}\left(\beta_1 - \left(\tfrac{n+1}{2}\right)^2 \beta_n\right)}, \quad (4.2)$$

$$\mu_e^W = \mu_0 \left(1 + \left(\tfrac{\|\mathbf{F}_0\|}{F_{ce}}\right)^2\right); \; F_{ce} = \sqrt{\tfrac{k_G\varphi}{c\lambda^2}} \; e^{\tfrac{\sigma_{\ln k}^2}{4}(4\beta_3 - \beta_1)}, \quad (4.3)$$

where $\beta_b = (1 - \sqrt{b})/\sqrt{b}(1 + \sqrt{b})$. Figure 1 details the boundary conditions
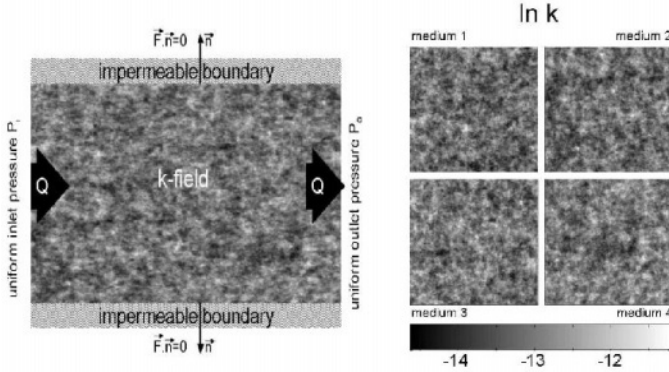
Figure 1   *Left:* Boundary conditions used for the numerical simulations. *Right:* The four isotropic realisations of $\ln k$.

and $\ln k$-fields considered here. In Figure 2, we compare simulation and homogenisation values for χ_e for the power-law fluid, together with 2D flow patterns ($\|\mathbf{F}\|$ plots). Numerical and theoretical values are in good agreement even for large $\sigma_{\ln k}^2$. 2D patterns show that flow concentrates into higher-k, as $\sigma_{\ln k}^2$ increases, and additionally, into lower tortuosity paths as n decreases. Figure 3 shows a very good agreement between the homogenised and numerical μ_e^W for Wissler fluids for $\sigma_{\ln k} = 1$. However for $\sigma_{\ln k}^2 = 10$, theory deviates from the numerics.
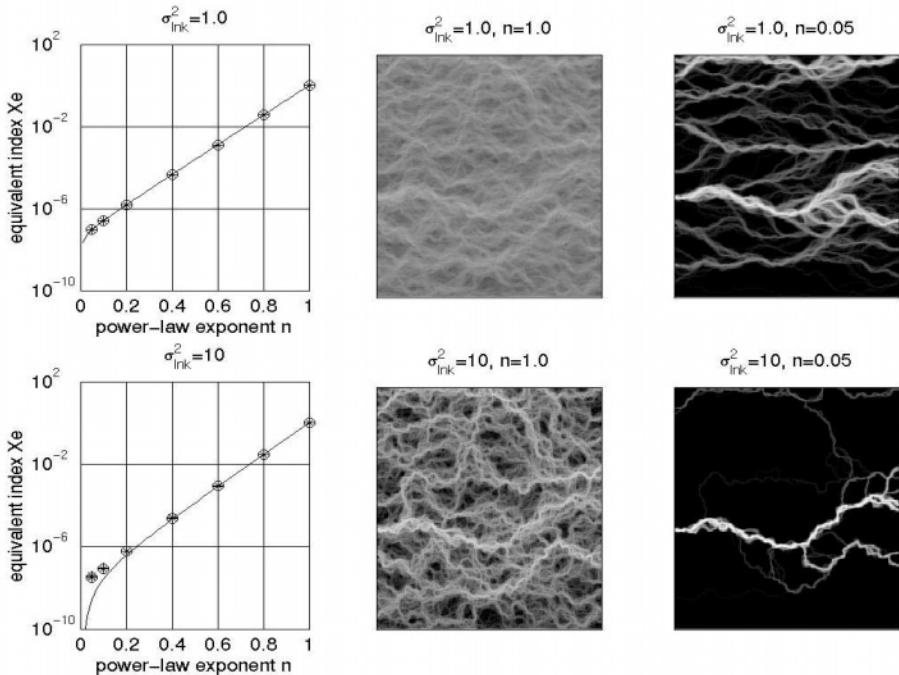
Figure 2 *Left:* Theoretical (line) and numerical (symbols, media 1-4) equivalent consistency index χ_e *vs* the power-law index n. *Centre and right:* Maps of the $\|\mathbf{F}\|$ for medium 1, for Newtonian (centre) and power-law (right), $n = 0.05$, fluids. High fluxes $\leftrightarrow$ light grey. The degree of heterogeneity is $\sigma = 1., 10.$, and $\chi = 1, \varphi = 0.2, c = 2.7$.
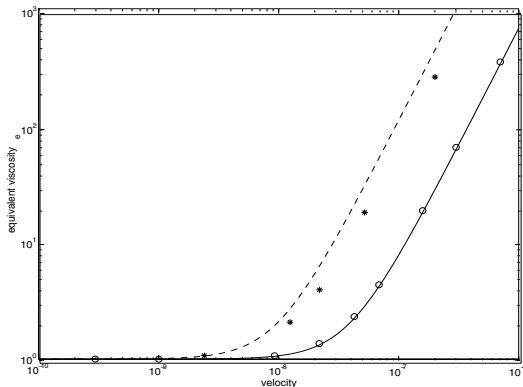

Figure 3 *Left:* Theoretical and numerical μ_e^W for medium 1. $\sigma_{\ln k}^2 = 1.$: solid line and circles ; $\sigma_{\ln k}^2 = 10.$ dashed line and stars. $\mu_0 = 1, \lambda = 1, \varphi = 0.2, c = 2.7$.

As a conclusion, we have developed a consistent methodology based on a dual homogenisation. This consistency leads to a larger domain of physical validity of the macro-scale results. The spectral representation of the

fluctuations allows us to obtain analytical and tractable results. Last, numerical simulations show a good agreement with the theory for moderate degree of heterogeneity. We are working at improving the spectral decomposition in order to lighten the statistical stationary assumption. Note that relationship similar to (1.2) may be derived in the context of heat transfer through, at least, a formal generalisation of Fourier's law relating the heat flux to the gradient of the temperature via a thermal conductivity. Then, our methodology and results may apply directly to homogenise heterogeneous heat transfer problems.

Acknowledgments

Appendix: Spectral decomposition

In order to solve the linearized equations (3.15) and (3.16) we assume the fluctuations are *stationary and ergodic random fields*. Under this hypothesis the fluctuations admit the following Fourier-Stieltjes representation ([4]):

$$a(\mathbf{x}) = \int_{R^d} e^{i\mathbf{w}\cdot\mathbf{x}} d\widehat{a}(\mathbf{w}); \ p(\mathbf{x}) = \int_{R^d} e^{i\mathbf{w}\cdot\mathbf{x}} d\widehat{p}(\mathbf{w}); \ f_i(\mathbf{x}) = \int_{R^d} e^{i\mathbf{w}\cdot\mathbf{x}} d\widehat{f}_i(\mathbf{w}) \tag{A.1}$$

The Fourier-Stieltjes spectral increments $d\widehat{a}$ etc... satisfy the following properties (we use dZ generally):

$$\langle dZ(\mathbf{w})\rangle = 0 \qquad \langle dZ^*(\mathbf{w})\rangle = \langle dZ(-\mathbf{w})\rangle$$

$$\langle dZ(\mathbf{w})dZ^*(\mathbf{w}')\rangle = S_{zz}(\mathbf{w})\delta(\mathbf{w} - \mathbf{w}')d\mathbf{w}' \tag{A.2}$$

where $*$ denotes the complex conjugate, S_{zz} is the spectral density of the random process $z(\mathbf{x})$ and δ denotes the Dirac symbol. A similar relation for cross spectral density S_{zy} holds:

$$\langle dZ(\mathbf{w})dY^*(\mathbf{w}')\rangle = S_{zy}(\mathbf{w})\delta(\mathbf{w} - \mathbf{w}')d\mathbf{w}' \tag{A.3}$$

The variances and covariances appearing in the closure problems are obtained from their spectral densities by the Wiener-Khinchine theorem as:

$$\langle u(\mathbf{x})v(\mathbf{x} + \xi)\rangle \equiv R_{uv}(\xi) = \int_{R^d} e^{i\mathbf{w}\cdot\xi} S_{uv}(\mathbf{w}) \, d\mathbf{w} \tag{A.4}$$

where ξ is the separation vector. For our purpose, we have used only $R_{uv}(\mathbf{0})$, that is:

$$\langle u(\mathbf{x})v(\mathbf{x}) \rangle \equiv R_{uv}(\mathbf{0}) = \int_{R^d} S_{uv}(\mathbf{w}) \, d\mathbf{w} \tag{A.5}$$

References

[1] Bear, J (1987) *Dynamics of fluids in porous media*, Dover ed.

[2] Vossoughi, S (1999) *Advances in the flow and rheology of non-Newtonian fluids*, Part B., D.A. Siginer et al. ed., Elsevier, Rheology series 8, 1225-1230.

[3] Fadili, A (2001) *Ecoulements diphasiques en réservoir pétroliers hétérogènes: homogénéisation stochastique*, Ph.D, INP Toulouse, n° 1762, pp. 301.

[4] Priestley, M B (1981) *Spectral analysis and time series, 1: univariate series*, Academic Press.

[5] Fadili, A Tardy, P M J and Pearson, J R A (2002) *A 3D filtration law for power-law fluids in heterogeneous large-scale porous media*, J.Non-Newtonian Fluid Mech., 106/2-3, (2002), 121-146.

[6] Fadili, A Tardy, P M J and Pearson, J R A (2002) *3D macro-scale analytical filtration law for power-law fluids in heterogeneous porous media*, Proc. Biot Conf. Poromechanics II, eds. Auriault et al., 431-436, Grenoble, France, August 2002.

[7] Fadili, A Tardy, P M J and Pearson, J R A (2002) *Stochastic homogenisation of non-Newtonian flows in heterogeneous porous media: 1. Theory*, in preparation.

[8] Tardy, P M J Fadili, A and Pearson, J R A (2002) *Stochastic homogenisation of non-Newtonian flows in heterogeneous porous media: 2. Numerical validation*, in preparation.

[9] Wissler, E H (1971) *Viscoelastic effects in the flow of non-Newtonian fluids through a porous medium*, Ind. Eng. Chem. Fundam., 10(3), 411-417.

ON MICROMECHANICS-BASED NONLOCAL MODELING OF ELASTIC MATRICES CONTAINING NON-SPHERICAL HETEROGENEITIES

I. Monetto[1] and W.J. Drugan[2]

[1] *Department of Structural and Geotechnical Engineering, University of Genoa*
Via Montallegro 1, 16145 Genova, Italy
monetto@diseg.unige.it

[2] *Department of Engineering Physics, University of Wisconsin - Madison*
1500 Engineering Drive, Madison, WI 53706-1687, USA
drugan@engr.wisc.edu

Abstract A micromechanics-based nonlocal constitutive equation relating the ensemble averages of stress and strain for a matrix containing a random distribution of non-spherical voids, cracks or inclusions but having macroscopically isotropic behavior is derived. The model of impenetrable particles considered consists of identical particles with fixed spheroidal shape and random orientation. It is shown how the effects of inclusion shape and spatial distribution can be separated. Terms related to inclusion shape reduce to certain integrals which can be evaluated analytically only in special cases. Terms describing effects of spatial distribution can be obtained explicitly for different statistical models, within the framework of up through two-point statistics. As verification of the formulation, completely explicit expressions are derived for the limiting case of spherical inclusions and for a standard statistical model on the basis of results found in the literature. The new constitutive equation can be used to produce quantitative estimates of the minimum size of a material volume element over which standard local constitutive equations provide a sensible description of the macroscopic constitutive response of the material.

1. MICROMECHANICS-BASED NONLOCAL MODELING OF TWO-PHASE ISOTROPIC COMPOSITES

Employing a generalization of the [3] and [4] variational formulation to random linear elastic composite materials, due to [11] and [12], [2] developed a micromechanics-based nonlocal constitutive equation relating the ensemble averages of stress and strain for random linear elastic composite materials. Two-phase composites consisting of any statistically uniform and isotropic distribution of isotropic phases, for which an ergodic assumption was made as well, were considered. The microstructure was described statistically by using up through two-point correlation functions. Nonlocal terms up through the second gradient of ensemble averaged strain were included. Based on the same variational formulation, a higher-order nonlocal constitutive equation is due to [1], who considered also the second non-zero nonlocal term, which under the assumptions noted is the fourth gradient of ensemble averaged strain. This nonlocal constitutive equation has the form:

$$< \sigma >_{ij} (\mathbf{x}) = \widehat{L}_{ijkl} < e >_{kl} (\mathbf{x}) + \widehat{L}_{ijklmn}^{(1)} \frac{\partial^2 < e >_{kl} (\mathbf{x})}{\partial x_m \partial x_n} +$$

$$+ \widehat{L}_{ijklmnop}^{(2)} \frac{\partial^4 < e >_{kl} (\mathbf{x})}{\partial x_m \partial x_n \partial x_o \partial x_p}, \tag{1.1}$$

where angle brackets denote ensemble average; σ_{ij} and e_{ij} are the stress and infinitesimal strain components; $\mathbf{x}$ is the position vector; $\widehat{L}_{ijkl}$, $\widehat{L}_{ijklmn}^{(1)}$ and $\widehat{L}_{ijklmnop}^{(2)}$ are isotropic tensors. The detailed forms of these tensors can be found in the references just cited; here, it is of interest to recall only that their components depend on the matrix elastic moduli, the shape and elastic properties of the inclusions as well as on the choice of the homogeneous comparison material. In particular, the shape and the spatial distribution of inclusions affect only the nonlocal tensor components through two radial integrals of the two-point correlation function $h(r)$ for the dispersion of heterogeneities, denoted as H and $\overline{H}$ and defined as:

$$H = \int_0^\infty h(r)\, r\, dr, \tag{1.2}$$

$$\overline{H} = \int_0^\infty h(r)\, r^3 dr. \tag{1.3}$$

The two-phase composite was further specialized to the case of a matrix embedding a random distribution of nonoverlapping identical spheres of a different material and completely explicit results were obtained.

For that case well-founded physical and mathematical bases for describing the material's statistics exist. Furthermore, the use of spheres as heterogeneities makes possible the analytical evaluation of both coefficients H and $\overline{H}$, which take into account details of the distribution of particles. However, despite the higher level of complexity introduced into the formulation as compared to the case of spheres, treatment of non-spherical particles would permit the preceding theory to be applied to a wider range of practical applications. A good example is particles of spheroidal shape. Short fibers in fibre-reinforced composites may be modeled as spheroids with aspect ratio of the order of 10 to 100; whereas a body containing penny-shaped cracks may be regarded as a limiting case of a composite with spheroids of aspect ratio tending to zero.

A main goal of this paper is the derivation of a micromechanics-based explicit nonlocal constitutive equation for a matrix containing a random distribution of non-spherical particles. With reference to composites having macroscopically isotropic behavior, note that constitutive equation (1.1) still applies and is completely explicit except for the evaluation of integrals H and $\overline{H}$. To determine these, the two-point correlation function $h(r)$ must be specified. Thus, the two-phase composite, already specialized to an isotropic distribution of isotropic phases, must be further specialized to the specific case of inclusion shape and distribution under consideration.

It is worthwhile to note that here attention is entirely focused on the formulation to derive the nonlocal corrections rather than on employing the constitutive model to produce quantitative results. In particular, it is proved that inclusion shape and spatial distribution induce mutually independent effects on the nonlocal corrections which can then be analyzed separately.

2. STATISTICAL CHARACTERIZATION OF MATERIAL MICROSTRUCTURE

The model of impenetrable particles here considered consists of nonoverlapping identical spheroids of semiaxes $a_1 = a_2 \neq a_3$ having random orientations. The shape is fixed by the aspect ratio $w = a_3/a_1$: $w < 1$ and $w > 1$ correspond to oblate and prolate spheroids, respectively; of course, $w = 1$ for the case of spheres. The spatial location and orientation of each spheroid are specified by the location $\mathbf{z} \in \mathbb{R}^3$ of the spheroid center and by the unit vector $\boldsymbol{\omega} \in \Omega$ directed along the semiaxis a_3, the unit hemi-sphere in $\mathbb{R}^3$ being denoted by Ω. The related indicator function $\chi_s(\mathbf{x} - \mathbf{z}; \boldsymbol{\omega}) = 1$ when $\mathbf{x} - \mathbf{z}$ lies in the domain of the reference spheroid, and $=0$ otherwise.

Preventing particles from overlapping introduces a higher level of complexity into the statistical characterization of the model. In order to make

possible some simplifications, whatever their locations the spheroids are assumed to take any orientation (there exist no preferred orientations) which is also independent of both locations and orientations of other spheroids. These assumptions add to those of isotropy, statistical uniformity and ergodicity on which the entire formulation is based. Under the above assumptions, a convenient statistical description of this dispersion is obtained by placing the particles within concentric hard "security" spheres of radius a (the semimajor axis of the spheroids being denoted by $a = \max\{a_1, a_3\}$) and referring to this random set of spheres to describe the statistics for the dispersion of the spheroid centers. The model of randomly oriented impenetrable particles within security spheres was used first by [8] who employed a fast Fourier sine transform to evaluate numerically the matrix probability functions in random media for a specific choice of the radial distribution function of the security sphere centers. Note that this assumption is much more restrictive than simply requiring the particles to be nonoverlapping; on the other hand, it makes possible the use of statistical models for the radial distribution function well-known in the case of spheres.

Now, recall that the two-point correlation function $h(r)$ for a statistically uniform two-phase material consisting of an isotropic distribution of phases satisfies the relation ([12]):

$$h(r) = \frac{1}{c_1(1 - c_1)}[P_2(r) - c_1^2], \tag{2.1}$$

where c_1 denotes the volume concentration of inclusions and $P_2(r)$ is the probability that two points $\mathbf{x}_1$ and $\mathbf{x}_2$ separated by $r = |\mathbf{x}_2 - \mathbf{x}_1|$ fall simultaneously in the inclusions. There are only two possibilities for such an event: either both $\mathbf{x}_1$ and $\mathbf{x}_2$ fall in the same spheroid (Event A) or $\mathbf{x}_1$ and $\mathbf{x}_2$ fall in two different spheroids (Event B). Let P_A and P_B the probabilities of Events A and B, respectively. The addition law for probabilities gives then:

$$P_2(r) = P_A + P_B. \tag{2.2}$$

The probability of Event A is:

$$P_A = n \left\{ \frac{1}{2\pi} \int_\Omega \left[\int_{\mathbb{R}^3} \chi_s(\mathbf{x}_1 - \mathbf{z}; \boldsymbol{\omega}) \chi_s(\mathbf{x}_2 - \mathbf{z}; \boldsymbol{\omega}) d\mathbf{z} \right] d\boldsymbol{\omega} \right\}, \tag{2.3}$$

where n is the number density of the spheroids ($c_1 = nV_s$, V_s denoting the spheroid volume). In this expression, notice that the total $\mathbf{z}$-space integral (between square brackets) is the intersection volume of two aligned spheroids (figure 1a), whereas the surface integral over the unit hemi-sphere Ω (between braces) takes the average of such an intersection volume over all orientations. Both integrals can be easily evaluated in closed form and
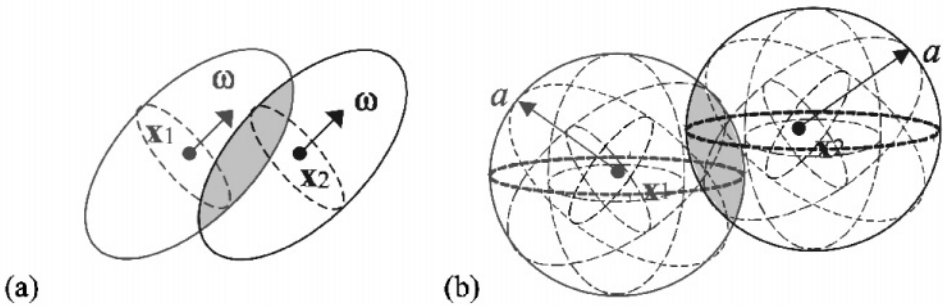
Figure 1 Locus of the centers of spheroids containing two given points $\mathbf{x}_1$ and $\mathbf{x}_2$: (a) Event A; (b) Event B.

the final result is a radially varying function which $=0$ when $r > 2a$. We can write for compactness:

$$P_A = c_a f_A(\rho)\chi_{2a}(r), \tag{2.4}$$

where $c_a = nV_a$ is the volume concentration of security spheres, V_a denoting their volume, χ_{2a} is the indicator function of a sphere of radius $2a$ ($\chi_{2a}(r) = 1$ when $r \leq 2a$, and $= 0$ otherwise) and hereafter, unless specified, $\rho = r/a$. Explicit expressions for function f_A are omitted for conciseness and will be reported elsewhere.

Analogously, the probability of Event B is:

$$P_B = n^2 \int_{\mathbb{R}^3} g(|\mathbf{z}'|) \left\{ \int_{\mathbb{R}^3} \left[\frac{1}{2\pi} \int_\Omega \chi_s(\mathbf{x}_1 - \mathbf{z}; \boldsymbol{\omega})d\boldsymbol{\omega} \right] \right.$$
$$\left. \left[\frac{1}{2\pi} \int_\Omega \chi_s(\mathbf{x}_2 - \mathbf{z}' - \mathbf{z}; \boldsymbol{\omega}')d\boldsymbol{\omega}' \right] d\mathbf{z} \right\} d\mathbf{z}', \tag{2.5}$$

having introduced the radial distribution function $g(r)$ for the dispersion of hard identical security spheres. It is worthwhile to note first that (2.5) reduces to $P_B = c_1^2$ for $g(|\mathbf{z}'|) = 1$. Secondly, each surface integral over the unit hemi-sphere Ω (between square brackets) returns a geometrical quantity, that is an inhomogeneous sphere of radius a, statistically equivalent to a spheroid randomly oriented. Let S denote a spherical shell of radius r, concentric with the reference spheroid. Varying r from 0 to a, the statistical density $\gamma(\rho)$ of the equivalent inhomogeneous sphere is defined as the ratio between the portion of S falling into the spheroid and the total surface of S. It follows that:

$$\gamma(\rho) = \begin{cases} 1, & 0 \leq \rho \leq c/a, \\ f(\rho), & c/a \leq \rho \leq 1, \end{cases} \tag{2.6}$$

$c = \min\{a_1, a_3\}$ being the semiminor axis of the spheroids and function $f(\rho)$ depending on the spheroid shape:

$$f(\rho) = \begin{cases} \frac{w}{\rho}\sqrt{\frac{1-\rho^2}{1-w^2}} & \text{for oblate spheroids } (w \leq 1), \\ 1 - \frac{1}{\rho}\sqrt{\frac{w^2\rho^2-1}{w^2-1}} & \text{for prolate spheroids } (w \geq 1). \end{cases} \tag{2.7}$$

Finally, the total **z**-space integral (between braces) in (2.5) represents the intersection volume of two such inhomogeneous spheres (figure 1b), which results in a radial function defined from 0 to $2a$. Analogously with (2.4), (2.5) can then be written for compactness as:

$$P_B = nc_a \int_{\mathbb{R}^3} f_B(\rho)\chi_{2a}(r)g(|\mathbf{z}'|)d\mathbf{z}', \tag{2.8}$$

where here $r = |\mathbf{x}_2 - \mathbf{x}_1 - \mathbf{z}'|$. In general, since its derivation involves some integrals of the statistical density γ, f_B may be either difficult or impossible to obtain analytically except for some special cases. To facilitate more explicit results, as the main goal of this paper, a convenient representation for g ($g(r) = 0$ for $r < 2a$ since overlapping is not allowed) is in the form suggested by [6]:

$$g(r) = 1 - \chi_{2a}(r) + \int_{2a}^{\infty} [g(y) - 1]\frac{d}{dy}(\chi_y(r))dy, \tag{2.9}$$

where χ_y is the indicator function of a sphere of radius $y \geq 2a$: $\chi_y(r) = 1$ when $r \leq y$, and $=0$ otherwise. Using (2.9) and interchanging the order of integration of the integrals so appearing, (2.8) can then be written as:

$$P_B = c_1^2 - nc_a \left[\int_{\mathbb{R}^3} f_B(\rho)\chi_{2a}(r)\chi_{2a}(|\mathbf{z}'|)d\mathbf{z}'\right] +$$

$$+nc_a \int_{2a}^{\infty} [g(y) - 1]\frac{d}{dy}\left[\int_{\mathbb{R}^3} f_B(\rho)\chi_{2a}(r)\chi_y(|\mathbf{z}'|)d\mathbf{z}'\right] dy. \tag{2.10}$$

Alternatively, having noted that both bracketed terms are convolutions, one obtains:

$$P_B = c_1^2 - nc_a(f_B\chi_{2a} * \chi_{2a})(r) +$$

$$+nc_a \int_{2a}^{\infty} [g(y) - 1]\frac{d}{dy}(f_B\chi_{2a} * \chi_y)(r)dy, \tag{2.11}$$

where $r = |\mathbf{x}_2 - \mathbf{x}_1|$. Finally, using (2.4) and (2.11) in (2.2) and the result in (2.1) gives the two-point correlation function for the dispersion of identical spheroids randomly oriented:

$$h(r) = \frac{c_a}{c_1(1-c_1)}[f_A(\rho)\chi_{2a}(r) - n(f_B\chi_{2a} * \chi_{2a})(r)] +$$
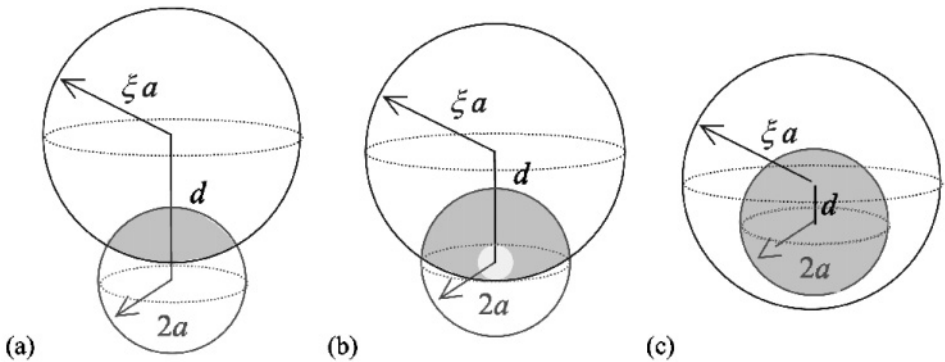
Figure 2 Intersection of two spheres of radius $2a$ and $\xi a \geq 2a$: (a) for $\xi a \leq d < (2+\xi)a$; (b) for $(\xi - 2)a \leq d < \xi a$; (c) for $0 \leq d < (\xi - 2)a$.

$$+\frac{nc_a}{c_1(1 - c_1)} \int_{2a}^{\infty} [g(y) - 1]\frac{d}{dy}(f_B\chi_{2a} * \chi_y)(r)dy = h^{ws}(r) + h^*(r), \quad (2.12)$$

which can be conveniently split into two parts: $h^{ws}(r)$ is the so-called well-stirred approximation corresponding to $g(r) = 1$ for $r \geq 2a$; and $h^*(r)$ is a correction term.

The two-point correlation function (2.12) is now employed to evaluate H and $\overline{H}$:

$$H = \int_0^{\infty} h(r)r\,dr = a^2 \int_0^{\infty} [h^{ws}(\rho) + h^*(\rho)]\rho d\rho, \quad (2.13)$$

$$\overline{H} = \int_0^{\infty} h(r)r^3\,dr = a^4 \int_0^{\infty} [h^{ws}(\rho) + h^*(\rho)]\rho^3 d\rho. \quad (2.14)$$

This task reduces to the evaluation of the following integrals:

$$\int_0^{\infty} \rho^m h^{ws}(\rho)d\rho = \frac{c_a}{c_1(1 - c_1)} \left\{ \int_0^2 \rho^m f_A(\rho)d\rho - n \int_0^{\infty} \rho^m (f_B\chi_{2a} * \chi_{2a})(\rho)d\rho \right\}, \quad (2.15)$$

$$\int_0^{\infty} \rho^m h^*(\rho)d\rho = \frac{nc_a}{c_1(1 - c_1)} \int_0^{\infty} \rho^m \left[\int_2^{\infty} [g(\xi) - 1]\frac{d}{d\xi}(f_B\chi_{2a} * \chi_{\xi a})(\rho)d\xi \right] d\rho, \quad (2.16)$$

where $\xi = y/a$. Setting $m = 1$ in (2.15) and (2.16) provides contributions to H, whereas $m = 3$ corresponds to terms appearing in the expression of $\overline{H}$.

The second integral in (2.15), which involves function f_A, can be easily evaluated for both $m = 1$ and $m = 3$ and the result depends only on the spheroid shape. In contrast, integrals which involve function f_B may be either difficult or impossible to evaluate analytically since f_B is not known explicitly, as already discussed. Nevertheless, more explicit results can be obtained on the basis of simple geometrical interpretations. The key point in the evaluation of these integrals is that their integrands are convolutions

and represent geometrically intersection volumes of two spheres whose centers are separated by r (figure 2): the former of radius $2a$ is inhomogeneous with density f_B; the latter of radius $y = \xi a \geq 2a$ is homogeneous. Thus, as regards the second term in the well-stirred approximation (2.15) where $\xi = 2$, it is straightforward to show that:

$$\int_0^\infty \rho^m (f_B \chi_{2a} * \chi_{2a})(\rho) d\rho = \frac{3}{4} V_a \left\{ \int_2^4 \rho^{m-1} \left[\int_{\rho-2}^2 \delta[4 - (\rho - \delta)^2] f_B(\delta) d\delta \right] d\rho \right\} +$$

$$+ 3V_a \left\{ \int_0^2 \rho^m \left[\int_0^{2-\rho} \delta^2 f_B(\delta) d\delta + \int_{2-\rho}^2 \frac{\delta[4 - (\rho - \delta)^2]}{4\rho} f_B(\delta) d\delta \right] d\rho \right\}. \quad (2.17)$$

Since $f_B(\delta)$ is not known explicitly, let us interchange the order of integration of all the integrals and evaluate first the ρ-integral. Combining terms, (2.17) finally reduces to:

$$\int_0^\infty \rho^m (f_B \chi_{2a} * \chi_{2a})(\rho) d\rho =$$

$$= \frac{V_a}{40} \int_0^2 f_B(\rho) \rho^2 [10(3 - m)(12 - \rho^2) + (m - 1)(240 + 40\rho^2 - \rho^4)] d\rho, \quad (2.18)$$

that is, a simple radial integral of function f_B depending only on the spheroid aspect ratio. On the other hand, as regards the double integral in (2.16), the first derivative with respect to the radius of the homogeneous sphere of the intersection volume just mentioned is involved. In this case we can find:

$$\int_0^\infty \rho^m \left[\int_2^\infty [g(\xi) - 1] \frac{d}{d\xi} (f_B \chi_{2a} * \chi_{\xi a})(\rho) d\xi \right] d\rho =$$

$$= \frac{3V_a}{2} \left\{ \int_2^\infty [g(\xi) - 1] \left[\int_{\xi-2}^\xi \rho^{m-1} \left(\int_{\xi-\rho}^2 \delta \xi f_B(\delta) d\delta \right) d\rho \right. \right.$$

$$\left. \left. + \int_\xi^{\xi+2} \rho^{m-1} \left(\int_{\rho-\xi}^2 \delta \xi f_B(\delta) d\delta \right) d\rho \right] d\xi \right\}. \quad (2.19)$$

Interchanging the order of integration of the ρ- and δ-integrals, evaluating the ρ-integral and combining terms, (2.19) finally reduces to:

$$\int_0^\infty \rho^m \left[\int_2^\infty [g(\xi) - 1] \frac{d}{d\xi} (f_B \chi_{2a} * \chi_{\xi a})(\rho) d\xi \right] d\rho =$$

$$= \frac{V_a}{2} \left[\int_2^\infty \xi[g(\xi) - 1] d\xi \right] \left[\int_0^2 f_B(\rho)[3(3 - m)\rho^2 + (m - 1)\rho^4] d\rho \right]$$

$$+ \frac{3V_a}{2} (m - 1) \left[\int_2^\infty \xi^3 [g(\xi) - 1] d\xi \right] \left[\int_0^2 \rho^2 f_B(\rho) d\rho \right], \quad (2.20)$$

where observe that the ξ- and ρ-integrals are mutually independent, as grouped above, and can thus be evaluated separately.

Introducing (2.18) and (2.20) into (2.15) and (2.16) and the results into (2.13) and (2.14), H and $\overline{H}$ assume the final forms:

$$H = \frac{c_a a^2}{c_1(1-c_1)} \left\{ Im_A + c_a \left[\int_0^2 \frac{\rho^2(\rho^2-12)}{2} f_B(\rho)d\rho + 3\Xi \int_0^2 \rho^2 f_B(\rho)d\rho \right] \right\}, \quad (2.21)$$

$$\overline{H} = \frac{c_a a^4}{c_1(1-c_1)} \left\{ \overline{Im}_A + \frac{c_a}{20} \left[\int_0^2 \rho^2(\rho^4 - 40\rho^2 - 240)f_B(\rho)d\rho \right] \right.$$
$$\left. + c_a \left[\Xi \int_0^2 \rho^4 f_B(\rho)d\rho + 3\overline{\Xi} \int_0^2 \rho^2 f_B(\rho)d\rho \right] \right\}, \quad (2.22)$$

having defined:

$$Im_A = \int_0^2 \rho f_A(\rho)d\rho, \quad \overline{Im}_A = \int_0^2 \rho^3 f_A(\rho)d\rho, \quad (2.23)$$

$$\Xi = \int_2^\infty \rho[g(\rho)-1]d\rho = \int_0^2 \rho d\rho + \lim_{s\to 0}\left[\int_0^\infty \rho[g(\rho)-1]e^{-s\rho}d\rho \right] = 2 + \lim_{s\to 0} f(s), \quad (2.24)$$

$$\overline{\Xi} = \int_2^\infty \rho^3[g(\rho)-1]d\rho = 4 + \lim_{s\to 0}\left[\int_0^\infty \rho^3[g(\rho)-1]e^{-s\rho}d\rho \right] = 4 + \lim_{s\to 0} \frac{d^2 f(s)}{ds^2}, \quad (2.25)$$

together with:

$$f(s) = \int_0^\infty \rho g(\rho)e^{-s\rho}d\rho - \frac{1}{s^2}. \quad (2.26)$$

3. EFFECTS OF INCLUSION SHAPE AND SPATIAL DISTRIBUTION ON THE NONLOCAL COEFFICIENTS

This section discusses the physical and analytical implications of the approach here followed in the evaluation of H and $\overline{H}$. Inclusion shape and spatial distribution have been proved to induce mutually independent effects which can be evaluated separately.

In (2.21) and (2.22) integrals Im_A, $\overline{Im}_A$ as well as all the radial integrals involving function f_B describe effects of inclusion shape through spheroid aspect ratio w. Im_A, $\overline{Im}_A$ are known analytically, as already mentioned, whereas evaluation of other integrals cannot be obtained in closed form except for particular cases. As an example, the case of spheres corresponds to taking the limit for $w \to 1$: Im_A and $\overline{Im}_A$ reduce to constants and all other radial integrals can be easily evaluated, so that H and $\overline{H}$ assume the forms:

$$H = \frac{a^2[2 + c_1(-9 + 5\Xi)]}{5(1-c_1)}, \quad \overline{H} = \frac{a^4[60 + c_1(-834 + 70\Xi + 175\overline{\Xi})]}{175(1-c_1)}. \quad (3.1)$$

As regards the spatial distribution of inclusions, this affects the nonlocal corrections only through integrals Ξ and $\overline{\overline{\Xi}}$ which are simple integrals of the radial distribution function. Thus, completely explicit expressions for Ξ and $\overline{\overline{\Xi}}$ require knowledge of $g(r)$. As an example, the best known model for the radial distribution function is due to [7] which [10] specialized for the case of hard identical spheres. Using this model for $g(r)$, $f(s)$ becomes:

$$f(s) = \frac{8sL(2s; c_a)}{12c_a[L(2s; c_a) + M(2s; c_a)\mathrm{e}^{2s}]} - \frac{1}{s^2}, \qquad (3.2)$$

from which integrals Ξ and $\overline{\overline{\Xi}}$ follow:

$$\Xi = \frac{c_a(22 - c_a)}{5(1 + 2c_a)}, \quad \overline{\overline{\Xi}} = \frac{4c_a(1310 + 1679c_a + 1629c_a^2 - 62c_a^3 + 7c_a^4)}{175(1 + 2c_a)^3}. \quad (3.3)$$

To conclude, it is interesting to observe that combining (3.1) and (3.3) where $c_a = c_1$ for spheres [2] and [1] results can be reproduced. Alternatively, improved results based on a different choice of the radial distribution function can be obtained; these will be reported elsewhere.

Acknowledgments

References

[1] Drugan, W. J. Micromechanics-based variational estimates for a higher-order nonlocal constitutive equation and optimal choice of effective moduli for elastic composites. *J. Mech. Phys. Solids*, 48:1359–1387, 2000.

[2] Drugan, W. J. and J. R. Willis. A micromechanics-based nonlocal constitutive equation and estimates of representative volume element size for elastic composites. *J. Mech. Phys. Solids*, 44:497–524, 1996.

[3] Hashin, Z. and S. Shtrikman. On some variational principles in anisotropic and nonhomogeneous elasticity. *J. Mech. Phys. Solids*, 10:335–342, 1962.

[4] Hashin, Z. and S. Shtrikman. A variational approach to the theory of the elastic behaviour of polycrystals. *J. Mech. Phys. Solids*, 10:343–352, 1962.

[5] Markov, K. Z. On the cluster bounds for the effective properties of microcracked solids. *J. Mech. Phys. Solids*, 46:357–388, 1998.

[6] Markov, K. Z. and J.R. Willis. On the two-point correlation function for dispersions of nonoverlapping spheres. *Math. Mod. Meth. Appl. Sciences*, 8:359–377, 1998.

[7] Percus, J. K. and G. J. Yevick. Analysis of classical statistical mechanics by means of collective coordinates. *Phys. Rev.*, 110:1–13, 1958.

[8] Quintanilla, J. Microstructure functions for random media with impenetrable particles. *Phys. Rev. E*, 60:5788–5794, 1999.

[9] Verlet, L. and J. J. Weis. Equilibrium theory of simple liquids. *Phys. Rev. A*, 5:939–952, 1972.

[10] Wertheim, M. S. Exact solution of the Percus-Yevick integral equation for hard spheres. *Phys. Rev. Lett.*, 10:321–323, 1963.

[11] Willis, J. R. Bounds and self-consistent estimates for the overall properties of anisotropic composites. *J. Mech. Phys. Solids*, 25:185–202, 1977.

[12] Willis, J. R. Elasticity theory of composites. In H. G. Hopkins and M. J. Sewell, editors, *Mechanics of Solids: The R. Hill 60th Anniversary Volume*, pages 653 – 686. Pergamon Press, Oxford, 1982.

ARTIFICIAL FERRO-MAGNETIC ANISOTROPY: HOMOGENIZATION OF 3D FINITE PHOTONIC CRYSTALS

F. Zolla[†], and S. Guenneau[‡1]

[†] *Institut Fresnel, UMR 6133, Faculté de saint-Jérôme, case 162, F13397 Marseille Cedex 20, France*

[‡] *Department of Mathematical Sciences, University of Liverpool, Liverpool L69 3BX, UK*

Abstract   In this paper, we attempt to replace heterogeneous ferro-magnetic photonic crystals by homogeneous structures with anisotropic matrices of permittivity and permeability, both deduced from the resolution of annex problems of electrostatic type on a periodic cell. The asymptotic analysis relies on the multi-scale method which is a tool in the theory of homogenization with rapidly oscillating coefficients [2]. We note a singular perturbation for the divergence of the electromagnetic field associated to scaled permittivity $\varepsilon(x/\eta)$ and permeability $\mu(x/\eta)$, which are periodic functions of period $\eta \ll 1$. We establish the sharp convergence of the oscillating field towards the homogenized one via the notion of two-scale convergence [1]. We finally solve numerically the associated system of partial differential equations with a Finite Element Method in order to exhibit the matrices of effective permittivity and permeability for given 2D ferro-magnetic periodic composites.

1.   INTRODUCTION

The theory of homogenization is concerned with the study of the behaviour of solutions of elliptic boundary value problems when the coefficients are periodic with a small period η [2][6]. Such situation corresponds, for instance, to the electromagnetic or elastic properties of a medium with large number of heterogeneities [8]. The main difficulty in homogenization problems is to pass to the limit in the product of two sequences both of which converge weakly and identify the limit. Due to oscillations, the limit of the product is not equal to the product of the limits, and so this

---

[1]Current address: Condensed Matter Theory Group, Blackett Laboratory, Imperial College, Prince Consort Rd., London SW7 2AZ, UK

problem is nontrivial. In order to analyze these oscillations in the physical space represented by the macroscopic (or slow) variable $\mathbf{x} = (x_1, x_2, x_3)$, one introduces the so-called microscopic (or fast) variable $\mathbf{y} = \mathbf{x}/\eta$, and one produces suitable test functions which are then used as multiplier in the original equation. The main results say that the weak limit of such solutions satisfies a suitable boundary value problem which has constant coefficients, that represent what is known as homogenized (or effective) medium. There are many ways to obtain the homogenized coefficients, deduced from a limiting procedure (e.g. 'Γ-convergence' of the energy functional [6], multiple-scale expansion method and 'H-convergence' [2]). We will use the 'two-scale convergence' [1] which consists in passing to the limit in a weak formulation of the initial problem with 'two-scale' test functions.

We will concentrate here on a problem of homogenization arising in electromagnetism and more precisely on periodic structures called 'photonic crystals'. We shall consider periodic structures defined by a unit cell Y_η of characteristic dimensions η ($Y_\eta = [0, \eta[^3$). The content of the cell will define the effective response of the macroscopic finite structure. Clearly, there must be some restrictions on the dimensions of the cell Y_η. If we are concerned about the response of the composite structure to electromagnetic radiation of frequency ω, the conditions should be $\eta \ll \lambda = \dfrac{2\pi c_0}{\omega}$, where c_0 denotes the speed of light. If this condition were not obeyed, there would be the possibility that the internal structure of the medium could diffract as well as refract radiation. This so-called long wavelength limit assumption ensures that the electromagnetic wave is too myopic to detect the internal structure and in this *limit* an effective permittivity and permeability is a valid concept. In this paper, we will discuss how the diffracted field can be related to ε_{eff} and μ_{eff} and provide some numerical results.

2.   SET UP OF THE PROBLEM

We consider a fixed domain Ω_f corresponding to a 3D ferro-magnetic diffracting object (see figure 1) lit by an incident electromagnetic field at a fixed frequency ω (its associated wavelength can be in resonance with the obstacle). The small heterogeneities of the object - of characteristic size η- induce oscillations of the field in the structure Ω_f, and in turn outside the structure $\mathbb{R}^3 \setminus \bar{\Omega}_f$. Therefore, we can introduce $(\mathbf{E}_\eta^d, \mathbf{H}_\eta^d)$ the diffracted field (which only makes sense outside the structure) deduced from the incident field $(\mathbf{E}^i, \mathbf{H}^i)$ illuminating the structure by $(\mathbf{E}_\eta^d, \mathbf{H}_\eta^d) = (\mathbf{E}_\eta, \mathbf{H}_\eta) - (\mathbf{E}^i, \mathbf{H}^i)$. It is worth noting that we can rigorously define the diffracted field, since the structure does not cover the overall space, which

emphasizes the importance of its boundary. Thus by defining the complex wave number k_0 as $k_0 = \omega(\varepsilon_0\mu_0)^{\frac{1}{2}}$, we obtain the following problem of electromagnetic scattering:

$$(\mathcal{P}_\eta) = \begin{cases} \operatorname{curl}\mathbf{E}_\eta + i\omega\mu_0\mu_\eta\mathbf{H}_\eta = 0 \\ \operatorname{curl}\mathbf{H}_\eta - i\omega\varepsilon_0\varepsilon_\eta\mathbf{E}_\eta = 0 \\ \mathbf{H}_\eta^d = O(\frac{1}{|\mathbf{x}|}), \ \mathbf{E}_\eta^d = O(\frac{1}{|\mathbf{x}|}) \\ k_0\mathbf{E}_\eta^d + \omega\mu(\frac{\mathbf{x}}{|\mathbf{x}|} \wedge \mathbf{H}_\eta^d) = o(\frac{1}{|\mathbf{x}|}) \end{cases} \tag{2.1}$$

where the so-called outgoing wave conditions of Silver-Müller play a fundamental role by ensuring existence and uniqueness of the solution of $(\mathcal{P}_\eta)$: the uniqueness is due to the fact that if $(\mathbf{E}_\eta^d, \mathbf{H}_\eta^d)$ is null, then they ensure that for a given open subset Ω strictly including Ω_η ($\varepsilon_\eta(x) = \mu_\eta(x) = 1$ in $\mathbb{R}^3 \setminus \bar{\Omega}$)

$$\mathcal{R}e \int_{\partial\Omega} (\mathbf{E}_\eta \wedge \bar{\mathbf{H}}_\eta) \cdot \frac{x}{\mathbf{x}} ds \geq 0 \tag{2.2}$$

with an equality in (2.2) if and only if $(\mathbf{E}_\eta, \mathbf{H}_\eta) = 0$ in $\mathbb{R}^3 \setminus \bar{\Omega}$ [5]. Of course, the two first equations of the system (2.1) make sense when assuming that $\mathbf{E}_\eta$ and $\mathbf{H}_\eta$ and all their derivatives are taken in the sense of distributions in the overall space $\mathbb{R}^3$. The radiation conditions are relevant in $C^\infty(\mathbb{R}^3 \setminus \bar{\Omega}_\eta)$. That is to say, $\mathbf{E}_\eta$ and $\mathbf{H}_\eta$ are continuous, as all their derivatives outside the obstacle (this is a consequence of the Helmholtz equation arising outside the obstacle, which induces analyticity of the diffracted electromagnetic field). From now on, we will always assume these hypotheses. If we take the curl of the former equations we then have two similar problems:

$$(\mathcal{P}_\eta^{\mathbf{E}}) = \begin{cases} \operatorname{curl}\left(\mu_\eta^{-1}\operatorname{curl}\mathbf{E}_\eta\right) - k_0^2\varepsilon_\eta\mathbf{E}_\eta = 0 \\ \mathbf{E}_\eta^d = O(\frac{1}{|\mathbf{x}|}) \\ \frac{\mathbf{x}}{|\mathbf{x}|} \wedge \operatorname{curl}\mathbf{E}_\eta^d + ik\mathbf{E}_\eta^d = o(\frac{1}{|\mathbf{x}|}) \end{cases}$$

$$(\mathcal{P}_\eta^{\mathbf{H}}) = \begin{cases} \operatorname{curl}\left(\varepsilon_\eta^{-1}\operatorname{curl}\mathbf{H}_\eta\right) - k_0^2\mu_\eta\mathbf{H}_\eta = 0 \\ \mathbf{H}_\eta^d = O(\frac{1}{|\mathbf{x}|}) \\ \frac{\mathbf{x}}{|\mathbf{x}|} \wedge \operatorname{curl}\mathbf{H}_\eta^d + ik\mathbf{H}_\eta^d = o(\frac{1}{|\mathbf{x}|}) \end{cases}$$

At this point, let us note a fundamental difference with our previous work on homogenization of dielectric PCF [5] in which it appeared much more difficult to perform the study of the problem $(\mathcal{P}_\eta^E)$ than the one of the problem $(\mathcal{P}_\eta^H)$, since μ was a constant function equal to μ_0 unlike ε_η. The magnetic field $\mathbf{H}_\eta$ was divergence free, in contrast with the electric field for which $\operatorname{div}\mathbf{E}_\eta$ behaves like $\dfrac{1}{\eta}$. Indeed, taking the divergence in

the second equation in $(\mathcal{P}\eta)$, we obtain $\operatorname{div}(\varepsilon_\eta \mathbf{E}_\eta) = 0$ which implies that $\operatorname{div}\mathbf{E}_\eta = -\dfrac{\nabla\,\varepsilon_\eta}{\varepsilon_\eta}\mathbf{E}_\eta \sim -\dfrac{\nabla_y\,\varepsilon}{\eta\varepsilon}\mathbf{E}_\eta$. The behavior of the gradient of $\mathbf{E}_\eta$ being related to the ones of the divergence and the curl of $\mathbf{E}_\eta$, it implies strong oscillations for the gradient of the electric field $\mathbf{E}_\eta$. Hence, in [5] we exclusively dealt with $(\mathcal{P}_\eta^H)$. Here, the Maxwell system is completely symmetric and the same difficulty occurs for the magnetic field $\mathbf{H}_\eta$. We arbitrarily choose the magnetic field as the variable (this is more convenient to make some comparisons with results established in [5], but all this study holds for the electric field *mutatis mutandis*). Thus, taking into account that $\mathbf{E}_\eta = \dfrac{i}{\omega\varepsilon_0\varepsilon_\eta}\operatorname{curl}\mathbf{H}_\eta$, we will come back to the couple $(\mathbf{E}_\eta, \mathbf{H}_\eta)$, solution of the initial problem $(\mathcal{P}_\eta)$ by taking the curl of $\mathbf{H}_\eta$, solution of the problem $(\mathcal{P}_\eta^H)$. To conclude this section, let us emphasize that in this paper, we explain in which sense the field $\mathbf{H}_\eta$ tends to a field $\mathbf{H}_{hom}$, solution of the so-called homogenized diffraction problem $(\mathcal{P}_{hom}^H)$, whose resolution leads to two annex problems of electrostatic types which will be discussed in full details in a forthcoming paper.

3. HOMOGENIZED MAXWELL SYSTEM FOR THE SCATTERING PROBLEM

In this section, we state the result of homogenization for a three-dimensional structure filled with a periodic arrangement of ferro-magnetic inclusions. The asymptotic analysis has been carried out thanks to the multiscale expansion technique applied to a scattering problem. We give the associated compactness result of two-scale convergence which establishes rigorously the theorem.

Main results

Let $\mathbf{H}_\eta$ be a sequence of locally square integrable functions on $\mathbb{R}^3$ solutions of

$$(\mathcal{P}_\eta^{\mathbf{H}}) \begin{cases} \operatorname{curl}\tilde{\varepsilon}^{-1}(\mathbf{x}, \tfrac{\mathbf{x}}{\eta})\operatorname{curl}\mathbf{H}_\eta - k_0^2\tilde{\mu}(\mathbf{x}, \tfrac{\mathbf{x}}{\eta})\mathbf{H}_\eta = 0 & \text{,in } \mathcal{D}'(\mathbb{R}^3) \\ \mathbf{H}_\eta^d = O(\tfrac{1}{|\mathbf{x}|}) & \text{,in } C^\infty(\mathbb{R}^3 - \bar{\Omega}_\eta) \\ \tfrac{\mathbf{x}}{|\mathbf{x}|} \wedge \operatorname{curl}\mathbf{H}_\eta^d + ik\mathbf{H}_\eta^d = o(\tfrac{1}{|\mathbf{x}|}) & \text{,in } C^\infty(\mathbb{R}^3 - \bar{\Omega}_\eta) \end{cases}$$

where $\tilde{\varepsilon}^{-1}(\mathbf{x}, \tfrac{\mathbf{x}}{\eta})$ and $\tilde{\mu}^{-1}(\mathbf{x}, \tfrac{\mathbf{x}}{\eta})$ respectively denote the inverse of relative permittivity and permeability of the media i.e. $\tilde{\varepsilon}^{-1}(\mathbf{x}, \tfrac{\mathbf{x}}{\eta}) = \varepsilon^{-1}(\tfrac{x}{\eta})$ (respectively $\tilde{\mu}^{-1}(\mathbf{x}, \tfrac{\mathbf{x}}{\eta}) = \mu^{-1}(\tfrac{x}{\eta})$) if $x \in \Omega_\eta$ and 1 elsewhere.

We suppose that $\mathbf{H}_\eta$, solution of the problem $(\mathcal{P}_\eta^{\mathbf{H}})$ has a two-scale expansion of the form:

$$\forall \mathbf{x} \in \Omega_f, \ \ \mathbf{H}_\eta(\mathbf{x}) = \mathbf{H}_0(\mathbf{x}, \frac{\mathbf{x}}{\eta}) + \eta \mathbf{H}_1(\mathbf{x}, \frac{\mathbf{x}}{\eta}) + \eta^2 \mathbf{H}_2(\mathbf{x}, \frac{\mathbf{x}}{\eta}) + ... \quad (3.1)$$

where $\mathbf{H}_i : \Omega_f \times Y \longmapsto \mathbb{C}^3$ is a smooth function of 6 variables, independent of η, such that $\forall \mathbf{x} \in \Omega_f$, $\mathbf{H}_i(\mathbf{x}, \cdot)$ is Y-periodic.

Our goal is to characterize the electromagnetic field when η tends to 0. If the coefficients $\mathbf{H}_i$ do not increase "too much" when η tends to 0, the limit of $\mathbf{H}_\eta$ will be $\mathbf{H}_0$, a rougher approximation to $\mathbf{H}_\eta$. Hence, we make the assumption that for all $\mathbf{x} \in \mathbb{R}^3$, $\mathbf{H}_i(\mathbf{x}, \frac{\mathbf{x}}{\eta}) = o(\frac{\mathbf{x}}{\eta^i})$, so that the expansion (also denoted by the German word 'ansatz') still makes sense in a neighbourhood of 0. If the above expansion is relevant, we can state the following fundamental result:

Theorem 1. *When η tends to zero, $\mathbf{H}_\eta$ solution of the problem $(\mathcal{P}_\eta^{\mathbf{H}})$, converges weakly in $L^2(\Omega_f)$ to the average of the first term of its asymptotic expansion on the basic cell Y, namely $\mathbf{H}_{hom}(\mathbf{x}) = \int_Y H_0(\mathbf{x}, \mathbf{y}) \, d\mathbf{y}$, which is the unique solution of the following problem $(\mathcal{P}_{hom}^{\mathbf{H}})$:*

$$(\mathcal{P}_{hom}^{\mathbf{H}}) = \begin{cases} \mathrm{curl}([\varepsilon_{hom}^{-1}](\mathbf{x})\mathrm{curl}\,\mathbf{H}_{hom}(\mathbf{x})) - k_0^2[\mu_{hom}]\mathbf{H}_{hom}(\mathbf{x}) = 0 \\ \mathbf{H}_{hom}^d(\mathbf{x}) = O(\frac{1}{|\mathbf{x}|}) \\ \frac{\mathbf{x}}{|\mathbf{x}|} \wedge \mathrm{curl}\,\mathbf{H}_{hom}^d(\mathbf{x}) + ik\mathbf{H}_{hom}^d(\mathbf{x}) = o(\frac{1}{|\mathbf{x}|}) \end{cases}$$

with

$$\begin{cases} [\varepsilon_{hom}](\mathbf{x}) = <\tilde{\varepsilon}(\mathbf{x}, \mathbf{y})(\mathbf{I} - \nabla_\mathbf{y}\mathbf{V}_Y(\mathbf{y})) >_Y & ,in \ \Omega_f \\ [\varepsilon_{hom}](\mathbf{x}) = \mathbf{I} & ,in \ \Omega_f^c \end{cases}$$

and

$$\begin{cases} [\mu_{hom}](\mathbf{x}) = <\tilde{\mu}(\mathbf{x}, \mathbf{y})(\mathbf{I} - \nabla_\mathbf{y}\mathbf{W}_Y(\mathbf{y})) >_Y & ,in \ \Omega_f \\ [\mu_{hom}](\mathbf{x}) = \mathbf{I} & ,in \ \Omega_f^c \end{cases}$$

Here, $< f >_Y$ is the average of f in Y (i.e. $\int_Y f(x, y) \, dy$). Furthermore, $\tilde{\varepsilon}(\mathbf{x}, \mathbf{y})$ and $\tilde{\mu}(\mathbf{x}, \mathbf{y})$ respectively denote

$$\tilde{\varepsilon}(\mathbf{x}, \mathbf{y}) = \begin{cases} 1 & , \ if \ \mathbf{x} \in \Omega_f^c \\ \varepsilon_r(\mathbf{y}) & , \ if \ \mathbf{x} \in \Omega_f \end{cases}$$

and

$$\tilde{\mu}(\mathbf{x}, \mathbf{y}) = \begin{cases} 1 & , \ if \ \mathbf{x} \in \Omega_f^c \\ \mu_r(\mathbf{y}) & , \ if \ \mathbf{x} \in \Omega_f \end{cases}$$

Besides, $\mathbf{V}_Y = (V_1, V_2, V_3)$ and $\mathbf{W}_Y = (W_1, W_2, W_3)$, where $V_j \ ,j \in \{1, 2, 3\}$ and $W_j \ ,j \in \{1, 2, 3\}$, are the unique solutions in $H_\sharp^1(Y)/\mathbb{R}$ (Hilbert

*space of Y-periodic square integrable functions with square integrable gradi-
ents, defined up to an additive constant) of one of the six following problems
$(\mathcal{K}_j)$ and $(\mathcal{M}_j)$ of electrostatic type:*

$$(\mathcal{K}_j) : \mathrm{div}_{\mathbf{y}}\Big[\varepsilon_r(\mathbf{y})\big(\nabla_{\mathbf{y}}(V_j(\mathbf{y}) - y_j)\big)\Big] = 0 \, , j \in \{1, 2, 3\}$$

$$(\mathcal{M}_j) : \mathrm{div}_{\mathbf{y}}\Big[\mu_r(\mathbf{y})\big(\nabla_{\mathbf{y}}(W_j(\mathbf{y}) - y_j)\big)\Big] = 0 \, , j \in \{1, 2, 3\}$$

As η tends to zero, we can replace the isotropic heterogeneous ferro-
magnetic diffracting obstacle of shape Ω_η, by a homogeneous obstacle of
shape Ω_f (see figure 1) with both anisotropic permittivity and permeability
which are given by what follows:

**Corollary 1. Developed form for the matrices of effective permit-
tivity and permeability**

The relative permittivity and permeability matrices of the homogenized
problem are equal to:

$$[\varepsilon_{hom}] = \begin{pmatrix} <\varepsilon_r(\mathbf{y})>_Y & 0 & 0 \\ 0 & <\varepsilon_r(\mathbf{y})>_Y & 0 \\ 0 & 0 & <\varepsilon_r(\mathbf{y})>_Y \end{pmatrix} - \begin{pmatrix} \varphi_{11} & \varphi_{12} & \varphi_{13} \\ \varphi_{21} & \varphi_{22} & \varphi_{23} \\ \varphi_{31} & \varphi_{32} & \varphi_{33} \end{pmatrix}$$

and

$$[\mu_{hom}] = \begin{pmatrix} <\mu_r(\mathbf{y})>_Y & 0 & 0 \\ 0 & <\mu_r(\mathbf{y})>_Y & 0 \\ 0 & 0 & <\mu_r(\mathbf{y})>_Y \end{pmatrix} - \begin{pmatrix} \psi_{11} & \psi_{12} & \psi_{13} \\ \psi_{21} & \psi_{22} & \psi_{23} \\ \psi_{31} & \psi_{32} & \psi_{33} \end{pmatrix}$$

where φ_{ij} and ψ_{ij} represent correction terms defined by:

$$\forall i, j \in \{1, 2, 3\}, \ \varphi_{ij} = < \varepsilon_r \frac{\partial V_j}{\partial y_i} >_Y = < \varepsilon_r \frac{\partial V_i}{\partial y_j} >_Y = - < \varepsilon_r \nabla V_i \cdot \nabla V_j >_Y$$

and

$$\forall i, j \in \{1, 2, 3\}, \ \psi_{ij} = < \mu_r \frac{\partial W_j}{\partial y_i} >_Y = < \mu_r \frac{\partial W_i}{\partial y_j} >_Y = - < \mu_r \nabla W_i \cdot \nabla W_j >_Y .$$

*Here, the brackets denote averaging over Y. Furthermore, V_j and W_j are
the unique solutions in $H^1_\sharp(Y)/\mathbb{R}$ of the six partial differential equations
$\mathcal{K}_j$ and $\mathcal{M}_j$. Hence, thanks to the symmetry of the matrices on the right
($\varphi_{ij} = \varphi_{ji}$ and $\psi_{ij} = \psi_{ji}$), the homogenized permittivity and permeability
are given by the knowledge of twelve terms φ_{ij} and ψ_{ij}, depending upon the
resolution of six annex problems $(\mathcal{K}_j)$ and $(\mathcal{M}_j)$.*

To identify the limit problem, one can substitute the ansatz (3.1) in
the first equation of $(\mathcal{P}^{\mathbf{H}}_\eta)$ and collect terms of the same orders of η (multi-
scale method). Nevertheless, to establish the convergence result of the main
theorem, it is more convenient to use the notion of two-scale convergence.

Definition 1. *We say that* $\mathbf{H}_\eta \rightharpoonup \mathbf{H}_0$ *if there exists* η_k *tending towards* 0 *(as* k *tends to infinity) such that for every* φ *in* $[L^2(\Omega, C_\sharp(Y))]^3$ *[1]*

$$\lim_{k \longmapsto +\infty} \int_\Omega \mathbf{H}_{\eta_k}(x) \cdot \varphi(x, \frac{x}{\eta_k})\, dx = \iint_{\Omega \times Y} \mathbf{H}(x, y) \cdot \varphi(x, y)\, dx dy \qquad (3.2)$$

Analogously, we should say that $\mathbf{H}_\eta \twoheadrightarrow \mathbf{H}_0$ *if* $\|\mathbf{H}_\eta\|_{L^2(\Omega)} \to \|\mathbf{H}_0\|_{L^2(\Omega \times Y)}$.

This approach amounts to take the variational form associated to the first equation of $(\mathcal{P}_\eta^\mathbf{H})$ with suitable test functions of the form (3.1) and then to take the limit when η tends to 0. A justification for this is given by the following lemma, the proof of which can be found in [4]:

Lemma 1. *Let* Ω *be a smooth bounded open subset in* $\mathbb{R}^3$, *and* $(\mathbf{H}_\eta)$ *be a bounded sequence in* $[L^2(\Omega)]^3$ *such that for a given sequence of coercive and bounded symmetric matrices* μ_η

$$\begin{cases} \text{div}(\mu_\eta \mathbf{H}_\eta) = 0 \\ \sup_\eta \int_\Omega \left(|\mathbf{H}_\eta|^2 + |\operatorname{curl} \mathbf{H}_\eta|^2 \right) dx < +\infty \\ \mathbf{H}_\eta \wedge n \quad \text{is bounded in } [H^{\frac{1}{2}}(\partial\Omega)]^3 \end{cases}$$

Then $\exists \mathbf{H}_0 \in H(\text{curl}, \Omega), \exists \mathbf{H}_1 \in L^2(\Omega, H_\sharp^1(\text{curl}, Y))$ *and a subsequence (still denoted by* $(\mathbf{H}_\eta)$*) such that:*

$$\begin{cases} \mathbf{H}_\eta \twoheadrightarrow \mathbf{H}_0(x, y) \\ \operatorname{curl} \mathbf{H}_\eta \rightharpoonup \operatorname{curl}_x \mathbf{H}_0(x, y) + \operatorname{curl}_y \mathbf{H}_1(x, y) \\ \text{div}(\mu_\eta \mathbf{H}_\eta) \rightharpoonup \text{div}_x(\mu_0(x, y) \mathbf{H}_0(x, y)) + \text{div}_y(\mathbf{H}_1(x, y)) = 0 \end{cases}$$

(for the sake of simplicity we denote by $\mu_0(x, y)$ *the limit of* μ_η, *assuming that there is no confusion in the present mathematical section with the value* $\mu_0 = 4.10^{-7}\pi$ *of the permeability of vacuum).*

4.   NUMERICAL ILLUSTRATION IN 2D

In the sequel we seek to determine the coefficients of the tensor of effective permittivity $[\varepsilon_{hom}]$ in 2D case (this procedure repeats *mutatis mutandis* for the effective permeability $[\mu_{hom}]$). More precisely, Ω_f is invariant itself with respect to the third component and we look at the particular case of TM polarization i.e. $\mathbf{H} = u(x_1, x_2)\mathbf{e}_3$. When ε does not depend on the third component namely $\varepsilon(\mathbf{y}) = \varepsilon(y_1, y_2)$ we get from the annex problem $(\mathcal{K}_j)$

$$[\varepsilon_{hom}] = \begin{pmatrix} [A_{hom}] & & 0 \\ & & 0 \\ 0 & 0 & <\varepsilon>_{Y^2} \end{pmatrix}$$
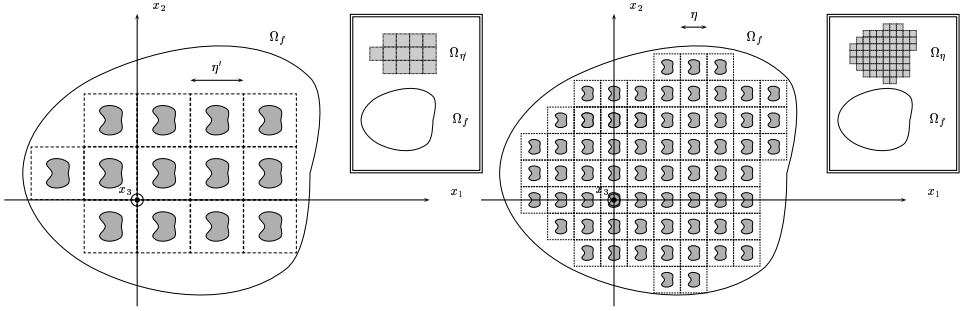
Figure 1 The fixed set Ω_f with two 'scaffolding' $\Omega_{\eta'}$ and Ω_η with $\eta < \eta'$ in the 2-D case.

where $Y^2 =]0;1[^2$ and $[A_{hom}]$ is the 2×2 matrix given by:

$$[A_{hom}] = \begin{pmatrix} \langle \varepsilon \rangle_{Y^2} - \langle \varepsilon \partial_1 V_1 \rangle_{Y^2} & - \langle \varepsilon \partial_1 V_2 \rangle_{Y^2} \\ - \langle \varepsilon \partial_2 V_1 \rangle_{Y^2} & \langle \varepsilon \rangle_{Y^2} - \langle \varepsilon \partial_2 V_2 \rangle_{Y^2} \end{pmatrix}$$

and V_j, $j \in \{1,2\}$, is the unique solution in $H^1_\sharp(Y^2)/\mathbb{R}$ of

$$(\mathcal{P}_j) \; : \; \text{div}\Big[\varepsilon(\mathbf{y})\big(\nabla(V_j(\mathbf{y}) - y_j))\big)\Big] = 0$$

Multiplying $\text{div}_y\big(\varepsilon \nabla_y(V_i - y_i)\big)$ by V_j in $(\mathcal{P}_j)$, $j \in \{1,2\}$, and integrating by parts over the basic cell Y^2 leads to the weak formulation:

$$\Big\langle \varepsilon(\mathbf{y})\big(\nabla_y(V_i - y_i)\big) \cdot \nabla V_j \Big\rangle_{Y^2} = 0 \tag{4.1}$$

To get the corresponding variational equation from the annex problem $(\mathcal{M}_j)$, one has to replace ε by μ in $(\mathcal{P}_j)$. In the discrete formulation the basic cell is meshed with triangles and node elements are used for the scalar fields V_i:

$$V_i = \sum_k^n \beta_i^k w_k^n(x,y) \; , \; \text{in } Y^2 \tag{4.2}$$

where β_i^k denotes the nodal value of the component V_i of the multi-scalar potential $\mathbf{V}$. Besides, w_k^n are basis functions of first order finite elements. The GetDP software [3] has been used to set up the finite element problem with some periodicity conditions imposed to the field on opposite sides of the basic cell Y. If we take ε as a piecewise constant function in (4.1) i.e. $\varepsilon = 4 + 3i$ in an elliptical inclusion (major and minor axes 0.3 and 0.4) and 1.25 elsewhere (cf. fig. 2), $[\varepsilon_{hom}]$ writes as

$$\begin{pmatrix} 1.9296204 + i0.2536979 & (-1.0533083 - i1.1849819)10^{-16} \\ (-44.417444 - i2.0555534)10^{-18} & 2.1127643 + i0.4618554 \end{pmatrix}$$
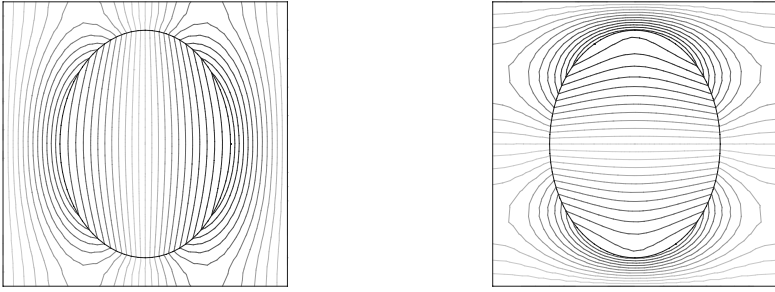
Figure 2 Potentials V_x (left) and V_y (right): the basic cell contains an elliptic inclusion of permittivity $\varepsilon = 4.0 + 3i$ with minor and major axes $a = 0.3$ and $b = 0.4$ in a matrix of silica ($\varepsilon = 1.25$).
.

with $< \varepsilon >_{Y2} = 2.2867255 + i1.1309734$ (see fig. 2 for the associated potentials V_x and V_y). We note that the off-diagonal terms are not strictly null: this artificial anisotropy induced by the mesh of the structure indicates the order of magnitude of the numerical error. Also, these numerical results have been checked with the so-called Method of Fictitious Charges, based on an integral approach (the reader can get any further details in [7]). Let us emphasize that with the Finite Element Method, we can deal with every type of geometry in the basic cell and that ε (or μ) can even be a tensor (provided it is symmetric, coercive and bounded). Also, we note that our result in 2D seems contradictory with the classical one [2] where ε (resp. μ) should be replaced by its inverse in the annex problem. Our result proves to be consistent with that one thanks to a duality relation generalizing a classical result for checkerboard problem due to Keller [7].

5. CONCLUSION

We note that there exists some ferro-magnetic medium whose relative permeability is lower than 1. It suggests that thanks to the homogenization process, one can adjust the effective permittivity and the effective permeability in such a way that $[\varepsilon_{hom}][\mu_{hom}] = \mathbf{I}$. The effective medium may therefore transmit light without deviation and reflect light as an ordinary medium (note that both effective permeability and permittivity can be anisotropic, although their product is the identity matrix). Another consequence is that bodies of various permittivity and permeability may verify $[\varepsilon_{hom}][\mu_{hom}] = \mathbf{I}$, and one has thus to define a class of equivalence for such heterogeneous structures, which behave in the same way for the long

384

wavelength, although they are quite different structures: similarly to the well-known lack of uniqueness of the solution to inverse problems, the homogenized diffracted field can be associated to various effective structures. Intuitively, one cannot distinguish such bodies in transmission (even if their shapes are quite different), since the transmitted waves do not see them!

Acknowledgments

References

[1] G. Allaire, Homogenization and two-scale convergence, SIAM J. Math. Anal. 23 (1992) 1482-1518.

[2] A. Bensoussan, A., J. L. Lions, J. L. and G. Papanicolaou, Asymptotic analysis for periodic structures, *North-Holland, Amsterdam* (1978).

[3] P. Dular, C. Geuzaine, F. Henrotte and W. Legros, A general environment for the treatment of discrete problems and its application to the finite element method, IEEE Trans. Mag. 34, No. 5 (1998) 3395-3398.

[4] S. Guenneau, Homogénéisation des quasi-cristaux et analyse des modes dans des fibres optiques de type cristal photonique, PhD Thesis, Université de Provence (2001).

[5] S. Guenneau, F. Zolla, Homogenization of three-dimensional finite photonic crystals, J. Elec. Waves and Appl. 14 (2000) 529-530/ Prog. in Elec. Res. 27 (2000) 91-127.

[6] V. Jikov, S. Kozlov and O. Oleinik, Homogenization of Differential Operators., *Springer-Verlag, Berlin* (1995).

[7] F. Zolla, S. Guenneau, A duality relation for the Maxwell system, Phys. Rev. E, Vol. 67 (2003), 026610.

[8] R. Landauer, Electrical conductivity in inhomogeneous media, Electrical and transport properties of inhomogeneous materials (ETOPIM '78). *AIP, New York* (1978).

HOMOGENIZED STIFFNESSES OF PERIODIC FIBRE-REINFORCED COMPOSITES

Julian Bravo-Castillero[†1], Raúl Guinovart-Diaz[†],
Reinaldo Rodriguez-Ramos[†], Federico J. Sabina[‡] and
Oscar C. Valdiviezo-Mijangos[⋆2]

[†] *Facultad de Matemática y Computación Universidad de La Habana*
San Lázaro y L, Vedado, Habana 4, CP–10400, Cuba.
jbravo@matcom.uh.cu, guino@matcom.uh.cu, reinaldo@matcom.uh.cu
[‡] *Instituto de Investigaciones en Matemáticas Aplicadas y en Sistemas*
Universidad Nacional Autónoma de México, Apartado Postal 20–726
Delegación de Alvaro Obregón, 01000 México, D.F., México
fjs@mym.iimas.unam.mx
[⋆] *Posgrado en Ciencias de la Tierra, U.N.A.M., Ciudad Universitaria*
04510 México, D.F., México.
ovm@mym.iimas.unam.mx

Keywords: Fibre-reinforced composite, effective properties, homogenization.

Abstract A two-phase fibre-reinforced composite is studied here, whose constituents are isotropic elastic arranged in a hexagonal array. The asymptotic homogenization method, applied to get the overall properties of this composite, yields exact closed-form solutions, which are amenable to a relatively easy computation. Limiting cases of rigid and empty fibres are considered. Hill's universal relations follow from the formulae. The exact formulae explicitly display Avellaneda and Swart's micro-structural parameters, which have a physical meaning, and provide formulae for them. A comparison between the hexagonal and square geometries is given.

---

[1]Present address: Instituto Tecnológico de Estudios Superiores de Monterrey, Campus Estado de México, División de Arquitectura e Ingenier'ia, Apartado Postal 6–3, Atizapán, 52926, México.
[2]Present address: Instituto Mexicano del Petróleo, Eje Central Lázaro Cárdenas 152, Col. San Bartolo Atepehuacan, Del. G.A. Madero, 07730 México, D.F., México.

1. INTRODUCTION

An important problem in micromechanics is posed as follows: in a fibre-reinforced composite, what is the influence of the elastic properties of the fibres and matrix on the overall elastic properties of the composite [1]. To answer this question, different micromechanical approaches are used according to a random or periodic distribution of the fibres. For the former case, various methods have been used, namely, dilute, self-consistent and Mori-Tanaka methods [1]–[3]. For the latter case, Fourier series have been used [3]–[5] and the method of cells [6], which cover a wide range of applications. Bounding methods [2], [3], [7] are very useful in the absence of exact or numerical solutions, especially when the bounds are very close. Composites with rapidly varying properties (periodic) can be studied by means of the asymptotic homogenization method [8]–[10]. Closed-form solutions may be obtained [9], [11]–[12], though the main emphasis of the technique nowadays is largely numerical, which relies on the solution of unit cell problems. See references in [11]–[12]. In this paper the problem of finding the effective properties of a two-phase fibre-reinforced composite is addressed. The constituent materials have isotropic elastic properties and the fibres are periodically arranged in a hexagonal array. Here there are two disparate length scales, i.e., the size of the periodic cell l and the width L of the composite, which allow the introduction of a geometric small parameter $\epsilon = l/L \ll 1$. The method of two scales can then be applied leading to local and global problems to be solved. The latter ones are solved over the unit periodic cell and give rise to the effective coefficients of the former one: the so-called homogenized problem. For a hexagonal array, the method also leads to exact closed-form formulae, which can be provided directly from [11] in a way that is suitable for a relatively easy computation. The limiting cases of empty and rigid fibres are considered.

2. STATEMENT OF THE PROBLEM

A two-phase fibre reinforced composite is studied here in which the properties of the constituents are homogeneous, isotropic and elastic. The Ox_3 direction is the axis of symmetry. The fibres have a circular cross-section and they are periodically distributed without overlapping in directions parallel to the Ox_1 axes and the lines with slope at an angle $\pi/3$, corresponding to hexagonal symmetry. Thus, the composite effective properties are transversely isotropic. The non-zero terms of the stress-strain constitutive relation may be written as a function of five independent parameters

k^*, l^*, n^*, p^* and m^* as follows:

$$\frac{1}{2}(\sigma_1 + \sigma_{22}) = k^*(\epsilon_{11} + \epsilon_{22}) + l^*\epsilon_{33},$$

$$\sigma_{33} = l^*(\epsilon_{11} + \epsilon_{22}) + n^*\epsilon_{33},$$

$$\sigma_{11} - \sigma_{22} = 2m^*(\epsilon_{11} - \epsilon_{22}),$$

$$\sigma_{32} = 2p^*\epsilon_{32}, \quad \sigma_{31} = 2p^*\epsilon_{31}, \quad \sigma_{12} = 2m^*\epsilon_{12}, \tag{2.1}$$

where σ_{ij} are the components of the stress tensor, the indices i, j range from 1 to 3, the components of the strain tensor ϵ_{ij} are defined by

$$\epsilon_{ij} = \frac{1}{2}\left(\frac{\partial u_i}{\partial x_j} + \frac{\partial u_j}{\partial x_i}\right), \tag{2.2}$$

here the components of the displacement vector are u_i; k^* is the plane-strain bulk modulus for lateral dilatation without longitudinal extension; l^* is the associated cross-modulus; n^* is the modulus for longitudinal uni-axial extension; p^* and m^* are, the rigidity moduli for shearing in the longitudinal and in any transverse directions, respectively. The engineering constants are related to these moduli through

$$E_a^* = n^* - l^{*2}/k^* = n^* - 4k^*\nu_a^{*2}, \quad \nu_a^* = l^*/2k^*,$$

$$E_t^* = 4k^*m^*/(k^* + m^*n^*/E_a^*) = 2(1 + \nu_t^*)m^*,$$

$$\nu_t^* = (k^* - m^*n^*/E_a^*)/(k^* + m^*n^*/E_a^*), \tag{2.3}$$

where the subindices a and t refer to an axial or transverse property, respectively. The Young moduli are denoted by E_a^*, E_t^* and the Poisson ratio by ν_a^* and ν_t^*. Also sub-indices 1 and 2 correspond to a quantity related to the matrix and the fibre, in that order. Bulk and rigidity moduli of the phases are defined by K and μ, respectively. The volume fraction per unit length occupied by the matrix is V_1 and the fibre, $V_2 = \pi R^2/\sin(\pi/3)$ so that $V_1 + V_2 = 1$. The Voigt or arithmetic mean of a certain property are given below as

$$K_v = K_1 V_1 + K_2 V_2, \quad \mu_v = \mu_1 V_1 + \mu_2 V_2. \tag{2.4}$$

The jump or contrast of a property across the matrix-fibre interface is denoted by means of the double bar notation as

$$\| K \| = K_1 - K_2, \quad \| \mu \| = \mu_1 - \mu_2. \tag{2.5}$$

The main purpose of this paper is to produce helpful exact formulae to compute overall stiffnesses and engineering moduli.

3.   TWO-PHASE ELASTIC COMPOSITE

In a recent study [11], a similar fibre-reinforced composite was analyzed with the same geometry except that both elastic constituents have transversely isotropic properties. The composite overall parameters are obtained by means of the asymptotic homogenization method and properties of doubly periodic functions. The final formulae can be used for isotropic components as well. The substitutions of these produce the formulae

$$
\begin{aligned}
k^* &= K_v + \mu_v/3 - V_2 \parallel K + \mu/3 \parallel^2 K_i/\mu_1, \\
l^* &= K_v - 2\mu_v/3 - V_2 \parallel K + \mu/3 \parallel\parallel K - 2\mu/3 \parallel K_i/\mu_1, \\
n^* &= K_v + 4\mu_v/3 - V_2 \parallel K - 2\mu/3 \parallel^2 K_i/\mu_1, \\
p^* &= \mu_1 \left[1 - 2V_2 \parallel \mu \parallel P_i/(\mu_1 + \mu_2)\right], \\
m^* &= \mu_1 - V_2 \parallel \mu \parallel M_i,
\end{aligned} \tag{3.1}
$$

where

$$
\begin{aligned}
K_i &= RD_i \left[V_1 + (1 + \kappa_1)D_i \mathcal{V}_p^T \mathcal{M}_k^{-1} \tilde{\mathcal{V}}_p \right] / B_i, \\
P_i &= \left[1 + \chi V_2 - \chi^2 \mathcal{V}_p^T \mathcal{M}_p^{-1} \tilde{\mathcal{V}}_p \right]^{-1}, \\
M_i &= (1 + \kappa_1)E_i / \left[1 + R^2 H_i - \mathcal{V}_m^T \mathcal{M}_m^{-1} \tilde{\mathcal{V}}_m \right]. \tag{3.2}
\end{aligned}
$$

The parameters B_i, D_i, E_i, H_i (i stands for isotropic); κ_1 and χ and the infinite order vectors $\mathcal{V}_p, \tilde{\mathcal{V}}_p, \mathcal{V}_m, \tilde{\mathcal{V}}_m$ and matrices $\mathcal{M}_k, \mathcal{M}_p, \mathcal{M}_m$ which appear in (3.2) can be found in [11], after some simpler substitutions of the isotropic properties. The super-index T denotes a transpose vector.

It is interesting to mention that explicit formulae can also be obtained for empty or rigid fibres in the limit when $\mu_2/\mu_1 \to 0, \infty$, respectively.

The above overall properties k^*, l^*, n^*, p^* and m^* of (3.1) are seen to depend on the isotropic characteristics of the components, the volume fraction filled by them and the radius R of the fibre circular cross-section. The three quantities K_i, P_i and M_i that appear in (3.1) are, in fact, relatively easy to compute. Thus simplifying considerably the computational effort. Enough accurate results are obtained after the infinite order vectors and matrices are truncated to the second order. The powers of R, a number less than one-half, appear frequently in the components. The series involved also converge very quickly.

The structure of (3.1) leads to an important result. The expression K_i may be eliminated from (3.1 a, b, c) to produce the well-known universal

relations of Hill [13] in terms of deviations from the so-called 'formula of mixtures', *viz.*,

$$\frac{\| K + \mu/3 \|}{\| K - 2\mu/3 \|} = \frac{k^* - K_v - \mu_v/3}{l^* - K_v + 2\mu_v/3} = \frac{l^* - K_v + 2\mu_v/3}{n^* - K_v - 4\mu_v/3}. \tag{3.3}$$

Thus the knowledge of one of the properties fixes the other two. The structure of (3.3) lead Avellaneda and Swart [14] to introduce two microstructural parameters A_k and A_m, having a simple physical interpretation, namely, they represent, respectively, the mean transverse hydrostatic strain and mean deviatoric strain in the fibre phase per unit applied transverse pressure and shear to yield

$$A_k = 1+ \| K - \mu/3 \| K_i/\mu_1, \quad A_m = M_i. \tag{3.4}$$

Hence an exact formulae is also obtained for A_k and A_m.

4.   NUMERICAL EXAMPLES

The material properties, of the binary composite considered here, were taken from [15]. The epoxy matrix Young's modulus is $E_1 = 3.45 GPa$ and Poisson's ratio is $\nu_1 = 0.35$; correspondingly, the glass fibres values are $E_2 = 73.1 GPa$ and $\nu_2 = 0.22$. It is of interest to show the exact results calculated using the asymptotic homogenization method (AHM) as a function of the fibre volumetric fraction V_2 up to the percolation limit, which is $V_2 = \pi/[4 \sin(\pi/3)]$. This is done in Figures 1 and 2.

As an example, the plane dimensionless properties dependence on the ratio μ_2/μ_1 against volume fraction V_2 is shown in Figures 1, 2. The shear modulus ratio μ_2/μ_1 ranges over 0 (empty fibre; full dotted line), 0.9 (dashed), 20 (dash-dotted), 120 (dotted) and ∞ (rigid fibre; continuous) for the ratio of transverse Poisson's ratio ν_t^*/ν_1 in Figure 1, and transverse Young's modulus E_t^*/E_1 in Figure 2. A typical fanning behaviour of the curves (non-intersecting) with fixed ratio μ_2/μ_1 as fan ribs is shown in Figure 2. Other parameters, namely, k^*/K_1 and m^*/μ_1 show a similar pattern, though it is not shown here. The empty and rigid cases bound all others. In Figure 2, the curve corresponding to empty fibres is monotone decreasing, characteristic of a fibre-weakened composite. As the material in the fibre becomes stiffer, the composite becomes stiffer so as to reach the limiting rigid behaviour, which is monotone increasing. Note that the composite is weakened (reinforced) when $\mu_2/\mu_1 < 1 (> 1)$.
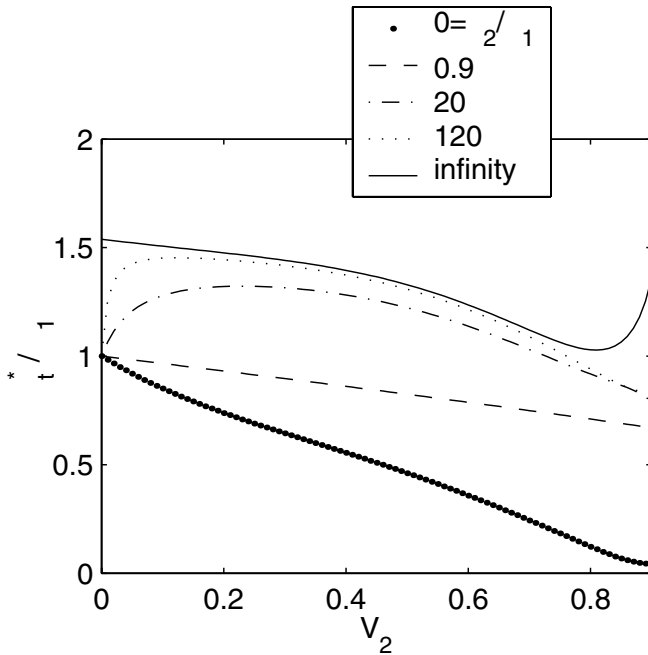
Figure 1 The dependence of normalized effective parameters as a function of $\mu_2/\mu_1 = 0$ (empty), 0.9, 20, 120 and ∞ (rigid) of plane transverse Poisson's ratio ν_t^*/ν_1 against volume fraction V_2. Note the bounding effect of empty and rigid fibres.

A different behaviour is shown in Figure 1 for ν_t^*/ν_1 as far as $\mu_2/\mu_1 > 1$; the curves are not longer monotone, but unimodal (a one maximum or minimum curve). Non-intersecting curves are obtained as well over the range of μ_2/μ_1 between 0 and ∞. The empty and rigid curves act as bounds again, the rigid curve does not start at $\nu_t^*/\nu_1 = 1$ for $V_2 = 0$, and displays a somewhat different behaviour as compared with the rest of the curves. Comparison with known bounds and experiments was done in [11]–[12].

The analysis carried out here refers to a hexagonal cell. A similar one can be done for a square array using [12]. It is interesting to compare results between the two geometries. For $\mu_2/\mu_1 = 20.27$, generally the same E_t^*/E_1 can be attained for a square array with a lesser fibre volume concentration than for a hexagonal one.
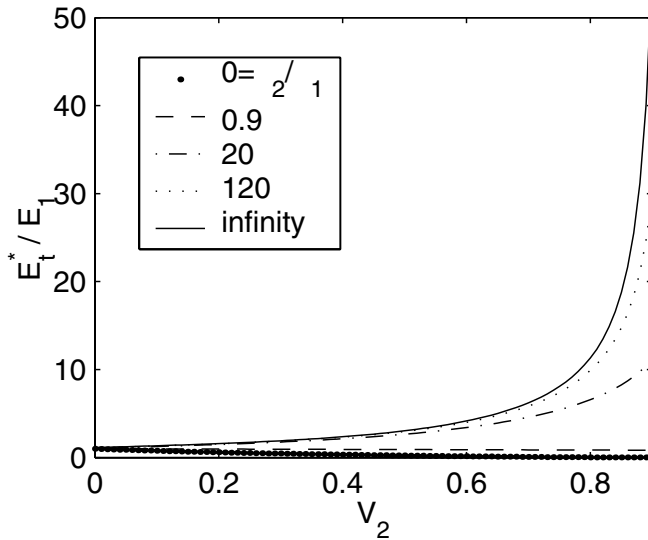
Figure 2 As Figure 1 but for transverse Young's modulus E_t^*/E_1. Again note the bounding effect of empty and rigid fibres.

5. CONCLUDING REMARKS

A binary periodic composite is considered here, whose phases are elastic isotropic media. Exact closed-form formulae are given for the overall properties and engineerings constants. The periodicity of the composite is hexagonal, so that the homogenized properties are transversely isotropic. The numerical implementation of the formulae is relatively easy since it involves the computation of rapidly convergent series. Infinite order matrices and vectors appear in the formulae, but they are truncated to the second order in the calculations producing accurate enough results, because high powers of $R \leq .5$ appear in the components.

The exact formulae (3.1), (3.4) and the universal relations (3.3) may be useful for checking numerical codes and experimental data.

References

[1] Christensen, R M (1991) *Mechanics of Composite Materials*. Malabar, Fl: Krieger.

[2] Benveniste, Y (1987) *Mech. Mat.* **6**, 147.

[3] Nemat-Nasser, S and Hori, M (1999) *Micromechanics: Overall Properties of Heterogeneous Materials*. Amsterdam: North-Holland.

[4] Iwakuma, T and Nemat-Nasser, S (1983) *Int. J. Solids Structures* **16**, 13.

[5] Luciano, R and Barbero, E J (1994) *Int. J. Solids Structures* **31**, 2933.

[6] Aboudi, J (1991) *Mechanics of Composite Materials. A Unified Micromechanical Approach*. Amsterdam: Elsevier.

[7] Bruno, O (1991) *Proc. R. Soc. Lond. A* **433**, 353.

[8] Bensoussan, A, Lions, J L and Papanicolau, G (1978) *Asymptotic Analysis for Periodic Structures*. Amsterdam: North-Holland.

[9] Pobedrya, B E (1984) *Mechanics of Composite Materials*. Moscow: Moscow State University, in Russian.

[10] Bakhvalov, N S and Panasenko, G P (1989) *Homogenization Averaging Processes in Periodic Media*. Dordrecht, Kluwer.

[11] Guinovart-Diaz, R, Bravo-Castillero, J, Rodriguez-Ramos. R and Sabina, F J (2001) *J. Mech. Phys. Solids* **49**, 1445.

[12] Rodriguez-Ramos, R, Sabina, F J, Guinovart-Diaz, R and Bravo-Castillero, J (2001) *Mech. Mat.* **33**, 223.

[13] Hill, R (1964) *J. Mech. Phys. Solids* **12**, 199.

[14] Avellaneda, M and Swart, P J (1998) *J. Acoust. Soc. Am.* **103**, 1449.

[15] Tsai, S W and Hahn, H T (1980) *Introduction to Composite Materials*. Westport: Technomic, Westport.

ASYMPTOTIC HOMOGENISATION IN STRENGTH AND FATIGUE DURABILITY ANALYSIS OF COMPOSITES

S. E. Mikhailov[1] and J. Orlik[2]

[1] *Div. of Mathematics, Glasgow Caledonian University, Glasgow, G4 0BA, UK*
s.mikhailov@gcal.ac.uk

[2] *Fraunhofer Institut für Techno- und Wirtschaftsmathematik*
Gottlieb-Daimler-Str. 49, D-67663 Kaiserslautern, Germany
orlik@itwm.fhg.de

Abstract Asymptotic homogenisation technique and two-scale convergence is used for analysis of macro-strength and fatigue durability of composites with a periodic structure under cyclic loading. The linear damage accumulation rule is employed in the phenomenological micro-durability conditions (for each component of the composite) under varying cyclic loading. Both local and non-local strength and durability conditions are analysed. The strong convergence of the strength as the structure period tends to zero is proved and its limiting value is estimated.

1. INTRODUCTION

Different homogenisation methods are widely used for obtaining homogenised macro-stress fields and effective elastic properties of composites. In [2, 6], the first approximation to the micro-stress field was derived from the properties of the components, micro-geometry of the composite and the applied macro-loads. Convergence of the micro-stresses to some limit, as the structure period tends to zero, can be proved by the two-scale homogenisation technique [1, 3]. The present paper is based on the fact that this limit is exactly the first term of the micro-stress field approximation, which is the product of the homogenised stress tensor, depending only on

macro-geometry and boundary conditions, and the so-called stress concentration tensor, related only to the micro-geometry and stiffness tensors of composite components.

Let B be a Banach space and $\tilde{\Omega}$ be an open or closed domain in a finite-dimensional space. Then $C(\tilde{\Omega}, B)$ denotes the space of continuous Banach-valued functions $f\colon \tilde{\Omega} \ni x \mapsto f(x) \in B$, that is such that $\|f(x_1) - f(x_2)\|_B \to 0$ as $\tilde{\Omega} \ni x_2 \to x_1$ for any $x_1 \in \tilde{\Omega}$. Let $\mathcal{M}(\tilde{\Omega})$ be the space of all bounded functions on $\tilde{\Omega}$.

2.   ELEMENTS OF STRENGTH ANALYSIS

For a bounded stress field $\sigma_{ij}(y)$, $i, j = 1, ..., 3$, any local strength condition for micro-stresses at a point $y \in \Omega \subset \mathbb{R}^k$ (k is 1, 2 or 3) can be written in the form $\Lambda\left(\sigma(y), y\right) < 1$, where $\Lambda \in C(\mathbb{R}^{3 \times 3}, \mathcal{M}(\Omega))$ is a normalised equivalent stress function, a material characteristic, which is non-negative and positively homogeneous of the order $+1$ w.r.t. σ.

Example 1. *For some materials* Λ *can be associated with the von Mises equivalent stress,* $\Lambda_M(\sigma(y), y) = \{[(\sigma_1(y) - \sigma_2(y))^2 + (\sigma_2(y) - \sigma_3(y))^2 + (\sigma_3(y) - \sigma_1(y))^2]\}^{1/2}/(\sqrt{2}\sigma_r(y))$, *or with the Tresca equivalent stress,*

$$\Lambda_T(\sigma(y), y) = \max_{k,m} |\sigma_k(y) - \sigma_m(y)|/\sigma_r(y),$$

where σ_1, σ_2, σ_3 *are the principal stresses and* σ_r *is a known uniaxial strength of material.*

Assuming body rupture means rupture of at least one of its points, the (initial) local strength condition for the whole body is then

$$\sup_{y \in \Omega} \Lambda\left(\sigma(y), y\right) < 1. \tag{2.1}$$

Such local strength condition, however, is generally not applicable to unbounded stress fields since the conditions will predict fracture under virtually any singular stress field.

For more general, especially singular stress fields, e.g. belonging to $L_2(\Omega)$, a (point) non-local strength condition $\Lambda^{\odot}(\sigma; y) < 1$ can be applied. Here $\Lambda^{\odot}(\sigma; y)$ is a normalised equivalent stress functional, which is defined on the tensor-functions $\sigma_{ij} \in L_2(\Omega)$ and is non-negative positively homogeneous of the order $+1$ w.r.t. σ, see [5].

Particularly for some materials $\Lambda^{\odot}$ can be related with a weighted averaging of $\sigma_{ij}(x)$, $x \in \Omega$ along some neighbourhood of the point y,

$$\Lambda^{\odot}(\sigma; y) := \Lambda\left(\sigma^{\odot}(y), y\right), \quad \sigma_{ij}^{\odot}(y) := \int_{\Omega} w_{ijkl}(y, x)\sigma_{kl}(x)dx, \tag{2.2}$$

where $\sigma_{ij}^{\odot} \in C(\bar{\Omega})$ is an auxiliary *non-local* stress tensor, and the weight $w \in C(\bar{\Omega}, L^2(\Omega))$ is a material characteristics, such as $\int_{\Omega} w_{ijkl}(y, x) dx = \delta_{ij}\delta_{kl}$. Then the non-local strength condition for the whole body is

$$\sup_{y \in \Omega} \Lambda\left(\sigma^{\odot}, y\right) < 1.$$

Example 2. *(i) If $w_{ijkl}(y, x) = \delta_{ij}\delta_{kl} \begin{cases} \frac{3}{4\pi d^3}, & |x - y| < d \\ 0, & |x - y| \geq d \end{cases}$ for 3D, where d is a material constant, then $\sigma_{ij}^{\odot}(y) = \frac{3}{4\pi d^3} \int_{|x-y|<d} \sigma_{ij}(x) dx$.*
(ii) If $w_{ijkl}(y, x) = \delta(x - y)\delta_{ij}\delta_{kl}$, where $\delta(x - y)$ is the Dirac function, then $\sigma_{ij}^{\odot}(y) = \sigma_{ij}(y)$, and the non-local strength-condition coincides with the local one.

3.   ELEMENTS OF FATIGUE DURABILITY ANALYSIS

Pure fatigue under cyclic loading is characterised by dependence of the durability on the loading history considered as a sequence of loading events but not on time or rate of loading. Then the cycle number n can be considered as a a discrete or continuous time-like parameter, more relevant to fatigue than the natural continuous time t. The Wöhler S–N durability diagram (Wöhler function) for a material under an uniaxial regular periodic cycling with constant stress range $\Delta\sigma = \sigma_{max} - \sigma_{min}$ and mean stress $\sigma_m = (\sigma_{max} + \sigma_{min})/2$, is a dependence of the critical number of cycles $n^*(\Delta\sigma, \sigma_m)$ to rapture, e.g. on $\Delta\sigma$. For a multiaxial in-phase periodic cycling, we consider $\Delta\sigma = \Delta\sigma_{ij}$ and $\sigma_m = \sigma_{mij}$ $(i, j = 1, 2, 3)$ as tensors. For simplicity, suppose further that $\sigma_{mij} = 0$ and $1/n^*(\Delta\sigma)$ is a continuous function. The approach discussed below works also for $\sigma_{mij} \neq 0$ under in-phase cycling if one considers $1/n^*(\Delta\sigma, \sigma_m)$ as a continuous function of the two tensor variables, and the corresponding conditions on σ_m as a function of coordinate and scaling parameter have to be applied as well.

If the material fatigue properties and/or stress field vary with the coordinate, one can write for a body Ω an (initial) durability condition under *periodic* cycling loading as

$$n < \inf_{y \in \Omega} n^*(\Delta\sigma(y), y), \tag{3.1}$$

where $n^*(\Delta\sigma(y), y)$ is the Wöhler diagram for a homogeneous material with the fatigue properties as at the point y, under the periodic cycling $\Delta\sigma_{ij}$ homogeneous in space coordinates.

Let us consider now a loading process with *varying* cycle parameters such that closed loops can be always identified but may be different. Let

$m = 1, 2, ...$ be a number of a closed loop with the stress range $\Delta\sigma_{ij}(m, y)$ in the loading history $\{\sigma(\cdot, y)\} = \{\sigma(m, y)\}_{m=1}^n$ at the point y. Let $n^*(\Delta\sigma, y)$ be the Wöhler function for the material of the point y. The Palmgren-Miner linear damage accumulation rule gives the durability condition for a cycle n in the form

$$\omega^N(\{\sigma(\cdot, y)\}; n, y) := \sum_{m=1}^n \frac{1}{n^*[\Delta\sigma(m, y), y]} < 1. \qquad (3.2)$$

where $\omega^N(\{\sigma(\cdot, y)\}; n, y)$ is called fatigue damage measure.

The corresponding body durability condition has the the form

$$\sup_{y \in \Omega} \omega^N(\{\sigma(\cdot, y)\}; n, y) < 1. \qquad (3.3)$$

Local fatigue durability condition (3.1) is generally not applicable to singular stress fields. For more general classes of stress fields, e.g. $L_2(\Omega)$, a non-local fatigue durability condition can be applied. For example, for the periodic cycling we can take

$$n < \inf_{y \in \Omega} n^{*\odot}(\Delta\sigma; y), \quad n^{*\odot}(\Delta\sigma; y) := n^*(\Delta\sigma^\odot(y), y), \qquad (3.4)$$

$$\Delta\sigma_{ij}^\odot(y) := \int_\Omega w_{ijkl}(y, x)\Delta\sigma_{kl}(x)dx \qquad (3.5)$$

where $w(y, x)$ is as above. For the non-periodic cycling, one can replace $\Delta\sigma(n, y)$ by $\Delta\sigma^\odot(n, y)$ in the linear damage accumulation rule (3.2).

4. ELEMENTS OF ASYMPTOTIC HOMOGENISATION

A boundary value problem of elasticity for a composite solid Ω having an $\varepsilon Y-$periodic structure, that is a large number of periodically distributed inclusions or pores with a scaling parameter ε, is presented by displacement $u_i^\varepsilon \in H^1(\Omega)$ and stress $\sigma_{ij}^\varepsilon \in L^2(\Omega)$ fields for each $\varepsilon > 0$. According to [6, 1, 3], the homogenised displacement and stress fields, $u_i^0 \in H^1(\Omega)$, $\hat\sigma_{ij} \in L^2(\Omega)$, present a solution to a uniquely solvable homogenised problem of elasticity in the domain Ω.

It is known [1, 3] that $\sigma_{ij}^\varepsilon \in L^2(\Omega)$ contains a subsequence, which two-scale converges to a function $\sigma^0 \in L^2(\Omega \times Y)$, that is,

$$\lim_{\varepsilon \to 0} |\int_\Omega \psi(x, \frac{x}{\varepsilon})\sigma_{ij}^\varepsilon(x)dx - \frac{1}{|Y|}\int_\Omega \int_Y \psi(x, \xi)\sigma_{ij}^0(x, \xi)dxd\xi| = 0, \qquad (4.1)$$

for any $\psi \in L^2(\Omega, C_{per}(Y))$. Furthermore,

$$\sigma_{ij}^0(x, \xi) = A_{ijkl}(\xi)\hat\sigma_{kl}(x), \qquad (4.2)$$

where $A_{ihjk}(\xi)$ is the stress concentration tensor [6, Chap.9, Sec.4], obtained after solution of an auxiliary periodic problem of elasticity and such that $\frac{1}{Y}\int_Y A_{ijkl}(\xi)d\xi = \delta_{ij}\delta_{kl}$.

5. HOMOGENISATION OF LOCAL STRENGTH AND DURABILITY CONDITIONS

In a periodic medium, all becomes dependent on the scaling parameter ε. Strength condition (2.1) and fatigue durability condition (3.1) become

$$\sup_{y\in\Omega}\Lambda^\varepsilon(\sigma^\varepsilon,y) < 1, \quad n < \inf_{y\in\Omega}n^{*\varepsilon}(\Delta\sigma^\varepsilon,y). \tag{5.1}$$

Suppose,

$$\Lambda^\varepsilon(\sigma^\varepsilon,y) := \Lambda(\sigma^\varepsilon,\frac{y}{\varepsilon}), \quad n^{*\varepsilon}(\Delta\sigma^\varepsilon,y) := n^*(\Delta\sigma^\varepsilon,\frac{y}{\varepsilon}). \tag{5.2}$$

Our aim is to derive macro-strength and macro-durability conditions like (2.1), (3.1) and (3.2)–(3.3), where the homogenised strength $\hat{\Lambda}$ function, Wöhler function $\hat{n}^*$, and damage measure $\hat{\omega}^N$ are functions of the homogenised stress $\hat{\sigma}_{ih}(x)$ and the composite micro-characteristics only. Let the notation $|\sigma|$ for a tensor σ_{ij} mean a matrix norm.

Proposition 1. (homogenisation of local normalised equivalent strength function) *Let a tensor function sequence $\sigma^\varepsilon(y) \in C(\bar{\Omega})$ converge to a tensor function $\sigma^0(y,\zeta) \in C(\bar{\Omega}, C_{per}(Y))$ uniformly w.r.t. y as $\varepsilon \to 0$, i.e.,*

$$\lim_{\varepsilon\to 0}\sup_{y\in\Omega}|\sigma^\varepsilon(y) - \sigma^0(y,\frac{y}{\varepsilon})| = 0 \tag{5.3}$$

and $\Lambda \in C(\mathbb{R}^{n\times n}, \mathcal{M}_{per}(Y))$. Then,

$$\lim_{\varepsilon\to 0}\sup_{y\in\Omega}\left|\Lambda\left(\sigma^\varepsilon(y),\frac{y}{\varepsilon}\right) - \Lambda\left(\sigma^0(y,\frac{y}{\varepsilon}),\frac{y}{\varepsilon}\right)\right| = 0 \tag{5.4}$$

If σ^0 is expressed by (4.2), then

$$\lim_{\varepsilon\to 0}\sup_{y\in\Omega}\Lambda\left(\sigma^\varepsilon(y),\frac{y}{\varepsilon}\right) \le \sup_{y\in\Omega}\hat{\Lambda}(\hat{\sigma}(y)), \ \ \hat{\Lambda}(\hat{\sigma}(y)) := \sup_{\zeta\in Y}\Lambda(A_{ijkl}(\zeta)\hat{\sigma}_{kl}(y),\zeta).$$

and the limit sufficient local macro-strength condition is $\sup_{y\in\Omega}\hat{\Lambda}(\hat{\sigma}(y)) < 1$.

<u>Proof:</u>
$$\sup_{y\in\Omega}\left|\Lambda\left(\sigma^\varepsilon(y),\frac{y}{\varepsilon}\right) - \Lambda\left(\sigma^0(y,\frac{y}{\varepsilon}),\frac{y}{\varepsilon}\right)\right| \le$$
$$\sup_{y\in\Omega}\sup_{\zeta\in Y}\left|\Lambda\left(\sigma^\varepsilon(y),\zeta\right) - \Lambda\left(\sigma^0(y,\frac{y}{\varepsilon}),\zeta\right)\right|. \tag{5.5}$$

Let us take any $\delta_1 > 0$. Belonging $\Lambda(\sigma, \zeta)$ to $C(\mathbb{R}^{n \times n}, \mathcal{M}_{per}(Y))$ implies that for any constant $C_1 > 0$ there exists $\delta_2 > 0$ such that $\sup_{\zeta \in Y} |\Lambda(\sigma', \zeta) - \Lambda(\sigma'', \zeta)| < \delta_1$ for any tensors σ', σ'' such that $|\sigma'|, |\sigma''| \leq C_1$ and $|\sigma' - \sigma''| < \delta_2$. Due to (5.3) and belonging $\sigma^0(y, \zeta)$ to $C(\bar{\Omega}, C_{per}(Y))$, one can choose such $\tilde{\varepsilon} > 0$ that $|\sigma^0(y, \zeta)|, |\sigma^\varepsilon(y)| \leq C_1$ for some $C_1 > 0$ for any $\varepsilon < \tilde{\varepsilon}$, $y \in \bar{\Omega}$ and $\zeta \in \bar{Y}$. Let us take $\tilde{\varepsilon} > 0$ even smaller such that $|\sigma^\varepsilon(y) - \sigma^0(y, \frac{y}{\varepsilon})| < \delta_2$ due to (5.3). Thus, $\sup_{\zeta \in Y} |\Lambda(\sigma^\varepsilon(y), \zeta) - \Lambda(\sigma^0(y, \frac{y}{\varepsilon}), \zeta)| < \delta_1$. This implies the convergence of the right hand side of (5.5) to zero as $\varepsilon \to 0$, that proves (5.4).

The rest of the proposition follows from (5.4), (4.2) and (5.1). ■

Note that although the hypotheses of Proposition 1 are satisfied for not any two-scale converging tensor function sequence $\sigma^\varepsilon(y) \in L^2(\Omega)$ appearing in the elastic composite analysis, the range of their validity is not empty. A trivial example is an infinite periodic composite with smooth inclusions, under a uniform load at infinity: then $\sigma^\eta(y)$ and $\sigma^0(y, y/\eta)$ simply coincide. Moreover, the hypotheses of Proposition 1 are always satisfied for the *non-local* counterpart of any two-scale converging tensor sequence, see Proposition 7 below.

Let us denote $n^{*-1}(\Delta\sigma, y) := 1/n^*(\Delta\sigma, y)$. Similarly to Proposition 1, we have

Proposition 2. (homogenisation of local fatigue durability diagram) *Let a periodic stress cycling have a tensor range sequence $\Delta\sigma^\varepsilon(y) \in C(\bar{\Omega})$, which converges to a tensor function $\Delta\sigma^0(y, \zeta)$ from $C(\bar{\Omega}, C_{per}(Y))$ uniformly w.r.t. y as $\varepsilon \to 0$ i.e.,*

$$\lim_{\varepsilon \to 0} \sup_{y \in \Omega} |\Delta\sigma^\varepsilon(y) - \Delta\sigma^0(y, \frac{y}{\varepsilon})| = 0.$$

Let $n^*(\Delta\sigma, \frac{y}{\varepsilon})$ be a durability diagram such that

$$n^{*-1} \in C(\mathbb{R}^{n \times n}, \mathcal{M}_{per}(Y))$$

.

$$Then \lim_{\varepsilon \to 0} \sup_{y \in \Omega} \left| n^{*-1}\left(\Delta\sigma^\varepsilon(y), \frac{y}{\varepsilon}\right) - n^{*-1}\left(\Delta\sigma^0(y, \frac{y}{\varepsilon}), \frac{y}{\varepsilon}\right) \right| = 0. \quad (5.6)$$

If σ^0 is expressed by (4.2), then

$$\lim_{\varepsilon \to 0} \inf_{y \in \Omega} n^*\left(\Delta\sigma^\varepsilon(y), \frac{y}{\varepsilon}\right) \geq \inf_{y \in \Omega} \hat{n}^*(\Delta\hat{\sigma}(y)),$$

$$where \quad \hat{n}^*(\Delta\hat{\sigma}(y)) := \inf_{\zeta \in Y} n^*(A_{ijkl}(\zeta)\Delta\hat{\sigma}_{kl}(y), \zeta)$$

and the limit sufficient local fatigue macro-durability condition under periodic cycling loading is $n < \inf_{y \in \Omega} \hat{n}^*(\hat{\sigma}(y))$.

Using Propositions 2 and the linear accumulation rule (3.2), (3.3), we can write the limiting expression for the Palmgren-Miner fatigue damage measure and the durability condition under *varying* cyclic loading.

Proposition 3. (homogenisation of local fatigue damage measure and durability condition) *Let a stress cycling have a range $\Delta\sigma^\varepsilon(m, y)$ from $C(\bar{\Omega})$, which converges to a tensor function $\Delta\sigma^0(m, y, \zeta)$ from $C(\bar{\Omega}, C_{per}(Y))$ uniformly w.r.t. y for each cycle number m, as $\varepsilon \to 0$, i.e.,*

$$\lim_{\varepsilon\to 0} \sup_{y\in\Omega} |\Delta\sigma^\varepsilon(m, y) - \Delta\sigma^0(m, y, \frac{y}{\varepsilon})| = 0$$

for any m. Let $n^*(\Delta\sigma, \frac{y}{\varepsilon})$ be a durability diagram such that

$$n^{*-1} \in C(\mathbb{R}^{n\times n}, \mathcal{M}_{per}(Y))$$

. Let

$$\omega^N(\{\sigma^\varepsilon(\cdot, y)\}; n, \frac{y}{\varepsilon}) = \sum_{m=1}^{n} n^{*-1}\left(\Delta\sigma^\varepsilon(m, y), \frac{y}{\varepsilon}\right)$$

. Then

$$\lim_{\varepsilon\to 0} \sup_{y\in\Omega} \left| \omega^N\left(\{\sigma^\varepsilon(\cdot, y)\}; n, \frac{y}{\varepsilon}\right) - \omega^N\left(\{\sigma^0(\cdot, y, \frac{y}{\varepsilon})\}; n, \frac{y}{\varepsilon}\right) \right| = 0, \qquad (5.7)$$

If σ^0 is expressed by (4.2), then

$$\lim_{\varepsilon\to 0} \sup_{y\in\Omega} \omega^N\left(\{\sigma^\varepsilon(\cdot, y)\}; n, \frac{y}{\varepsilon}\right) \le \sup_{y\in\Omega} \hat{\omega}^N(\{\hat{\sigma}(\cdot, y)\}; n), \qquad where$$

$$\hat{\omega}^N(\{\hat{\sigma}(\cdot, y)\}; n) := \sup_{\zeta\in Y} \omega^N\left(\{A_{ijkl}(\zeta)\hat{\sigma}_{kl}(\cdot, y)\}; n, \zeta\right) =$$

$$\sup_{\zeta\in Y} \sum_{m=1}^{n} \frac{1}{n^*\left(A_{ijkl}(\zeta)\Delta\hat{\sigma}_{kl}(m, y), \zeta\right)} \le \sum_{m=1}^{n} \frac{1}{\hat{n}^*(\Delta\hat{\sigma}(m, y))} \qquad (5.8)$$

and the limit sufficient local fatigue macro-durability condition under variable cyclic loading is

$$\sup_{y\in\Omega} \hat{\omega}^N(\{\hat{\sigma}(\cdot, y)\}; n) < 1.$$

Proof: Using (5.6), we have

$$\lim_{\varepsilon\to 0} \sup_{y\in\Omega} |\omega^N(\{\sigma^\varepsilon(\cdot, y)\}; n, y) - \omega^N(\{\sigma^0(\cdot, y, \frac{y}{\varepsilon})\}; n, y)| \le$$

$$\sum_{m=1}^{n} \lim_{\varepsilon\to 0} \sup_{y\in\Omega} \left| n^{*-1}\left(\Delta\sigma^\varepsilon(m, y), \frac{y}{\varepsilon}\right) - n^{*-1}\left(\Delta\sigma^0(m, y,), \frac{y}{\varepsilon}\right) \right| = 0.$$

This proves (5.7), and the rest of the proposition does directly follow. ■

Note that according to (5.8), the limit composite damage measure is generally not expressed but only estimated by the damage measure based on the limit composite durability diagram.

6. HOMOGENISATION OF NON-LOCAL STRENGTH AND DURABILITY CONDITIONS

Let us consider for a periodic medium the limits of *non-local* micro–strength and micro–durability conditions $\sup_{y\in\Omega} \Lambda^{\odot\varepsilon}(\sigma^\varepsilon; y) < 1, \quad n < \inf_{y\in\Omega} n^{*\odot\varepsilon}(\Delta\sigma^\varepsilon; y)$ as $\varepsilon \to 0$. Representations (2.2), (3.4) become

$$\Lambda^{\odot\varepsilon}(\sigma^\varepsilon; y) := \Lambda^\varepsilon\left(\sigma^{\odot\varepsilon}(y), y\right), \quad n^{*\odot\varepsilon}(\Delta\sigma^\varepsilon; y) := n^{*\varepsilon}\left(\Delta\sigma^{\odot\varepsilon}(y), y\right),$$

$$\sigma_{ij}^{\odot\varepsilon}(y) := \int_\Omega w_{ijkl}^\varepsilon(y,x)\sigma_{kl}^\varepsilon(x)dx, \quad y \in \Omega.$$

Suppose the functions Λ^ε and $n^{*\varepsilon}$ have form (5.2). Let further $w_{ijkl}^\varepsilon(y,x) := w_{ijkl}(y,\frac{y}{\varepsilon},x,\frac{x}{\varepsilon})$. Then

$$\Lambda^\varepsilon(\sigma^{\odot\varepsilon},y) = \Lambda(\sigma^{\odot\varepsilon}(y),\frac{y}{\varepsilon}), \quad n^{*\varepsilon}(\Delta\sigma^{\odot\varepsilon},y) = n^*(\Delta\sigma^{\odot\varepsilon}(y),\frac{y}{\varepsilon}),$$

$$\sigma_{ij}^{\odot\varepsilon}(y) = \int_\Omega w_{ijkl}(y,\frac{y}{\varepsilon},x,\frac{x}{\varepsilon})\sigma_{kl}^\varepsilon(x)dx, \qquad (6.1)$$

Lemma 1. *Let $\sigma^\varepsilon \in L^2(\Omega)$ be a sequence of tensor functions $\sigma^\varepsilon(x)$ two–scale converging to a tensor $\sigma^0 \in L^2(\Omega \times Y)$ as $\varepsilon \to 0$. Let $w \in C(\bar\Omega, C_{per}(Y, L^2(\Omega, C_{per}(Y))))$. Then the sequence*

$$\tilde\sigma^{\odot\varepsilon}(y,\zeta) := \int_\Omega w(y,\zeta,x,\frac{x}{\varepsilon})\sigma^\varepsilon(x)dx, \qquad (6.2)$$

is bounded in $C(\bar\Omega, C_{per}(Y))$ and does strongly converge in this space to

$$\sigma^{\odot 0}(y,\zeta) = \frac{1}{|Y|}\int_\Omega\int_Y w(y,\zeta,x,\xi)\sigma^0(x,\xi)d\xi dx. \qquad (6.3)$$

Proof: Since the sequence $\sigma^\varepsilon \in L^2(\Omega)$ two-scale converges, it converges also weakly and, consequently is bounded in $L^2(\Omega)$, that is, $\|\sigma^\varepsilon\|_{L^2(\Omega)} < C < \infty$.

The periodicity in ζ is evident for the both functions $\tilde\sigma^{\odot\varepsilon}(y,\zeta)$ and $\sigma^{\odot 0}(y,\zeta)$, and it is sufficient to prove the proposition in the space $C(\bar\Omega\times\bar Y)$.

From (6.2) we have,

$$\sup_{y\in\bar{\Omega}}\sup_{\zeta\in\bar{Y}}|\tilde{\sigma}^{\odot\varepsilon}(y,\zeta)| \leq \sup_{y\in\bar{\Omega}}\sup_{\zeta\in\bar{Y}}\left[\int_{\Omega}\left|w(y,\zeta,x,\frac{x}{\varepsilon})\right|^2 dx\right]^{\frac{1}{2}}\|\sigma^{\varepsilon}\|_{L^2(\bar{\Omega})} \leq$$

$$\sup_{y\in\bar{\Omega}}\sup_{\zeta\in\bar{Y}}\left[\int_{\Omega}\sup_{\xi\in Y}|w(y,\zeta,x,\xi)|^2 dx\right]^{\frac{1}{2}} C = \|w\|_{C(\bar{\Omega},C_{per}(Y,L^2(\Omega,C_{per}(Y))))}C.$$

That is, the sequence $\tilde{\sigma}^{\odot\varepsilon}(y,\zeta)$ is equi-bounded in $C(\bar{\Omega}\times\bar{Y})$. Let us check the continuity,

$$|\tilde{\sigma}^{\odot\varepsilon}(y_1,\zeta_1) - \tilde{\sigma}^{\odot\varepsilon}(y_2,\zeta_2)| =$$

$$\left|\int_{\Omega}\left[w(y_1,\zeta_1,x,\frac{x}{\varepsilon}) - w(y_2,\zeta_2,x,\frac{x}{\varepsilon})\right]\sigma^{\varepsilon}(x)dx\right| \leq$$

$$\left[\int_{\Omega}\sup_{\xi\in Y}|w(y_1,\zeta_1,x,\xi) - w(y_2,\zeta_2,x,\xi)|^2 dx\right]^{\frac{1}{2}}\|\sigma^{\varepsilon}\|_{L^2(\bar{\Omega})} =$$

$$\|w(y_1,\zeta_1,\cdot,\cdot) - w(y_2,\zeta_2,\cdot,\cdot)\|_{L^2(\Omega,C_{per}(Y))}C.$$

The term $\|w(y_1,\zeta_1,\cdot,\cdot) - w(y_2,\zeta_2,\cdot,\cdot)\|_{L^2(\Omega,C_{per}(Y))}$ tends to zero as $\sqrt{|y_1 - y_2|^2 + |\zeta_1 - \zeta_2|^2} \to 0$ uniformly w.r.t. $\{y_i,\zeta_i\} \in \bar{\Omega}\times\bar{Y}$, $i = 1, 2$, since $w \in C(\bar{\Omega}, C_{per}(Y, L^2(\Omega, C_{per}(Y))))$. Thus, the sequence $\tilde{\sigma}^{\odot\varepsilon}(y,\zeta)$ does not only belong to $C(\bar{\Omega}\times\bar{Y})$ but is also equi-bounded and equi-continuous. From the Ascoli-Arzelá theorem, the sequence is then compact in $C(\bar{\Omega}\times\bar{Y})$.

On the other hand, as follows from the two-scale convergence of σ^{ε}, the sequence $\tilde{\sigma}^{\odot\varepsilon}(y,\zeta)$ converges point-wise to $\sigma^{\odot 0}(y,\zeta)$ for any $\{y,\zeta\} \in \bar{\Omega}\times\bar{Y}$. Since the sequence is also equi-bounded, this means it converges to $\sigma^{\odot 0}(y,\zeta)$ weakly in $C(\bar{\Omega}\times\bar{Y})$ (see, e.g., [4]). However, each compact and weakly converging sequence in a Banach space converges also strongly (see, e.g., [7, Section 20.2]). This proves the lemma. ∎

Proposition 4. *Let* $\sigma^{\varepsilon} \in L^2(\Omega)$ *be a sequence of tensor functions* $\sigma^{\varepsilon}(x)$ *two–scale converging to a tensor* $\sigma^0 \in L^2(\Omega \times Y)$. *Suppose,* $w \in C(\bar{\Omega}, C_{per}(Y, L^2(\Omega, C_{per}(Y))))$. *Then the sequence* $\sigma^{\odot\varepsilon}(y)$ *given by (6.1) is bounded in* $C(\bar{\Omega})$ *and does converge to the tensor function* $\sigma^{\odot 0}(y, \frac{y}{\varepsilon})$, *given by (6.3), uniformly w.r.t.* y *as* $\varepsilon \to 0$, *i.e.,*

$$\lim_{\varepsilon\to 0}\sup_{y\in\bar{\Omega}}\left|\sigma^{\odot\varepsilon}(y) - \sigma^{\odot 0}(y,\frac{y}{\varepsilon})\right| = 0.$$

<u>Proof:</u> Let us note that $\sigma^{\odot\varepsilon}(y) = \tilde{\sigma}^{\odot\varepsilon}(y,\frac{y}{\varepsilon})$, where the sequence $\tilde{\sigma}^{\odot\varepsilon}$ is given by (6.2) and belongs to and is equi-bounded in $C(\bar{\Omega}, C_{per}(Y))$

according to Lemma 1. This implies the sequence $\sigma^{\odot\varepsilon}(y)$ belongs to and is equi-bounded in $C(\bar{\Omega})$. Then, owing to Proposition 1,
$\sup_{y\in\bar{\Omega}}\left|\sigma^{\odot\varepsilon}(y) - \sigma^{\odot 0}(y,\frac{y}{\varepsilon})\right| = \sup_{y\in\bar{\Omega}}\left|\tilde{\sigma}^{\odot\varepsilon}(y,\frac{y}{\varepsilon}) - \sigma^{\odot 0}(y,\frac{y}{\varepsilon})\right| \le$
$\sup_{y\in\bar{\Omega}}\sup_{\zeta\in\bar{Y}}\left|\tilde{\sigma}^{\odot\varepsilon}(y,\zeta) - \sigma^{\odot 0}(y,\zeta)\right| \to 0.$ ∎

Applying Proposition 1 to the non-local stresses (6.3) and taking into account their convergence proved in Proposition 4, we arrive at the following proposition on homogenisation of non-local strength conditions.

Proposition 5. *Let $\sigma^\varepsilon \in L^2(\Omega)$ be a sequence of tensor functions two–scale converging to a tensor $\sigma^0 \in L^2(\Omega \times Y)$. Suppose the non-local stress $\sigma^{\odot\varepsilon}(y)$ is given by (6.1) with the weight $w \in C(\bar{\Omega}, C_{per}(Y, L^2(\Omega, C_{per}(Y))))$. Suppose $\Lambda \in C(\mathbb{R}^{n\times n}, \mathcal{M}_{per}(Y))$. Then*

$$\lim_{\varepsilon\to 0}\sup_{y\in\Omega}\left|\Lambda\left(\sigma^{\odot\varepsilon}(y),\frac{y}{\varepsilon}\right) - \Lambda\left(\sigma^{\odot 0}(y,\frac{y}{\varepsilon}),\frac{y}{\varepsilon}\right)\right| = 0,$$

where $\sigma^{\odot 0}(y,\zeta)$ is given by (6.3). If σ^0 is expressed by (4.2), then

$$\lim_{\varepsilon\to 0}\sup_{y\in\Omega}\Lambda\left(\sigma^{\odot\varepsilon}(y),\frac{y}{\varepsilon}\right) \le \sup_{y\in\Omega}\hat{\Lambda}^{\odot}(\hat{\sigma};y),$$

$$\text{where}\quad \hat{\Lambda}^{\odot}(\hat{\sigma};y) := \sup_{\zeta\in Y}\Lambda\left(\int_{\Omega}\hat{w}_{ijkl}(y,\zeta,x)\hat{\sigma}_{kl}(x)dx,\zeta\right),$$

$$\hat{w}_{ijkl}(y,\zeta,x) = \frac{1}{|Y|}\int_{Y} w_{ijpq}(y,\zeta,x,\xi)A_{pqkl}(\xi)d\xi.$$

Finally the limit sufficient non-local macro-strength condition is
$\sup_{y\in\Omega}\hat{\Lambda}^{\odot}(\hat{\sigma};y) < 1.$

Changing the notations, we obtain a similar proposition on homogenisation of non-local fatigue durability diagram n^* and then of the fatigue damage measure ω.

The approach developed in the paper is based on the two-scale convergence for stresses (4.1) following from [1], see also [3], for the linear elasticity. It will also work for more complex material behaviour, e.g. plasticity or small-cyclic fatigue if the convergence (4.1) holds true for such cases.

Acknowledgments

References

[1] Allaire, G (1992) *Homogenisation and Two-Scale Convergence*, SIAM J. Math. Anal., **23** , 1482-1518.

[2] Bakhvalov, N and Panasenko, G (1984) *Homogenisation: Averaging Processes in Periodic Media. Mathematical Problems in the Mechanics of Composite Materials*, Dordrecht-Boston-London:Kluwer.

[3] Cioranescu, D and Donato, P (1999) *An Introduction to Homogenization.* New York: Oxford University Press.

[4] Kolmogorov, A N and Fomin, S B (1957) *Elements of the theory of functions and functional analysis.* Rochester, N.Y.: Graylock Press.

[5] Mikhailov, S E (1995) *A Functional Approach to Non-local Strength Conditions and Fracture Criteria: I. Body and Point Fracture*, Eng. Fract. Mech., **52**, 731-743.

[6] Pobedrya, B E (1984) *Mechanics of Composite Materials*, Moscow State University Publishing.

[7] Trenogin, V A (1980) *Functional Analysis*, Moscow: Nauka.

Chapter 7
Models associated with elastic plates, shells, rods and thin-walled composite structures

ON A KIND OF SINGULAR PERTURBATIONS FOR TRANSMISSION PROBLEMS

E. Sanchez-Palencia

L.M.M. - CNRS UMR 7607, Université Pierre et Marie Curie

4 place Jussieu - 75252 PARIS CEDEX 05, France

sanchez@lmm.jussieu.fr

Keywords: Partial differential equations, singular perturbations, unbounded energy, transmission problems.

Abstract   We consider a kind of variational singular perturbation problems with piecewise constant coefficients and unbounded energy. The method of matched asymptotic expansions allows us to give a rigorous proof of the asymptotic behaviour (leading order term) in two examples with elliptic and parabolic limit, respectively.

1. Introduction

We consider a kind of singular perturbation problems inspired by thin shell theory.

Let V be a (real) Hilbert space, a and b two symmetric positive and continuous bilinear forms on V. Moreover $a + b$ is coercive on V, but a in general is not (b may also not be coercive). We then consider the family of variational problems with small parameter ε :

Find $u^\varepsilon \in V$ such that $\forall w \in V$:

$$a(u^\varepsilon, w) + \varepsilon^2 b(u^\varepsilon, w) = \langle f, w \rangle \tag{1}$$

The left hand side is coercive on V with coerciveness constant $O(\varepsilon^2)$ which vanishes as ε tends to zero. Under the hypothesis

$$a(w, w) = 0 \implies w = 0 \tag{2}$$

the form a is the square of a norm on V, and we may construct the "limit problem".

Find $u \in V_a$ such that $\forall w \in V_a$

$$a(u, w) = \langle f, w \rangle \tag{3}$$

where V_a is the completion of V with the norm $a^{1/2}$. Obviously $V_a \supset V$ and the duals satisfy $V_a' \subset V'$. The problems (1) and (3) make sense for $f \in V'$ and $f \in V_a'$ respectively. It is then classical (see for instance [4]) that when both conditions are satisfied u^ε converges to u in the strong topology of V_a. Otherwise, if $f \in V'$ but $f \notin V_a'$, the limit problem does not make sense as a variational problem ; in that case it may either make sense in another framework or not make sense at all. It is then easily seen that the energy of the solution of (1) tends to infinity so that classical a priori estimates are of no use. It appears in specific examples that the energy of u^ε concentrates in certain regions. The way to study the asymptotic behaviour of u^ε is the method of matched asymptotic expansions (see for instance [1]) involving a change of variables $x \to y$ which implies a dilatation of the singular region. This process changes the asymptotic expression of the energy which, in the appropriate spaces, remains bounded, then, standard a priori estimates allow us to prove convergence.

The objective of this paper is to show some examples of transmission problems (involving piecewise constant coefficients) where the limit problem (3) does not make sense at all for singular loadings. Hence, no convergence holds in the x variable. Energy concentrates along the segment $x_2 = 0$ and the alternative description in the y variable and a scaling of u^ε allows us to establish rigorously the leading order of the asymptotic behaviour. It should be pointed out that in the first example (section 3) the limit problem is elliptic (independently of the fact that it does not make sense for certain f) and the asymptotic description involves a differential equation with respect to the variable normal to the singular curve, whereas the tangential variable is a parameter. Moreover the topology of this limit discards additive functions of the tangential variable. The corresponding indeterminacy of the limit is connected with lower order (non singular) terms which match with the outer region. Oppositely, in the example of section 4, the limit problem is parabolic and both variables are involved in the description of the asymptotic behaviour, accounting for propagation of singularities along the characteristics.

2. Remarks on a simple transmission problem

Let us consider in the interval $I = (-1, +1)$

$$-\partial[\alpha(x)\partial u] = f \quad \text{for } x \in I \tag{4}$$

$$(\pm 1) = 0 \tag{5}$$

where $a(x)$ denotes the piecewise constant function

$$\alpha(x) = \begin{cases} \alpha_+ \text{ for } x > 0 \\ \alpha_- \text{ for } x < 0 \end{cases} \tag{6}$$

and $\alpha_\pm$ are strictly positive constants.

Classically for $f \in H^{-1}(I)$ this is a variational problem in $H_0^1(I)$. Moreover, if f is sufficiently smooth, for instance $f \in H^s(I)$, $s > -1/2$, it is immediately seen that $-a\partial u$ is a primitive of f and then a continuous function ; u is of class H^{s+2} for $x > 0$ and $x < 0$ and u satisfies the transmission conditions :

$$[\![u]\!] = 0, \tag{7}$$

$$[\![\alpha\partial u]\!] = 0 \tag{8}$$

where $[\![\ ]\!]$ denotes the jump at $x = 0$. This is the usual definition of the transmission problem.

For $f \in H^{-1}(I)$ a unique solution $u \in H_0^1(I)$ exists and (4) make sense in distribution theory (whereas (8) is not satisfied in general). In particular, denoting by $F \in L^2(I)$ a primitive of f we have

$$\alpha\partial u = -F + C, \tag{9}$$

$$\partial u = \alpha^{-1}(-F + C). \tag{10}$$

This situation changes for more singular f. For instance, if $f = \delta_0'$ (where δ_λ denotes the Dirac mass at $x = \lambda$), it is clear that (4) does not make sense in distribution theory. Indeed, if it did, we would have

$$-\alpha\partial u = \delta_0 + C, \tag{11}$$

i.e., the block $\alpha\partial u$ is a distribution, but there is no distribution u solving (11) as the product of δ_0 by a function bearing a jump at the origin does not make sense. Nevertheless, in the case $\alpha_+ = \alpha_-$ this difficulty disappears, and (4), (5) with $f = \delta_0'$ has a solution $u \in H^s$, $s > 1/2$ (this is an elementary example of Lions-Magenes theory [5]).

Remark 2.1.   The very reason of the impossibility of solving (4), (5) with $f = \delta_0'$ is that *"any definition of u should be very unstable"*. Indeed, let us replace δ_0' by δ_λ'. Taking $\lambda \neq 0$, (4) makes sense, and (10) becomes

$$\partial u = \alpha^{-1}(-\delta_\lambda + C), \tag{12}$$

so that u has at $x = \lambda$ a jump of intensity $-(\alpha_-)^{-1}$ or $-(\alpha_+)^{-1}$ for $\lambda < 0$ and $\lambda > 0$ respectively.∎

3. An example with elliptic limit

In this section we consider an example of the problem (1) which is elliptic (for $\varepsilon > 0$ as well as for $\varepsilon = 0$) in the domain

$$\Omega = (0, \pi) \times (-1, +1) . \tag{13}$$

410

The forms a and b are given by

$$a(u, w) = \int_\Omega \alpha(x_2)\partial_i u \partial_i w \; dx \tag{14}$$

$$b(u, w) = \int_\Omega \partial_{ij} u \partial_{ij} w \; dx \tag{15}$$

where $\alpha(x_2)$ is the function defined in (6) and standard summation convention of repeated indices is used. The energy space for $\varepsilon > 0$ is $V = H_0^2(\Omega)$, so that :

$$-\partial_i \left[\alpha(x_2)\partial_i u^\varepsilon \right] + \varepsilon^2 \Delta^2 u^\varepsilon = f \quad \text{in } \Omega \tag{16}$$

$$u^\varepsilon = \partial_n u^\varepsilon = 0 \quad \text{on } \partial\Omega \tag{17}$$

where $V_a = H_0^1(\Omega)$, and the limit problem is

$$-\partial_i \left[\alpha(x_2)\partial_i u \right] = f \quad \text{in } \Omega \tag{18}$$

$$u = 0 \quad \text{on } \partial\Omega . \tag{19}$$

We shall take

$$f = F(x_1)\delta'(x_2) \tag{20}$$

with $F \in L^2(0, \pi)$. Clearly, $f \in V' = H^{-2}$ but $f \notin V_a' = H^{-1}$. For reasons analogous to those of section 2, (18) with (20) does not make sense in distribution theory. Nevertheless, it is possible to write a "formal transmission condition" along $x_2 = 0$. Indeed, denoting

$$\alpha \, \mathrm{grad} \, u = \sigma = (\sigma_1, \sigma_2) \tag{21}$$

and assuming that the singularity is mainly concerned with the variable x_2, we have :

$$-\frac{\partial}{\partial x_2}\sigma_2 = F(x_1)\delta'(x_2) \tag{22}$$

or equivalently, the leading term of the singularity is the measure :

$$-\sigma_2 \simeq F(x_1)\delta(x_2) \tag{23}$$

In order to study the asymptotic behaviour of u^ε, we make the change

$$x_1 = y_1 \; , \quad x_2 = \varepsilon y_2 \; , \quad u^\varepsilon(x) = v^\varepsilon(y) \tag{24}$$

$$D_i = \partial/\partial y_i . \tag{25}$$

Then (1) becomes the new problem $\mathcal{P}_\varepsilon$:

$$\begin{cases} \text{Find } v^\varepsilon \in H_0^2(B_\varepsilon) \; , \; B_\varepsilon = (0, \pi) \times (-1/\varepsilon, 1/\varepsilon) \\ \text{such that } \forall w \in H_0^2(B_\varepsilon) \; : \\ a_0(v^\varepsilon, w) + \varepsilon^2 a_1(v^\varepsilon, w) + \varepsilon^4 a_2(v^\varepsilon, w) = \langle \Phi, w \rangle \end{cases} \tag{26}$$

where

$$\langle \Phi, w \rangle = -\int_0^\pi F(y_1) D_2 w(y_1, 0) dy_1 \tag{27}$$

$$\begin{cases} a_0(v, w) = \int_{B_\varepsilon} \alpha(y_2) D_2 v D_2 w dy + \int_{B_\varepsilon} D_2^2 v D_2^2 w dy \\ a_1(v, w) = \int_{B_\varepsilon} \alpha(y_2) D_1 v D_1 w dy + \int_{B_\varepsilon} 2 D_1 D_2 v D_1 D_2 w dy \\ a_2(v, w) = \int_{B_\varepsilon} D_1^2 v D_1^2 w dy \end{cases} \tag{28}$$

We observe that the "inner" formulation of the problem (see (26)) is somewhat analogous to the initial ("outer") one (see (1) with (14), (15), (20)) with some differences ; the domain of definition B_ε depends on ε and tends to the strip $B_0 = (0, \pi) \times \mathbb{R}y_2$ as ε tends to zero (but the functions v^ε may be extended with value 0 to B_0). Moreover, the "limit form" a_0 in (28) involves terms coming from a and b (see (14), (15)) so that the "boundedness of the energy" is a different concept in the outer and inner formulations. Moreover, the limit form a_0 is only concerned with $D_2 w$, not with w itself ; correspondingly, the functional (27) in the right hand side is also concerned with $D_2 w$.

Usual techniques (a priori estimates and weak compactness) allow us to prove the convergence of $D_2 v^\varepsilon$ to a well defined limit. Indeed :

Theorem 3.1. *Let v^ε be the solution of (26) and let $\hat{v}$ be defined as the solution of the Lax-Milgram problem :*

$$\begin{cases} \text{Find } \hat{v} \in \mathcal{V} \text{ such that } \forall w \in \mathcal{V} \\ \int_{B_0} (\alpha \hat{v} w + D_2 \hat{v} D_2 w) \, dy = -\int_0^\pi F(y_1) w(y_1, 0) dy_1 \end{cases} \tag{29}$$

where $\mathcal{V} = L^2\left((0, \pi); H^1(\mathbb{R}y_2)\right)$. Then

$$D_2 v^\varepsilon \longrightarrow \hat{v} \text{ strongly in } \mathcal{V} \tag{30}$$

Remark 3.1 We note that the convergence only takes place for the derivative $D_2 v^\varepsilon$; this amounts to a convergence *up to additive functions* of y_1. Equivalently, convergence may be stated in spaces of appropriate equivalence classes (see [7] for other problems in this context).∎

The explicit solution of the limit problem (29) is easily written, as it is in fact an ordinary differential equation in y_2 with parameter y_1 :

$$\hat{v}(y_1, y_2) = -F(y_1) \left[\alpha_+^{1/2} + \alpha_-^{1/2}\right]^{-1} \begin{cases} e^{-(\alpha_+)^{1/2} y_2} & \text{for } y_2 > 0 \\ e^{+(\alpha_-)^{1/2} y_2} & \text{for } y_2 < 0 \end{cases} \tag{31}$$

According to (30) and Remark 3.1, we also may write

$$v^\varepsilon \longrightarrow v \tag{32}$$

where v is any primitive in y_2 of $\hat{v}$ defined up to $+C(y_1)$; the convergence being of course that of (30). Because of the exponential decay of $\hat{v}$ for $|y_2| \to \infty$ in (31), the integral of $\alpha(y_2)D_2v(y_1, y_2)$ between $y_2 = -\infty$ and $= +\infty$ is easily computed:

$$\int_{-\infty}^{+\infty} \alpha(y_2)D_2v(y_1, y_2)dy_2 = -F(y_1) \tag{33}$$

which should be compared with (23). Indeed, after the dilatation $x_1 \longrightarrow y_2$ we have

$$\alpha(y_2)D_2v^\varepsilon(y_1, y_2)dy_2 = \sigma_2^\varepsilon(x_1, x_1)dx_2$$

where σ^ε is defined as in (21) but for the problem in ε. Consequently (33) shows that v describes explicitly the concentrated mass of (23).

Remark 3.2. We saw in section 2 that in this kind of problems, the limit equation in the variables x does not make sense. The limit process does not amount to solving that problem. In fact we perturbed it with the $\varepsilon^2 b$ terms and we considered the asymptotic behaviour of the corresponding perturbed solutions u^ε (after changing them in $v^\varepsilon(y)$). It is clear that this asymptotic behaviour does depend on the perturbation term, which is given by the physical (or other) definition of the problem, but this does not solve the limit problem, which does not make sense.■

4. A model problem for shell theory with parabolic limit

We consider again the domain Ω in (13) and the vector problem in the context of (1) with two unknowns $(u_1, u_2) = u$ defined by the bilinear forms

$$a(u, w) = \int_\Omega \alpha(x_2) [\gamma_1(u)\gamma_1(w) + \gamma_2(u)\gamma_2(w)] \, dx \tag{34}$$

$$b(u, w) = \int_\Omega \sum_{|\alpha|=2} (\partial_\alpha u_2)(\partial_\alpha w_2)dx \tag{35}$$

where $a(x_2)$ is again defined by (6) and

$$\gamma_1(w) = \partial_1 w_1 \; ; \; \gamma_2(w) = \partial_2 w_1 - w_2 \tag{36}$$

in the space $V = H_0^1(\Omega) \times H_0^2(\Omega)$, $V' = H^{-1} \times H^{-2}$. We shall take

$$\langle f, v \rangle = \int_0^\pi F(x_1)v_2(x_1, 0)dx_1 \tag{37}$$

with given $F \in L^2(0, \pi)$, or equivalently

$$f = (0, F(x_1)\delta(x_2)) . \tag{38}$$

The space V_a is not very easy to describe in an explicit way, but it is clear that w_2 appears in its norm without derivative, so that its trace is not defined. Then, obviously, $f \in V' \ f \notin V'_a$.

Remark 4.1. The system of equations for the limit problem ($\varepsilon = 0$) is

$$\begin{cases} -\partial_1 \left[\alpha\partial_1 u_1\right] - \partial_2 \left[\alpha(\partial_2 u_1 - u_2)\right] = f_1 \\ -\alpha(\partial_2 u_1 - u_2) = f_2 \end{cases} \tag{39}$$

or equivalently

$$\begin{cases} -\alpha(x_2)\partial_1^2 u_1(x_1, x_2) = f_1(x_1, x_2) - \partial_2 f_2(x_1, x_2) \\ \alpha(x_2)u_2(x_1, x_2) = \alpha(x_2)\partial_2 u_1(x_1, x_2) + f_2(x_1, x_2) \end{cases} \tag{40}$$

which is essentially the first equation of (40) for u_1 (and then an elliptic problem in x_2 with parameter x_1) and u_2 is then computed from the second equation (40). Obviously we have propagation of singularities along the characteristics $x_2 = const$, (note that the problem is parabolic in x_1, x_2). Nevertheless, the derivatives with respect to x_2 at the right hand side of (40) imply very strong singularities of the solution u along the characteristics. For instance, if f is given by (38) the right hand side of the first equation is singular as $\delta'(x_2)$, so that u_1 will also be so, and au_2 from the second equation (40) will be singular as $\delta''(x_2)$. Moreover when a is constant this gives u_2 itself singular as $\delta''(x_2)$. This situation is classical in shell theory (see [2], [3]). Moreover, when the function a is given by (6) the equation for u_2 does not make sense as in section 2.∎
In order to study the asymptotic behaviour of u^ε as ε tends to zero we make the change (inspired by the considerations in Remark 4.1) :

$$x_1 = y_1 , \quad x_2 = \eta y_2 ; \quad \eta = \varepsilon^{1/3} \tag{41}$$

$$u_1^\varepsilon(x) = \frac{1}{\eta^2} v_1^\eta(y) , \quad u_2^\varepsilon(x) = \frac{1}{\eta^3} v_2^\eta(y) \tag{42}$$

then the variational problem becomes :

$$\eta^{-2}a_c(v^\eta, w) + a_0(v^\eta, w) + a_s(v^\eta, w) = \int_0^\pi F(y_1)w_2(y_1, 0)dy_1 \tag{43}$$

in the space $H_0^1 \times H_0^2$ of the domain

$$\Omega_\eta = (0, \pi) \times (-1/\eta, +1/\eta) . \tag{44}$$

where

$$a_c(v, w) = \int_{\Omega_\eta} \alpha(y_2)(D_2v_1 - v_2)(D_2w_1 - w_2)dy$$

$$a_0(v, w) = \int_{\Omega_\eta} \left[\alpha(y_2)(D_1v_1)(D_1w_1) + (D_2^2v_2)(D_2^2w_2) \right] dy$$

$$a_s(v, w) = \eta^2 \int_{\Omega_\eta} [2(D_1D_2v_2)(D_1D_2w_2)] dy +$$

$$+ \eta^4 \int_{\Omega_\eta} \left[(D_1^2v_2)(D_1^2w_2) \right] dy$$

Remark 4.2. We observe that in the present case, the problem in the inner variables y is a singular perturbation formed by the terms a_0 and a_s and an additional penalty term in $\eta^{-2}a_c$, which implies a constraint for η tending to zero: the limit "lives" in the kernel of the form a_c.■

In order to define the limit problem we consider the union for $\eta < 1$ of the spaces $H_0^1 \times H_0^2$ of the domains (44) (note that the elements of that space may be extended with value zero to $\Omega = (0, \pi) \times \mathbb{R}y_2$) and we construct the completion of that space with the norm

$$[a_c(w, w) + a_0(w, w)]^{1/2}$$

Let $\mathcal{V}$ be the Hilbert space so obtained. We shall also define the subspace of $\mathcal{V}$ with the constraint evoked in Remark 4.2 :

$$G = \{w \in \mathcal{V} \; ; \; \partial_2 w_1 - w_2 = 0\} \tag{45}$$

which is a closed subspace of $\mathcal{V}$. The limit problem is :

$$\text{Find } v \in G \text{ such that} \forall w \in G \; :$$
$$a_0(v, w) = \int_0^\pi F(y_1)w_2(y_1, 0)dy_1 \tag{46}$$

Lemma 4.1. The right hand side of (46) is a continuous functional on $\mathcal{V}$.

Proof.   It was proved in [6], Lemma 4.1 that if $v \in \mathcal{V}$, taking the restriction to $(0, \pi) \times (-1, +1)$, we have

$$v_1 \in L^2\left((0, \pi); H^1(-1, +1)\right)$$

with the obvious continuity in the norms. On the other hand, from the definition of $\mathcal{V}$ follows that

$$D_2^2 v_2 \in L^2\left((0, \pi) \; ; \; L^2(-1, +1)\right)$$
$$D_2 v_1 - v_2 \in L^2\left((0, \pi) \; ; \; L^2(-1, +1)\right)$$

so that

$$v_2 \in L^2\left((0,\pi)\ ;\ H^2(-1,+1)\right) \tag{47}$$

and taking the trace at the origin in $H^2(-1,+1)$, the conclusion follows.∎
The limit problem (46) is then a classical variational problem in G and its solution v is well defined. Moreover, we have :

Theorem 4.1. Let v^η and v be the solutions of (43) and (46) respectively. Then

$$v^\eta \to v \quad \text{strongly in } \mathcal{V} . \tag{48}$$

The proof is analogous to that of theorem 3.1 in [6].
Using the constraint $v_2 = \partial_2 v_1$ in the space G it is easy to write the solution of the limit problem (46) in terms of v_1 :

$$\left(-\alpha(y_0)D_1^2 + D_2^6\right)v_1 = -\delta'(y_2)F(y_1) \quad \text{in } (0,\pi) \times \mathbb{R}y_2 \tag{49}$$

$$v_1(0,y_2) = v_1(\pi,y_2) = 0, \tag{50}$$

which may be easily solved by separation of variables. As $v \in G$, we have exponential decreasing for $\mid y_2 \mid \to \infty$.

Remark 4.3. Many variants of the previous problem are possible. Let us mention the following one : we consider

$$\langle f,v\rangle = \int_0^\pi M(x_1)\partial_2 v_2(x_1,0)dx \tag{51}$$

instead of (37). All the previous developments hold true (note in particular that (47) allows us to take traces of D_2v_2). The only difference is concerned with the re-scaling (42) : the exponents of η in the denominators of (42) should be 3 and 4 instead of 2 and 3 respectively.∎

References

[1] Il'in A.M. 1992. *Matching of asymptotic expansions of solutions of boundary value problems*, Am. Math. Soc., Providence.

[2] Karamian P., Sanchez-Hubert J. 2002. Boundary layers in thin elastic shells with devleoppable middle surface, *Eur. J. Mech. A/Solids*, **21**, p. 13-47.

[3] Karamian-Surville P., Sanchez-Hubert J., Sanchez-Palencia E. 2002. Propagation of singularities and structure of layers in shells. Hyperbolic case. *Comp. and Struct.*, **80**, p. 747-768.

[4] Lions J.L. 1973. *Perturbations singulières dans les problèmes aux limites et en contrôle optimal*. Springer, Berlin.

[5] Lions J.L. et Magenes E. 1968. *Problèmes aux limites homogènes et applications*, vol. 1. Dunod, Paris.

[6] Sanchez-Palencia E. 2000. On a singular perturbation going out of the energy space, *J. Math. Pures Appl.*, **79**, 591-602.

[7] Sanchez-Palencia E. 2002. On the structure of layers for singularity perturbed equations in the case of unbounded energy, *Control, Optim. Cal. Var.*, issue dedicated to J.L. Lions, vol. **7**, 941-963. .

ASYMPTOTICS OF LAMINATED SHELLS. MEMBRANE - BENDING COUPLING AND NUMERICAL IMPLEMENTATION

H. Ranarivelo and J. Sanchez-Hubert

Laboratoire de Mécanique, Modélisation Mathématique et Numérique

Université de Caen, BP 5186, 14032 Caen, France

jsanchez@lmm.jussieu.fr

Keywords: Shell theory, anisotropy, numerical implementation.

Abstract   In this paper, we give a method to compute the generalized elasticity coefficients including coupling terms which appear in thin shell theory when the material is heterogeneous. A new program to compute this coefficients is implemented in the finite element code Modulef. As an example we consider an inhibited bilayered thin shell with hyperbolic middle surface involving a composite material with unidirectional fibres. We observe that the presence of anisotropy modifies the quantitative results obtained for isotropic homogeneous material but not the qualitative trends of the solutions.

1.   INTRODUCTION

Heterogeneous plate and shallow shell theories were considered in [11], Chap.6, Remark 3.9 and [5]. The description of these problems includes coupling between membrane stress and bending. A corresponding theory for thin shells was worked out in [4] starting from a theory of shells in the framework of the Koiter's hypotheses, and in [3] starting directly from three-dimensional elasticity. Asymptotic two-scale method was used in [3] to derive thin shell theory (see also [12]). Very many papers were published concerning thin shells and their numerical computation in the isotropic case, but very few in the general anisotropic and heterogeneous case. In this paper, we give a method to compute the generalized elasticity coefficients which appear in the variational formulation of the shell theory, in particular the coupling ones, in the framework of [3]. These coefficients are computed in contravariant components. This implies implementation of subroutines in the Modulef code. Precisely, construction of matrices

including the rigidity coefficients in the covariant basis. As an example, numerical simulation is done by using the Ganev-Argyris finite element [1] in the case of a multilayered and anisotropic shell. Precisely, in that example, each ply is a composite material with unidirectional fibers. Checking out, by post-processing, the generalized coefficients at Gauss points, we observe that the coupling coefficients do not vanish, in general, and their numerical values are not very small with respect to the membrane and bending coefficients. So, they may be taken into account in numerical computations.

The paper is organized as follows, in the Sect.2 we recall the main results of the asymptotic theory developed in [3]. They will be used in the following sections. Sect.3 is devoted to the local behavior, we give the expression of the contravariant elasticity coefficients in terms of the rigidity coefficients given in a Cartesian frame. In particular, we give explicitly the generalized coefficients in the case of a multilayered shell. Numerical simulation is given in Sect. 4 concerning a bilayered shell, we observe that the coupling coefficients do not vanish and consequently modify the quantitative results obtained for isotropic homogeneous shells. Nevertheless the qualitative results hold true, in particular we observe the boundary layer phenomena for inhibited shell when the loading does not vanish at a free boundary (see [6], [7], [8]).

2.   MAIN RESULTS OF THE ASYMPTOTIC THEORY

In this section, we summarize the main results obtained in [3]. We consider the asymptotic behavior as the relative thickness tends to zero. The asymptotic process is based directly on the variational formulation of the problem and not on the equations. The asymptotic expansions are performed by using a formal two-scale method, in the next subsection, we give some indications on notations .

2.1.   MAIN NOTATIONS

The current curvilinear coordinates are $y = \left(y^1, y^2, y^3\right)$ where y^1, y^2 are the parameters defining the middle surface $\mathcal{S}$ of the shell and y^3 denotes the distance from $\mathcal{S}$ in the normal direction. Vectors with three components in the physical space are written in boldface, for instance the displacement is $\mathbf{u} = (u_1, u_2, u_3)$. The Greek indices run on 1,2 and the Latin ones on 1,2,3.

Moreover, as upper and lower indices will be used for contravariant and covariant variables respectively, the set of the terms in the asymptotic

expansions will be written in parentheses, for instance

$$\mathbf{u} \simeq \mathbf{u}^{(0)} + \varepsilon \mathbf{u}^{(1)} + \varepsilon^2 \mathbf{u}^{(2)} + \cdots . \tag{2.1}$$

In the context of laminated shells, the large scale variables are only $y = (y^1, y^2, 0)$ or merely $y = (y^1, y^2)$. The small scale variable is $z = (0, 0, z^3)$.

In any case, we shall consider y and z as three-dimensional variables with

$$\frac{\partial}{\partial y^3} = 0, \quad \frac{\partial}{\partial z^\alpha} = 0. \tag{2.2}$$

Moreover, we shall use the usual notations

$$e_{ijy} = \frac{1}{2} \left(\frac{\partial u_i}{\partial y^j} + \frac{\partial u_j}{\partial y^i} \right) \tag{2.3}$$

$$e_{ijz} = \frac{1}{2} \left(\frac{\partial u_i}{\partial z^j} + \frac{\partial u_j}{\partial z^i} \right) \tag{2.4}$$

The middle surface $\mathcal{S}$ is define by the mapping

$$\overrightarrow{\psi} : \left(y^1, y^2 \right) \in \Omega \to \overrightarrow{\psi} \left(y^1, y^2 \right) \in \mathcal{E}^3, \tag{2.5}$$

where Ω is some domain of the $\left(y^1, y^2 \right) -$ plane and $\mathcal{E}^3$ denote the Euclidean space with coordinates (x_1, x_2, x_3), then $\mathcal{S}$ is the image of Ω. At each point of $\mathcal{S}$ we consider the two tangent vectors

$$\mathbf{a}_\alpha = \frac{\partial \overrightarrow{\psi}}{\partial y^\alpha} \tag{2.6}$$

and the normal unit vector

$$\mathbf{a}_3 = \frac{\mathbf{a}_1 \wedge \mathbf{a}_2}{|\mathbf{a}_1 \wedge \mathbf{a}_2|} \tag{2.7}$$

The coefficients of the first fundamental form are

$$a_{\alpha\beta} = \mathbf{a}_\alpha \bullet \mathbf{a}_\beta \tag{2.8}$$

Obviously, the surface $\mathcal{S}$ is assumed to be smooth up to its boundary $\partial \mathcal{S}$. As it is classical, we then define the normal curvilinear coordinates $\left(y^1, y^2, y^3 \right)$ so that

$$\mathbf{x} = \overrightarrow{\psi} \left(y^1, y^2 \right) + y^3 \mathbf{a}_3.$$

Then the vectors of the local basis are

$$\mathbf{g}_i \left(y^1, y^2, y^3 \right) = \frac{\partial \mathbf{x}}{\partial y^i},$$

and, of course, the above defined vectors $\mathbf{a}_i$ are $\mathbf{g}_i\left(y^1, y^2, 0\right)$. The metric tensor a_{ij} of the curvilinear coordinates is $g_{ij} = \mathbf{g}_i \bullet \mathbf{g}_j$ and the $a_{\alpha\beta}$ defined in (2.8) are $g_{\alpha\beta}\left(y^1, y^2, 0\right)$. We also shall use the contravariant basis defined by $\mathbf{g}^i \bullet \mathbf{g}_j = \delta_j^i$. The Christoffel symbols of the surface are defined as

$$\Gamma_{\alpha\beta}^\lambda\left(y^1, y^2\right) = \Gamma_{\alpha\beta}^\lambda\left(y^1, y^2, 0\right) \tag{2.9}$$

We also recall that the surface and volume elements are given by

$$\begin{cases} dS = \left(\det a_{\alpha\beta}\right)^{\frac{1}{2}} dy^1 dy^2, \\ dV = \left(\det a_{ij}\right)^{\frac{1}{2}} dy^1 dy^2 dy^3 \end{cases} \tag{2.10}$$

respectively. As in normal coordinates $a_{\alpha 3} = 0$ and $a_{33} = 1$, for small y^3 we have

$$dV = \left(1 + \mathcal{O}\left(y^3\right)\right) dS dy^3. \tag{2.11}$$

The thin shell is defined by considering a small parameter ε such that 2ε is the thickness of the shell. Then the thin shell occupies the domain $\mathcal{S}_\varepsilon$ defined in curvilinear coordinates by

$$\mathcal{S}_\varepsilon = \left\{\mathbf{x}; \left(y^1, y^2, y^3\right) \in \Omega \times \left]-\varepsilon, \varepsilon\right[\right\}. \tag{2.12}$$

The shell is assumed to be fixed by a part Γ_ε of its lateral surface

$$\Gamma_\varepsilon = \partial_0 \mathcal{S} \times \left]-\varepsilon, \varepsilon\right[, \tag{2.13}$$

where $\partial_0 \mathcal{S}$ denotes a part of the lateral boundary of $\mathcal{S}$.

2.2. MECHANICAL BEHAVIOR OF THE SHELL

Let a^{ijkh} be the elasticity coefficients, expressed in the covariant basis associated with the curvilinear coordinates of $\mathcal{S}_\varepsilon$. We shall consider them to be functions of $\left(y^1, y^2, \frac{y^3}{\varepsilon}\right)$ defined on $\mathcal{S}_\varepsilon$, they satisfy the symmetry and positivity properties :

$$a^{ijkh} = a^{khij} = a^{jikh} \tag{2.14}$$

$$a^{ijkh}\xi_{ij}\xi_{kh} \geq C\xi_{ij}\xi_{ij}, \quad \forall \xi_{ij} \text{ such that } \xi_{ij} = \xi_{ji} \tag{2.15}$$

The elasticity coefficients are assumed to be smooth functions of y^1, y^2, oppositely they are not necessarily smooth with respect to $z^3 = y^3/\varepsilon$, for instance in the case of a laminated shell they are piecewise smooth of z^3.

The density of the applied forces are assumed to be

$$\varepsilon^3 F^i \left(y^1, y^2\right) \tag{2.16}$$

by unit surface on $\mathcal{S}$.

The components of the strain tensor are given by

$$\gamma_{kh}\left(\mathbf{u}\right) = e_{kh}\left(\mathbf{u}\right) - \Gamma^m_{kh} u_m. \tag{2.17}$$

Denoting by $\mathcal{V}_\varepsilon$ the space of the kinematically admissible displacements, the variational formulation of the elasticity problem is

$$\text{Find } \mathbf{u}^\varepsilon \in \mathcal{V}_\varepsilon \text{ such that}$$
$$\int_{\mathcal{S}_\varepsilon} a^{ijkh} \gamma_{kh}\left(\mathbf{u}\right) \gamma_{ij}\left(\mathbf{v}\right) dV = \varepsilon^3 \int_{\mathcal{S}} F^i v_i dS \quad \forall \mathbf{v} \in \mathcal{V}_\varepsilon. \tag{2.18}$$

In order to work up the two-scale method, we consider the variables

$$y = \left(y^1, y^2, 0\right), \quad z = \left(0, 0, z^3 = y^3/\varepsilon\right) \tag{2.19}$$

By analogy with the plate theory (see [2] and [11]), we search for expansions of $\mathbf{u}^\varepsilon$ of the form

$$\mathbf{u}^\varepsilon \simeq \mathbf{u}^{(0)}\left(y\right) + \varepsilon \mathbf{u}^{(1)}\left(y, z\right) + \varepsilon^2 \mathbf{u}^{(2)}\left(y, z\right) + \cdots$$

Then, by expanding γ_{ij} under the form

$$\gamma_{ij}\left(\mathbf{u}^\varepsilon\right) \simeq \gamma^{(0)}_{ij} + \varepsilon \gamma^{(1)}_{ij} + \cdots \tag{2.20}$$

it was proved (see [3], [12]) that :

1 $\mathbf{u}^0\left(y\right)$ is a pure bending, defined as solution of

$$\gamma_{\alpha\beta y}\left(\mathbf{u}^0\right) = 0,$$

   satisfying the kinematic boundary conditions

2 $\mathbf{u}^1\left(y, z\right)$ is equal to a Love-Kirchhoff displacement field given by $\mathbf{u}^0$ plus a term $\widehat{\mathbf{u}}^{(1)}$ independent of z.

3 The components $\gamma^{(1)}_{ij}$ are of the form

$$\gamma^{(1)}_{ij} = C_{ij}\left(\mathbf{u}^0\right) z^3 + E_{ij}\left(\widehat{\mathbf{u}}^{(1)}\right) + e_{ijz}\left(\mathbf{u}^{(2)}\right)$$

   where

$$C_{33} = E_{33} = 0.$$

4 At last, it was proved that the coefficients $C_{\alpha 3}$ and $E_{\alpha 3}$ have not influence on the stress tensor, so they may be taken equal to zero. Then we have

$$\gamma_{\alpha\beta}^{(1)} = -\rho_{\alpha\beta}\left(\mathbf{u}^0\right) z^3 + \gamma_{\alpha\beta y}\left(\widehat{\mathbf{u}}^{(1)}\right) + e_{\alpha\beta z}\left(\mathbf{u}^{(2)}\right) \tag{2.21}$$

$$\gamma_{i3z}^{(1)} = e_{i3z}\left(\mathbf{u}^{(2)}\right)$$

where $\rho_{\alpha\beta}$ are the components of the variations of the curvature.

The local equation, i.e. with respect to z, is then

$$\int_{-1}^{1} a^{ijkh}\left[C_{kh}\left(\mathbf{u}^0\right) z^3 + E_{kh}\left(\widehat{\mathbf{u}}^{(1)}\right) + e_{khz}\left(\mathbf{u}^{(2)}\right)\right] e_{ijz}\left(\mathbf{w}\right) dz^3 = 0$$

$$\forall \mathbf{w} \in \left[H^1\left(-1, 1\right)\right]^3 \tag{2.22}$$

(2.22) is an equation for $\mathbf{u}^{(2)}$ when the quantities C_{kh} are considered as data. The solution is then defined as an element of $\left[H^1\left(-1, 1\right)\right]^3 / \mathbb{R}^3$, it is linear with respect to $C_{kh}\left(\mathbf{u}^0\right)$ and $E_{kh}\left(\widehat{\mathbf{u}}^{(1)}\right)$ (which, are constant in z). With $\mathbf{u}^{(2)}$ defined in a such way, $\gamma_{\alpha\beta}^{(1)}$ is known and we may define the leading terms of the membrane constraints and moments in the shell :

$$T^{ij} = \varepsilon^2 \int_{-1}^{1} a^{ijkh}\gamma_{kh}^{(1)}dz^3 \tag{2.23}$$

$$M^{ij} = \varepsilon^3 \int_{-1}^{1} a^{ijkh}\gamma_{kh}^{(1)}z^3 dz^3 \tag{2.24}$$

with $T^{i3} = M^{i3} = 0$. Indeed, according to (2.22), we have

$$\int_{-1}^{1} \sigma^{(1)ij} e_{ijz}\left(\mathbf{w}\right) dz^3 = 0$$

and, as $\mathbf{w}$ is an arbitrary vector, it follows that

$$0 = \sigma_{,j}^{(1)ij} \simeq \frac{1}{\varepsilon}\sigma_{,3}^{(1)i3} + \cdots \Rightarrow \sigma_{,3}^{(1)i3} \equiv 0.$$

Consequently, $\sigma^{(1)i3}$ are constants with respect to z^3 and, on account of the boundary conditions at $z^3 = \pm 1$, we have

$$\sigma^{(1)i3} = 0. \tag{2.25}$$

As (2.25) is satisfied at any $z \in (-1, 1)$, at the leading order of the stress, *each point of a ply is in a plane - stress state*. Moreover, as $C_{\alpha i}$ and $E_{\alpha i}$ may be taken equal to zero, taking account of the linearity, we may write $T^{\alpha\beta}$ and $M^{\alpha\beta}$ under the form

$$\begin{cases} \varepsilon^{-2} T^{\alpha\beta} = A_{11}^{\alpha\beta\lambda\mu} \gamma_{\lambda\mu} - A_{12}^{\alpha\beta\lambda\mu} \rho_{\lambda\mu} \\ \varepsilon^{-3} M^{\alpha\beta} = A_{21}^{\alpha\beta\lambda\mu} \gamma_{\lambda\mu} - A_{22}^{\alpha\beta\lambda\mu} \rho_{\lambda\mu} \end{cases} \tag{2.26}$$

where the coefficients $A_{\nu\delta}^{\alpha\beta\lambda\mu}$ are well defined by relations of the form

$$\begin{cases} A_{11}^{\alpha\beta\lambda\mu} = \int\limits_{-1}^{1} c^{\alpha\beta\lambda\mu} \left(y^1, y^2, z^3\right) dz^3 \ : \ \text{membrane coefficients} \\ A_{22}^{\alpha\beta\lambda\mu} = \int\limits_{-1}^{1} c^{\alpha\beta\lambda\mu} \left(y^1, y^2, z^3\right) \left(z^3\right)^2 dz^3 \ : \ \text{bending coefficients} \\ A_{12}^{\alpha\beta\lambda\mu} = A_{21}^{\alpha\beta\lambda\mu} = \int\limits_{-1}^{1} c^{\alpha\beta\lambda\mu} \left(y^1, y^2, z^3\right) z^3 dz^3 \ : \ \text{coupling coefficients} \end{cases}$$

$$(2.27)$$

where the coefficients $c^{\alpha\beta\lambda\mu}$ are the *contravariant elasticity coefficients in the plane -stress state*, they will be defined in the next section (see 3.4). They satisfy the symmetry and positivity properties.

At the present level, the energy form is written in terms of the *curvilinear generalized elasticity coefficients* $A_{\nu\delta}^{\alpha\beta\lambda\mu}$. In order to implement the problem for multilayered shells we have to use the numerical coefficients for each ply $\mathcal{C}_k$, $k = 1, 2, \cdots N$. This is the object of the next section.

3. LOCAL MECHANICAL BEHAVIOR OF EACH PLY $C_{\overline{K}}$

3.1. COMPONENTS OF THE REDUCED LOCAL ELASTICITY COEFFICIENTS

The mechanical behavior of each ply $\mathcal{C}_{\overline{k}}$ is known in a Cartesian basis $\left(\mathbf{e}_1^{\overline{k}}, \mathbf{e}_2^{\overline{k}}, \mathbf{e}_3^{\overline{k}}\right)$ which is chosen, for example, such that $\mathbf{e}_3^{\overline{k}}$ coincides with the unit normal vector $\mathbf{a}_3 \left(y^1, y^2\right)$ of the surface. In such a basis, the local behavior writes

$$\overline{\sigma}^{i'j'} = \overline{a}_{\overline{k}}^{i'j'k'h'} \overline{\gamma}_{k'h'} \tag{3.1}$$

where the elasticity coefficients $\overline{a}_{\overline{k}}^{i'j'k'h'}$ are the mechanical ones in each ply, they are assumed to be known for a given material. We shall call them *effective elasticity coefficients.* They are expressed in terms of characteristic mechanical modulus of the material. In (3.1) the indices may be upper or lower ones because contravariant and covariant coincide in the Cartesian basis.

Condition (2.25) allows us to write the constitutive law in terms of plane stresses i.e.under the form

$$\overline{\sigma}^{\alpha'\beta'} = \overline{c}^{\alpha'\beta'\lambda'\mu'}\overline{\gamma}_{\lambda'\mu'} \tag{3.2}$$

where the coefficients $\overline{c}^{\alpha'\beta'\lambda'\mu'}$ will be called *reduced elasticity coefficients.*

3.2.   EXPRESSION OF THE GENERALIZED CONTRAVARIANT ELASTICITY COEFFICIENTS IN TERMS OF THE REDUCED ONES

The vectors constituting the local basis $\{\mathbf{a}_\mu\}$ may be expressed in the Cartesian basis $\left\{\mathbf{e}_{\alpha'}^{\overline{k}}\right\}$ and, by inversion, we have relations of the form

$$\mathbf{e}_{\mu'}^{\overline{k}} = P_{\mu'}^{\beta}\mathbf{a}_\beta \quad \Leftrightarrow \quad \left[\mathbf{e}_{\mu'}^{\overline{k}}\right] = \left[P_{\overline{k}}\right][\mathbf{a}_\beta]$$

We note that the coefficients $P_{\mu'}^{\beta}$ of the matrix $[P]$, where β is a row index and μ' a line index, may also be written with indices $P_{\beta\mu'}$ with the same convention, for convenience in the formulae we shall use this possibility. Then, from

$$\sigma = \sigma^{\alpha\beta}\mathbf{a}_\alpha \otimes \mathbf{a}_\beta = \overline{\sigma}^{\alpha'\beta'}\mathbf{e}_{\alpha'}^{\overline{k}} \otimes \mathbf{e}_{\beta'}^{\overline{k}}$$

we have

$$\overline{\sigma}^{\alpha'\beta'} = P_\lambda^{\alpha'}P_\mu^{\beta'}\sigma^{\lambda\mu} \quad \Leftrightarrow \quad \left[\overline{\sigma}^{\alpha'\beta'}\right] = \left[U_{\overline{k}}\right]\left[\sigma^{\lambda\mu}\right]$$

In the same way, we have

$$\gamma = \gamma_{\lambda\mu}\mathbf{a}^\lambda \otimes \mathbf{a}^\mu = \gamma_{\lambda\mu}a^{\lambda\xi}a^{\mu\eta}\mathbf{a}_\xi \otimes \mathbf{a}_\eta = \gamma_{\lambda\mu}a^{\lambda\xi}a^{\mu\eta}P_{\xi\alpha'}P_{\eta\beta'}\mathbf{e}^{\alpha'} \otimes \mathbf{e}^{\beta'} = \overline{\gamma}_{\alpha'\beta'}\mathbf{e}^{\alpha'} \otimes \mathbf{e}^{\beta'}$$

or equivalently

$$[\gamma_{\lambda\mu}] = [V]\left[\overline{\gamma}_{\alpha'\beta'}\right] \quad \Leftrightarrow \quad \left[\overline{\gamma}_{\alpha'\beta'}\right] = \left[V_{\overline{k}}\right]^{-1}[\gamma_{\lambda\mu}]$$

namely

$$\overline{\gamma}_{\alpha'\beta'} = a^{\lambda\xi}a^{\mu\eta}P_{\xi\alpha'}P_{\eta\beta'}\gamma_{\lambda\mu}$$

then, from (3.2) we get the generalized contravariant elasticity coefficients:

$$c_{\overline{k}}^{\alpha\beta\lambda\mu} = a^{\lambda\xi}a^{\mu\eta}P_{\xi\delta'}P_{\eta\nu'}\overline{a}_{\overline{k}}^{\alpha\beta\delta'\nu'} \quad \Leftrightarrow \quad \left[c_{\overline{k}}^{\alpha\beta\lambda\mu}\right] = U_{\overline{k}}\left[\overline{c}_{\alpha'\beta'k'h'}\right]\left[V_{\overline{k}}\right]^{-1} \tag{3.3}$$

Consequently, when the effective elasticity coefficients in a ply $\mathcal{C}_k$ are known, then the contravariant coefficients for each ply are well determined and the elasticity coefficients in the right hand side of (2.27) are given by

$$
c^{\alpha\beta\lambda\mu}\left(y^1,y^2,z^3\right) =
\begin{cases}
c_1^{\alpha\beta\lambda\mu}\left(y^1,y^2\right) & \text{for } -1 \leq z^3 \leq z_1^{3-} \\
c_2^{\alpha\beta\lambda\mu}\left(y^1,y^2\right) & \text{for } z_1^{3+} \leq z^3 \leq z_2^{3-} \\
\qquad\qquad\cdots \\
c_k^{\alpha\beta\lambda\mu}\left(y^1,y^2\right) & \text{for } z_{k-1}^{3+} \leq z^3 \leq z_k^{3-} \\
\qquad\qquad\cdots \\
c_N^{\alpha\beta\lambda\mu}\left(y^1,y^2\right) & \text{for } z_{N-1}^{3+} \leq z^3 \leq 1
\end{cases}
\tag{3.4}
$$

3.3. PARTICULAR CASE OF A COMPOSITE MATERIAL WITH UNIDIRECTIONAL FIBRES

In this section, we consider the case when the material constituting each ply $\mathcal{C}_{\bar{k}}$ is a composite with unidirectional fibres. Taking the vector $\mathbf{e}_1^{\bar{k}}$ of the Cartesian basis in the tangential direction to the fibre at $Q \in \mathcal{C}_{\bar{k}}$, we may locally define the orientation of the fibre by the angle

$$
\theta_{\bar{k}} = \left(\mathbf{e}_1^{\bar{k}}, \mathbf{a}_1\right)
\tag{3.5}
$$

Then, the coefficients of the previous matrix $P^{\bar{k}}$ are defined by using the relations

$$
\mathbf{e}_\alpha = P_\alpha^\beta \mathbf{a}_\beta.
\tag{3.6}
$$

namely

$$
\begin{pmatrix}
\dfrac{\cos\theta_{\bar{k}}}{\|\mathbf{a}_1\|} + \dfrac{\mathbf{a}^{21}}{\|\mathbf{a}^2\|}\sin\theta_{\bar{k}} & -\|\mathbf{a}^2\|\sin\theta_{\bar{k}} & 0 \\
\dfrac{\sin\theta_{\bar{k}}}{\|\mathbf{a}_1\|} - \dfrac{\mathbf{a}^{21}}{\|\mathbf{a}^2\|}\cos\theta_{\bar{k}} & \|\mathbf{a}^2\|\cos\theta_{\bar{k}} & 0 \\
0 & 0 & 1
\end{pmatrix}
$$

As the Cartesian basis $\left\{\mathbf{e}_i^{\bar{k}}\right\}$ is the orthotropy basis for the considered material, condition (2.25) leads to

$$
\bar{c}_{\alpha\beta\lambda\mu}^{\bar{k}} = \bar{a}_{\alpha\beta\lambda\mu}^{\bar{k}} - \frac{\bar{a}_{\alpha\beta33}^{\bar{k}}\,\bar{a}_{33\lambda\mu}^{\bar{k}}}{\bar{a}_{3333}^{\bar{k}}}
\tag{3.7}
$$

In (3.7), computation of the coefficients $\bar{c}^{\bar{k}}_{\alpha\beta\lambda\mu}$ needs the data of four elastic modulus of the material (see [9]) :

$$
\begin{cases}
\overline{E}^{\bar{k}}_1 \text{ and } \overline{E}^{\bar{k}}_2 = \overline{E}^{\bar{k}}_3 : \text{longitudinal and transverse Young's moduli, respectively,} \\
\overline{\nu}^{\bar{k}}_{12} \text{ Poisson coefficient in the } (\mathbf{e}_1, \mathbf{e}_2) \text{ and } (\mathbf{e}_1, \mathbf{e}_3) - planes, \\
\overline{G}^{\bar{k}}_{12} \text{ shear modulus in the } (\mathbf{e}_1, \mathbf{e}_2) \text{ and } (\mathbf{e}_1, \mathbf{e}_3) - planes.
\end{cases}
\tag{3.8}
$$

then we have

$$
\begin{cases}
\bar{c}^{\bar{k}}_{1111} = \dfrac{\left(\overline{E}^{\bar{k}}_1\right)^2}{\overline{E}^{\bar{k}}_1 - \overline{E}^{\bar{k}}_2 \left(\nu^{\bar{k}}_{12}\right)^2}, \\[2ex]
\bar{c}^{\bar{k}}_{2222} = \dfrac{\overline{E}^{\bar{k}}_2}{\overline{E}^{\bar{k}}_1} \bar{c}^{\bar{k}}_{1111}, \\[2ex]
\bar{c}^{\bar{k}}_{1122} = \overline{\nu}^{\bar{k}}_{12} \bar{c}^{\bar{k}}_{2222}, \\[2ex]
\bar{c}^{\bar{k}}_{1212} = \overline{G}^{\bar{k}}_{12}
\end{cases}
\tag{3.9}
$$

Then, (3.4) gives the contravariant elasticity coefficients $c^{\alpha\beta\lambda\mu}$ and (2.27) the generalized contravariant elasticity coefficients $A^{\alpha\beta\lambda\mu}_{\nu\delta}$.

4. NUMERICAL SIMULATIONS

4.1. IMPLEMENTATION IN THE MODULEF CODE

For the numerical experiments, the Modulef code is used. Modulef gives finite element analysis to compute thin shells in the isotropic homogeneous case. The modular structure of this code and its interactive character will allow us to implement programs to compute the generalized contravariant elasticity coefficients in the case of multilayered shells. The so reprogrammed modulus is precisely that of the computation of the generalized coefficients introduced in Sect. (2) and (3). The choice of the Ganev - Argyris element for all the numerical tests will allow us to solve, not on the middle surface, but on the plane domain Ω of the parameters. Let us note that as the implementation involves $(u_1, u_2, u_3) \in H^1 \times H^1 \times H^2$ a reliable conformal discretization is obtained with Ganev triangles for u_1, u_2 and Argyris triangles for u_3.

As it is classical, let us introduce a generalized unknown with 12 components

$$
[U(y^1, y^2)] = [u_1 \ u_{1,1} \ u_{1,2} \ u_2 \ \cdots \ u_{3,22}]
$$

then, the variational formulation becomes

$$\varepsilon A_m\left(U,V\right) + \varepsilon^2 A_c\left(U,V\right) + \varepsilon^3 A_f\left(U,V\right) = \varepsilon^3 \left\langle F,V\right\rangle \; \forall V \in \mathcal{V}$$

where

$$A_m\left(U,V\right) = \int_\Omega \left[U\right]\left[A_m\right]_{12\times12}\left[V\right]dy^1dy^2$$

and the analogous relations for A_c and A_f. The matrices $\left[A_m\right]$, $\left[A_c\right]$ and $\left[A_f\right]$ are computed with the elasticity coefficients (2.27).

The essential modification in Modulef consists in the construction of the above matrices. This previously needs the construction of the local and reduced coefficients of rigidity $\overline{c}^{\overline{k}}$ (see Sect.3) and the knowledge of four characteristics of the material in each ply (see 3.12). The main programs may be found as annex in [10].

4.2. NUMERICAL SIMULATION

As an example, we consider a thin shell constituted by two parallel plies made with a composite material with unidirectional fibers.

$$C_1 : z^3 \in \left]-1,0\right[, \; C_2 : z^3 \in \left]0,1\right[.$$

The map of the middle surface is

$$\overrightarrow{\psi} : \left(y^1,y^2\right) \in \Omega \to \left(y^1,\; y^2,\; y^1y^2\right)$$

(hyperbolic shell) where

$$\Omega = \left]0,1\right[\times \left]0,1\right[.$$

The directions of the fibers are defined, according to (3.9), by

$$\theta_1 = 0, \;\; \theta_2 = \frac{\pi}{4}$$

respectively.

For each ply, with a local orthonormal orthotropy basis $(\mathbf{e}_1,\mathbf{e}_2,\mathbf{e}_3)$, the elasticity moduli are

$$\overline{E}_1^{\overline{k}} = 84 \, GPa., \; \overline{E}_2^{\overline{k}} = 5.6 \, GPa, \; \overline{G}_{12}^{\overline{k}} = 2.1 \, GPa, \; \overline{\nu}_{12}^{\overline{k}} = 0.32$$

The relative thickness of the shell is $\varepsilon = 10^{-4}$. The generalized coefficients $A_{\gamma\delta}^{\alpha\beta\lambda\mu}$ are computed at each Gauss point. For instance, in the triangle with the nodes

$$A_1 = \left(1,\; 0.990680635\right), \; A_2 = \left(1,\; 1\right), \; A_3 = \left(0.990680635,\; 1\right)$$

at the Gauss point (0.997676806, 0.995327023), we obtain for the elasticity coefficients the values given in table 1.

Membrane	Coupling	Bending
A_{11}^{1111}	A_{12}^{1111}	A_{22}^{1111}
3.93469693E-05	-1.55805042E-05	1.31156564E-05
A_{11}^{1112}	A_{12}^{1112}	A_{22}^{1112}
-3.58176537E-06	2.81319676E-07	-1.19392179E-06
A_{11}^{1122}	A_{12}^{1122}	A_{22}^{1122}
5.31921149E-06	6.7729936E-07	1.7730705E-06
A_{11}^{1212}	A_{12}^{1212}	A_{22}^{1212}
5.4798033E-06	6.07729936E-07	1.8266011E-06
A_{11}^{1222}	A_{12}^{1222}	A_{22}^{1222}
8.06505495E-07	2.36123294E-06	2.68835165E-07
A_{11}^{2222}	A_{12}^{2222}	A_{22}^{2222}
2.43021952E-05	8.22597544E-06	8.10073173E-06

Table 1

In particular, it appears that the coupling coefficients do not vanish, moreover they are not very small with respect to the membrane and bending ones. Other examples may be found in [10] leading to the same conclusion.

The influence of the anisotropy on the mechanical behavior may be seen making comparisons with results obtained for this shell in the isotropic case (see [8]). For instance if the shell is fixed by $y^1 = 0$ and $y^2 = 0$ and free elsewhere (we note that it is an inhibited shell i.e. the middle surface is geometrically rigid), comparison between the numerical results for isotropic and anisotropic cases show that the general trends of the solutions are the same. In particular, there is accumulation of energy along the free boundaries $y^1 = 1$ and $y^2 = 1$. Obviously, the quantitative results are different in both cases see [10].

Examples with parabolic middle surface for inhibited shell may be found in [10] leading to the same conclusions as in the previous hyperbolic case.

5.   CONCLUDING REMARKS

Computation of the generalized elasticity coefficients for anisotropic shells were given. We showed on an example that the coupling coefficients are of the same order as the membrane and bending ones so that they should be taken into account in numerical computations. They are also relevant in the study of the structure of the inner and boundary layers (see [7] and [8]).

References

[1] Bernadou M., *Méthodes d'éléments finis pour les problèmes de coques minces,* Masson, Paris;1994.

[2] Caillerie D.,*Thin elastic and periodic plates*, Math. Methods Appl. Sci., N° 6, 1984, pp. 159-191.

[3] Caillerie D. & Sanchez Palencia É., *Elastic thin shells : asymptotic theory in the anisotropic and heterogeneous cases,* Math. Models and meth. in Appl. Sci., vol. 5, N°4, 1995, pp. 473-496.

[4] Caillerie D. & Sanchez Palencia É., *A new kind of singular stiff problems and application to thin elastic shell,* Math. models Meth. in Appl. Sci., vol. 5, 1995, pp.47-66.

[5] Ciarlet P.G. & Paumier J.C., *A justification of the Marguerre - von Karman equations,* Comput. Mech., vol.1, 1986, pp. 177-202.

[6] Karamian P., Sanchez-Hubert J. & Sanchez Palencia É;, *A model problem for boundary layers of thin elastic shells,* Math. Modell. Num. Anal. 2000; 34 : 1-30.

[7] Karamian P. & J. Sanchez - Hubert, *Boundary layers in thin elastic shells with developable middle surface*, European Journal of Mechanics A/Solids (to appear)

[8] Karamain-Surville P., Sanchez-Hubert J., Sanchez Palencia É.,*Propagation of singularities and structure of layers in shells. Hyperbolic case,* Computers and Structures, Vol. 80, 2002, pp 747-768.

[9] Lekhnitskii S.G., *Theory of elasticity of an anisotropic elastic body*, Holden-Day series in mathematical physics, San Francisco, 1963

[10] Ranarivelo H., *Contribution à l'étude du comportement anisotrope de coque mince,* thèse de l'Université de Caen, 2002.

[11] Sanchez-Hubert J. & Sanchez Palencia É. *Introduction aux méthodes asymptotiques et à l'homogénéisation,* Masson, 1992.

[12] Sanchez-Hubert J. & Sanchez Palencia É. *Coques élastiques minces : propriétés asymptotiques,* Masson, 1997.

EXACT SINGULAR SOLUTIONS FOR AN INHOMOGENEOUS THICK ELASTIC PLATE

A. J. M. Spencer

School of Mathematical Sciences, University of Nottingham, Nottingham NG7 2RD, UK

Abstract   The author and co-workers have developed and applied [1-7] a procedure for deriving a large class of exact solutions of the three-dimensional field equations of linear elasticity for plates that are isotropic but inhomogeneous in the through-thickness direction. Here the technique is applied to several problems in which the corresponding two- dimensional problem involves a singular stress field. A feature is that in every case the presence of inhomogeneity results in an increase in the order of the singularity.

1.   INTRODUCTION

In a series of earlier papers, Rogers and Spencer [1], Rogers [2], Spencer [3,4,5], Mian and Spencer [6] and Spencer and Selvadurai [7] have developed and applied a procedure for deriving exact solutions of the equations of linear elasticity for materials that are isotropic but inhomogeneous in a specified direction.

The origins of the method reside in classical solutions by Michell [7] for plane stress of moderately thick elastic plates, and a reformulation of Michell's equations by Kaprielian, Rogers and Spencer [8]. The principal result obtained in [1-5] is that any solution of the classical thin plate or classical laminate theory equations (which describe a two-dimensional theory) can be applied, by straightforward substitutions, to generate an exact solution of the three-dimensional linear elasticity equations for a material with arbitrary inhomogeneity in a specified direction, which is here taken to be the direction normal to the surface of a thick flat plate. Thus, if this direction is taken to be the z direction of a system of rectangular Cartesian coordinates $Oxyz$, the Lamé elastic moduli (or Young's modulus and

Poisson's ratio) can be arbitrary specified functions of z, subject only to the usual strain-energy positive-definiteness requirements.

A disadvantage of the method is that, although it constructs exact solutions of the field equations, the solutions are usually not sufficiently general to allow satisfaction of the standard point-by point boundary conditions at the edge of a plate. However they normally admit specification of the usual combinations of stress resultants and moments, or of average or mid-plane displacements, at a boundary edge. Hence the solutions should strictly be regarded as interior solutions in a plate, and for completeness need to be supplemented by edge boundary layer solutions. There are some interesting solutions in two-dimensional elasticity theory which do not involve any boundaries, and which describe the effects of concentrated forces, force pairs, and higher order singularities, in plates. The main purpose of this paper is to derive the corresponding exact solutions for several problems involving singularities in an inhomogeneous plate.

2.   GENERAL THEORY

The governing equations were formulated in terms of rectangular Cartesian coordinates (x, y, z) in [6]. Here we employ cylindrical polar coordinates (r, θ, z). In this system, displacement components are denoted by u, v and w, components of the stress tensor σ by σ_{rr}, $\sigma_{r\theta}$, ..., and components of the infinitesimal strain tensor $\mathbf{e}$ by

$$
\begin{aligned}
e_{rr} &= \frac{\partial u}{\partial r}, \quad e_{\theta\theta} = \frac{u}{r} + \frac{1}{r}\frac{\partial v}{\partial \theta}, \quad 2e_{r\theta} = \frac{1}{r}\frac{\partial u}{\partial \theta} + \frac{\partial v}{\partial r} - \frac{v}{r}, \\
2e_{rz} &= \frac{\partial u}{\partial z} + \frac{\partial w}{\partial r}, \quad 2e_{\theta z} = \frac{\partial v}{\partial z} + \frac{1}{r}\frac{\partial w}{\partial \theta}, \quad e_{zz} = \frac{\partial w}{\partial z},
\end{aligned}
\tag{2.1}
$$

For an isotropic elastic solid, the stress-strain relations can be expressed in the form

$$
[\sigma_{rr},\, \sigma_{\theta\theta},\, \sigma_{zz}] = \lambda\,[e,\, e,\, e] + 2\mu\,[e_{rr}, e_{\theta\theta}, e_{zz}],
\tag{2.2}
$$

$$
[\sigma_{\theta z},\, \sigma_{rz},\, \sigma_{r\theta}] = 2\mu\,[e_{\theta z},\, e_{rz},\, e_{r\theta}]
\tag{2.3}
$$

where λ and μ are the Lamé elastic moduli and $e = e_{rr} + e_{\theta\theta} + e_{zz}$. The equations of equilibrium are

$$\frac{\partial \sigma_{rr}}{\partial r} + \frac{1}{r}\frac{\partial \sigma_{r\theta}}{\partial \theta} + \frac{\partial \sigma_{rz}}{\partial z} + \frac{\sigma_{rr} - \sigma_{\theta\theta}}{r} = 0,$$

$$\frac{\partial \sigma_{r\theta}}{\partial r} + \frac{1}{r}\frac{\partial \sigma_{\theta\theta}}{\partial \theta} + \frac{\partial \sigma_{\theta z}}{\partial z} + \frac{2\sigma_{r\theta}}{r} = 0,$$

$$\frac{\partial \sigma_{rz}}{\partial r} + \frac{1}{r}\frac{\partial \sigma_{\theta z}}{\partial \theta} + \frac{\partial \sigma_{zz}}{\partial z} + \frac{\sigma_{rz}}{r} = 0. \qquad (2.4)$$

We consider a plate or slab of linearly elastic material, which is not necessarily thin, bounded by the planes $z = \pm h$. The material is isotropic, but may be inhomogeneous in the z direction, so that, in general, λ and μ are specified functions of z. The dependence of λ and μ on z need not be continuous, so that the important special case of a laminated or layered material, in which λ and μ are piecewise constant functions of z, is included. The case in which the dependence is continuous corresponds to a functionally graded material.

The underlying idea is that exact solutions of the three-dimensional elasticity equations for the inhomogeneous plate are generated by solutions of the classical two-dimensional thin elastic plate or classical laminate theory equations. The following is a summary of required results that are described in detail in [5].

Let $\overline{u}(r,\theta), \overline{v}(r,\theta)$ and $\overline{w}(r,\theta)$ be displacements which may be interpreted as average or mid-surface displacements of a *thin* plate, and denote

$$\Delta = \frac{\partial \overline{u}}{\partial r} + \frac{\overline{u}}{r} + \frac{1}{r}\frac{\partial \overline{v}}{\partial \theta}, \quad \Omega = \frac{\partial \overline{v}}{\partial r} + \frac{\overline{v}}{r} - \frac{1}{r}\frac{\partial \overline{u}}{\partial \theta}. \qquad (2.5)$$

It is supposed that $\overline{u}(r,\theta), \overline{v}(r,\theta)$ and $\overline{w}(r,\theta)$ satisfy the equations

$$\kappa_1 \frac{\partial \Delta}{\partial r} - \frac{1}{r}\frac{\partial \Omega}{\partial \theta} + \kappa_2 \frac{\partial \nabla^2 \overline{w}}{\partial r} = 0,$$

$$\kappa_1 \frac{1}{r}\frac{\partial \Delta}{\partial \theta} + \frac{\partial \Omega}{\partial r} + \kappa_2 \frac{1}{r}\frac{\partial \nabla^2 \overline{w}}{\partial \theta} = 0, \quad \nabla^4 \overline{w} = 0, \qquad (2.6)$$

where κ_1 and κ_2 are the constants

$$\kappa_1 = \frac{4\int_{-h}^{h}\{\mu(\lambda+\mu)/(\lambda+2\mu)\}dz}{2h\overline{\mu}},$$

$$\kappa_2 = -\frac{4\int_{-h}^{h}\{\mu(\lambda+\mu)/(\lambda+2\mu)\}zdz}{2h\overline{\mu}}, \qquad (2.7)$$

and $\overline{\mu}$ is the through-thickness average value of μ, thus

$$2h\bar{\mu} = \int_{-h}^{h} \mu dz. \tag{2.8}$$

Equations (2.6) can be interpreted as the classical equations for bending and stretching of a *thin* elastic plate. It follows from (2.6) that Δ and Ω are harmonic functions, so that

$$\nabla^2\Delta = 0, \quad \nabla^2\Omega = 0, \quad \nabla^2 = \frac{\partial^2}{\partial r^2} + \frac{1}{r}\frac{\partial}{\partial r} + \frac{1}{r^2}\frac{\partial^2}{\partial\theta^2}. \tag{2.9}$$

If the plate is symmetric, so that $\lambda(z) = \lambda(-z)$ and $\mu(z) = \mu(-z)$, then $\kappa_2 = 0$, and the stretching deformations $\bar{u}$ and $\bar{v}$, uncouple from the bending deformations $\bar{w}$.

It is shown in [5] that if $\bar{u}, \bar{v}$ and $\bar{w}$ satisfy (2.6) then an *exact* solution of the three-dimensional elasticity equations (2.1)-(2.4) is

$$u(r,\theta,z) = \bar{u} - z\frac{\partial\bar{w}}{\partial r} + F(z)\frac{\partial\Delta}{\partial r} + B(z)\frac{\partial\nabla^2\bar{w}}{\partial r},$$
$$v(r,\theta,z) = \bar{v} - z\frac{1}{r}\frac{\partial\bar{w}}{\partial\theta} + F(z)\frac{1}{r}\frac{\partial\Delta}{\partial\theta} + B(z)\frac{1}{r}\frac{\partial\nabla^2\bar{w}}{\partial\theta},$$
$$w(r,\theta,z) = \bar{w} + G(z)\Delta + C(z)\nabla^2\bar{w}, \tag{2.10}$$

where the functions $B(z), C(z), G(z)$ and $F(z)$ are determined by the equations

$$\frac{dG}{dz} = -\frac{\lambda}{\lambda + 2\mu}, \quad \frac{dC}{dz} = z\frac{\lambda}{\lambda + 2\mu},$$

$$\frac{d}{dz}\left\{\mu\left(\frac{dF}{dz} + G\right)\right\} = \mu\kappa_1 - \frac{4\mu(\lambda + \mu)}{\lambda + 2\mu},$$
$$\frac{d}{dz}\left\{\mu\left(\frac{dB}{dz} + C\right)\right\} = \mu\kappa_2 + z\frac{4\mu(\lambda + \mu)}{\lambda + 2\mu}, \tag{2.11}$$

and the boundary conditions

$$\frac{dF}{dz} + G = 0, \quad \frac{dB}{dz} + C = 0, \quad at\ z = \pm h. \tag{2.12}$$

The definitions (2.7) of κ_1 and κ_2 ensure that the lateral surfaces $z = \pm h$ of the plate are free from tractions, so that

$$\sigma_{rz} = 0, \quad \sigma_{\theta z} = 0, \quad \sigma_{zz} = 0, \quad at\ z = \pm h. \tag{2.13}$$

Other values of κ_1 and κ_2 still yield exact solutions of the three-dimensional field equations, but do not satisfy (2.13).

From (2.2), (2.3) and (2.11) the stress associated with the displacement (2.10) is

$$\sigma_{rr} = \frac{2\lambda\mu}{\lambda+2\mu}(\Delta - z\nabla^2\overline{w}) + 2\mu\left\{\frac{\partial\overline{u}}{\partial r} - z\frac{\partial^2\overline{w}}{\partial r^2} + F\frac{\partial^2\Delta}{\partial r^2} + B\frac{\partial^2\nabla^2\overline{w}}{\partial r^2}\right\},$$

$$\sigma_{\theta\theta} = \frac{2\lambda\mu}{\lambda+2\mu}(\Delta - z\nabla^2\overline{w}) + 2\mu\left\{\frac{\overline{u}}{r} + \frac{1}{r}\frac{\partial\overline{v}}{\partial\theta} - z\left(\frac{1}{r}\frac{\partial\overline{w}}{\partial r} + \frac{1}{r^2}\frac{\partial^2\overline{w}}{\partial\theta^2}\right)\right\}$$
$$+ 2\mu\left\{F\left(\frac{1}{r}\frac{\partial\Delta}{\partial r} + \frac{1}{r^2}\frac{\partial^2\Delta}{\partial\theta^2}\right) + B\left(\frac{1}{r}\frac{\partial\nabla^2\overline{w}}{\partial r} + \frac{1}{r^2}\frac{\partial^2\nabla^2\overline{w}}{\partial\theta^2}\right)\right\},$$

$$\sigma_{r\theta} = \mu\left\{\frac{1}{r}\frac{\partial\overline{u}}{\partial\theta} + \frac{\partial\overline{v}}{\partial r} - \frac{\overline{v}}{r} - z\left(\frac{2}{r}\frac{\partial^2\overline{w}}{\partial r\partial\theta} - \frac{2}{r^2}\frac{\partial\overline{w}}{\partial\theta}\right)\right\}$$
$$+ \mu\left\{F\left(\frac{2}{r}\frac{\partial^2\Delta}{\partial r\partial\theta} - \frac{2}{r^2}\frac{\partial\Delta}{\partial\theta}\right) + B\left(\frac{2}{r}\frac{\partial^2\nabla^2\overline{w}}{\partial r\partial\theta} - \frac{2}{r^2}\frac{\partial\nabla^2\overline{w}}{\partial\theta}\right)\right\},$$

$$\sigma_{rz} = \mu\left\{\left(\frac{dF}{dz} + G\right)\frac{\partial\Delta}{\partial r} + \left(\frac{dB}{dz} + C\right)\frac{\partial\nabla^2\overline{w}}{\partial r}\right\},$$

$$\sigma_{\theta z} = \mu\left\{\left(\frac{dF}{dz} + G\right)\frac{1}{r}\frac{\partial\Delta}{\partial\theta} + \left(\frac{dB}{dz} + C\right)\frac{1}{r}\frac{\partial\nabla^2\overline{w}}{\partial\theta}\right\},$$

$$\sigma_{zz} = 0. \tag{2.14}$$

Explicit expressions for $G(z), C(z), F(z)$ and $B(z)$ can be obtained by integration of (2.11), and are given in [5]. If the plate is symmetric, so that λ and μ are even functions of z, then F and C are even functions of z, and G and B are odd functions of z.

3.   CONCENTRATED FORCE IN AN INHOMOGENEOUS THICK PLATE

The exact three-dimensional solution for a concentrated line force in an inhomogeneous plate of arbitrary thickness was derived in [5]. We take the required solution of (2.6) to be of the form

$$\overline{u}(r,\theta) = (\alpha\ln r + \beta)\cos\theta, \quad \overline{v}(r,\theta) = (-\alpha\ln r + \beta)\sin\theta,$$
$$\overline{w}(r,\theta) = \gamma r\ln r\,\cos\theta \tag{3.1}$$

where α, β are constants, and it follows that

$$\Delta = (\alpha + 2\beta)\frac{\cos\theta}{r}, \quad \Omega = (-\alpha + 2\beta)\frac{\sin\theta}{r}, \quad \nabla^2\overline{w} = 2\gamma\frac{\cos\theta}{r}, \tag{3.2}$$

and that (2.6) are satisfied provided that

$$\alpha(\kappa_1 - 1) + 2\beta(\kappa_1 + 1) + 2\gamma\kappa_2 = 0. \qquad (3.3)$$

Then, from (2.10), the corresponding three-dimensional displacement in the thick plate is

$$u(r, \theta, z) = \left\{ \alpha \ln r + \beta - \gamma z(1 + \ln r) - F\frac{\alpha + 2\beta}{r^2} - B\frac{2\gamma}{r^2} \right\} \cos \theta,$$

$$v(r, \theta, z) = \left\{ -\alpha \ln r + \beta + \gamma z \ln r - F\frac{\alpha + 2\beta}{r^2} - B\frac{2\gamma}{r^2} \right\} \sin \theta,$$

$$w(r, \theta, z) = \left\{ \gamma r \ln r + G\frac{\alpha + 2\beta}{r} + C\frac{2\gamma}{r} \right\} \cos \theta. \qquad (3.4)$$

Then, from (2.14), the stress is given as

$$\sigma_{rr} = \left\{ \frac{2\mu}{\lambda + 2\mu} \frac{\{2\alpha(\lambda + \mu) + 2\beta\lambda - \gamma(3\lambda + 2\mu)z\}}{r} \right.$$
$$\left. + \frac{4\mu\{F(\alpha + 2\beta) + 2B\gamma\}}{r^3} \right\} \cos \theta,$$

$$\sigma_{\theta\theta} = \left\{ \frac{2\mu}{\lambda + 2\mu} \frac{\{2\alpha\lambda + 2\beta(\lambda + \mu) - \gamma(3\lambda + 2\mu)z\}}{r} \right.$$
$$\left. - \frac{4\mu\{F(\alpha + 2\beta) + 2B\gamma\}}{r^3} \right\} \cos \theta,$$

$$\sigma_{r\theta} = \mu \left\{ \frac{\{-(\alpha + 2\beta) + 2\gamma z\}}{r} + \frac{4\mu\{F(\alpha + 2\beta) + 2B\gamma\}}{r^3} \right\} \sin \theta,$$

$$\sigma_{rz} = \mu \left\{ -\left(\frac{dF}{dz} + G \right) \frac{(\alpha + 2\beta)}{r^2} - \left(\frac{dB}{dz} + C \right) \frac{2\gamma}{r^2} \right\} \cos \theta,$$

$$\sigma_{\theta z} = \mu \left\{ -\left(\frac{dF}{dz} + G \right) \frac{(\alpha + 2\beta)}{r^2} - \left(\frac{dB}{dz} + C \right) \frac{2\gamma}{r^2} \right\} \sin \theta. \qquad (3.5)$$

In general, the stress components σ_{rz} and $\sigma_{\theta z}$ give rise to non-zero stress resultants $\int_{-h}^{h} \sigma_{rz}\, dz$ and $\int_{-h}^{h} \sigma_{\theta z}\, dz$. However, these stress resultants are zero, and so only in-plane resultant forces are present, if γ is chosen such that

$$(\alpha + 2\beta) \int_{-h}^{h} \mu \left(\frac{dF}{dz} + G \right) dz + 2\gamma \int_{-h}^{h} \mu \left(\frac{dB}{dz} + C \right) dz = 0. \qquad (3.6)$$

From (2.7), (2.8) and (2.11) it can be shown that

$$\int_{-h}^{h} \mu \left(\frac{dF}{dz} + G \right) dz = -2h(\kappa_1 \widehat{\mu} + \kappa_2 \overline{\mu}),$$

$$\int_{-h}^{h} \mu \left(\frac{dB}{dz} + C \right) dz = -2h(\kappa_2 \widehat{\mu} + \kappa_3 \overline{\mu}), \qquad (3.7)$$

where

$$2h\widehat{\mu} = \int_{-h}^{h} z\mu(z)dz, \quad \kappa_3 = \frac{4 \int_{-h}^{h} \{\mu(\lambda + \mu)/(\lambda + 2\mu)\} z^2 dz}{2h\overline{\mu}}. \qquad (3.8)$$

Therefore (3.6) can be written as

$$(\alpha + 2\beta)(\kappa_1 \widehat{\mu} + \kappa_2 \overline{\mu}) + 2\gamma(\kappa_2 \widehat{\mu} + \kappa_3 \overline{\mu}) = 0. \qquad (3.9)$$

If the plate is symmetric, then $\kappa_2 = 0$ and $\widehat{\mu} = 0$, and therefore in this case $\gamma = 0$.

The resultant force exerted by a cylinder of radius r with its axis coincident with the $z-$axis on the material outside the cylinder acts in the $x-$direction and has magnitude P, where

$$P = -2 \int_{-h}^{h} \int_{-\pi}^{\pi} (\sigma_{rr} \cos \theta - \sigma_{r\theta} \sin \theta) r d\theta dz. \qquad (3.10)$$

from which it can be shown, from (2.7), (2.8) and (3.5) that

$$P = -2\pi h \overline{\mu} \{\alpha(\kappa_1 + 1) + 2\beta(\kappa_1 - 1) + 2\gamma\kappa_2\}, \qquad (3.11)$$

and hence, from (3.3), $P = -4\pi h \overline{\mu}(\alpha - 2\beta)$, which is the same as the classical result for a homogeneous thin plate subject to the deformation (3.1). Since P is independent of r, the solution can be interpreted as describing the displacement and stress in the plate due to a line force at $r = 0$ acting in the x direction. As in standard plane theories for a homogeneous material, the displacement and stress are singular as $r \to 0$, thus contradicting the underlying small strain assumption of linear elasticity theory. Therefore, as in the theory for homogeneous materials, the solution should be regarded as an asymptotic solution as $r \to \infty$. It is of interest that P does not depend on γ, and so even for a non-symmetric plate P is not affected by the bending displacement mode that is included in (3.1). Another feature is that although in the inhomogeneous plate the stress includes terms of order r^{-3} as well as terms of order r^{-1}, these higher order terms do not contribute to P.

The coefficients α, β and γ need to be expressed in terms of P and the elastic moduli. It follows from the above analysis that

$$\alpha = -\frac{P}{8\pi h\overline{\mu}}\left\{1 + \frac{\kappa_3\overline{\mu} - \kappa_2\widehat{\mu}}{\overline{\mu}(\kappa_1\kappa_3 - \kappa_2^2)}\right\}, \quad \beta = \frac{P}{16\pi h\overline{\mu}}\left\{1 - \frac{\kappa_3\overline{\mu} - \kappa_2\widehat{\mu}}{\overline{\mu}(\kappa_1\kappa_3 - \kappa_2^2)}\right\},$$

$$\gamma = \frac{P(\kappa_2\overline{\mu} - \kappa_1\widehat{\mu})}{8\pi h\overline{\mu}^2((\kappa_1\kappa_3 - \kappa_2^2)}. \tag{3.12}$$

If the plate is symmetric, then $\kappa_2 = 0$ and $\widehat{\mu} = 0$, and (3.12) reduce to

$$\alpha = -\frac{P}{8\pi h\overline{\mu}}\left\{1 + \frac{1}{\kappa_1}\right\}, \quad \beta = \frac{P}{16\pi h\overline{\mu}}\left\{1 - \frac{1}{\kappa_1}\right\}, \quad \gamma = 0. \tag{3.13}$$

If the plate is homogeneous, then it is easily shown that (3.12) reduce further to the classical solution.

The stress and displacement due to distributed in-plane forces can be constructed by superposition of solutions for concentrated forces.

The solution for a line-load acting on the surface of a half -space can be derived in a similar way and was described in [5].

4.   HIGHER ORDER POINT SINGULARITIES

Stress and displacement singularities of higher order can be derived by differentiation, just as for homogeneous materials, and as described by, for example, Timoshenko and Goodier [10, Chap. 4]. Consider for example a pair of equal opposite concentrated forces of magnitude P situated at $x = \pm\delta$, $y = 0$ and directed in the positive and negative x directions respectively. Denote the displacement (3.4) by $\mathbf{u}(x, y, z)$ and the stress (3.5) by $\sigma(x, y, z)$. In the terminology of Love [9, Chap.9] this comprises a 'force pair without moment'. Then the displacement $\mathbf{u}_1$ and stress σ_1 due to the pair of forces are given by superposition as

$$\mathbf{u}_1 = \mathbf{u}(x + \delta, y, z) - \mathbf{u}(x - \delta, \ y, \ z)\}, \ \sigma_1 = \sigma(x + \delta, \ y, \ z) - \sigma(x - \delta, \ y, \ z). \tag{4.1}$$

Hence in the limit $\delta \to 0$, $\mathbf{u}_1 = 2\delta\partial\mathbf{u}/\partial x$, $\sigma_1 = 2\delta\partial\sigma/\partial x$, and it is assumed that $P \to \infty$, $\delta \to 0$ in such a way that $Q = 2P\delta$ is finite. Details were given in [5]

By superposing two such force pairs, with lines of action along the x and y axes respectively. there results the displacement corresponding to a centre of dilatation. This result can also be obtained by considering solutions of (2.6) in which $\overline{u}, \overline{v}$, and $\overline{w}$ depend only on r.

In a similar way, a 'force pair with moment' is formed by two concentrated forces, of equal magnitude P, with the first acting in the positive x-direction at $(0, \delta)$, and the second in the negative x-direction at $(0, -\delta)$.

Hence the pair of forces exert a moment of magnitude $2\delta P = Q$ about the z-axis. In this case the displacement $\mathbf{u}_2$ and the stress σ_2 are given by $\mathbf{u}_1 = 2\delta\partial\mathbf{u}/\partial y$, $\sigma_1 = 2\delta\partial\sigma/\partial y$. By superposing two such force pairs oriented along the x and y axes there follows the solution for a centre of rotation about the z-axis. This also may be derived by considering solutions in which $\overline{u}, \overline{v}$, and $\overline{w}$ depend only on r.

Higher order singularities may be described by higher order derivatives of $\mathbf{u}$ and σ with respect to x and y. An example was given in [5]

5.   VOLTERRA DISLOCATIONS

The displacement

$$\overline{u} = \alpha\cos\theta\ln r + \varepsilon\theta\sin\theta, \quad \overline{v} = -\alpha\sin\theta\ln r + \varepsilon\theta\cos\theta + \beta\sin\theta,$$
$$\overline{w} = \delta r\theta\sin\theta + \gamma r\ln r\cos\theta, \tag{5.1}$$

where α. β, γ, δ and ε are constants, satisfies (2.6) provided that

$$(\kappa_1 - 1)(\alpha + \varepsilon) + (\kappa_1 + 1)\beta + 2\kappa_2(\delta + \gamma) = 0. \tag{5.2}$$

By substituting (5.1) into (2.10), it follows that the displacement

$$u = (\alpha - \gamma z)\cos\theta\ln r + (\varepsilon - \delta z)\theta\sin\theta - \gamma z\cos\theta$$
$$\quad - \{(\alpha + \beta + \varepsilon)F(z) + 2(\delta + \gamma)B(z)\}\,r^{-2}\cos\theta,$$
$$v = -(\alpha - \gamma z)\sin\theta\ln r + (\varepsilon - \delta z)\theta\cos\theta + (\beta - \delta z)\sin\theta$$
$$\quad - \{(\alpha + \beta + \varepsilon)F(z) + 2(\delta + \gamma)B(z)\}\,r^{-2}\sin\theta,$$
$$w = \gamma r\ln r\cos\theta + \delta r\theta\sin\theta + \{(\alpha + \beta + \varepsilon)G(z) + 2(\delta + \gamma)C(z)\}\,r^{-1}\cos\theta, \tag{5.3}$$

satisfies the equations of three-dimensional elasticity, for any specified dependence of λ and μ on z. If θ is restriced to the range $0 \le \theta < 2\pi$, then in plane elasticity the in-plane components of (5.1) represent a deformation in which the tangential component of displacement $\overline{v}$ is discontinuous by an amount $2\varepsilon\pi$ across $\theta = 0$. If θ is replaced by $\theta + \pi/2$, the displacement is one in which the radial component $\overline{u}$ is discontinuous on this plane. In general, for a non-symmetrical plate, the discontinuity in v induces a slope discontinuity in w. The associated stress is, from (2.14)

$$\sigma_{rr} = \left[\left\{\frac{2\lambda\mu}{\lambda+2\mu}\{\alpha+\beta+\varepsilon-2(\gamma+\delta)z\}+2\mu\{\alpha-\gamma z\}\right\}\frac{1}{r}\right.$$

$$\left. +4\mu\left\{(\alpha+\beta+\varepsilon)F(z)+2(\delta+\gamma)B(z)\right\}\frac{1}{r^3}\right]\cos\theta,$$

$$\sigma_{\theta\theta} = \left[\left\{\frac{2\lambda\mu}{\lambda+2\mu}\{\alpha+\beta+\varepsilon-2(\gamma+\varepsilon)z\}+2\mu\{\beta+\varepsilon-z(2\delta+\gamma)\}\right\}\frac{1}{r}\right.$$

$$\left. -4\mu\left\{(\alpha+\beta+\varepsilon)F(z)+2(\delta+\gamma)B(z)\right\}\frac{1}{r^3}\right]\cos\theta,$$

$$\sigma_{r\theta} = \left[-\mu(\alpha+\beta-\varepsilon-2\gamma z)\frac{1}{r}\right.$$

$$\left. +4\mu\left\{(\alpha+\beta+\varepsilon)F(z)+2(\delta+\gamma)B(z)\right\}\frac{1}{r^3}\right]\sin\theta,$$

$$\sigma_{rz} = -\mu[(\alpha+\beta+\varepsilon)\{F(z)+G(z)\}+2(\delta+\gamma)\{B(z)+C(z)\}]\frac{1}{r^2}\cos\theta,$$

$$\sigma_{\theta z} = -\mu[(\alpha+\beta+\varepsilon)\{F(z)+G(z)\}+2(\delta+\gamma)\{B(z)+C(z)\}]\frac{1}{r^2}\sin\theta,$$

$$(5.4)$$

The solution contains the five constants α. β, γ, δ and ε which must satisfy (5.2) so that four of them are independent. The constant ε is a measure of the magnitude of the dislocation. If the out-of-plane stress resultants are zero, then by analogy with (3.9)

$$(\alpha+\beta+\varepsilon)(\kappa_1\widehat{\mu}+\kappa_2\overline{\mu})+2(\gamma+\delta)(\kappa_2\widehat{\mu}+\kappa_3\overline{\mu})=0 \qquad (5.5)$$

Another possible condition is that the resultant force on a cylinder enclosing the dislocation should be zero. The condition for this is (3.10) with $P=0$, which gives, by analogy with (3.11)

$$\{\alpha(\kappa_1+1)+\beta(\kappa_1-1)+\varepsilon(\kappa_1-3)\}\overline{\mu}+4\gamma\widehat{\mu}=0 \qquad (5.6)$$

Furthermore, if the transverse displacement $\overline{w}$ is continuous, then $\delta=0$. Stress resultants on surfaces $r=const.$ can be prescribed by superposing continuous solutions of the equations.

A solution for a screw dislocation was given by Spencer and Selvadurai [7].

6. A SEMI-INFINITE CRACK

The displacement

$$\bar{u} = r^{1/2}(a\cos\frac{1}{2}\theta + b\cos\frac{3}{2}\theta), \quad \bar{v} = r^{1/2}(c\sin\frac{1}{2}\theta - b\sin\frac{3}{2}\theta),$$
$$\bar{w} = er^{3/2}\cos\frac{1}{2}\theta, \tag{6.1}$$

where a, b, c and e are constants, satisfies (2.6) provided that

$$(3\kappa_1 + 1)a + (\kappa_1 + 3)c + 4\kappa_2 e = 0 \tag{6.2}$$

In plane theory, the above expressions for $\bar{u}$ and $\bar{v}$ lead to the solution for a semi-infinite opening (mode I) crack lying in the half-plane $y = 0$, $x < 0$. The corresponding three-dimensional solution of the field equations is, from (2.10)

$$u = r^{1/2}\{(a - \frac{3}{2}ez)\cos\frac{1}{2}\theta + b\cos\frac{3}{2}\theta)\}$$
$$-r^{-3/2}\{(\frac{1}{4}(3a+c)F(z) + eB(z)\}\cos\frac{1}{2}\theta\}$$
$$v = r^{1/2}\{(c + \frac{1}{2}ez)\sin\frac{1}{2}\theta - b\sin\frac{3}{2}\theta)\}$$
$$-r^{-3/2}\{(\frac{1}{4}(3a+c)F(z) + eB(z)\}\sin\frac{1}{2}\theta\},$$
$$w = r^{3/2}e\cos\frac{1}{2}\theta + r^{-1/2}\{\frac{1}{2}(3a+c)G(z) + 2eC(z)\}\cos\frac{1}{2}\theta. \tag{6.3}$$

The corresponding stress is

$$\sigma_{rr} = \frac{2\lambda\mu}{\lambda + 2\mu}\{\frac{1}{2}(3a+c) - 2ez\}r^{-1/2}\cos\frac{1}{2}\theta$$
$$+\mu\{(a - \frac{3}{2}ez)\cos\frac{1}{2}\theta + b\cos\frac{3}{2}\theta\}r^{-1/2}$$
$$+\mu\left\{\frac{3}{4}(3a+c)F(z) + 3eB(z)\right\}r^{-5/2}\cos\frac{1}{2}\theta,$$
$$\sigma_{\theta\theta} = \frac{2\lambda\mu}{\lambda + 2\mu}\{\frac{1}{2}(3a+c) - 2ez\}r^{-1/2}\cos\frac{1}{2}\theta$$
$$+\mu\{(2a+c - \frac{5}{2}ez)\cos\frac{1}{2}\theta - b\cos\frac{3}{2}\theta\}r^{-1/2}$$

$$-\mu\left\{\frac{3}{4}(3a+c)F(z)+3eB(z)\right\}r^{-5/2}\cos\frac{1}{2}\theta,$$

$$\sigma_{r\theta} = -\mu\left\{\frac{1}{2}(a+c-ez)\sin\frac{1}{2}\theta+b\sin\frac{3}{2}\theta\right\}r^{-1/2}$$

$$+\mu\left\{\frac{3}{4}(3a+c)F(z)+3eB(z)\right\}r^{-5/2}\sin\frac{1}{2}\theta,$$

$$\sigma_{rz} = -\mu[\frac{1}{4}(3a+c)\{F(z)+G(z)\}+e\{B(z)+C(z)]r^{-3/2}\cos\frac{1}{2}\theta,$$

$$\sigma_{\theta z} = -\mu[\frac{1}{4}(3a+c)\{F(z)+G(z)\}+e\{B(z)+C(z)]r^{-3/2}\sin\frac{1}{2}\theta,$$

$$(6.4)$$

In general the available constants cannot be chosen so as to prescribe zero tractions on the crack surfaces, but they can be chosen to be such that no resultant tractions act on these surfaces.

The problem of an anti-plane strain (mode III) crack was discussed in [7]. The mode II (sliding) crack may be analysed in a similar manner to the mode I crack described above.

7. DISCUSSION

A feature of all the solutions presented above is that the order of the singularity in the three-dimensional solution for inhomogeneous material exceeds by two the order of the singularity in the corresponding two-dimensional problem. From (2.14) it is clear that this situation will obtain in any case in which the two-dimensional solution is singular. It is not clear how this result should be interpreted. There is an inherent contradiction in applying linear elasticity to singular problems, because linear elasticity assumes that displacement gradients are small, whereas at a singularity they become infinite. Nevertheless it is usually considered that linear elasticity solutions are valid asymptotically at large distances from a singularity where, for example, 'large' means large compared to a crack-tip radius. However the analysis seems to suggest that even smooth inhomogeneities may give rise to unexpectedly large local concentrations of strain energy density, which may have implications for failure and fracture analysis.

References

[1] T.G. Rogers and A.J.M. Spencer, Thermoelastic stress analysis of moderately thick inhomogeneous and laminated plates. Int. J. Solids Structures 25 (1989) 1467-1482

[2] T.G. Rogers, Exact three-dimensional bending solutions for inhomogeneous and laminated elastic plates. In Elasticity, Mathematical methods and applications, G.Eason and R.W. Ogden, eds., Ellis Horwood, Chichester 1990, 301-313

[3] A.J.M. Spencer, Three-dimensional elasticity solutions for stretching of inhomogeneous and laminated plates. In Elasticity, Mathematical methods and applications, G.Eason and R.W. Ogden, eds., Ellis Horwood, Chichester, 1990, 347-356

[4] A.J.M. Spencer, A stress function formulation for a class of exact solutions for functionally graded elastic plates. In IUTAM Symposium on transformation problems in composite and active materials, Y.A Bahei-el-Din and G.J. Dvorak, eds., Kluwer Academic Publishers, Dordrecht, 1998, 161-172

[5] A.J.M. Spencer, Concentrated force solutions for an inhomogeneous thick elastic plate. Z. angew Math.Phys. 51 (2000) 573-590

[6] M. Abid Mian and A.J.M. Spencer, Exact solutions for functionally graded and laminated elastic materials. J. Mech. Phys. Solids 46 (1998) 2283-2295

[7] A.J.M. Spencer and A.P.S. Selvadurai, Some generalized anti-plane strain problems for an inhomogeneous elastic halfspace. J. Engineering Mathematics 34 (1998) 403-416

[8] J.H. Michell, On the direct determination of stress in an elastic solid, with applications to the theory of plates. Proc. London Math. Soc. 31 (1900) 100-124

[9] P.V. Kaprielian, T.G. Rogers and A.J.M. Spencer, Theory of laminated elastic plates I. Isotropic laminae. Phil. Trans. Roy .Soc. Lond. A324 (1988) 565-594

[10] A.E.H. Love, A treatise on the mathematical theory of elasticity, 4th edition, Cambridge University Press, Cambridge, 1927.

[11] S. Timoshenko and J.N. Goodier, Theory of Elasticity, McGraw Hill, New York, 1951.

STRETCH, FLEXURE AND TWIST IN FINITE ELASTICITY

David F. Parker

School of Mathematics, University of Edinburgh,
The King's Buildings, Edinburgh, EH9 3JZ, UK

D.F.Parker@ed.ac.uk

Abstract   The classical stretching, torsion and flexure solutions of linear elasticity
are important ingredients of asymptotic treatments of slender structures.
They each describe solutions in a cylindrical elastic region, with zero trac-
tion applied over the lateral boundary. For rods, bars and tubes of arbitrary
cross-section, anisotropy and transverse non-uniformity, they provide the
relevant flexural, torsional and extensional rigidities, which relate resul-
tant forces and moments to appropriate curvatures, twist and stretch in
the deformed configuration. To leading order, these then characterize the
constitutive behaviour.

In finite elasticity, it is less clear how to choose the canonical states of
deformation which should yield equivalent nonlinear constitutive laws in
a one-dimensional theory. The helical solutions of Ericksen[1] provide a
two-parameter set of such solutions, but this family must be enlarged by
considering other solutions with no body forces or lateral tractions. Static
solutions having strain a periodic function of the axial material coordinate
provide such a four-parameter set of canonical deformations of a typical
cross-section. These solutions are shown to play a central rôle in the asymp-
totic description of slender elastic bodies, within which both the rotation
and strain may become large.

1.   INTRODUCTION

The equilibrium, and indeed the dynamics, of slender rods, wires and
tubes has long been treated in technical theories by considering the shape
$\boldsymbol{x} = \boldsymbol{r}(s)$ of a representative curve (frequently called the *curve of centres*).
Associated with each point of the curve is a *stress resultant* $\boldsymbol{F}(s)$ and a
stress couple $\boldsymbol{M}(s)$. Each value of s is associated with a *cross-section* of the
material. Then the vectors $\boldsymbol{F}(s_0)$ and $\boldsymbol{M}(s_0)$ measure the resultant force
and moment (about $\boldsymbol{r}(s_0)$) imparted by the material in $s > s_0$ upon the

material in $s < s_0$. A standard exercise in statics, involving the resultant externally applied load $\boldsymbol{L}(s)\,\delta s$ and moment $\boldsymbol{P}(s)\,\delta s$ arising from the body forces and surface tractions acting upon material in the interval $(s, s + \delta s)$, yields the equilibrium equations

$$\boldsymbol{F}'(s) + \boldsymbol{L}(s) = \boldsymbol{0} \ , \qquad \boldsymbol{M}'(s) + \boldsymbol{r}'(s) \times \boldsymbol{F}(s) + \boldsymbol{P}(s) = \boldsymbol{0} \ . \quad (1.1)$$

However, the theory is incomplete without *constitutive laws* relating $\boldsymbol{F}$ and $\boldsymbol{M}$ to the material configuration. A secondary issue is the evaluation of both $\boldsymbol{L}$ and $\boldsymbol{P}$ as integrals, which presumes knowledge of the deformed configuration of each cross-section. An asymptotic derivation, based upon the full three-dimensional analysis, naturally incorporates this knowledge and allows for very general material cross-sections.

In the linear theory of (initially straight) beams, the four canonical solutions describing stretching, torsion and bending in each principal plane provide both the constitutive laws for slender beam theory and describe the deformations of typical cross-sections relative to a local orthogonal triad of basis vectors. The resulting *elastica theory* and its analogies with rigid body dynamics were developed a century ago (see e.g. Love[2]). In developing related theories for nonlinear elasticity, it is pertinent to seek similar canonical deformation states in which stress resultants and stress couples are linked mathematically to the stretch, the curvatures and the twist. Just as, in elastica theory, the constitutive laws for the one-dimensional theory are unaffected by externally applied tractions and body forces even though these are responsible for $\boldsymbol{L}$ and $\boldsymbol{P}$, in the finite-elastic theory the canonical configurations correspond to static deformations without surface traction or body force. The helical deformations of Ericksen [1, 3] and Muncaster [4, 5] provide elegant examples of such deformations, in which the Cauchy-Green strain is independent of the axial coordinate. The treatment allows for initially straight bars of any cross-section, with anisotropy and material composition depending on the two lateral coordinates. It has an elegant variational formulation. The theory also is readily extended to initially twisted or curved bars. However, the associated set of canonical deformations possesses only two independent parameters, not the four of elastica theory. The explanation is that elastica theory allows only a two parameter set of solutions having constant stretch, twist and curvatures, without distributed loading. Typically, a more general solution without applied loads or moments involves curvatures and twist which are periodic in the coordinate s. This is the motivation for seeking canonical finite-elastic configurations which are periodic in an axial material coordinate. Within an approximate treatment of large deformations of slender rods,

bars or tubes, such deformations then become the leading-order state of deformation at a typical material cross-section.

Section 2 describes the kinematics and statics of pre-twisted, pre-curved rods using curvilinear material coordinates. Deformations with periodically varying strain are identified in Section 3 as solutions to a variational problem, which predicts formulae for the stress resultant and stress couple. These canonical deformations are used, in Section 4, to deduce constitutive laws for finite flexure, twist and stretch. In Section 5, linearization for slender rods recovers the standard St.-Venant solutions, so showing the current theory to naturally generalize elastica theory.

2.   FINITE DEFORMATIONS OF SLENDER BARS

The finite elastic theory is developed for slender bars or tubes which, in a reference (unstressed) configuration, have cross-section which varies only gradually with respect to an axial coordinate. Specifically, if $\boldsymbol{I}_K$ ($K = 1, 2, 3$) denotes a fixed orthonormal triad, with X_K ($K = 1, 2, 3$) the associated Lagrangian coordinates, there exists a *reference curve* $\boldsymbol{X} = \boldsymbol{R}(Y)$ and a second orthonormal triad $\{\boldsymbol{E}_1, \boldsymbol{E}_2, \boldsymbol{E}_3 \equiv \boldsymbol{R}'(Y)\}$ (n.b. $|\boldsymbol{R}'(Y)| = 1$) such that the reference configuration may be written as

$$\boldsymbol{X} = X_K \boldsymbol{I}_K = \boldsymbol{R}(Y) + Y_\alpha \boldsymbol{E}_\alpha(Y) \qquad (K = 1, 2, 3; \; \alpha = 1, 2) \quad (2.1)$$

with the material occupying the region parameterized by $Y \in (0, L)$, $(Y_1, Y_2) \in \mathcal{D}(\varepsilon Y)$ for some $\varepsilon \ll 1$. A typical magnitude of $(Y_1^2 + Y_2^2)^{1/2}$ on $\partial \mathcal{D}$ is O(1), while $L = O(\varepsilon^{-1})$, or larger.

Since $\boldsymbol{E}_3(Y)$ is the unit tangent to the reference curve and since there exists a vector $\bar{\boldsymbol{\kappa}} \equiv \bar{\kappa}_J \boldsymbol{E}_J$ such that

$$\boldsymbol{E}'_J(Y) = \bar{\boldsymbol{\kappa}} \times \boldsymbol{E}_J,$$

the quantities $\bar{\kappa}_\alpha(Y)$ ($\alpha = 1, 2$) may be regarded as reference *curvatures* with $\bar{\kappa}_3(Y)$ the reference *twist* of the bar. Special cases having each $\bar{\kappa}_J$ constant correspond to helical bars, including (for $\bar{\kappa}_2 = \bar{\kappa}_3 = 0$) a simply curved bar and (for $\bar{\kappa}_1 = \bar{\kappa}_2 = 0$) a uniformly twisted (corkscrew) bar.[1]

Deformed configurations are written in terms of the (non-orthogonal) curvilinear coordinate system $(Y_1, Y_2, Y_3 {\equiv} Y)$. Since $\boldsymbol{E}_J = H_{JK} \boldsymbol{I}_K$, where $H_{JK} = \boldsymbol{E}_J \cdot \boldsymbol{I}_K$ are components of the orthogonal matrix $\mathbf{H}$, then

$$H'_{JL}(Y) = \bar{S}_{JK} H_{KL} \qquad \text{with} \quad \bar{S}_{JK} = -\epsilon_{JKL} \bar{\kappa}_L.$$

---

[1]The theory developed here applies not just to these generalizations of straight bars, but also to bars for which the $\bar{\kappa}_J$, like $\partial \mathcal{D}$, depend only gradually on Y and so may be written as functions of εY.

Also, the Jacobian matrix $\partial X_K / \partial Y_L$ has elements given by

$$\frac{\partial X_K}{\partial Y_L} = H_{RK} V_{RL} \qquad \text{and} \qquad \mathbf{V} = \begin{pmatrix} 1 & 0 & \bar{\kappa}_3 Y_2 \\ 0 & 1 & -\bar{\kappa}_3 Y_1 \\ 0 & 0 & \Delta \end{pmatrix}$$

in which $\Delta = 1 + \bar{\kappa}_2 Y_1 - \bar{\kappa}_1 Y_2 \equiv \Delta(Y_1, Y_2)$ is the Jacobian of the coordinate transformation (differing from 1 due to the varying orientations of the plane material cross-sections $Y = $ constant).

A deformed configuration is represented as

$$\boldsymbol{x} \equiv x_j \boldsymbol{I}_j = \boldsymbol{r}(Y) + u_i(Y_\alpha, Y) \boldsymbol{e}_i(Y), \qquad Y_\alpha \in \mathcal{D}(\varepsilon Y) \tag{2.2}$$

in which $\boldsymbol{x} = \boldsymbol{r}(Y)$ is the deformed *curve of centres* with unit tangent $\boldsymbol{e}_3 \equiv \boldsymbol{r}'(Y)/|\boldsymbol{r}'(Y)|$ and with $\boldsymbol{e}_1$, $\boldsymbol{e}_2$ and $\boldsymbol{e}_3$ forming a (rotating) orthogonal triad of unit vectors. The *stretch* is $\Lambda \equiv |\boldsymbol{r}'(Y)|$, while the *curvatures* κ_α ($\alpha = 1, 2$) and *twist* κ_3, in the deformed state, are defined by $\boldsymbol{e}_i'(Y) = \boldsymbol{\kappa} \times \boldsymbol{e}_i$ with $\boldsymbol{\kappa} = \kappa_j \boldsymbol{e}_j$, so that $\boldsymbol{e}_i' = S_{ij} \boldsymbol{e}_j$ with $S_{ij} = -\epsilon_{ijk} \kappa_k$.

Within the bar, the deformation gradient has components

$$\frac{\partial x_j}{\partial X_K} = \frac{\partial x_j}{\partial Y_L} \frac{\partial Y_L}{\partial X_K} = \frac{\partial x_j}{\partial Y_L} U_{LS} H_{SK}$$

in which $\mathbf{U} \equiv \mathbf{V}^{-1}$ is the matrix

$$\mathbf{U} = \begin{pmatrix} 1 & 0 & -\bar{\kappa}_3 \Delta^{-1} Y_2 \\ 0 & 1 & \bar{\kappa}_3 \Delta^{-1} Y_1 \\ 0 & 0 & \Delta^{-1} \end{pmatrix} \equiv \mathbf{U}(Y_\alpha, \varepsilon Y). \tag{2.3}$$

The Cauchy-Green strain has components $G_{JK} = H_{RJ} p_{jR} p_{jS} H_{SK}$, in which $p_{jS} \equiv (\partial x_j / \partial Y_L) U_{LS}$ are components of $\mathbf{p}$ the deformation gradient relative to axes parallel to the local reference triad $\{\boldsymbol{E}_S(Y)\}$. For *any* bar, the strain-energy density W satisfies $W = W(\mathbf{pH}, Y_\alpha, Y) = W(\hat{\mathbf{H}} \mathbf{pH}, Y_\alpha, Y)$ for all proper orthogonal $\hat{\mathbf{H}}$. For bars with material composition depending only gradually on Y this specializes to

$$W = W(\mathbf{p}, Y_\alpha, \varepsilon Y) = W(\hat{\mathbf{H}} \mathbf{p}, Y_\alpha, \varepsilon Y). \tag{2.4}$$

The associated Piola-Kirchhoff stress components $\tau_{Jj} \equiv \partial W / \partial x_{j,J}$ then allow introduction of stress components

$$\sigma_{Sj} = H_{SJ} \tau_{Jj} = \frac{\partial W}{\partial p_{jS}} \equiv \sigma_{Sj}(\mathbf{p}, Y_\alpha, Y), \tag{2.5}$$

in terms of which the Euler equations become

$$0 = \frac{\partial \tau_{Jj}}{\partial X_J} = U_{MQ} H_{QJ} \frac{\partial \tau_{Jj}}{\partial Y_M} = U_{MQ} H_{QJ} \left(H_{SJ} \frac{\partial \sigma_{Sj}}{\partial Y_M} + \delta_{M3} H_{SJ}'(Y) \sigma_{Sj} \right)$$

$$= U_{MS} \frac{\partial \sigma_{Sj}}{\partial Y_M} + \Delta^{-1} \bar{S}_{S3} \sigma_{Sj} = U_{MS} \frac{\partial \sigma_{Sj}}{\partial Y_M} + \Delta^{-1} (\bar{\kappa}_2 \sigma_{1j} - \bar{\kappa}_1 \sigma_{2j}). \tag{2.6}$$

Equations (2.6) are simplified using a variational formulation. The stored elastic energy in a material region $\mathcal{R} \equiv \mathcal{D}(\varepsilon Y) \times [Y_0, Y_0 + L]$ is

$$E \equiv \iiint_{\mathcal{R}} W(\mathbf{p}, Y_\alpha, \varepsilon Y) \, \Delta(Y_\alpha, \varepsilon Y) \, \mathrm{d}\boldsymbol{Y} \, .$$

Treating first variations arising from displacements $x_j \mapsto x_j + \eta_j(Y_\alpha, Y)$, so that $p_{jS} \mapsto p_{jS} + \dfrac{\partial \eta_j}{\partial Y_L} U_{LS}$ and $\delta W \mapsto \sigma_{Sj} \dfrac{\partial \eta_j}{\partial Y_L} U_{LS}$, leads to

$$\delta E = -\iiint_{\mathcal{R}} \eta_j(Y_\alpha, Y) \frac{\partial}{\partial Y_L}(\Delta U_{LS}\sigma_{Sj}) \mathrm{d}\boldsymbol{Y} + \iint_{\partial \mathcal{R}} \eta_j \Delta U_{LS}\sigma_{Sj} n_L \mathrm{d}S \, ,$$

in which $U_{LS} n_L \mathrm{d}S$ are components of a vector element of reference area. From this, it is seen that the Euler-Lagrange equations are

$$\frac{\partial}{\partial Y_L}(\Delta U_{LS}\sigma_{Sj}) = 0 \, , \tag{2.7}$$

which, after differentiation, using (2.3), is found to be equivalent to (2.6). Also, on the lateral surface $\partial \mathcal{D} \times [Y_0, Y_0 + L]$, the natural boundary conditions $n_L U_{LS}\sigma_{Sj} = 0$ correspond to a traction-free surface.

Over any cross-section $Y = $ constant, the stress resultant $\boldsymbol{F} = F_j \boldsymbol{I}_j$ and stress couple $\boldsymbol{M} = M_j \boldsymbol{I}_j$ have components defined through

$$F_j \equiv \iint_{\mathcal{D}} \sigma_{3j}(Y_\alpha, Y) \, \mathrm{d}Y_1 \mathrm{d}Y_2 = F_j(Y)$$

$$M_j \equiv \iint_{\mathcal{D}} \epsilon_{jpq}[x_p(Y_\alpha, Y) - r_p(Y)]\sigma_{3q} \, \mathrm{d}Y_1 \mathrm{d}Y_2$$

$$= \iint_{\mathcal{D}} \epsilon_{jpq} x_p(Y_\alpha, Y)\sigma_{3q}(Y_\alpha, Y) \, \mathrm{d}Y_1 \mathrm{d}Y_2 - \epsilon_{jpq} r_p(Y) F_q(Y) \, . \tag{2.8}$$

Then, when the lateral boundary $\partial \mathcal{D} \times [Y_0, Y_0 + L]$ is traction-free and body forces are absent, use of $\epsilon_{jpq} x_p \partial / \partial Y_L (\Delta U_{LS}\sigma_{Sq}) = 0$ in integration of equations (2.7) shows that equilibrium configurations are governed by

$$\frac{\mathrm{d}\boldsymbol{F}}{\mathrm{d}Y} = \boldsymbol{0} \qquad \text{and} \qquad \frac{\mathrm{d}}{\mathrm{d}Y}[\boldsymbol{M} + \boldsymbol{r}(Y) \times \boldsymbol{F}] = \boldsymbol{0} \, . \tag{2.9}$$

Thus (consistent with the Euler equations and boundary conditions) the stress resultant $\boldsymbol{F}$ and moment $\boldsymbol{M} + \boldsymbol{r}(Y) \times \boldsymbol{F}$ are independent of Y.[2]

---

[2]In general, with body forces $\boldsymbol{b}(Y_\alpha, Y) = b_j \boldsymbol{I}_j$ these are replaced by

$$\frac{\mathrm{d}\boldsymbol{F}}{\mathrm{d}Y} = -\iint_{\mathcal{D}} \boldsymbol{b}(Y_\alpha, Y) \, \mathrm{d}Y_1 \mathrm{d}Y_2 \equiv -\boldsymbol{L}(Y) \, ,$$

$$\frac{\mathrm{d}}{\mathrm{d}Y}[\boldsymbol{M} + \boldsymbol{r}(Y) \times \boldsymbol{F}] = -\iint_{\mathcal{D}} (\boldsymbol{x} - \boldsymbol{r}) \times \boldsymbol{b}(Y_\alpha, Y) \, \mathrm{d}Y_1 \mathrm{d}Y_2 \equiv -\boldsymbol{P}(Y) \, .$$

3. CANONICAL DEFORMATIONS

In the special case ($\varepsilon \to 0$) in which $\bar{\kappa}_j$, Δ, W and $\mathcal{D}$ are strictly independent of Y, *canonical deformations* $x_j = x_j(Y_\alpha, Y)$ exist with A-periodic strain [6, 7] such that for some proper orthogonal matrix $\mathbf{B}$

$$F_{jL}(Y_\alpha, Y + A) = B_{jk}F_{kL}(Y_\alpha, Y), \quad F_{jL}(Y_\alpha, Y) \equiv \frac{\partial x_j}{\partial Y_L}.$$

Associated with $\mathbf{B}$ is a unit vector $\mathbf{B}$, such that $\mathbf{Bb} = \mathbf{b}$, $|\mathbf{b}| = 1$ and a skew-symmetric (rotation) matrix $\mathbf{Q}$ such that

$$\mathbf{B} = e^{\Theta\mathbf{Q}} = \mathbf{I} + \mathbf{Q}\sin\Theta + \mathbf{Q}^2(1 - \cos\Theta)$$

so that $\mathbf{B}$ describes a rotation about $\mathbf{b} \equiv b_j\mathbf{I}_j$ through angle Θ. The elements of $\mathbf{Q}$ are $Q_{jk} = -\epsilon_{ijk}b_i$, so that $\mathbf{Qb} = \mathbf{0}$ and $\mathbf{Q}^3 = -\mathbf{Q}$. The corresponding configuration may be represented as

$$x_j(Y_\alpha, Y) = c_j + ab_jY + \bar{x}_j(Y_\alpha, Y) \text{ with } \bar{x}_j(Y_\alpha, Y + A) = B_{jk}\bar{x}_k(Y_\alpha, Y).$$

These are canonical deformations in which any two cross-sections labelled by Y and $Y + A$ differ only by a translation through distance aA parallel to $\mathbf{b}$ and a rotation through angle Θ about an axis parallel to $\mathbf{b}$ and passing through $\boldsymbol{x} = c_j\mathbf{I}_j$. Special cases ($\mathbf{G}$ independent of Y) include flexure of a strip ($a = 0$), combined torsion and extension of a bar and helical solutions [1].

In *all* periodic deformations, the stress components satisfy $\sigma_{Sj}(Y_\alpha, Y + A) = B_{jk}\sigma_{Sk}(Y_\alpha, Y)$ so that the stress resultant and stress couple satisfy

$$F_j(Y + A) = B_{jk}F_k(Y), \quad M_j(Y + A) = B_{jk}M_k(Y),$$

so yielding the results $F_j = b_jF$ and $M_j + \epsilon_{jkl}\bar{x}_k(0, Y)F_l = b_jM$. Thus, the traction over the cross-section at *each* value Y is equipollent to the same *wrench*, consisting of a *force* $\boldsymbol{F} = F\boldsymbol{b}$ and a *moment* $M\boldsymbol{b}$ about *any point* $\boldsymbol{x} = (c_j + \lambda b_j)\mathbf{I}_j = \boldsymbol{c} + \lambda\boldsymbol{b}$ on the *canonical axis*.

The constitutive relations for the scalars F and M are readily obtained from a variational description. Define the *cross-sectional energy* as

$$\mathcal{E}(Y) \equiv \iint_\mathcal{D} W(\mathbf{p}, Y_\alpha)\,\Delta(Y_\alpha)\,\mathrm{d}Y_1\mathrm{d}Y_2, \tag{3.1}$$

so that the strain energy within $\mathcal{D} \times [Y_0, Y_0 + A]$ is

$$E \equiv \int_{Y_0}^{Y_0+A} \mathcal{E}(Y)\,\mathrm{d}Y \equiv E(a, A, \Theta). \tag{3.2}$$

Stationary values of E are then sought for variations of a, A and Θ, with the unit vector $\boldsymbol{b}$, skew-symmetric matrix $\mathbf{Q}$ ($Q_{ij} = \epsilon_{ikj}b_k$) and translation vector $\boldsymbol{c}$ held fixed and with configurations given by

$$x_j(Y_\alpha, Y) = c_j + ab_j Y + \bar{x}_j(Y_\alpha, Y)\,, \qquad \bar{x}_j(Y_\alpha, Y + A) = B_{jk}\bar{x}_k(Y_\alpha, Y)\,.$$

From (3.2) and (2.5), it follows that

$$
\begin{aligned}
\frac{\partial E}{\partial a} &= \iiint_{\mathcal{R}} \Delta\sigma_{Qj}\frac{\partial p_{jQ}}{\partial a}\mathrm{d}\boldsymbol{Y} = \iiint_{\mathcal{R}} \Delta\sigma_{Qj}U_{LQ}\frac{\partial}{\partial Y_L}\left(\frac{\partial x_j}{\partial a}\right)\mathrm{d}\boldsymbol{Y} \\
&= \iint_{\partial\mathcal{R}} \frac{\partial x_j}{\partial a}\Delta U_{LQ}\sigma_{Qj}n_L\,\mathrm{d}S - \iiint_{\mathcal{R}} \frac{\partial x_j}{\partial a}\frac{\partial}{\partial Y_L}(\Delta U_{LQ}\sigma_{Qj})\,\mathrm{d}\boldsymbol{Y} \\
&= \left[\iint_{\mathcal{D}} \left(Yb_j + \frac{\partial \bar{x}_j}{\partial a}\right)\sigma_{3j}\,\mathrm{d}Y_1\mathrm{d}Y_2\right]_{Y_0}^{Y_0+A} = Ab_j F_j = A\boldsymbol{b}\cdot\boldsymbol{F}
\end{aligned}
$$

so that

$$F = \boldsymbol{b}\cdot\boldsymbol{F} = A^{-1}\frac{\partial E}{\partial a} \equiv F(a, A, \Theta)\,. \tag{3.3}$$

Analogously, using identities involving $\partial p_{jQ}/\partial\Theta$ and $\partial\bar{x}_j/\partial\Theta$ yields

$$
\begin{aligned}
\frac{\partial E}{\partial \Theta} &= b_l\iint_{\mathcal{D}} \epsilon_{lkm}[x_k(Y_\alpha, Y_0) - r_k(Y_0)]\sigma_{3m}(Y_\alpha, Y_0)\mathrm{d}Y_1\mathrm{d}Y_2 + \epsilon_{lkm}b_l r_k(Y_0)F_m \\
&= \boldsymbol{b}\cdot[\boldsymbol{M} + \boldsymbol{r}(Y_0)\times\boldsymbol{F}] = \boldsymbol{b}\cdot\boldsymbol{M} = M \equiv M(a, A, \Theta)\,. \tag{3.4}
\end{aligned}
$$

Additionally, it is found (since $\mathbf{B}^T\mathbf{b} = \mathbf{b}$) that

$$\frac{\partial E}{\partial A} = \mathcal{E}(Y_0 + A) + ab_j B_{jk}F_k = \mathcal{E}(Y_0 + A) + aF\,. \tag{3.5}$$

Since this shows that $\mathcal{E}(Y_0 + A)$ is independent of Y_0, then $E = A\mathcal{E}$ and

$$\mathcal{E} + A\frac{\partial\mathcal{E}}{\partial A} = \frac{\partial E}{\partial A} = \mathcal{E} + \frac{a}{A}\frac{\partial}{\partial a}(A\mathcal{E})\,.$$

This implies that $\mathcal{E} = \widehat{E}(d, \Theta)$, with $d \equiv aA$, so that the *wrench* involves $\boldsymbol{F} = F\boldsymbol{b}$ and $\widehat{\boldsymbol{M}} \equiv M\boldsymbol{b}$, where

$$F = A^{-1}\frac{\partial E}{\partial a} = A^{-1}\frac{\partial\widehat{E}}{\partial d}\,, \qquad M = \frac{\partial E}{\partial\Theta} = A^{-1}\frac{\partial\widehat{E}}{\partial\Theta}\,, \tag{3.6}$$

with d and Θ being the axial and angular displacements of cross-sections for which Y differs by one period A of the canonical deformation.

4.   CONSTITUTIVE LAWS FOR THE ROD

For arbitrary constant $\mathcal{D}$ and $\bar{\kappa}_J$, extremals of E determine canonical deformations in which the *curve of centres*

$$\boldsymbol{x} = \boldsymbol{r}(Y) \equiv aY\boldsymbol{b} + \bar{\boldsymbol{x}}(0, Y) \quad \text{with} \quad \bar{x}_j(Y_\alpha, Y + A) = B_{jk}\bar{x}_k(Y_\alpha, Y)$$

describes a curve periodically coiled around a helix (here $\boldsymbol{c} = \boldsymbol{0}$, without loss of generality). Each portion $[Y_0, Y_0 + A]$ has the same shape, parameterized by a, A, Θ and Y. The stress resultant and stress couple are

$$\boldsymbol{F} = F\boldsymbol{b}, \qquad \boldsymbol{M} = M\boldsymbol{b} + F\boldsymbol{b} \times \boldsymbol{r}(Y) = M\boldsymbol{b} + F\boldsymbol{b} \times \bar{\boldsymbol{x}}(0, Y). \quad (4.1)$$

The unit tangent $\boldsymbol{t}$ and stretch Λ are given by

$$\boldsymbol{t} = \boldsymbol{t}(Y) \equiv \boldsymbol{r}'(Y)/|\boldsymbol{r}'(Y)|, \qquad \Lambda = |\boldsymbol{r}'(Y)| \tag{4.2}$$

(N.B. $\Lambda\boldsymbol{t} \times \boldsymbol{F} = -F\boldsymbol{b} \times \boldsymbol{r}'(Y) = -\boldsymbol{M}'(Y)$, as in classical beam theory).

The constitutive relations for $\boldsymbol{t} \cdot \boldsymbol{F}$ and for the intrinsic components of $\boldsymbol{M}$ need to be related to the deformed material configuration. The orthonormal triad $\{\boldsymbol{e}_1, \boldsymbol{e}_2, \boldsymbol{e}_3\}$ is chosen with $\boldsymbol{e}_3 = \boldsymbol{t}$ and with

$$\boldsymbol{e}_3 \cdot \iint_{\mathcal{D}} (\boldsymbol{x} - \boldsymbol{r}) \times \boldsymbol{e}_\alpha Y_\alpha \, \Delta \, \mathrm{d}Y_1 \mathrm{d}Y_2 = 0, \quad \iint_{\mathcal{D}} (\boldsymbol{x} - \boldsymbol{r}) \cdot \boldsymbol{e}_\alpha Y_\alpha \Delta \, \mathrm{d}Y_1 \mathrm{d}Y_2 > 0,$$

so identifying $\boldsymbol{e}_1(Y)$, $\boldsymbol{e}_2(Y)$ and $\boldsymbol{e}_3(Y)$ at each cross section. Alternatively, since $\boldsymbol{x} = \boldsymbol{r} + u_i\boldsymbol{e}_i$, this gives

$$\iint_{\mathcal{D}} (u_1 Y_2 - u_2 Y_1)\Delta \, \mathrm{d}Y_1 \mathrm{d}Y_2 = 0, \quad \iint_{\mathcal{D}} (u_1 Y_1 + u_2 Y_2)\Delta \, \mathrm{d}Y_1 \mathrm{d}Y_2 > 0.$$

At each cross section, the curvatures κ_α and material twist $\kappa_3 \equiv \tau$ are computed from $\kappa_j = \frac{1}{2}\Lambda^{-1}\epsilon_{jkl}\boldsymbol{e}'_k \cdot \boldsymbol{e}_l$ (or $\Lambda\kappa_1 = \boldsymbol{e}'_2 \cdot \boldsymbol{e}_3$, etc.). Resolving $\boldsymbol{b}$, $\bar{\boldsymbol{x}}(0, Y)$, $\boldsymbol{F}$ and $\boldsymbol{M}$ into intrinsic components as $\boldsymbol{b} = \tilde{b}_j\boldsymbol{e}_j$, $\bar{\boldsymbol{x}}(0, Y) = \tilde{u}_l\boldsymbol{e}_l$, $\boldsymbol{F} = \tilde{F}_j\boldsymbol{e}_j$ and $\boldsymbol{M} = \tilde{M}_j\boldsymbol{e}_j$ then gives

$$\tilde{F}_j = \tilde{b}_j F, \qquad \tilde{M}_j = \tilde{b}_j M + \epsilon_{jkl}\tilde{b}_k\tilde{u}_l F, \tag{4.3}$$

with *each* of $\tilde{b}_j$, $\tilde{u}_l$, $\tilde{\kappa}_j$ and Λ being periodic in Y, with F and M given by (3.3) and (3.4) (or by (3.6)). For each value a, with $|a|$ not greatly exceeding 1, we expect one (or more) helical solutions to exist for each (moderate) ratio Θ/A. As A is increased, we anticipate bifurcation from stable helical solutions to solutions with A-periodic strain. The helical solutions typically cover only a 2-parameter region of Λ, κ_j space, while, for each period A, a stable periodic solution may be expected to cover a 3-parameter region. Accordingly, a 4-parameter region will be covered by the parameters a, A, Θ and $Y \in [Y_0, Y_0 + A)$. These canonical behaviours, computed from minimization of E in (3.2) when $\bar{\kappa}_J$, W and $\mathcal{D}$ are taken to be *independent of Y*, are the natural candidates for finite-elastic constitutive laws, even for nonuniformly pre-twisted, pre-curved rods.

5.   THE SMALL STRAIN LIMIT

For initially straight rods ($\boldsymbol{E}_J \equiv \boldsymbol{I}_J$), configurations $\boldsymbol{x} = \boldsymbol{r}(Y) + Y_\alpha \boldsymbol{e}_\alpha + \epsilon w_j(\boldsymbol{Y})\boldsymbol{e}_j$, with $\boldsymbol{\kappa} = \epsilon \hat{\boldsymbol{\kappa}}(Y)$, $\Lambda = 1 + \epsilon \hat{a}(Y)$ (so that $\boldsymbol{e}'_j(Y) = \epsilon \hat{\boldsymbol{\kappa}} \times \boldsymbol{e}_j$) involve small strain. For isotropic materials (with Lamé constants λ, μ), the linearized Euler equations become

$$(\lambda + \mu)(w_{1,11} + w_{2,12}) + \mu(w_{1,11} + w_{1,22})$$
$$= \lambda \hat{\kappa}_2(Y) - (\lambda + \mu)w_{3,13} - \mu w_{1,33} ,$$
$$(\lambda + \mu)(w_{1,12} + w_{2,22}) + \mu(w_{2,11} + w_{2,22})$$
$$= -\lambda \hat{\kappa}_1(Y) - (\lambda + \mu)w_{3,23} - \mu w_{2,33} ,$$
$$\mu(w_{3,11} + w_{3,22}) = -(\lambda + \mu)(w_{1,13} + w_{2,23}) - (\lambda + 2\mu)w_{3,33} ,$$

where $,_j$ denotes $\partial/\partial Y_j$. Imposing the appropriate boundary conditions over $\partial \mathcal{D}$ leads, when $\hat{\kappa}_j$ and $\hat{a}$ are constants, to the 4-parameter set of solutions

$$w_1 = -\sigma \hat{a} Y_1 - \sigma \hat{\kappa}_1 Y_1 Y_2 + \tfrac{1}{2}\sigma \hat{\kappa}_2(Y_1^2 - Y_2^2) ,$$
$$w_2 = -\sigma \hat{a} Y_2 + \tfrac{1}{2}\sigma \hat{\kappa}_1(Y_1^2 - Y_2^2) + \sigma \hat{\kappa}_2 Y_1 Y_2 , \quad w_3 = \hat{\kappa}_3 \Psi(Y_\alpha) , \qquad (5.1)$$

in which $\sigma = \tfrac{1}{2}\lambda/(\lambda + \mu)$ is Poisson's ratio. The displacements multiplying $\hat{a}$ describe Poisson contraction, those multiplying $\hat{\kappa}_1$ and $\hat{\kappa}_2$ describe flexure, while $\Psi(Y_\alpha)$ is the warping function for the cross-section $\mathcal{D}$ (the two standard *bending functions* for $\mathcal{D}$ arise when $\hat{\kappa}'_1$ and $\hat{\kappa}'_2$ are constants, so introducing into w_3 contributions proportional to $\hat{\kappa}'_1$ and $\hat{\kappa}'_2$).

Configurations (5.1), although involving standard solutions of linear elasticity, *do not require that displacements or rotations be small*.

With the standard choice of $Y_\alpha = 0$ as the centroid of $\mathcal{D}$ with $\boldsymbol{e}_1$ and $\boldsymbol{e}_2$ along principal inertia axes, the stress couple components become

$$\tilde{M}_j = A_j \hat{\kappa}_j \qquad \text{(no summation)} , \qquad\qquad \tilde{F}_3 = A_4 \hat{a} , \qquad\qquad (5.2)$$

for some constants $A_1, \ldots, A_4$. Inserting these into the equilibrium equations (see (2.9)) $\boldsymbol{F} = F\boldsymbol{b}$, $\boldsymbol{M}'(Y) = \Lambda F\boldsymbol{b} \times \boldsymbol{e}_3$ gives, when Λ is replaced by 1 (as is consistent with the small strain approximation), the elastica equations which are known to be analogous to those for the spinning of an asymmetric top.

It is a standard result that, for $A_1 = A_2$, every solution has $\tilde{b}_3 = \boldsymbol{b} \cdot \boldsymbol{e}_3$ either constant or periodic (and expressible in terms of elliptic functions). While $\tilde{b}_1$ and $\tilde{b}_2$ are not always periodic, each of $\tilde{b}_l$ and $\hat{\kappa}_j$ is expressible in terms of circular and elliptic functions. Generally, if $A_1 \neq A_2$, the angle $\cos^{-1} \tilde{b}_3$ between the tangent $\boldsymbol{t}$ and $\boldsymbol{b}$ oscillates non-periodically. However,

454

special solutions will have $\tilde{b}_l$ and $\hat{\kappa}_j$ periodic in Y.[3] These periodic-strain solutions are the small strain limit of minimizers for (3.2). Since the constitutive laws (5.2) apply to both periodic and non-periodic configurations, it seems plausible to base nonlinear constitutive laws upon (4.3) in all deformations, even when $\bar{\boldsymbol{\kappa}}$, $\mathcal{D}$ and W depend explicitly on Y and when body forces and surface tractions are present.

References

[1] Ericksen, J L (1977) *Bending a Prism to Helical Form*, Arch. Rat. Mech. Anal. **66**, 1-18.

[2] Love, A E H (1926) *A Treatise on the Mathematical Theory of Elasticity* (4th edition), Dover reprint (1944), New York.

[3] Ericksen, J L (1977) *On the formulation of St.-Venant's Problem*, in *Nonlinear Analysis and Mechanics: Heriot-Watt Symposium, Volume I* ed. R.J. Knops, 158-186.

[4] Muncaster, R G (1979) *St.-Venant's Problem in Nonlinear Elasticity: A Study of Cross-sections*, in *Nonlinear Analysis and Mechanics: Heriot-Watt Symposium, Volume IV* ed. R.J. Knops, 17-75.

[5] Muncaster, R G (1979) *Invariant Manifolds in Mechanics I: The General Construction of Coarse Theories from Fine Theories*, Arch. Rat. Mech. Anal. **84**, 353-373.

[6] Ericksen, J L (1979) *Periodic Solutions for Elastic Prisms*, Quart. Appl. Math. **37**, 443-446.

[7] Parker, D F (1987) *Dynamical Equations for the Finite Elastic Bending, Torsion, and Stretching of Rods*, Quart. Appl. Math. **45**, 533-548.

[8] Parker, D F and Tsoy, E N (1999) *Explicit Solitary and Periodic Solutions for Optical Cascading*, J. Engng. Math. **36**, 149-162.

---

[3]It is anticipated, though not yet confirmed, that by seeking solutions linear in the Jacobian elliptic functions cn, sn and dn, as performed in nonlinear optics [8], families of explicit solutions may be determined.

ASYMPTOTIC ANALYSIS OF HEAT TRANSFER IN A SYSTEM OF CHANNELS CONNECTED BY THIN CONDUCTING WALLS

A. Selsil, A.B. Movchan, N.V. Movchan

Department of Mathematical Sciences, University of Liverpool, Liverpool, U.K.

aselsil@liv.ac.uk, abm@liv.ac.uk, nvm@liv.ac.uk

Keywords: Asymptotics, multi-channel system, heat transfer.

Abstract   The aim of this work is to investigate the *temperature distribution* in a system of n thin channels, of thickness ε, with each channel separated by a thin conducting wall, of thickness ε^2. The problem considered is a $2D$ problem, with *nonhomogeneous heat equations* in the channels and *homogeneous heat equations* in the walls. Neumann boundary conditions are set on the upper and lower horizontal parts of the external boundary of the system, and *ideal thermal contact* is assumed between each layer. We use an *asymptotic method* to obtain a set of *solvability conditions*, which lead to a coupling between the temperatures in the channels. A particular example, incorporating chemical reactions inside the channels, highlights industrial applications of this work.

Introduction

The motivation for this work came from problems that arise in chemical engineering. In particular, the book by Hayes and Kolaczkowski [3] presents the theory of catalytic combustion where thermal interaction occurs between adjacent channels of a multi-channel system. In this paper we develop an asymptotic model that enables us to reduce the dimension of the problem and to describe accurately the thermal interaction through a thin wall of low thermal conductivity. The paper is organised as follows: in the first section we consider a model asymptotic problem involving the heat source density independent of the temperature; in the second part we relate the asymptotic algorithm to a steady-state chemical reaction which

generates the heat source density; the concluding section indicates directions for further development.

1.   A SIMPLE MODEL PROBLEM

Consider a system (shown in Fig. 1) which consists of two infinite channels Ω_1 and Ω_2 of width ε, separated by a thin conducting wall Ω_0 of width ε^2, where ε is a small positive parameter, $0 < \varepsilon \ll 1$. Assume that each channel Ω_j, $j = 1, 2$, is filled with a fluid whose temperature $T^{(j)}$ satisfies a *nonhomogeneous* heat equation

$$\mu_j \nabla^2 T^{(j)} - \frac{\partial T^{(j)}}{\partial t} + f^{(j)} = 0 \ \text{ in } \Omega_j, \quad j = 1, 2, \tag{1.1}$$

where μ_j denotes the thermal diffusivity, and $f^{(j)}$ is the heat source density (independent of $T^{(j)}$ and ε). The distribution of the temperature $T^{(0)}$ within the wall Ω_0 is described by a homogeneous heat equation

$$\mu_0 \nabla^2 T^{(0)} - \frac{\partial T^{(0)}}{\partial t} = 0 \ \text{ in } \Omega_0, \tag{1.2}$$

where μ_0 is the thermal diffusivity of the wall.

We assume that the temperatures $T^{(1)}$, $T^{(2)}$ and $T^{(0)}$ satisfy the *ideal thermal contact* conditions on the surfaces γ^+ and γ^- of the wall Ω_0, that is,

$$T^{(1)} = T^{(0)}, \ \mu_1 \frac{\partial T^{(1)}}{\partial y} = \mu_0 \frac{\partial T^{(0)}}{\partial y} \ \text{ on } \gamma^+, \tag{1.3}$$

$$T^{(2)} = T^{(0)}, \ \mu_2 \frac{\partial T^{(2)}}{\partial y} = \mu_0 \frac{\partial T^{(0)}}{\partial y} \ \text{ on } \gamma^-. \tag{1.4}$$

On the upper and lower horizontal external boundaries Γ^+ and Γ^- of the system we set the following flux conditions

$$\mu_1 \frac{\partial T^{(1)}}{\partial y} = \varepsilon p^+ \ \text{ on } \ \Gamma^+, \tag{1.5}$$

$$\mu_2 \frac{\partial T^{(2)}}{\partial y} = \varepsilon p^- \ \text{ on } \ \Gamma^-, \tag{1.6}$$

where $p^\pm$ are given functions of x and t, and are independent of ε.

Our objective is to find the temperature distribution in such a system and to analyse how changing the temperature in one channel affects the temperature in the other.

We assume that the diffusivity μ_0 of the wall is small compared to the diffusivities μ_1 and μ_2 of the channels, namely, μ_0 is taken in the form

$$\mu_0 = \varepsilon^3 \mu^*, \tag{1.7}$$
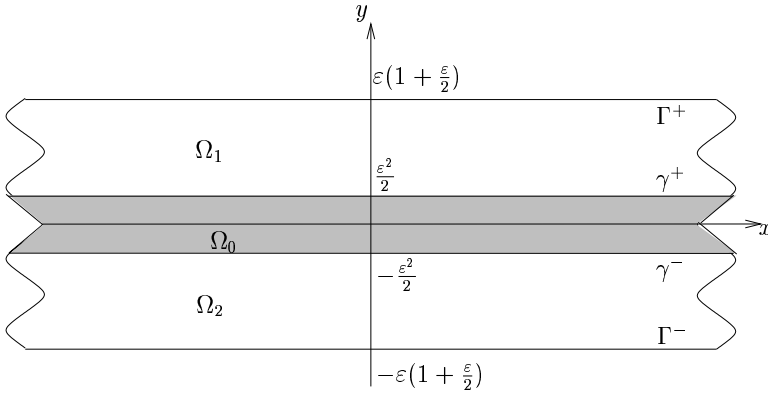
Figure 1   Two infinite channels separated by a thin conducting wall.

where μ^* has the same order of magnitude as μ_1 and μ_2.

Using an asymptotic technique similar to those described in [1] and [2], we shall construct asymptotic expansions for the temperatures $T^{(j)}$ in the following form

$$T^{(j)} = T_0^{(j)} + \varepsilon T_1^{(j)} + \varepsilon^2 T_2^{(j)} + \ldots, j = 0, 1, 2, \qquad (1.8)$$

and derive a set of conditions which "couple" the temperatures $T_0^{(1)}$ and $T_0^{(2)}$ in the two channels.

We begin by introducing new *scaled variables*

$$\tau_j = \frac{y_j}{\varepsilon} \text{ in } \Omega_j, \quad j = 1, 2, \quad \tau_0 = \frac{y}{\varepsilon^2} \text{ in } \Omega_0, \qquad (1.9)$$

where $\tau_i \in [-1/2, 1/2], i = 0, 1, 2; \; y_j = y + (-1)^j \varepsilon (1 + \varepsilon)/2, j = 1, 2.$

In these new variables the conditions (1.3) - (1.6) can be rewritten as follows:

$$T^{(1)}\Big|_{\tau_1 = -\frac{1}{2}} = T^{(0)}\Big|_{\tau_0 = \frac{1}{2}}, \quad \frac{\mu_1}{\varepsilon} \frac{\partial T^{(1)}}{\partial \tau_1}\Big|_{\tau_1 = -\frac{1}{2}} = \frac{\mu_0}{\varepsilon^2} \frac{\partial T^{(0)}}{\partial \tau_0}\Big|_{\tau_0 = \frac{1}{2}}, \qquad (1.10)$$

$$T^{(2)}\Big|_{\tau_2 = \frac{1}{2}} = T^{(0)}\Big|_{\tau_0 = -\frac{1}{2}}, \quad \frac{\mu_2}{\varepsilon} \frac{\partial T^{(2)}}{\partial \tau_2}\Big|_{\tau_2 = \frac{1}{2}} = \frac{\mu_0}{\varepsilon^2} \frac{\partial T^{(0)}}{\partial \tau_0}\Big|_{\tau_0 = -\frac{1}{2}}, \qquad (1.11)$$

$$\frac{\mu_1}{\varepsilon} \frac{\partial T^{(1)}}{\partial \tau_1}\Big|_{\tau_1 = \frac{1}{2}} = \varepsilon p^+, \quad \frac{\mu_2}{\varepsilon} \frac{\partial T^{(2)}}{\partial \tau_2}\Big|_{\tau_2 = -\frac{1}{2}} = \varepsilon p^-. \qquad (1.12)$$

Substituting (1.8) into (1.1) and (1.2) we obtain

$$\frac{\partial^2 T_0^{(j)}}{\partial \tau_j^2} = 0, \quad \frac{\partial^2 T_1^{(j)}}{\partial \tau_j^2} = 0, \; \tau_j \in (-1/2, 1/2), \; j = 0, 1, 2.$$

The latter implies that the functions $T_0^{(j)}, T_1^{(j)}$ in (1.8) are linear in τ_j, that is,

$$T_i^{(j)}(x, \tau_j, t) = c_1^{(i,j)}(x, t) + c_2^{(i,j)}(x, t)\tau_j, \; i = 0, 1, \; j = 0, 1, 2. \qquad (1.13)$$

From the flux conditions in (1.10)-(1.12), after substitution of condition (1.7), it follows that

$$\frac{\partial T_i^{(1)}}{\partial \tau_1}\bigg|_{\tau_1 = \pm 1/2} = 0, \; \frac{\partial T_i^{(2)}}{\partial \tau_2}\bigg|_{\tau_2 = \pm 1/2} = 0, \; i = 0, 1,$$

and therefore, the functions $T_0^{(1)}, T_0^{(2)}$ and $T_1^{(1)}, T_1^{(2)}$ are independent of τ_j.

The remaining two conditions in (1.10), (1.11), together with (1.13), give

$$T_0^{(0)}(x, 1/2, t) = c_1^{(0,0)}(x, t) + c_2^{(0,0)}(x, t)/2 = T_0^{(1)}(x, t),$$

$$T_0^{(0)}(x, -1/2, t) = c_1^{(0,0)}(x, t) - c_2^{(0,0)}(x, t)/2 = T_0^{(2)}(x, t).$$

Thus, eliminating $c_1^{(0,0)}(x, t)$ and $c_2^{(0,0)}(x, t)$, we obtain

$$T_0^{(0)}(x, \tau_0, t) = \frac{1}{2}(T_0^{(1)}(x, t) + T_0^{(2)}(x, t))$$

$$+(T_0^{(1)}(x, t) - T_0^{(2)}(x, t))\tau_0, \; \tau_0 \in [-1/2, 1/2].$$

In order to find the unknown functions $T_0^{(1)}(x, t)$ and $T_0^{(2)}(x, t)$, we derive a set of boundary value problems for the next terms $T_2^{(1)}$ and $T_2^{(2)}$ in the asymptotic representations (1.8) for the temperatures $T^{(1)}$ and $T^{(2)}$ in the two channels:

$$\frac{\partial^2 T_2^{(j)}}{\partial \tau_j^2} = -\frac{\partial^2 T_0^{(j)}}{\partial x^2} + \frac{1}{\mu_j}\left(\frac{\partial T_0^{(j)}}{\partial t} - f^{(j)}\right), \; \tau_j \in (-1/2, 1/2); \qquad (1.14)$$

$$\mu_1 \frac{\partial T_2^{(1)}}{\partial \tau_1}\bigg|_{\tau_1 = -1/2} = \mu^*(T_0^{(1)} - T_0^{(2)}) = \mu_2 \frac{\partial T_2^{(2)}}{\partial \tau_2}\bigg|_{\tau_2 = 1/2}, \qquad (1.15)$$

$$\frac{\partial T_2^{(1)}}{\partial \tau_1}\bigg|_{\tau_1 = 1/2} = \frac{p^+}{\mu_1}, \; \frac{\partial T_2^{(2)}}{\partial \tau_2}\bigg|_{\tau_2 = -1/2} = \frac{p^-}{\mu_2}, \qquad (1.16)$$

whose solvability conditions form a system of equations for $T_0^{(1)}$ and $T_0^{(2)}$:

$$\mu_1 \frac{\partial^2 T_0^{(1)}}{\partial x^2} - \frac{\partial T_0^{(1)}}{\partial t} - \mu^*(T_0^{(1)} - T_0^{(2)}) = -p^+ - \int_{-\frac{1}{2}}^{\frac{1}{2}} f^{(1)} d\tau_1, \qquad (1.17)$$

$$\mu_2 \frac{\partial^2 T_0^{(2)}}{\partial x^2} - \frac{\partial T_0^{(2)}}{\partial t} + \mu^*(T_0^{(1)} - T_0^{(2)}) = p^- - \int_{-\frac{1}{2}}^{\frac{1}{2}} f^{(2)} d\tau_2. \qquad (1.18)$$

Equations (1.17) and (1.18) are *coupled* via the term $(T_0^{(1)} - T_0^{(2)})$ which characterises the *jump* in temperature across the wall. The system (1.17), (1.18), together with the initial conditions at $t = 0$ and conditions as $x \to \pm\infty$ (or $x = 0$, $x = L$ for channels of finite length L), can then be solved (analytically or numerically) for the given source densities $f^{(1)}$, $f^{(2)}$ and the fluxes p^+, p^-.

As a particular example, we consider the case when there is no dependence on time, each channel is of length $L = 1[m]$, the fluxes p^+, p^-, measured in $[\frac{Km}{s}]$ and the source densities $f^{(1)}, f^{(2)}$, measured in $[\frac{K}{s}]$, are given by

$$p^+ = -10, \ p^- = 4, \ \int_{-1/2}^{1/2} f^{(1)} d\tau_1 = 0, \ \int_{-1/2}^{1/2} f^{(2)} d\tau_2 = 12,$$

the temperatures $T_0^{(1)}$ and $T_0^{(2)}$ satisfy the boundary conditions

$$T_0^{(1)}(0) = 760[K], \ T_0^{(2)}(0) = 730[K], \ \frac{dT_0^{(1)}}{dx}(1) = 0\left[\frac{K}{m}\right], \ \frac{dT_0^{(2)}}{dx}(1) = 0\left[\frac{K}{m}\right],$$

and the thermal diffusivities μ_1, μ_2 and m are equal to $0.2[\frac{m^2}{s}]$, $0.1[\frac{m^2}{s}]$ and $18[\frac{m^2}{s}]$, respectively. The resulting temperature distribution in each channel is shown in Figure 2(A). For comparison, we also present the solution for the uncoupled ($\mu^* = 0$) case (Figure 2(B)).
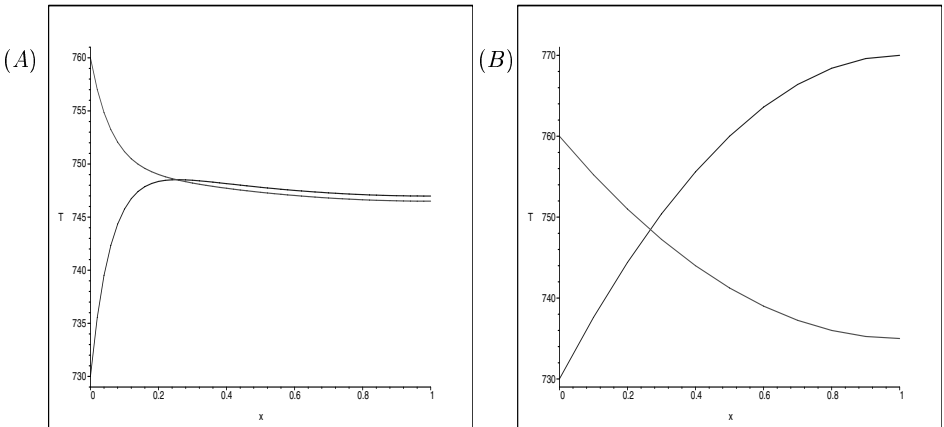
Figure 2 (A): Coupled temperature distribution (i.e. with the $(T_0^{(1)} - T_0^{(2)})$ terms), (B): Uncoupled temperature distribution (i.e. $\mu^* = 0$).

2.   STEADY FLOW

Assume now that a steady-state chemical reaction takes place in each channel, and the fluid moves steadily with a nonzero velocity $\mathbf{v}^{(j)}, j = 1, 2$. In this case the temperatures $T^{(1)}$ and $T^{(2)}$ satisfy the following equations in Ω_1 and Ω_2 respectively :

$$\mu_j \nabla^2 T^{(j)} - \mathbf{v}^{(j)} \cdot \nabla T^{(j)} - \frac{1}{\rho_j C_p^{(j)}}(\Delta H^{(j)})(-R^{(j)}) = 0, \ j = 1, 2, \quad (2.1)$$

where ρ_j is the fluid density, $C_p^{(j)}$ is the specific heat capacity, $(-R^{(j)})$ is the reaction rate, and $(\Delta H^{(j)})$ is the heat of the reaction. A positive value of $(\Delta H^{(j)})$ represents an endothermic reaction and a negative value represents an exothermic reaction.

We shall take the reaction rates $(-R^{(j)})$ in a simplified Arrhenius form (see, for example, [3], [4]),

$$(-R^{(j)}) = \mathcal{A}^{(j)} e^{-\frac{E^{(j)}}{RT^{(j)}(0)}} Y^{(j)}, \ j = 1, 2,$$

where $\mathcal{A}^{(j)}$ are constants known as the pre-exponential factors, $E^{(j)}$ is the activation energy, R is a gas constant, and $Y^{(j)}$ is the concentration of a reactant in the channel Ω_j which satisfies the equation

$$D_j \nabla^2 Y^{(j)} - \rho_j \mathbf{v}^{(j)} \cdot \nabla Y^{(j)} - (-R^{(j)}) = 0, \ j = 1, 2, \quad (2.2)$$

where D_j is the diffusion coefficient.

Equations (2.1) and (2.2) are complemented by the homogeneous heat equation (1.2) for the temperature $T^{(0)}$ inside the wall, the ideal thermal contact conditions (1.3)-(1.6) for the temperatures $T^{(j)}$ $(j = 0, 1, 2)$, the *non-slip* conditions for the velocities

$$\mathbf{v}^{(j)} = \mathbf{0} \text{ on } \gamma^{\pm} \cup \Gamma^{\pm},$$

and the conditions for the concentrations

$$\frac{\partial Y^{(1)}}{\partial y_1} = 0 \text{ on } \Gamma^+ \cup \gamma^+, \ \frac{\partial Y^{(2)}}{\partial y_2} = 0 \text{ on } \Gamma^- \cup \gamma^-.$$

We assume, in addition, that the flow in each channel is uni-directional[1], that is,

$$\mathbf{v}^{(j)} = (v^{(j)}(y_j), 0), \ j = 1, 2,$$

---

[1] This is a physically plausible assumption, since the channels are thin (of width ε).

where $v^{(j)}$ satisfies the equation

$$\nabla^2 v^{(j)} = G^{(j)}/\eta^{(j)},$$

with $G^{(j)}$ the pressure gradient, and $\eta^{(j)}$ the viscosity. The latter implies that the velocity distribution in each channel has the form

$$\mathbf{v}^{(j)} = ((G^{(j)}/2\eta^{(j)})y_j^2 + A^{(j)}y_j + B^{(j)}, 0), \ j = 1, 2, \tag{2.3}$$

where the constants $A^{(j)}$ and $B^{(j)}$ are obtained from the boundary conditions on $\Gamma^\pm$ and $\gamma^\pm$, and they are given by

$$A^{(j)} = 0, \ B^{(j)} = -\frac{G^{(j)}\varepsilon^2}{8\eta^{(j)}}, \ j = 1, 2.$$

Using the coordinate transformation (1.9) and the representations (2.3) for the velocities $\mathbf{v}^{(j)}$ in each channel, we rewrite the system (2.1), (2.2) in the form

$$\mu_j\left(\frac{\partial^2 T^{(j)}}{\partial x^2} + \frac{1}{\varepsilon^2}\frac{\partial^2 T^{(j)}}{\partial \tau_j^2}\right) - \Upsilon^{(j)}(4\tau_j^2 - 1)\frac{\partial T^{(j)}}{\partial x} - \frac{1}{\rho_j C_p^{(j)}}(\Delta H^{(j)})(-R^{(j)}) = 0,$$

$$D_j\left(\frac{\partial^2 Y^{(j)}}{\partial x^2} + \frac{1}{\varepsilon^2}\frac{\partial^2 Y^{(j)}}{\partial \tau_j^2}\right) - \Upsilon^{(j)}\rho_j(4\tau_j^2 - 1)\frac{\partial Y^{(j)}}{\partial x} - (-R^{(j)}) = 0, \quad (2.4)$$

where $\Upsilon^{(j)} = \dfrac{\varepsilon^2 G^{(j)}}{8\eta^{(j)}}$ is assumed to be of order $O(1)$, $j = 1, 2$.

We shall take the asymptotic expansions for the temperatures $T^{(j)}$ and the concentrations $Y^{(j)}$ in the form

$$T^{(j)} = T_0^{(j)} + \varepsilon T_1^{(j)} + \varepsilon^2 T_2^{(j)} + \ldots, j = 0, 1, 2, \tag{2.5}$$

$$Y^{(j)} = Y_0^{(j)} + \varepsilon Y_1^{(j)} + \varepsilon^2 Y_2^{(j)} + \ldots, j = 1, 2. \tag{2.6}$$

Substituting these into equations (2.1), (2.2), (1.2) and the boundary conditions we obtain (in the same way as in Section 1) that the functions $T_0^{(j)}, T_1^{(j)}, Y_0^{(j)}$ and $Y_1^{(j)}$ ($j = 1, 2$) are independent of τ_j, and the functions $T_2^{(j)}$ and $Y_2^{(j)}$ solve the following problems:

$$\mu_j\frac{\partial^2 T_2^{(j)}}{\partial \tau_j^2} = \frac{(\Delta H^{(j)})}{\rho_j C_p^{(j)}}A_o^{(j)}e^{-\frac{E^{(j)}}{RT_0^{(j)}(0)}}Y_0^{(j)} + \Upsilon^{(j)}(4\tau_j^2 - 1)\frac{dT_0^{(j)}}{dx} - \mu_j\frac{d^2 T_0^{(j)}}{dx^2},$$

$$\mu_1\frac{\partial T_2^{(1)}}{\partial \tau_1}\bigg|_{\tau_1=-1/2} = \mu^*(T_0^{(1)} - T_0^{(2)}) = \mu_2\frac{\partial T_2^{(2)}}{\partial \tau_2}\bigg|_{\tau_2=1/2},$$

$$\frac{\partial T_2^{(1)}}{\partial \tau_1}\bigg|_{\tau_1=1/2} = 0, \ \frac{\partial T_2^{(2)}}{\partial \tau_2}\bigg|_{\tau_2=-1/2} = 0; \tag{2.7}$$

$$D_j \frac{\partial^2 Y_2^{(j)}}{\partial \tau_j^2} = \mathcal{A}^{(j)} e^{-\frac{E^{(j)}}{RT_0^{(j)}(0)}} Y_0^{(j)} + \Upsilon^{(j)} \rho_j (4\tau_j^2 - 1) \frac{dY_0^{(j)}}{dx} - D_j \frac{d^2 Y_0^{(j)}}{dx^2},$$

$$\frac{\partial Y_2^{(j)}}{\partial \tau_j}\bigg|_{\tau_j=\pm 1/2} = 0, \ j = 1, 2. \tag{2.8}$$

The solvability conditions for (2.7) and (2.8) give the system of coupled differential equations for the leading terms $T_0^{(j)}$ and $Y_0^{(j)}$ ($j = 1, 2$) in the expansions (2.5), (2.6):

$$\mu_1 \frac{d^2 T_0^{(1)}}{dx^2} + \frac{2}{3} \Upsilon^{(1)} \frac{dT_0^{(1)}}{dx} - \mu^* (T_0^{(1)} - T_0^{(2)}) = \frac{(\Delta H^{(1)})}{\rho_1 C_p^{(1)}} \mathcal{A}^{(1)} e^{-\frac{E^{(1)}}{RT_0^{(1)}(0)}} Y_0^{(1)},$$

$$\mu_2 \frac{d^2 T_0^{(2)}}{dx^2} + \frac{2}{3} \Upsilon^{(2)} \frac{dT_0^{(2)}}{dx} + \mu^* (T_0^{(1)} - T_0^{(2)}) = \frac{(\Delta H^{(2)})}{\rho_2 C_p^{(2)}} \mathcal{A}^{(2)} e^{-\frac{E^{(2)}}{RT_0^{(2)}(0)}} Y_0^{(2)},$$

$$D_j \frac{d^2 Y_0^{(j)}}{dx^2} + \frac{2}{3} \Upsilon^{(j)} \rho_j \frac{dY_0^{(j)}}{dx} - \mathcal{A}^{(j)} e^{-\frac{E^{(j)}}{RT_0^{(j)}(0)}} Y_0^{(j)} = 0, \ j = 1, 2. \tag{2.9}$$

As a particular example, we solve the system (2.9) numerically, using Maple, for the following values of the parameters (having an endothermic reaction in channel 1 and an exothermic reaction in channel 2):

$$D^{(1)} = D^{(2)} = 2 \left[\frac{m^2}{s}\right], \quad \Upsilon^{(1)} = \Upsilon^{(2)} = 3 \left[\frac{1}{ms}\right]$$

$$\mu_1 = \mu_2 = 0.3 \left[\frac{m^2}{s}\right], \quad C_p^{(1)} = C_p^{(2)} = 0.5 \left[\frac{J}{molK}\right]$$

$$E^{(1)} = E^{(2)} = 2 \left[\frac{J}{mol}\right], \quad R = 3 \left[\frac{J}{mol.K}\right], \quad \mu^* = 3 \left[\frac{m^2}{s}\right]$$

$$\mathcal{A}^{(1)} = \mathcal{A}^{(2)} = 3 \left[\frac{mol}{kg.s}\right], \quad \Delta H^{(1)} = 2 \, [K], \quad \Delta H^{(2)} = -2 \, [K],$$

assuming that both channels are of finite length $L(= 1 \, [m])$, and the temperatures $T_0^{(1)}$, $T_0^{(2)}$ and the concentrations $Y_0^{(1)}$, $Y_0^{(2)}$ satisfy the following boundary conditions:

$$Y_0^{(1)}(0) = 0.3, \quad \frac{dY_0^{(1)}}{dx}(1) = 0 \left[\frac{1}{m}\right], \quad Y_0^{(2)}(0) = 0.1, \quad \frac{dY_0^{(2)}}{dx}(1) = 0 \left[\frac{1}{m}\right],$$
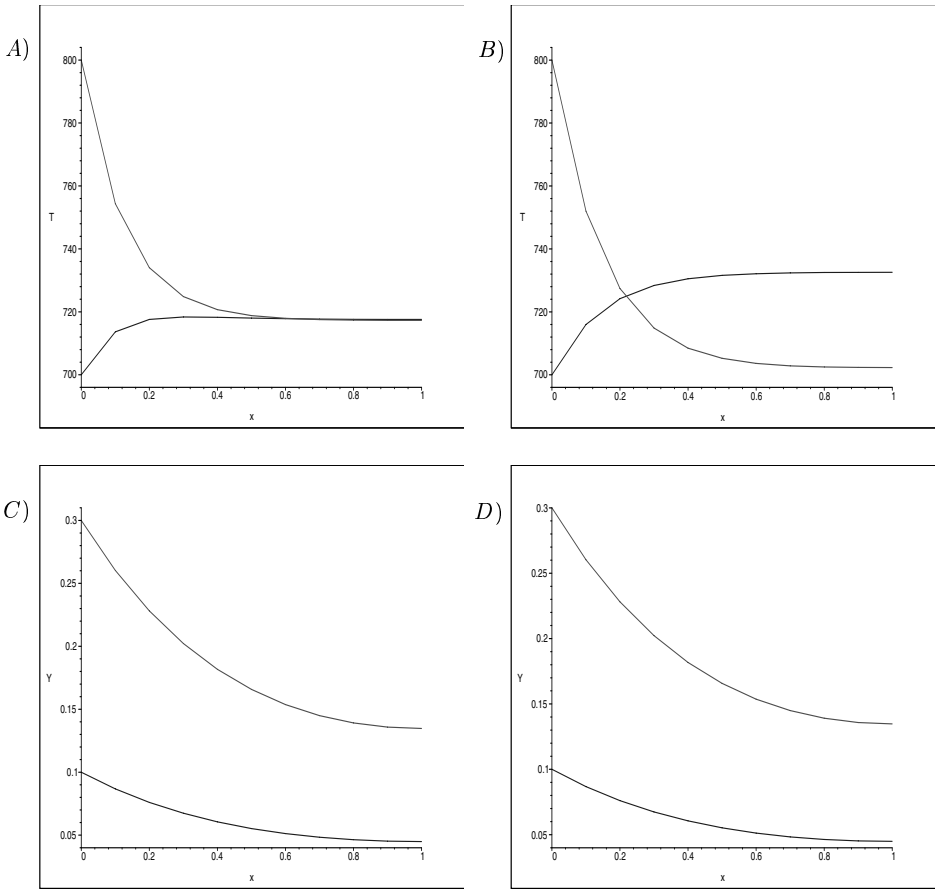
Figure 3   (A): Temperature distribution - Conducting wall resulting in coupling of temperatures; (B): Temperature distribution - Non-conducting wall resulting in uncoupled temperatures; (C): Concentration distribution - In the case when the wall is conducting; (D): Concentration distribution - In the case when the wall is non-conducting.

$$T_0^{(1)}(0) = 800 \ [K], \ T_0^{(2)}(0) = 700 \ [K],$$

$$\frac{dT_0^{(1)}}{dx}(1) = 0 \ \left[\frac{K}{m}\right], \ \frac{dT_0^{(2)}}{dx}(1) = 0 \ \left[\frac{K}{m}\right].$$

The results of numerical calculations are shown in Figures 3 (A) and (C). In order to highlight the effect of coupling, in Figures 3 (B) and (D) we present the graphs for the uncoupled ($\mu^* = 0$) case.

Conclusion

In this paper we analysed the effect of heat transfer across a thin conducting wall on the temperature distribution in the adjacent channels. Using the asymptotic technique of [1], [2], we derived the system of differential equations which "couples" the temperatures in the two channels. To highlight the effect of such a "coupling", we compared the results of numerical calculations with those for the uncoupled case (when there is no heat transfer across the wall). We would like to mention that, although in this paper we considered the system of only two channels (separated by a thin conducting wall), all the results can be easily generalised to the case of multi-channel interactions with multiple heterogeneous chemical reactions taking place in each channel.

Acknowledgement

References

[1] Kozlov, V.A., Maz'ya V.G., Movchan, A.B. (1999) *Asymptotic Analysis of Fields in Multi-Structures*, Oxford University Press.

[2] Avila-Pozos, O. (1999) Mathematical models of layered structures with an imperfect interface. Ph.D Thesis, Chpt. 2, University of Bath.

[3] Hayes, R.E., Kolaczkowski, S.T. (1997) *Introduction to Catalytic Combustion*, Gordon and Breach Publishers.

[4] Rose, L.M. (1974) *The Application of Mathematical Modelling to Process Development and Design*, Applied Science Publishers, Ltd.

Chapter 8
Asymptotics of fields near non-smooth boundaries

EFFECT OF A THIN COATING ON THE STRESS SINGULARITY AT THE VERTEX OF A THIN CONICAL INCLUSION

D. Esparza & N.V. Movchan

Department of Mathematical Sciences

University of Liverpool, Liverpool, L69 3BX, UK

Abstract   In this work we analyse the behaviour of the stress field near the vertex of a thin conical inclusion connected to the surrounding medium via a thin soft layer. We assume that all three materials are homogeneous, elastic and isotropic. The soft thin coating is modelled as an interface where the normal stresses remain continuous, but there is a jump in the displacement across the boundary. We analyse the effect of the coating on the stress singularity, and specify the load that would generate the strongest singularity. Results are compared with those for a perfectly bonded conical inclusion.

1.   INTRODUCTION

In this paper we investigate the effect of a thin conical layer, which connects a conical inclusion and an elastic matrix, on the stress singularity at the vertex of the inclusion. Using the method of [1] we derive the constitutive equations of the interface which models the effect of the "coating" layer. We analyse the stress singularity at the vertex of the cone for different aspect ratios of the elastic parameters of the inclusion, the thin layer and the matrix. This investigation is based on the results of [4], and is explained in detail in [2].

2.   FORMULATION OF THE PROBLEM

Consider a "coated" conical inclusion embedded in an elastic matrix (see Fig. 1). Let us define the following domains: $k_\varepsilon = \{\mathbf{x} \in \mathbb{R}^3 : x_3 > 0, \varepsilon^{-1} x_3^{-1} \|\mathbf{x}'\| < R_1, \mathbf{x}' = (x_1, x_2)\}$, occupied by a thin circular conical inclusion with elastic constants λ_o, μ_o, the "coating" $k_\varepsilon^* = \{\mathbf{x} \in \mathbb{R}^3 : x_3 > 0, \varepsilon^{-1} x_3^{-1} \|\mathbf{x}'\| \in (R_1, R_1 + \varepsilon R_0)\}$ with elastic constants λ^*, μ^*, and the elastic matrix $K_\varepsilon = \mathbb{R}^3 \setminus (\overline{k_\varepsilon \cup k_\varepsilon^*})$ with elastic constants λ, μ. The elastic materials are all homogeneous and isotropic. We assume that the

"width" $(\varepsilon^2 R_0)$ of the layer k_ε^* is sufficiently small in comparison with the radius (εR_1) of the intersection of the inclusion k_ε and the unit sphere $\mathbb{S} = \{\mathbf{x} \in \mathbb{R}^3 : \|\mathbf{x}\| = 1\}$.

The displacement fields $\mathbf{u}^o, \mathbf{u}^*$, and $\mathbf{u}$ in $k_\varepsilon, k_\varepsilon^*$ and K_ε satisfy the Lamé equations:

$$\mathbf{L}^o(\frac{\partial}{\partial x})\mathbf{u}^o(\varepsilon; \mathbf{x}) := \mu_o\Delta\mathbf{u}^o + (\lambda_o + \mu_o)\nabla\nabla \cdot \mathbf{u}^o = \mathbf{0}, \ \mathbf{x} \in k_\varepsilon,$$

$$\mathbf{L}^*(\frac{\partial}{\partial x})\mathbf{u}^*(\varepsilon; \mathbf{x}) := \mu^*\Delta\mathbf{u}^* + (\lambda^* + \mu^*)\nabla\nabla \cdot \mathbf{u}^* = \mathbf{0}, \ \mathbf{x} \in k_\varepsilon^*,$$

$$\mathbf{L}(\frac{\partial}{\partial x})\mathbf{u}(\varepsilon; \mathbf{x}) := \mu\Delta\mathbf{u} + (\lambda + \mu)\nabla\nabla \cdot \mathbf{u} = \mathbf{0}, \ \mathbf{x} \in K_\varepsilon, \qquad (2.1)$$
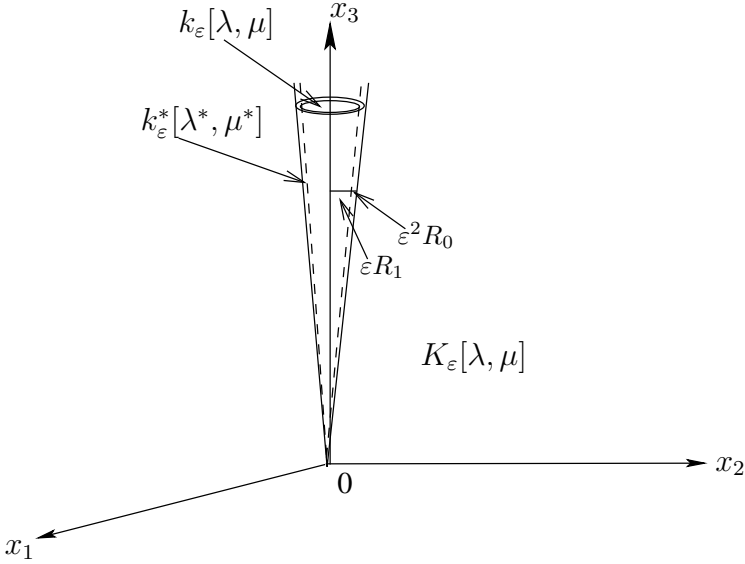
Figure 1 Conical inclusion k_ε with a conical coating k_ε^*, embedded in a elastic matrix $K_\varepsilon = \mathbb{R}^3 \setminus (\overline{k_\varepsilon \cup k_\varepsilon^*})$.

where $\mathbf{L}^o, \mathbf{L}^*, \mathbf{L}$ are the Lamé operators for the inclusion, the layer and the matrix, respectively.

Conditions at the Interfaces
We assume that there is a perfect bonding at the two interfaces between the inclusion and the layer, and between the layer and the surrounding matrix. The latter implies the continuity in displacements and stresses across

each interface:

$$\mathbf{u}^o(\varepsilon;\mathbf{x}) = \mathbf{u}^*(\varepsilon;\mathbf{x}), \ x_3^{-1}\|\mathbf{x}'\| = \varepsilon R_1,$$
$$\mathbf{u}^*(\varepsilon;\mathbf{x}) = \mathbf{u}(\varepsilon;\mathbf{x}), \ x_3^{-1}\|\mathbf{x}'\| = \varepsilon R_1 + \varepsilon^2 R_0, \tag{2.2}$$
$$\boldsymbol{\sigma}^{o(n)}(\mathbf{u}^o;\varepsilon,\mathbf{x}) = \boldsymbol{\sigma}^{*(n)}(\mathbf{u}^*;\varepsilon,\mathbf{x}), \ x_3^{-1}\|\mathbf{x}'\| = \varepsilon R_1,$$
$$\boldsymbol{\sigma}^{*(n)}(\mathbf{u}^*;\varepsilon,\mathbf{x}) = \boldsymbol{\sigma}^{(n)}(\mathbf{u};\varepsilon,\mathbf{x}), \ x_3^{-1}\|\mathbf{x}'\| = \varepsilon R_1 + \varepsilon^2 R_0. \tag{2.3}$$

In (2.3) $\boldsymbol{\sigma}^{o(n)}$, $\boldsymbol{\sigma}^{*(n)}$ and $\boldsymbol{\sigma}^{(n)}$ denote the normal stresses generated by $\mathbf{u}^o$, $\mathbf{u}^*$, and $\mathbf{u}$ at each boundary.

3.   BOUNDARY LAYER SOLUTION

We want to analyse the behaviour of the solution in the vicinity of the vertex. In the vicinity of the origin we take the solutions in the form (see [4]):

$$\mathbf{u}^o(\varepsilon;\mathbf{x}) = \rho^{1+\varepsilon^2\Lambda_2}\mathbf{v}^o(\varepsilon;\theta,\varphi), \ \mathbf{x} \in k_\varepsilon,$$
$$\mathbf{u}^*(\varepsilon;\mathbf{x}) = \rho^{1+\varepsilon^2\Lambda_2}\mathbf{v}^*(\varepsilon;\theta,\varphi), \ \mathbf{x} \in k_\varepsilon^*,$$
$$\mathbf{u}(\varepsilon;\mathbf{x}) = \rho^{1+\varepsilon^2\Lambda_2}\mathbf{v}(\varepsilon;\theta,\varphi), \ \mathbf{x} \in K_\varepsilon, \tag{3.1}$$

where (ρ,θ,φ) are the spherical coordinates $(\rho \geq 0, \theta \in [0,\pi], \varphi \in [0,2\pi))$, and Λ_2 is the stress singularity exponent. We construct an asymptotic expansion for each of the three displacement vectors $\mathbf{v}^o, \mathbf{v}^*, \mathbf{v}$ using the technique described in [3], [4].

For the case where there is no inclusion and no layer ($\varepsilon = 0$), the leading order approximations $\boldsymbol{\Phi}^o, \boldsymbol{\Phi}^*, \boldsymbol{\Phi}$ for the fields $\mathbf{v}^o, \mathbf{v}^*, \mathbf{v}$ have the form

$$\mathbf{v}^o \sim \boldsymbol{\Phi}^o(\theta,\varphi) = \sum_{j=1}^{6} c_j \boldsymbol{\Phi}^{(1,j)}(\theta,\varphi) \text{ on } g_\varepsilon,$$

$$\mathbf{v}^* \sim \boldsymbol{\Phi}^*(\theta,\varphi) = \sum_{j=1}^{6} c_j \boldsymbol{\Phi}^{(1,j)}(\theta,\varphi) \text{ on } g_\varepsilon^*,$$

$$\mathbf{v} \sim \boldsymbol{\Phi}(\theta,\varphi) = \sum_{j=1}^{6} c_j \boldsymbol{\Phi}^{(1,j)}(\theta,\varphi) \text{ on } \mathbb{S} \setminus (\overline{g_\varepsilon \cup g_\varepsilon^*}), \tag{3.2}$$

where $g_\varepsilon, g_\varepsilon^*$ are the intersections of $k_\varepsilon, k_\varepsilon^*$ with the unit sphere $\mathbb{S}$. The functions $\boldsymbol{\Phi}^o, \boldsymbol{\Phi}^*, \boldsymbol{\Phi}$ are projections of linear vector fields on $\mathbb{S}$; they satisfy the Lamé equation and are given in [4].

In a neighbourhood of the point $\mathcal{N}(0,0,1)$ new scaled variables are introduced:

$$\xi_i = \frac{x_i}{\varepsilon x_3}, \ i = 1, 2. \tag{3.3}$$

Since we assume that the conical coating has the width $\varepsilon^2 R_0$, within the layer we introduce the second set of variables,

$$\zeta = \frac{\|\boldsymbol{\xi}\| - R_1}{\varepsilon}, \ \varphi' = \varphi, \ \zeta \in (0, R_0), \ \varphi' \in [0, 2\pi). \tag{3.4}$$

We also assume that the layer is soft, that is,

$$\lambda^* = \varepsilon \lambda_o^*, \ \mu^* = \varepsilon \mu_o^*, \tag{3.5}$$

where λ_o^*, μ_o^* have the same order as $\lambda, \mu, \lambda_o, \mu_o$. In stretched variables, the Lamé operator $\mathbf{L}^*$ and the traction operator $\mathbf{B}^*$ can be represented as

$$\mathbf{L}^*(\frac{\partial}{\partial \mathbf{x}}) = \varepsilon^{-2} \mathcal{L}_0^*(\frac{\partial}{\partial \boldsymbol{\xi}}) + \varepsilon^{-1} \mathcal{L}_1^*(\frac{\partial}{\partial \boldsymbol{\xi}}, \frac{\partial}{\partial x_3}) + O(1)$$

$$= \varepsilon^{-3} l_0^*(\frac{\partial}{\partial \zeta}, \frac{\partial}{\partial \varphi}) + \varepsilon^{-2} l_1^*(\frac{\partial}{\partial \zeta}, \frac{\partial}{\partial \varphi}, \frac{\partial}{\partial x_3}) + O(\varepsilon^{-1}), \tag{3.6}$$

$$\mathbf{B}^*(\frac{\partial}{\partial \mathbf{x}}, \mathbf{n}) = \varepsilon^{-1} \mathcal{B}_0^*(\frac{\partial}{\partial \boldsymbol{\xi}}, \mathbf{n}) + \mathcal{B}_1^*(\frac{\partial}{\partial \boldsymbol{\xi}}, \frac{\partial}{\partial x_3}, \mathbf{n}) + O(\varepsilon)$$

$$= \varepsilon^{-1} \mathbf{b}_0^*(\frac{\partial}{\partial \zeta}, \frac{\partial}{\partial \varphi}, \mathbf{n}) + \mathbf{b}_1^*(\frac{\partial}{\partial \zeta}, \frac{\partial}{\partial \varphi}, \frac{\partial}{\partial x_3}, \mathbf{n}) + O(\varepsilon), \tag{3.7}$$

where $\mathcal{L}_0^*, \mathcal{L}_1^*, l_0^*, l_1^*$ and $\mathcal{B}_0^*, \mathcal{B}_1^*, \mathbf{b}_0^*, \mathbf{b}_1^*$ are matrix differential operators, which have a block-diagonal structure and are given in [2]. The vectors $\mathbf{v}^*, \mathbf{v}^o, \mathbf{v}$ can then be written as follows:

$$\mathbf{v}^o \sim \boldsymbol{\Phi}(\varphi, \theta) + \varepsilon \mathbf{w}^{o(1)}(\boldsymbol{\xi}) + \varepsilon^2 \mathbf{w}^{o(2)}(\boldsymbol{\xi}), \ \|\boldsymbol{\xi}\| < R_1,$$

$$\mathbf{v}^* \sim \boldsymbol{\Phi}(\varphi, \theta) + \varepsilon \mathbf{w}^{*(1)}(\zeta, \varphi) + \varepsilon^2 \mathbf{w}^{*(2)}(\zeta, \varphi), \ \zeta \in [0, R_0],$$

$$\mathbf{v} \sim \boldsymbol{\Phi}(\varphi, \theta) + \varepsilon \mathbf{w}^{(1)}(\boldsymbol{\xi}) + \varepsilon^2 \mathbf{w}^{(2)}(\boldsymbol{\xi}), \ \|\boldsymbol{\xi}\| > R_1 + \varepsilon R_0, \ \varphi \in [0, 2\pi), \tag{3.8}$$

where $\mathbf{w}^{o(1)}, \mathbf{w}^{o(2)}, \mathbf{w}^{(1)}, \mathbf{w}^{(2)}, \mathbf{w}^{*(1)} \mathbf{w}^{*(2)}$ are unknown functions. Using (3.6), (3.7) and the expression for $\mathbf{v}^*$ in (3.8), we can derive the representations for the functions $\mathbf{w}^{*(1)}, \mathbf{w}^{*(2)}$ (as shown in [2]) in the form

$$\mathbf{w}^{*(1)}(\zeta, \varphi) = \mathbf{W}^{*(1)}(\varphi)\zeta + \mathbf{U}^{*(1)}(\varphi), \tag{3.9}$$

$$\mathbf{w}^{*(2)}(\zeta, \varphi) = \mathbf{F}^*(\varphi)\zeta^2 + \mathbf{W}^{*(2)}(\varphi)\zeta + \mathbf{U}^{*(2)}(\varphi), \ \varphi \in [0, 2\pi), \tag{3.10}$$

where $\mathbf{W}^{*(1)}, \mathbf{U}^{*(1)}$ and $\mathbf{F}^*, \mathbf{W}^{*(2)}, \mathbf{U}^{*(2)}$ are unknown functions of φ. From (3.9), we can see that the stress field generated by the displacement $\mathbf{w}^{*(1)}$ is independent of ζ within the thin layer. However, it is also clear that there is a jump in the displacement across the layer. Thus, the functions $\mathbf{W}^{*(1)}$ and $\mathbf{W}^{*(2)}$ can be written in terms of the jump in $\mathbf{w}^{*(1)}, \mathbf{w}^{*(2)}$ across the thin layer, respectively. Similarly, $\mathbf{F}^*, \mathbf{U}^{*(1)}$, and $\mathbf{U}^{*(2)}$ can be written

in terms of the functions $\mathbf{w}^{o(1)}, \mathbf{w}^{o(2)}, \mathbf{w}^{(1)}, \mathbf{w}^{(2)}$ evaluated at $\|\boldsymbol{\xi}\| = R_1$ and at $\|\boldsymbol{\xi}\| = R_1 + \varepsilon R_o$. Therefore, the boundary value problem for the "coated" inclusion is transformed into a boundary value problem for an infinite medium with an imperfectly bonded inclusion with a non-zero jump in displacement across the interface:

$$\mathcal{L}_0 \mathbf{w}^{(2)} + \mathcal{L}_1 \mathbf{w}^{(1)} = 0, \ \|\boldsymbol{\xi}\| > R_1,$$

$$\mathcal{L}_0^o \mathbf{w}^{o(2)} + \mathcal{L}_1^o \mathbf{w}^{o(1)} = 0, \ \|\boldsymbol{\xi}\| < R_1,$$

$$\mathcal{B}_0 \mathbf{w}^{(2)} + \mathcal{B}_1 \mathbf{w}^{(1)} - \mathcal{B}_0^o \mathbf{w}^{o(2)} - \mathcal{B}_1^o \mathbf{w}^{o(1)} = \boldsymbol{f}_1(R_1, \varphi) + \mathbf{g}_1(R_1, \varphi),$$

$$\mathcal{B}_0 \mathbf{w}^{(2)} + \mathcal{B}_1^{(1)} \mathbf{w}^{(1)} = \boldsymbol{f}_2(R_1, \varphi) + \mathbf{g}_2(R_1, \varphi), \ \varphi \in [0, 2\pi), \qquad (3.11)$$

where

$$\boldsymbol{f}_1 = \frac{\mu_o^*}{R_1} \begin{pmatrix} 2(w_\zeta^{(1)} - w_\zeta^{o(1)})(R_1, \varphi) \\ 2(w_\varphi^{(1)} - w_\varphi^{o(1)})(R_1, \varphi)) \\ (w_z^{(1)} - w_z^{o(1)})(R_1, \varphi) \end{pmatrix} + \frac{1}{R_1} \begin{pmatrix} \mu_o^* \dfrac{d}{d\varphi}(w_\varphi^{(1)} - w_\varphi^{o(1)})(R_1, \varphi)) \\ \lambda_o^* \dfrac{d}{d\varphi}(w_\zeta^{(1)} - w_\zeta^{o(1)})(R_1, \varphi)) \\ 0 \end{pmatrix},$$

and

$$\boldsymbol{f}_2 = \begin{pmatrix} (\lambda_0^* + 2\mu_o^*)\{\dfrac{1}{R_0}(w_r^{(2)} - w_r^{o(2)})(R_1, \varphi) + \dfrac{\partial w_r^{(1)}}{\partial r}(R_1, \varphi) + R_0 F_\zeta^*(\varphi)\} \\ \mu_o^*\{\dfrac{1}{R_0}(w_\varphi^{(2)} - w_\varphi^{o(2)})(R_1, \varphi) + \dfrac{\partial w_\varphi^{(1)}}{\partial r}(R_1, \varphi), +R_0 F_\varphi^*(\varphi)\} \\ \mu_o^*\{\dfrac{1}{R_0}(w_z^{(2)} - w_z^{o(2)})(R_1, \varphi) + \dfrac{\partial w_z^{(1)}}{\partial r}(R_1, \varphi), +R_0 F_z^*(\varphi)\} \end{pmatrix}.$$

Here $\mathbf{g}_1, \mathbf{g}_2$ are functions of φ, R_1, and they are given in [2]. Both functions $\mathbf{w}^{(1)}, \mathbf{w}^{(2)}$ decay at infinity as $O(\|\mathbf{x}\|^{-1})$.

By applying the Divergence Theorem to the first two equations in (3.11) in a circle of radius R enclosing the inclusion, and then taking the limit as $R \to \infty$, we obtain the coefficients in the asymptotic representation for $\mathbf{w}^{(2)}$ at infinity, as explained in detail in [2], [4]. These coefficients are then used when deriving the solvability conditions for the problem (3.11) which, as shown in [2], [4], can be expressed as an eigenvalue problem for a 6×6 matrix:

$$M \, \boldsymbol{c} \; = \; \Lambda_2 \, \boldsymbol{c}. \qquad (3.12)$$

Here $\boldsymbol{c} = (c_1, c_2, \ldots, c_6)^T$ is the vector of the coefficients in the representation (3.2), Λ_2 is the stress singularity exponent (see (2.3)), and M is a 6×6 matrix whose elements depend on $\lambda, \mu, \lambda_o, \mu_o, \lambda_o^*, \mu_o^*$ and are given in [2].

The eigenvector $\boldsymbol{c}$ determines the stress field generated by the external load in the vicinity of the origin in the elastic medium without an inclusion. We shall call this stress field *a stress mode*. The stress field becomes

singular at the vertex of the cone if $\Lambda_2 < 0$. By solving the eigenvalue problem (3.12) we find 6 eigenvalues $\Lambda_2^{(j)}, j = 1, 2, \ldots, 6$, and the corresponding eigenvectors (the stress modes) that generate these singularities. In the paper we adopt the following notations: we denote the eigenvalues associated with an axisymmetric load by $\Lambda_2^{(1)}, \Lambda_2^{(2)}, \Lambda_2^{(3)}$; these correspond to compression or tension along the x-, y-, and z- axes. The eigenvalues associated with a non-axisymmetric load are denoted by $\Lambda_2^{(4)}, \Lambda_2^{(5)}, \Lambda_2^{(6)}$; they correspond to shear load in the xy-, xz- and yz- planes, respectively. We assume that the matrix, the inclusion and the coating layer have the same Poisson's ratio ν, that is,

$$\nu = \nu_o = \nu_o^*. \tag{3.13}$$

This relation allows us to write

$$\lambda = \frac{2\mu\nu}{1 - 2\nu}, \quad \lambda_o = \frac{2\mu_o\nu}{1 - 2\nu}, \quad \lambda_o^* = \frac{2\mu_o^*\nu}{1 - 2\nu}. \tag{3.14}$$

Although we do not present the elements of the matrix M (which are given in [2]), here we write the representation for its eigenvalues:

$$\Lambda_2^{(1)} = \frac{1}{2}\left\{ \frac{f_1}{f_2} + \sqrt{\left(\frac{f_1}{f_2}\right)^2 + \frac{(1+\nu)(1-2\nu)}{1-\nu}\frac{f_3}{f_2}} \right\}$$

$$\Lambda_2^{(2)} = \frac{1}{2}\left\{ \frac{f_1}{f_2} - \sqrt{\left(\frac{f_1}{f_2}\right)^2 + \frac{(1+\nu)(1-2\nu)}{1-\nu}\frac{f_3}{f_2}} \right\}$$

$$\Lambda_2^{(3)} = \Lambda_2^{(4)} = -\frac{(1-2\nu)(1-\mu_o/\mu)}{1 + (3-4\nu)\mu_o/\mu}$$

$$\Lambda_2^{(5)} = \Lambda_2^{(6)} = -\frac{5 - 2\nu - 8\nu^2}{4(1-\nu)(3-4\nu)} \frac{\dfrac{\mu_o}{\mu}R_0 + \dfrac{\mu_o^*}{\mu}R_1(1 - \mu_o/\mu)}{\dfrac{\mu_o}{\mu}R_0 + \dfrac{\mu_o^*}{\mu}R_1(1 + \mu_o/\mu)},$$

$$\tag{3.15}$$

where

$$f_1 = (1-\nu)\frac{\mu_o^*}{\mu}R_1(1 - \mu_o/\mu)[\frac{\mu_o}{\mu}(1+\nu) + (1-2\nu)]$$
$$\qquad -\frac{\mu_o}{\mu}(1-2\nu)R_0[\frac{\mu_o}{\mu}(1+\nu) - 1],$$

$$f_2 = \frac{\mu_o}{\mu}(1-2\nu)R_0 + (1-\nu)\frac{\mu_o^*}{\mu}R_1(\frac{\mu_o}{\mu} + 1 - 2\nu),$$

$$f_3 = (1-\nu)\frac{\mu_o^*}{\mu}(1 - \mu_o/\mu)^2 R_1 + \frac{\mu_o}{\mu}(1 - \mu_o/\mu)R_0. \tag{3.16}$$

4.   RESULTS

In Figs. 2 to 5 we plot the eigenvalues $\Lambda_2^{(j)}(j = 1, \ldots 6)$ as functions of ν for different values of the ratios μ_o/μ and μ_o^*/μ. In each case we compare the graphs with the corresponding (dotted) curve for a perfectly bonded inclusion. The curve for $\mu_o^*/\mu = 2.5$ is always the farthest from the dotted curve.

For the case of the eigenvalue $\Lambda_2^{(1)}$ (Fig. 2), all the curves lie above the $\Lambda = 0$ axis when $\mu_o/\mu < 1$ (the inclusion is softer than the matrix), while $\Lambda_2^{(1)}$ takes positive and negative values when $\mu_o/\mu > 1$ (the matrix is softer than the inclusion). Therefore, the presence of the layer generates a stronger singularity for an axisymmetric load with tension along the z-axis when $\mu_o/\mu > 1$. If we consider an axisymmetric load with compression along the z- axis (Fig. 3), we find that, for all the ratios of μ_o/μ considered, the presence of the layer generates a singularity in the stress field, since $\Lambda_2^{(2)}$ takes negative values. However, in comparison with the case of perfect bonding, the presence of the layer generates a stronger singularity if $\mu_o/\mu < 1$, and a weaker one if $\mu_o/\mu > 1$.

The eigenvalue $\Lambda_2^{(3)}$ (same as $\Lambda_2^{(4)}$) does not depend on R_0 or μ_o^*/μ, and therefore the presence of the thin layer has no effect on the singularity in the stress field for the shear in the xy- plane. In Fig. 4 we show the plot for $\Lambda_2^{(3)}$, where we vary the ratio μ_o/μ between 0.5 and 4.5 and obtain negative values for $\mu_o/\mu < 1$.

For the eigenvalue $\Lambda_2^{(5)} = \Lambda_2^{(6)}$, the presence of the thin layer generates a stronger singularity than the case of perfect bonding when $\mu_o/\mu < 1$, as shown in Fig. 5. If $\mu_0/\mu > 1$, the eigenvalue takes positive and negative values depending on the ratio μ_o^*/μ. Since the eigenvalue for the perfect bonding is positive if $\mu_o/\mu > 1$, then the presence of the layer can generate a singularity in the stress field for the shear loads in the xz- and yz- planes.

5.   CONCLUSIONS

We have studied the behaviour of the stress field near the vertex of a coated conical inclusion embedded in an elastic matrix. We have analysed the effect of the thin coating on the stress singularity. By taking the same Poisson ratio for all materials, we found the expression for the stress singularity exponent and associated stress mode which generates this singularity. We found that compared to the case of perfect bonding the presence of the layer can generate a stronger singularity for a non-axisymmetric load.

Acknowledgments

References

[1] Bigoni D., Serkov S.K., Valentini M., & Movchan A.B., (1998), Asymptotic models of dilute composites with imperfectly bonded inclusions, *Int. J. Solids Structures*, **35**, 3239-3258.

[2] Esparza D., (2002), *Elasticity problems in domains with non-smooth boundaries*, Ph.D. Thesis, University of Liverpool, 140pp.

[3] Kondrat'ev V.A., (1967), Boundary problems for elliptic equations in domains with conical or angular points, *Trans. Moscow Math. Soc.*, **16**, 227-313.

[4] Movchan A.B., and Movchan N.V., (1995), *Mathematical Modeling of Solids with Non-Regular Boundaries*, CRC Press, 325 pp.
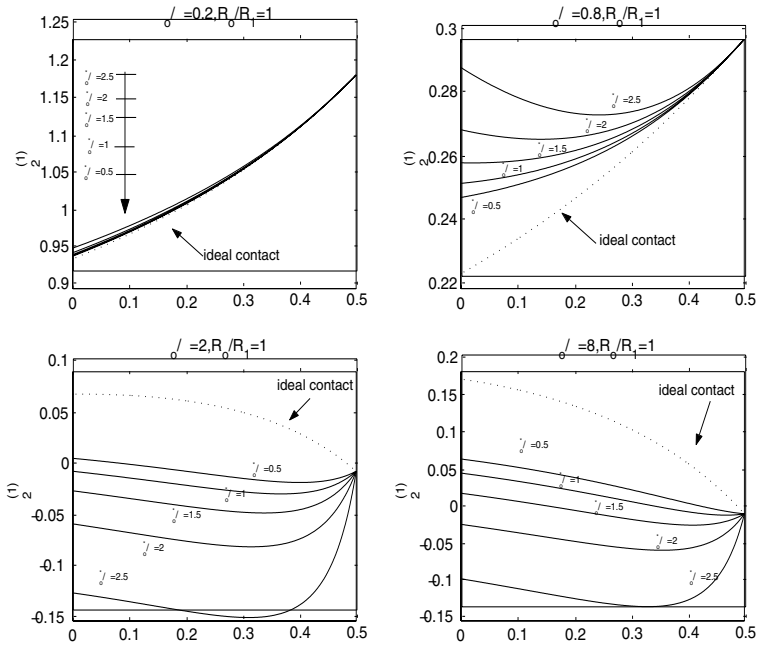
Figure 2   Eigenvalue $\Lambda_2^{(1)}$, for $\mu_o/\mu = 0.2, 0.8, 2, 8$, and $\mu_o^*/\mu = 0.5, 1, 1.5, 2, 2.5$. The curve for the ideal contact $(R_0/R_1 = 0)$ is shown by a dotted line.
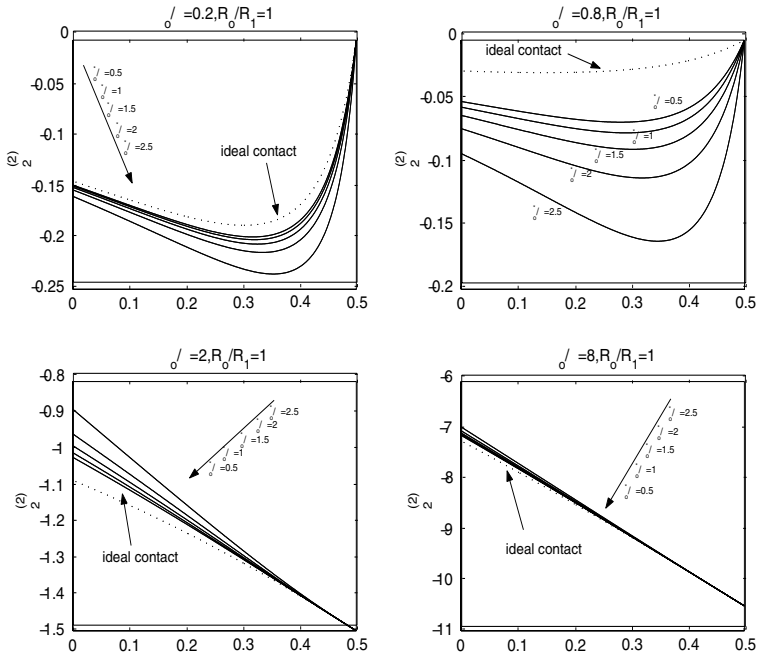
Figure 3   Eigenvalue $\Lambda_2^{(2)}$, for $\mu_o/\mu = 0.2, 0.8, 2, 8$, and $\mu_o^*/\mu = 0.5, 1, 1.5, 2, 2.5$. The curve for the ideal contact $(R_0/R_1 = 0)$ is shown by a dotted line.
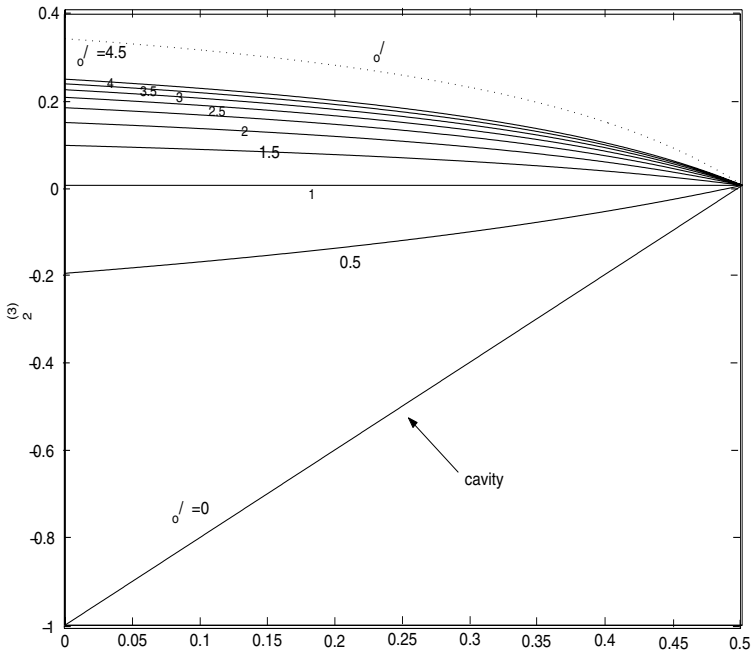
Figure 4   Eigenvalue $\Lambda_2^{(3)} = \Lambda_2^{(4)}$, for $\mu_o/\mu = 0.5, 1, 1.5, 2, 2.5, 3, 3.5, 4, 4.5$. The case for $\mu_0 = 0$ corresponds to a circular cavity.
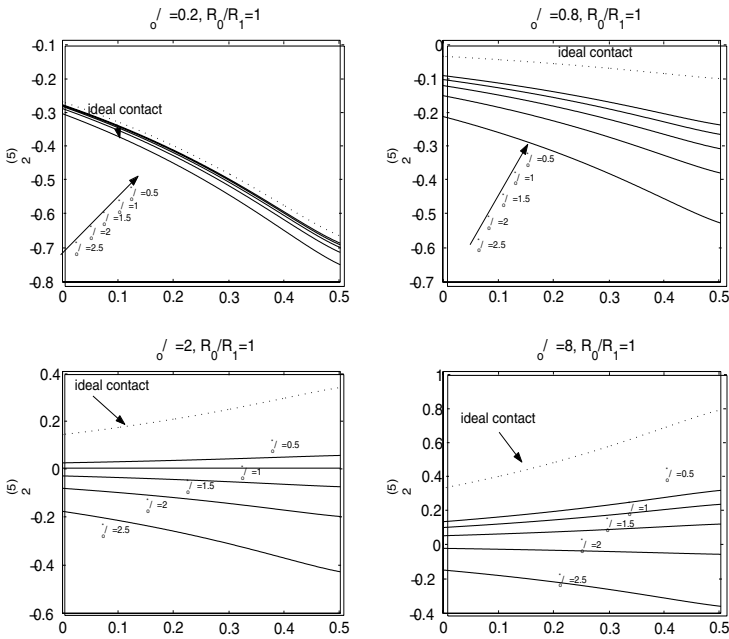
Figure 5   Eigenvalue $\Lambda_2^{(5)} = \Lambda_2^{(6)}$, for $\mu_o/\mu = 0.2, 0.8, 2, 8$, and $\mu_o^*/\mu = 0.5, 1, 1.5, 2, 2.5$. The curve for the ideal contact $(R_0/R_1 = 0)$ is shown by a dotted line.

3D SINGULARITIES WITH APPLICATIONS TO FATIGUE CRACK GROWTH

Karsten Kolk[1], Günther Kuhn[1] and Gennady Mishuris[2]

[1] *University of Erlangen–Nuremberg, Institute of Applied Mechanics*
Egerland Str. 5, 91058 Erlangen, Germany
kolk@ltm.uni-erlangen.de
[2] *Rzeszów University of Technology, Department of Mathematics*
W.Pola 2, 35-959, Rzeszów, Poland
miszuris@prz.rzeszow.pl

Abstract   3D singularities and its application to fatigue crack growth simulation are considered in this paper. The calculation of such singularities is briefly described. The focus lies on the usage of the appearing singularities, e. g. design of special crack front elements and specimens with a predefined crack front shape. Finally, the angle of a crack front and the outer boundary are determined in case of surface breaking cracks.

1.   INTRODUCTION

The numerical determination of three-dimensional crack front shapes - as they appear in experiments - is essential for a realistic 3D simulation of fatigue crack growth. From the engineering point of view it is also important for life time estimations.

It is well–known, that along any 3D crack front stresses show a singular behavior in the crack front near field within the framework of linear elastic fracture mechanics. In contrast to 2D, it has to be distinguished between two certain singularities. Along a smooth crack front a wedge singularity is present. At corners, particularly in the vicinity where the crack front intersects the free surface, a corner singularity has to be taken into account. Knowing the present singularity at every point along the crack front offers

a variety of new aspects – design of specimens (section 5), design of crack front elements (section 3) and additionally the determination of the crack front angle at the intersection of the crack front and the free surface (section 4).

2.   3D SINGULARITY ANALYSIS

An arbitrary 3D body $\Omega \subset \mathbb{R}^3$ with a singular point O and its coordinates $\boldsymbol{x}_O$ is considered. The domain Ω consists of homogeneous, isotropic and linear–elastic material. The corresponding elastic solution in the vicinity of the singular point O related to the spherical coordinate system, which is centered in O, is asymptotically expanded in the form

$$u_i\left(\rho, \theta, \varphi, O\right) = \sum_{L=1}^{\infty} K_L^\star(O)\rho^{\alpha_L} g_i^L(\theta, \varphi, O) \ . \tag{2.1}$$

This procedure traces back to [1] and is recently published in [3]. α_L denote the asymptotic exponents satisfying $\alpha_L > -0.5$ from the elastic energy point of view , cp. [3], and g_i^L are the corresponding angular functions. The vicinity Ω_O^ε around O is given by

$$\Omega_O^\varepsilon := \Omega \cap \Omega^\varepsilon \ , \ \ \Omega^\varepsilon := \{\boldsymbol{x} \in \mathbb{R}^3 : |\boldsymbol{x} - \boldsymbol{x}_O| < \varepsilon\} \ , \ \ \boldsymbol{x}_O \in \Omega \subset \mathbb{R}^3 \ . \tag{2.2}$$

All solutions (eigenstates) are searched satisfying the Lamé–Navier equation regarding to local boundary conditions [3]. This problem is solved by a weak FEM approximation (Galerkin–Petrov method) and the governing equations reads

$$\int_{\Omega_O^\varepsilon} \sigma_{ij}(\mathbf{u})\,\varepsilon_{ij}(\mathbf{v})\,\mathrm{d}\Omega(\boldsymbol{x}) = 0 \ . \tag{2.3}$$

The displacements u_i $(i = 1, 2, 3)$ are approximated by

$$\mathbf{u} = \rho^\alpha \mathbf{U}_\alpha(\theta, \varphi) \tag{2.4}$$

and the test functions v_i by

$$\mathbf{v} = \Phi(\rho)\,\mathbf{V}(\theta, \varphi) \tag{2.5}$$

with

$$\Phi(\rho) \in C^\infty \ , \ \mathrm{supp}(\Phi) = [0, \varepsilon) \ . \tag{2.6}$$

The test function $\mathbf{v}$ is chosen in such a way that combined with homogeneous local boundary conditions the r.h.s. of (2.3) vanishes. After a sophisticated discretization followed by the evaluation of equation (2.3) one obtains a quadratic eigenvalue problem in terms of α. An α–shift of $\bar{\alpha} = \alpha + \frac{1}{2}$ yields

$$[\mathbf{P} + \bar{\alpha}\mathbf{Q} + \bar{\alpha}^2\mathbf{R}]\mathbf{d} = \mathbf{0} \tag{2.7}$$

with better structured matrices. Then, the eigenvalue problem is linearized within the solution procedure and solved with the help of the mathematical package ARPACK [7]. g_i^L are the associated eigenvectors. Because the asymptotic behavior is focused, the interval $-0.5 < \alpha_L < 1$ is considered excluding the rigid body motion modes as they are known.

For a smooth part of the crack front the well-known value is $\alpha_1 = 0.5$ with a multiplicity of three. It is the classical square–root displacement field which is equivalent to the square–root stress singularity. Along non-smooth parts of the crack front, particularly where the crack front intersects the free surface the values of α_L are not a–priori known. They depend on material parameters as well as on the geometrical situation around the singular point.

3.   CRACK FRONT ELEMENTS

As mentioned in the previous section, stress singularities appear in the neighborhood of crack fronts. With standard elements, e. g. quadratic quadrilateral elements, such singularities can not be modelled correctly. It leads to a relatively fine mesh in such areas with an increasing number of degrees of freedom (DOF) to register these asymptotical behavior. Furthermore, when solving the related system of linear equations the convergence is slower if singularities are present and not properly modelled.

To overcome this drawback crack front elements incorporating the relevant singularity or singularities are necessary. For the standard case of the classical square–root singularity a variety of elements are available. They can be grouped into two classes. The first class contains standard elements with appropriate shape functions showing the desired singular behavior. The second class consists of standard elements with eight or nine nodes. The mid-side nodes which are perpendicular to the crack front are moved to one quarter close to the crack front. These elements are the popular and widely used quarter–point elements. However, such kind of elements are missing for the neighborhood of singular points as considered in section 2 for three–dimensional analyses.

To have a common concept for embedded as well as for surface breaking cracks the following types of crack front elements can be proposed. They belong to the first group with appropriate shape functions. The functions are formulated to approximate the displacement field $u_j(\boldsymbol{x})$

$$u_j\left(\boldsymbol{x}(\boldsymbol{\eta})\right) = \sum_{m=1}^{p} u_j^m N^m(\boldsymbol{\eta}) \; ; \; \boldsymbol{\eta} = (\eta_1, \eta_2)^{\mathrm{T}} \qquad (3.1)$$

near the crack front.

It is defined via p nodal displacements u_j^m and shape functions $N^m(\boldsymbol{\eta})$ which fulfill the usual requirements

$$N^m(\boldsymbol{\eta}^n) = \delta_{mn} \quad , \quad \sum_{m=1}^{p} N^m(\boldsymbol{\eta}) = 1 \text{ and} \tag{3.2}$$

$$\sum_{m=1}^{p} \frac{\partial N^m(\boldsymbol{\eta})}{\partial \eta_1} = \sum_{m=1}^{p} \frac{\partial N^m(\boldsymbol{\eta})}{\partial \eta_2} = 0 \tag{3.3}$$

where $\boldsymbol{\eta}^n$ denote the local co–ordinates of node n.

It has to be distinguished between three different types of elements as shown in figure 1 a. Type I elements are located along the smooth part of the crack front. Type II elements are located on the crack front and share one node with the singular point whereas type III elements are placed on the outer boundary sharing one singular point. All these elements are macro–elements consisting of two standard elements – QUAD8 and/or TRIA6 elements.
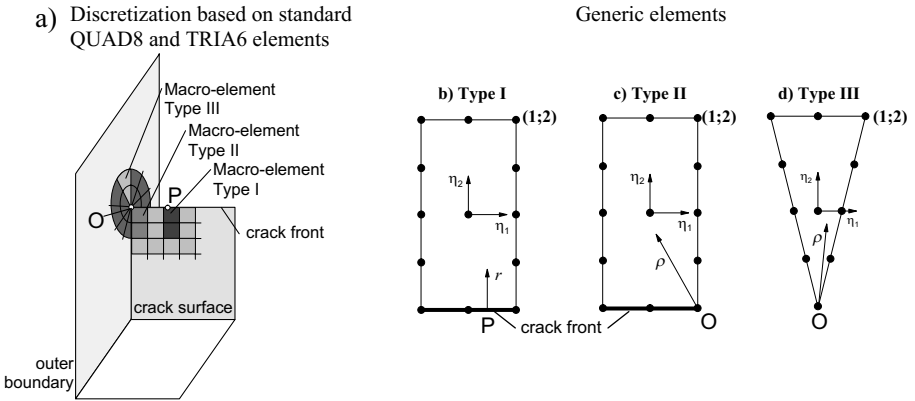
Figure 1   Crack front elements

To include the $\sqrt{r}$–behavior of the displacement as r tends to zero into the shape functions of the element type I (see figure 1 b) a separation of variables $N^m(\boldsymbol{\eta}) = f^m(\eta_1)g^m(r(\eta_2))$ is performed. It is enough to have a quadratical distribution tangential to the crack front. But, having the same order of approximation as well as the desired $\sqrt{r}$ distribution normal to the crack front, the following functions are proposed

$$f^m(\eta_1) := \operatorname{span}\left\{1, \eta_1, \eta_1^2\right\} \ , \tag{3.4}$$

$$g^m(r) := \operatorname{span}\left\{1, \sqrt{r}, r, r^{1.5}, r^2\right\} \ . \tag{3.5}$$

At non–smooth parts of the crack front, e. g. the intersection of the crack front and the outer boundary a similar approach but with other functions

is necessary. The general outline of the shape functions for the element types II and III (figure 1 c-d) is

$$N^m(\boldsymbol{\eta}) = f^m\left(\rho(\eta_1, \eta_2), \eta_1, \eta_2\right) \tag{3.6}$$

with

$$f^m(\rho, \eta_1, \eta_2) := \text{span}\left\{1, \rho^{\alpha_1}, \rho^{\alpha_2}, \rho^{\alpha_3}, \rho, \rho^{\alpha_4}, h(\eta_1, \eta_2)\right\} \ . \tag{3.7}$$

There can be up to four different exponents α_L taken into account. If one exponent has a multiplicity greater then one it will be considered only once. The matching function $h(\eta_1, \eta_2)$ is used to adjust the remaining parameters in the shape functions depending on the total number of nodes in the macro–element.

For the element type II the matching function has to assure the same approximation of displacements for $\eta_1 = -1$ along η_2 as in an element type I along the same direction. The element type III is at $\eta_2 = 2$ connected to a quadratic standard element. Therefore, matching of the quadratic distribution for $\eta_2 = 2$ along η_1 is required.

4.   SURFACE BREAKING CRACKS

In case of surface breaking cracks the crack front intersects the outer boundary at an angle γ, cp. figure 3 a. γ is defined as the angle between the normal vector on the outer boundary and the tangent vector of the crack front. If the angle were a-priori known, it would be useful for the 3D simulation of fatigue crack growth.

For the determination of this angle an assumption is made. The crack front is shaped in such a way that the square–root singularity holds along the whole crack front even in the vicinity of the intersection point. This assumption is investigated for mode–I conditions considering the four point bending specimen as shown in figure 2.
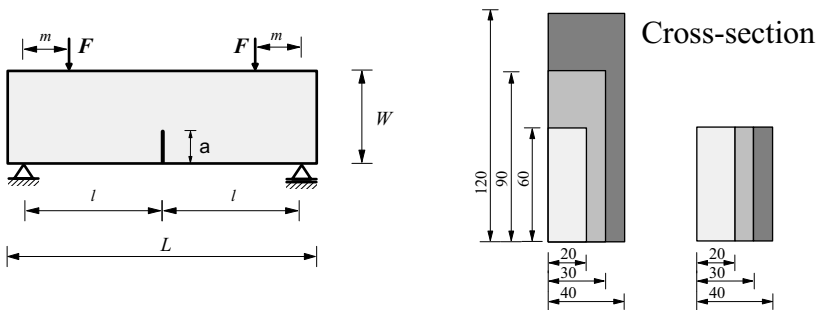
Figure 2   Sketch of the 4–point bending specimen

The asymptotic exponent related to the symmetrical crack opening depends on the material and the geometrical situation. The material is PMMA (Poisson ratio $\nu = 0.36$ and Young's modulus $E = 3.6$GPa). The geometrical situation is visualized in figure 3 a.
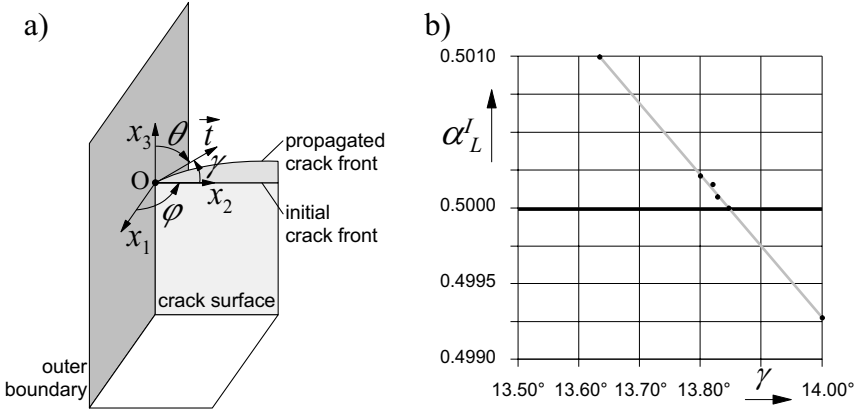
Figure 3 a) Geometrical situation around the singular point b) Crack front angle satisfying the square–root singularity

To assure the eigenvalue α_L^I related to a symmetrical crack opening with high precision, different meshes were tested within the framework of the singularity analysis. The (θ, φ)–plane of the domain Ω_O^ε is spanned by $(\theta, \varphi) \in (0°; 180°) \times (0°; 180°)$. The crack intersects this domain at $\varphi = 90°$ and $\theta \in (\theta^\star; 180°)$. An analytical solution for this setup is given in [2] for $\theta^\star = 90°$ and $\nu = 0.3$ with $\alpha_L^I = 0.5477$. The best mesh yields $\alpha_L^{I\ num} = 0.5479$ for this case ($\nu = 0.3$) with an error less then 0.04%. Based on this discretization the angle $\theta^\star$ has to be found satisfying the square root singularity at both ends of the crack front. If $\theta^\star = 76.155°$, which is equivalent to $\gamma = 13.845°$, the value of α_L^I is equal to 0.50000669. As there will be no further change of the geometrical situation at both ends of the crack front during the stable mode–I crack propagation, the specified angle γ will not change either.

A practically linear relationship between the crack front angle γ and the asymptotic exponent α_L^I is shown in figure 3 b. The predicted crack front angle could be confirmed in experimental investigations [4], cp. figure 4.

The shape of the crack fronts is almost independent of the specimen dimensions during the stable fatigue crack growth. Then, the assumption of a valid square–root singularity in the vicinity of the intersection between the crack front and the outer boundary could be confirmed by the agreement of the angle γ.
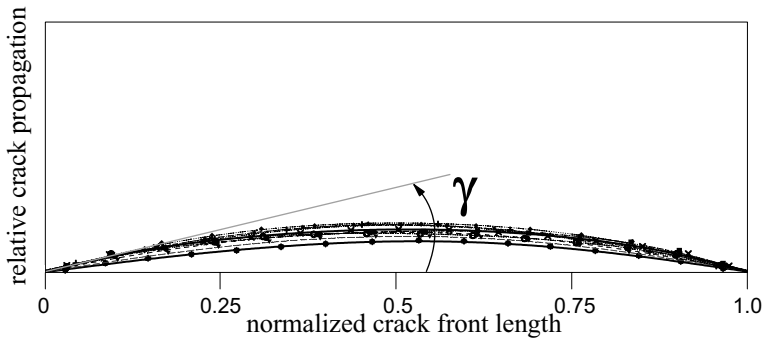
Figure 4 Experimentally observed crack front shapes

One can conclude, at least for pure the mode–I loading, that the crack front will be shaped in such a way that the square–root singularity holds along the whole crack front. Additionally, a very interesting result has been observed in numerical simulations. Namely, if one take the crack front shape from the experiment and introduce it into the calculation, then the resulting SIF K_I has been a constant along the whole crack front.

These two results are already included in an iterative forward predictor–corrector procedure, cp. [6].

5.   DESIGN OF SPECIMENS

For a given specimen with a surface breaking crack under mode–I conditions the crack front will be shaped satisfying $K_I = const$ and having a certain crack front angle γ, cp. section 4. In contrast to section 4 one can follow the other way. How should a specimen designed getting a straight crack front? It would be useful for many experimental investigations. Usually, the crack starts growing from a starting notch. But the radius of the notch influences the crack growth behavior at the very beginning and has to be close to zero [8]. Within this procedure the real experiment always starts with a curved crack front instead of a desired straight crack front.

Hence, the following question appears. How could the geometrical situation in the area where the crack front intersects the outer boundary be changed in order to keep the crack front angle $\gamma = 0°$? As a possible solution we propose to insert an additional notch into the specimen.

The specimen ($L = 200\,\text{mm}$, $W = 50\,\text{mm}$ and $B = a = 25\,\text{mm}$) with its special geometry is subjected to tension ($\sigma_0 = 100\,\text{MPa}$) and shown in figure 5. The additional notch is characterized by the opening angle β and the depth h. The geometry is divided into a core and a boundary layer zone. The core specimen corresponds to a classical single edge cracked specimen

Front view

σ_0 · · · · · σ_0

W

a

L

Top view

core

boundary layer

h

t

B

h

p

$\beta/2$
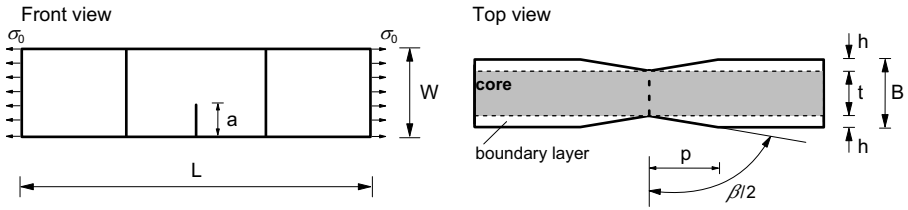
Figure 5 Sketch of a square–root singular specimen

(SEC–specimen) expanded by a boundary layer zone. The specimen is made of PMMA (Young's modulus $E = 3.6\,\text{GPa}$ and Poission ratio $\nu = 0.36$).

In the following the notch angle β has to be found satisfying the square root singularity in the vicinity of the intersection between the crack front and the outer boundary.

The (θ, φ)–plane of the domain Ω_O^ε in the singularity analysis is spanned by $(\theta, \varphi) \in (0°; 180°) \times (0°; \zeta)$. The crack intersects this domain at $\varphi = \frac{\zeta}{2}$ and $\theta \in (90°; 180°)$. ζ is defined by $\zeta = 360° - \beta$. The eigenvalue α_L^I related to a symmetrical opening of the crack surfaces (mode–I) was equal to 0.500106 for the crack front angle $\gamma = 0°$ and the notch angle $\beta = 166.8°$ for $\nu = 0.36$. To have this notch angle on hand for other materials figure 6 is shown.

As ν tends to zero the notch angle tends to 180°. This corresponds well to the plane strain conditions and to results obtained by [3].

With the notch angle on hand, numerical investigations [5] are performed to determine a reliable size of the notch depth h having a constant K_I distribution along the whole crack front. All global dimensions were kept constant and only the depth h was varied. It can be clearly seen in figure 7 a) a certain minimum depth has to be reached to come from a

180°

β

$\nu = 0.2$
$\beta = 174.08°$

175°

$\nu = 0.1$
$\beta = 177.12°$

$\nu = 0.36$
$\beta = 166.8°$

170°

$\nu = 0.3$
$\beta = 169.5°$

165°

$\nu = 0.45$
$\beta = 160.75°$

160°

$\nu = 0.499$
$\beta = 156.49°$

155°

$\nu = 0.49999$
$\beta = 156.2°$

150°

0.0   0.1   0.2   0.3   0.4   0.5

ν

Figure 6 Notch angle satisfying the square–root singularity

convex distribution of $K_I^n(s) = K_I(s)/(\sigma_0\sqrt{\pi a})$ to a constant one. s denotes the coordinate of the normalized crack front length. The constance is given in terms of the maximum deviation $\Delta K_I^{\max} = \max\left[(K_I(s) - \bar{K}_I)/\bar{K}_I\right]$ of the mean value $\bar{K}_I$, cp. figure 7 b). The changing algebraic sign corresponds to the transition from the convex to a practically constant distribution of K_I^n. Although the distribution of $K_I^n(s)$ is slightly increasing

Figure 7 Notch depth obtaining a constant K_I^n–distribution

at both ends it can be treated as constant because ΔK_I^{max} is always less then 0.7% for $h \geq 2\,\text{mm}$. It may indicate that the notch angle β should be slightly larger and the corresponding singular exponent closer to 0.5. But this problem is subjected to a forthcoming sensitivity analysis.

For the range of $2\,\text{mm} \leq \text{h} \leq 6\,\text{mm}$ the "constant" distribution has almost the same level. If the depth h is more increasing the SIF $K_I^n(s)$ keeps still practically constant but the level is decreasing. The remaining crack front length t is also decreasing. That is why, there can not be assumed the plane strain conditions any more. It is a transition from the plane strain to the plane stress conditions in the crack near field. From the associated displacement field it is known that the respective stress intensity factors $(K_I^{n,\circ}, K_I^{n,*})$ differ at a factor M

$$M(\nu) = K_I^{n,\circ}/K_I^{n,*} \sim (5+\nu)/(5+\nu-4\nu^2)$$

between these two conditions. This factor M can be depicted in figure 7 a). Assuming two dimensional plane strain conditions it leads to $K_I^{n,\circ} = 2.82658$ and for the plane stress conditions one obtains $K_I^{n,*} = K_I^{n,\circ}/M = 2.553212$ for $\nu = 0.36$. As one can see in figure 7 a), $K_I^n(s)$ tends exactly to the value of $K_I^{n,*}$ as the crack length t tends to zero $(h \to 12.5\,\text{mm})$.

The qualitative behavior of getting a straight crack front by introducing an additional notch has been confirmed by the performance of an appropriate experiment.

Finally, the name square–root singularity specimen can be proposed for the specimen in figure 5, because the square–root singularity holds along the whole crack front and the crack front is straight.

6.   CONCLUSION

The application of 3D singularities to fatigue crack growth simulation has been shown. The determination of such singularities has been explained briefly. With known asymptotic exponents three aspects are going to arise. Firstly, the design of special crack front elements has been proposed for the accurate simulation of the displacement field near the crack front. Secondly, concerning mode–I fatigue crack growth, the crack front angle γ is specified regarding to the assumption of a valid square–root singularity along the whole crack front. Thirdly, a new class of specimens – square–root singularity specimens – has been proposed. With the help of these specimens a straight crack front can be generated under mode–I loading during stable crack growth. This new specimen offers the chance of neglecting the "negative" influence of the Poisson ratio in experiments.

References

[1] Bazant, ZP and Estenssoro, LF (1979) *Surface singularity and crack propagation*, Int. J. Solids Structures, **15**, 405–426.

[2] Benthem, JP (1977) *State of stress at the vertex of a quarter–infinite crack in a half space*, Int. J. Solids Structures, **13**, 479–492.

[3] Dimitrov, A, Andrä, H and Schnack, E (2001) *Efficient computation of order and mode of corner singularities in 3D–elasticity*, Int. J. Meth. Engng, **52**, 805–827.

[4] Kuhn, G, Kolk, K and Heyder, M (2002) *3D fatigue crack propagation – simulation and experiment*, Presentation at the International Workshop on Contact and Fracture Problems, Bad Honnef, May, 27–29.

[5] Kolk, K and Kuhn, G (2001) *3D crack growth simulation,* in Z. Waszczyszyn, J. Pamin, eds., *Solids, Structures and Coupled Problems in Engineering. CD. 2nd ECCM, Cracow.*

[6] Kolk, K and Kuhn, G (2002) *A predictor–corrector procedure for the determination of the shape of 3D crack fronts,* in H.A. Mang, F.G. Rammersdorfer, J. Eberhardsteiner eds., *Fifth World Congress on Computational Mechanics. Vienna. Austria.*

[7] Lehoucq, RB, Sorenson, DC and Yang, C (1998) *ARPACK User's Guide Solution of Large Scale Eigenvalue Problems with Implicitly Restarted Arnoldi Methods*, Internet publication, ftp://ftp.caam.rice.edu/pub/software/ARPACK.

[8] Plank, R (1997) *Ermüdungsrissausbreitung unter nicht-proportionaler Mixed-Mode-Beanspruchung*, Fortschr.–Ber. VDI Reihe 18 Nr. 207, VDI, Düsseldorf, Germany.

Chapter 9
Mathematical models
of gas and fluid flows

A DIFFUSING VORTEX CIRCLE IN A VISCOUS FLUID

L.E. Fraenkel[1] and J.B. McLeod[2]

[1] *Department of Mathematical Sciences, University of Bath, Bath BA2 7AY, UK*
lef@maths.bath.ac.uk
[2] *Department of Mathematics, University of Pittsburgh, Pittsburgh, PA 15260, USA*

Abstract   This paper concerns the evolution, according to the Navier-Stokes equations, of vorticity $\boldsymbol{\omega} = \omega \mathbf{e}^{\varphi}$ initially concentrated on a circle as in Figure 1. The aim is to prove existence, for small times, of an exact solution $\omega = \omega_A + \omega_1 + \rho$, where ω_A is a formal approximation that is known explicitly. The leading perturbation ω_1 is the semi-explicit solution of a linear problem; the remainder ρ must be shown to exist and to be suitably small.

The following results are presented. (i) Saffman's formulae for the centroid of vorticity and its velocity are derived with a little more generality than is used in [4] and from a different starting point; possibly there is a gain of clarity. (ii) Theorem 1 establishes existence and uniqueness of ω_1. (iii) Theorem 2 presents an *a priori* bound for ρ.

The final stage of the work remains to be done. It seems very probable that existence and suitable smallness of ρ will follow from Theorem 2, but the proof of this is not yet complete.

1.   INTRODUCTION

This paper describes work on an initial-value problem for the Navier-Stokes equations. Fluid is assumed to occupy the whole (Euclidean, three-dimensional) space $\mathbb{R}^3$; the initial velocity (at time $t = 0$) is that induced by vorticity concentrated on, and tangential to, a circle that we visualize as horizontal (Figure 1). According to plausible reasoning, the circle moves upwards, initially with infinite velocity; the vorticity diffuses, being mainly contained for small $t > 0$ in a (vaguely defined) ring of small cross-section outside which the vorticity is exponentially small.

$$z = x_3$$

$$x = (r\cos\varphi, r\sin\varphi, z)$$

circle $\{z = 0,\, r = a\}$

x_1

circulation κ at time 0

φ

vorticity $\boldsymbol{\omega}(x, 0)$

x_2
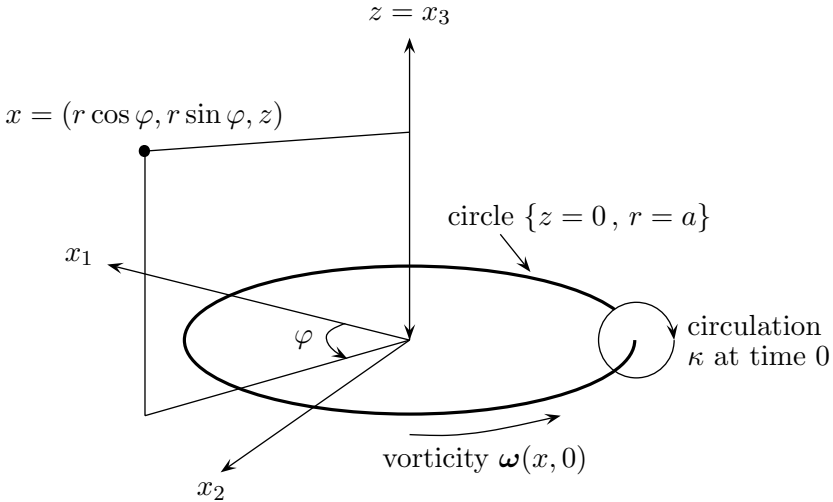
Figure 1

Thin vortex rings of this kind in a viscous fluid are the subject of various approximate formulae ; there is a long list of references in [1]. Not all these formulae refer to an initial-value problem and not all agree with others. The present work is intended to provide a rigorous basis for such approximations. In particular, we wish to confirm Saffman's admirable formula in [4] for the velocity of the *centroid of vorticity* defined there.

Let x_1, x_2, x_3 be Cartesian co-ordinates such that the frame $(0x_1, 0x_2, 0x_3)$ moves, relative to the fluid at infinity, with the velocity $(0, 0, U(t))$ of the centroid of vorticity, the axes remaining parallel to their initial positions (shown in Figure 1). The *fluid velocity* relative to this moving frame is written $\mathbf{v}(x, t)$, where $x \in \mathbb{R}^3$, and the *vorticity* is $\boldsymbol{\omega} := \operatorname{curl} \mathbf{v} = \nabla_\wedge \mathbf{v}$. In the present situation it follows that, when $U(t)$ and $\boldsymbol{\omega}(x, t)$ are known, the fluid velocity is given by

$$\mathbf{v}(x, t) \;=\; -(0, 0, U(t)) + \nabla_\wedge \int_{\mathbb{R}^3} \frac{1}{4\pi |x - x'|} \; \boldsymbol{\omega}(x', t) dx'. \qquad (1.1)$$

With this equation understood, our problem is to find $\boldsymbol{\omega}(x, t)$ and $U(t)$ such that

$$\left(\frac{\partial}{\partial t} - \Delta \right) \boldsymbol{\omega} \;=\; -\frac{1}{\nu} \{ (\mathbf{v} \cdot \nabla)\boldsymbol{\omega} - (\boldsymbol{\omega} \cdot \nabla)\mathbf{v} \} \quad \text{in} \quad \mathbb{R}^3 \times (0, \bar{t}) \qquad (1.2)$$

for some small $\bar{t} > 0$; also such that

$$\boldsymbol{\omega}(x, 0) \;=\; \kappa\, \delta(z)\delta(r - a)\mathbf{e}^\varphi, \qquad (1.3)$$

where the kinematic viscosity ν, the circulation κ and the radius a are given positive constants; $t := \nu T$, where T denotes physical time; $\delta(\cdot)$ denotes the Dirac generalized function; cylindrical co-ordinates z, r, φ are defined by $x =: (r\cos\varphi,\ r\sin\varphi, z)$ and $\mathbf{e}^\varphi := (-\sin\varphi,\ \cos\varphi, 0)$. Thus $\boldsymbol{\omega}(x,t) = \omega(z,r,t)\mathbf{e}^\varphi$.

The use of t simplifies the heat operator in (1.2) and many subsequent formulae. If we were to use non-dimensional variables $\hat{x} := x/a$, $\hat{t} := t/a^2$, $\hat{\mathbf{v}} := \mathbf{v}a/\nu$ and $\hat{\omega} := \omega a^2/\nu$, then the only parameter of the problem would be the Reynolds number κ/ν. Our results are valid whenever $0 < \kappa/\nu < \infty$, but the time interval $(0, \bar{t}/a^2)$ shrinks as κ/ν increases.

The basic theory of the Navier-Stokes equations [3]does not apply to this problem, because the initial kinetic energy of the fluid is infinite, but Giga and Miyakawa, in an impressive paper [2], have proved the existence of Navier-Stokes solutions for which the initial vorticity is concentrated on curves. However, the generality of their theorem forces Giga and Miyakawa to impose a restriction of small initial vorticity. Because the present paper concerns a particular axially symmetric flow, no hypothesis of small initial vorticity is needed and more explicit results are possible.

For small values of t/a^2, the right-hand member of (1.2) is expected to be small, because $\boldsymbol{\omega}$ should be approximately constant on small circles in a meridional plane ($\varphi = $ const.) centred at $z = 0$, $r = a$, so that $\mathbf{v}$ is approximately tangential to such circles and approximately of constant magnitude on each of them. If these non-linear terms are neglected, there results the formal approximation

$$\omega_A(z,r,t) \;=\; \frac{\kappa}{4\pi t}\quad \exp\left(-\frac{s^2}{4t}\right)\left(\frac{a}{r}\right)^{\frac{1}{2}} B\left(\frac{ar}{2t}\right), \qquad (1.4)$$

where $s := \{z^2 + (r-a)^2\}^{\frac{1}{2}}$ and B is a known function such that $B(y) \to 1$ as $y \to \infty$. More precisely,

$$B(y) = (2\pi y)^{\frac{1}{2}} e^{-y} I_1(y) \qquad (0 \le y < \infty), \qquad (1.5)$$

where I_1 is the modified Bessel function of the first kind and of order 1 (as in [5], p.77).

We seek a solution of (1.1)to (1.3) having the form

$$\left.\begin{aligned}\omega(z,r,t) &= \omega_A(z,r,t) + t^{-\frac{1}{2}}\{\omega_{11}(\sigma)\cos\theta + \omega_{12}(\sigma)\sin\theta\} + \rho(z,r,t),\\ \text{where}\quad & z =: s\cos\theta,\quad r-a =: s\sin\theta,\quad \sigma := s/(4t)^{\frac{1}{2}}.\end{aligned}\right\}$$
$$(1.6)$$

The functions ω_{11} and ω_{12} refer to an inner region near $z = 0, r = a$ and satisfy linear, ordinary integro-differential equations for $0 < \sigma < \infty$. The remainder function ρ must satisfy a non-linear, partial integro-differential equation on $\mathbb{R} \times (0, \infty) \times (0, \bar{t})$ and represents the difficult part of the problem: ρ must be shown to exist and to be suitably bounded.

2.   THE CENTROID OF VORTICITY AND ITS VELOCITY

This section begins with a slightly more general version of Saffman's basic equations in [4]; the argument is perhaps more transparent than the treatment in [4].

Let X_1, X_2, X_3 be Cartesian co-ordinates such that the frame $(0X_1, 0X_2, 0X_3)$ is fixed relative to the fluid at infinity (which is at rest). Let T denote the time, $\mathbf{u}(X, T)$ the fluid velocity relative to the axes $0X_j$ and $\boldsymbol{\zeta}(X, T) := \nabla_\wedge \mathbf{u}(X, T)$ the vorticity, where now $\nabla := (\partial/\partial X_1, \partial/\partial X_2, \partial/\partial X_3)$.

We consider a viscous flow in all of $\mathbb{R}^3$ that is due solely to vorticity, and assume *a priori* that $\boldsymbol{\zeta}$ is smooth, say each $\zeta_j(., T) \in C^{2,\mu}(\mathbb{R}^3)$ (second derivatives are Hölder continuous with Hölder exponent $\mu \in (0, 1)$); that, for some $\delta > 0$,

$$|\boldsymbol{\zeta}| = O(R^{-5-\delta}) \quad \text{as} \quad R := |X| \to \infty \tag{2.1}$$

(uniformly over the directions X/R and over T); and that

$$\int_{\mathbb{R}^3} \boldsymbol{\zeta} \, dX = \mathbf{0}. \tag{2.2}$$

If it is known or assumed that $|\mathbf{u}| = o(R^{-2})$ as $R \to \infty$, then (2.2) is a *result* rather than a hypothesis. The formula

$$\mathbf{u}(X, T) = \nabla_\wedge \int_{\mathbb{R}^3} \frac{1}{4\pi|X - X'|} \boldsymbol{\zeta}(X', T) dX' \tag{2.3}$$

now implies that each $u_j(., T) \in C^{3,\mu}(\mathbb{R}^3)$ and that $|\mathbf{u}| = O(R^{-3})$ as $R \to \infty$. For fluid of density 1, the *impulse* is

$$\mathbf{I} := \frac{1}{2} \int_{\mathbb{R}^3} \mathbf{X}_\wedge \boldsymbol{\zeta} \, dX \tag{2.4}$$

(we write $\mathbf{X}$ for $X := (X_1, X_2, X_3)$ when its vector nature requires emphasis). Like the Euler equations for an inviscid fluid, the Navier-Stokes

equations imply that *the impulse is constant: $d\mathbf{I}/dT = \mathbf{0}$*; we assume that $\mathbf{I} \neq \mathbf{0}$. Saffman defines the *centroid of vorticity* by

$$\mathbf{c}(T) := \frac{1}{2} \int_{\mathbb{R}^3} \frac{\mathbf{I} \cdot (\mathbf{X} \wedge \boldsymbol{\zeta})}{|\mathbf{I}|^2} \mathbf{X} \, dX, \tag{2.5}$$

partly because this leads to correct results for known vortex configurations that move through inviscid fluid without change of form or of velocity. We now choose co-ordinates such that *the axis $0X_3$ is in the direction $\mathbf{I}/|\mathbf{I}|$*; then

$$\mathbf{I} = (0, 0, I_3), \quad I_3 = \frac{1}{2} \int_{\mathbb{R}^3} (X_1 \zeta_2 - X_2 \zeta_1) dX, \tag{2.6}$$

$$\mathbf{c}(T) = \int_{\mathbb{R}^3} \frac{X_1 \zeta_2 - X_2 \zeta_1}{2 I_3} \mathbf{X} \, dX, \tag{2.7}$$

$$\mathbf{U}(T) := \frac{d\mathbf{c}(T)}{dT} = \frac{1}{2 I_3} \int_{\mathbb{R}^3} \left(X_1 \frac{\partial \zeta_2}{\partial T} - X_2 \frac{\partial \zeta_1}{\partial T} \right) \mathbf{X} \, dX. \tag{2.8}$$

The vorticity form of the Navier-Stokes equations is

$$\frac{\partial \zeta_i}{\partial T} = \nu \Delta \zeta_i - \sum_{j=1}^{3} \partial_j (u_j \zeta_i - u_i \zeta_j) \qquad \left(\partial_j := \frac{\partial}{\partial X_j}, \; i = 1, 2, 3 \right), \tag{2.9}$$

where $\nabla \cdot \mathbf{u} = 0$ and $\nabla \cdot \boldsymbol{\zeta} = 0$. Hence, for a smooth $f(X)$ such that $f = O(R^2)$ and $|\nabla f| = O(R)$ as $R \to \infty$, we have

$$\int_{\mathbb{R}^3} f \frac{\partial \zeta_i}{\partial T} \, dX = \nu \int_{\mathbb{R}^3} (\Delta f) \zeta_i \, dX + \sum_{j=1}^{3} \int_{\mathbb{R}^3} (\partial_j f)(u_j \zeta_i - u_i \zeta_j) dX. \tag{2.10}$$

Applying this identity to (2.8), first with $f(X) = X_1 X_k, i = 2$ and then with $f(X) = X_2 X_k, i = 1$ (and with $k = 1, 2, 3$ in both cases), also using (2.2) when $f(X) = X_1^2$ or X_2^2, we obtain

$$2 I_3 U_k(T) = 3 \int_{\mathbb{R}^3} X_k (u_1 \zeta_2 - u_2 \zeta_1) dX \quad \text{for} \quad k = 1, 2, \tag{2.11}$$

$$2 I_3 U_3(T) = \int_{\mathbb{R}^3} \{ X_1 (u_3 \zeta_2 - u_2 \zeta_3) + X_2 (u_1 \zeta_3 - u_3 \zeta_1) + 2 X_3 (u_1 \zeta_2 - u_2 \zeta_1) \} dX. \tag{2.12}$$

The identity (integration by parts)

$$\int_{\mathbb{R}^3} \mathbf{X} \cdot (\boldsymbol{\zeta} \wedge \mathbf{u}) dX = \frac{1}{2} \int_{\mathbb{R}^3} |\mathbf{u}|^2 dX \tag{2.13}$$

494

allows us to write (2.12) as

$$2I_3U_3(T) = 3\int_{\mathbb{R}^3} X_3(u_1\zeta_2 - u_2\zeta_1)dX + \frac{1}{2}\int_{\mathbb{R}^3}|\mathbf{u}|^2dX. \qquad (2.14)$$

For a known flow, (2.11) and (2.14) give the velocity of the centroid of vorticity.

We transform to a co-ordinate frame moving vertically with the centroid of vorticity by defining

$$\mathbf{e}^3 := (0,0,1), \qquad x := X - c_3(T)\mathbf{e}^3, \qquad t := \nu T, \qquad (2.15)$$

$$\mathbf{v}(x,t) := \mathbf{u}(X,T) - U_3(T)\mathbf{e}^3, \qquad \boldsymbol{\omega}(x,t) := \boldsymbol{\zeta}(X,T). \qquad (2.16)$$

Then $\partial/\partial X_j = \partial/\partial x_j$ and $\partial/\partial T = \nu\partial/\partial t - U_3(T)\partial/\partial x_3$, so that $\partial/\partial T + \mathbf{u}.\nabla = \nu\partial/\partial t + \mathbf{v}.\nabla$ and the new vorticity equation (1.2) is essentially the same as the previous (2.9). (The factor ν in $\nu\partial/\partial t$ is tiresome here but convenient elsewhere in the paper.) The impulse is now

$$I_3 = \frac{1}{2}\int_{\mathbb{R}^3}(x_1\omega_2 - x_2\omega_1)dx, \qquad (2.17)$$

and the velocity of the centroid of vorticity (relative to the fluid at infinity) becomes

$$2I_3\mathbf{U}(T) = 3\int_{\mathbb{R}^3}\mathbf{x}(v_1\omega_2 - v_2\omega_1)dx + \left(\frac{1}{2}\int_{\mathbb{R}^3}|\mathbf{u}|^2dx\right)\mathbf{e}^3; \qquad (2.18)$$

in the first integral we have been able to replace $x_3 + c_3(T)$ by x_3 because

$$\int_{\mathbb{R}^3}\mathbf{u}\wedge\boldsymbol{\zeta}dX = \mathbf{0}. \qquad (2.19)$$

For *axial symmetry*, with co-ordinates $x =: (r\cos\varphi, r\sin\varphi, z)$, with unit vectors

$$\mathbf{e}^z := (0,0,1), \qquad \mathbf{e}^r := (\cos\varphi, \sin\varphi, 0), \qquad \mathbf{e}^\varphi := (-\sin\varphi, \cos\varphi, 0), \qquad (2.20)$$

with vorticity $\omega(z,r,t)\mathbf{e}^\varphi$ and with fluid velocity $v^z(z,r,t)\mathbf{e}^z + v^r(z,r,t)\mathbf{e}^r$, we have

$$I_3 = \frac{1}{2}\int_{\mathbb{R}^3}r\omega\,dx, \qquad v_1\omega_2 - v_2\omega_1 = v^r\omega, \qquad (2.21)$$

and (2.18) reduces to

$$U_1 = U_2 = 0, \quad 2I_3U_3(T) = 3\int_{\mathbb{R}^3}zv^r\omega dx + \frac{1}{2}\int_{\mathbb{R}^3}|\mathbf{u}|^2dx. \qquad (2.22)$$

As Saffman emphasizes in [4], an advantage of this formula in the problem (1.1) to (1.3) is that a formal first approximation to U_3 can be calculated from the ω_A in (1.4), whereas other formulae for U_3 require a better approximation to ω. More explicitly, we expect that, for the problem (1.1) to (1.3),

$$U(t) := U_3(T) = U_0(t)\{1 + O\left(\varepsilon \log \frac{8}{\varepsilon}\right)\}, \qquad \varepsilon := \frac{\sqrt{4t}}{a}, \qquad (2.23)$$

with

$$U_0(t) = \frac{\kappa}{4\pi a}\{\log \frac{8a}{\sqrt{4t}} + \frac{1}{2}(\gamma - \log 2 - 1)\}. \qquad (2.24)$$

Here $\gamma = 0.5772...$ is Euler's constant and we have used the *inner approximation*

$$\omega_A(z, r, t) \sim \frac{\kappa}{4\pi t} \exp(-\sigma^2), \quad \sigma := \frac{s}{\sqrt{4t}} \in [0, \infty), \qquad (2.25)$$

based on $t \downarrow 0$ *with σ fixed* (so that $s \downarrow 0$). The formula (2.24) is due to Saffman [4]. At present the O-term in (2.23) is merely a hope; equation (2.23) will become a result when $\omega_1 + \rho$ is proved to exist and to be suitably small.

3.   SUITABLE FORMS OF THE GOVERNING EQUATIONS

We introduce a stream function ψ due to vorticity, and a total stream function

$$\Psi(z, r, t) = -\frac{1}{2}U(t)r^2 + \psi(z, r, t), \qquad (3.1)$$

such that (with the notation defined between (2.19) and (2.21)), $v^z = r^{-1}\partial\Psi/\partial r$ and $v^r = -r^{-1}\partial\Psi/\partial z$ and $\Psi(z, 0, t) = 0$. In place of (1.1) we have

$$\psi(z_0, r_0, t) = \iint_\Pi P(z_0 - z, r_0, r)\, \omega(z, r, t)\, dzdr, \qquad (3.2)$$

where $\Pi := \{(z, r)| -\infty < z < \infty, r > 0\}$ denotes a meridional half-plane ($\varphi =$const.) and

$$P(z_0 - z, r_0, r) := \frac{r_0 r}{4\pi} \int_{-\pi}^{\pi} \frac{\cos\lambda}{\{(z - z_0)^2 + r^2 - 2rr_0\cos\lambda + r_0^2\}^{\frac{1}{2}}}\, d\lambda. \quad (3.3)$$

The kernel P can be written in terms of complete elliptic integrals.

For *inner approximations* (based on $t \downarrow 0$ with $s/\sqrt{4t}$ fixed), it is useful that, if we define $\alpha := z/a = s \cos\theta/a$ and $\beta := (r-a)/a = s \sin\theta/a$, then

$$P(z_0 - z, r_0, r) = \frac{a}{2\pi} \left\{ \log \frac{8}{|(\alpha, \beta) - (\alpha_0, \beta_0)|} \sum_{n=0}^{\infty} p_n(\alpha - \alpha_0, \beta, \beta_0) \right.$$
$$\left. + \sum_{n=0}^{\infty} q_n(\alpha - \alpha_0, \beta, \beta_0) \right\}, \quad (3.4)$$

where the p_n and q_n are homogeneous polynomials of degree n. In particular,

$$
\begin{aligned}
p_0 &= 1, & q_0 &= -2, \\
p_1 &= \tfrac{1}{2}(\beta + \beta_0), & q_1 &= -\tfrac{1}{2}(\beta + \beta_0), \\
p_2 &= \tfrac{1}{16}\{3(\alpha - \alpha_0)^2 + (\beta - \beta_0)^2\}, & q_2 &= \tfrac{1}{16}\{-(\alpha - \alpha_0)^2 + 3\beta^2 + 2\beta\beta_0 + 3\beta_0^2\}.
\end{aligned}
$$

Both series in (3.4) converge uniformly and absolutely if $|(\alpha, \beta)| \leq 1 - \delta$ and $|(\alpha_0, \beta_0)| \leq 1 - \delta$ for some $\delta > 0$. The converse of (3.2) is

$$\omega = -\frac{1}{r}L\psi, \quad \text{where} \quad L := \left(\frac{\partial}{\partial z}\right)^2 + \left(\frac{\partial}{\partial r}\right)^2 - \frac{1}{r}\frac{\partial}{\partial r}. \quad (3.5)$$

In terms of the stream function Ψ, the vorticity equation (1.2) becomes

$$\left(\frac{\partial}{\partial t} - L_1\right)\omega = \frac{1}{\nu}\left\{\frac{\partial\Psi}{\partial z}\frac{\partial}{\partial r}\left(\frac{\omega}{r}\right) - \frac{\partial\Psi}{\partial r}\frac{\partial}{\partial z}\left(\frac{\omega}{r}\right)\right\}, \quad (3.6)$$

where

$$L_1 := \left(\frac{\partial}{\partial z}\right)^2 + \left(\frac{\partial}{\partial r}\right)^2 + \frac{1}{r}\frac{\partial}{\partial r} - \frac{1}{r^2}. \quad (3.7)$$

For inner approximations we use variables $\sigma := s/\sqrt{4t}, \theta$ and $\tau = t$, where $\partial/\partial\tau$ means that σ and θ are held constant; also, $\sqrt{4\tau}/a$ serves as a 'small parameter'. Then (3.6) and (3.7) become

$$\left(\frac{\partial}{\partial\tau} - \frac{1}{2\tau}\sigma\frac{\partial}{\partial\sigma} - L_1\right)\omega = \frac{1}{\nu}\frac{1}{4\tau\sigma}\left\{\frac{\partial\Psi}{\partial\sigma}\frac{\partial}{\partial\theta}\left(\frac{\omega}{r}\right) - \frac{\partial\Psi}{\partial\theta}\frac{\partial}{\partial\sigma}\left(\frac{\omega}{r}\right)\right\}, \quad (3.8)$$

$$L_1 = \frac{1}{4\tau}\Delta_\sigma + \frac{1}{\sqrt{4\tau}}\frac{1}{r}\left(\sin\theta\frac{\partial}{\partial\sigma} + \cos\theta\frac{1}{\sigma}\frac{\partial}{\partial\theta}\right) - \frac{1}{r^2}, \quad (3.9)$$

where

$$\Delta_\sigma := \left(\frac{\partial}{\partial\sigma}\right)^2 + \frac{1}{\sigma}\frac{\partial}{\partial\sigma} + \frac{1}{\sigma^2}\left(\frac{\partial}{\partial\theta}\right)^2, \quad r = a + \sqrt{4\tau}\sigma\sin\theta. \quad (3.10)$$

4.   A SECOND APPROXIMATION FOR THE INNER REGION

If in (3.5) and (3.8) we replace L and L_1 by $(4\tau)^{-1}\Delta_\sigma$, and then replace r by a, the resulting equations are satisfied by

$$\omega_0(\sigma, \tau) = \frac{\kappa}{4\pi} \frac{e^{-\sigma^2}}{\tau}, \tag{4.1}$$

$$\Psi_0(\sigma) = \frac{\kappa a}{2\pi} \left\{ \left(\log \frac{1}{\sigma} - \int_\sigma^\infty \frac{e^{-\lambda^2}}{\lambda} \, d\lambda \right) - 2 - \frac{1}{8} (\gamma - \log 2 - 1) \right\}. \tag{4.2}$$

The constant in Ψ is such that (3.1) and (3.2) are also satisfied to the lowest order when (2.24) and (3.4) are used.

We now seek a second approximation $\omega_0(\sigma, \tau) + \omega_1(\sigma, \theta, \tau)$ by substituting this into (3.2) and (3.8), by assuming that ω_1 will be $O\left(\tau^{-\frac{1}{2}}\right)$ and not $o\left(\tau^{-\frac{1}{2}}\right)$ and by neglecting all terms that appear to be $o\left(\tau^{-\frac{3}{2}}\right)$. The resulting equation is

$$\frac{\partial \omega_1}{\partial \tau} - \frac{1}{4\tau} \left\{ \Delta_\sigma + 2\sigma \frac{\partial}{\partial \sigma} + b(\sigma) \frac{\partial}{\partial \theta} \right\} \omega_1 - \frac{c_0}{4\tau} e^{-\sigma^2} \frac{\partial}{\partial \theta} (A\omega_1)$$

$$= (4\tau)^{-\frac{3}{2}} f_1(\sigma, \theta), \tag{4.3}$$

where

$$b(\sigma) := -\frac{\kappa}{2\pi\nu} \frac{1 - e^{-\sigma^2}}{\sigma^2}, \quad c_0 := \frac{2\kappa}{\pi\nu}, \tag{4.4}$$

$$\left.\begin{array}{l} (A\omega_1)(\sigma_0, \theta_0, \tau) \\[2mm] \qquad := \frac{1}{2\pi} \iint_E \log \frac{1}{|\sigma e^{i\theta} - \sigma_o e^{i\theta_o}|} \, \omega_1(\sigma, \theta, \tau) \sigma \, d\sigma \, d\theta, \\[2mm] E := \{(\sigma, \theta) | 0 < \sigma < \infty, \, -\pi < \theta \le \pi\}. \end{array}\right\} \tag{4.5}$$

The forcing function f_1 has the form

$$f_1(\sigma, \theta) = \frac{\kappa^2}{2\pi^2\nu a} h_1(\sigma) \cos \theta, \tag{4.6}$$

where h_1 is a known function that is $O(\sigma)$ for $\sigma \downarrow 0$ and is $O(e^{-\sigma^2} \sigma \log \sigma)$ for $\sigma \to \infty$. The factor $\cos \theta$ in (4.6) permits the separation of variables in ω_1 that is shown in (1.6), but such a decomposition is not needed for the following result.

Theorem 1. *Equation (4.3) has a unique solution $\omega_1(\sigma, \theta, \tau) = (4\tau)^{-\frac{1}{2}}$ $\omega_*(\xi, \eta)$, where $\xi := \sigma \cos \theta$ and $\eta := \sigma \sin \theta$, such that $\omega_* \in C^2(\mathbb{R}^2)$ and*

$$\omega_*(\xi, \eta) = O(e^{-\sigma^2} \sigma \log \sigma) \quad as \quad \sigma \to \infty. \tag{4.7}$$

Remarks.   1. If it should be desirable to seek a third approximation $\omega_0 + \omega_1 + \omega_2$ in the inner region (before considering a remainder ρ), with ω_2 also satisfying a linear equation, then Theorem 1 extends to existence and uniqueness of ω_2.

2. The proof of Theorem 1, while not unduly long (20 pages of hand-written notes, including all details), cannot be included here for reasons of space. However, we can state the essential step. Let

$$\omega_1(\sigma, \theta, \tau) =: (4\tau)^{-\frac{1}{2}} e^{-\frac{1}{2}\sigma^2} q_1(\sigma, \theta); \tag{4.8}$$

then (4.3) becomes

$$-\left\{ \Delta_\sigma - \sigma^2 + b(\sigma) \frac{\partial}{\partial \theta} \right\} q_1 - c_0 e^{-\frac{1}{2}\sigma^2} \frac{\partial}{\partial \theta} A \left(e^{-\frac{1}{2}\sigma^2} q_1 \right) = e^{\frac{1}{2}\sigma^2} f_1(\sigma, \theta). \tag{4.9}$$

Assume that a solution q_1 of (4.9) exists; multiply the equation by σq_1 and integrate over E; there results

$$\iint_E \left\{ \left(\frac{\partial q_1}{\partial \sigma} \right)^2 + \left(\frac{1}{\sigma} \frac{\partial q_1}{\partial \theta} \right)^2 + \sigma^2 q_1^2 \right\} \sigma d\sigma d\theta = \iint_E e^{\frac{1}{2}\sigma^2} f_1 q_1 \sigma d\sigma d\theta. \tag{4.10}$$

It is obvious why the term $\partial q_1/\partial \theta$ in (4.9) does not contribute to this equation; that $\partial A(\cdot)/\partial \theta$ does not contribute is not quite obvious, but is true. Equation (4.10) provides an *a priori* bound for q_1 in an appropriate Sobolev space.

5.   THE PROBLEM FOR THE REMAINDER

We set $\omega = \omega_A + \omega_1 + \rho$, where ω_A and ω_1 are known functions given by (1.4) and by Theorem 1, respectively. If pressed, we could reduce the forcing function in the problem for ρ by introducing a second inner pertur-bation $\omega_2(\sigma, \theta, \tau)$. Let $N(\omega) = 0$ denote the vorticity equation (3.6) with Ψ expressed in terms of ω by (3.1),(3.2) and (2.22); $N(\omega)$ stands for the left-hand member of (3.6) minus the right-hand member. Then

$$N(\omega) = N(\omega_A) + N'(\omega_A)(\omega_1 + \rho) + F(\omega_A, \omega_1 + \rho), \tag{5.1}$$

where F is formally of order $(\omega_1 + \rho)^2$. The essence of the problem for ρ is the linear equation $N'(\omega_A)\rho = f$; if this has a suitably bounded solution ρ

for every f in an appropriate class, then in $N(\omega) = 0$ the terms of order $\omega_1 \rho$ and of order ρ^2 can be controlled.

Although linear, the equation $N'(\omega_A)\rho = f$ is more difficult than (4.3) because it contains many terms, because the co-ordinate σ is appropriate for an inner region but is unsuitable for $s \geq$ const. > 0 and because the term $\partial\rho/\partial t$ cannot be handled as simply as $\partial\omega_1/\partial\tau$ was. Nevertheless, if β is a smooth non-decreasing function of σ such that, with $\varepsilon := \sqrt{4\tau}/a$,

$$\beta(\sigma,\tau) = \frac{1}{2}\sigma^2 \quad \text{for} \quad \sigma \leq \varepsilon^{-\frac{1}{2}} \ (\text{for} \quad s \leq \varepsilon^{\frac{1}{2}}a), \tag{5.2}$$

$$\beta(\sigma,\tau) = \frac{a}{\sqrt{4\tau}} \quad \text{for} \quad \sigma \geq 3\varepsilon^{-\frac{1}{2}} \ (\text{for} \quad s \geq 3\varepsilon^{\frac{1}{2}}a), \tag{5.3}$$

then the transformation

$$\rho(z,r,t) =: re^{-\beta(\sigma,\tau)}u(z,r,t), \tag{5.4}$$

which is comparable with (4.8), leads to an inequality resembling the identity (4.10).

In order to state a result, we must define

$$\gamma(\sigma,\tau) := 2\sigma\frac{\partial\beta}{\partial\sigma} - \left(\frac{\partial\beta}{\partial\sigma}\right)^2 - 4\tau\frac{\partial\beta}{\partial\tau} = \begin{cases} \sigma^2 & \text{for} \quad \sigma \leq \varepsilon^{-\frac{1}{2}}, \\ 2\dfrac{a}{\sqrt{4\tau}} & \text{for} \quad \sigma \geq 3\varepsilon^{-\frac{1}{2}}. \end{cases} \tag{5.5}$$

The Banach space V_0 is the completion of the set $C_c^\infty(\Pi \times (0,\bar{t}])$, of infinitely differentiable functions having compact support in $\Pi \times (0,\bar{t}]$, in the norm defined by

$$\| \varphi \|_{V_0}^2 := \max_{0 \leq t \leq \bar{t}} \int_\Pi \varphi(z,r,t)^2 \, dm$$

$$+ \iint_{Q_{\bar{t}}} \left\{ |\nabla\varphi|^2 + \frac{\gamma(\sigma,\tau)}{4t}\varphi^2 \right\} dm \, dt, \tag{5.6}$$

where $dm := r^3 dz dr$ and $Q_{\bar{t}} := \Pi \times (0,\bar{t})$. Note that $dz dr/4t = \sigma d\sigma d\theta$.

Let $Mu = e^\beta f$ be the equation to which $N'(\omega_A)\rho = f$ is transformed by (5.4). The definition of a *weak solution* $u \in V_0$ of $Mu = e^\beta f$ is of a conventional kind but is too long to be stated here (because a special Hilbert space, designed to go well with V_0, is used to house test functions).

Theorem 2. *If $\bar{t}$ is sufficiently small, if*

$$\|f\|^2 := \iint_{Q_{\bar{t}}} \frac{4t}{1+\gamma(\sigma,\tau)}e^{2\beta}f^2 dm \, dt < \infty, \tag{5.7}$$

if $u \in V_0$ and if u is a weak solution of $Mu = e^{\beta} f$, then

$$\| u \|_{V_0} \leq 4\sqrt{3}\|f\|. \tag{5.8}$$

Remarks. 1. The proof is long and somewhat technical; there can be no question of including it here. We merely remark that the transformation (5.4) and the quadratic form to which it leads are all-important, like their simpler analogues in (4.8) and in (4.10).

2. It is *almost* certain that the *a priori* bound in Theorem 2 leads to a smooth, suitably bounded solution ρ of the full non-linear problem for ρ, but we have not yet completed the details of this.

References

[1] Y. Fukumoto and H. K. Moffatt, Motion and expansion of a viscous vortex ring. Part 1. A higher-order asymptotic formula for the velocity. *J.Fluid Mech.* **417** (2000), 1-45.

[2] Y. Giga and T. Miyakawa, Navier-Stokes flow in R^3 with measures as initial vorticity and Morrey spaces. *Commun. PDEs* **14** (1989), 577-618.

[3] O. A. Ladyzhenskaya, *The mathematical theory of viscous incompressible flow.* New York: Gordon and Breach (1963).

[4] P. G. Saffman, The velocity of viscous vortex rings. *Stud. Appl. Math.* **49** (1970), 371-380.

[5] G. N. Watson, *Theory of Bessel functions.* Cambridge: University Press (1952).

LOW AXIAL REYNOLDS NUMBER, HIGH SWIRL RATIO, VORTEX BREAKDOWN IN A SLOWLY VARYING TUBE

D.A. MacDonald

Department of Mathematical Science

P.O. Box 147

The University

Liverpool L69 3BX, U.K.

sx10@liv.ac.uk

Keywords: Vortex breakdown, low Reynolds number, unsteady flow.

Abstract   For time $\bar{t} < 0$ viscous fluid is in slow flow through a long straight axially symmetric tube whose radius varies slowly with axial distance, $\bar{x}$. When $\bar{t} = 0$ the tube is impulsively rotated about its axis with angular velocity, $\bar{\Omega}$ at which angular speed it is thereafter maintained (Figure 1a). During the transition from zero angular velocity to solid body rotation, the flow in the tube can briefly exhibit striking physical behaviour[1]. In this paper, the solution of the parabolic governing equations given in [1] is subjected to close scrutiny. In particular, the neglected axial diffusion terms are evaluated using the parabolic solution and are shown to be almost everywhere negligible.

1.   INTRODUCTION

When viscous fluid with swirl is introduced into a stationary circular tube, of constant or slowly increasing cross-section, the radial pressure gradient, at sufficiently high rates of incoming swirl, satisfies the approximate equation

$$\frac{\partial \bar{p}}{\partial \bar{r}} = \rho \, \frac{\bar{v}^2}{\bar{r}} ,$$

where $\bar{v}(\bar{r}, \bar{x})$ denotes the azimuthal velocity component and dimensional quantities are denoted by a bar. This equation leads to

$$\left(\frac{\partial \bar{p}}{\partial \bar{x}} \right)_{\bar{r} = \bar{a}} - \left(\frac{\partial \bar{p}}{\partial \bar{x}} \right)_{\bar{r} = 0} = 2 \rho \int_0^{\bar{a}} \frac{\bar{v}}{\bar{r}} \frac{\partial \bar{v}}{\partial \bar{x}} \, d\bar{r} ,$$

where $\bar{p}$ denotes the fluid pressure and $\bar{r} = \bar{a}(\bar{x})$ gives the equation of the tube wall. But, for flow which is nowhere reversed in direction, $\bar{v}\,\partial\bar{v}/\partial\bar{x} < 0$. Indeed, at sufficiently high rates of incoming swirl and at suitable values of the axial Reynolds number, the rate of decrease of $\frac{\partial\bar{v}}{\partial\bar{x}}$ with increase of $\bar{x}$ is sufficiently large to produce **an adverse pressure gradient on the tube axis**, this being a necessary precursor of the phenomenon of **vortex breakdown**, in which a stagnation point develops on the axis of the tube, with a finite region of recirculating fluid, frequently referred to as a *bubble*, downstream (Harvey [2]).

The terminology *vortex breakdown*, is adopted from the field of aerodynamics, where the *bursting* of vortices shed from the edges of delta wings has attracted much attention since being first described in 1957. These wing vortices have been observed to burst in two distinct ways: in one the vortex filament bells out symmetrically from the front stagnation point to form a bubble; in another, the filament is deformed into a spiral. Both forms of breakdown are captured on the striking photograph taken by Lambourne and Bryer [3] where the *bursting* of the vortex filaments is evident.

In Harvey's experiments the working fluid was air and the axial Reynolds numbers based on tube radius appears to have been about 4500. In the experiments of Sarpkaya [4] the working fluid was water and the bubble type breakdown was observed at axial Reynolds numbers as low as 800 for a swirl parameter $\lambda = \Gamma/(\bar{W}\,\bar{a}_0^2) = 3.0$, where Γ is a measure of the swirl imparted to the fluid entering the test section of tubing.

2. VORTEX BREAKDOWN AT LOW AXIAL REYNOLDS NUMBERS

M.G.Hall [5], S. Leibovich [6] and T. Sarpkaya [4] have all presented definitions of vortex breakdown at high Reynolds numbers. However, these definitions are satisfied by two very different *low Reynolds number* tube flows, each of which can be solutions of linearised Navier-Stokes equations.

2.1. AN INFINITELY LONG TUBE,$-\infty < X < \infty$, ROTATING WITH CONSTANT ANGULAR VELOCITY Ω_1 WHEN $X < 0$, CONSTANT ANGULAR VELOCITY Ω_2 WHEN $X > 0$

Consider **steady** flow in a long tube, $-\infty < \bar{x}/\bar{a}_0 < \infty$, with an upstream section, $(\bar{x} < 0)$, rotating with constant angular velocity, $\bar{\Omega}_1$, and a downstream section rotating with constant angular velocity, $\bar{\Omega}_2$. When $\bar{\Omega}_2/\bar{\Omega}_1 < 1$ the swirl is decreasing with increase of $\bar{x} > 0$ and in the case

when $\bar{\Omega}_2 = 0$ and $G < -256.41$, where

$$G = -\frac{1}{2}Re^A\Gamma^2, \qquad \Gamma = \frac{\bar{\Omega}_1\bar{a}}{\bar{W}},$$

where Re^A denotes the axial Reynolds number, $\bar{W}\,\bar{a}/\nu$, a *bubble* with axis the $\bar{x}$ axis is predicted, (MacDonald [7], Figure 2, Lavan Nielsen & Fejer [8], L.N.F.).

L.N.F. have also presented numerical solutions to the full non-linear equations for axial Reynolds numbers up to 10.0 (at which value a swirl ratio of 7.92 was just sufficient to produce incipient flow reversal on the tube axis). They concluded that their analytic solution, derived on the assumption that $Re^A \to 0$ and $\Gamma \to \infty$ in such a way that $Re^A\,\Gamma^2$ remains constant, and their numerical solution were in good agreement for $Re^A < 1.0$. The finite Re^A problem has been discussed in the numerical work of Crane and Burley [9] and Silvester Thatcher and Duthie [10], each of whom have confirmed the accuracy of the numerical results of L.N.F.

2.2.   UNSTEADY FLOW IN A LONG TUBE OF SLOWLY VARYING CROSS SECTION

Consider slow viscous flow in a slowly varying tube, say $a = 1/2\,(3 \pm \tanh(x))$ where $x \in (-\infty, \infty)$ is a slowly varying dimensionless axial coordinate. For time $\bar{t} < 0$ the tube is stationary and, for $\bar{t}\bar{\Omega} \geq 0$, it rotates with constant angular velocity, $\bar{\Omega}$, about its axis , Figure 1b (MacDonald [1]). Here, $Re^A = O(1)$, and $\epsilon = \bar{W}\,\bar{a}_0^2/\nu\,\bar{L} \to 0$, where $\bar{L}$ is a length typical of changes in the axial direction, $\bar{a}_0$ is a reference axial radius - say the tube radius far upstream- and the swirl parameter, $\lambda = \bar{\Omega}\,\bar{a}_0/\bar{W} \to \infty$, in such a way that $\Gamma = \lambda^2\,\epsilon$ is finite. The flow in the diverging tube $a = 1/2\,(3 + \tanh(x))$ includes, for certain $t\;(>0)$, where $t = \bar{t}\nu/\bar{a}_0^2$, when Γ is sufficiently large, a transitory bubble, streamlines of which have been drawn for $\Gamma = 40$ and $t = 0.6$, MacDonald [1].

When the tube is **converging** the rotation of the wall increases the shear stress at the wall and at suitably large Γ a recirculation region occurs adjacent to the **wall**; MacDonald [1] presents streamlines showing this region for the case when $a = 1/2\,(3 - \tanh(x))$, $t = 0.6$ and $\Gamma = 40$.

3.   THE NON-DIMENSIONAL EQUATIONS

To consider the motion of viscous incompressible fluid, of viscosity ν, in a long axially symmetric tube of slowly-varying cross-section, we shall refer the motion to cylindrical polar coordinates, $\bar{x}, \bar{r}, \bar{\theta}$, with corresponding velocity components $\bar{w}, \bar{u}, \bar{v}$, where the $\bar{x}$ axis is assumed to coincide with the axis of the tube, which is assumed to have radius $\bar{a}(\bar{x})$
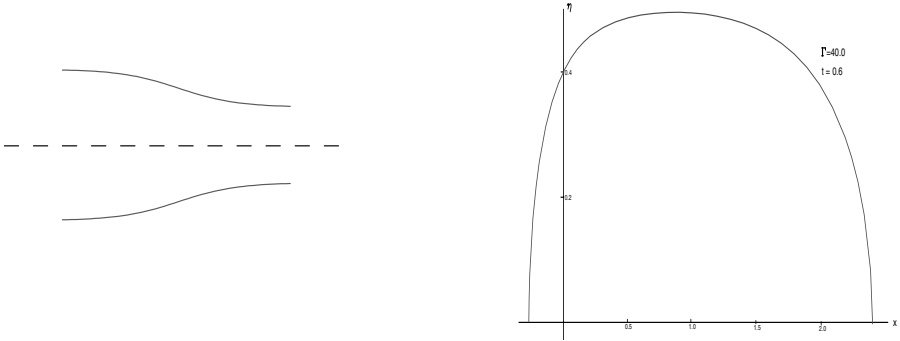
Figure 1 *(a) Left:* A typical flow configuration. When $t < 0$, the tube is stationary with viscous fluid in steady slow flow from left to right. At $t = 0$, the tube is impulsively rotated with constant angular velocity about its axis (Not to scale).
(b) Right: The assemblage of points, in an axial plane, where $w_{\eta\eta} + w_\eta/\eta = 0$, when $a = 1/2(3 + \tanh(x))$.

at axial position $\bar{x}$. Let $\bar{L}$ and $\bar{a}_0$ denote representative lengths in the axial and radial directions and introduce the non-dimensional variables $x = \bar{x}/\bar{L}, \quad r = \bar{r}/\bar{a}_0, \quad w = \bar{w}/\bar{W}, \quad v = \bar{v}/\Omega\,\bar{a}_0$, where $\bar{Q}$ $(= \pi\bar{a}_0^2\bar{W})$ denotes the rate of volume flow through the tube, which is assumed constant.

We assume that, (i),

$$\bar{a}_0/\bar{L} << 1.$$

This is the slowly-varying assumption which permits the axial diffusion terms in the Navier-Stokes equations to be neglected when compared to the radial diffusion terms.

When $t = 0$ the tube is impulsively rotated about its axis with angular velocity $\bar{\Omega}$, at which angular speed it is thereafter maintained.

Then when, (ii),

$$\bar{t}_{\bar{a}} >> \bar{t}_{\bar{r}} \,,$$

i.e. when the time for axial diffusion of momentum $>>$ the time for radial diffusion of momentum ,

$$\frac{\bar{\Omega}\,\bar{a}_0^2}{\nu} \equiv Re^R >> 1 \,. \qquad (3.1)$$

This constitutes our second assumption . Re^R is termed the swirl Reynolds number. We note that

$$\frac{\bar{W}}{\bar{\Omega}\,\bar{L}} = \frac{\bar{W}\,\bar{a}_0^2}{\nu\,L}\frac{\nu}{\bar{a}_0^2\,\Omega} = o\,(\varepsilon),$$

$$\text{where} \qquad \varepsilon = \frac{W\,a_0^2}{\nu\,L} \qquad (3.2)$$

is the Blasius parameter, which $\to 0$ when $\bar{a}_0/\bar{L} \to 0$ and $W\bar{a}_0/\nu = 0(1)$. Finally, we note from 3.2 that

$$\bar{W}\,\bar{a}_0/\nu \ = \ 0(1) \quad \Leftrightarrow \quad \bar{a}_0/L \ = \ 0(\varepsilon).$$

As $Re^R >> 1$ and $Re^A = O(1)$, we introduce the dimensionless pressure $p = \bar{p}/(\rho\,(\bar{\Omega}\,\bar{a}_0)^2)$. Hence, with $v = \bar{v}/(\bar{\Omega}\bar{a}_0)$, and - from the mass conservation equation - $u = \bar{u}\bar{L}/(\bar{W}\,\bar{a}_0)$, we obtain from the non-dimensional Navier-Stokes equations, on taking the limits $\bar{a}_0/L \to 0,$ $\varepsilon \to 0,$ $Re^R \to \infty$, with

$$\Gamma \ = \ \varepsilon\left(\frac{\bar{\Omega}\,\bar{a}_0}{\bar{W}}\right)^2$$

held fixed, the linearised equations

$$\frac{\partial p}{\partial r} = \frac{v^2}{r} \qquad (3.3)$$

$$\frac{\partial v}{\partial t} = \frac{\partial^2 v}{\partial r^2} + \frac{1}{r}\frac{\partial v}{\partial r} - \frac{v}{r^2} \qquad (3.4)$$

$$\frac{\partial w}{\partial t} = -\Gamma\frac{\partial p}{\partial x} + \frac{\partial^2 w}{\partial r^2} + \frac{1}{r}\frac{\partial w}{\partial r} \,. \qquad (3.5)$$

4.   BOUNDARY AND INITIAL CONDITIONS

The initial condition is that for all $x \in (-\infty, \infty)$

$$v = 0, \ \ r \neq a(x), \qquad w = 2/a^2\,(1 - \eta^2), \quad \eta = r/a(x)\,, \qquad t = 0. \quad (4.1)$$

The boundary conditions are

$$v = a, \quad w = 0, \quad r = a, \quad \forall\, t > 0. \tag{4.2}$$

Finally, our solution must satisfy the integral equation

$$\int_0^1 \eta\, w(x, \eta, t)\, d\eta = \frac{1}{2\, a^2}. \tag{4.3}$$

When $\hat{t} \equiv t/a(x)^2 > \hat{t}_{asy}$, where $\hat{t}_{asy} \sim 0.3$ the solution for the axial velocity component, $w(x, \eta)$, is (MacDonald, [1]) approximately

$$w(\xi, \eta, \hat{t}) = \frac{2}{a^2}\,(1 - \eta^2) - \alpha a^3 a' \sum_{k=1}^{\infty} \frac{e^{-\alpha_k^2 \hat{t}}}{\alpha_k^4 J_0(\alpha_k)} \times$$

$$\Big[16(J_0(\alpha_k) - J_0(\alpha_k \eta)) + 2\alpha_k^2 J_0(\alpha_k \eta) + 2(\alpha_k \eta)^2 J_2(\alpha_k \eta)$$

$$+\hat{t}4\,\alpha_k^2\left[2(J_0(\alpha_k) - J_0(\alpha_k \eta)) + (\alpha_k \eta) J_1(\alpha_k \eta)\right]\Big]. \tag{4.4}$$

and $J_1(\alpha_k) = 0$, for $k = 0, 1, 2, \ldots$. This approximate solution, which is derived on the assumption that the azimuthal velocity component is fully developed, see MacDonald, [1], satisfies the initial condition, $w(\xi, \eta, 0) = 2/a^2(1 - \eta^2)$, the boundary condition, $w(\xi, 1, \hat{t}) = 0$, the symmetry condition, $\frac{\partial w}{\partial \eta}(\xi, 0, \hat{t}) = 0$, the mass conservation equation,

$$\int_0^1 \eta\, w(\xi, \eta, \hat{t})\, d\eta = \frac{1}{2\, a^2},$$

and is asymptotically correct for 'large' finite $\hat{t}$.

The solution enables the stream function, $\psi(x, \eta, \hat{t})$, to be calculated, and the curves of constant ψ give the streamlines at time $t = a(x)^2 \hat{t}$. These show, when $t = 0.6$ and $a = 1/2(3 + \tanh(x))$ a bubble with axis the tube axis, when $\Gamma = 40.0$.

It is surprising that with parabolic equations, which use no upstream conditions, we are able to reproduce the same phenomena as L.N.F. produced with elliptic equations and we propose in this paper to investigate this matter in greater depth.

5. THE EQUATIONS CORRECT TO $O(\varepsilon)$

As $\bar{a}_0/L = O(\varepsilon)$, when $W\bar{a}_0/\nu = O(1)$, the Navier Stokes equations, correct to order ε, are

$$\frac{\partial p}{\partial r} = \frac{v^2}{r}$$

$$\frac{\partial v}{\partial t} + \varepsilon \left(u \frac{\partial v}{\partial r} + w \frac{\partial v}{\partial x} + \frac{u\, v}{r} \right) = \frac{\partial^2 v}{\partial r^2} + \frac{1}{r} \frac{\partial v}{\partial r} - \frac{v}{r^2}$$

$$\frac{\partial w}{\partial t} + \varepsilon \left(u \frac{\partial w}{\partial r} + w \frac{\partial w}{\partial x} \right) = -\Gamma \frac{\partial p}{\partial x} + \frac{\partial^2 w}{\partial r^2} + \frac{1}{r} \frac{\partial w}{\partial r} \,.$$

The initial condition is that when $t = 0$,

$$w(x, r, t) = 2/a^2(1 - \eta^2) + \varepsilon \frac{a'}{a^3} \left(\frac{2}{9} - \eta^2 + \eta^4 - \frac{2}{9}\eta^6 \right), \qquad \eta = \frac{r}{a}.$$

The boundary conditions are unchanged from eqns 4.2, and condition 4.3 must also hold.

As $\Gamma \gg \varepsilon$, the solution of this non-linear **parabolic** problem will be close to the solution to our linear problem.

The next approximation, to order ε^2, results in the full equations for the axial and azimuthal velocity components, with some simplification for the equation governing the radial velocity component. Hence there is no tractable elliptic problem and, as our theory requires $\varepsilon \to 0$, we conclude that the only possible deficiency with our parabolic formulation is when

$$\frac{\partial^2 w}{\partial r^2} + \frac{1}{r} \frac{\partial w}{\partial r} \ll \left(\frac{\bar{a}_0}{L} \right)^2 \frac{\partial^2 w}{\partial x^2} \,.$$

6. THE SOLUTION 3.9 EXAMINED

It can be shown from equation 3.9 that

$$\frac{\partial^2 w}{\partial x^2} = (12 - 20\eta^2)\frac{a''}{a^3} + 4\left(\frac{a'}{a^2}\right)^2 (5 - 14\eta^2) + 6\left(\frac{a''}{aa'}\right)^2 (1 - \eta^2)$$

$$- \frac{2a'''}{a'a^2}(1 - \eta^2) + w\left(\frac{a'''}{a'} - 3\left(\frac{a''}{a'}\right)^2 - 2\frac{a''}{a} \right) + \frac{\partial w}{\partial x}\left(3\frac{a''}{a'} + 2\frac{a'}{a} \right)$$

$$+ \Gamma a(a')^3 \sum_k \frac{e^{-\alpha_k^2 \hat{t}}}{J_0(\alpha_k)} \left[F_0(\eta) + F_1(\eta)\hat{t} + F_2(\eta)\hat{t}^2 + F_3(\eta)\hat{t}^3 \right] ,$$

508
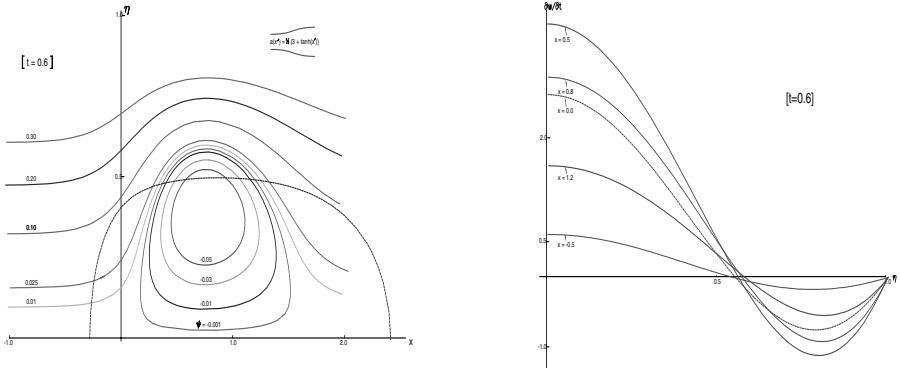
Figure 2 (a) *Left:* Streamlines in an axial plane through the recirculation region, $\Gamma = 40$, $a = \frac{1}{2}(3+\tanh(x))$ [inset not to scale]. Also shown broken is the curve of intersection of an axial plane with the surface on which $D = 0$.
(b) *Right:* $\frac{\partial w}{\partial t}$ when $\Gamma = 40$, $a = \frac{1}{2}(3 - \tanh(x))$ and $x = -0.5$, 0.0, 0.8, 1.2.

where, with $C(\hat{t}) = c_0 + c_1\hat{t} + c_2\hat{t}^2$,

$$\frac{\partial w}{\partial x} = -4\frac{a'}{a^3}(1 - 2\eta^2) + \frac{a''}{a'}[w - \frac{2}{a^2}(1 - \eta^2)] - \Gamma(aa')^2 \sum_k \frac{e^{-\alpha_k^2\hat{t}}}{\alpha_k^4 J_0(\alpha_k)}C(\hat{t})$$

and

$$F_0 = \eta J_1(\alpha_k\eta)[\frac{6}{\alpha_k^3}(8 - \alpha_k^2) + 2\frac{\eta^2}{\alpha_k}] + \eta J_0(\alpha_k\eta)[-16\frac{\eta}{\alpha_k^2} + 2\eta(1 - \eta^2)],$$

$$F_1 = (56\frac{\eta}{\alpha_k} - 8\alpha_k\eta + 12\alpha_k\eta^3)J_1(\alpha_k\eta) + \frac{16}{\alpha_k^2}(J_0(\alpha_k\eta) - J_0(\alpha_k))$$

$$- 4(1 + 4\eta^2)J_0(\alpha_k\eta),$$

$$F_2 = 40\alpha_k\eta J_1(\alpha_k\eta) + 24(\alpha_k\eta)^2 J_0(\alpha_k\eta) +$$
$$8\ [(2 - \alpha_k^2)J_0(\alpha_k\eta) - 2J_0(\alpha_k)],$$
$$F_3 = -2\alpha_k^2[16(J_0(\alpha_k) - J_0(\alpha_k\eta)) + 8\alpha_k\eta J_1(\alpha_k\eta)],$$

$$c_0 = 48J_0(\alpha_k) - 6(8 - \alpha_k^2(1 - \eta^2))J_0(\alpha_k\eta)$$
$$- 2\alpha_k\eta(2 - \alpha_k^2(1 - \eta^2))J_1(\alpha_k\eta),$$
$$c_1 = \alpha_k^2(40\,J_0(\alpha_k) - 4(10 - \alpha_k^2 + 2\alpha_k^2\eta^2)J_0(\alpha_k\eta) + 4\alpha_k\eta J_1(\alpha_k\eta)),$$
$$c_2 = \alpha_k^4\,(16\,J_0(\alpha_k) - 16J_0(\alpha_k\eta) + 8\alpha_k\eta\,J_1(\alpha_k\eta)).$$

Further,

$$\frac{\partial^2 w}{\partial \eta^2} + \frac{1}{\eta}\frac{\partial w}{\partial \eta} = -\frac{8}{a^2} - \Gamma a^3 a' \sum_k \frac{e^{-\alpha_k^2\hat{t}}}{J_0(\alpha_k)}\left(4\eta^2(1 - \alpha_k^2\hat{t})\frac{J_1(\alpha_k\eta)}{\alpha_k\eta}\right.$$
$$\left. + \ (\frac{16}{\alpha_k^2}(1 + \alpha_k^2\hat{t}) - 2(1 - \eta^2))J_0(\alpha_k\eta)\right).$$

Examination of $\frac{\partial^2 w}{\partial x^2}$ and $\frac{\partial^2 w}{\partial r^2} + \frac{1}{r}\frac{\partial w}{\partial r}$ shows that

$$\frac{\partial^2 w}{\partial r^2} + \frac{1}{r}\frac{\partial w}{\partial r} >> (\frac{\bar{a}_0}{L})^2\frac{\partial^2 w}{\partial x^2}$$

almost everywhere within the flow field, save close to an instantaneous closed surface on which

$$D \equiv \frac{\partial^2 w}{\partial \eta^2} + \frac{1}{\eta}\frac{\partial w}{\partial \eta} = 0, \qquad\qquad \eta = \frac{r}{a}. \qquad (6.1)$$

The assemblage of points satisfying 6.1 in an axial plane when $a(x) = 0.5(3 + \tanh(x))$ and $t = 0.6$, $\Gamma = 40$ is shown on Figure 1b; Figure 2a superimposes Figure 1b onto the streamlines through the recirculation region for this case.

From 3.5 we see that on the curve shown broken on Figure 2a

$$\frac{\partial w}{\partial t} = -\Gamma\frac{\partial p}{\partial x},$$

i.e. the pressure gradient at any point of the broken curve is *favourable*, whenever $\frac{\partial w}{\partial t} > 0$. Figure 2b shows $\frac{\partial w}{\partial t}$ against η for selected values of x. From Figure 2a we notice that **the pressure gradient is favourable in the upper reaches of the bubble**. Above the bubble, the pressure gradient must be large and favourable, to drive the appreciable forward flow in the relatively thin annulus through which the mass flow through the tube must pass. The pressure gradient in the lower half of the bubble, on the
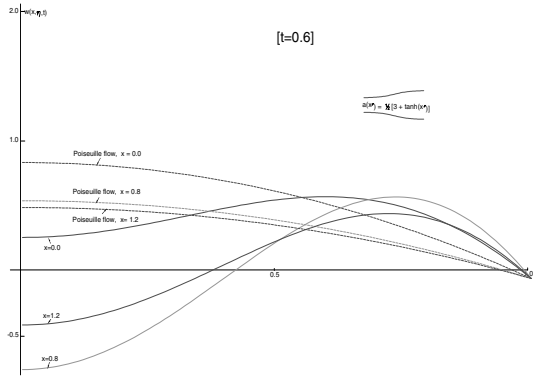
Figure 3 The axial velocity component, $w(x, \eta, t)$, at axial positions $x = 0.0$, 0.8, 1.2 when $\Gamma = 40$, $a = \frac{1}{2}(3 - \tanh(x))$ [Inset not to scale]. Also, shown broken, are the curves $2/a^2(1 - \eta^2)$.

other hand, is adverse (the flow on the axis, for example, is *upstream*). It follows, therefore, that the transition region in which the pressure changes from being adverse to being favourable must lie *within the bubble*. For fixed x, as r increases the increasingly favourable pressure gradient in the upper reaches of the bubble accelerates the flow to its value at the edge of the annulus of fast moving fluid. From Figure 3, which shows the axial velocity component as a function of η when $x = 0.0$, 0.8, 1.2, we see that at $x = 0.8$ the axial velocity component is instantaneously zero when $\eta \approx 0.39$. At this value of x, $\partial p/\partial x < 0$, whenever $\eta \geq \eta_0$, where $\eta_0 \approx 0.39$.

References

[1] D.A. MacDonald Transient recirculation in a slowly varying tube impulsively rotated about its axis with constant angular velocity, Physics of Fluids, **12**, no. 12, 3168-3180 (2000) .

[2] J.K. Harvey Some observations on the vortex breakdown phenomenon, Jl. Fluid Mech., **14** 585-592, (1962).

[3] N.C. Lambourne and D.W. Bryer The breakdown of certain types of vortices, A.R.C., R. & M. No. 3282, 1-36 (1961).

[4] T. Sarpkaya On stationary and travelling vortex breakdowns, Jl. Fluid Mech., **45**, 545-559, (1971).

[5] M.G. Hall Vortex breakdown, Ann. Rev. Fluid Mech., **4**, 195-218, (1972).

[6] S.Leibovich The structure of vortex breakdown, Ann. Rev. Fluid Mech., **10**, 221-246 (1978).

[7] D.A. MacDonald The zeros of $J_1^2(\zeta) - J_0(\zeta) J_1(\zeta) = 0$ with an application to swirling flow in a tube, SIAM Jl. on Appl. Math., **50**, 40-48 (1991).

[8] Z. Lavan, H. Nielsen and A.A. Fejer Separation and flow reversal in swirling flow in circular ducts, Physics of Fluids, **12**, No. 9, 1747-1757 (1969) .

[9] C.M Crane and D.M. Burley Numerical studies of laminar flow in ducts and pipes, Jl. of Computational and Applied Math., **2**, 95-111 (1976).

[10] D.J. Silvester, R.W. Thatcher and J.C. Duthie The specification and numerical solution of a benchmark swirling flow problem, Computers and Fluids, **12**, 281-292 (1984).

SUPERSONIC LEADING-EDGE NOISE

C.J. Powles
Department of Mathematics,
Keele University,
Staffordshire, ST5 5BG, UK.
c.j.powles@maths.keele.ac.uk

Keywords: Blade-vortex interaction, supersonic flow, linear theory, arbitrary gust form.

Abstract   We consider the production of sound when a convected gust in a supersonic mean flow strikes the leading edge of a fan blade. The blade is modelled as an infinite span flat rigid plate, and a gust of arbitrary form is considered. By the application of Fourier transforms the boundary value problem for the velocity potential is solved, and an integral expression for the sound field is found, which is applicable everywhere inside the Mach wedge. For gusts localised in the span direction, a far field approximation is derived. This approximation is valid inside a Mach cone, and may be evaluated analytically for specified gust shapes. For certain gusts the exact solutions may be calculated, giving results which are valid everywhere. Thus our integral expression enables a study to be made of the way in which the radiated acoustic field depends on properties of the incoming gusts. The new feature of this analysis is the fact that we deal with an arbitrary gust form: previous authors have considered the properties of individual gusts in some detail, focusing principally on harmonic gusts and jets.

1.   INTRODUCTION

An important mechanism of noise generation in modern high performance aeroengines is the interaction between fan blades and turbulent gusts in the air flow. A comprehensive investigation of a complex engine would without doubt require a considerable computational effort, but analytical results for simple model problems are important in providing understanding. Here we consider a single fan blade in isolation, which we take to be moving at supersonic velocity relative to the mean air flow, and which we model as a flat half plane.

The interaction between a gust and a flat half plane has been considered in the past by many authors. Prior to the 1970s there was considerable interest in the problem of calculating the unsteady forces acting on the plane due to the gust. More recently however, attention has turned to the acoustical problem. The general approach in previous papers has been to consider a definite gust form. The case of a subsonic blade velocity and an arbitrary gust form has recently been considered by Chapman [2].

The supersonic problem has been investigated by Ffowcs Williams and Guo [3] and Guo [4, 5, 6], who considered the special case of a cylindrical jet gust in some detail. Some work has also been done in extending this theory to more realistic models, taking into account, for example, corner effects (see Peake [7]). Here we shall take the simplest configuration, the leading edge half plane, but we shall consider the effect of an arbitrary gust.

We begin by deriving a boundary value problem which describes the system in question, and we go on to solve this using Fourier transforms. Inverting these we derive a double integral formula for the pressure field generated by an arbitrary gust. For the case of a gust which is localised in the span direction, we go on to derive a single integral approximation of the pressure field, which is valid in the acoustic far field. An example of the field generated by a simple gust is given, which illustrates some general properties of the fields.

2.   THE BOUNDARY VALUE PROBLEM

The system in question is shown in figure 1, which shows part of a semi-infinite flat plate located in the plane $y = 0$, $x > 0$. We choose a system of wind tunnel coordinates with the z-axis lying along the leading edge. The mean flow of fluid is in the positive x direction, with speed $U = Mc_0$, where c_0 is the speed of sound and M is the Mach number, in this case taken to be greater than 1.

The gust is convected with the mean fluid flow, and we assume the disturbances are small enough that linear theory may be applied. We also assume that inviscid theory is applicable. Then the only interaction between the gust and the wing must take place through the y-component of the gust velocity in the plane $y = 0$, which we describe as a function $f(t - x/U, z)$. The acoustic disturbance is described by a particle velocity $\mathbf{u}$ and a pressure p, and we may define a velocity potential φ:

$$\mathbf{u} = \nabla\varphi, \qquad\qquad p = -\rho_0 \left(\frac{\partial}{\partial t} + U\frac{\partial}{\partial x} \right)\varphi, \qquad (2.1)$$
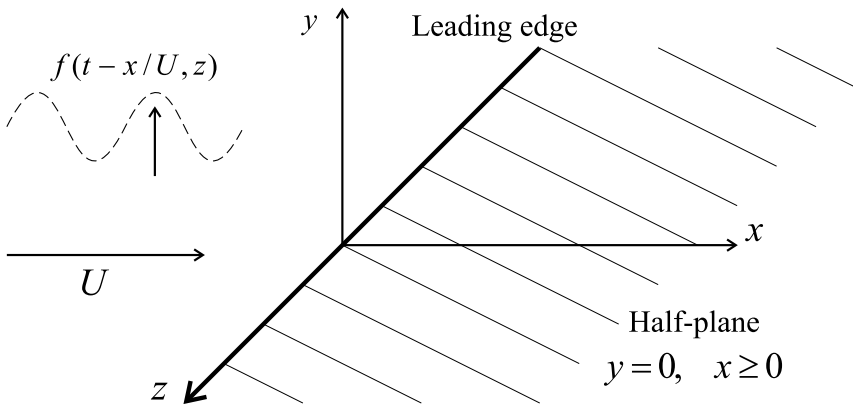
Figure 1   Flat half-plane blade in a mean flow containing a gust.

where ρ_0 = density of fluid. We know this potential must obey the convected wave equation

$$\frac{1}{c_0^2}\left(\frac{\partial}{\partial t} + U\frac{\partial}{\partial x}\right)^2 \varphi - \nabla^2 \varphi = 0. \tag{2.2}$$

Now since we assume the plate is rigid, the total velocity, acoustic plus gust, must be zero on the surface of the blade. Also, since the flow is supersonic and thus all sound is swept downstream, we know that the upstream acoustic velocity must equal zero. This gives our boundary condition in terms of a Heaviside unit-step function:

$$\frac{\partial \varphi}{\partial y} = -f(t - x/U, z)\mathrm{H}(x) \qquad\qquad y = 0^{\pm}. \tag{2.3}$$

We also dictate that our solution must obey a radiation condition, and an associated causality condition. The first of these means we require solutions which are outgoing and finite at infinity, and the second that there should be no acoustic disturbance in the fluid before the gust strikes the leading edge.

We shall find it convenient to introduce a set of Doppler adjusted coordinates: $\bar{x} = x/(M^2 - 1)$, $\bar{y} = y/(M^2 - 1)^{1/2}$, $\bar{z} = z/(M^2 - 1)^{1/2}$. These allow the final formulae and also the equations for Mach cones and wedges to be expressed in a compact form.

3.   EXACT SOLUTION

The problem is solved by the application of Fourier transforms. We transform from x,z, and t to the wavenumbers k,m, and the frequency ω,

defining our transform as

$$\Phi(k, y, m, \omega) = \int\limits_{-\infty}^{\infty} \int\limits_{-\infty}^{\infty} \int\limits_{-\infty}^{\infty} \varphi(x, y, z, t) e^{i(\omega t - kx - mz)} \mathrm{d}x \mathrm{d}z \mathrm{d}t. \qquad (3.1)$$

Then transforming the wave equation we obtain a simple ordinary differential equation for Φ,

$$\frac{\partial^2 \Phi}{\partial y^2} - \gamma^2(k, m, \omega)\Phi = 0. \qquad (3.2)$$

where we have defined the function $\gamma(k, m, \omega)$ as

$$\gamma(k, m, \omega) = \left\{ k^2 + m^2 - \frac{(\omega - Uk)^2}{c_0^2} \right\}^{1/2}. \qquad (3.3)$$

We choose the branch of the square root such that $\mathrm{Re}(\gamma(k, m, \omega)) \geq 0$. From the symmetry of the problem we know that φ must be an odd function of y, and so the solution of 3.2 which obeys the radiation condition is

$$\Phi(k, y, m, \omega) = A(k, m, \omega)\mathrm{sgn}(y)e^{-\gamma(k, m, \omega)|y|}, \qquad (3.4)$$

where $A(k, m, \omega)$ is a function to be determined from the boundary condition. To transform the boundary condition, we define the gust transform term

$$F(\omega, m) = \int\limits_{-\infty}^{\infty} \int\limits_{-\infty}^{\infty} f(t', z) e^{i(\omega t' - mz)} \mathrm{d}t' \mathrm{d}z, \qquad (3.5)$$

$(t' = t - x/U)$. Then the boundary condition is transformed to

$$\frac{\partial \Phi}{\partial y} = \frac{-iUF(\omega, m)}{\omega - Uk} \qquad\qquad y = 0^{\pm}. \qquad (3.6)$$

Applying this to our solution 3.4, we may determine the function $A(k, m, \omega)$. Thus we have a complete solution for Φ, which when inserted to the inverse transform of 3.1 gives the solution φ as a triple integral:

$$\varphi(x, y, z, t) = \frac{1}{(2\pi)^3} \int\limits_{-\infty}^{\infty} \int\limits_{-\infty}^{\infty} \int\limits_{-\infty}^{\infty} \frac{iU\mathrm{sgn}(y)F(\omega, m)}{(\omega - Uk)\gamma(k, m, \omega)} \qquad (3.7)$$

$$\times e^{-i(\omega t - kx - mz)} e^{-\gamma(k, m, \omega)|y|} \mathrm{d}k\mathrm{d}m\mathrm{d}\omega.$$

This integral includes a pole term $(\omega - Uk)^{-1}$, as well as the branch points due to the function $\gamma(k, m, \omega)$. Our principle interest however lies
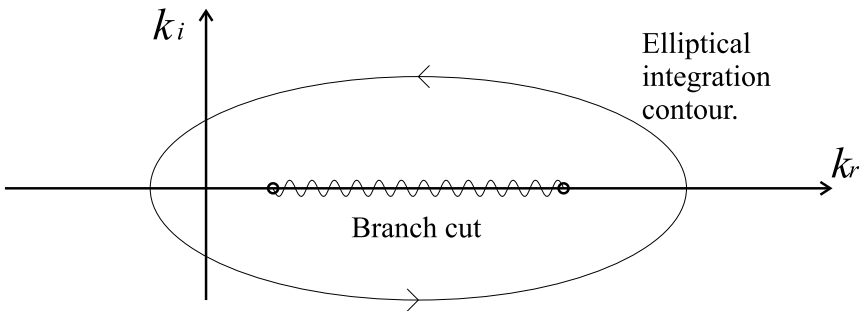
Figure 2 Elliptical integration contour enclosing the branch cut in the k plane. Valid for $\bar{x} > |\bar{y}|$.

not with the potential, but rather with the acoustic pressure perturbation $p(x, y, z, t)$. This is given by 2.1, and when we transform the differential operators to take them inside the integral, they give an $(\omega - Uk)$ term, cancelling the pole. Then the integral of interest is slightly simpler in form than that for the potential.

The resulting integral may be partially integrated for an arbitrary gust, since the gust transform term $F(\omega, m)$ is independent of the streamwise wavenumber k. Isolating the k integral, we find there are two branch points on the real line. Using Landau and Lighthill's method to find the causal solution (see, for instance, Howe [8, pp36-37]), we find that the integration contour must run below these points. It is found that there are two regions of validity for the integral. For $\bar{x} < |\bar{y}|$ the integration contour may be closed in the lower k plane, giving an answer of zero. This tells us of the existence of a Mach wedge, outside of which no pressure disturbance may reach, due to the supersonic mean flow convecting all disturbances downstream. Alternatively, for $\bar{x} > |\bar{y}|$ the contour must be closed in the upper k plane. In this case, using an appropriate substitution, we deform the integration contour onto an ellipse enclosing the branch points (see figure 2), and thus reduce the k integral to a standard expression (see [1, equation 9.1.21]) for a Bessel function of the first kind, of order zero. Then the general pressure integral for an arbitrary gust is

$$p(x, y, z, t) = \frac{-\rho_0 M c_0 \mathrm{sgn}(y)}{(2\pi)^2 (M^2 - 1)^{1/2}} \int\limits_{-\infty}^{\infty} \int\limits_{-\infty}^{\infty} F(\omega, m) e^{-i\omega(t - M\bar{x}/c_0)} e^{imz} \qquad (3.8)$$

$$\times J_0 \left(\left\{ \omega^2/c_0^2 + m^2(M^2 - 1) \right\}^{1/2} (\bar{x}^2 - \bar{y}^2)^{1/2} \right) \mathrm{d}m \mathrm{d}\omega.$$

When evaluating this integral for specific gusts, the causality condition dictates that the integration contour in the complex ω plane should run above any singularities.

4. APPROXIMATION FOR LOCALISED GUSTS

The exact integral formula 3.8 is rather complicated, and in practice may only be evaluated analytically for gusts of a very simple form. Thus it is convenient to consider possible simplifications or approximations to the formula. An approximation is available if we consider the field due to a gust which is localised in the span direction.

A point source in a supersonic flow generates a perfect Mach cone. A source which is distributed over some finite area produces a cone-like region of disturbance, which in the far-field may be modelled as a cone. Then for gusts which only strike a localised region of the leading edge, we may derive a simple approximation valid in the far field, inside the cone $\bar{x} > (\bar{y}^2 + \bar{z}^2)^{1/2}$.

We begin by making the substitution $m = \frac{\omega}{c_0}(M^2-1)^{-1/2}\sinh(\chi)$ which simplifies the argument of the Bessel function. Then we take a standard Hankel approximation [1, equation 9.2.1], for argument greater than order, to the Bessel function. For the Bessel function of order zero, this is accurate except when the argument is very small, so from 3.8 we expect that our approximation may be inaccurate near the Mach wedge.

The integration contour in the χ plane is taken to be the real χ axis, for positive ω. We express the cosine in our approximation as the sum of two complex exponentials, and thus the pressure is approximated by the sum of two double integrals. The χ integrals are in an ideal form for stationary phase analysis, being of the form

$$I(x,y,z,\omega) = \int_{-\infty}^{\infty} G(\omega,\chi)e^{-i\frac{\omega}{c_0}(\bar{z}\sinh(\chi)\pm(\bar{x}^2-\bar{y}^2)^{1/2}\cosh(\chi))}\mathrm{d}\chi, \qquad (4.1)$$

where

$$G(\chi) = F(\omega, \frac{\omega}{c_0}(M^2-1)^{-1/2}\sinh\chi)\cosh^{1/2}\chi. \qquad (4.2)$$

Then carrying out the analysis, we find

$$p(x,y,z,t) \simeq p_1(x,y,z,t) + p_2(x,y,z,t), \qquad (4.3)$$

where

$$p_{1,2}(x,y,z,t) = \frac{-\rho_0 M c_0 \mathrm{sgn}(y)}{(2\pi)^2(M^2-1)}\frac{1}{\bar{R}_h}\int_{-\infty}^{\infty} e^{-i\omega(t-M\bar{x}/c \mp \bar{R}_h/c)} \qquad (4.4)$$

$$\times F(\omega, \pm \frac{\omega}{c_0}(M^2 - 1)^{-1/2} \tan(\bar{\theta}_h)) d\omega.$$

Here we have defined the variables

$$\bar{R}_h = (\bar{x}^2 - \bar{y}^2 - \bar{z}^2)^{1/2}; \tag{4.5}$$

$$\tan(\bar{\theta}_h) = \frac{-\bar{z}}{(\bar{x}^2 - \bar{y}^2 - \bar{z}^2)^{1/2}}. \tag{4.6}$$

The quantity $\bar{R}_h$ is fundamental in the analysis of localised gusts. The contours of $\bar{R}_h$ are hyperbolic surfaces asymptotic to the Mach cone. The stationary phase argument relies on $\bar{R}_h$ being large, so we expect our simple approximation may fail near the Mach cone.

This approximation is simple enough that it may be analytically integrated for many gusts, giving information about the far-field when an exact integration of 3.8 may not be possible.

5.   EXAMPLE

Consider a simple two dimensional sinusoidal gust

$$f(t - x/U, z) = v_0 e^{-i\omega_0(t - x/U)}. \tag{5.1}$$

For this gust the exact sound field is calculated from 3.8 as

$$p(x, y, t) = \frac{-\rho_0 M c_0 v_0 \text{sgn}(y)}{(M^2 - 1)^{1/2}} e^{i\omega_0(t - x/U)} J_0 \left(\frac{\omega_0}{c_0}(\bar{x}^2 - \bar{y}^2)^{1/2} \right). \tag{5.2}$$

This pressure field is illustrated in figure 3. It is illustrative of the general fact that the pressure magnitude is greatest on the Mach wedge.

This example and the three dimensional result 4.4 can be used to illustrate the general nature of the far field decay. In the case of localised gusts which give rise to a three dimensional sound field the general decay term is $1/\bar{R}_h$, while in the case of a two dimensional field, as in 5.2, the decay is as $1/\bar{r}_h^{1/2}$, where $\bar{r}_h$ is defined as $\bar{r}_h = (\bar{x}^2 - \bar{y}^2)^{1/2}$. This may be compared to the subsonic case, where it is a general result that three-dimensional fields decay as $1/R$ and two dimensional fields decay as $1/r^{1/2}$, where R and r are spherical and cylindrical radii respectively. In our supersonic flow problem we have a similar decay factor, but ours are hyperbolic in nature, with the decay being away from the Mach cone or wedge.

6.   FURTHER WORK

At the moment work is ongoing in the calculation of a number of examples of the fields due to specific gusts. The formulae 3.8 and 4.4 allow
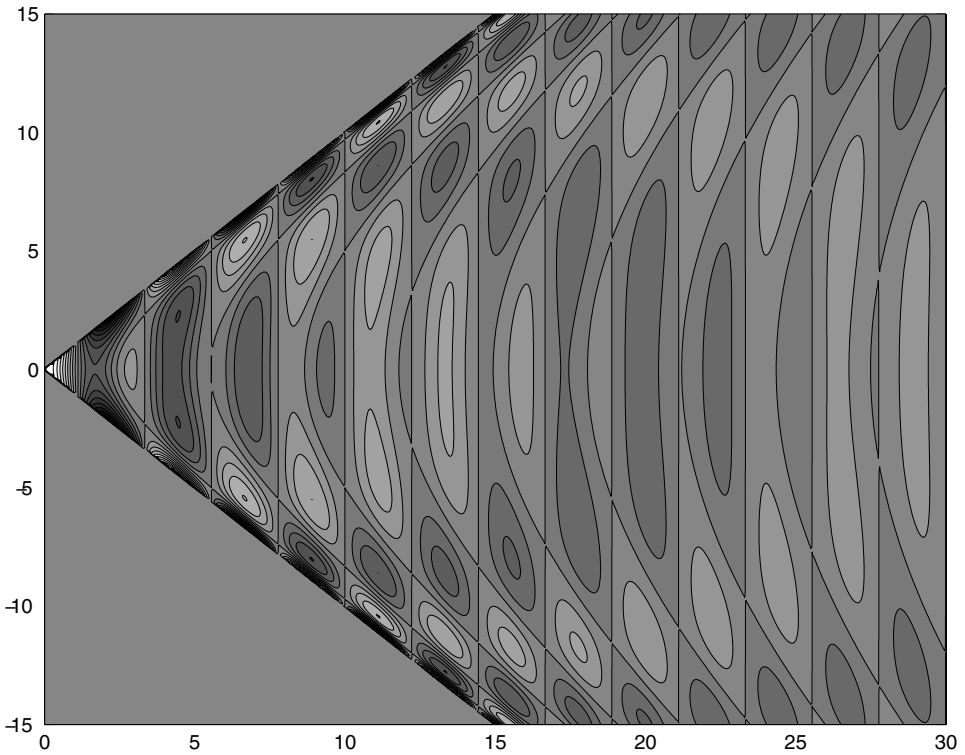
Figure 3   Pressure contours in the x,y plane due to a sinusoidal gust.

a study to be made of the way in which different gust features, such as sharp edges, affect the generated field. The formulae are of a form which allows easy numerical evaluation in those instances where analytical results can not be obtained. Thus we are developing a fuller understanding of the behaviour of the generated sound fields.

The linear inviscid theory presented here could be extended beyond our very simple model geometry to take account of the effects of a side edge or a trailing edge, and we could also consider the effects of mean loading on the blade.

We have given a very brief description of the work and the methods. Currently a more detailed description of the work, including the full derivations of the formulae and consideration of a wide range of examples, is being prepared for submission for publication in the Journal of Sound and Vibration.

Acknowledgments

References

[1] ABRAMOWITZ, M and STEGUN, I A (1966) *Handbook of Mathematical Functions.* National Bureau of Standards, Washington.

[2] CHAPMAN, C J (2002) *High speed leading-edge noise*, Proc. Roy. Soc. Lond. A. In Press.

[3] FFOWCS-WILLIAMS, J E and GUO, Y P (1988) *Sound generated from the interruption of a steady flow by a supersonically moving aerofoil*, J. Fluid Mech. **195**, 113-135.

[4] GUO, Y P (1989a) *On sound generation by a jet flow passing a semi-infinite aerofoil*, AIAA Paper 89-1070.

[5] GUO, Y P (1989b) *Sound generation by a supersonic aerofoil cutting through a steady jet flow*, J. Fluid Mech. **216**, 193-212.

[6] GUO, Y P (1991) *Energetics of sound radiation from flow aerofoil interaction*, J. Sound Vib. **151**, 247-262.

[7] PEAKE, N (1993) *The interaction between a steady jet flow and a supersonic blade tip*, J. Fluid Mech. **248**, 543-566.

[8] HOWE, M S (1998) *Acoustics of Fluid-Structure Interactions.* Cambridge: Cambridge University Press.

Chapter 10
Non-linear waves

ENVELOPE EQUATIONS FOR MODULATED NON-CONSERVATIVE WAVES

Vadim N. Biktashev

Department of Mathematical Sciences, University of Liverpool, Liverpool, L69 7ZL, UK

vnb@liv.ac.uk

Abstract   Modulated waves, i.e. waves that are locally plane and periodic, but at large distances and/or over long intervals of time change their characteristics, appear in many applications. An efficient way to study such waves is the method of envelope equations, when the original wave equations are replaced by equations describing the slowly varying parameters of the waves. The practical approaches to this problem are numerous; however, many of them have limitations, either in achievable accuracy, or in the wave equations to which they could apply (e.g. only conservative systems), or both. In this paper we discuss an approach of this kind, which appear to be free from these disadvantages. This approach is illustrated for *autowaves*, which, in the author's opinion, should play the same role in the theory of waves, as auto-oscillations=limit cycles play in the theory of oscillations: as the basic, least degenerate type of solutions.

1.   INTRODUCTION.

When differential equations, describing a natural or technological process, are too complicated to be solved exactly, one needs to do it approximately. This can be done either numerically, or analytically, e.g. by using some asymptotic methods. Approximate methods may not only serve for pure purposes of calculation, but also be an "instrument of understanding" of complex systems.

The simplest case is if the right-hand sides of the differential equations contain small parameters, and the system becomes much simpler, e.g. can be treated exactly, if these parameters are equal to zero. Then for nonzero

but small values of the parameters, solutions can be obtained by perturbation techniques.

The perturbation technique may also be applied to systems without any small parameters. This may be the case if we are interested in solutions from a special class, depending on such parameters. A well known example is small-amplitude oscillations in a nonlinear system. By scaling the dynamic variables to normalise the amplitude of oscillations, one can bring this problem to a problem explicitly depending on the small parameter, which becomes linear if this small parameter is equated to zero.

There is a less trivial example of the same kind. This is the famous geometric optics approximation. The classical interpretation of geometric optics is that consideration is restricted to solutions with wavelengths small in comparison with other characteristic scales of the problem [1]. This works well with classical, linear wave equations, which admit wave solutions with arbitrarily short wavelengths. In general, this restriction may be impractical, e.g. if wave solution may not exist with wavelengths less than a certain minimum. Then the idea of the geometric optics is reformulated as the idea of modulated waves[2], or slowly varying waves [3]: the characteristic sizes of the problem, in particular of the initial conditions for the equations, should be much larger than a typical wavelength. This means that in relatively small regions, the waves are close to plane and periodic, but the parameters of these waves, including direction of propagation and the period, slowly change in time and/or in space, becoming significantly different at large distances and/or after long time intervals.

The classical geometric optics approximation for linear wave equations heavily relies on the specific properties of these equation, e.g. the superposition principle. This is no good for nonlinear waves. A well known method for nonlinear waves is the Whitham procedure (modulation theory) [2, 4]. One form of the method uses knowledge of conservation laws, available for many wave systems originating from physics, and derives the evolution equations for slowly varying parameters from these conservation laws. Another form of the method also uses the properties of physical origin, namely, the fact that the field equations can be written in the form of a Lagrange variational principle. The evolution equations are then derived also from a Lagrangian principle, where the averaged Lagrangian is rewritten as a function of the new independent variables describing the slowly-varying solutions. This method has been applied to many classical nonlinear equations, such as nonlinear Klein-Gordon equation, Korteweg-deVries equation and others. Recent development in this direction can be found e.g. in [5].

2.   THE PROBLEM.

There is an important class of nonlinear waves, for which Whitham's approach can not be applied — so called *autowaves*. Speaking physically, these are waves that propagate unchanged not because there is no dissipation, but because the dissipation is compensated by the constant supply of energy. Examples are electric pulses in nerve and heart tissues, and waves in some chemical reactions where the consumed reagents are either supplied, or are stored in substantial amounts so that their decrease during the wave period is negligible. Mathematically, such systems are most often described by systems of partial differential equation of reaction-diffusion type,

$$\partial u/\partial t = D \triangle u + f(u). \tag{2.1}$$

Here $u = u(x,t) \in \mathbb{R}^\ell$ is a column-vector of concentrations of the reagents, $f(u) \in \mathbb{R}^\ell$ is a column-vector of nonlinear reaction terms (interesting behaviour starts from $\ell \geq 2$), D is an $\ell \times \ell$ matrix of diffusion coefficients of the reagents, which we assume symmetric; the space coordinates $x \in \mathbb{R}^n$ where the dimension of physical space, n, can be equal to 1, 2 or 3, and $\triangle$ is the Laplacian in $\mathbb{R}^n$.

Systems of the form (2.1), describing real autowave systems, do not have any conserved quantities at all, and, in particular, are not Hamiltonian. The simplest autowave solutions of (2.1) are the plane periodic waves,

$$u(x,t) = U\left((k,x) - \omega(k^2)t + \varphi_0, k^2\right) = U(\xi, \eta), \tag{2.2}$$

$$\text{where} \qquad \xi = (k,x) - \omega(k^2)t + \varphi_0, \quad \eta = k^2, \quad k \in \mathbb{R}^n \tag{2.3}$$

$$\text{and} \qquad \eta DU_{\xi\xi}(\xi, \eta) + \omega(\eta)U_\xi(\xi, \eta) + f(U) = 0. \tag{2.4}$$

Here k is the wavevector, $0 \leq \eta_1 \leq k^2 \leq \eta_2 < \infty$, ω is the frequency, and φ_0 is an arbitrary initial phase. Brackets $(,)$ denote the scalar product in the physical space $\mathbb{R}^n$.

Modulated autowaves (see fig. 1) are solutions of the form

$$u(x,t) = U\left(\varphi, (\nabla\varphi)^2\right) + v(x,t), \tag{2.5}$$

where $\nabla\varphi$ is a local wavevector slowly varying in space and time, and v is a small correction, so that

$$\varphi = \epsilon^{-1}\Phi(\epsilon x, \epsilon t, \epsilon), \qquad \epsilon \ll 1, v \ll 1. \tag{2.6}$$

The question is, what conditions should the phase ("eikonal") variable $\varphi(x,t)$ satisfy. It happens, that the condition can be written in the form of a partial differential equation, the *evolution equation,* which will be the analogue of the eikonal equation in the geometric optics. Our purpose is

to develop a method of derivation of this equation for every given reaction-diffusion system (2.1). One thing we should always bear in mind: as a rule, this *cannot be done entirely analytically*, there usually will be some bits to do numerically. One reason for that is quite obvious: the basic solutions (2.2) can not be found analytically.

3. HEURISTIC DERIVATION OF THE EVOLUTION EQUATION

By substituting (2.5) into (2.1), we get a ℓ-component vector equation for two unknown functions: vector function $v \in \mathbb{R}^\ell$ and scalar function φ. So, the equation is under-determined. In linear approximation in v it takes the form

$$v_t(x,t) = D\nabla^2 v(x,t) + \mathcal{F}[\varphi(x,t)]v(x,t) + h[\varphi(x,t)], \qquad (3.1)$$

where the Jacobian matrix $\mathcal{F}$ and the free term h depend on the unknown $\varphi(x,t)$ so that

$$\mathcal{F}[\varphi] = \left.\frac{\partial f(u)}{\partial u}\right|_{u=U}, \qquad \text{and} \qquad (3.2)$$

$$h[\varphi] = -\left(\omega((\nabla\varphi)^2) + \varphi_t\right)U_\xi - U_\eta\frac{\partial}{\partial t}(\nabla\varphi)^2$$

$$+D\left(U_\eta\nabla^2(\nabla\varphi)^2 + 2U_{\xi\eta}\left(\nabla\varphi, \nabla\left((\nabla\varphi)^2\right)\right)\right.$$

$$\left.+U_\xi\nabla^2\varphi + U_{\eta\eta}\left(\nabla((\nabla\varphi)^2)\right)^2\right). \qquad (3.3)$$

Here the function U is assumed with arguments $U = U(\varphi, (\nabla\varphi)^2)$.

Figure 1: Modulated waves in a reaction+diffusion system. Notice the cores of the spiral waves, and the shock structure between the spiral wave domains. Everything else is modulated waves.
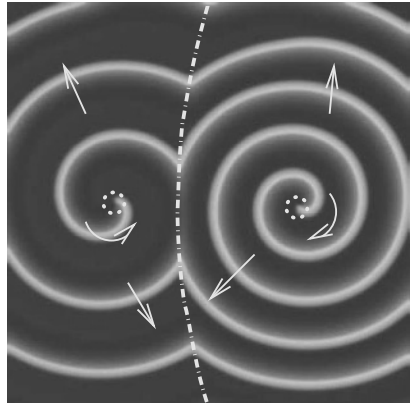
The requirement that v is small leads to certain restrictions on the function φ. These restrictions are just the desired evolution equation.

Since the local wavevector $k = \nabla\varphi$ varies slowly, the coefficients $\mathcal{F}$ and the free term h are approximately periodic functions of only one variable $\xi = \varphi(x,t) \approx (k,x) - \omega(k^2)t$ (locally). Then the boundedness of solutions v of (3.1) at large times requires, via the Fredholm alternative, that

$$\oint \langle W_0(\xi,\eta), h[\varphi]\rangle \, d\xi = 0, \tag{3.4}$$

where $W_0(\xi,\eta) \in \mathbb{R}^\ell$ is the 0-eigenfunction of the adjoint $\mathcal{L}^+$ of the linearised operator $\mathcal{L}$,

$$\begin{aligned}\mathcal{L}v &= \eta D v_{\xi\xi} + D \triangle_y v + \omega v_\xi + \mathcal{F}(\xi)v, \\ \mathcal{L}^+ w &= \eta D w_{\xi\xi} + D \triangle_y w - \omega w_\xi + \mathcal{FT}(\xi)w. \end{aligned} \tag{3.5}$$

Now we substitute (3.3) into condition (3.4). The resulting equality does not depend x and t explicitly, but only on time and space derivatives of φ, and so can be viewed as the required evolution equation. It makes sense if the derivatives of φ are no longer considered constant, but allowed to slowly vary in time and space, i.e. "unfrozen". Generically, this equation will contain a term with $\frac{\partial}{\partial t}(\nabla\varphi)^2$. However, the coefficient at that term can be made to disappear, by the following transformation. Notice that if $U(\xi,\eta)$ is a base wave solution of (2.4), then $U(\xi + \chi(\eta),\eta)$ is also a solution, for arbitrary χ. This function $\chi(\eta)$ can be chosen in such a way that $\oint \langle W_0(\xi,\eta), DU_{\xi\eta}(\xi,\eta)\rangle \, d\xi = 0$, see [6, 7] for details. Ultimately, we have

$$\varphi_t + \omega((\nabla\varphi)^2) = P\left((\nabla\varphi)^2\right)\nabla^2\varphi + Q\left((\nabla\varphi)^2\right)(\nabla\varphi\nabla)(\nabla\varphi)^2 \tag{3.6}$$

where

$$P(\eta) = \oint \langle W_0(\xi,\eta), DU_\xi(\xi,\eta)\rangle \, d\xi,$$

$$Q(\eta) = 2\oint \langle W_0(\xi,\eta), DU_{\xi\eta}(\xi,\eta)\rangle \, d\xi. \tag{3.7}$$

The key points of this heuristic derivation are elimination of the secular growth (Fredholm alternative), and "freezing" and "unfreezing" the derivatives of φ. The latter procedure is potentially flawed. E.g., the ignored non-periodicity of $\mathcal{F}$ and h leads to an error of the order of ϵ even at a distance of one period, though the final equation (3.6) keeps the terms $\mathcal{O}(\epsilon)$ preserved. Thus, more sophisticated tools are required.

4. PERTURBATION OF A MANIFOLD OF STABLE EQUILIBRIA

The ideas of the more accurate asymptotic approaches can be introduced using a finite dimensional example. Consider a perturbed system of ODEs

$$u_t = f(u) + \epsilon h(u), \quad u \in \mathbb{R}^n \qquad (4.1)$$

and assume that at $\epsilon = 0$ it has an m-dimensional attracting manifold of equilibria $U(a)$ with coordinates $a \in A \subset \mathbb{R}^m$, $m < n$, so that $f(U(a)) = 0$, $\forall a \in A$.

For $\epsilon \neq 0$, there is an invariant manifold in the vicinity of U, with a slow dynamics on it:

$$u = U(a(t)) + \epsilon v(t) \qquad (4.2)$$

Here $v = \mathcal{O}(1)$, and a, v are ϵ-slowly varying functions, i.e. they depend upon t only via the combination ϵt, and $v(t)$ can be found as a functional of a in all orders of ϵ. To make (4.2) unambiguous, we require that $v(t)$ is always orthogonal to U at the point $a(t)$, say

$$\langle W_j(a), v \rangle = 0, \quad j = 1..m, \qquad (4.3)$$

where W_j are eigenvectors of the transposed Jacobian matrix, $\mathcal{FT}(a)W_j(a) = \overline{\lambda_j}(a)W_j(a)$, biorthogonal ($\langle W_j(a), V_{j'}(a) \rangle = \delta_{j,j'}$) to the eigenvectors of the Jacobian $F = \partial f(U(a))/\partial u$ itself, including the tangent vectors to the stationary manifold $V_j(a) = \partial U(a)/\partial a_j$, corresponding to
$\lambda_j(a) = 0, j = 1 \ldots m$.

Substitution of the Ansatz (4.2) into (4.1), introducing notation for the flow on the slow manifold, $\dot{a}_j = \epsilon \mathcal{G}_j$, $\mathcal{G} = \mathcal{O}(1)$ and expanding $v(t)$ in the eigenvector basis, $v(t) = \sum_j^n V_j(a(t))v_j(t)$, $v_j \in \mathbb{R}$, leads to

$$\dot{v}_j = \lambda_j(a)v_j + (h_j(a) - \mathcal{G}_j(t))$$
$$+ \epsilon \left\{ \sum_k^n h_{jk}v_k + \sum_{k,l}^n (K_{jkl}\mathcal{G}_k v_l + f_{jkl}v_k v_l) \right\} + \mathcal{O}(\epsilon^2). \qquad (4.4)$$

where $\mathcal{G}_j \equiv 0$ for $j > m$, h_{jk}, f_{jkl} etc. are Taylor coefficients of the functions h and f, and $K_{jkl} = \langle \partial W_j(a)/\partial a_k, V_l(a) \rangle = - \langle W_j, \partial V_l(a)/\partial a_k \rangle$. Imposing now conditions of orthogonality (4.3), $v_j(t) \equiv 0$, $j = 1 \ldots m$, we determine iteratively $a_j(t)$ and $v_j(t)$ with higher and higher precision, by considering alternately (4.4) for $j = m+1 \ldots n$ as equations for v_j, and $j = 1 \ldots m$ as equations for $\mathcal{G}_j$. E.g., in the second order we get

$$\dot{a}_j = \epsilon h_j + \epsilon^2 \left\{ -\sum_k h_{jk}h_k/\lambda_k + \sum_{k,l} \left(K_{jkl}h_k h_l/\lambda_l + f_{jkl}h_k h_l/(\lambda_k \lambda_l) \right) \right\}$$
$$+ \mathcal{O}(\epsilon^3). \qquad (4.5)$$

We see, that this iterative procedure yields successively more and more precise evolution equations. The significant feature of the procedure is that their solutions approximate exact solutions not only with successively decreasing (in asymptotic sense) error, but also become valid at successively growing time scales. This becomes possible only by *keeping terms of different order in the same equation.*

5.   SUBCENTER MANIFOLD EXPANSION

The described method is associated with the method of the (sub)centre manifold, which is both a fundamentally important theoretical concept and an efficient practical tool.

The procedure of alternating increase of asymptotic precision of the $\mathcal{G}(a)$ and $v(a)$ leads to building asymptotic series in ϵ for these functions. If these series converge for some ϵ, this means that for each of those ϵ we will have an invariant manifold

$$\mathcal{U}(a, \epsilon) = U(a) + \epsilon v(a, \epsilon) \tag{5.1}$$

and the flow on that manifold defined by

$$\dot{a} = \mathcal{G}(a, \epsilon). \tag{5.2}$$

The unique dependence of v on a arises when we select a unique solution to the differential equation, say the one that remains finite for $t \to -\infty$.

In the extended phase space $\mathbb{R}^n \times \mathbb{R} = \{u, \epsilon\}$, manifold U is an intersection of the manifold $\mathcal{U}$ by the hyperplane $\epsilon = 0$. It be easily seen that the difference between $\mathcal{U}$ and U at small ϵ is along V_0, which means that $\mathcal{U}$ is tangent to the centre subspace of U. Thus it is a centre manifold or a sub-centre manifold; the technical difference is not important for us here, as all we use is the formalism.

This motivates an alternative approach to building the asymptotic evolution equation: from the very beginning, to look for representations of (5.1) and (5.2) in the form of power series in ϵ straightaway, instead of coming to (5.1) via the complicated procedure described above. This certainly is a very efficient method from a practical viewpoint.

And as far as actual calculations rather than their motivation in this finite-dimensional example are concerned, the subcenter manifold approach and the method described in Section 4 are strikingly similar. Method of Section 4, modified for a PDE problem in the form of the "method of the detecting operator", has been applied for the problem of the modulated strongly nonlinear waves, including autowaves in reaction-diffusion system (2.1) and conservative waves in the nonlinear Klein-Gordon equation, in [7]. Here we treat the modulated autowaves using the formalism of the

subcenter manifold. This is based on the idea of [8] originally applied to another class of problems (nearly linear waves).

6. FUNCTIONAL SUBCENTER MANIFOLD OF MODULATED WAVES

We consider modulated waves defined by (2.5) as a "functional manifold". Thus, the whole phase distribution $\varphi(x)$, in its entirety, is a coordinate on this manifold.

We consider the starting PDE system (2.1) as an ordinary differential equation in a Banach space $\mathcal{Y}$,

$$\frac{\mathrm{d}\hat{u}}{\mathrm{d}t} = \hat{f}(\hat{u})$$

where $\hat{u} : \mathbb{R} \to \mathcal{Y}; \quad t \mapsto u(x,t)$. The Ansatz is

$$u(x,t) = \mathcal{U}[\varphi(x,t)], \tag{6.1}$$

where square brackets [] denote functional dependence, i.e. $[\varphi]$ denotes dependence on φ and *all its spatial derivatives*, $\mathcal{U}(\varphi, \partial\varphi/\partial x_i, \partial^2\varphi/\partial x_i \partial x_j, \dots)$. In Banach-vector form,

$$\hat{u}(t) = \hat{\mathcal{U}}(\hat{\varphi}(t)), \tag{6.2}$$

where $\hat{\varphi}$ is a vector of a "smaller" functional space $\mathcal{X}$, representing the spatial distribution of the phase $\varphi(x,t)$ at a particular time instant t: $\hat{\varphi} : \mathbb{R} \to \mathcal{X}; \quad t \mapsto \varphi(x,t)$, and $\hat{\mathcal{U}} : \mathcal{X} \to \mathcal{Y}$.

Space $\mathcal{X}$ is "smaller" than $\mathcal{Y}$, e.g. in the sense that it consists of scalar functions rather than $\mathbb{R}^\ell$-valued functions as $\mathcal{Y}$. Another (non-formalised) difference is that $\hat{\varphi}$ represents functions $\varphi(x,t)$ with slowly varying spatial derivatives.

Evolution of the phase $\varphi(x,t)$ is sought in the form

$$\frac{\partial\varphi}{\partial t} = \mathcal{G}[\varphi(x,t)] \quad \text{or} \quad \frac{\mathrm{d}\hat{\varphi}}{\mathrm{d}t} = \hat{\mathcal{G}}(\hat{\varphi}(t)) \tag{6.3}$$

where $\hat{\mathcal{G}} : \mathcal{X} \to \mathcal{X}$ (assuming $\mathcal{X}$ is linear).

Then, the operators $\hat{\mathcal{U}}$ and $\hat{\mathcal{G}}$ are sought in the form of formal power series in the small parameter ϵ,

$$\mathcal{U} = \sum_{n=0}^{\infty} \mathcal{U}^{(n)} \epsilon^n, \; \mathcal{G} = \sum_{n=0}^{\infty} \mathcal{G}^{(n)} \epsilon^n, \quad \text{or} \quad \hat{\mathcal{U}} = \sum_{n=0}^{\infty} \hat{\mathcal{U}}^{(n)} \epsilon^n, \; \hat{\mathcal{G}} = \sum_{n=0}^{\infty} \hat{\mathcal{G}}^{(n)} \epsilon^n. \tag{6.4}$$

Then we use the finite-dimensional procedure discussed above, expressed in terms of $\hat{\mathcal{U}}$ and $\hat{\mathcal{G}}$, as a guidance, but immediately translate obtained

expressions to the straightforward form, without hats. The orbit derivative of (6.1) by the system (6.3) yields

$$\partial u/\partial t = \mathcal{U}_\varphi \mathcal{G} + \mathcal{U}_{\nabla\varphi}\nabla\mathcal{G} + \mathcal{O}(\epsilon^2) \tag{6.5}$$

since, as we mentioned, $\mathcal{U}$ is function of φ and all its derivatives, and derivatives of higher orders are, according to (2.6), of higher asymptotic orders in ϵ.

In turn, differentiation of $\mathcal{U}$ by spatial variables, using the chain rule, yields

$$\partial \mathcal{U}/\partial x_i = \mathcal{U}_\varphi \varphi_i + \mathcal{U}_{\varphi_j}\varphi_{ij} + \mathcal{O}(\epsilon^2). \tag{6.6}$$

Here and below, we denote spatial derivatives of φ by subscripts corresponding to the spatial coordinates, so φ_i means $\partial\varphi/\partial x_i$ etc.; and assume summation by repeated indices.

Now, substitution of spatial and (6.5) into (2.1), with account of expansions (6.4), yields

$$\begin{aligned}
&\mathcal{U}_\varphi^{(0)}\mathcal{G}^{(0)} + \mathcal{U}_\varphi^{(1)}\mathcal{G}^{(0)} + \mathcal{U}_\varphi^{(0)}\mathcal{G}^{(1)} + \mathcal{U}_{\varphi_i}^{(0)}\mathcal{G}_{\varphi_j}^{(0)}\varphi_{ij} + O(\epsilon^2) \\
&= f(\mathcal{U}^{(0)}) + \mathcal{F}(\mathcal{U}^{(0)})\mathcal{U}^{(1)} \\
&+ D\left(\mathcal{U}_{\varphi\varphi}^{(0)}\varphi_i\varphi_i + 2\mathcal{U}_{\varphi\varphi_j}^{(0)}\varphi_i\varphi_{ij} + \mathcal{U}_\varphi^{(0)}\varphi_{ii} + \mathcal{U}_{\varphi\varphi}^{(1)}\varphi_i\varphi_i\right) + \mathcal{O}(\epsilon^2). \tag{6.7}
\end{aligned}$$

Then we consider sequentially different orders in ϵ of this equation.

Order $\mathcal{O}(1)$.   Equating terms of (6.7) of the order $\mathcal{O}(1)$ we have

$$-\mathcal{U}_{\varphi^{(0)}}\mathcal{G}^{(0)} = f(\mathcal{U}^{(0)}) + D\mathcal{U}_{\varphi\varphi}^{(0)}\varphi_i\varphi_i. \tag{6.8}$$

This coincides with the equation (2.4) for the basic waves if $\mathcal{U}^{(0)} = U$, $\mathcal{G}^{(0)} = -\omega$, and $\varphi_i\varphi_i$ is identified with η. Together with the requirement of periodicity in φ, this order provides a nonlinear eigenvalue problem determining the basic solution $\mathcal{U}^{(0)} = U$ and the main frequency $-\mathcal{G}^{(0)} = \omega$ as functions of the local value of the slowly varying phase gradient $\eta = \varphi_i\varphi_i = (\nabla\varphi)^2$.

Order $\mathcal{O}(\epsilon)$.   This order gives a linear equation for $\mathcal{U}^{(1)}$:

$$\mathcal{L}\mathcal{U}^{(1)} = h, \tag{6.9}$$

where the linear operator $\mathcal{L}$ is

$$\mathcal{L} = \eta D\partial_{\varphi\varphi} + \omega(\eta)\partial_\varphi + \mathcal{F} \tag{6.10}$$

and the free term h depends on $\mathcal{G}^{(1)}$,

$$h = \mathcal{G}^{(1)}\mathcal{U}_\varphi^{(0)} + \mathcal{U}_{\varphi_i}^{(0)}\mathcal{G}_{\varphi_j}^{(0)} - D\mathcal{U}_{\varphi\varphi}^{(0)}\varphi_{ii} - 2D\mathcal{U}_{\varphi\varphi_j}^{(0)}\varphi_i\varphi_{ij}. \tag{6.11}$$

This is a differential problem in φ and as such is exactly 2π-periodic. Operator $\mathcal{L}$ is singular, its zero eigenfunction is the Goldstone mode $V_0 = \partial U/\partial \varphi$. By Fredholm, (6.9) is solvable iff the free term is orthogonal to the zero-eigenfunction W_0, of the adjoint operator $\mathcal{L}^+$,

$$\mathcal{L}^+ = \eta D \partial_\varphi^2 - \omega(\eta)\partial_\varphi + \mathcal{FT}. \tag{6.12}$$

This leads to the following result:

$$\mathcal{G}^{(1)} = \left(\oint \left\langle W_0, D\mathcal{U}_\varphi^{(0)} \right\rangle \mathrm{d}\varphi \right) \varphi_{ii} + 2 \left(\oint \left\langle W_0, D\mathcal{U}_{\varphi\varphi_j}^{(0)} \right\rangle \mathrm{d}\varphi \right) \varphi_i \varphi_{ij}. \tag{6.13}$$

Noting that $\mathcal{U}^{(0)}$ depends on φ only via $\eta = \varphi_i^2$, we arrive ultimately to the evolution equation precisely coinciding, up to the notation difference, with (3.6), with identical definitions of P and Q.

7.   DISCUSSION

In this paper, we describe a new method of derivation of the envelope equations for strongly nonlinear, non-conservative waves. The method is illustrated for the generic reaction-diffusion system (2.1), without any assumptions on the exact form of the reaction term $f(u)$ or diffusion matrix D. It has been demonstrated that the detecting operator technique, closely related to the sub-centre manifold technique, is equally applicable classical conservative nonlinear wave equations, such as the nonlinear Klein-Gordon equation, and produces the same results[7], so we may expect the present method to be similarly flexible. The detecting operator technique described in [7] is rather involved, and construction of the detecting operator itself is a non-algorithmic part of the procedure. The method described here is free from that disadvantage and provides a much easier, algorithmic way, producing the same results.

References

[1] L. D. Landau and E. M. Lifshitz. *The Classical Theory of Fields*, volume 2 of *Course of Theoretical Physics*. Pergamon Press, Oxford, 197.

[2] G. B. Whitham. *Linear and Nonlinear Waves*. Wiley, New York, 1974.

[3] L. N. Howard and N. Kopell. Slowly varying waves and shock structures in reaction-diffusion equations. *Stud. Appl. Math.*, 56(2):95–146, 1977.

[4] P. L. Bhatnagar. *Nonlinear Waves in One-Dimensional Dispersive Systems*. Clarendon Press, Oxford, 1979.

[5] A. M. Kamchatnov "New approach to periodic solutions of integrable equations and nonlinear theory of modulational instability", *Physics Reports*, 286:199-270, 1997.

[6] V. N. Biktashev. Diffusion of autowaves. *Physica D*, 40:83–90, 1989.

[7] V. N. Biktashev. On the geometrical optics for nonlinear waves. In L. Debnath, editor, *Nonlinear Dispersive Wave Systems*, pages 481–506. World Scientific, Singapore, 1992.

[8] A. J. Roberts. A sub-centre manifold description of the evolution and interaction of nonlinear dispersive waves. In L. Debnath, editor, *Nonlinear Dispersive Wave Systems*, pages 127–155. World Scientific, Singapore, 1992.

NONLINEAR WAVES IN A BI-LAYER AND COUPLED KLEIN-GORDON EQUATIONS

Karima R. Khusnutdinova

Department of Mathematical Sciences, Loughborough University,
Loughborough LE11 3TU, UK
and
Institute of Mechanics, Ufa Branch of the Russian Academy of Sciences,
Karl Marx Str. 6, Ufa 450000, Russia
K.Khusnutdinova@lboro.ac.uk

Keywords: Bi-layer, coupled Klein-Gordon equations, Lie group classification, conservation laws, nonlinear waves.

Abstract   A system of coupled Klein-Gordon equations is suggested to model one-dimensional nonlinear wave processes in a bi-layer. The type of coupling depends on the type of the interface and constitutes an arbitrary element of the Lie group classification problem, which is solved for these equations. The classification results are used to find conservation laws and particular invariant solutions.

1.   INTRODUCTION

After the intensive study of nonlinear wave processes in recent decades, it has become clear that the same equations, such as the Korteweg – de Vries equation and the nonlinear Schrödinger equation, appear in many different physical situations (see, for example, [1, 2] and the references therein). Since heterogeneity constitutes an essential feature of many physical problems, it makes sense to try to find some simple mathematical models which allow us to study peculiarities of nonlinear wave processes in heterogeneous media.

A possible way to derive such continuum models is to consider the long-wave dynamics of discrete models. One of the most famous models of this type is the Frenkel-Kontorova model [3]. Proposed initially to describe dislocations in metals, it has found numerous applications, and has been generalized in order to describe different phenomena (see the review [4]).

The original FK model deals with the situation when an additional semi-infinite plane of atoms is inserted into a perfect crystal lattice. The atoms of the "interface" layer are treated as a one-dimensional chain subjected to an external periodic potential produced by the surrounding atoms. For long waves, in dimensionless variables, one can obtain the integrable sine-Gordon equation whose kink and anti-kink solutions give the approximate description of the lattice behaviour in the vicinity of the dislocation core (see [4]).

In the FK model, one part of the crystal is treated as rigid and motionless. The natural generalization of this model is that of coupled chains of particles [5], i.e., of two one-dimensional periodic chains with linear links between elements and non-linear interaction between the chains. The long wave dynamics of this system is described, in dimensionless variables, by the coupled Klein-Gordon equations

$$u_{tt} - u_{xx} = f_u(u, w), \quad w_{tt} - c^2 w_{xx} = f_w(u, w), \tag{1.1}$$

where the subscripts denote partial derivatives, c is the ratio of the acoustic velocities of non-interacting components, and $f(u, w)$ describes the interaction between the chains.

Although originating as a generalization of the FK model, for appropriate choices of the function $f(u, w)$, the coupled Klein-Gordon equations (1.1) can also be considered as a long-wave limit of a simple lattice model for one-dimensional nonlinear wave processes in a bi-layer. Similar lattice models were proposed by Slepyan and his coworkers in connection with crack propagation in composites (see, for example, [6]). In that case the model parameters are determined by the type of the interface and materials forming the bi-layer. It is also worth noting that the same equations describe some processes in the DNA double helix [7] (see also [8] and the references therein).

In all these models the function $f(u, w)$ should be found experimentally, and therefore, its analytic form is not unique. It is known that the existence of a sufficiently large group of symmetries allows a certain analytic investigation of properties of the equations (see, for example, [9, 10]). Thus, the problem of group classification of coupled Klein-Gordon equations (1.1) naturally arises in connection with the model discussed above.

Equations of the type (1.1) with $c = 1$ (and arbitrary functions of u and w on the right-hand side) were studied in [11], where the cases admitting Lie-Bäcklund symmetries were picked out, and completely or partially integrable examples were presented. If $f_{uw}(u, w) = 0$, the system (1.1) splits into two independent Klein-Gordon equations, whose group classification was given by S.Lie [12] (or see [13] instead). The results of the Lie group classification of equations (1.1) for $c \neq 1, f_{uw}(u, w) \neq 0$ are presented in

this paper, and are used to find conservation laws and to construct particular invariant solutions. In conclusion, we discuss some possible applications of this model.

2. LIE POINT SYMMETRIES

The classification is given up to the following equivalence transformations (which preserve the differential structure of the equations and change only the arbitrary element, see, for example, [9])

$$\tilde{t} = \alpha t + \beta, \quad \tilde{x} = \alpha x + \gamma, \quad \tilde{u} = \lambda u + \mu, \quad \tilde{w} = \lambda w + \nu, \quad \tilde{f} = \frac{\lambda^2}{\alpha^2} f + \rho,$$

where $\alpha, \beta, \gamma, \lambda, \mu, \nu$, and ρ are arbitrary constants and $\alpha\lambda \neq 0$;

$$\begin{array}{cccc}
t \to -t, & x \to x; & t \to t, & x \to -x; \\
u \to -u, & w \to w; & u \to u, & w \to -w; \\
t \to t, & x \to \dfrac{x}{c}, & u \to w, & w \to u, \quad c \to \dfrac{1}{c}.
\end{array}$$

(Equations related by equivalence transformations admit similar groups).

The generator of the admitted Lie point group is sought in the form

$$X = \xi^1 \frac{\partial}{\partial t} + \xi^2 \frac{\partial}{\partial x} + \eta^1 \frac{\partial}{\partial u} + \eta^2 \frac{\partial}{\partial w}. \tag{2.1}$$

Using the methods of the group analysis of differential equations (see [9, 10]), the coordinates of the generator can be found as follows:

$$\xi^1 = C_1 t + C_2, \quad \xi^2 = C_1 x + C_3,$$
$$\eta^1 = C_4 u + \varphi(t, x), \quad \eta^2 = C_4 w + \chi(t, x),$$

where the functions $\varphi(t, x)$ and $\chi(t, x)$ satisfy the equations

$$\varphi_{tt} - \varphi_{xx} = (2C_1 - C_4) f_u + (C_4 u + \varphi) f_{uu} + (C_4 w + \chi) f_{uw},$$
$$\chi_{tt} - c^2 \chi_{xx} = (2C_1 - C_4) f_w + (C_4 u + \varphi) f_{uw} + (C_4 w + \chi) f_{ww}. \tag{2.2}$$

Here C_i, $i = \overline{1,4}$ are arbitrary constants.

It follows from (2.2) that when $f(u, w)$ is an arbitrary function, equations (1.1) admit a 2-dimensional algebra with the basis

$$X_1 = \frac{\partial}{\partial t}, \quad X_2 = \frac{\partial}{\partial x}, \tag{2.3}$$

and extension of the admitted algebra (2.3) is possible in those cases when function $f(u, w)$ satisfies the equation

$$(a_1 u + a_2) f_u + (a_1 w + a_3) f_w + a_4 f = a_5 u + a_6 w + a_7, \tag{2.4}$$

where $a_i, i = \overline{1,7}$ are constant coefficients.

For the analysis of the classifying relation (2.4) we first find how its coefficients transform under the equivalence transformations. Then, we find all solutions of the equation (2.4) up to equivalence transformations. Finally, solving the determining equations (2.2) for all cases obtained we find the generators additional to (2.3). The results of group classification are presented in Table 1.

Comments on Table:

- A, B, C, D, and σ are arbitrary constants, δ is positive real constant, $\tilde{\delta}$ is nonnegative real constant; $\varepsilon = \pm 1$, $\tilde{\varepsilon} = 0, \pm 1$.

- The constants λ and μ take real or imaginary values.

- $\psi(t, x) = \dfrac{1}{\delta(c^2 - 1)}\{[A\delta c^2 + B(1 + \delta^2 c^2)]t^2 + [A\delta + B(1 + \delta^2)]x^2\}.$

- In subcases the group of equivalence transformations can be wider than in general case. For example, if $f(u, w) = F(\delta u - w) + Au$, where $F'''(z) \neq 0$, additional transformations have the form:

$$\tilde{u} = u + \theta tx + \omega t + \tau x, \quad \tilde{w} = w + \delta(\theta tx + \omega t + \tau x) \qquad (2.5)$$

with arbitrary constants θ, ω, and τ;

$$\tilde{u} = u + \frac{c^2 t^2 + x^2}{2(c^2 - 1)}(\tilde{A} - A), \quad \tilde{w} = w + \frac{c^2 t^2 + x^2}{2(c^2 - 1)}\delta(\tilde{A} - A), \quad (2.6)$$

where $\tilde{A}$ satisfies the equation $\dfrac{d\tilde{A}}{da} = \Phi(\tilde{A}, c, \delta)$, $\tilde{A}\Big|_{a=0} = A$;

$$\tilde{u} = u + \frac{\kappa(A, c, \delta)}{2\delta(c^2 - 1)}[(1 + \delta^2 c^2)t^2 + (1 + \delta^2)x^2],$$

$$\tilde{w} = w + \frac{\kappa(A, c, \delta)}{2(c^2 - 1)}[(1 + \delta^2 c^2)t^2 + (1 + \delta^2)x^2], \qquad (2.7)$$

$$\tilde{f} = f + \kappa(A, c, \delta)(\delta u - w).$$

Here Φ and κ are arbitrary functions of their arguments. In accordance with these transformations, one may suppose that in the case under consideration $A = B = 0$.

<center>*Table 1*   Lie group classification of equations (1.1) ($c^2 \neq 1$, $f_{uw} \neq 0$).</center>

$f(u,w)$	Admitted generators (basis)
Arbitrary function	$X_1 = \dfrac{\partial}{\partial t}, \quad X_2 = \dfrac{\partial}{\partial x}$
$u^\sigma F(\dfrac{u}{w}), \quad \sigma \neq 0,$ if $\sigma \neq 2$, $F(z) \neq \varepsilon\left(\delta - \dfrac{1}{z}\right)^\sigma$ if $\sigma = 2$, $F(z) \neq A + \dfrac{B}{z^2} + \dfrac{1}{z}$	$X_3 = (\sigma - 2)(t\dfrac{\partial}{\partial t} + x\dfrac{\partial}{\partial x}) -$ $2(u\dfrac{\partial}{\partial u} + w\dfrac{\partial}{\partial w})$
$\exp u \; F(\tilde{\delta}u - w),$ $F(z) \neq \varepsilon \exp z$	$X_3 = t\dfrac{\partial}{\partial t} + x\dfrac{\partial}{\partial x} - 2(\dfrac{\partial}{\partial u} + \tilde{\delta}\dfrac{\partial}{\partial w})$
$F(\dfrac{u}{w}) + \tilde{\varepsilon}\ln u \;,$ $F(z) \neq \tilde{\varepsilon}\ln\left(\delta - \dfrac{1}{z}\right)$	$X_3 = t\dfrac{\partial}{\partial t} + x\dfrac{\partial}{\partial x} + u\dfrac{\partial}{\partial u} + w\dfrac{\partial}{\partial w}$
$F(\delta u - w) + Auw +$ $(\varepsilon - \delta A)\dfrac{u^2}{2}, \; F'''(z) \neq 0.$ If a) $\lambda^2 = \dfrac{\delta\varepsilon - A}{\delta(1-c^2)} \neq 0$, $\quad \mu^2 = \dfrac{\delta\varepsilon c^2 - A}{\delta(1-c^2)} \neq 0;$ b) $\lambda = 0, \quad \mu^2 = -\dfrac{A}{\delta} = -\varepsilon;$ c) $\lambda^2 = \dfrac{A}{\delta c^2} = \varepsilon, \quad \mu = 0$	$X_i = \varphi_i(t,x)(\dfrac{\partial}{\partial u} + \delta\dfrac{\partial}{\partial w}),$ $\quad i = \overline{3,6}$ $\varphi_3 = \cos\lambda x \cos\mu t, \; \varphi_4 = \sin\lambda x \sin\mu t,$ $\varphi_5 = \cos\lambda x \sin\mu t, \; \varphi_6 = \sin\lambda x \cos\mu t;$ $\varphi_3 = x\cos\mu t, \quad \varphi_4 = \cos\mu t,$ $\varphi_5 = x\sin\mu t, \quad \varphi_6 = \sin\mu t;$ $\varphi_3 = t\cos\lambda x, \quad \varphi_4 = \cos\lambda x,$ $\varphi_5 = t\sin\lambda x, \quad \varphi_6 = \sin\lambda x$
$F(\delta u - w) + \varepsilon uw - \delta\varepsilon\dfrac{u^2}{2},$ $F'''(z) \neq 0,$ $\lambda^2 = \dfrac{\varepsilon}{\delta(c^2-1)}$	$X_i = \varphi_i(t,x)(\dfrac{\partial}{\partial u} + \delta\dfrac{\partial}{\partial w}), \; i = \overline{3,6}$ $\varphi_3 = \cos\lambda x \cos\lambda t, \; \varphi_4 = \sin\lambda x \sin\lambda t,$ $\varphi_5 = \cos\lambda x \sin\lambda t, \; \varphi_6 = \sin\lambda x \cos\lambda t$

3.   INVARIANT SOLUTIONS AND CONSERVATION LAWS

The results of classification allow us to find conservation laws and to construct particular invariant solutions (self-similar, traveling waves, etc.)

Table 1 (continued)
Lie group classification of equations (1.1) ($c^2 \neq 1$, $f_{uw} \neq 0$).

$f(u, w)$	Admitted generators (basis)
$F(\delta u - w) + Au,$	$X_i = \varphi_i(t, x)(\dfrac{\partial}{\partial u} + \delta \dfrac{\partial}{\partial w}),\ \ i = \overline{3,6}$
$F'''(z) \neq 0.$	$\varphi_3 = tx,\ \ \varphi_4 = t,\ \ \varphi_5 = x,\ \ \varphi_6 = 1$
(i) $F(z) = \varepsilon z^\sigma + Bz,$	$X_7 = t\dfrac{\partial}{\partial t} + x\dfrac{\partial}{\partial x} + \dfrac{2}{2 - \sigma}(u\dfrac{\partial}{\partial u} +$
$\sigma \neq 0, 1, 2$	$w\dfrac{\partial}{\partial w}) + \dfrac{1 - \sigma}{2 - \sigma}\psi(t, x)(\dfrac{\partial}{\partial u} + \delta \dfrac{\partial}{\partial w})$
(ii) $F(z) = \varepsilon \exp z + Bz$	$X_7 = t\dfrac{\partial}{\partial t} + x\dfrac{\partial}{\partial x} + 2\dfrac{\partial}{\partial w} +$
	$\psi(t, x)(\dfrac{\partial}{\partial u} + \delta \dfrac{\partial}{\partial w})$
(iii) $F(z) = \varepsilon \ln z + Bz$	$X_7 = t\dfrac{\partial}{\partial t} + x\dfrac{\partial}{\partial x} + u\dfrac{\partial}{\partial u} + w\dfrac{\partial}{\partial w} +$
	$\dfrac{1}{2}\psi(t, x)(\dfrac{\partial}{\partial u} + \delta \dfrac{\partial}{\partial w})$
(iv) $F(z) = \varepsilon z \ln z$	$X_7 = t\dfrac{\partial}{\partial t} + x\dfrac{\partial}{\partial x} + 2(u\dfrac{\partial}{\partial u} + w\dfrac{\partial}{\partial w}) +$
	$\dfrac{\varepsilon}{\delta(c^2 - 1)}[(1 + \delta^2 c^2)t^2 +$
	$(1 + \delta^2)x^2](\dfrac{\partial}{\partial u} + \delta \dfrac{\partial}{\partial w})$
$\dfrac{A}{2}u^2 + \dfrac{B}{2}w^2 + uw +$	$X_{\varphi, \chi} = \varphi(t, x)\dfrac{\partial}{\partial u} + \chi(t, x)\dfrac{\partial}{\partial w},$
$+ Cu + Dw$	where $\varphi_{tt} - \varphi_{xx} = A\varphi + \chi,$
Here if	$\chi_{tt} - c^2\chi_{xx} = \varphi + B\chi$
a) $AB \neq 1, C = D = 0;$	$X_3 = u\dfrac{\partial}{\partial u} + w\dfrac{\partial}{\partial w};$
b) $AB = 1,$	$X_3 = (u + \dfrac{D - BC}{2(A + B)}t^2)\dfrac{\partial}{\partial u} +$
	$(w - \dfrac{A(D - BC)}{2(A + B)}t^2 + \dfrac{AC + D}{A + B})\dfrac{\partial}{\partial w}$

The system (1.1) with an arbitrary function $f(u, w)$ is Lagrangian with the density

$$L = \frac{1}{2}(u_t^2 + w_t^2 - u_x^2 - c^2 w_x^2) + f(u, w).$$

Indeed, the variation of the functional $\mathcal{L} = \int_{t_1}^{t_2} \int_{x_1}^{x_2} L\,dx\,dt$,

$$\frac{\delta \mathcal{L}}{\delta u} = f_u(u,w) - u_{tt} + u_{xx} = 0, \quad \frac{\delta \mathcal{L}}{\delta w} = f_w(u,w) - w_{tt} + c^2 w_{xx} = 0$$

gives equations (1.1). Therefore, knowing infinitesimal operators (2.1) and using the Noether theorem (see [10]), one can find conservation laws

$$A_t^1 + A_x^2 = 0,$$

where $A^i = L\xi^i + (\eta^\alpha - \xi^k u_k^\alpha)\dfrac{\partial L}{\partial u_i^\alpha}$, $\alpha = 1,2, i = 1,2$; and $u^1 = u, u^2 = w$; $u_1^\alpha = u_t^\alpha, u_2^\alpha = u_x^\alpha$. The operators (2.3) are admitted with any function $f(u,w)$. The corresponding conservation laws of energy and momentum have the form

$$\frac{\partial}{\partial t}[\frac{1}{2}(u_t^2 + w_t^2 + u_x^2 + c^2 w_x^2) - f(u,w)] - \frac{\partial}{\partial x}[u_t u_x + c^2 w_t w_x] = 0,$$

$$\frac{\partial}{\partial t}[u_t u_x + w_t w_x] - \frac{\partial}{\partial x}[f(u,w) + \frac{1}{2}(u_t^2 + w_t^2 + u_x^2 + c^2 w_x^2)] = 0.$$

In those cases where the dimension of the admitted algebra is larger than 2, there are additional conservation laws, which can be easily written down explicitly.

Let us also find some particular invariant solutions of equations (1.1) in the case $f(u,w) = \cos(\delta u - w)$. Introducing $\tilde{u} = \delta u, \tilde{w} = w$ as new dependent variables, we rewrite equations as

$$u_{tt} - u_{xx} = -\delta^2 \sin(u - w), \quad w_{tt} - c^2 w_{xx} = \sin(u - w) \qquad (3.1)$$

(the tildes are omitted). Although this case is not the most beneficial from the point of view of symmetries admitted (6-dimensional Lie algebra), it is interesting as a possible generalization of the FK model. Here, $\delta^2 = m_2/m_1$ has a meaning of the ratio of masses of particles in the "lower" and the "upper" chains. For $\delta^2 \to 0$, setting $u = 0$, we obtain for w the sine-Gordon equation, being the long-wave approximation of the FK model. Thus, the FK model appear as a natural limit of the coupled equations (3.1).

Equations (3.1) admit the generator

$$X_1 + vX_2 + \alpha X_4 = \frac{\partial}{\partial t} + v\frac{\partial}{\partial x} + \alpha t(\frac{\partial}{\partial u} + \frac{\partial}{\partial w})$$

(see Table 1), where v and α are arbitrary constants. The solution which is invariant with respect to this generator for $v^2 \neq 1, c^2$, and $\dfrac{1 + \delta^2 c^2}{1 + \delta^2}$, has the form

$$u = \sigma^{-1}[\delta^2(v^2 - c^2)p(x - vt) + \eta], \quad w = \sigma^{-1}[(1 - v^2)p(x - vt) + \eta], \quad (3.2)$$

where $\quad \sigma = \delta^2(v^2 - c^2) + v^2 - 1,$

$$\eta = \alpha(1 + \delta^2)vtx - \frac{\alpha}{2}[(1 + \delta^2c^2)t^2 + (1 + \delta^2)x^2] + A(x - vt) + B,$$

$$p'' = -\lambda \sin p - a, \qquad\qquad (3.3)$$

$$\lambda = \frac{\delta^2(v^2 - c^2) + v^2 - 1}{(v^2 - 1)(v^2 - c^2)}, \qquad a = \frac{\alpha(1 - c^2)}{(v^2 - 1)(v^2 - c^2)}.$$

Here the prime denotes derivative with respect to the argument of the function; A and B are arbitrary constants. Let us set $A = B = 0$.

If $\lambda < 0$, then introducing $\tilde{p} = p + \pi$, equation (3.3) can be rewriten in the form $\tilde{p}'' = -|\lambda| \sin \tilde{p} - a$. Therefore, analyzing (3.3), one can suppose $\lambda > 0$. The energy integral of (3.3) may be written in the form

$$(p')^2 + 2\lambda(1 - \cos p) + 2ap - 2E^* = 2E, \quad E^* = \lambda - \sqrt{\lambda^2 - a^2} - a \arcsin \frac{a}{\lambda}.$$

If the condition $|a| < \lambda$ is satisfied, then any value of E from the interval

$$0 < E < 2\lambda - \pi|a| - 2E^*$$

defines a bounded periodic solution of (3.3) describing nonlinear oscillations near the point of equilibrium $\quad p = -\arcsin \frac{a}{\lambda} \quad$ in the region $p \in [p_1, p_2]$. Here p_1 and p_2 are the roots of the equation

$$\lambda(1 - \cos p) + ap - E^* = E$$

on the interval $(-\pi + \arcsin \frac{a}{\lambda}, \pi + \arcsin \frac{a}{\lambda})$. It is assumed here that $\arcsin \frac{a}{\lambda} \in (-\frac{\pi}{2}, \frac{\pi}{2})$.

If $\alpha = 0$, equation (3.3) turns out to be the equation describing oscillations of the mathematical pendulum, which is integrable in terms of elliptic functions (see, for example, [14]). In this case solutions of the system (3.1) describing periodic waves have the form:

$$u = 2U \arcsin\{k \operatorname{sn} [\sqrt{\lambda}(x - vt), k]\} = Ww \qquad (3.4)$$

— "fast" waves, propagating with velocities $\quad v^2 \in (S, M) \cup (L, +\infty),$ where $S = \min\{1, c^2\}, M = \dfrac{1 + \delta^2c^2}{1 + \delta^2}, L = \max\{1, c^2\},$

$$u = 2U \arcsin\{\operatorname{dn} [\sqrt{|\lambda|}(x - vt), k]\} = Ww, \qquad (3.5)$$

— "slow" waves, propagating with velocities $v^2 \in [0, S) \cup (M, L)$. Here

$$U = \frac{\delta^2(v^2 - c^2)}{\delta^2(v^2 - c^2) + v^2 - 1}, \qquad W = \frac{\delta^2(v^2 - c^2)}{1 - v^2}, \quad 0 < k < 1.$$

In the $k = 1$ limiting case, "slow" periodic waves become solitary waves,

$$u = 4U \arctan\{\exp \sqrt{|\lambda|}(x - vt)\} = Ww.$$

Using the fact that equations (3.1) admit reflections

$$t \to -t, \quad x \to x; \qquad t \to t, \quad x \to -x; \qquad u \to -u, \quad w \to -w,$$

one can obtain solutions with other combinations of signs.

If $\delta \to 0$ ($m_1 \gg m_2$), solitary waves may propagate with the velocities $v^2 \in [0, c^2)$. In that case the displacement of particles is independent on the velocity of wave propagation. If the masses m_1 and m_2 are comparable, solitary waves may propagate with the velocities $v^2 \in [0, S) \bigcup (M, L)$. Therefore, if the acoustic velocities of non-interacting components are different ($c^2 \neq 1$), a gap appears in the velocity spectrum of the solitary waves, i.e., the system acts as a kind of a filter of solitary waves. Here the relative displacement (of "upper" particles relative to "lower" ones) remains the same as in the FK model (per period of the chain), but the absolute displacement depends on the velocity of the wave.

Solutions for nonlinear waves in the presence of additional shear forces (acting either on both chains in the opposite directions or on just one chain) can be constructed using (3.2) with $\alpha \neq 0$ and the equivalence transformations (2.5) – (2.7), which were found above. Using other linear combinations of the generators from Table 1 we can find other invariant solutions.

4.   CONCLUSION

The simple lattice-based model proposed here can be used for studying the peculiarities of propagation and interaction of one-dimensional non-linear waves in a bi-layer. It can be useful for problems related to energy exchange between the layers, long-short wave resonance, delamination, etc. The model can be modified to take into account other degrees of freedom by considering chains of interacting mechanical dipoles [15] instead of chains of point masses. These topics will be discussed elsewhere.

Acknowledgments

References

[1] Dodd, R K, Eilbek, J C, Gibbon, J D, and Morris, H C (1984) *Solitons and Nonlinear Wave Equations*. London: Academic Press Inc.

546

[2] Scott, A (1999) *Nonlinear Science: Emergence and Dynamics of Coherent Structures.* New York: Oxford University Press Inc.

[3] Kontorova, T A, and Frenkel, Ya I (1938) *On the theory of plastic deformation and twinning I, II*, Zh. Eksp. Teor. Fiz. **8** (1) 89 - 95, (12) 1340 -1348.

[4] Braun, O M and Kivshar, Yu S (1998) *Nonlinear dynamics of the Frenkel-Kontorova model*, Phys. Rep. **306**, 1-108.

[5] Akhatov, I Sh, Baikov, V A, and Khusnutdinova, K R (1995) *Nonlinear dynamics of coupled chains of particles*, J. Appl. Maths Mechs **59** (3) 353 - 361.

[6] Slepyan, L I (1998) *Some Basic Aspects of Crack Dynamics.* In: Cherepanov, G P ed. *Fracture. A Topical Encyclopedia of Current Knowledge.* Malabar, Florida: Krieger Publishing Co.

[7] Yomosa, S (1983) *Soliton excitations in deoxyribonucleic acid (DNA) double helices*, Phys. Rev. A **27** (4) 2120 - 2125.

[8] Yakushevich, L V (1998) *Nonlinear Physics of DNA.* Chichester: Wiley.

[9] Ovsiannikov, L V (1982) *Group Analysis of Differential Equations.* New York: Academic Press.

[10] Olver, P (1986) *Applications of Lie Groups to Differential Equations.* New York: Springer-Verlag.

[11] Zhiber, A V, Ibragimov, N H, and Shabat, A B (1979) *Equations of Liouville type*, Dokl. Akad. Nauk SSSR. **249** (1) 26 - 29.

[12] Lie, S (1881) *Discussion der Differentialgleichung $\frac{\partial^2 z}{\partial x \partial y} = F(z)$* , Arch. für Math. og Naturv. **6** (1) 112 - 124.

[13] Ibragimov, N H ed. (1994) *CRC Handbook of Lie Group Analysis of Differential Equations, Vol. 1, Symmetries, exact solutions and conservation laws.* Boca Raton: CRC Press.

[14] Kamke, E (1967) *Differentialgleichungen. Lösungsmethoden und Lösungen. Teil 1, 8th ed.* Leipzig: Akademics Verlag, Greest & Portig.

[15] Khusnutdinova, K R (1992) *Nonlinear Waves in a Double Row Particle System*, Vestn. MGU, **1** (2) 71-76.

Chapter 11
Combustion models

NONMODAL INSTABILITY AS THE MECHANISM OF ACCELERATION OF CELLULAR FLAMES

Vladimir Karlin

University of Central Lancashire, Preston PR1 2HE, UK

VKarlin@uclan.ac.uk

Keywords: Nonmodal instability, cellular flame, Sivashinsky equation

Abstract A detailed analysis of the evolution of unstable flame fronts governed by the Sivashinsky equation was undertaken in order to understand physical mechanism of acceleration of laminar premixed flames. Rates of the linear nonmodal growth of the perturbations were estimated. The estimation is based on the analysis of the resolvent and the C_0-semigroup generated by the linear operator associated with the Sivashinsky equation. The results are in good quantitative agreement with direct numerical simulations. They confirm a possibility of a huge linear transient amplification of certain types of small perturbations generated by noise. These amplified perturbations increase the flame surface area and, as a result, the flame speed.

1. INTRODUCTION

Experiments with large-scale expanding flames in open atmosphere revealed that they can experience substantial acceleration [1]. Further research showed that the phenomenon can be observed on much smaller scales in pressurised enclosures [2]. This acceleration was linked with the intrinsic long wave instability of flame fronts which is also known as the Darrieus-Landau or the hydrodynamic flame instability, see e.g. [3]. Wide variety of time and space scales involved makes it inefficient to study this phenomenon on the basis of the general Navier-Stokes system and necessitates development of simplified mathematical models. In particular, an asymptotic model of cellularization of hydrodynamically unstable flames was obtained in [4]. The model is known as the Sivashinsky equation and in this work we use it to analyse the evolution of the unstable flame fronts.

The Sivashinsky equation governs evolution of the perturbation $\Phi(x_1, x_2, t)$ of the plane flame front moving in the direction orthogonal to the x_1, x_2-plane with the laminar flame speed u_b:

$$\partial_t \Phi - 2^{-1} |\nabla \Phi|^2 = \Delta \Phi - (\gamma/4\pi)(-\Delta)^{1/2}\Phi, \qquad t > 0. \qquad (1.1)$$

Here, space coordinates are measured in units of the flame front width δ_{th}, time is in units of δ_{th}/u_b, and initial position of the flame $\Phi(x_1, x_2, 0)$ is given. The contrast of densities of burnt and unburnt gas mixtures $\gamma = 1 - \rho_b/\rho_u$ and gradient of the perturbation are assumed to be small. For one-dimensional perturbations (1.1) takes the form

$$\partial_t \Phi - 2^{-1}(\partial_x \Phi)^2 = \partial_{xx} \Phi - (\gamma/2)\mathcal{H}[\partial_x \Phi], \quad |x| < \infty, \quad t > 0, \qquad (1.2)$$

where $\mathcal{H}$ denotes the Hilbert transformation.

If $\Phi^{(1)}(x, t)$ is a Λ_1-periodic solution to (1.2) for $\gamma = \gamma_1$, then $\Phi^{(2)}(x, t) = \Phi^{(1)}(\gamma_2 x/\gamma_1, \gamma_2^2 t/\gamma_1^2)$ is a $(\gamma_1\Lambda_1/\gamma_2)$-periodic solution to (1.2) for $\gamma = \gamma_2$. This makes it possible to study (1.2) for any γ, though proper scaling of independent variables may be required in order to give a physically correct interpretation of the results obtained in this paper for $\gamma = 0.8$.

A wide class of explicit solutions to (1.2) was obtained in [5] by using the pole decomposition technique. The Λ-periodic, or "cellular", steady coalescent N-pole solutions to (1.2) have the following form

$$\Phi_{N,\Lambda}(x, t) = V_{N,\Lambda}t + 2\sum_{n=1}^{N} \ln|\cosh 2\pi b_n/\Lambda - \cos 2\pi x/\Lambda|, \qquad (1.3)$$

where real $\Lambda > 0$ and integer N lying in the range $0 \le N \le N_\Lambda = \operatorname{ceil}(\gamma\Lambda/8\pi + 1/2) - 1$ are otherwise arbitrary parameters. Real numbers b_n, $n = 1, \ldots, N$ are the imaginary parts of poles introduced by the pole decomposition technique. They should satisfy a system of nonlinear algebraic equations available elsewhere. The increase of the flame speed due to the "cellularization" is exactly $V_{N,\Lambda} = 2\pi N\Lambda^{-1}(\gamma - 4\pi N/\Lambda)$.

Presence of the $V_{N,\Lambda}t$ term in (1.3) confirms that cellularization of the flame front results in an increase of its propagation speed. However, values of $V_{N,\Lambda}$ are too small to match the increase of flame speeds obtained in experiments. Obviously, there should be something else in (1.1) if it is advanced enough to model the experiment adequately.

An indication of a sophisticated nature of the Sivashinsky equation comes from numerical experiments. In order to study (1.1) numerically, the infinite domain of definition of its space variables needs to be replaced by a finite one and a method to extend the solution up to the infinity should be provided. Thus, (1.1) is considered in a square of size L and its solutions are assumed to be L-periodic. The latter is physically reasonable if

$L \gg 8\pi/\gamma$, where $8\pi/\gamma$ is the wavelength of the most amplified harmonics in the dispersion relation associated with (1.1).

Such effectuated numerical solutions to (1.2) converge to $\Phi_{N_L,L}$ for a wide variety of initial conditions if $L < L_c \approx 68\pi/\gamma$. In larger computational domains $L > L_c$, they do not stabilize to any steady state at all, see e.g. [6], [7]. Instead, being essentially nonsteady, they remain very close to $\Phi_{N_L,L}$, developing on the surface of the flame front small cusps randomly in time as this is shown in Fig. 1a. Associated flame speed grows as a result of the increased flame surface area.
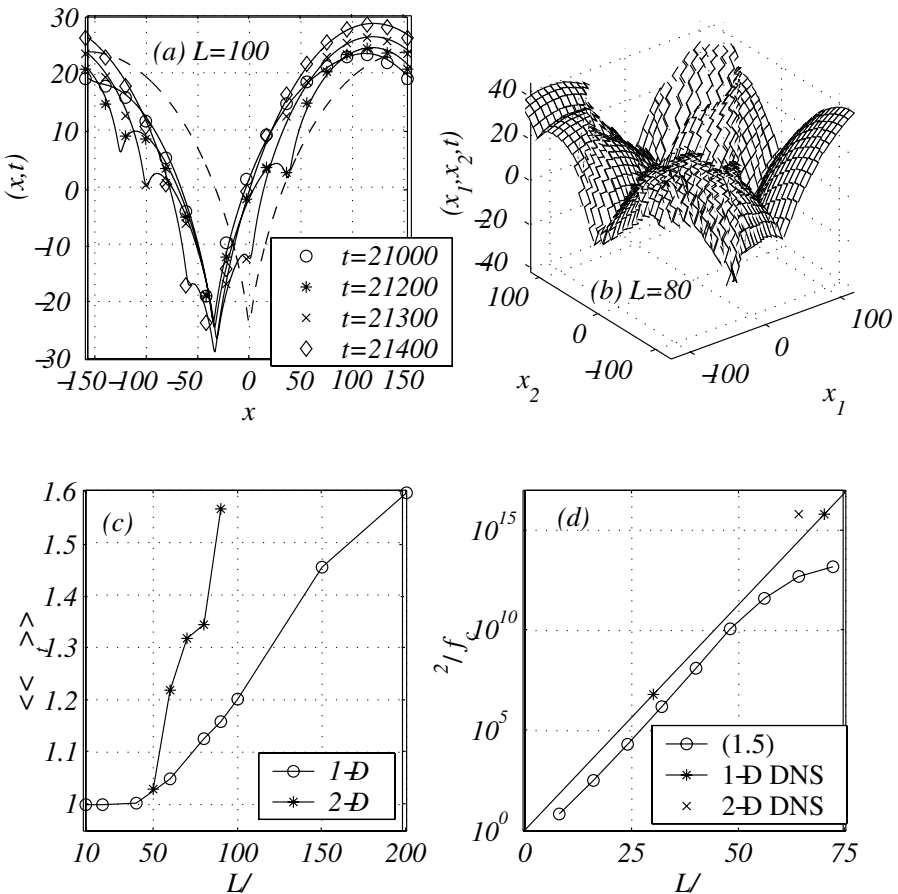
Figure 1 (a) Small cusps on the flame surface corresponding to $\Phi_{N_L,L}(x,t)$. A profile of $\Phi_{N_L,L}$ is plotted with a dashed line. (b) A crack on the surface of a 2-D flame at $t = 27000$. (c) Increase of the averaged flame speed $\langle <\Phi_t> \rangle$ obtained in 1-D and 2-D numerical simulations and normalized by $V_{N_L,L}$ and $2V_{N_L,L}$ correspondingly. (d) Critical strength of noise versus flame size.

The behaviour of the two-dimensional flame fronts is similar [7]. For small $L < L_c \approx 64\pi/\gamma$ solutions to (1.1) converge to $\Phi_{N_L,L}(x_1, x_2, t) = \Phi_{N_L,L}(x_1, t) + \Phi_{N_L,L}(x_2, t)$. The perturbations begin to appear randomly in time for $L > L_c$. They resemble cracks and are illustrated in Fig. 1b. Graphs of the time and space averaged increase of the flame speed $\langle\langle\Phi_t\rangle\rangle$ obtained in one- and two-dimensional computations and normalized by $V_{N,L}$ and $2V_{N,L}$ correspondingly are depicted in Fig. 1c.

In this work rates of the linear nonmodal growth of the perturbations were estimated by means of the numerical analysis of the resolvent and the C_0-semigroup generated by the linear operator associated with the Sivashinsky equation. The relevance of the most amplifiable perturbations to the small cusps appearing on the surface of large enough flames in numerical simulations was established and the effect itself was suggested as the mechanism of the increase of the flame speed.

2.   NONMODAL AMPLIFICATION

High sensitivity of $\Phi_{N_L,L}$ to certain perturbations was suggested in [8] as an explanation of the fundamental change in the behaviour of the numerical solutions to (1.2) for $L = L_c$. The idea was based on a particular asymptotic solution to an approximation of the Sivashinsky equation linearized in a neighbourhood of $\Phi_{N,L}$. In sequel, a model equation with a stochastic right hand side, explicitly introducing noise of physical origins, was proposed and investigated, see e.g. [9].

The direct confirmation of the idea of high sensitivity can be obtained by the estimation of possible linear amplification of perturbations of $\Phi_{N,\Lambda}$. Substituting $\Phi(x, t) = \Phi_{N,\Lambda}(x, t) + \varphi(x, t)$ into (1.2) and linearizing it with respect to the L-periodic perturbations $\varphi(x, t)$, one obtains

$$\partial_t\varphi = (\partial_x\Phi_{N,\Lambda})\partial_x\varphi + \partial_{xx}\varphi - (\gamma/2)\mathcal{H}[\partial_x\varphi] = \mathcal{A}_{N,\Lambda}\varphi. \qquad (2.1)$$

The eigenvalue problem for an operator $\mathcal{A}'_{N,\Lambda}$ similar to $\mathcal{A}_{N,\Lambda}$ was studied in [10] and indicated that $\Phi_{N_L,L}$ is the only steady coalescent pole solution to (1.2) with no eigenvalues located in the right half of the complex plane for any $L > 0$. The eigenvalues of both operators coincide and the eigenfunctions of $\mathcal{A}'_{N,\Lambda}$ are just x-derivatives of those of $\mathcal{A}_{N,\Lambda}$.

The eigenfunctions of $\mathcal{A}_{N,\Lambda}$ are nonorthogonal. Hence, solutions to (2.1) may undergo a substantial amplification over a finite period of time, though they are likely to decay for $t \to \infty$, if $N = N_L$. This amplification would result from a peculiar mixing of a few severely nonorthogonal eigenmodes, rather than from a single one. Accordingly, it is called the nonmodal amplification and the nonmodal instability if the amplification is strong

enough to bring the nonlinearity of the problem into the play. In what follows we are interested in $\Phi_{N_L,L}$ only and the index L is dropped.

The link between the resolvent $(z\mathcal{I} - \mathcal{A}_N)^{-1}$ and the C_0-semigroup $e^{t\mathcal{A}_N}$ in the form of the Laplace transformation provides a robust lower bound on the maximal possible amplification of the initial condition in (2.1). Carrying out the straightforward estimation of the integral in a norm of the Laplace transformation of $e^{t\mathcal{A}_N}$, one arrives at

$$\sup_{t>0} \|e^{t\mathcal{A}_N}\| \geq \sup_{\mathrm{Re}(z)>0} \left[\mathrm{Re}(z) \|(z\mathcal{I} - \mathcal{A}_N)^{-1}\| \right] = \mathcal{K}_{\mathcal{A}_N}. \qquad (2.2)$$

Thus, the lower bound $\mathcal{K}_{\mathcal{A}_N}$ on $\|e^{t\mathcal{A}_N}\|$ can be effectively estimated by calculating norms of the resolvent of a finite-dimensional approximation to $\mathcal{A}_N$. The 2-norm represents the energy of solutions to (2.1) and is an appropriate choice in this investigation. Plotting level lines of $\|(z\mathcal{I} - \mathcal{A}_N)^{-1}\|$ not only simplifies the search of the supremum but, also, provides boundaries of pseudospectra of $\mathcal{A}_N$, see e.g. [11]. Examples of the latter can be found in [7]. Values of $\mathcal{K}_{\mathcal{A}_N}$ shown in Fig. 1d are large enough to amplify round-off errors to the level of the solution itself.

If f is the order of the amplitude of perturbations associated with the round-off errors, then $L_c = L_c(f)$. Two values of $L_c(f)$ obtained in our one-dimensional calculations with the 32- and 64-bit arithmetic are shown in Fig. 1d. It is convenient to invert the relation $L_c = L_c(f)$ and write it in the form $f_c = f_c(L)$, where f_c is a critical noise strength for the given size L of the flame. The reciprocal of $\mathcal{K}_{\mathcal{A}_N}$ is an estimation of the upper bound on this critical strength, i.e. $f_c \leq \mathcal{K}_{\mathcal{A}_N}^{-1}$. Here, the strength of perturbations means their 2-norm. The corresponding graph is plotted in Fig. 1d. It is in a very good agreement with the results of our direct numerical simulations.

3. MOST GROWING PERTURBATIONS

Polar decomposition of $e^{t\mathcal{A}_N}$ can be used to demonstrate that the set of its right singular vectors $\psi_n(x,t)$, $n = 1, 2, \ldots$ forms an orthogonal basis in the space of valid initial conditions for any $t > 0$. Corresponding singular values $\sigma_n(t)$ provide the magnitude of amplification of $\psi_n(x,t)$, taken as the initial condition $\varphi(x,0)$, by the time instance t. Approximating $\mathcal{A}_N$ by a finite-dimensional matrix, both $\sigma_n(t)$ and $\psi_n(x,t)$ can be effectively calculated by using singular value decomposition (SVD) algorithms of numerical linear algebra.

A few largest singular values of $e^{t\mathcal{A}_N}$ are shown in Fig. 2a. One may see that $\sigma_{1,2}(t)$ match $\mathcal{K}_{\mathcal{A}_N}$ and that the dimension of the subspace of the most growing perturbations is very low. Appearance of $\psi_{1,2}(x,t)$, which will be most amplified by $t = 10^3$, is depicted in Fig. 2b. Figure 2c shows a few largest coefficients of the expansions of $\psi_1(x,t)$ and $\varphi_1(x,t) = e^{t\mathcal{A}_N}\psi_1(x,t)$
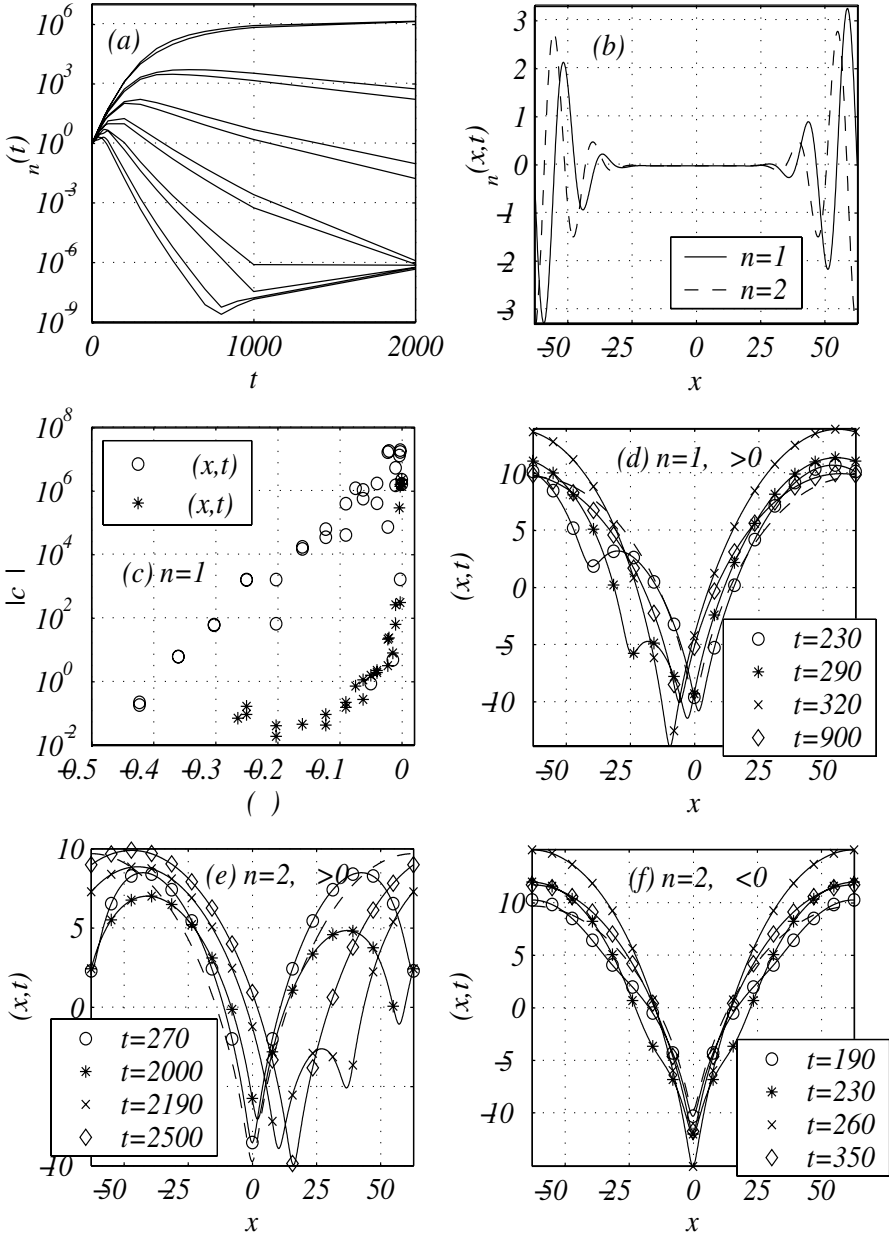
Figure 2 (a) Largest singular values of $e^{t\mathcal{A}_N}$. (b) Right singular vectors of $e^{t\mathcal{A}_N}$ corresponding to $\sigma_1(t) \approx 9.2 \times 10^5$ and $\sigma_2(t) \approx 7.4 \times 10^5$ for $t = 10^3$. (c) Coefficients of expansions of $\psi_1(x,t)$ and $\varphi_1(x,t) = e^{t\mathcal{A}_N}\psi_1(x,t)$ in the basis of the eigenfunctions of $\mathcal{A}_N$ for $t = 10^3$. (d)-(f) Solutions to (1.2) for $\Phi(x,0) = \Phi_N + \varepsilon\psi_n(x,10^3)$; (d) $n = 1$, $\varepsilon = 10^{-3}$, (e) $n = 2$, $\varepsilon = 10^{-3}$, (f) $n = 2$, $\varepsilon = -10^{-3}$. Here $L = 40\pi$.

in the basis of the eigenfunctions of $\mathcal{A}_N$ for $t = 10^3$. This confirms, that the perturbation is formed by more than one eigenmode.

Evolution of both types of the most growing perturbations governed by the nonlinear Sivashinsky equation is illustrated in Figs. 2d - 2f. The initial conditions were $\Phi(x, 0) = \Phi_N(x, 0) + \varepsilon \psi_n(x, 10^3)$, where $\varepsilon = \pm 10^{-3}$, and $n = 1, 2$. The asymmetric singular mode $\psi_1(x, 10^3)$, see Fig. 2b, results in appearance of a small cusp to the left or to the right from the trough depending on the sign of ε. After merging of the cusp with the trough, the flame profile converges slowly to $\Phi_N(x + \Delta x, t)$, $\mathrm{sign}(\varepsilon)\Delta x > 0$. The symmetric singular mode $\psi_2(x, 10^3)$ produces two symmetric dents moving towards the trough on both sides of the profile if $\varepsilon < 0$, see Fig. 2f. By $t \approx 500$ the flame profile returns exactly to $\Phi_N(x, t)$. For $\varepsilon > 0$ two small cusps move towards the boundaries of the computational domain creating a quasi-steady structure shown in Fig. 2e for $t = 270$. This structure survives until $t \approx 1800$, but eventually bifurcates and the solution converges to $\Phi_N(x + \Delta x, t)$, $\Delta x < 0$.

Behaviour of perturbations $\psi_{1,2}(x, 10^3)$ of the amplitude $\varepsilon = 10^{-6}$ was not as picturesque, but they managed to produce a visible effect on Φ_N. Same can be said about $\psi_{3,4}(x, 10^3)$ of the amplitude $\varepsilon = 10^{-3}$. Perturbations corresponding to $\psi_n(x, 10^3)$ of higher orders did not grow significantly and did not cause any noticeable changes to Φ_N for ε up to 10^{-2}. The dominating singular modes $\psi_{1,2}(x, t)$ stabilize to the profiles shown in Fig. 2b by $t \approx 200$. Prior to that time the associated amplification $\sigma_{1,2}(t)$ is already about 10^3, but $\psi_{1,2}(x, t)$ does not coincide with neither $\psi_{1,2}(x, 10^3)$ nor $\psi_{3,4}(x, 10^3)$. Thus, dependence of ψ_n on time makes studies of the effect of transient amplification on short time scales $t < 200$ quite complicated.

Computer round-off errors act permanently and the perturbations generated by them can be of any type, including those special types which can be hugely amplified. When the size of the flame grows, the perturbations of that special type, linearly amplified during the finite period of time, become so large that the nonlinearity of the Sivashinsky equation cannot be neglected. The result can be seen as a sequence of small cusps, appearing on the flame surface randomly in time.

4.   CONCLUSIONS

Nonmodal instability of steady coalescent pole solutions to the Sivashinsky equation has been established by means of the estimation of possible transitional amplification of perturbations and was demonstrated in direct numerical simulations. As the size of the flame increases, the nonmodal amplification of noise grows. Hence, the number of the cusps generated by

noise on the flame surface grows as well, contributing to its total surface area and, eventually, in its acceleration.

From the physical point of view, a possibility of nonmodal instability of flames was demonstrated in this paper for quite a hypothetic case $\gamma \ll 1$. It is too optimistic to expect the same level of nonmodal amplification for realistic values of γ, but the continuity principle provides a good chance that the effect itself will be present. Examples from hydrodynamics show that the nonmodal amplification does not need to be as huge as we observed it in the Sivashinsky equation in order to be a dominating effect, because the level of noise in physical systems is usually much higher than the computer round-off errors. Further research is required in order to validate the mechanism of nonmodal instability for realistic cellular flames.

Unlike (1.2), the solutions, representing the expanding flames, depend on time essentially making coefficients of the associated linearized equation time-dependent. Investigation of transitional amplification in a system with time-dependent coefficients is currently a challenge.

Acknowledgments

References

[1] Y.A. Gostintsev, A.G. Istratov, and Y.V. Shulenin. *Phys Combust Expl*, 24(5):63–70, 1988.

[2] D. Bradley, R.A. Hicks, M. Lawes, C.G.W. Sheppard, and R. Woolley. *Combust Flame*, 115:126–144, 1998.

[3] J.K. Bechtold and M. Matalon. *Combust Flame*, 67:77–90, 1987.

[4] G.I. Sivashinsky. *Acta Astronaut*, 4:1177–1206, 1977.

[5] O. Thual, U. Frisch, and M. Hénon. *J Physique*, 46(9):1485–1494, 1985.

[6] M. Rahibe, N. Aubry, and G.I. Sivashinsky. *Combust Theory Model*, 2(1):19–41, 1998.

[7] V. Karlin. *Proc Combust Inst*, 2002. (to appear).

[8] G. Joulin. *J Physique*, 50:1069–1082, 1989.

[9] P. Cambray, K. Joulain, and G. Joulin. *Combust Sci Technol*, 103:265–282, 1994.

[10] D. Vaynblat and M. Matalon. *SIAM J Appl Math*, 60(2):679–702, 2000.

[11] L.N. Trefethen. *SIAM Rev*, 39(3):383–406, 1997.

CATALYTIC COMBUSTION: MAKING THE CONNECTION BETWEEN THE PHYSICAL/CHEMICAL PROCESSES AND THE MATHEMATICAL MODEL OF THE REACTOR

S.T. Kolaczkowski

Department of Chemical Engineering,
University of Bath, Bath BA2 7AY, UK

cestk@bath.ac.uk

Abstract   Catalytic monoliths are used in a wide number of applications, and in particular in catalytic combustion. To explain the difference between homogeneous and catalytic combustion reactions, a simple experiment is described, which could be performed readily, to illustrate these two types of combustion processes. In addition, examples of the form of the equations representing catalytic combustion reactions in a monolith are outlined, illustrating how the physical/chemical processes are included in a mathematical model of the reactor. This, in turn, leads to a complex system of coupled equations with non-linear terms. When numerical methods are employed, the solvers can crash, and being aware of the physical significance of the terms in the equation can lead to a method of breaking down the problem into a manageable form.

Introduction

The use of monoliths as support structures for catalysts, and their subsequent use in reactors, has created some interesting challenges for modellers of such systems. The catalytic monolith consists of a structure that contains a large number of parallel channels through which a fluid flows. For example, in one popular and important application of this technology, the catalytic converter, the fluid is the exhaust gas from the engine of a vehicle. The catalytic system oxidises the emissions of CO to CO_2, and hydrocarbons to carbon dioxide and water, whereas the oxides of nitrogen (NO_x) are reduced to nitrogen. The catalytic converter is a catalytic reactor, through which the reactants flow in the gas stream. The process consists

of interactions in the transfer of energy, between the gas and the solid layer, where the catalyst is dispersed and energy is released from the chemical reactions. A complete description of this process is available in Hayes and Kolaczkowski (1997).

The modelling of the performance of such reactors, and related applications where catalytic monoliths are used to support catalytic combustion reactions, creates difficulties as a result of the complexity of the coupled system of equations that describe fluid flow, chemical reactions, and heat and mass transfer in these systems.

Before explaining the connection between physical/chemical processes in catalytic combustion, it is important to understand how it differs from 'conventional' or homogeneous combustion. This is illustrated with the aid of two relatively simple experiments and a description of the stoichiometry of combustion reactions to help visualise these complex processes.

Homogeneous gas phase combustion

Gas phase combustion chemistry is very complex and there are many references in the literature, e.g. Glassman (1987), Spalding (1979), Griffiths and Barnard (1995). The mechanistic steps are very complex. For example, the simplified representation of the overall stoichiometry for the combustion of methane, may be represented by:

$$CH_4 + 2O_2 \rightarrow CO_2 + 2H_2O. \tag{1}$$
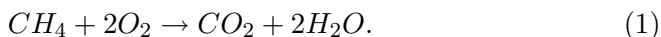
However, in reality, this could consist of about 149 reactions, as listed in Frenklach et al (1992).

It is relatively easy to observe homogeneous combustion with the aid of a blowlamp, or blowtorch (Kolaczkowski, 2002). This is a device that has a cartridge of fuel connected to a small burner and could be used to strip paint, to solder joints in plumbing, or, in a cooking application, to caramelise the surface of crème brulé. The fuel could consist of a mixture of propane/butane, and, in a simplified form, the overall stoichiometry for complete combustion may be represented by:

$$C_3H_8 + 5O_2 \rightarrow 3CO_2 + 4H_2O, \tag{2}$$

for propane, and

$$C_4H_{10} + 6.5O_2 \rightarrow 4CO_2 + 5H_2O, \tag{3}$$
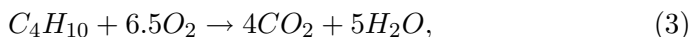
for butane. When the gas mixture is ignited, it burns with a visible flame that has a well defined shape, and temperatures in the region of 2300^oC may be reached in the hot zone of the flame.

Heterogeneous catalytic combustion reactions

To illustrate catalytic combustion reactions, a hot air gun could be used and adapted in the following manner (Kolaczkowski, 2002). A hot air gun is an electrically heated device that, with the aid of a fan, draws air and passes it over the electrically heated elements. It is similar to an electrically heated hair drier, but higher temperatures are achieved. In excess of $400^{o}C$ can be reached readily. This can also be used for stripping paint and soldering joints in plumbing. The hot air gun could be connected to a high temperature quartz tube that contains a sample of catalytic monolith. This is shown as a schematic in Figure 1. A fuel line from a propane/butane cartridge could be connected to the air inlet to the hot air gun. The fuel will then mix with air in the fan, be preheated by the electrical heating elements, and then fed into the catalytic monolith. A monolith that has a 35mm o.d. and is 20mm long would be suitable, using platinum on alumina as a catalyst. It could have about 62 cells/cm^2, and each channel could be square-shaped (1mm x 1mm).

A fuel mixture of propane and butane could be selected for the experiment, as (a) the fuel is readily available in a small cartridge, and (b) at the exit air temperature from the hot air gun (about $400^{o}C$) this fuel mixture is easily oxidised in the presence of a platinum catalyst.

If the temperature was raised to about $400^{o}C$, and then fuel gradually added, it could be shown that the temperature of the monolith starts to increase rapidly up to about $800^{o}C$ (at which point, the supply of fuel would need to be adjusted to maintain that temperature). Combustion would be flameless and the monolith would glow a bright orange/yellow colour. When the fuel was turned off, the temperature would gradually decrease, as heat transferred from the solid structure to the gas flowing through the monolith. The transient nature of the system would be very apparent. As fuel is then turned on, reactions would again be initiated on the surface of the catalyst, and as a result of the energy liberated in the catalyst layer, the temperature of the solid would rise, the rate of reaction would increase, and heat would be transferred by axial conduction, radiation, and convection to the gas. If the flow of gas was stopped, then the solid phase would cool down more slowly.

A mathematical representation of this catalytic monolith would result in the formulation of a boundary value problem. This arises from a number of physical sources, for example:

(a) at the ends of the monolith, heat transfer occurs by radiation from the end faces of the monolith to the surrounding area,

(b) in the axial direction, along the walls of the monolith structure, heat is transferred by radiation and axial conduction. This can occur in both directions, as described in the experiment in which the fuel is turned on and off.

Technically, energy exchange by radiation would also occur between the gas and the wall and the surrounding areas. However, as the volume of gas in the channels is very small, exchange by radiation with the gas is insignificant.

Mathematically, the transient nature of the problem can be represented by a series of coupled partial differential equations with highly non-linear terms (e.g. see Hayes et al (2003)). The non-linear nature of the problem arises from terms that are exponentially dependent on temperature, and these terms feature in the equations describing both the material and the energy balances at the surface of the catalyst.

For the purpose of the paper, we neglect heat losses from the sides of the monolith in contact with the glass tube.

Single channel model: form of the mathematical equations

If all the channels in the monolith can be assumed to behave in a similar manner, then it is only necessary to model one of the channels. A complete discussion of the problem is available in Hayes and Kolaczkowski (1997), and only a few of the key equations for a steady state condition will be presented in this paper to illustrate some of the physical and chemical processes taking place.

1D steady state plug flow model

Representing the gas flow in the channel as one dimensional and in plug flow, then for the system illustrated in Figure 2, where A represents a reactant (e.g. propane), the following equations may be written:

(a) Steady state gas phase mole balance equation

The mole balance on the volume element ΔV gives:

$$
\begin{aligned}
&[\text{Moles of A in}] - [\text{Moles of A out}] = \\
&[\text{Moles of A reacted in homogeneous reaction}] + \\
&[\text{Moles of A transported to catalyst surface}]. \quad (4)
\end{aligned}
$$

The final mole balance equation is:

$$-\frac{1}{A_C}\frac{dF_A}{dz} = (-R_A)_H + \frac{4}{D_H}k_{m,A}C_b(Y_{A,b} - Y_{A,S}). \tag{5}$$

(b) Steady state solid catalyst phase mole balance equation

[Moles of A transported to catalyst surface] =

[Moles of A reacted in the catalytic reaction]. (6)

$$k_{m,A}C_b(Y_{A,b} - Y_{A,S}) = \eta(-R_A)_S. \tag{7}$$

(c) Steady state gas phase energy balance equation

[Enthalpy increase as a result of temperature rise] =

[Heat generated in gas phase reaction] +

[Heat added to gas from surface]. (8)

$$v_m\rho C_p\frac{dT_b}{dz} = -\Delta H_R(-R_A)_H + \frac{4}{D_H}h(T_S - T_b). \tag{9}$$

(d) Steady state 1D solid phase energy balance equation

[Heat released by reaction] = [Heat transferred from solid] =

(10)

[Conduction out] − [Conduction in] +

[Loss by radiation] + [Loss by convection]. (11)

$$-\eta\Delta H_R(-R_A)_S = -\frac{d}{dz}\left(k_W\delta_W\frac{dT_S}{dz}\right) + q_{rad} + h(T_S - T_b). \tag{12}$$

(e) Momentum balance

If pressure drop is significant, then this should also be included, however, in many practical applications, the pressure drop across the monolith is small, and only an overall momentum balance across the whole of the reactor is considered to estimate the pressure drop.

(f) Boundary conditions at either ends of the monolith wall

These depend on what happens at the ends of the monolith.

(i) If it was insulated and did not lose heat to the surroundings, then:

$$\frac{dT_S}{dz} = 0, \quad \text{at } z = 0 \text{ and } z = L. \tag{13}$$

(ii) If the end was radiating to the space surrounding it at some temperature $T_{1,\alpha}$, and $T_{2,\alpha}$, then:

$$\left(k_W\frac{dT_S}{dz}\right)_{z=0} = \varepsilon\sigma(T_S^4 - T_{1,\infty}^4), \quad \text{at } z = 0, \tag{14}$$

and

$$\left(-k_W \frac{dT_S}{dz}\right)_{z=L} = \varepsilon\sigma(T_S^4 - T_{2,\infty}^4), \quad \text{at } z = L. \tag{15}$$

(g) Boundary conditions in the gas phase

$$Y_{A,b} = Y_{A,b_o}; \quad T_b = T_{bo} \quad \text{at } z = 0, \tag{16}$$

$$\frac{dY_{A,b}}{dz} = 0; \quad \frac{dT_b}{dz} = 0 \quad \text{at } z = L. \tag{17}$$

One big advantage of solving the set of equations for a real physical system (rather than an abstract mathematical equation) is that all the terms in the equation have a physical significance, and this, to an engineer, provides a clear indication of the range of values to be expected in the solution to the problem. For example, the rate of reaction for propane could be represented by an equation of the following form (Bennett et al, 1991):

$$(-R_{C_3H_8})_S = 2.4 \times 10^5 \exp\left(-\frac{1.08 \times 10^4}{T_S}\right) C_{C_3H_8} \quad \text{mol m}^{-2} \text{ s}^{-1}. \tag{18}$$

This rate expression features in the equations describing both the material balance and the energy balance at the surface of the catalyst.

For a fixed value of: $C_{C_3H_8} = 0.113 \quad \text{mol m}^{-3}$

if $T_S = 291\text{K}$, then $(-R_{C_3H_8}) = 2 \times 10^{-12} \quad \text{mol m}^{-2} \text{ s}^{-1}$,

if $T_S = 673\text{K}(400^oC)$, then $(-R_{C_3H_8}) = 3 \times 10^{-3} \quad \text{mol m}^{-2} \text{ s}^{-1}$,

if $T_S = 1073\text{K}(800^oC)$, then $(-R_{C_3H_8}) = 1.2 \quad \text{mol m}^{-2} \text{ s}^{-1}$.

These large variations in the rate of reaction, illustrate why difficulties may be encountered with the numerical routines.

As the heat of reaction for propane is $-2045 \text{ kJ mol}^{-1}$, then the mole fraction of propane would need to be 6.26×10^{-3}, in order to achieve a temperature rise of 400^oC. At a gas inlet temperature of 400^oC and atmospheric pressure, this would correspond to a molar concentration of 0.113 mol/m^3. So the concentration of propane, $C_{C_3H_8}$, can only vary from 0.113 mol m^{-3} at the inlet to 0 mol m^{-3} at the outlet. Whilst it may, from a mathematical point of view, be interesting to search for a solution in which $C_{C_3H_8}$ has a negative value, this would never occur in practice so is irrelevant. Likewise, there is a limit as to how small or big the value of T_S would be. It would never be negative, and in practice, very large values (e.g. above 1200^oC) would also cause problems as the material would become damaged and its properties, and even physical form, would change. For this particular catalyst system, this would occur at 900^oC .

In equations (5), (7) and (16), the component mole fraction, $Y_{A,b}$, could only have a value between these limits: $0 \leq Y_{A,b} \leq 1$.

In this way, we can look at each of the terms in the model and gather information about the magnitude and limits of the terms.

Having constructed a mathematical model of such a reactor, numerical methods are often used to solve what has become a complex system of coupled equations, with non-linear terms. Subsequently, additional techniques often need to be applied to prevent the solvers from 'crashing. This can arise from the way in which the solvers search for a possible solution, and the non-linear nature of the problem results in substitutions into the equations that are not physically significant and prevent convergence on the physical solution.

An example of these 'tricks or techniques is illustrated in Kolaczkowski and Worth (1995). The starting point was a differential-algebraic-integral system with first order initial value problems and second order boundary value problems. In the approach described, the problem is divided into three parts.

"Firstly, solid phase conduction and radiation are neglected, and the equations which now form a differential-algebraic system (DAE) are solved. Using the solution found, the radiation fluxes are then calculated utilising the approximations of the integral equations. In order to keep the radiation effect on temperature, the DAEs are solved again including radiation. A further solution of the radiation equations is carried out before axial conduction is included by solving the boundary value problem. The next solution of the DAE now shows the effect of radiation and axial conduction and if necessary the process is iterated to find a converged solution."

Coupled endothermic and exothermic reactions in a compact reactor

In addition to these problems encountered in the modelling of a catalytic combustion process, if this technique was used to provide energy in a manner in which there was direct interaction between the catalytic monolith and the heat sink, then additional complexities arise, creating instabilities with solution methods. One way of approaching this problem is to make use of asymptotic analysis as a method of simplifying the problem. This could help to screen quickly alternative design concepts, and could then be incorporated at the front end of a more rigorous numerical scheme, in order to help identify estimated values of unknown parameters, to initiate the numerical process.

The use of the method of asymptotic analysis has already been shown (e.g. Antipov et al (2001); Kolaczkowski et al (1999); Antipov et al (2001)) to provide an effective method of analysing problems on catalytic monoliths. In a new project between the Universities of Bath and Liverpool

in the UK, the method is being used to screen alternative design configurations and operating conditions for a new design of compact reactor, in which catalytically supported combustion reactions balance catalytically supported endothermic reactions. For further information on the concept, see Charlesworth et al (1995), or Zanfir (2002). The reacting system, in a simplified form, is illustrated in Figure 3.

The need to balance heat flow from one side of a channel to another suggests that unstable operating conditions are possible. The system of equations clearly leads to a boundary value problem, which is complicated by a matrix of channels in which the neighbouring channels on either side of a heat source act as a heat sink, with different exponential terms in neighbouring channels that are dependent on temperature.

On the catalytic combustion side, the rate expression could be of a similar form to equation (18). This is relatively easy to handle, however, to model the entire system even in a semi-rigorous manner will be very challenging, especially if more realistic forms of the rate expression are to be used for the reforming reactions. For example, according to Xu and Froment (1989), the reforming reactions may be represented by the following three overall reactions.

For reaction 1:

$$CH_4 + H_2O \rightleftharpoons CO + 3H_2 \quad \Delta H^o_{298} = 206 \text{ kJ mol}^{-1}, \tag{19}$$

$$(-r_{CH_4})_1 = \frac{k_1}{p_{H_2}^{2.5}} \left(p_{CH_4} \, p_{H_2O} - \frac{p_{H_2}^3 \, p_{CO}}{K_1} \right) \frac{1}{(\text{DEN})^2}. \tag{20}$$

For reaction 2:

$$CO + H_2O \rightleftharpoons CO_2 + H_2 \quad \Delta H^o_{298} = -41 \text{ kJ mol}^{-1}, \tag{21}$$
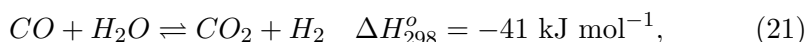
$$(-r_{CO})_2 = \frac{k_2}{p_{H_2}} \left(p_{CO} \, p_{H_2O} - \frac{p_{H_2} \, p_{CO_2}}{K_2} \right) \frac{1}{(\text{DEN})^2}. \tag{22}$$

For reaction 3:

$$CH_4 + 2H_2O \rightleftharpoons CO_2 + 4H_2 \quad \Delta H^o_{298} = 165 \text{ kJ mol}^{-1}, \tag{23}$$

$$(-r_{CH_4})_3 = \frac{k_3}{p_{H_2}^{3.5}} \left(p_{CH_4} \, p_{H_2O}^2 - \frac{p_{H_2}^4 \, p_{CO_2}}{K_3} \right) \frac{1}{(\text{DEN})^2}, \tag{24}$$

where

$$\text{DEN} = 1 + \text{K}_{CO}p_{CO} + \text{K}_{H_2}p_{H_2} + \text{K}_{CH_4}p_{CH_4} + \text{K}_{H_2O}p_{H_2O}/p_{H_2}. \tag{25}$$

What is important to note, is that these reactions are reversible, which means they are limited by equilibrium. Also, the heat of reactions are very

different, with reactions (1) and (3) consuming heat, and reaction (2) releasing heat. The rates of these reactions are very different, and as products are produced from a feed of CH_4 and H_2O, they interact with reactions (2) and (3). The situation is very complex, as the species start to disappear and appear along the reactor. The k_1, k_2, k_3 terms are reaction rate constants; the K_1, K_2, K_3 are equilibrium constants; and $K_{CO}, K_{H_2}, K_{CH_4}, K_{H_20}$ are adsorption constants. All of these terms are exponentially dependent on temperature. If we were to oversimplify the equations in our model of the system, to obtain a mathematically tractable expression, then it would not represent the physical situation, however, we can use such techniques in order to help us to screen non-viable or unstable operating conditions, and to help identify the starting point in order to utilise numerical techniques.

Concluding Remarks

With the aid of a description of a simple experiment, it was shown how the physical/chemical processes that take place in a catalytic combustion experiment, may be represented by a mathematical model of the reactor.

In the presentation of examples of more generic expressions to model a catalytic monolith, although transient terms were not included, these are important in a number of applications (e.g. catalytic converters). However, as the speed of the response of the gas in the monolith is generally several orders of magnitude higher than that of the solid, transient terms in the gas phase may be ignored. If the transient response is to be modelled, then transient terms need to be retained in the solid phase, adding to the complexity.

By understanding the physical significance of the terms in the equations, it is possible to combine this knowledge with the use of mathematical techniques to simplify the problem, screen non-viable or unstable operating conditions, and identify a starting point for the numerical routines.

Acknowledgments

Nomenclature

A_C Cross-sectional area of a channel, m^2
$C_{C_3H_8}$ Mean bulk concentration of propane, mol m^{-3}

566

C_b Mean bulk concentration, mol m^{-3}

C_p Constant pressure heat capacity, J kg^{-1} K^{-1}

D_H Hydraulic diameter, m

DEN Is a denominator and the term is defined by equation (25)

F_A Molar flow of component A, mol s^{-1}

h Heat transfer coefficient, W m^{-2} K^{-1}

ΔH_R Heat of reaction, J mol^{-1}

ΔH_{298}^o Standard enthalpy change due to reaction, kJ mol^{-1}

k_1, k_3 Rate coefficients, kmol bar$^{1/2}$ kg$_{cat}^{-1}$ h^{-1}

k_2 Rate coefficient, kmol, kg$_{cat}^{-1}$ h^{-1} bar^{-1}

k_W Thermal conductivity of the wall, W m^{-1} K^{-1}

$k_{m,A}$ Mass transfer coefficient of species A, m s^{-1}

K_1, K_3 Equilibrium constants, bar^2

K_2 Equilibrium constant,

$K_{CO}, K_{H_2}, K_{CH_4}$ Adsorption constants, bar^{-1}

K_{H_2O} Adsorption constant

p_j Partial pressure of component j, bar

q_{rad} Radiant heat flux, W m^{-2}

$(-r_{CH_4})_1$ Rate of disappearance of CH_4 in reaction 1, kmol kg$_{cat}^{-1}$ h^{-1}

$(-r_{CO})_2$ Rate of disappearance of CO in reaction 2, kmol kg$_{cat}^{-1}$ h^{-1}

$(-r_{CH_4})_3$ Rate of disappearance of CH_4 in reaction 3, kmol kg$_{cat}^{-1}$ h^{-1}

$(R_A)_H$ Rate of disappearance of species A by homogeneous reaction, mol m^{-3} s^{-1}

$(R_A)_H$ Rate of disappearance of species A at conditions (of temperature, pressure and concentration) at the surface of the catalyst, mol m^{-2} s^{-1}

$T_{1\alpha}, T_{2,\alpha}$ Temperature of body surrounding the monolith, K

T_b Bulk gas mean temperature, K

T_S Surface solid temperature, K

v_m Mean mass average gas velocity, m s^{-1}

$Y_{A,b}, Y_{A,S}$ Mole fraction of component A in the bulk and at the surface

z Axial co-ordinate, m

Greek Symbols

δ_w Reactor wall thickness, m

ε Emissivity of a surface

η Effectiveness factor

ρ Mass density, kg m^{-3}

σ Stephan - Boltzman constant, 5.67×10^{-8} W m^{-2} K^4

References

[1] Antipov, Y.A., Avila-Pozos, O., Kolaczkowski, S.T., Movchan, A.B. (2001) Mathematical model of delamination cracks on imperfect interfaces, International Journal of Solids and Structures, 38, 6665-6697.

[2] Antipov, Y.A., Movchan, A.B., Kolaczkowski, S.T. (2001) Models of fracture of cellular monolith structures, International Journal of Solids and Structures, 38, 1659-1668.

[3] Bennett, C.J., Kolaczkowski, S.T. and Thomas, W.J. (1991) Determination of heterogeneous reaction kinetics and reaction rates under mass transfer controlled conditions for a monolith reactor, Trans. I. Chem. E., 69B, 209-220.

[4] Charlesworth, R., Gough, A. and Ramshaw, C. (1995) Combustion and steam reforming of methane on thin layer catalysts for use in catalytic plate reactors, 4th UK National Conference on Heat Transfer, 26-27 Sept., C510/099/95, I. Mech. E., 85-89.

[5] Frenklach, M., Wang, H. and Rabinowitz, M.J. (1992) Optimization and analysis of large chemical kinetic mechanisms using the solution mapping method-combustion of methane, Prog Energy Combust Sci, 18, 47-73.

[6] Glassman, I. (1987) Combustion, second edition, Academic Press Inc.

[7] Griffiths, J.F. and Barnard, J.A. (1995) Flame and Combustion, 3rd edition, Blakie Academic & Professional, Chapman & Hall.

[8] Hayes, R.E., Kolaczkowski, S.T. (1997) Introduction to Catalytic Combustion, Gordon and Breach, New York.

[9] Hayes, R.E., Bertrand, F.H., Audet, C. and Kolaczkowski, S.T. (2003) Catalytic Combustion Kinetics: using a direct search algorithm to evaluate kinetic parameters from light-off curves, Canadian Journal of Chemical Engineering, in press.

[10] Kolaczkowski, S. T. (2002) Demonstration of homogeneous combustion experiment (with blowlamp), and catalytic combustion experiment (with aid of hot air blower and catalytic monolith) at the IUTAM Symposium, 8 - 11 July 2002, University of Liverpool, UK).

[11] Kolaczkowski, S.T., Lin, P., Movchan, A.B., Serkov, S.K., Spence, A. (1999) Thermal stress analysis and homogenization for catalytic combustor monoliths, Eur. J. Appl. Math., 10, 185-220.

[12] Kolaczkowski, S.T., Worth, D.J. (1995) Modelling channel interactions in a non-adiabatic multichannel catalytic combustion reactor, Catalysis Today, 26, 275-282.

[13] Spalding, D.B. (1979) Combustion and Mass Transfer: A Textbook with Multiple-choice Exercises for Engineering Students, Pergamon Press Ltd.

[14] Xu, J., Froment, G.F. (1989) Methane steam reforming, methanation and water-gas shift: 1. intrinsic kinetics, AIChE Journal, Vol 35 No 1, pp 88-103.

[15] Zanfir, M. (2002) Catalytic plate reactors for endothermic-exothermic reaction coupling, PhD Thesis, University College London.

Figure captions:

Figure 1. Schematic of the catalytic combustion experiment demonstrated in the lecture.

Figure 2. (a) Volume element used for the gas phase. (b) Volume element used to develop the energy balance for the wall (adapted from Hayes and Kolaczkowski, 1997).

Figure 3. The compact reactor, in which catalytic combustion reactions exchange heat across the wall to support the steam reforming reactions.
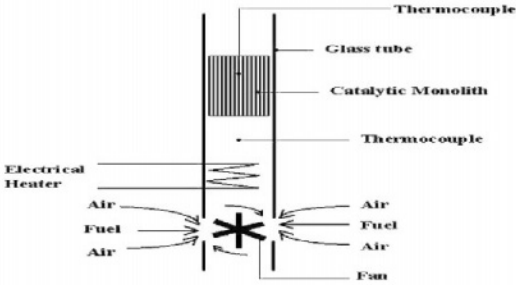
Figure 1
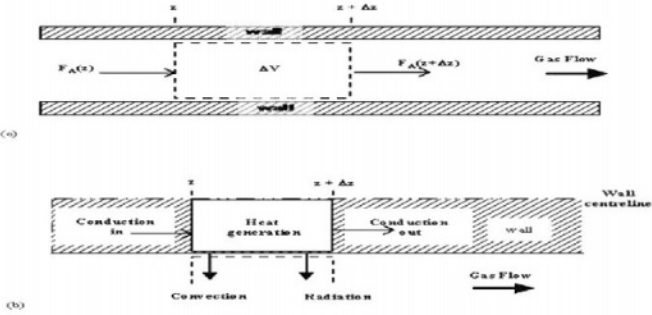
Figure 2
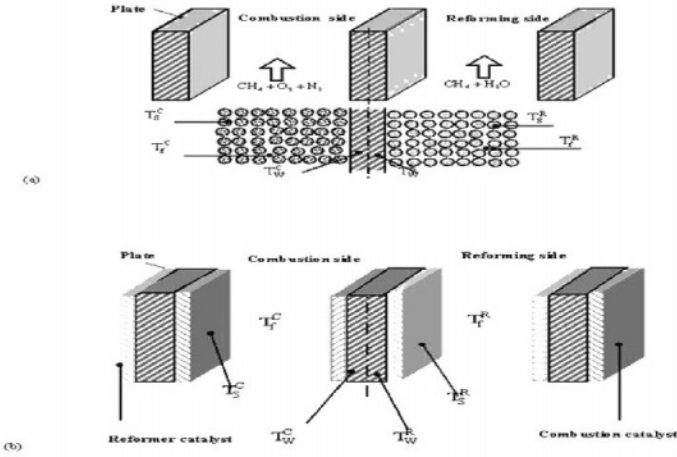
Figure 3

Chapter 12
Asymptotic approximations for orbital perturbations

THE USE OF LIE SERIES GENERATING FUNCTIONS TO DERIVE ASYMPTOTIC SERIES EXPRESSIONS FOR ORBITAL PERTURBATIONS

P.J. Message
Applied Mathematics Division,
Department of Mathematical Sciences,
University of Liverpool,
L69 3BX, U.K.
sx20@liverpool.ac.uk

Abstract   This paper describes a new method, using Lie series transformations, for the development of asymptotic series expressions for the perturbations of the orbits in a planetary or satellite system. The aim is to overcome difficulties of slow convergence encountered in near-commensurability cases, in the use of traditional methods. The paper begins with a brief description of the Lie series type of transformation, then briefly describes the parameter sets used to describe the orbits in a planetary or satellite system, and how they may be put into a Hamiltonian formulation, then it addresses difficulties particular to cases of near small-integer commensurability of the orbital periods, with especial reference to the case of Saturn's satellite Hyperion, and ends with an indication of the current work on the use of the generating function for the Lie series transformation to derive expressions for the short-period perturbations.

1.   INTRODUCTION.

In a meeting having asymptotic methods as a topic, it seems appropriate to describe work in progress on a new method for the derivation of asymptotic expansions expressing those perturbations of orbits in a planetary or satellite system, which arise from the mutual gravitational attractions within the system. A brief indication of the background of the topic also seems appropriate.

Well-founded theoretical predictions of positions of satellites in the systems of the outer planets are essential for the planning of space missions, as well as for the proper analysis of observational data, and improvement

of the estimates of the physical parameters of the system. The ongoing work reported on here particularly involves the development of analytical expressions for the motion of Saturn's satellite Hyperion, the closeness of whose orbital period to four-thirds of that of the most massive satellite, Titan, leads to particular difficulties in the use of the usual perturbation methods.

In a planetary or satellite system, in which most of the mass is concentrated in one body (the Sun, in the Solar System, or the primary planet, in a satellite system), the motion of each body usually deviates only slowly from what it would be in the absence of the other members of the system. So, in order to make use of this to study the evolution of the system, we use the concept of the *instantaneous Kepler orbit* (usually an ellipse) of each planet (or satellite). At each instant, it is that orbit, corresponding to the position and velocity of the body at that instant, according to Kepler's laws of motion, that is, to two-body motion, as if the other bodies (other than the primary) were absent. At a different instant, this will define a different Kepler orbit, because of the perturbing attractions of the other bodies of the system, but the changes will usually be slow, and the parameters defining the instantaneous orbit will usually change only slowly. (Exceptions arise for the outer satellites of Jupiter, because of the very considerable perturbing effect of the Sun.)

Expressions for these changes *perturbations* in the parameters of the instantaneous orbit are usually derived by iterative solution of the differential equations governing the changes in the orbital parameters, in ways similar to those used in perturbation theory in other fields. These expressions are almost always only obtainable as asymptotic series in powers of the *perturbation parameters* (usually the ratios of the masses of the perturbing other members of the system, to the mass of the primary.) This is because of terms with denominators which are linear combinations of the orbital mean motions, and these denominators become zero in an everywhere dense set of points in parameter space, and so the series cannot be uniformly convergent. Also special difficulties are faced in cases of close small-integer near-commensurability of orbital period (where the orbital periods of two planets - or satellites - are close in ratio to the ratio of two small integers). Indeed, in cases of very close commensurability of orbital period, the actual motions are often fundamentally different from those which occur in the absence of such commensurabilities.

To study the longer time scale evolution of the system, we often seek to isolate the underlying evolution of the system by defining a dynamical system, the *long-period problem*, which is free of the *short-period perturbations*), which are those whose frequencies are linear combinations of the angular motions (*mean motions*) corresponding to the orbital periods of

the planets. Of the methods available for this, let us consider the use, for this separation, of the *Lie series* type of contact transformation, as introduced by Hori ([2]) for which the generating function readily gives explicit expressions for the original co-ordinates and momenta in terms of the transformed ones, and vice versa. While such transformations have been used to carry out this separation of the long-period problem from the short-period effects, we should note that the generating function also carries enough information to construct analytical expressions for the short-period perturbations themselves. The recent and ongoing researches described in this paper concern the use of the Lie series generating function to derive multiple Fourier series expressions for the short-period perturbations of the parameters of the orbit of Saturn's satellite Hyperion, whose motion shows the effects of its very close near-commensurability of orbital period with Titan, the most massive satellite of the system, to the extent that there has previously been no successful analytical derivation of expressions for the short-period peturbations.

This paper begins with a brief description of the Lie series type of transformation, then of the parameters used to describe the orbits in a planetary or satellite system (with a Hamiltonian formulation) and, very briefly, special features associated with small-integer commensurability of the orbital periods, and an indication of the current work on the orbit of Hyperion.

2.   LIE SERIES TRANSFORMATIONS.

In a Hamiltonian dynamical system, the state of motion at any instant is given by the *co-ordinates* $q = (q_1, q_2, ..., q_n)$, and their *conjugate momenta* $p = (p_1, p_2, ..., p_n)$, and the equations of motion may be put into Hamilton's form

$$\frac{\mathrm{d}q_i}{\mathrm{d}t} = \frac{\partial \mathcal{H}}{\partial p_i}, \quad \text{and} \quad \frac{\mathrm{d}p_i}{\mathrm{d}t} = -\frac{\partial \mathcal{H}}{\partial q_i}, \quad \text{for} \quad i = 1, 2, ..., n. \qquad (2.1)$$

where $\mathcal{H}$ is the *Hamiltonian function*, and n is the number of *degrees of freedom* of the system.   It follows that, for any function $f(q, p)$,

$$\frac{\mathrm{d}f}{\mathrm{d}t} = \{f, \mathcal{H}\} \qquad (2.2)$$

where the *Poisson bracket* of any two functions f and g is given by

$$\{f, g\} = \sum_{i=1}^{n} \left\{ \frac{\partial f}{\partial q_i} \frac{\partial g}{\partial p_i} - \frac{\partial g}{\partial q_i} \frac{\partial f}{\partial p_i} \right\}. \qquad (2.3)$$

If $\mathcal{W}(q, p)$ is any function with the necessary derivatives, and ϵ is any real number, then consider the transformation from q and p to

$Q = (Q_1, Q_2, Q_3, \ldots, Q_n)$ and $P = (P_1, P_2, P_3, \ldots, P_n)$, given by

$$Q_i = q_i + \epsilon \frac{\partial \mathcal{W}}{\partial p_i} + \frac{1}{2} \epsilon^2 \left\{ \frac{\partial \mathcal{W}}{\partial p_i}, \mathcal{W} \right\}$$
$$+ \frac{1}{3!} \epsilon^3 \left\{ \left\{ \frac{\partial \mathcal{W}}{\partial p_i}, \mathcal{W}, \right\}, \mathcal{W} \right\} + \ldots \text{etc.},$$

and

$$P_i = p_i - \epsilon \frac{\partial \mathcal{W}}{\partial q_i} + \frac{1}{2} \epsilon^2 \left\{ \frac{\partial \mathcal{W}}{\partial q_i}, \mathcal{W} \right\}$$
$$- \frac{1}{3!} \epsilon^3 \left\{ \left\{ \frac{\partial \mathcal{W}}{\partial q_i}, \mathcal{W}, \right\}, \mathcal{W} \right\} + \ldots \text{etc.}$$
$$\text{(for} \quad i = 1, 2, 3, \ldots, n). \tag{2.4}$$

It may be regarded as representing the evolution over a time interval of length ϵ of a hypothetical dynamical system whose Hamiltonian function is $\mathcal{W}$, and so is a contact transformation. Therefore (Q, P), like (q, p), are governed by equations of motion of Hamilton's type, $\frac{\mathrm{d}Q_i}{\mathrm{d}t} = \frac{\partial \mathcal{H}'}{\partial P_i}$ and $\frac{\mathrm{d}P_i}{\mathrm{d}t} = -\frac{\partial \mathcal{H}'}{\partial Q_i}$, for an appropriate Hamiltonian function $\mathcal{H}'$. The transformation (2.4) is a *Lie series transformation*, and $\mathcal{W}$ is its *generating function*, which we choose according to what we want the transformation to accomplish.

More compactly, if we define $\mathcal{L}$ to be the operator taking any function $f(q, p)$ to its Poisson bracket with $\mathcal{W}$, that is $\mathcal{L}(f) = \{f, \mathcal{W}\}$, and we write repeated applications of it as $\mathcal{L}^k(f) = \mathcal{L}(\mathcal{L}^{k-1}(f))$ (understanding $\mathcal{L}^1(f)$ as $\mathcal{L}(f)$), then the equations (2.4) which define the transformation may be written

$$Q_i = q_i + \sum_{k=1}^{\infty} \frac{1}{k!} \epsilon^k \mathcal{L}^k(q_i), \quad \text{and} \quad P_i = p_i + \sum_{k=1}^{\infty} \frac{1}{k!} \epsilon^k \mathcal{L}^k(p_i),$$
$$\text{for} \quad i = 1, 2, \ldots, n, \tag{2.5}$$

Note that, considering the equation corresponding to (2.2) in this hypothetical motion, and using Taylor's theorem, for any function f,

$$f(Q, P) = f(q, p) + \sum_{k=1}^{\infty} \frac{1}{k!} \epsilon^k \mathcal{L}^k \big(f(q, p)\big) \tag{2.6}$$

The inverse of the transformation is given by reversing the sign of ϵ, and so

$$f(q, p) = f(Q, P) + \sum_{k=1}^{\infty} \frac{1}{k!} (-\epsilon)^k \mathcal{L}^k \big(f(Q, P)\big) \tag{2.7}$$

3.   THE PARAMETERS OF THE INSTANTANEOUS ORBIT.

In a system of one planet (or satellite), with only gravitational forces in action, the motion about the Sun (or primary planet) is in a fixed ellipse, followed according to Kepler's laws of planetary motion, so that the primary is at a focus, and the radius vector covers area at a constant rate. The parameters usually used to specify this orbit are:

- to specify the size and shape, the *major semi-axis* (a) and the *eccentricity* (e),

- to specify the orientation of the plane of the orbit, the *orbital inclination* (i), and the *longitude of the ascending node* (denoted here by Ω), which is the angle, measured in the reference plane, from the agreed initial line, which defines the *ascending node*: that direction on the intersection of the orbit plane with the reference plane, corresponding to the passage of the body from South to North,

- and to specify the orientation of the orbit in its plane, the *argument of the near apse* (ω), which is the angle between the ascending node to the *near apse*, which is the nearest point on the ellipse to the primary.

In addition, we need to specify where the body is in its orbit at the instant in question. To do this, let us make use of the *mean anomaly* (denoted by ℓ), which, in unperturbed Keplerian motion, is an angle increasing linearly with time, taking the successive values $0, 2\pi, 4\pi, \ldots$, etc., at successive returns to the near apse. In perturbed motion, it remains the same function of the position and velocity, but of course will no longer be usually exactly linear in time.

To avoid indeterminacy when the inclination (i) is near to zero, we use the *longitude of the near apse* (denoted by ϖ), which is $\Omega + \omega$, and to avoid indeterminacy when the eccentricity (e) is near zero, we use the *mean longitude* (denoted by λ), which is $\varpi + \ell$.

4.   FORMULATION OF PERTURBED ORBITAL MOTION IN HAMILTONIAN FORM.

Suppose there are N bodies in the system, apart from the primary. The motion relative to the primary gives a dynamical system of $3N$ degrees of freedom. Take the three co-ordinates corresponding to the i'th body to be the mean longitude (λ_i), the longitude of the near apse (ϖ_i), and the longitude of the ascending node (Ω_i) of its orbit relative to the primary. The momenta conjugate to these are found to be

$\Lambda_i = \beta_i\sqrt{\mu_i a_i}$, $\Pi_i = \Lambda_i\{\sqrt{1-e_i^2}-1\}$, and $N_i = \Lambda_i\sqrt{1-e_i^2}(\cos i_i - 1)$, respectively, where a_i, e_i, and i_i refer to the orbit of the i'th planet (or satellite), β_i is a function of the masses of the bodies, and μ_i is the product of the constant of gravitation with the sum of the masses of the primary and the i'th body.

In the unperturbed problem, in which the mutual attractions of the bodies other than the primary are not taken into account, the Hamiltonian is of course such as to give zero rate of change to all of the dynamical variables except the mean longitude (λ_i) of each body, which then has the constant rate of change, the *mean motion in longitude*, $n_i = \sqrt{\mu_i a_i^{-3}}$ given by Kepler's third law of planetary motion. This is provided for by taking $\mathcal{H}_0 = \sum_{i=1}^{N}\beta_i^2\mu_i^3\Lambda_i^{-2}$

In the perturbed problem however, the Hamiltonian of course contains the terms which express the perturbations of the instantaneous orbits due to the mutual gravitational attractions of the bodies in the system. We find that

$$\mathcal{H} = \mathcal{H}_0 - \epsilon\mathcal{R}, \tag{4.1}$$

where ϵ is a function of the masses of the bodies which is zero when all of the masses, other than that of the primary, are zero. Thus ϵ is an appropriate choice for perturbation parameter. Also the *disturbing function*, $\mathcal{R}$, may be expressed as a multiple Fourier series in the angular co-ordinates:

$$\mathcal{R} = \sum_j \mathcal{K}_j\cos\mathcal{N}_j, \tag{4.2}$$

where $\mathcal{N}_j$ is the linear combination of the co-ordinates given by $\mathcal{N}_j = \sum_{i=1}^{N}(j_i\lambda_i + j_{N+i}\varpi_i + j_{2N+i}\Omega_i)$, and $\mathcal{K}_j$ is a function of the momenta, and the summation is over all sets $j = (j_1, j_2, j_3, \ldots, j_{3N})$ of integers j_r with j_1 non-negative and with $\sum_{r=1}^{3N} j_r = 0$.

5. IDENTIFICATION OF THE SHORT-PERIOD TERMS.

The fastest changing co-ordinates are the mean longitudes λ_i, and so those arguments, $\mathcal{N}_j$, of terms of (4.2) which are fastest changing are those which contain one or more of the λ_i, that is, those in which not all of the coefficients $j_1, j_2, \ldots, j_N$ are zero. These are the *short-period* terms. The others, in which $j_1 = j_2 = \cdots = j_N = 0$, are the *long-period* terms. So the short-period part of the disturbing function is $\mathcal{R}_{\mathcal{SP}} = \sum_{j,\mathcal{SP}} \mathcal{K}_j\cos\mathcal{N}_j$, the "$\mathcal{SP}$" here indicating that the summation is over the short-period terms

only.　　　Let us denote the long-period part of the disturbing function by $\mathcal{R}_{\mathcal{LP}}$, so that

$$\mathcal{R} = \mathcal{R}_{\mathcal{LP}} + \mathcal{R}_{\mathcal{SP}}. \tag{5.1}$$

6.　　CHOOSING A TRANSFORMATION TO REMOVE THE SHORT-PERIOD TERMS.

We will use the Lie series transformation to reach a Hamiltonian function in which no short-period terms appear, so that the underlying long-period evolution of the system may be studied in isolation. That is, we seek to arrange that the Hamiltonian function $\mathcal{H}'(Q, P)$ has no short-period terms. We now use the fact that, since the contact transformation (2.4) is not explicitly dependent on the time, then it leaves the value of the Hamiltonian function unchanged, that is,

$$\mathcal{H}'(Q, P) = \mathcal{H}(q, p). \tag{6.1}$$

But now, from (2.7),

$$\mathcal{H}(q, p) = \mathcal{H}(Q, P) + \sum_{k=1}^{\infty} \frac{1}{k!} (-\epsilon)^k \mathcal{L}^k \big(\mathcal{H}(Q, P) \big) \tag{6.2}$$

Then substituting from (6.2) into (6.1) gives, implicitly, the partial differential equation for the generating function $\mathcal{W}$ needed to accomplish the separation of terms which we seek. We will proceed by equating terms of the same order in ϵ, but before we do that we must be prepared for the fact that it will prove necessary to expand $\mathcal{W}$ in powers of ϵ, that is,

$$\mathcal{W}(Q, P) = \mathcal{W}_0(Q, P) + \sum_{k=1}^{\infty} \epsilon^k \mathcal{W}_k(Q, P) \tag{6.3}$$

so that each Poisson bracket involving $\mathcal{W}$ will give rise to a series in powers of ϵ. We will also find that the Hamiltonian function for the transformed system will in general also need terms in all powers of ϵ, so that

$$\mathcal{H}'(Q, P) = \mathcal{H}'_0(Q, P) + \sum_{k=1}^{\infty} \epsilon^k \mathcal{H}'_k(Q, P) \tag{6.4}$$

Then substituting (6.3) and (6.4) into (6.2), and then substituting this and (6.4) into (6.1) gives, more explicitly, the equation from which $\mathcal{W}$ and $\mathcal{H}'$ will be derived. We proceed by equating, separately, the terms of each power in ϵ to give the equations from which to derive the separate parts $\mathcal{H}'_k$ and $\mathcal{W}_k$ of $\mathcal{H}'$ and $\mathcal{W}$ respectively. The terms independent of

ϵ give $\mathcal{H}'_0(Q, P) = \mathcal{H}_0(Q, P)$ so that, of course, the transformed unperturbed problem is the same as the untransformed one. We will now equate terms linear in ϵ, noting (4.1), so that $\mathcal{L}(\mathcal{H})$ is $\{\mathcal{H}_0, \mathcal{W}_0\} - \epsilon\{\mathcal{R}, \mathcal{W}_0\}$, and also noting (5.1), so that there results $\mathcal{H}'_1(Q, P) = -\mathcal{R}_{\mathcal{LP}} - \mathcal{R}_{\mathcal{SP}} + \{\mathcal{H}_0(Q, P), \mathcal{W}_0(Q, P)\}$. Our aim of keeping the transformed problem free of short-period terms is served if make the choice $\mathcal{H}'_1(Q, P) = -\mathcal{R}_{\mathcal{LP}}$ leaving the partial differential equation for $\mathcal{W}_0$ as, $\{\mathcal{H}_0(Q, P), \mathcal{W}_0(Q, P)\} = \mathcal{R}_{\mathcal{SP}}$, in which the left-hand side is the rate of change which $\mathcal{W}_0$ would experience in the unperturbed problem, with Q and P, and quantities dependent on them, being given the time dependence they would have in that problem, so that this equation becomes $\sum_{i=1}^{N} n_i \frac{\partial \mathcal{W}_0}{\partial \lambda_i} = \sum_{j,\mathcal{SP}} \mathcal{K}_j \cos \mathcal{N}_j$, which is satisfied by

$$\mathcal{W}_0 = \sum_{j,\mathcal{SP}} \frac{\mathcal{K}_j}{\rho_j} \sin \mathcal{N}_j, \tag{6.5}$$

where $\rho_j = \sum_{i=1}^{N} j_i n_i$.

Equating now the terms in the square of ϵ, we find the equation

$$\mathcal{H}'_2(Q, P) = \{-\mathcal{R}_{\mathcal{LP}} - \mathcal{R}_{\mathcal{SP}}, \mathcal{W}_0\} + \{\mathcal{H}_0, \mathcal{W}_1\}$$
$$+ \frac{1}{2}\Big\{\{\mathcal{H}_0(Q, P), \mathcal{W}_0\}, \mathcal{W}_0\Big\}. \tag{6.6}$$

Put $\{-\mathcal{R}_{\mathcal{LP}} - \mathcal{R}_{\mathcal{SP}}, \mathcal{W}_0\} + \frac{1}{2}\Big\{\{\mathcal{H}_0(Q, P), \mathcal{W}_0\}, \mathcal{W}_0\Big\} = -\mathcal{R}_{2,\mathcal{LP}} - \mathcal{R}_{2,\mathcal{SP}}$, say, in which $\mathcal{R}_{2,\mathcal{SP}}$ contains the short-period terms, which will be identifiable when $\mathcal{W}_0$ has been solved for, and $\mathcal{R}_{2,\mathcal{LP}}$ contains the remainder, which are the long-period terms. Then, since we want the transformed Hamiltonian function to contain the long-period terms, we choose $\mathcal{H}'_2(Q, P) = -\mathcal{R}_{2,\mathcal{LP}}(Q, P)$, leaving, as the partial differential equation for $\mathcal{W}_1$, $\{\mathcal{H}_0(Q, P), \mathcal{W}_1(Q, P)\} = \mathcal{R}_{2,\mathcal{SP}}$, so that, if we write $\mathcal{K}_{2,j}$ for the coefficient of $\cos \mathcal{N}_j$ in $\mathcal{R}_{2,\mathcal{SP}}$, this equation becomes $\sum_{i=1}^{N} n_i \frac{\partial \mathcal{W}_1}{\partial \lambda_i} = \sum_{j,\mathcal{SP}} \mathcal{K}_{2,j} \cos \mathcal{N}_j$, which is satisfied by

$$\mathcal{W}_1 = \sum_{j,\mathcal{SP}} \frac{\mathcal{K}_{2,j}}{\rho_j} \sin \mathcal{N}_j. \tag{6.7}$$

In a similar manner, we may derive in turn $\mathcal{H}'_3(Q, P)$ and $\mathcal{W}_2(Q, P)$, then $\mathcal{H}'_4(Q, P)$ and $\mathcal{W}_3(Q, P)$, and higher terms in turn.

7. MOTION CLOSE TO SMALL-INTEGER ORBITAL COMMENSURABILITY.

Practical usefulness of the series expansions (6.5) and (6.7) of course requires them to consist of terms which diminish sufficiently rapidly. Now,

indeed, as a consequence of the *d'Alembert property* of Fourier expansions for co-ordinates in Keplerian elliptic motion, the coefficients $\mathcal{K}_j$ do become generally successively smaller for successively larger values of the multiples j_r. There is an extensive literature discussing the questions of convergence of series of the types (6.5) and (6.7) which arise in the various methods of solving the equations for the perturbations of orbital parameters. (See, e.g., [1], and [11].) However, in cases in which the ratio of two orbital periods, and therefore of the corresponding mean motions n_i, are close to a commensurability with small integer multiples, the corresponding linear multiples ρ_j will take small values, for terms for which the coefficients $\mathcal{K}_j$ are not small. In such cases of close enough commensurability, expressions for the short-period terms of the type (6.5) and (6.7) will not even give any approximation to the actual motion, and solutions of a quite different type apply (see, e.g., [3] and [4]). Then we call such terms *critical terms*, and they must not be included with the short-period terms, and so they remain as part of the long-period problem, whose solution may then take a quite different form.

8. THE MOTION OF SATURN'S SATELLITE HYPERION.

Saturn's satellite Hyperion, whose motion has been the subject of theoretical research here in Liverpool over many years, was discovered by Bond at Harvard in 1848, and independently by Lassell at Liverpool at about the same time. Soon after it was discovered, it was noticed that its orbital motion showed some exceptional features. The eccentricity of its orbit is unusually large (about 0.1), and its apse is moving in a retrograde sense, in place of the usual forward motion. It was shown by Newcomb ([9]) that these are a consequence of the very close commensurability of its orbital period with that of Titan, by far the most massive of Saturn's satellites, and whose orbital period is very close to three quarters of that of Hyperion. So we must consider as critical terms in the disturbing function, $\mathcal{R}$, those for which the angular argument $\mathcal{N}_j$ contains the mean longitudes of Hyperion and Titan (λ_H and λ_T respectively) in the combination $4\lambda_H - 3\lambda_T$. The fact that this near commensurability is so very close leads to the breakdown of usual methods of perturbation theory, and the relevant solution of the long-period problem proves to be of a very special type. (See [8].) Very briefly, the critical argument $\theta = 4\lambda_H - 3\lambda_T - \varpi_H$ (where ϖ_H is the longitude of the apse of Hyperion), instead of changing monotonically, as is usual for arguments of the disturbing function, librates about a mean value of 180 degrees, the main term having a free amplitude about 36 degrees, with a period of about 21 months. The next largest term has an

amplitude of about 13.7 degrees, and has as argument the time linear part (denoted by ζ) of the difference $\varpi_T - \varpi_H$ of the apse longitudes of the two satellites, with a period of about 18 3/4 years. Earlier papers ([5], [6], and [7]) give more details, and describe how methods have been developed to derive expressions for the long-period parts of the perturbations of the orbital parameters, as multiple Fourier series with the arguments τ (the argument of the free 21-month libration) and ζ, and how expressions have been obtained for the necessary partial derivatives, to enable differential correction to be carried out, using observational data, to lead to improved estimates of the relevant orbital and physical parameters.

9. ASYMPTOTIC EXPRESSIONS FOR THE SHORT-PERIOD TERMS FROM THE LIE SERIES GENERATING FUNCTION.

It is found that the methods usually employed to derive analytical expressions for the short-period perturbations of the parameters of the orbit encounter particular difficulties in the case of Hyperion, in the extremely slow convergence of the relevant series, and previously such expressions have only been able to be obtained using numerical integration of the appropriate equations of motion. Now $\mathcal{W}$, the generating function for the Lie series transformation, contains implicitly the necessary information, and provides a means to overcome the difficulty, and to derive explicit analytical expressions for the short-period perturbations of the orbital parameters.

As an example of the use of this, currently being developed, consider the main short-period terms in the longitude of the apse (ϖ). These are given by $\frac{\partial \mathcal{W}}{\partial \Pi}$, which may be expressed as

$$-\frac{\sqrt{1-e^2}}{na^2 e}\frac{\partial \mathcal{W}}{\partial e}. \tag{9.1}$$

The method being used to derive expressions for $\mathcal{W}$, and its derivatives with respect to the orbital parameters, is described in the earlier papers which are referred to in the previous section. Preliminary values, derived from the expression (9.1), for the coefficients of the largest short-period terms in the apse longitude of Hyperion give, in degrees,

$$1.085\sin\varphi + 0.456\sin2\varphi + 0.320\sin3\varphi + 0.296\sin4\varphi + 0.056\sin5\varphi \tag{9.2}$$

(where φ is $\lambda_H - \lambda_T$, the difference between the mean longitudes of the two satellites). These values are in fair agreement with the result of Fourier analysis of results from numerical integration, as given by Taylor ([10]), who gives

$$1.039\sin\varphi + 0.421\sin2\varphi + 0.312\sin3\varphi + 0.280\sin4\varphi \tag{9.3}$$

Work is in hand to extend this to further terms, and to provide corresponding expressions for the short-period perturbations in the other parameters of the orbit.

References

[1] Arnol'd, V.I., 1963, "Small denominators and problems of stability of motion in Classical and Celestial Mechanics", *Usp. Mat. Nauk* **18**, pp.91-192, (and *Russian Mathematical Surveys*, **18**, pp. 85-193).

[2] Hori, G., 1966, "Theory of General Perturbation with Unspecified Canonical Variable", in Publications of the Astronomical Society of Japan, **18**, pp.287-296.

[3] Message, P.J., 1966, "On nearly-commensurable periods in the restricted problem of three bodies, with calculations of the long-period variations in the interior 2:1 case", in *Proceedings of International Astronomical Union Symposium No. 25*, pp. 197-222.

[4] Message, P.J., 1987, "Planetary Perturbation Theory from Lie Series, including Resonance and Critical arguments" in *"Long-term Dynamical Behaviour of natural and Artificial N-Body Systems"* ed. A.E. Roy, Kluwer, 47-72.

[5] Message, P.J., 1989, "The use of computer algorithms in the construction of a theory of the long-period perturbations of Saturn's satellite Hyperion", in *Celestial Mechanics*, **45**, pp. 45-53.

[6] Message, P.J., 1993, "On the Second-order long-period motion of Hyperion" in *Celestial Mechanics*, **56**, pp. 277-284.

[7] Message, P.J., 1999a, "The use of Lie series in the construction of a perturbation theory and some recent results in the theory of the motion of Hyperion", in *Celestial Mechanics*, **73**, pp. 349-358.

[8] Message, P.J., 1999b, "Orbits of Saturn's satellites: Some Aspects of Commensurabilities and Periodic Orbits" in *"The Dynamics of Small Bodies in the Solar System"* ed. B.A.Steves and A.E. Roy, Kluwer, 207-225.

[9] Newcomb, S., 1891, "The Motion of Hyperion, a new case in Celestial Mechanics" *Astronomical Papers of the American Ephemeris*, **III**.

[10] Taylor, D.B., 1992, "A synthetic theory for the perturbations of Titan on Hyperion" in *Astronomy and Astrophysics*, **265**, pp.825-832.

[11] Whiteman, K.J., 1977, "Invariants and stability in classical mechanics", in *Rep. Prog. Phys.*, **40**, pp. 1033-1069.

Chapter 13
Advanced numerical techniques

INVERSE ITERATION FOR NONLINEAR EIGENVALUE PROBLEMS IN ELECTROMAGNETIC SCATTERING

A. Spence[1] and C. G. Poulton[2]

[1] *Department of Mathematical Sciences, University of Bath, Bath BA2 7AY, UK*

[2] *High Frequency and Quantum Electronics Laboratory, University of Karlsruhe, 76128 Karlsruhe, Germany*

Abstract   We present an extension of the well-known method of "inverse iteration" for the standard eigenvalue problem to the nonlinear problem of finding dispersion relations for electromagnetic waves moving through a doubly-periodic structure. Numerical results are presented to illustrate the performance of the technique. A further improvement is described that allows an efficient "path following" algorithm where a curve of solutions is computed in $(\omega, \mathbf{k}_{bloch})$ space. We present dispersion relations calculated via this new method and compare the efficiency of this algorithm with that of more traditional methods.

1.   INTRODUCTION

We consider the classical problem in electromagnetism of calculating a dispersion relation in a structured doubly-periodic material; the aim is to find a relationship between the frequency ω and the Bloch wavevector $\mathbf{k}_{\text{bloch}}$ of the wave. There are several methods available to solve this problem in the literature, and these can be roughly grouped into *linear* and *nonlinear* approaches, according to the form of the eigenvalue problem which results from the application of the method. The linear approaches include finite difference methods and finite element methods. Among the nonlinear approaches are plane-wave expansions, transfer matrix methods and approaches based on integral equations[1, 2, 3]. In each case listed, the problem is reduced to an eigenvalue problem of the form $A(\omega, \mathbf{k}_{\text{bloch}})\mathbf{x} = \mathbf{0}$ where $A(\omega, \mathbf{k}_{\text{bloch}})$ is an $n \times n$ Hermitian matrix depending either linearly or nonlinearly on the parameters, and $\mathbf{x}$ is a complex eigenvector which is related somehow to the expansion of the propagating fields in the material. Clearly the problem is equivalent to finding zeros of the determinant of

$A(\omega, \mathbf{k}_{\text{bloch}})$, and if no zeros exist for a given value of ω then there exists a 'photonic band-gap', a region for which all propagation in the material is critically damped.

The linear methods are characterized by very large matrices and hence put heavy demands on computing power, however the matrices involved have the advantages of sparsity and of special structure. The non-linear methods by contrast typically involve the solution of relatively small, dense matrix systems which depend on the parameters $(\omega, \boldsymbol{k}_{\text{bloch}})$ in a non-linear manner. In this paper we concentrate on ways of facilitating the solution of these non-linear methods.

By way of illustration we employ an approach based on a multipole expansion of an integral equation, and which is known generally as the 'Rayleigh method'. The advantage of this procedure is that it converges quickly and accurately to the solution, and also that the resulting fields can then be represented semi-analytically, which allows the solution to be easily checked. The procedure however involves the solution of a dense, complex-valued matrix problem of the type stated previously. It is the intention of this paper to use the Rayleigh method as an example of a non-linear eigenvalue problem which can be quickly and effectively solved using an extension of the inverse iteration technique.

Previous methods for solving non-linear eigenvalue problems have involved using a multitude of successive determinant evaluations while varying one of the parameters with the second parameter held fixed. This approach is expensive in terms of computer time and also runs the risk of 'missing' a mode. More sophisticated search procedures have also been employed, notably numerical packages such as BRENT[4], and while procedures such as these fare better they are not optimized for problems which depend on more than one parameter. In comparison the new approach based on inverse iteration not only gives a quadratic convergence to the solution but is also easily extended into a 'path-following' algorithm for finding the solution in a space of two or more parameters.

Dispersion curves

Any wave moving through a periodic material can be expressed as a series of Bloch waves, or waves which possess a fixed spatial frequency. For each Bloch wave we can designate a Bloch vector, which we denote $\boldsymbol{k}_{\text{bloch}}$, and a characteristic frequency ω . The relation $\omega(\boldsymbol{k}_{\text{bloch}})$ is known as a dispersion relation, and the traditional depiction of the dispersion relation is to plot ω only for the values of $\boldsymbol{k}_{\text{bloch}}$ which lie on the edge of the Brillouin zone's first irreducible segment. We note that in any such two-dimensional plot the path of $\boldsymbol{k}_{\text{bloch}}$ is always fixed, and so the two-variable problem

which we introduced originally is in fact a problem for a single variable, which we can label k.

There are many methods available for calculating the dispersion relations. For the purpose of demonstrating our search procedure we have used a multipole method often known as 'the Rayleigh method', after its invention by the great scientist in 1892. Due to limited space, we simply state the endpoint of the method and direct the interested reader to the reference [6] for details of the derivation and of the physical background.

The problem of finding the dispersion relation can be reduced to the algebraic system

$$(\mathcal{M}(\omega) + \mathcal{S}(\omega, k))\, \mathbf{B} = \mathbf{0} \, , \tag{1.1}$$

Here the matrix $\mathcal{M}$ results from the boundary conditions of the inclusions in the array, and $\mathcal{S}$ is a matrix of structure coefficients which characterize the array's periodic geometry. Zeros of the determinant of the above system correspond to propagating modes, and these modes can be reconstructed using the nullspace vector $\mathbf{B}$.

The system written above is Hermitian, complex valued, dense, and is a non-linear eigenvalue problem for the variables ω and k - indeed the complexity of the dependence of the terms $\mathcal{M}(\omega)$ and $\mathcal{S}(\omega, k)$ on their dependent variables means that the system is very non-linear indeed. Fortunately the system can be formulated so that it converges rapidly away from the main diagonal - this means that accurate results can be obtained with relatively small matrices.

2.   INVERSE ITERATION METHOD

We now describe a method to find the solutions of the nonlinear eigenvalue problem (1.1). Our method is a natural extension of the Rayleigh Quotient Iteration for the symmetric eigenvalue problem (see [8]). The method we derive is essentially a combination of the approach in [9] and [5]. An interesting alternative approach is discussed in [10] where the steps in the Newton method discussed in [5] are reorganized to provide the "Residual Correction Method". We shall discuss this approach later.

2.1.   THEORY

First consider the one-parameter nonlinear eigenvalue problem

$$A(\omega)\mathbf{x} = \mathbf{0} \, , \tag{2.1}$$

where $A(\omega)$ is an $n \times n$ Hermitian matrix, with $A(\omega)$ at least twice continuously differentiable with respect to ω, a real parameter. Here $\mathbf{x}$ is a complex vector normalized by

$$\mathbf{x}^{H}\mathbf{x} = 1 \, . \tag{2.2}$$

We denote derivatives of $A(\omega)$ by $A_\omega(\omega)$, etc., and note that $A_\omega(\omega)$ is also Hermitian. Clearly (2.1) is equivalent to the problem

$$\det A(\omega) = 0 , \tag{2.3}$$

and since $A(\omega)$ is Hermitian its determinant is real. Thus our problem is one of finding zeros of a real valued function. It is well known that the most desirable situation occurs when the zero is locally unique. We give a precise condition to ensure this happens in the following nondegeneracy Theorem.

Theorem: Let $(\mathbf{x}^*, \omega^*)$ solve (2.1) and (2.2) so that $\det A(\omega^*) = 0$. Assume:

$$\text{(i)} \quad \text{Null}A(\omega^*) = \text{span}\{\mathbf{x}^*\} , \tag{2.4}$$

and

$$\text{(ii)} \quad \mathbf{x}^{*H} A_\omega(\omega^*)\mathbf{x}^* \neq 0 , \tag{2.5}$$

Then

$$\frac{d}{d\omega}(\det A(\omega^*))|_{\omega=\omega^*} \neq 0 . \tag{2.6}$$

Before giving the proof we remark that (2.4) implies that the nullspace is one dimensional and hence $A(\omega^*)$ has a simple zero eigenvalue, and (2.6) shows that the determinant crosses through zero with nonzero speed at $\omega = \omega^*$. We shall see that expressions like the quadratic form on the left hand side of (2.5) occur several times in this paper, and the fact that (2.5) holds is crucial to the success of the algorithm we discuss.

Proof: First it is easily shown that the matrix $M(\omega)$ defined by

$$M(\omega) = \begin{pmatrix} A(\omega) & \mathbf{x}(\omega) \\ \mathbf{x}(\omega)^H & 0 \end{pmatrix} ,$$

is nonsingular at $\omega = \omega^*$ and hence $\det M(\omega^*) \neq 0$. Also $M(\omega)$ is nonsingular for ω near ω^*. Thus the $(n+1) \times (n+1)$ linear system

$$\begin{pmatrix} A(\omega) & \mathbf{x}(\omega) \\ \mathbf{x}(\omega)^H & 0 \end{pmatrix} \begin{pmatrix} \mathbf{u}(\omega) \\ f(\omega) \end{pmatrix} = \begin{pmatrix} 0 \\ 1 \end{pmatrix} , \tag{2.7}$$

has a unique solution for ω near ω^*. Moreover, Cramer's Rule shows that

$$f(\omega) = \det A(\omega)/ \det M(\omega) ,$$

and hence $f(\omega^*) = 0$ and $\mathbf{u}(\omega^*) = \mathbf{x}(\omega^*) = \mathbf{x}^*$.Differentiating with respect to ω and evaluating at $\omega = \omega^*$ shows

$$\frac{d}{d\omega} \det A(\omega)|_{\omega=\omega^*} = f_\omega(\omega^*) \det M(\omega^*) . \tag{2.8}$$

Finally, differentiating the first equation of (2.7), left multiplying by $\mathbf{x}(\omega)^H$ and evaluating at $\omega = \omega^*$ gives (noting $\mathbf{x}^{*H}\mathbf{x}^* = 1$)

$$f_\omega(\omega^*) = -\mathbf{x}(\omega^*)^H A_\omega(\omega^*)\mathbf{x}(\omega^*) \ . \tag{2.9}$$

Since $\det M(\omega^*) \neq 0$, equations (2.8) and (2.9) provide the result of the theorem.

2.2.   DERIVATION OF THE ALGORITHM

Assume $(\mathbf{x}^i, \omega^i)$ is an approximation to $(\mathbf{x}^*, \omega^*)$, a solution of (2.1). The appropriate equation to improve $\mathbf{x}^i$ is easily derived using Taylor's Theorem. We have

$$0 = A(\omega^*)\mathbf{x}^* = A(\omega^i)\mathbf{x}^i + A(\omega^i)(\mathbf{x}^* - \mathbf{x}^i) + (\omega^* - \omega^i)A_\omega(\omega^i)\mathbf{x}^i + \ldots$$

Neglecting higher order terms and replacing $(\mathbf{x}^*, \omega^*)$ by $(\mathbf{x}^{i+1}, \omega^{i+1})$ gives

$$A(\omega^i)\mathbf{y}^{i+1} = -A_\omega(\omega^i)\mathbf{x}^i \ , \tag{2.10}$$

where

$$\mathbf{y}^{i+1} = \mathbf{x}^{i+1}/(\omega^{i+1} - \omega^i) \ ,$$

so that $\mathbf{y}^{i+1}$ is merely a scaled form of the improved estimate $\mathbf{x}^{i+1}$. To update ω^i we again use Taylor's theorem. We have

$$0 = A(\omega^*) = A(\omega^i) + (\omega^* - \omega^i)A_\omega(\omega^i) + \ldots$$

Neglecting quadratic and higher order terms and replacing ω^* by ω^{i+1} gives

$$A(\omega^i) + (\omega^{i+1} - \omega^i)A_\omega(\omega^i) = 0 \tag{2.11}$$

and, after left and right multiplication by $\mathbf{x}^{i+1}$, we obtain

$$\omega^{i+1} = \omega^i - \frac{\mathbf{x}^{i+1^H} A(\omega^i)\mathbf{x}^{i+1}}{\mathbf{x}^{i+1^H} A_\omega(\omega^i)\mathbf{x}^{i+1}} \tag{2.12}$$

where, as convergence occurs, the denominator is nonzero by (2.5). Note that even though $\mathbf{x}^{i+1}$ is complex, the correction to ω^i is real since A and A_ω are Hermitian. Equations (2.10) and (2.12) provide the basis for the algorithm.

Algorithm (Nonlinear Inverse Iteration): Given $(\mathbf{x}^i, \omega^i)$ with $\mathbf{x}^{i^H}\mathbf{x}^i = 1$:

(i) Solve: $A(\omega^i)\mathbf{y}^{i+1} = -A_\omega(\omega^i)\mathbf{x}^i$.

(ii) Rescale: $\mathbf{x}^{i+1} = \mathbf{y}^{i+1}/ \parallel \mathbf{y}^{i+1} \parallel_2$.

(iii) Update ω: $\omega^{i+1} = \omega^i - \dfrac{\mathbf{x}^{i+1^H} A(\omega^i)\mathbf{x}^{i+1}}{\mathbf{x}^{i+1^H} A_\omega(\omega^i)\mathbf{x}^{i+1}}$.

(iv) Repeat until convergence.

We prove that this algorithm has quadratic convergence in the following subsection, but first we illustrate the expected quadratic convergence in Table 1.

i	ω^i	$\omega^i - \omega^*$	$(\omega^{i+1} - \omega^*)/(\omega^i - \omega^*)^2$
0	2.098478317619202	0.00991457723203	169.288654112512
1	2.105204619002223	0.01664087861505	7.08344766150259
2	2.090525280504449	0.00196154011728	7.10231325846239
3	2.088591067529145	0.00002732714197	9.64975033688122
4	2.088563747593345	0.00000000720617	9821.12343644970
5	2.088563740387682	0.00000000000051	0
6	2.088563740387172	0.00000000000000	0

Table 1: Illustration of the convergence of the inverse iteration method.

To study the convergence of the algorithm we picked the point within the first Brillouin zone $k_b = (\pi/2, 0)$ and took an initial starting guess which was known to be close to the true value ω^* . In the table we plot the values of $\omega^i - \omega^*$ and of $(\omega^{i+1} - \omega^*)/(\omega^i - \omega^*)^2$. On the first iteration the algorithm is in fact driven away from the true solution; this occurs because the initial choice for the vector $\mathbf{x}^0$ is arbitrary and is hence not necessarily close to $\mathbf{x}^*$. We then observe that as i increases the values of $(\omega^{i+1} - \omega^*)/(\omega^i - \omega^*)^2$ become approximately constant, showing quadratic convergence.

We mention that in our experiments we experienced no loss of accuracy due to ill-conditioning of $A(\omega^i)$ when implementing the solve step (i) above. However in some cases it might be appropriate to carry out some steps of iterative refinement (see, for example, Section 2.5 in [11]).

It is interesting to compare our method with the "Residual Correction Method" of [10].

Algorithm (Residual Correction Method): Given a fixed real σ and a complex vector $\mathbf{x}^i$ with $\mathbf{x}^{i^H}\mathbf{x}^i = 1$:

(i) Find ω^{i+1} the root of $\mathbf{x}^{i^H} A(\omega^{i+1})\mathbf{x}^i = 0$.

(ii) Solve: $A(\sigma)\mathbf{d}^i = -A(\omega^{i+1})\mathbf{x}^i$.

(iii) Set: $\mathbf{x}^{i+1} = \mathbf{x}^i + \mathbf{d}^i$ and renormalize $\mathbf{x}^{i+1}$.

(iv) Repeat until convergence.

In [10] it is shown that this method has *linear* convergence and some examples are given. Note that one option for (i) above is to take

$$\omega^{i+1} = \omega^i - \frac{\mathbf{x}^{i^H} A(\omega^i)\mathbf{x}^i}{\mathbf{x}^{i^H} A_\omega(\omega^i)\mathbf{x}^i}.$$

(cf. step (iii) in our Nonlinear Inverse Iteration Algorithm). In cases when n is large (and perhaps sparse) and where evaluations of $A(\omega)$ are not expensive then this method may have advantages over the approach discussed here. However in our case n is small and because of costs we seek to minimise the number of evaluations of $A(\omega)$. Thus we prefer to keep the quadratically convergent method discussed here.

2.3.   CONVERGENCE

In this subsection we provide the details of the proof that the nonlinear inverse iteration algorithm converges quadratically. Let $(\mathbf{x}^*, \omega^*)$ denote the exact solution with $(\mathbf{x}^i, \omega^i)$ and $(\mathbf{x}^{i+1}, \omega^{i+1})$ denoting successive estimates obtained from the nonlinear inverse iteration algorithm. The key tool in the convergence analysis is to use the *orthogonal decomposition* utilized in [8]. Let

$$\mathbf{x}^i = c^i \mathbf{x}^* + s^i \mathbf{z}^i \ , \tag{2.13}$$

where c^i and s^i are complex constants, and $\mathbf{z}^i$ is an unknown vector in the plane of $\mathbf{x}^i$ and $\mathbf{x}^*$ satisfying $\| \mathbf{z}^i \|_2 = 1$ and the orthogonality condition

$$\mathbf{x}^{*^H} A_\omega(\omega^*) \mathbf{z}^i = 0 \ . \tag{2.14}$$

Here c^i and s^i may be identified with $\cos \theta^i$ and $\sin \theta^i$ where θ^i is the (complex) angle between $\mathbf{x}^i$ and $\mathbf{x}^*$ (see pp.63,64 of [8]). To see the roles played by c^i and s^i we note from (2.13) that

$$\| \mathbf{x}^i - c^i \mathbf{x}^* \|_2 = |s^i| \ ,$$

and if $|s^i| \to 0$ then $|c^i| \to 1$, and so $\mathbf{x}^i$ tends to the desired direction $\mathbf{x}^*$. Similarly we write

$$\mathbf{x}^{i+1} = c^{i+1} \mathbf{x}^* + s^{i+1} \mathbf{z}^{i+1} \ , \tag{2.15}$$

where again $\mathbf{z}^{i+1}$ is an unknown vector satisfying $\| \mathbf{z}^{i+1} \|_2 = 1$ and

$$\mathbf{x}^{*^H} A_\omega(\omega^*) \mathbf{z}^{i+1} = 0 \ . \tag{2.16}$$

We remark that $\mathbf{z}^i$ and $\mathbf{z}^{i+1}$ only appear in the convergence analysis and never need to be computed. We shall prove quadratic convergence of the nonlinear inverse iteration algorithm by showing that

$$|s^{i+1}| = O\left(|s^i|^2\right) + O\left(|s^i|(\omega^i - \omega^*)\right) \tag{2.17}$$

and

$$\omega^{i+1} - \omega^* = O\left((\omega^i - \omega^*)^2\right). \tag{2.18}$$

The fact that quadratic terms are neglected in the use of Taylor's Theorem to derive of the formula to update ω^i (given by (2.12)) shows directly that $\omega^{i+1} - \omega^* = O\left((\omega^i - \omega^*)^2\right)$. However the fact that (2.17) also holds is more complicated, but essentially involves substituting (2.13) and (2.15) into step (i) of the nonlinear inverse iteration algorithm and then using Taylor's Theorem expanded about ω^* . It is convenient to introduce d^* defined by

$$d^* = \mathbf{x}^{*^H} A_\omega(\omega^*)\mathbf{x}^*. \tag{2.19}$$

From step (i) of the algorithm we have

$$\| \mathbf{y}^{i+1} \|_2 \{A(\omega^*) + (\omega^i - \omega^*)A_\omega(\omega^*) + O\left((\omega^i - \omega^*)^2\right)\}(c^{i+1}\mathbf{x}^* + s^{i+1}\mathbf{z}^{i+1})$$
$$= -\{A_\omega(\omega^*) + (\omega^i - \omega^*)A_{\omega\omega}(\omega^*) + O\left((\omega^i - \omega^*)^2\right)\}(c^i\mathbf{x}^* + s^i\mathbf{z}^i). \tag{2.20}$$

Multiply on the left by $\mathbf{x}^{*^H}$ to obtain (using (2.14) and (2.16))

$$\| \mathbf{y}^{i+1} \|_2 \ (\omega^i - \omega^*)\left\{c^{i+1}d^* + s^{i+1}\mathbf{x}^* A_\omega(\omega^*)\mathbf{z}^{i+1} + O(\omega^i - \omega^*)\right\}$$
$$= -c^i d^* + O(|s^i|) + O(\omega^i - \omega^*). \tag{2.21}$$

Next multiply (2.20) on the left by $\mathbf{z}^{i+1^H}$ to obtain (again using (2.14) and (2.16)).

$$\| \mathbf{y}^{i+1} \|_2 \ \{s^{i+1}(\mathbf{z}^{i+1})A(\omega^*)\mathbf{z}^{i+1} + O(\omega^i - \omega^*)) + O((\omega^i - \omega^*)^2)\}$$
$$= -s^i \left\{\mathbf{z}^{i+1^H} A_\omega(\omega^i)z^i\right\} - (\omega^i - \omega^*)\left\{c^i\mathbf{z}^{i+1^H} A_{\omega\omega}(\omega^*)\mathbf{x}^*\right\}. \tag{2.22}$$

Now dividing (2.22) by (2.21) we lose the $\| \mathbf{y}^{i+1} \|_2$ terms and obtain, after rearrangement,

$$\frac{s^{i+1}\{\mathbf{z}^{k+1}(A(\omega^*) + O(\omega^i - \omega^*))\mathbf{z}^{k+1} + O((\omega^i - \omega^*)^2)}{c^{i+1} + O(\omega^i - \omega^*)}$$
$$= \frac{(\omega^i - \omega^*)\{O(|s^i|) + O(\omega^i - \omega^*)\}}{c^i + O(\omega^i - \omega^*)} \tag{2.23}$$

Hence

$$|s^{i+1}| = O(|s^i||\omega^i - \omega^*|) + O(|\omega^i - \omega^*|^2).$$

Finally, if $\omega^i - \omega^* = O(|s^i|)$ then

$$|s^{i+1}| = O(|s^i|^2) \ ,$$

ensuring the quadratic convergence observed in practice.

2.4. TWO PARAMETER PROBLEMS

The application of interest in this paper (1.1) is a two parameter non-linear eigenvalue problem of the form

$$A(\omega, k)\mathbf{x} = \mathbf{0} \ , \tag{2.24}$$

where k is a second real parameter. In particular we wish to compute a path in the $\omega - k$ plane where

$$\det A(\omega, k) = 0 \ . \tag{2.25}$$

For the problem (2.24) we assume ω and $\mathbf{x}$ are smooth functions of k. Thus differentiating (2.24) with respect to k gives

$$\left(A_\omega(\omega(k), k)\frac{d\omega}{dk} + A_k(\omega(k), k)\mathbf{x}(k)\right) + A(\omega(k), k)\frac{d\mathbf{x}(k)}{dk} = \mathbf{0} \ ,$$
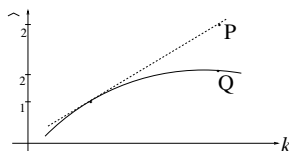
Figure 1 Schematic to illustrate the approximation of (ω_2, k_2) by $(\hat{\omega}_2, k_2)$.

where the subscript k denotes partial differentiation with respect to k. Left multiplication by $\mathbf{x}(k)^H$ and the fact that $\mathbf{x}(k)^H A(\omega(k), k) = \mathbf{0}$ gives

$$\frac{d\omega}{dk} = -\frac{\mathbf{x}(k)^H A_k(\omega(k), k)\mathbf{x}(k)}{\mathbf{x}(k)^H A_\omega(w(k), k)\mathbf{x}(k)} . \tag{2.26}$$

Assume that $\det A(\omega_1, k_1) = 0$. For a given k_2 close to k_1 we seek w_2 where $\det A(\omega_2, k_2) = 0$. The nonlinear inverse iteration algorithm is used to find ω_2 but an accurate starting value for the iteration is obtained from the formula

$$\hat{\omega}_2 = \omega_1 + (k_2 - k_1)\frac{d\omega}{dk}(k_1)$$

where $\frac{d\omega}{dk}$ is obtained using (2.26) evaluated at (ω_1, k_1). In Figure 1, Q is the desired point (ω_2, k_2) and P the estimate $(\hat{\omega}_2, k_2)$.

3.   NUMERICAL RESULTS

In Table 2 we compare the performance of the inverse iteration method with two other methods which are used for the same problem. The physical situation which we consider is for the calculation of the lowest dispersion curve for the TE mode moving in a doubly periodic array of perfectly conducting cylinders. Because the matrix $A(\omega, \mathbf{k}_{\text{bloch}})$ is dense but not particularly large, the majority of the computational expense comes from evaluating the matrix itself rather than solving the linear system. For this reason we give the number of matrix evaluations as well as the net computation time taken.

Method	matrix calls	time/s
'näive' procedure	2434	334
BRENT	1491	208
inverse iteration	429	63

Table 2: Performance of the inverse iteration method for the calculation of a single band of a dispersion curve consisting of 50 points.

The first method which is used for a comparison is a 'näive' search procedure, which fixes k and samples the search region in ω, looking for crossings, i.e. places where the determinant changes sign. The search region is limited by physical considerations, namely, that the transverse

group velocity $d\omega/dk$ cannot be greater than the speed of light. If a crossing is found, then the search region is further divided and the procedure repeats itself until the determinant is deemed sufficiently small. The second method is similar, in that it begins the search by sampling the search region and looking for crossings. When a crossing is found however, the BRENT search procedure is used to find the zero of the determinant. In both methods a simple interpolation path-following procedure is employed, by which the approximate position of the next point is predicted using the current slope on the dispersion curve. The inverse iteration procedure was employed for the same physical parameters, and used the path-following technique given in section 2.4. It can be seen that the inverse iteration algorithm performs markedly better than the two other methods.

Acknowledgments

References

[1] K. M. Leung and Y.F. Liu. *Full vector wave calculation of photonic band structures in face-centred cubic dielectric media.* Phys. Rev. Lett., 65:2646–2649, 1990.

[2] J. B. Pendry and P. M. Bell. *Transfer matrix techniques for electromagnetic waves*, volume 315 of *NATO ASI Series E:Applied Sciences*, page 203. Kluwer, Dordrecht, 1996.

[3] R. C. McPhedran, N. A. Nicorovici, L. C. Botten, and Ke-Da Bao. *Green's function, lattice sum and Rayleigh's identity for a dynamic scattering problem*, volume 96 of *IMA Volumes in Mathematics and its Applications*, pages 155–186. Springer-Verlag, New York, 1997.

[4] W. H. Press, S. A. Teukolsky, W.T. Vetterling, and B.P. Flannery, *Numerical Recipes in Fortran 77*, section 9.3, CUP, Cambridge MA, 1992.

[5] A. Ruhe *Algorithms for the Nonlienear Eigenvalue Problem*, SIAM J.Numer. Anal. vol 10, pages 674–689. 1973.

[6] P. M. Anselone and L. B. Rall, *The Solution of Characteristic Value-Vector Problems by Newton's Method*, Numerische Mathematik, vol 11, pages 38–45, 1968.

[7] P. Lancaster, *Lambda-Matrices and Vibrating Systems*, Pergamon, Oxford. 1966.

[8] B. N. Parlett, *The Symmetric Eigenvalue Problem*, 2nd edition, SIAM, Philadelphia, 1998.

[9] P. Lancaster, *A Generalised Rayleigh Quotient Iteration for Lambda-Matrices*, Arch. Rat. Mech. Anal. vol 8 pages 309–322, 1961.

[10] A. Neumaier, *Residual Inverse Iteration for the Nonlinear Eigenvalue Problem* SIAM J.Numer. Anal. vol 20, pages 914–923. 1983.

[11] J. W. Demmel, *Applied Numerical Linear Algebra*, SIAM, Philadelphia, 1997.

FAST ITERATIVE SOLUTION OF COUPLED 3-DIMENSIONAL FLUID-STRUCTURE INTERACTION PROBLEMS

Martyn D Hughes and Ke Chen

Department of Mathematical Sciences, University of Liverpool,
Liverpool L69 3BX, UK

Keywords: Linear systems, iterative methods, preconditioning, sparse approximate inverses, *a priori* patterns, sparsification, diagonal blocks.

Abstract

Modelling the interaction of an acoustic field in a fluid and a structure submerged in the fluid leads to a system of complex linear equations with a complicated sparsity structure and, for adequate modelling, the systems are very large. Solution of such systems by direct methods is too slow. Iterative methods, which in theory are capable of giving a solution of acceptable accuracy to large linear systems in a much shorter time than direct methods, either do not converge at all or converge too slowly for this problem. However, if the matrix of the linear system is suitably preconditioned, iterative methods will converge much more quickly. We have developed some preconditioners particularly applicable to this problem. We present test results for the case of a hollow steel sphere in water.

INTRODUCTION

The problem of the interaction of an acoustic field in a fluid medium (such as the sea) with an arbitrarily-shaped elastic structure (such as a submarine or other vessel) submerged in the fluid, where the acoustic wavelength is comparable with the size of the structure, cannot be solved analytically by the use of asymptotic methods since these are not valid in this intermediate frequency range. Hence the only feasible methods of solution of this problem are numerical methods.

The acoustic field is governed by the Helmholtz equation, but is formulated in equivalent integral equation form over the surface of the structure to avoid the problem of the infinite fluid domain. This has the added advantage that the problem is reduced from a 3-dimensional problem to a 2-dimensional one. The integral equation is then reduced to discrete form using the boundary element method. The behaviour of the structure under the influence of the acoustic field is modelled using finite element analysis. These models are coupled by insisting that the fluid particle velocity normal to the surface is continuous.

Direct methods of solution are too slow for the large linear systems necessary for adequate modelling of the situation, and iterative methods converge too slowly or not at all without any preconditioning. The aim of our work is to develop better preconditioners to accelerate the convergence of the best modern iterative solution methods.

Our new results are presented for a hollow steel sphere in water, with no incoming wave.

1. THE MODELS

We now describe the outlines of the boundary element and finite element models, together with the coupling method. Full details of the models are given in [1].

1.1. THE ACOUSTIC FIELD

Assuming single frequency harmonic waves of the form $\Phi(p,t) = \varphi(p)e^{-i\omega t}$, where $\Phi(p,t)$ is the excess pressure at the point p at time t, and ω is the frequency, the acoustic field can be modelled by the Helmholtz equation, $\nabla^2\varphi(p) + k^2\varphi(p) = 0$, where $k = \omega/c$ is the acoustic wave number, c being the wave speed.

To ensure that all waves are outgoing at infinity, we use the Sommerfeld radiation condition

$$\lim_{r\to\infty} r\left\{\frac{\partial\varphi(r)}{\partial r} - ik\varphi(r)\right\} = 0. \tag{1.1}$$

Formulating the Helmholtz equation in equivalent boundary integral equation form over the surface of the structure gives

$$\int_S \left\{\varphi(q)\frac{\partial G_k(p,q)}{\partial n_q} - G_k(p,q)\frac{\partial\varphi(q)}{\partial n_q}\right\} dS_q = \frac{1}{2}\varphi(p), \tag{1.2}$$

where $G_k(p,q) = \frac{e^{ik|p-q|}}{4\pi|p-q|}$ is the free-space Green's function for the Helmholtz equation.

To avoid problems of non-existence and non-uniqueness of the solutions of the integral equation at the natural frequencies of the structure, we use the Burton and Miller formulation [2],

$$\left(-\frac{1}{2}\mathcal{I} + \mathcal{M}_k + \alpha\mathcal{N}_k\right)\varphi = \left[\mathcal{L}_k + \alpha\left(\frac{1}{2}\mathcal{I} + \mathcal{M}_k^T\right)\right]\frac{\partial\varphi}{\partial n}, \qquad (1.3)$$

where $\mathcal{L}_k$ and $\mathcal{M}_k$ are the single and double layer Helmholtz potential operators, $\mathcal{M}_k^T$ and $\mathcal{N}_k$ are their normal derivatives, and α is a coupling parameter.

This integral equation is discretized using the boundary element (BE) method. We use the collocation method, with triangular elements for the surface of the structure and piecewise constant interpolation functions for the solution, which gives a linear system of the form

$$A\underline{\varphi} = i\omega\rho B\underline{v} - \underline{c}, \qquad (1.4)$$

where A and B are from the above Burton and Miller equation, ρ is the fluid density, $\underline{\varphi}$ is the pressure, $\underline{v}$ the velocity, and $\underline{c}$ the incident wave pressure. The matrix of the system is dense and complex.

1.2.   THE STRUCTURE

The behaviour of the structure under the influence of the acoustic field is modelled using the finite element (FE) method. Prism-shaped elements are formed by projection from the triangular surface boundary elements to the centre of the sphere and we use piecewise quadratic interpolation functions on the triangular faces and piecewise linear functions on the rectangular faces.

We then use minimization of the energy of the structure to derive a linear system, which is of the form $(K - \omega^2 M)\underline{q} = \underline{f}$, where K is the stiffness matrix, M the mass matrix, $\underline{q}$ the displacement, and $\underline{f} = \underline{f}^k + \underline{f}^\varphi$ the total load due to the applied forces $(\underline{f}^k)$ and the fluid pressure $(\underline{f}^\varphi)$. The matrix of the system is real, symmetric, and sparse.

1.3.   THE COUPLED SYSTEM

We use the requirement that the fluid particle velocity should be continuous at the surface of the structure to couple the BE and FE systems.

The load due to the fluid pressure, $\underline{f}^\varphi$, can be written in terms of the pressure, $\underline{\varphi}$, as $\underline{f}^\varphi = -L\underline{\varphi}$, where L is a matrix derived from the basis functions used in the BE and FE analyses. Also, the velocity, $\underline{v}$, can be written in terms of the displacement, $\underline{q}$, as $\underline{v} = -i\omega L'\underline{q}$, where L' is a matrix derived from the basis functions used in the FE analysis.

The coupled problem is to solve, simultaneously, the equations

$$A\underline{\varphi} = i\omega\rho B\underline{v} - \underline{c},\tag{1.5}$$

and

$$(K - \omega^2 M)\underline{q} = \underline{f}^k - L\underline{\varphi}\tag{1.6}$$

using the equation $\underline{v} = -i\omega L'\underline{q}$.

This gives the coupled but partitioned system for $\underline{\varphi}$ and $\underline{q}$

$$\begin{bmatrix} A & -\omega^2\rho BL' \\ L & K - \omega^2 M \end{bmatrix} \begin{bmatrix} \underline{\varphi} \\ \underline{q} \end{bmatrix} = \begin{bmatrix} -\underline{c} \\ \underline{f}^k \end{bmatrix}.\tag{1.7}$$

A typical matrix of this system has the following pattern of nonzeros

BE block $\rightarrow$
A
36×36
Complex, dense

$\leftarrow$ Coupling strip
$-\omega^2\rho BL'$
36×444
Complex, sparse

Coupling strip $\rightarrow$
L
444×36
Real, sparse

$\leftarrow$ FE block
$K - \omega^2 M$
444×444
Real, sparse, symmetric
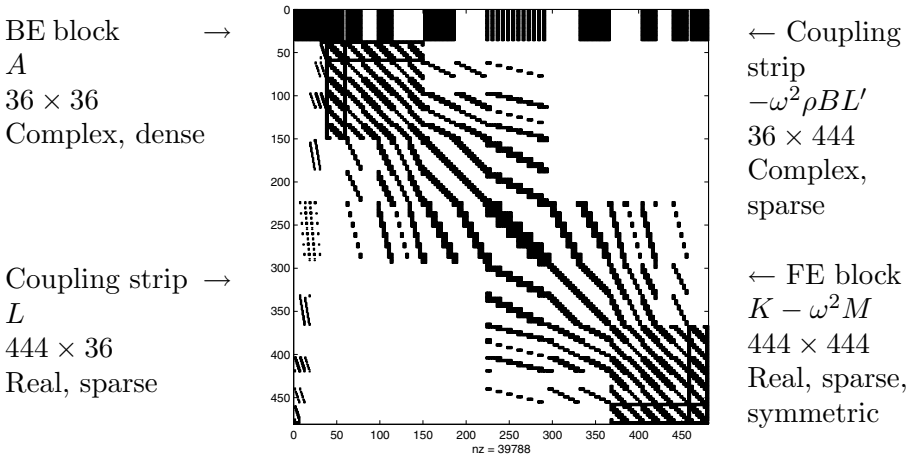
Figure 1   Pattern of coupled matrix

With the parameter values that we have been using, the maximum size of the entries in the right hand parts is of the order of 10^{11} times that for those in the left hand parts.

2.   SOLVING THE LINEAR SYSTEM

We use two iterative methods - the generalized minimum residual method (GMRES) and the conjugate gradients squared method (CGS). There is

no convergence of either method for our coupled system without any preconditioning. This is mainly because the eigenvalues of the matrix are too spread out. Ideally, the eigenvalues should be clustered, say at 1, and there should be few near zero. Preconditioning can achieve this.

2.1. PRECONDITIONING THE SYSTEM

In preconditioning, another matrix, M, is applied to the system, either on the left or the right (or possibly both), so that, in the right case for example, the system is changed from $Ax = b$ to

$$AMy = b \qquad (x = My). \qquad (2.1)$$

The solution, x, is the same as the original but the governing eigenvalues are those of AM instead of A. The ideal preconditioner is a compromise between the extremes of $M = A^{-1}$(the true inverse of A) and $M = I$, with $M \approx A^{-1}$, and hence $AM \approx I$, so that the eigenvalues of AM are clustered close to 1, but also such that the calculations are easy at each iteration. The preconditioner should also be sparse to make it efficient in use.

2.2. SIMPLE PRECONDITIONERS

We first consider the simplest preconditioners. These are the inverses of sparse approximations to A, such as those with the diagonal entries, or block diagonal entries, of A, or incomplete factorizations of A.

In this case, a simple diagonal preconditioner produces slow convergence for GMRES but not CGS. Scaling of the matrix on the right by a diagonal matrix, to equalize the maximum size of the entries of A, also produces slow convergence of GMRES but not CGS.

The table below shows the number of iterations required for GMRES to converge to a tolerance of 10^{-5} using the diagonal inverse matrix alone (diag), and the scaling matrix alone (scale).

2.3. THE SPARSE APPROXIMATE INVERSE METHOD (SPAI)

The performance of the solvers can be greatly improved using more sophisticated preconditioners, including ones involving approximations to the inverse of A itself. We are using such preconditioners, generated by an algorithm called SPAI (SParse Approximate Inverse).

A major advantage of this method, particularly for this problem, is that it is easily parallelizable.

The method can be used to generate a left or a right preconditioner; consider the case of a right preconditioner.

Table 1   Simple preconditioning results

Size	Method	GMRES
480	scale	52
	diag	70
702	scale	94
	diag	142
2754	scale	206
	diag	129

The method determines how good an approximation M is to A^{-1} by minimizing the Frobenius norm, $||AM - I||_F$. From the definition of the Frobenius norm, this minimization problem separates into n independent least squares problems

$$\min_{m_k} ||Am_k - e_k||_2, \qquad k = 1, 2, \ldots, n, \qquad (2.2)$$

where m_k and e_k are the kth columns of M and I respectively. For sparse A (as in this case) and M these problems are small and quick to solve.

Hence the method is implemented column-by-column (or row-by-row for a left preconditioner) and so is easy to parallelize. Run sequentially, the method is not competitive with other methods for speed but it can be when run in parallel. Separation of the columns/rows also means that effort can be concentrated on the difficult ones, which may be a particular advantage for this problem.

One well-known implementation of the method is the adaptive approach of Grote and Huckle [3]. In this method we start with a simple pattern for M (usually diagonal) and add a few entries at a time (usually 5), chosen by a minimization procedure for the error involved in adding the elements to the column, until an error tolerance or a maximum number of nonzeros in the column has been reached. The choice of entry positions can be restricted, for example to those of A. It is important that the total number of nonzeros per column is kept fairly small; just one full column defeats the object since more work is involved in this case than in a direct method of solution.

2.4.   *A PRIORI* PATTERNS

Alternatively, if we can find a good sparsity structure for the approximate inverse beforehand, this can be used as an *a priori* pattern, with

the method being used to solve the least squares problem for all the corresponding entries in a column at once. This avoids the adaptive procedure and so can be much faster, but it is important that the *a priori* pattern is sufficiently sparse. This is an inherent problem since the true inverse is almost certain to be full. See Huckle [4] and Chow [5] for more details of this method.

To choose a good *a priori* pattern, we need to know which of the entries in the true inverse of A are the most important. We can use the theory of the relationship between the pattern of A, denoted by $S(A)$, and the pattern of its inverse, denoted by $S(A^{-1})$.

Using the Cayley-Hamilton theorem and rearranging, we have

$$A^{-1} = -(\alpha_1 I + \alpha_2 A + \alpha_3 A^2 + \alpha_4 A^3 + \cdots + \alpha_n A^{n-1})/\alpha_0. \qquad (2.3)$$

Hence the pattern of A^{-1} is contained in the pattern $\bigcup_{j=0}^{n-1} S(A^j)$, or

$$S(A^{-1}) \subseteq S((I + A)^{n-1}) \qquad (2.4)$$

so we can use $S((I + A)^m)$ for small m as an approximate pattern for A^{-1}, and hence as an *a priori* pattern. Provided that A has a full diagonal, we can thus use A, A^2, A^3 etc. as *a priori* patterns.

Unless the matrix is very sparse, it is clearly necessary to remove some of the entries from the matrix before using it or its powers as *a priori* patterns, in order to avoid the pattern being too dense. It is obviously essential for full matrices. This can be done using various methods, including a simple dropping strategy based on a threshold using the mean of the entries, either globally or per column. This process is called sparsification.

2.5.   NEW METHOD - BLOCK DIAGONAL PRECONDITIONERS

Extensive experiments have shown that the adaptive SPAI method is slow and does not produce very effective preconditioners in this case without a large number of nonzeros. The *a priori* method, using the pattern of the original matrix, is faster and the resulting preconditioners are quite effective. They are obviously no more dense than the original matrix.

Rather than using SPAI on the whole matrix, we propose to take advantage of the block structure of the matrix in this case. In particular, we can use the fact that the BE and FE parts form diagonal blocks to produce an approximate block diagonal inverse preconditioner, using SPAI for the two blocks separately.

We can use either the adaptive method or the *a priori* method for one or the other, or for both parts. Since the (full) BE part is relatively small compared to the (sparse) FE part, we can afford to fill this completely to

produce a very accurate inverse, while still keeping the overall number of nonzeros small. However, it is more efficient with SPAI to use sparsification to reduce the number of nonzeros, if possible.

The resulting preconditioners are as effective as those using the *a priori* method for the whole matrix, but the method is considerably faster and there are less nonzeros in the preconditioner. There is obvious scope for parallelization of the SPAI for the BE and FE parts.

3.   RESULTS

We have carried out tests using GMRES and CGS to solve the linear systems using right preconditioners generated using the generic SPAI method for the whole matrix, both adaptively and *a priori*, and the new block method with different combinations of adaptive and *a priori* methods for the two parts. We did not sparsify either part. Some of the results are set out in the following table.

All the tests were carried out using programs written in Matlab, with data from programs written in Fortran. The solvers were the Matlab solvers, suitably adapted. The methods used were:

1 - SPAI used adaptively for the whole matrix with 10 percent maximum nonzeros per column and the choice of new entry position restricted to the pattern of A.

2 - the *a priori* method using the pattern of A.

3 - the block diagonal inverse method, using SPAI adaptively for both parts with 10 percent maximum nonzeros per column and the choice of new entry positions restricted to the patterns of the respective parts.

4 - the block diagonal method, using the *a priori* method for both parts separately, using the full patterns of the respective parts.

The figures in the Total time, Nnz/col and Direct time columns are the average cpu time per column required to generate the preconditioner and carry out GMRES, the average number of nonzeros per column in the preconditioner, and the average cpu time per column taken by the Matlab direct solver, respectively. The results columns show the number of iterations required to converge to a tolerance of 10^{-5}, together with the time taken per column. GMRES was not restarted. All the times are in seconds.

Although the number of nonzeros in the *a priori* cases is higher than in the adaptive cases, this is offset by the advantages in terms of much greater speed of generation of the preconditioner and very much improved effectiveness in use. Also, the percentage of nonzeros in the matrix decreases as the size increases so that this disadvantage becomes less important. Bearing in mind the simple parallelizability of the SPAI method, the competitiveness

Table 2 SPAI results

Size	Method	Direct time	Total time	Nnz/ col	GM	GM time	CGS	CGS time
480	1	0.005	1.98	48	62	0.004	62	0.004
	2		0.4	83	13	0.001	12	0.001
	3		0.91	42	62	0.004	69	0.004
	4		0.14	65	12	0.001	12	0.001
702	1	0.007	3.9	67	90	0.009	82	0.005
	2		0.54	89	20	0.002	19	0.002
	3		2.52	58	98	0.01	104	0.006
	4		0.26	76	21	0.002	19	0.002
1368	1	0.012	9.22	92	160	0.026	319	0.026
	2		0.7	95	56	0.006	50	0.115
	3		6.97	84	208	0.038	270	0.021
	4		0.49	88	55	0.005	48	0.112
2754	2	0.063	3.44	130	40	0.008	46	0.006
	4		0.41	83	40	0.007	40	0.004
4494	2	0.148	2.92	119	115	0.022	159	0.018
	4		0.7	91	115	0.021	159	0.017
5364	2	0.22	2.87	117	127	0.026	147	0.017
	4		0.8	93	127	0.026	147	0.015

of the block *a priori* method with the direct solver in terms of speed is clear from the results.

4.   CONCLUSIONS AND FUTURE WORK

It is evident from the results so far that the block diagonal method using an *a priori* pattern is best in terms of speed and effectiveness of the resulting preconditioners for this problem. However, the number of nonzeros in the preconditioners is not as small as we would like and we intend to explore the use of sparsification strategies further.

The accuracy of the results compares well with those obtained using the Matlab direct solver, but there is a difference between the accuracy of the parts corresponding to the BE and FE parts. This is due to the different scales of the BE and FE parts and the greater accuracy of the approximate BE inverse and is the subject of further investigation.

There is a correlation between the ordering of the nodes in the discretization of the physical system and the pattern of the true inverse of the system matrix and we intend to investigate the effect of this on *a priori* patterns, We also intend to work on the effective parallelization of the methods.

Our results so far are for comparatively small cases and we need to ensure that the methods are equally applicable to much larger cases. Work on reducing the time and memory requirements to enable large cases to be tested is currently being done.

There are other methods that can be used to solve this problem, some of which might involve less storage and computation time. For example, the fast multipole method [6], in which only the near-field matrix entries are calculated, could be used for the acoustic field to produce the BE part of a block diagonal preconditioner. We intend to investigate some of these other methods.

Acknowledgment

References

[1] Amini S, Harris P J and Wilton D T (1992) *Coupled Boundary and Finite Element Methods for the Solution of the Dynamic Fluid-Structure Interaction Problem*, Lecture Notes in Engineering, Vol. 77, Springer-Verlag.

[2] Burton A J and Miller G F (1971) *The Application of Integral Equation Methods for the Numerical Solution of Boundary Value Problems*, Proc. Roy, Soc. Lon., A232, pp. 201-210.

[3] Grote M J and Huckle T (1997) *Parallel Preconditioning with Sparse Approximate Inverses*, SIAM J. of Sci. Comp., Vol. 18, No. 3, pp. 838-853.

[4] Huckle T (1999) *Approximate Sparsity Patterns for the Inverse of a Matrix and Preconditioning*, App. Num. Math., Vol. 30, pp 291-303.

[5] Chow E (2000) *A Priori Sparsity Patterns for Parallel Sparse Approximate Inverse Preconditioners*, SIAM J. of Sci. Comp., Vol. 21, No. 5, pp. 1804-1822.

[6] Greengard L and Rokhlin V (1997) *A Fast Algorithm for Particle Simulations*, J. of Comp. Phys., No. 135, pp. 280-292.

PRECONDITIONING FOR FINGER PATTERN MATRICES ARISING FROM WAVELET DISCRETISATIONS OF BOUNDARY INTEGRAL EQUATIONS

Stuart C. Hawkins and Ke Chen

Department of Mathematical Sciences, University of Liverpool,

Liverpool L69 3BX, U.K.

stuarth@liv.ac.uk, k.chen@liv.ac.uk

Abstract   A new preconditioning strategy is introduced for finger pattern matrices arising from the application of the discrete wavelet transform to discretisations of BIEs. The new strategy is compared against some existing preconditioning strategies and its advantage is demonstrated for low bandwidth preconditioners, and for problems with off diagonal features.

1.   INTRODUCTION

There is much interest in solving linear systems

$$Ax = b, \tag{1.1}$$

where A is a large and dense matrix. Such systems arise from boundary element discretisations of boundary integral equations (BIEs). Applications include the acoustic scattering problem.

Fast solution of (1.1) can be difficult. Direct solution methods are generally not applicable because A is too large. Iterative solution methods are impeded by the high cost of matrix vector multiplication with a large dense matrix, and the difficulty of preconditioning a matrix with no easily exploited structure.

A wavelet discretisation of a BIE leads to a nearly sparse linear system [1, 2]

$$\tilde{A}\tilde{x} = \tilde{b}. \tag{1.2}$$

in the sense that, subject to thresholding, $\tilde{A}$ is sparse with a finger pattern. To concentrate on preconditioning issues we may view (1.2) as being derived from (1.1) by application of a discrete wavelet transform (DWT).

We say that a matrix or submatrix is smooth when nearby entries are similar, and that A has an off diagonal feature when it has an off diagonal region that is not smooth. For example, corner singularities in a BIE can produce in boundary element discretisations one or more columns that differ greatly from their neighbours.

For the case when A has no off diagonal features Chen [3] proposed applying a DWT and using a preconditioner for (1.2) based on a reordering of $\tilde{A}$. For the case when A has off diagonal features Ford and Chen [4] used the method of [3] after reordering A.

In this paper we present a new wavelet preconditioning strategy for matrices A that have off diagonal features. The principal feature of the new strategy is a new reordering of $\tilde{A}$. Preordering of A before application of the DWT is not required. The latter property is particularly useful when $\tilde{A}$ arises directly from wavelet discretisations of BIEs, in which case preordering is not possible.

The paper is structured as follows. In Section 2 the discrete wavelet transform is described. Section 3 describes the new ordering for the wavelet basis. Section 4 describes the preconditioning strategies developed from the ordering. Numerical results are presented in Section 5.

2. THE DISCRETE WAVELET TRANSFORM

We are interested in discrete wavelet transforms (DWTs) because, loosely speaking, they convert smoothness into sparsity. There are many types of discrete wavelet transform, depending on which kind of continuous wavelet is employed. Some of these are described in Strang and Nguyen [5]. We focus only on the Daubechies wavelets, but our ideas are easily extended to others.

Let $x = (x_1, x_2, \ldots, x_n)^T \in \mathbb{C}^n$. We assume that $n = 2^L$ for some $L \in \mathbb{N}$. The DWT of x is the vector $\tilde{x} = (s^{(L)}, d^{(L)}, d^{(L-1)}, \ldots, d^{(1)})^T$ with

$$s^{(0)} = x,$$

$$s_j^{(k)} = \sum_{l=1}^{4} h_l s_{\langle l+2(j-1)\rangle_{n/2^{k-1}}}^{(k-1)}, \qquad j = 1, 2, \ldots, n/2^k, \qquad (2.1)$$

$$d_j^{(k)} = \sum_{l=1}^{4} g_l s_{\langle l+2(j-1)\rangle_{n/2^{k-1}}}^{(k-1)}, \qquad j = 1, 2, \ldots, n/2^k, \qquad (2.2)$$

where $h_1, \ldots, h_4, g_1, \ldots, g_4$ are the Daubechies 4 wavelet filter coefficients, and $\langle n \rangle_m$ denotes $c + 1$ where c is the remainder of $n - 1$ modulo m.

It is possible to write $\tilde{x} = W^T x$ where W is an orthogonal matrix. Thus $x = W\tilde{x}$, and $\tilde{x}$ represents the vector x in the new basis $w_1, w_2, \ldots, w_n$ given by the columns of W.
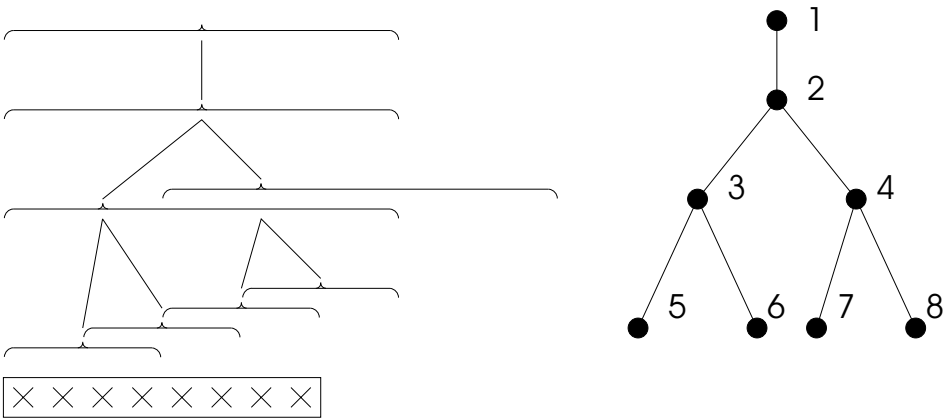
Figure 1   The supports of the wavelet basis vectors in $\mathbb{C}^8$ (left) and the associated tree structure labelled with the natural ordering (right). Wrap around in the supports is illustrated by overhanging brackets.

The basis vectors $w_1, w_2, \ldots, w_n$ split naturally into sets $\{w_1\}$, $\{w_2\}$, $\{w_3, w_4\}$, $\{w_5, \ldots, w_8\}, \ldots, \{w_{n/2+1}, \ldots, w_n\}$. These are the wavelet basis vectors at levels $-1, 0, 1, \ldots, L-1$ respectively.

Define the support of w_i to be the set of indices of the non zero entries of w_i. It can be deduced from (2.1) and (2.2) that the size of the support of the wavelets increases with their level.

The supports of the wavelets when $L = 3$ are illustrated in Figure 1. Natural parent child relationships can be seen, and the resulting tree structure is also illustrated.

Since $\tilde{x} = W^T x$ each entry in $\tilde{x}$ is a linear combination of the entries in x. In fact the entry $\tilde{x}_i$ is a linear combination of those entries of x that are indexed by the support of w_i. That is, the entry $\tilde{x}_i$ depends upon x_j whenever j is in the support of w_i.

The DWT of the matrix A is $\tilde{A} = W^T A W$. Note that $\tilde{A}_{ij} = w_i^T A w_j$ and that when A is a band matrix, $|\tilde{A}_{ij}|$ is large when the supports of w_i and w_j are close or overlap. Note that the support of w_i wholly contains the support of w_j when w_j is a descendant of w_i.

Consider what happens to an area of non smoothness in a vector x under a DWT. Similar behaviour occurs in a matrix. Suppose x_j is a non smooth entry. Then $\tilde{x}_i$ is large whenever j is in the support of w_i. Containment of these supports will be the main idea behind our reordering.

3.   REORDERING

When A has no off diagonal features reordering $\tilde{A}$ with the Per ordering of Chen [3] produces a band structure. Preconditioning is much easier for matrices with this structure. In this section we present a new ordering for when A has off diagonal features.

The tree in Figure 1 approximates the undirected graph of a finger pattern matrix and reordering the finger pattern matrix is equivalent to reordering the nodes in the tree. Most nodes in the tree have two children, which can be labelled the left child and right child. Node 1 is unique in having only one child, and we will label Node 2 the left child of Node 1.

Denote by $\mathcal{I}$ the sequence ordering the nodes by the Per ordering [3]. Under the Per ordering a band structure in A becomes a broader band structure in $\tilde{A}(\mathcal{I}, \mathcal{I})$ because, loosely speaking, the wavelets are ordered by the location of their supports. We use the Matlab notation $\tilde{A}(\mathcal{I}, \mathcal{I})$ to denote the reordering of the rows and columns of $\tilde{A}$ using $\mathcal{I}$.

The Per ordering is not sufficient when off diagonal features are present in A, which is the case this paper is concerned with, unless A is pre-ordered [4]. Clearly the ordering should take account of the location of the off diagonal feature but the Per ordering does not.

We now introduce our new ordering for the case when off diagonal features are present. The new ordering builds in information about the location of the diagonal feature, and we name it singularity-ordered tree traversal (STT). The aim is to order together wavelets whose support contains the location of the feature.

Suppose that the off diagonal feature is located in the kth row or column and let c_w denote the centre of the support of the wavelet w. Now $d_k(w) = |c_w - k|$ defines a metric on the set of wavelets. We say that $w_i \preceq w_j$ whenever w_i and w_j have the same parent and $d_k(w_i) \le d_k(w_j)$. With the relation $\preceq$ reorganise the tree so that if $w_i \preceq w_j$ then w_i is the left child and w_j is the right child.

The nodes in the tree can now be ordered using a Tarry ordering [6]. The rules governing the STT ordering are described in Ordering 1.

Ordering 1 (STT).

1 if w_i is an ascendant of w_j then $w_i \le w_j$,

2 if $w_i \preceq w_j$ then the descendants of $w_i \le$ the descendants of w_j.

To illustrate the two orderings consider how the standard DWT and the Per and STT orderings scatter a non smooth feature in a vector $x \in \mathbb{R}^8$. The key is to group large entries in $\tilde{x}$ close together, and the large entries correspond to those wavelets whose supports contain 1. The Per ordering,

with the large entries underlined, is $(\underline{5}, \underline{3}, 6, \underline{2}, \underline{1}, 7, \underline{4}, \underline{8})$. The large entries are scattered. The STT ordering with $k = 1$ is $(\underline{1}, \underline{2}, \underline{3}, \underline{5}, 6, \underline{4}, \underline{8}, 7)$. The large entries are in two groups. The effect is more pronounced but less easily demonstrated when there are more nodes.

Remark 1. *The STT ordering is easily extended to the case where there are several special features. Replacing k by a set of indices Λ, we define $d_\Lambda(w) = \min_{k \in \Lambda} |c_w - k|$. The ordering follows on substituting d_Λ for d_k in the discussion above.*

4.   PRECONDITIONING STRATEGIES

We now consider how to use the STT ordering to construct a preconditioner. Matrix sparsity patterns that are suited to LU factorisation include $\text{band}_k(\cdot)$, the k band part, and $\text{arrow}_{k,l}(\cdot)$, the bordered band part, that is, the k band part augmented with the bottom l rows and right l columns.

Let $\mathcal{J}$ denote the new STT ordering. The new preconditioned linear system is then

$$1 \quad M^{-1}\tilde{A}(\mathcal{J}, \mathcal{J}) \, \tilde{x}(\mathcal{J}) = \tilde{b}(\mathcal{J}) \text{ where } M = \text{arrow}_{k,l}(\tilde{A}(\mathcal{J}, \mathcal{J})).$$

Similarly let $\mathcal{I}$ be the Per ordering, and $\mathcal{K}$ the preordering of A described by Ford and Chen [4]. Let $\widehat{A}$ be the DWT of $A(\mathcal{K}, \mathcal{K})$, $\widehat{b}$ the DWT of $b(\mathcal{K})$ and $\widehat{x}$ the DWT of $x(\mathcal{K})$. We also consider the following reformulations of (1.1).

$$2 \quad M^{-1}\tilde{A} \, \tilde{x} = \tilde{b} \text{ where } M = \text{band}_k(\tilde{A}),$$

$$3 \quad M^{-1}\tilde{A}(\mathcal{I}, \mathcal{I}) \, \tilde{x}(\mathcal{I}) = \tilde{b}(\mathcal{I}) \text{ where } M = \text{band}_k(\tilde{A}(\mathcal{I}, \mathcal{I})),$$

$$4 \quad M^{-1}\widehat{A}(\mathcal{I}, \mathcal{I}) \, \widehat{x}(\mathcal{I}) = \widehat{b}(\mathcal{I}) \text{ where } M = \text{arrow}_{k,l}(\widehat{A}(\mathcal{I}, \mathcal{I})).$$

The STT preconditioning algorithm is as follows.

Algorithm 1.

 1 Specify location of off diagonal feature.

 2 Construct STT ordering $\mathcal{J}$.

 3 Construct $M = arrow_{k,l}(\tilde{A}(\mathcal{J}, \mathcal{J}))$.

 4 Solve system using GMRES preconditioned with M.

The cost of preconditioning GMRES using these strategies involves the fixed cost of computing an LU factorisation of M, and a cost per iteration of back/forward substitution with L and U. Both costs increase with k for Strategies 1,2,3 and 4, and also with l for Strategies 1 and 4.

Our experience is that the factorisation cost is small compared with the cost of the iterative solver. Back/forward substitution with L and U becomes much more expensive as k and l increase. However each iteration also involves a matrix vector product with $\tilde{A}$ or $\widehat{A}$. This is much more expensive than the back/forward substitution with L and U because these matrices are sparse whilst $\tilde{A}$ and $\widehat{A}$ are dense.

5.   NUMERICAL EXPERIMENTS

In this section we present results of numerical experiments with Algorithm 1 for four test cases. In all cases GMRES was implemented with the zero initial guess vector until the residual norm of the approximate solution was reduced by a factor of 10^6. Experiments were performed with matrices of various sizes. The results presented are for matrices of size 256×256 and are typical of the results obtained.

Calderon Zygmund matrices.   The Calderon Zygmund matrix A given by

$$A = \begin{cases} 3/2, & i = j, \\ 1/|i - j|, & \text{otherwise}, \end{cases}$$

models a Calderon Zygmund operator.

Many operators found in BIEs can be approximated by a Calderon Zygmund operator. Much of the theory for the application of wavelets to such BIEs is based on this fact (see for example Beylkin, Coifman and Rokhlin [1]). Realistic off diagonal features can be produced by augmenting A with a non zero column. This column produces several dense columns in $\tilde{A}$. This is a similar effect to that produced in wavelet discretisations of BIEs by a corner in the boundary. For an example, see the matrix compression strategy of Rathsfeld [2].
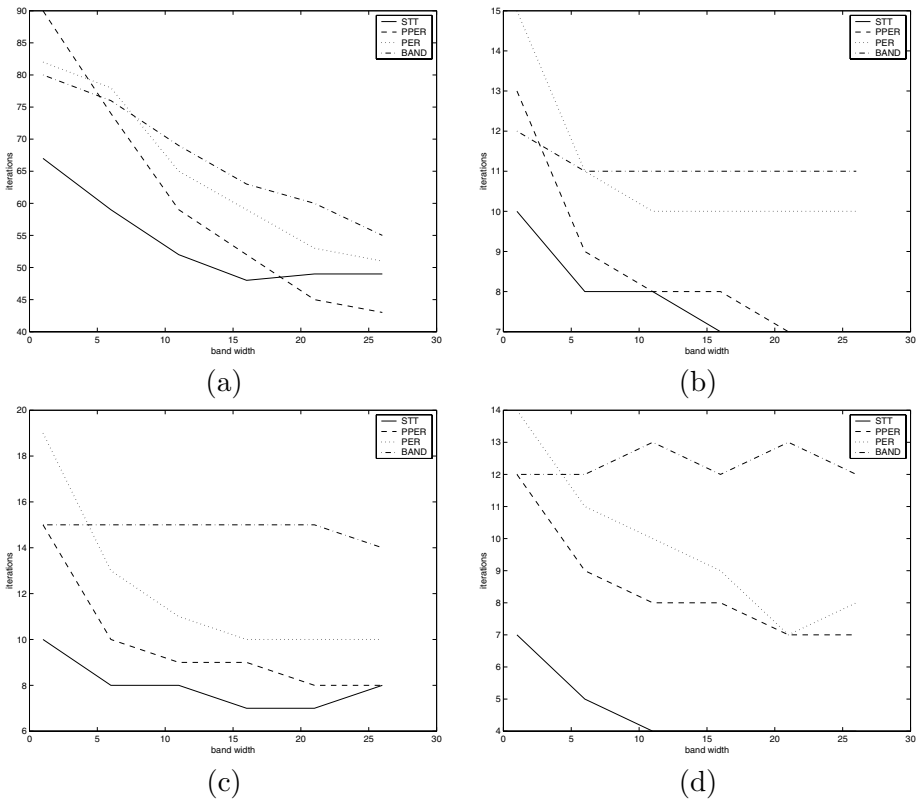
Figure 2   Number of GMRES iterations plotted against bandwidth for (a) the Exterior Helmholtz problem and the Calderon Zygmund problem with (b) no off diagonal features (c) small off diagonal feature (d) large off diagonal feature. Observe that the advantage of STT is greatest for (d) where a large off diagonal feature is present.

The number of GMRES iterations taken for this problem with preconditioning strategies 1–4 from Section 4 are plotted against preconditioner bandwidth in Figure 2 (b) for no off diagonal features, (c) a small off diagonal feature, and (d) a large off diagonal feature. For ease of presentation only the results for border width $l = 45$ are plotted for strategies 3 (STT) and 4 (preordered Per). Decreasing l increases the number of iterations required, but the results shown are representative. We see that GMRES with STT preconditioning gives the fewest iterations. The advantage of STT over the other methods is most significant when the off diagonal feature is large, see Figure 2 (d).

The Exterior Helmholtz Equation. Acoustic scattering from infinitely long bodies is described by the 2D exterior Helmholtz equation

$$\triangle u(p) + k^2 u(p) = 0, \quad p \in \mathbb{R}^2 \setminus D, \tag{5.1}$$

with Neumann boundary condition

$$\frac{\partial u}{\partial n_p}(p) = f(p), \quad p \in \partial D, \tag{5.2}$$

for a peanut shaped domain $D \subseteq \mathbb{R}^2$ with boundary ∂D. The boundary is smooth but produces off diagonal non smooth areas in A [4].

A solution to (5.1) can be obtained by solving the related boundary integral formulation due to Burton and Miller. The Burton and Miller formulation is important because, like (5.1), it has a unique solution for all wavenumbers k [7, 8]. Many BIEs derived from (5.1) do not have this property. From the Burton and Miller formulation we obtain the matrix A by piecewise constant collocation discretisation of the operator

$$-\frac{1}{2}\mathcal{I} + \mathcal{M}_k + i\mathcal{N}_k$$

where $\mathcal{I}$ is the identity, $\mathcal{M}_k$ is the double layer potential

$$\mathcal{M}_k u(p) = \int_{\partial D} \frac{\partial G_k}{\partial n_q}(p, q) u(q) dq,$$

and $\mathcal{N}_k$ is the hypersingular operator

$$\mathcal{N}_k u(p) = \frac{\partial}{\partial n_p}(\mathcal{M}_k u(p)).$$

Here n_q denotes the unit outward normal to ∂D at q, and G_k is the fundamental solution of (5.1). The boundary element solution of (5.1) involves solving a linear system (1.1). See, for example, Atkinson [9] and Kress [10].

The number of GMRES iterations taken for this problem with preconditioning strategies 1–4 from Section 4 are plotted against preconditioner bandwidth in Figure 2 (a). Again, for ease of presentation only the results for border width $l = 45$ are plotted for strategies 3 (STT) and 4 (preordered Per). We see that when the bandwidth of the preconditioner is small GMRES with STT preconditioning gives the fewest iterations. GMRES with preordered Per preconditioning gives the fewest iterations when the bandwidth of the preconditioner is large.

6.   CONCLUSIONS

We have introduced a new preconditioning strategy for dense matrices with off diagonal features. The new strategy is based on application of a

DWT, and a singularity ordered tree traversal reordering of the resulting finger pattern matrix. The ordering places the most significant entries close to the diagonal.

We have compared the new strategy with 3 existing strategies. For low bandwidth preconditioners STT gives faster convergence than the others.

STT requires no preordering of A and so is suitable for generalisation to finger pattern matrices that arise directly from a wavelet discretisation.

References

[1] G. Beylkin, R. Coifman, and V. Rokhlin. Fast wavelet transforms and numerical algorithms I. *Comm. Pure. and Appl. Math.*, 37:141–183, 1991.

[2] A. Rathsfeld. On the stability of piecewise linear wavelet collocation and the solution of the double layer equation over polygonal curves. Technical report, Weierstrass-Institut für Angewandte Analysis und Stochastik, 1997.

[3] K. Chen. Discrete wavelet transforms accelerated sparse preconditioners for dense boundary element systems. *Electronic Transactions on Numerical Analysis*, 8:138–153, 1999.

[4] J. Ford and K. Chen. Wavelet-based preconditioners for dense matrices with non-smooth local features. *BIT*, 41:282–307, 2001.

[5] G. Strang and T. Nguyen. *Wavelets and filter banks*. Wellesley–Cambridge Press, 1996.

[6] Bernard Carré. *Graphs and Networks*. Oxford University Press, 1979.

[7] S. Amini, P. J. Harris, and D. T. Wilton. *Coupled Boundary and Finite Element Methods for the Solution of the Dynamic Fluid-Structure Interaction Problem*. Springer-Verlag, 1992.

[8] D. Colton and R. Kress. *Integral Equation Methods in Scattering Theory*. John Wiley & Sons, 1983.

[9] K. E. Atkinson. *The Numerical Solution of Integral Equations of the Second Kind*. Cambridge University Press, 1997.

[10] R. Kress. *Linear Integral Equations*. Springer-Verlag, 2nd edition, 1999.

Appendix: IUTAM symposium programme

IUTAM Symposium Programme

Asymptotics, Singularities and Homogenisation in Problems of Mechanics

8 - 11 JULY 2002

Monday, 8 July

09:00 - 09:20 Welcome address by *J.W. Bruce*
Pro-Vice-Chancellor of Liverpool University

09:20 - 10:00 *J.R. Willis*
Dynamic perturbation of a propagating crack: implications for crack stability

10:00 - 10:40 *H. Gao*
Extending fracture mechanics concepts to biological nanocomposite materials

10:40 - 11:20 *D. Bigoni, E. Radi, D. Capuani*
Instabilities and near tip crack fields in elastic, incompressible solids

11:40 - 12:20 *A.J.M. Spencer*
Exact singular solutions for an inhomogeneous thick elastic plate

12:20 - 13:00 *Yu.A. Antipov, V.V. Silvestrov*
Method of hyperelliptic surfaces for vector functional-difference equations

13:40 - 14:20 *F.J. Sabina, J. Bravo-Castillero, R. Rodriguez-Ramos, R. Guinovart-Diaz*
Analysis of fibre-reinforced materials via the asymptotic homogenization method

14:20 - 15:00 *M. Gei, E. Radi*
Near-Tip fields of mode III steady-state crack propagation in elastic-plastic strain gradient solids

15:00 - 15:40 *A. Cherkaev*
Damageable structures of waiting links

15:40 - 16:20 *I.S. Jones*
Methods of assessment of thermal striping fatigue damage

16:20 - 17:00 *O. Obrezanova, A.B. Movchan, J.R. Willis*
Dynamic crack stability

17:00 - 17:40 *I. Monetto, W.J. Drugan*
On micromechanics-based non-local modelling of elastic matrices containing non-spherical heterogeneities

18:00 - 19:00 <u>Poster session I</u>:

M.D. Hughes, K. Chen
Fast iterative solution of coupled 3-dimensional fluid-structure
interaction problems
G.T. Piliposian, P.G. Appleby
A simple model of the origin and transport of ^{222}Rn and ^{210}Pb in the
atmosphere
S.B. Platts, N.V. Movchan
Filtering and polarisation of elastic waves by 2D phononic crystals
P.G. Appleby, A. Ploger, L. Camarero
The transport of fallout radionuclides in a high mountain lake
A. Selsil, A.B. Movchan, N.V. Movchan
Asymptotic analysis of heat transfer in a system of channels
connected by thin conducting walls
G.S. Mishuris, K. Kolk, G. Kuhn
3D Singularities and its application to fatigue crack growth simulation
S.E. Mikhailov, J. Orlik
Asymptotic homogenisation in strength and durability
analysis of composites
M.L. Shendeleva
Wave analogies in thermal wave reflection and refraction at an interface
V.N. Biktashev
Envelope equations for modulated non-conservative waves
M. Brun, D. Bigoni, D. Capuani
Boundary elements for non-linear elasticity
M. Perelmuter
Fracture criterion for cracks with bridged zone
C.G. Poulton, S. Guenneau, A. Nicolet, A.B. Movchan
Investigation of the coupling between light and sound waves in periodic
structures with finite element and Rayleigh methods
R. Suckley, V.N. Biktashev
Geometry of the slow manifold in the Hodgkin-Huxley
system of equations
E. Babenkova, J. Kaplunov
The two-term asymptotic expansion in the case of low-frequency
vibrations of elongated elastic rectangle
C.J. Powles
Supersonic leading-edge noise
I.M. Mohamed, J.B. Lawrie
A parametric investigation of the acoustic power in a two dimensional
waveguide with membrane bounded cavity

J.B. Lawrie, R. Kirby
Analysing the performance of a dissipative silencer: a mode-matching
approach

Tuesday, 9 July

09:00 - 09:40 *I.D. Abrahams*
        On the approximate factorization of Wiener-Hopf kernels
        with applications in structural acoustics
09:40 - 10:20 *R.C. McPhedran, N. Nicorovici, C.G. Poulton,*
        L.C. Botten
        Localized states in photonic crystals: A multipole method
10:20 - 11:00 *J.S. Jensen, O. Sigmund*
        Periodic band gap structures as optimal designs
11:00 - 11:40 *F. Zolla, S. Guenneau*
        Artificial ferro-magnetic anisotropy: Homogenization of 3D
        finite photonic crystals
12:00 - 12:40 *S.T. Kolaczkowski*
        Catalytic combustion: making the connection between the
        physical/chemical processes and the mathematical model of
        the reactor
12:40 - 13:20 *V. Karlin*
        Nonmodal instability as the mechanism of acceleration of
        cellular flames
14:00 - 14:40 *C.G. Poulton, A. Spence*
        Numerical methods for the solution of non-linear eigenvalue
        problems arising in electromagnetism
14:40 - 15:20 *M. Hori, T. Ichimura, H. Nakagawa*
        Application of homogenization techniques to two
        earthquake problems
15:20 - 16:00 *A. Fadili, J.R.A. Pearson, P.M.J. Tardy*
        Stochastic homogenisation of fluid flows in heterogeneous
        porous media
16:20 - 17:00 *E. Sanchez-Palencia*
        On a kind of singular perturbations for transmission
        problems
17:00 - 17:40 *S. Sorokin, O.A. Ershova, S.V. Grishina*
        Asymptotic analysis of vibrations and wave propagation in
        sandwich plates with parametric stiffness modulation
17:40 - 18:20 *P.G. Martinsson, G. Rodin*
        Boundary algebraic equations for lattice problems

18:20 - 19:00 *J. Sanchez-Hubert, H. Ranarivelo*
Asymptotics of laminated shells. Membrane - bending coupling and numerical implementation

Wednesday, 10 July

08:20 - 09:00 *L. Berlyand*
Discrete network approximation for effective properties of high contrast random highly packed solid and fluid composites

09:00 - 09:40 *L.E. Fraenkel*
A diffusing vortex circle in a viscous fluid

09:40 - 10:20 *C.J. Chapman*
The asymptotic theory of fluid-structure interaction with heavy fluid loading

10:40 - 11:20 *J. Sivaloganathan*
Singular minimisers, configurational forces and implications for fracture in nonlinear elasticity

11:20 - 12:00 *E. Cherkaev*
Coupled effective properties of a random mixture

12:00 - 12:40 *S. Vladimirov, M.P. Hertzberg and N.F. Cramer*
Dynamics of charged rotators and lattice waves in a plasma environment

12:40 - 13:20 *C.M. Linton*
Embedding formulas and singularities in acoustic scattering

Thursday, 11 July

08:20 - 09:00 *A. Lacey*
Singular behaviour of solutions to some parabolic models of shear-band formation

09:00 - 09:40 *D.F. Parker*
Stretch, flexure and twist in finite elasticity

09:40 - 10:20 *Y. Fu, Y.P. Lin*
A WKB analysis of the buckling of an everted neo-Hookean cylindrical tube

10:40 - 11:20 *H. Ockendon*
Models for the textile industry

11:20 - 12:00 *R. Craster, Yu. V. Obsonov*
Model multi-phase composites

12:00 - 12:40 *W.J. Drugan*
>   Comparisons of exact and gradient-approximate nonlocal
>   constitutive equations from a Hashin-Shtrikman-Willis
>   variational principle for random elastic composite materials

13:20 - 14:00 *A. Nicolet, S. Guenneau, F. Zolla, C. Geuzaine,*
>   *B. Kuhlmey, G. Renversez*
>   Numerical investigation of photonic crystal fibres by means
>   of finite elements and matrix of diffraction methods

14:00 - 14:40 *B. Gralak, A. Tip*
>   Calculation of dispersion relation in absorptive photonic
>   crystals

14:40 - 15:20 *S.E. Mikhailov, I.V. Namestnikova*
>   Non-local approach to fatigue crack initiation and
>   propagation

15:20 - 16:00 *G. Mishuris*
>   Asymptotic behaviour of mode III interface crack for various
>   thin nonhomogeneous anisotropic interfaces

16:20 - 17:00 *A.G. Aslanyan, A.B. Movchan, O. Selsil*
>   Estimates for the first six eigenfrequencies for a massive
>   body supported by thin cylindrical rods

17:00 - 17:40 *J. Kaplunov, V. Kovalev, M. Wilde*
>   Asymptotic analysis of higher order peripheral modes in
>   acoustic wave scattering by elastic cylinders and spheres

17:40 - 18:20 *K. Khusnutdinova*
>   Non-linear dynamics of bi-layer and coupled Klein-Gordon
>   equations

18:20 - 19:20 <u>Poster session II</u>:

D.A. MacDonald
On linear vortex breakdown in a slowly-varying tube impulsively rotated
about its axis with constant angular velocity
P.J. Message
The use of asymptotic series for Lie series generating functions in
deriving multiple Fourier series expressions for orbital perturbations
O. Avila-Pozos, A.B. Movchan, S.V. Sorokin
Propagation of elastic waves along interfaces in layered beams
S. Guenneau, C.G. Poulton, A.B. Movchan
Oblique propagation of electromagnetic and elasic waves for an array of
cylindrical fibres
D.J. Hasanyan, G.T. Piliposyan, A.H. Kamalyan, M.I. Karakhanyan
Some dynamical problems for a functionally inhomogeneous elastic

material, including anti-plane deformations
S. Haq
Models of dislocation in lattice structures
V.V. Zalipaev
Summation of Gaussian beams in 3D problems of radiation and scattering of elastic waves
D. Esparza, N.V. Movchan
Effect of interface bonding on the stress singularity at the vertex of a thin conical inclusion
S.C. Hawkins, K. Chen
Preconditioning for finger pattern matrices arising from wavelet discretisations of boundary integral equations
J.P. Bercial
Asymptotic analysis of the wave equation in a 3D layer containing a dynamic crack
J. Servant, S. Guenneau, A.B. Movchan, C.G. Poulton
Scattering by a single circular cylinder in oblique incidence
I.S. Jones, O. Selsil, A.B. Movchan
A thermoelasticity problem in a domain with an edge crack: Asymptotic analysis

Index

Mechanics

SOLID MECHANICS AND ITS APPLICATIONS

Series Editor: G.M.L. Gladwell

Aims and Scope of the Series

The fundamental questions arising in mechanics are: *Why?*, *How?*, and *How much?* The aim of this series is to provide lucid accounts written by authoritative researchers giving vision and insight in answering these questions on the subject of mechanics as it relates to solids. The scope of the series covers the entire spectrum of solid mechanics. Thus it includes the foundation of mechanics; variational formulations; computational mechanics; statics, kinematics and dynamics of rigid and elastic bodies; vibrations of solids and structures; dynamical systems and chaos; the theories of elasticity, plasticity and viscoelasticity; composite materials; rods, beams, shells and membranes; structural control and stability; soils, rocks and geomechanics; fracture; tribology; experimental mechanics; biomechanics and machine design.

1. R.T. Haftka, Z. Gürdal and M.P. Kamat: *Elements of Structural Optimization*. 2nd rev.ed., 1990
    ISBN 0-7923-0608-2
2. J.J. Kalker: *Three-Dimensional Elastic Bodies in Rolling Contact.* 1990 ISBN 0-7923-0712-7
3. P. Karasudhi: *Foundations of Solid Mechanics.* 1991   ISBN 0-7923-0772-0
4. *Not published*
5. *Not published.*
6. J.F. Doyle: *Static and Dynamic Analysis of Structures.* With an Emphasis on Mechanics and Computer Matrix Methods. 1991   ISBN 0-7923-1124-8; Pb 0-7923-1208-2
7. O.O. Ochoa and J.N. Reddy: *Finite Element Analysis of Composite Laminates.*
    ISBN 0-7923-1125-6
8. M.H. Aliabadi and D.P. Rooke: *Numerical Fracture Mechanics.*   ISBN 0-7923-1175-2
9. J. Angeles and C.S. López-Cajún: *Optimization of Cam Mechanisms.* 1991
    ISBN 0-7923-1355-0
10. D.E. Grierson, A. Franchi and P. Riva (eds.): *Progress in Structural Engineering.* 1991
    ISBN 0-7923-1396-8
11. R.T. Haftka and Z. Gürdal: *Elements of Structural Optimization.* 3rd rev. and exp. ed. 1992
    ISBN 0-7923-1504-9; Pb 0-7923-1505-7
12. J.R. Barber: *Elasticity.* 1992   ISBN 0-7923-1609-6; Pb 0-7923-1610-X
13. H.S. Tzou and G.L. Anderson (eds.): *Intelligent Structural Systems.* 1992
    ISBN 0-7923-1920-6
14. E.E. Gdoutos: *Fracture Mechanics.* An Introduction. 1993   ISBN 0-7923-1932-X
15. J.P. Ward: *Solid Mechanics*. An Introduction. 1992   ISBN 0-7923-1949-4
16. M. Farshad: *Design and Analysis of Shell Structures*. 1992   ISBN 0-7923-1950-8
17. H.S. Tzou and T. Fukuda (eds.): *Precision Sensors, Actuators and Systems*. 1992
    ISBN 0-7923-2015-8
18. J.R. Vinson: *The Behavior of Shells Composed of Isotropic and Composite Materials*. 1993
    ISBN 0-7923-2113-8
19. H.S. Tzou: *Piezoelectric Shells*. Distributed Sensing and Control of Continua. 1993
    ISBN 0-7923-2186-3
20. W. Schiehlen (ed.): *Advanced Multibody System Dynamics*. Simulation and Software Tools. 1993   ISBN 0-7923-2192-8
21. C.-W. Lee: *Vibration Analysis of Rotors.* 1993   ISBN 0-7923-2300-9
22. D.R. Smith: *An Introduction to Continuum Mechanics.* 1993   ISBN 0-7923-2454-4
23. G.M.L. Gladwell: *Inverse Problems in Scattering*. An Introduction. 1993 ISBN 0-7923-2478-1

Mechanics

Mechanics

SOLID MECHANICS AND ITS APPLICATIONS
Series Editor: G.M.L. Gladwell

Mechanics

SOLID MECHANICS AND ITS APPLICATIONS
    Series Editor: G.M.L. Gladwell

69. P. Pedersen and M.P. Bendsøe (eds.): *IUTAM Symposium on Synthesis in Bio Solid Mechanics*. Proceedings of the IUTAM Symposium held in Copenhagen, Denmark. 1999
    ISBN 0-7923-5615-2
70. S.K. Agrawal and B.C. Fabien: *Optimization of Dynamic Systems*. 1999
    ISBN 0-7923-5681-0
71. A. Carpinteri: *Nonlinear Crack Models for Nonmetallic Materials*. 1999
    ISBN 0-7923-5750-7
72. F. Pfeifer (ed.): *IUTAM Symposium on Unilateral Multibody Contacts*. Proceedings of the IUTAM Symposium held in Munich, Germany. 1999   ISBN 0-7923-6030-3
73. E. Lavendelis and M. Zakrzhevsky (eds.): *IUTAM/IFToMM Symposium on Synthesis of Non-linear Dynamical Systems*. Proceedings of the IUTAM/IFToMM Symposium held in Riga, Latvia. 2000   ISBN 0-7923-6106-7
74. J.-P. Merlet: *Parallel Robots*. 2000   ISBN 0-7923-6308-6
75. J.T. Pindera: *Techniques of Tomographic Isodyne Stress Analysis*. 2000 ISBN 0-7923-6388-4
76. G.A. Maugin, R. Drouot and F. Sidoroff (eds.): *Continuum Thermomechanics.* The Art and Science of Modelling Material Behaviour. 2000   ISBN 0-7923-6407-4
77. N. Van Dao and E.J. Kreuzer (eds.): *IUTAM Symposium on Recent Developments in Non-linear Oscillations of Mechanical Systems*. 2000   ISBN 0-7923-6470-8
78. S.D. Akbarov and A.N. Guz: *Mechanics of Curved Composites*. 2000   ISBN 0-7923-6477-5
79. M.B. Rubin: *Cosserat Theories: Shells, Rods and Points*. 2000   ISBN 0-7923-6489-9
80. S. Pellegrino and S.D. Guest (eds.): *IUTAM-IASS Symposium on Deployable Structures: Theory and Applications.* Proceedings of the IUTAM-IASS Symposium held in Cambridge, U.K., 6–9 September 1998. 2000   ISBN 0-7923-6516-X
81. A.D. Rosato and D.L. Blackmore (eds.): *IUTAM Symposium on Segregation in Granular Flows.* Proceedings of the IUTAM Symposium held in Cape May, NJ, U.S.A., June 5–10, 1999. 2000   ISBN 0-7923-6547-X
82. A. Lagarde (ed.): *IUTAM Symposium on Advanced Optical Methods and Applications in Solid Mechanics*. Proceedings of the IUTAM Symposium held in Futuroscope, Poitiers, France, August 31–September 4, 1998. 2000   ISBN 0-7923-6604-2
83. D. Weichert and G. Maier (eds.): *Inelastic Analysis of Structures under Variable Loads*. Theory and Engineering Applications. 2000   ISBN 0-7923-6645-X
84. T.-J. Chuang and J.W. Rudnicki (eds.): *Multiscale Deformation and Fracture in Materials and Structures*. The James R. Rice 60th Anniversary Volume. 2001   ISBN 0-7923-6718-9
85. S. Narayanan and R.N. Iyengar (eds.): *IUTAM Symposium on Nonlinearity and Stochastic Structural Dynamics.* Proceedings of the IUTAM Symposium held in Madras, Chennai, India, 4–8 January 1999   ISBN 0-7923-6733-2
86. S. Murakami and N. Ohno (eds.): *IUTAM Symposium on Creep in Structures*. Proceedings of the IUTAM Symposium held in Nagoya, Japan, 3-7 April 2000. 2001   ISBN 0-7923-6737-5
87. W. Ehlers (ed.): *IUTAM Symposium on Theoretical and Numerical Methods in Continuum Mechanics of Porous Materials.* Proceedings of the IUTAM Symposium held at the University of Stuttgart, Germany, September 5-10, 1999. 2001   ISBN 0-7923-6766-9
88. D. Durban, D. Givoli and J.G. Simmonds (eds.): *Advances in the Mechanis of Plates and Shells The Avinoam Libai Anniversary Volume*. 2001   ISBN 0-7923-6785-5
89. U. Gabbert and H.-S. Tzou (eds.): *IUTAM Symposium on Smart Structures and Structonic Systems*. Proceedings of the IUTAM Symposium held in Magdeburg, Germany, 26–29 September 2000. 2001   ISBN 0-7923-6968-8

Mechanics

SOLID MECHANICS AND ITS APPLICATIONS

Series Editor: G.M.L. Gladwell

Mechanics

SOLID MECHANICS AND ITS APPLICATIONS

Series Editor: G.M.L. Gladwell

Mechanics

FLUID **MECHANICS AND ITS APPLICATIONS**

Series Editor: R. Moreau

Aims and Scope of the Series

The purpose of this series is to focus on subjects in which fluid mechanics plays a fundamental role. As well as the more traditional applications of aeronautics, hydraulics, heat and mass transfer etc., books will be published dealing with topics which are currently in a state of rapid development, such as turbulence, suspensions and multiphase fluids, super and hypersonic flows and numerical modelling techniques. It is a widely held view that it is the interdisciplinary subjects that will receive intense scientific attention, bringing them to the forefront of technological advancement. Fluids have the ability to transport matter and its properties as well as transmit force, therefore fluid mechanics is a subject that is particularly open to cross fertilisation with other sciences and disciplines of engineering. The subject of fluid mechanics will be highly relevant in domains such as chemical, metallurgical, biological and ecological engineering. This series is particularly open to such new multidisciplinary domains.

Mechanics

FLUID MECHANICS AND ITS APPLICATIONS

Series Editor: R. Moreau

Mechanics

FLUID MECHANICS AND ITS APPLICATIONS
Series Editor: R. Moreau

46. U. Frisch (ed.): *Advances in Turbulence VII.* Proceedings of the Seventh European Turbulence Conference, held in Saint-Jean Cap Ferrat, 30 June–3 July 1998. 1998   ISBN 0-7923-5115-0
47. E.F. Toro and J.F. Clarke: *Numerical Methods for Wave Propagation.* Selected Contributions from the Workshop held in Manchester, UK. 1998   ISBN 0-7923-5125-8
48. A. Yoshizawa: *Hydrodynamic and Magnetohydrodynamic Turbulent Flows*. Modelling and Statistical Theory. 1998   ISBN 0-7923-5225-4
49. T.L. Geers (ed.): *IUTAM Symposium on Computational Methods for Unbounded Domains*. 1998   ISBN 0-7923-5266-1
50. Z. Zapryanov and S. Tabakova: *Dynamics of Bubbles, Drops and Rigid Particles*. 1999   ISBN 0-7923-5347-1
51. A. Alemany, Ph. Marty and J.P. Thibault (eds.): *Transfer Phenomena in Magnetohydrodynamic and Electroconducting Flows*. 1999   ISBN 0-7923-5532-6
52. J.N. Sørensen, E.J. Hopfinger and N. Aubry (eds.): *IUTAM Symposium on Simulation and Identification of Organized Structures in Flows*. 1999   ISBN 0-7923-5603-9
53. G.E.A. Meier and P.R. Viswanath (eds.): *IUTAM Symposium on Mechanics of Passive and Active Flow Control*. 1999   ISBN 0-7923-5928-3
54. D. Knight and L. Sakell (eds.): *Recent Advances in DNS and LES*. 1999 ISBN 0-7923-6004-4
55. P. Orlandi: *Fluid Flow Phenomena*. A Numerical Toolkit. 2000   ISBN 0-7923-6095-8
56. M. Stanislas, J. Kompenhans and J. Westerveel (eds.): *Particle Image Velocimetry*. Progress towards Industrial Application. 2000   ISBN 0-7923-6160-1
57. H.-C. Chang (ed.): *IUTAM Symposium on Nonlinear Waves in Multi-Phase Flow*. 2000   ISBN 0-7923-6454-6
58. R.M. Kerr and Y. Kimura (eds.): *IUTAM Symposium on Developments in Geophysical Turbulence* held at the National Center for Atmospheric Research, (Boulder, CO, June 16–19, 1998) 2000   ISBN 0-7923-6673-5
59. T. Kambe, T. Nakano and T. Miyauchi (eds.): *IUTAM Symposium on Geometry and Statistics of Turbulence*. Proceedings of the IUTAM Symposium held at the Shonan International Village Center, Hayama (Kanagawa-ken, Japan November 2–5, 1999). 2001   ISBN 0-7923-6711-1
60. V.V. Aristov: *Direct Methods for Solving the Boltzmann Equation and Study of Nonequilibrium Flows*. 2001   ISBN 0-7923-6831-2
61. P.F. Hodnett (ed.): *IUTAM Symposium on Advances in Mathematical Modelling of Atmosphere and Ocean Dynamics.* Proceedings of the IUTAM Symposium held in Limerick, Ireland, 2–7 July 2000. 2001   ISBN 0-7923-7075-9
62. A.C. King and Y.D. Shikhmurzaev (eds.): *IUTAM Symposium on Free Surface Flows*. Proceedings of the IUTAM Symposium held in Birmingham, United Kingdom, 10–14 July 2000. 2001   ISBN 0-7923-7085-6
63. A. Tsinober: *An Informal Introduction to Turbulence*. 2001   ISBN 1-4020-0110-X; Pb: 1-4020-0166-5
64. R.Kh. Zeytounian: *Asymptotic Modelling of Fluid Flow Phenomena*. 2002   ISBN 1-4020-0432-X
65. R. Friedrich and W. Rodi (eds.): *Advances in LES of Complex Flows.* Prodeedings of the EUROMECH Colloquium 412, held in Munich, Germany, 4-6 October 2000. 2002   ISBN 1-4020-0486-9
66. D. Drikakis and B.J. Geurts (eds.): *Turbulent Flow Computation*. 2002 ISBN 1-4020-0523-7
67. B.O. Enflo and C.M. Hedberg: *Theory of Nonlinear Acoustics in Fluids*. 2002   ISBN 1-4020-0572-5

Mechanics

FLUID **MECHANICS AND ITS APPLICATIONS**

Series Editor: R. Moreau